



HAL
open science

TiO₂ Nanoparticles Coupled To Photosensitizers For Applications In Photocatalysis And Photodynamic Therapy

Zahraa Youssef

► **To cite this version:**

Zahraa Youssef. TiO₂ Nanoparticles Coupled To Photosensitizers For Applications In Photocatalysis And Photodynamic Therapy. Chemical and Process Engineering. Université de Lorraine; Université libanaise, 2017. English. NNT: 2017LORR0231 . tel-01907765

HAL Id: tel-01907765

<https://hal.univ-lorraine.fr/tel-01907765>

Submitted on 17 Jan 2020

HAL is a multi-disciplinary open access archive for the deposit and dissemination of scientific research documents, whether they are published or not. The documents may come from teaching and research institutions in France or abroad, or from public or private research centers.

L'archive ouverte pluridisciplinaire **HAL**, est destinée au dépôt et à la diffusion de documents scientifiques de niveau recherche, publiés ou non, émanant des établissements d'enseignement et de recherche français ou étrangers, des laboratoires publics ou privés.



AVERTISSEMENT

Ce document est le fruit d'un long travail approuvé par le jury de soutenance et mis à disposition de l'ensemble de la communauté universitaire élargie.

Il est soumis à la propriété intellectuelle de l'auteur. Ceci implique une obligation de citation et de référencement lors de l'utilisation de ce document.

D'autre part, toute contrefaçon, plagiat, reproduction illicite encourt une poursuite pénale.

Contact : ddoc-theses-contact@univ-lorraine.fr

LIENS

Code de la Propriété Intellectuelle. articles L 122. 4

Code de la Propriété Intellectuelle. articles L 335.2- L 335.10

http://www.cfcopies.com/V2/leg/leg_droi.php

<http://www.culture.gouv.fr/culture/infos-pratiques/droits/protection.htm>



Thèse En Cotutelle

Une thèse soumise pour l'obtention du titre de Docteur
Spécialité : Génie des Procédés et des Produits

l'Université de Lorraine

Ecole Doctoral RP2E

Science et Ingénierie, Ressources, Procédés, Produits et Environnement

ET

l'Université Libanaise

Ecole Doctorale des Sciences et Technologies (EDST)

Présentée et soutenue publiquement le 19 Décembre 2017 by:

Zahraa YOUSSEF

Nanoparticules de TiO₂ Couplées à Des Photosensibilisateurs Pour Des Applications En Photocatalyse Et En Thérapie Photodynamique

Membre du jury :

Valérie KELLER-SPITZER	<i>DR-CNRS, Université de Strasbourg (ICPEES)</i>	Rapporteur
Jean-Olivier DURAND	<i>DR-CNRS, Université de Montpellier 2 (ICGM)</i>	Rapporteur
Pierre PICHAT	<i>DR-CNRS, Ecole Centrale de Lyon (IFoS, STMS)</i>	Examinateur
Florent POYER	<i>IR-CNRS, Institut Curie, Université Paris-Sud (INSERM)</i>	Examinateur
Thibault ROQUES-CARMES	<i>MC-CNRS, Université de Lorraine (LRGP-ENSIC)</i>	Directeur (France)
Tayssir HAMIEH	<i>Pr-CNRS, Université Libanaise (MCEMA)</i>	Directeur (Lebanon)
Céline FROCHOT	<i>DR-CNRS, Université de Lorraine (LRGP-ENSIC)</i>	Co-Directeur (France)
Joumana TOUFAILY	<i>Pr-CNRS, Université Libanaise (MCEMA)</i>	Co-Directeur (Lebanon)
Valérie JOUAN-HUREAUX	<i>IE-CNRS, Université de Lorraine (CRAN)</i>	Invitée



Cotutelle Thesis

A thesis submitted for obtaining the PhD degree
Speciality: Process and Product Engineering

University of Lorraine
Doctoral School RP2E
Science and Engineering, Resources, Processes, Products and Environment

And

Lebanese University
Doctoral School of Science and Technology (EDST)

Presented and defended on December 19th, 2017 by:

Zahraa YOUSSEF

TiO₂ Nanoparticles Coupled To Photosensitizers For Applications In Photocatalysis And Photodynamic Therapy

Jury members:

Valérie KELLER-SPITZER	<i>DR-CNRS, University of Strasbourg (ICPEES)</i>	Reviewer
Jean-Olivier DURAND	<i>DR-CNRS, University of Montpellier 2 (ICGM)</i>	Reviewer
Pierre PICHAT	<i>DR-CNRS, Central School of Lyon (IFoS, STMS)</i>	Examiner
Florent POYER	<i>IR-CNRS, Curie Institute, University of Paris-Sud (INSERM)</i>	Examiner
Thibault ROQUES-CARMES	<i>MC-CNRS, University of Lorraine (LRGP-ENSIC)</i>	Director (France)
Tayssir HAMIEH	<i>Pr-CNRS, Lebanese University (MCEMA)</i>	Director (Lebanon)
Céline FROCHOT	<i>DR-CNRS, University of Lorraine (LRGP-ENSIC)</i>	Co-Director (France)
Joumana TOUFAILY	<i>Pr-CNRS, Lebanese University (MCEMA)</i>	Co-Director (Lebanon)
Valérie JOUAN-HUREAUX	<i>IE-CNRS, University of Lorraine (CRAN)</i>	Invited

This work was realized in co-supervision between the University of Lorraine (LRGP) and the Lebanese University (MCEMA). This gave me the opportunity to get in contact with people of various nationalities and cultures, which added to my personality and made this experience vivid.

I would like to dedicate my gratitude to Mr. Jean-Olivier DURAND and Mrs. Valérie KELLER-SPITZER for having accepted to be the reviewers of this thesis. I also associate with these thanks the members of the jury, Mr. Pierre PICHAT, Mr. Florent POYER and Mrs. Valérie JOUAN-HUREAUX for being a part of the jury. A big thank you to Mrs. Valérie JOUAN-HUREAUX for all the helping hand you gave me in the biological experiments, I really appreciate, and for Mrs. Muriel BARBERI-HEYOB for the hospitality extended to me during my work in CRAN.

First I wish to thank my advisor, Mr. Thibault ROQUES-CARMES, for all his support, availability and belief in my capabilities. My tender-hearted co-advisor Mrs. Celine Frochot, I can't express my gratitude enough for the knowledge and experience that you share, for the support and the care.

My Lebanese advisor and co-advisor Mr. Tayssir Hamieh and Mrs. Joumana Toufaily, thank you for having faith in my competences and for the opportunity you gave me so that I am standing where I am today.

Philippe, I will always have 'une petite question' for you, thank you for your patience answering all my endless questions and for always stretching out a helping hand for me. Ludo, you're like the 'superman' of the lab, I owe you a thousand 'merci'. Alberto, your arrival to the lab was the most exciting event on my third PhD year; you're more like the 'lucky charm'. Dearest Regis, thank you for all the fatherly support and guidance. For all the great PDT team members, sweetest Amina, Samir, Mathilde, Francis, Ludovine, thank you for making me feel that I belong to a family.

For all my old colleagues, Amirah whom I miss taking to and sharing moments with, Chadlia and Rima thank you for being part of this journey.

My greatest friends who supported me all the way from Lebanon, dearest Fatima, Sukaina, Olfat and sweet cousin Nour, and those who shared with me this 'Nancéienne' experience, Hawraa, Batoul, Enaam, Zeinab, Roukaya, and a bunch of wonderful friends that I was lucky to meet in Nancy, thank you for always being there for me.

I would like to express my infinite acknowledgment to all my LRGP, LCPM and CRAN lab mates for embracing me and for the nice moments we had.

My deepest gratitude, from the bottom of my heart, is dedicated to my family, father, mother, brother and sister. Thank you for always having my back, listening to me and taking care of me when I was down even when you're far from me. I love you more than these words can express.

Last but not least, I would like to thank the 'Association of Specialization and Scientific Orientation' in Lebanon for funding this thesis.

Thank you, Merci, شكرا

ABSTRACT	8
RÉSUMÉ	9
INTRODUCTION	10
Résumé du rapport en français	15

Chapter I: Bibliographic background

1. Titanium dioxide	46
1.1. Definition, origin and crystal forms	46
1.2. Surface chemistry: Chemical groups on the surface of TiO₂	49
1.3. Different applications of TiO₂	51
1.4. Photoreactivity of TiO₂ and the production of reactive oxygen species (ROS)	52
2. Photocatalysis	54
2.1. Water pollution issue	54
2.2. Wastewater treatment methods	55
2.3. Photocatalytic wastewater treatment	56
2.3.1. The use of semiconductors in photocatalysis	57
2.3.2. TiO₂ semiconductor in photocatalysis	57
2.3.3. Limitations of TiO₂ in photocatalysis	58
3. Photodynamic therapy (PDT)	59
3.1. About cancer	59
3.2. Angiogenesis: Growth of tumors	62
3.3. Metastasis	63
3.4. Types of cancer treatments	64
3.4.1. Surgical resection	64
3.4.2. Radiotherapy	64
3.4.3. Chemotherapy	65
3.4.4. Immunotherapy	66
3.5. Anti-cancer photodynamic therapy (PDT)	66
3.5.1. Historical background on PDT	66
3.5.2. Overview on PDT: Definition and principle	68
3.5.3. Mechanism of action	69
3.5.4. Main components in PDT	71
3.5.4.1. Light	71
3.5.4.2. Photosensitizers (PS)	72
3.5.5. The use of nanoparticles in PDT	79
3.5.6. The use of TiO₂ in PDT	82

4.	Strategies to modify TiO ₂ for enhancing its efficiency	84
4.1.	How to extend the absorption of TiO ₂ to visible and limit electron-hole recombination? ...	84
4.1.1.	Semiconductor-semiconductor coupling: Heterojunction	85
4.1.2.	Metal ion doping	86
4.1.3.	Non-metal ion doping	86
4.1.4.	Non-metal codoping.....	87
4.1.5.	Mixed-Phase Titania.....	87
4.1.6.	Sensitization of titania with organic compounds/inorganic metal complexes.....	87
4.2.	How to increase its selectivity in PDT?.....	88

Subchapter I.1: The application of NP-Photosensitizer systems in photocatalysis

1.	Introduction	96
2.	Titania/PS systems.....	98
2.1.	Nature of the PS.....	102
2.2.	Metallo-PS.....	105
2.3.	Photocatalytic mechanisms under UV, solar and visible light	112
2.4.	Bonds between PS and TiO ₂ surface.....	115
2.5.	PS loadings and different geometries	126
3.	PS/ZnO systems.....	129
4.	PS/Fullerene systems.....	134
5.	PS/Graphene systems	140
6.	Conclusions	141

Subchapter I.2: The application of NP-Photosensitizer systems in photodynamic therapy

1.	Background.....	150
2.	Zinc oxide Nanoparticles (ZnO NPs)	153
3.	Titanium dioxide nanoparticles (TiO ₂ NPs)	159
4.	Fullerene	168
5.	Graphene and graphene oxide	180
5.1.	Graphene and single wall carbon nanotubes (SWCNTs)	181
5.2.	Graphene oxide.....	186
6.	Conclusion.....	203

Chapter II: Photocatalytic water treatment by modified titania and silica nanoparticles

1.	Introduction	215
2.	Experimental procedures	216
2.1.	Materials	216
2.2.	Preparation of the photosensitizer-nanoparticles	217
2.2.1.	Activation of the photosensitizers	217
2.2.2.	Synthesis of the core-shell functionalized silica-based nanoparticles	217
2.2.3.	Preparation of APTES modified hybrid NPs.....	220
2.2.4.	Control nanoparticles.....	220
2.2.5.	Silicon dioxide NPs: silane modification and PS grafting.....	220
2.3.	Characterization of the modified NPs	221
2.3.1.	Physico-chemical characterizations	221
2.3.2.	Photophysical measurements.....	221
2.4.	Photocatalytic tests	222
2.4.1.	Solar light	222
2.4.2.	Visible light.....	223
3.	Results and discussion.....	223
3.1.	Characterization of the modified catalysts	223
3.1.1.	Transition electron microscopy (TEM) and high resolution-TEM (HR-TEM)..	223
3.1.2.	X-ray diffraction (XRD).....	225
3.1.3.	Dynamic light scattering (DLS).....	226
3.1.4.	Fourier Transform Infrared Spectroscopy (FTIR).....	227
3.1.5.	Zeta-potential (ζ-potential)	229
3.2.	Photophysical properties	230
3.2.1.	UV-visible absorption spectroscopy.....	230
3.2.2.	Fluorescence and singlet oxygen measurements	231
4.	Photocatalysis activity	233
4.1.	Photocatalysis under solar light	233
4.2.	Photocatalysis under visible light	237
5.	ROS measurements: HO [•] and ¹ O ₂	239
6.	Conclusions	242
	Supporting information	246
	Annexes	257

Chapter III: Photodynamic therapy of glioblastoma by modified titania and silica nanoparticles

1. Introduction	265
2. Materials and methods.....	267
2.1. Materials.....	267
2.2. Preparation of the titania and silica NPs.....	267
2.2.1. Activation of Chlorin e6 PS	268
2.2.2. Preparation of core-shell NPs coupled to Ce6.....	268
2.2.3. Preparation of APTES-modified NPs coupled to Ce6.....	268
2.3. Physico-chemical and photophysical characterizations.....	269
2.4. <i>In vitro</i> studies	269
2.4.1. Cell culture conditions.....	269
2.4.2. Cellular uptake	269
2.4.3. Estimation of Ce6 concentration in each dose of NPs	270
2.4.4. Fluorescence microscopy	270
2.4.5. Photodynamic therapy efficiency	271
2.4.6. Statistical analysis.....	271
2.4.7. ROS measurement.....	271
3. Results and discussion.....	272
3.1. Physico-chemical characterization	272
3.2. Photophysical properties	278
3.3. Cellular uptake of NPs.....	281
3.4. Fluorescence microscopy	282
3.5. Photodynamic therapy	283
3.6. ROS measurement	285
4. Conclusion.....	288
Supporting information	293
Annexes.....	296
 CONCLUSION AND PERSPECTIVES	298
List of abbreviations	301

ABSTRACT

This work addresses the development of TiO₂ and SiO₂ nanoparticles (NPs) modified by light-sensitive organic molecules termed photosensitizers (PS) for application in photocatalytic water treatment and anti-cancer photodynamic therapy (PDT). The NPs' core was either coated with a polysiloxane layer formed by two silane reagents (aminopropyl triethoxysilane (APTES) and tetraethyl orthosilicate (TEOS)) emerging a core-shell nanosystem, or simply modified by APTES alone. In both systems, the APTES mediated the amide covalent linkage between the NPs and the PS. Monocarboxylic tetraphenyl porphyrin (P1-COOH) and chlorin e6 (Ce6) were used as photosensitizers. The photodegradation of two model pollutants, methylene blue and methyl orange, was used to assess the photocatalytic efficiency of the prepared catalysts under simulated solar and pure visible lights. The results reveal that the APTES-modified nanosystems sensitized with P1-COOH and Ce6 exhibit a superior photocatalytic activity than the PS-sensitized core-shell system under both solar and visible light. In particular, TiO₂-APTES-Ce6 NPs possess the best efficiency under solar and visible light irradiation. Similar sensitized nanosystems with a SiO₂ core were also prepared in order to assess the contribution of the support in the photocatalytic degradation process. The reactive oxygen species (ROS) involved in the photodegradation process were also analyzed. Moreover, to investigate the anti-cancerous efficiency of those NPs, *in vitro* tests were conducted on the glioblastoma cell line U87 (brain tumor) at different concentrations of NPs. Cells were illuminated at 652 nm using a diode laser device with a fluence of 10 J/cm². Unlike the core-shell NPs, TiO₂-APTES-Ce6 revealed a good phototoxicity as the cell viability was decreased by 89% after illumination. In addition, the uptake of the best performing TiO₂-APTES-Ce6 NPs into the U87 cells was further investigated. It is remarkable that the TiO₂-APTES-Ce6 nanosystem showed the best photocatalytic and PDT performances among the systems investigated and, also over the core-shell system. This may be attributed to the minimal crowding and masking of the surface of TiO₂ achieved in the case of TiO₂-APTES-Ce6 NPs, thus, an efficient photo-induced excitation of functionalized TiO₂ under visible light became possible. In addition the charge transfer from the Ce6 to the titania catalyst reduces the electronic recombinations. Actually, the end-use properties required for both processes appear similar, *i.e.* photogeneration of ROS (HO• and singlet oxygen (¹O₂)) using visible illumination in order to oxidize cancer cells and/or organic pollutants. In addition, the charge transfer detected in photocatalysis occurs also in PDT. Consequently, we can say that in this work, an example of a product design approach was employed to design efficient functionalized nanoparticle system for two different applications. This study indicates that the recent advances in photocatalytic materials can be easily implemented in PDT and *vice versa*.

RÉSUMÉ

Le travail de thèse concerne le développement de nanoparticules de TiO_2 et SiO_2 modifiées par des molécules photosensibles greffées sur la surface pour des applications en photocatalyse pour le traitement des effluents et thérapie photodynamique (PDT) pour le traitement de certains cancers. Deux modes de modifications ont été envisagés. Le premier repose sur le recouvrement des nanoparticules par une couche d'organosilane composée de (3-aminopropyl)triéthoxysilane (APTES) et d'orthosilicate de tétraéthyle (TEOS). La deuxième concerne le greffage direct d'APTES sur la surface. Pour ces deux systèmes le groupement APTES permet de relier le photosensibilisateur (PS) aux nanoparticules. Deux types de PSs ont été étudiés, à savoir la porphyrine tétraphényl monocarboxylique (P1-COOH) et la chlorine e6 (Ce6). Ces nanosystèmes hybrides ont permis d'étendre l'activité photocatalytique de ces systèmes vers la lumière visible et solaire. Ils sont très efficaces pour dégradés des polluants modèles tels que l'orange de méthyle et le bleu de méthylène. Les propriétés photocatalytiques dépendent fortement du mode de greffage (cœur/coquille vs simple greffage), de la nature du PS, du type de lumière utilisée, et de la nature des particules. Les meilleures performances sont obtenues avec des nanoparticules de dioxyde de titane modifiée par de l'APTES en présence de Ce6 sous lumière visible. Elles proviennent du faible taux de recouvrement de la surface par la couche de silane et du transfert de charge entre le PS photoactivé et le matériau semi-conducteur. En parallèle, nous avons étudié l'efficacité de ces nanosystèmes hybrides pour détruire des cellules cancéreuses par le procédé de thérapie photodynamique. Pour ce faire, les tests ont été *in vitro* sur des cellules de glioblastome U87 (tumeur cérébrale) en présence de quantités croissantes de nanoparticules. Les cellules ont été irradiées à une longueur d'onde de 652 nm *via* une diode laser (10 J/cm^2). Pour les particules de dioxyde de titane et de silice, la meilleure efficacité en PDT a été obtenue lorsque le PS Ce6 est attaché par simple greffage ($\text{TiO}_2\text{-APTES-Ce6}$ et $\text{SiO}_2\text{-APTES-Ce6}$). En présence de $\text{TiO}_2\text{-APTES-Ce6}$ ($200 \mu\text{g/mL}$), la viabilité cellulaire diminue de 89% sous irradiation. Il est remarquable de constater que le système $\text{TiO}_2\text{-APTES-Ce6}$ présente les meilleures performances parmi tous les systèmes étudiés dans deux types d'applications différentes. Les propriétés d'usage recherchées dans ces deux procédés apparaissent similaires, à savoir la photogénération d'espèces réactives de l'oxygène (ROS : radicaux HO^\bullet et oxygène singulet) sous lumière visible afin d'oxyder soit des cellules cancéreuses soit des polluants organiques. Le système $\text{TiO}_2\text{-APTES-Ce6}$ permet de produire à la fois des radicaux HO^\bullet et de l'oxygène singulet.

INTRODUCTION

Since the last century, nanotechnology became an interesting and challenging matter of research. Nanotechnology defines the use of matter that falls at the nanoscale to manufacture structures and materials of various types and new functionalities. Since the Nobel laureate Richard P. Feynman presented ‘nanotechnology’ in his famous lecture “There’s Plenty of Room at the Bottom” in 1959, the domain of nanotechnology has been witnessing revolutionary and innovative advancements. Nanotechnology as research domain investigates the electrical, optical, magnetic and structural activities of materials at the molecular as well as the submolecular level. On this basis, a potential economic and technical revolution at the level of the medical and biotechnological devices and processes can be mediated through nanotechnology.

As a definition, nanoparticles (NPs) represent a wide array of materials including particulate substances that possess a size below 100 nm. The size of the NPs can influence their physicochemical properties. They are categorized into various classes based on their size, shape and different properties. Those classes encompass carbon-based, metal, ceramic, polymeric, lipid-based and semiconductor NPs. The unique properties of NPs such as their antibacterial activity, high resistance to oxidation and high thermal conductivity rendered it suitable for a wide range of commercial, industrial and domestic applications. NPs have been employed in energy harvesting and storage, mechanical industry, cosmetics, clothing, optical and electronic devices, sensors, bactericidal applications, imaging, biological labeling, drugs and medication including the treatment of certain cancers and in the catalytic domain [1, 2].

Nanotechnology have been employed for environmental applications aiming to the development of environment-friendly products, sensors for environmental stages and the removal of harmful and toxic substances from contaminated materials and waters. In the domain of drugs and medications, various semiconductor and metallic NPs showed a great potential for the diagnosis and treatment of cancer. This potential is based on their properties of absorption, enhanced light scattering associated with a surface-plasmon resonance (SPR) and proper antibacterial efficiencies. TiO_2 , ZnO and BiVO_4 are some examples of the NPs that have been employed for this goal [2].

Semiconductor nanomaterials are nanosized particles of wide band-gaps and light-emitting capability. They hold properties between metals and non-metals. The wide band-gap of the semiconductor NPs is tunable allowing modifications in the materials properties. On this account, semiconductor NPs became extensively used in photocatalysis, cellular imaging, solar energy conversion, water splitting, optics, electronics, etc. [1, 2].

Titanium dioxide (TiO_2) is a wide band-gap semiconductor that has been involved in a vast array of applications including photocatalysis, photovoltaics, cosmetics, new material manufacture, anti-bacterial, etc. Upon UV-light illumination, TiO_2 NPs dispersed in aquatic solutions are capable of producing reactive oxygen species (ROS) such as hydroxyl radicals (HO^\bullet), superoxide anions ($\text{O}_2^{\bullet-}$), hydrogen peroxide (H_2O_2), etc. The size and morphology of the NPs influence the quantity of generated ROS [3].

In photocatalysis, semiconductor NPs, especially TiO_2 , have been extensively used. Photocatalysis is referred to as the process of acceleration of a chemical reaction in the presence of photocatalyst substances capable of absorbing light at appropriate wavelengths matching to their band structure. In 1972, Fujishima and Honda demonstrated the efficiency of TiO_2 in the photo-electrochemical water splitting; since then, TiO_2 paved its way towards extensive use in environmental purification applications [4].

Photodynamic therapy (PDT) is a minimally-invasive process used for the destruction of cancer cells using a photoactivable photosensitizer (PS) molecule, light and available molecular oxygen. Most of the photosensitizers (PSs) used in PDT are hydrophobic thus inducing some selectivity and aggregation issues that may jeopardize their efficiency. In contrast, a facilitated delivery through the blood and an enhanced uptake by the cancer cells due to the Enhanced Permeability and Retention (EPR) effect can be achieved by the use of NPs in PDT applications [5, 6]. Several *in vitro* researches applied on TiO_2 NPs have proven that the generated ROS produced by light-activated TiO_2 can trigger the oxidative destruction of different molecules. Relying on this, TiO_2 NPs were regarded as potential candidates as PSs in anti-cancer photodynamic therapy (PDT). Upon light irradiation, neoplastic cells containing TiO_2 NPs can be damaged under the effect of produced ROS [3].

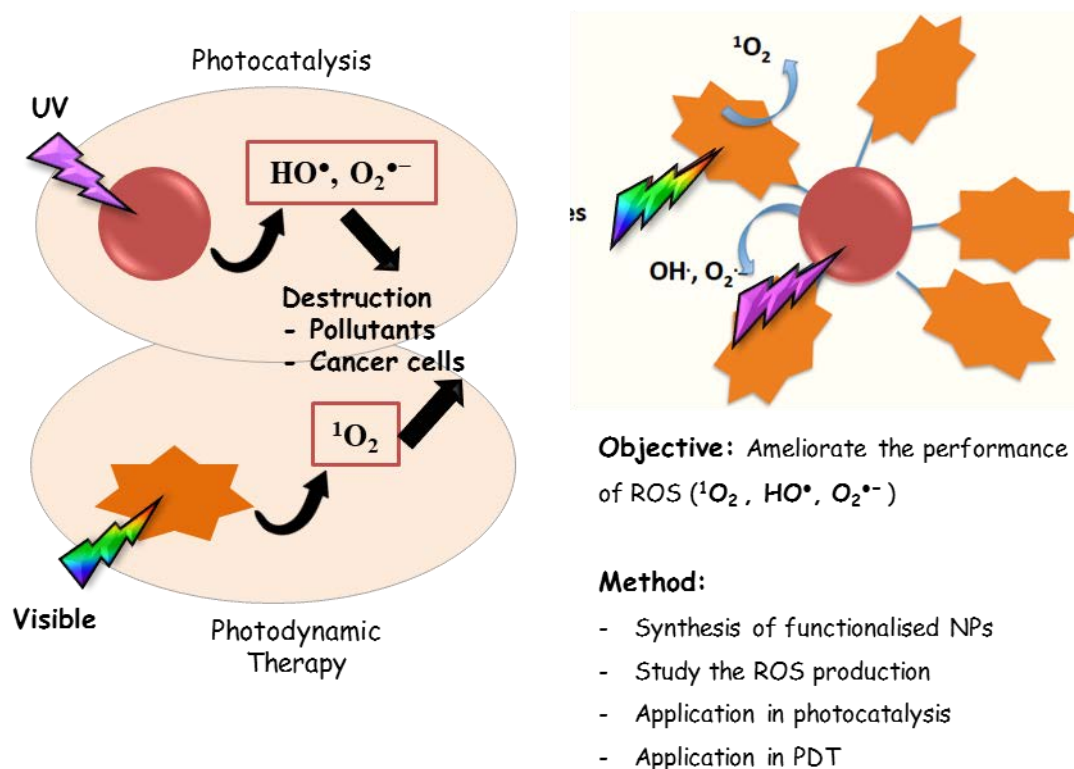
Despite the various advantageous properties of TiO_2 and its efficient use in photocatalytic treatment of polluted water and in the eradication of cancer cells by PDT, the application with titania encounters some limiting disadvantages. The most affecting disadvantage is the wide band-gap of TiO_2 NPs that restricts its light-activation to a wavelength (~ 387 nm) falling in the UV region of light. Upon irradiation, TiO_2 produces charge carriers, holes and electrons, which induce redox reactions leading to the generation of ROS. However, the recombination of those charge carriers suppresses the ROS production which is considered another limitation of TiO_2 [4].

In the domain of photocatalysis, for the sake of the commercialization and practical industrialization of NPs, research efforts are driven towards the applications consuming the solar and visible light [4]. As for PDT, in contrast to visible light, UV irradiation is incapable of deep penetration into the human tissues which hinders the use of UV-activated TiO_2 for the treatment of deeply localized cancers. TiO_2 also lacks selectivity to cancer cells [7].

For this reason, various strategies have been applied to modify the light-activation properties of TiO_2 aiming to extend the photoresponse of those NPs towards the visible region of light and decrease the electron-hole recombination. Among those strategies, dye-sensitization appears to be attractive. Dye-sensitization is the linking of a visible-light-activated organic porphyrin- or chlorin-based PS onto TiO_2 either covalently or *via* simple adsorption. This strategy enables an extension of the absorption profile of the hybrid TiO_2 NPs towards visible light and reduces the recombination of the charge carriers. Visible-light photocatalysis becomes possible due to surface sensitization of titania [8]. In terms of PDT, since the EPR effect allows better internalization of NPs into the malignant cells, the conjugation of the PS to TiO_2 permits the use of lower amounts of PS and restricts the limitations induced by the use of the PS alone [5, 6].

In this study (**scheme 1**), the surface of the “de facto standard” TiO_2 photocatalyst, Degussa P25, was modified *via* silane reagents to assure a covalent linkage of the PS to the NPs. Two strategies were conducted for this modification. In the first strategy, two silane reagents, 3-aminopropyl triethoxysilane (APTES) and tetraethyl orthosilicate (TEOS), polymerize and condense growing a polysiloxane shell around the TiO_2 core. Hydrophilic polyethylene glycol (PEG-250) was grafted onto the core-shell NPs. The second strategy was much simpler where only APTES modified the surface of the TiO_2 NPs. In both nanosystems, APTES assists as a bridging molecule facilitating the covalent conjugation of Monocarboxylic tetraphenyl porphyrin (P1-COOH) or chlorin e6 (Ce6) to the surface of the hybrid NPs. Amorphous silica NPs were modified and hybridized in a similar procedure as crystalline TiO_2 to elucidate the contribution and the effect of the support. The hybridized NPs were used in two distinct applications. The first application was the degradation of model organic pollutants that are methylene blue (MB) and methyl orange (MO) from water under solar and pure visible light. The second application was the *in vitro* PDT of glioblastoma under visible light irradiation (652 nm).

Project: The elaboration and study of TiO₂ nanoparticles coupled to Photosensitizers



Scheme 1: Schematic representation of the formation of reactive oxygen species (ROS) from TiO₂ coupled to a photosensitizer (PS).

The following report is constituted of three main chapters that assure a detailed description of the work conducted:

Chapter I: Bibliographic background on TiO₂ NPs, photocatalysis and PDT.

Subchapter I.1: A detailed review on the application of PS-conjugated TiO₂ and other materials, ZnO, fullerene and graphene, in photocatalysis (*To be submitted in Dyes and Pigments Journal*)

Subchapter I.2: A detailed review on the application of PS-conjugated TiO₂ and other materials, ZnO, fullerene and graphene, in PDT (*Published in Cancer Nanotechnology*).

Chapter II: The photocatalytic degradation of model organic pollutants from water mediated by core-shell and APTES-modified TiO₂-PS and SiO₂-PS NPs under solar and visible lights (*Submitted in Journal of Photochemistry and Photobiology A: Chemistry*).

Chapter III: The *in vitro* study of the photodynamic efficiency of TiO₂-PS and SiO₂-PS NPs towards the eradication of glioblastoma U87 cells under visible light (*To be submitted to Journal of Photochemistry and Photobiology B: Biology*).

References for the introduction

- [1] I. Khan, K. Saeed, and I. Khan, "Nanoparticles: Properties, applications and toxicities," *Arab. J. Chem.*, May 2017.
- [2] H. Saba, 'A review on nanoparticles: their synthesis and types.' *Research Journal of Recent Sciences* , ISSN 2277 (2015): 2502."
- [3] B. Geiseler, M. Miljevic, P. Müller, and L. Fruk, "Phototriggered Production of Reactive Oxygen Species by TiO₂ Nanospheres and Rods," *J. Nanomater.*, vol. 2012, pp. 1–9, 2012.
- [4] V. Etacheri, C. Di Valentin, J. Schneider, D. Bahnemann, and S. C. Pillai, "Visible-light activation of TiO₂ photocatalysts: Advances in theory and experiments," *J. Photochem. Photobiol. C Photochem. Rev.*, vol. 25, pp. 1–29, Dec. 2015.
- [5] D. K. Chatterjee, L. S. Fong, and Y. Zhang, "Nanoparticles in photodynamic therapy: An emerging paradigm," *Adv. Drug Deliv. Rev.*, vol. 60, no. 15, pp. 1627–1637, Dec. 2008.
- [6] N. Mehraban and H. Freeman, "Developments in PDT Sensitizers for Increased Selectivity and Singlet Oxygen Production," *Materials*, vol. 8, no. 7, pp. 4421–4456, Jul. 2015.
- [7] A. Master, M. Livingston, and A. Sen Gupta, "Photodynamic nanomedicine in the treatment of solid tumors: Perspectives and challenges," *J. Controlled Release*, vol. 168, no. 1, pp. 88–102, May 2013.
- [8] S. G. Kumar and L. G. Devi, "Review on Modified TiO₂ Photocatalysis under UV/Visible Light: Selected Results and Related Mechanisms on Interfacial Charge Carrier Transfer Dynamics," *J. Phys. Chem. A*, vol. 115, no. 46, pp. 13211–13241, Nov. 2011.

Résumé Détaillé Du Rapport En Français

Photocatalyse

La protection de l'environnement, et particulièrement de l'eau, demeure un enjeu fondamental, en raison de sa détérioration à cause des activités industrielles et anthropiques. A l'heure actuelle la contamination se répercute également sur l'eau douce qui se trouve détériorée par divers polluants provenant de diverses sources. Celles-ci peuvent être industrielles, provenir de l'agriculture intensive, du transport, des déchets domestiques, des produits de santé, des déchets urbains, de la pollution aérienne soluble dans l'eau [1-4]. Les procédés de traitement dans les stations d'épuration ne permettent pas d'éliminer toute la pollution présente dans les effluents et des traces de polluants demeurent présentes dans les eaux en sortie des stations. Les procédés photochimiques d'oxydation avancée apparaissent comme une bonne alternative en pleine expansion pour la décontamination de l'eau [5-7]. Elle présente une complémentarité intéressante aux techniques habituelles de floculation, précipitation, adsorption sur charbon activé ou osmose inverse en tant que traitements tertiaires de finition. En outre, le rejet de ces polluants pose également des problèmes pour le fonctionnement de l'écosystème. Il devient donc nécessaire de développer des technologies innovantes et de nouveaux procédés de façon à éliminer, à un coût acceptable, les traces de mélanges de nano et micropolluants les plus indésirables tout en préservant l'écosystème.

Parmi ces techniques d'oxydation avancée, la photocatalyse hétérogène présente l'avantage d'oxyder de très nombreux contaminants de l'eau tels que les engrais, les pesticides, les colorants, les molécules pharmaceutiques jusqu'à leur destruction complète (minéralisation) [8-10]. La méthode repose sur l'action simultanée de photons et d'une couche de catalyseur (**Fig. 1**). Le catalyseur le plus utilisé est le dioxyde de titane (TiO_2) pour des raisons d'efficacité, stabilité et de faible coût de production [11,12]. L'activité photocatalytique de TiO_2 est basée sur la génération de paires électron-trou à la surface du matériau sous rayonnement ultraviolet. La forme anatase présentant une bande interdite (gap) de 3,23 eV (384 nm) qui correspond au domaine ultraviolet est photoactive. Un photon d'énergie supérieure ou égale au gap pourra être absorbé par le TiO_2 . Les électrons de la bande de valence sont alors excités et promus dans la bande de conduction. Il en résulte la création de porteurs de charges sous forme de photoélectrons e^- et de trous électroniques h^+ . Ces paires électron-trou peuvent alors migrer vers la surface du matériau pour former des sites oxydants et réducteurs. Des réactions d'oxydoréduction peuvent avoir lieu avec des groupements accepteurs ou donneurs adsorbés en surface. Le fort pouvoir oxydant des trous h^+ peut entraîner la formation de radicaux hydroxyles $\cdot\text{OH}$ ou $\text{R}\cdot$ très réactifs, *via* l'oxydation de l'eau, des groupements OH

superficiels ou encore de produits organiques R adsorbés à la surface. Ces radicaux sont des oxydants très puissants qui peuvent à leur tour réagir avec les polluants adsorbés à la surface du matériau. Les méthodes de traitement par voie photochimique sont de plus en plus utilisées pour la dépollution de l'eau lorsque ces substances sont présentes à l'état de traces.

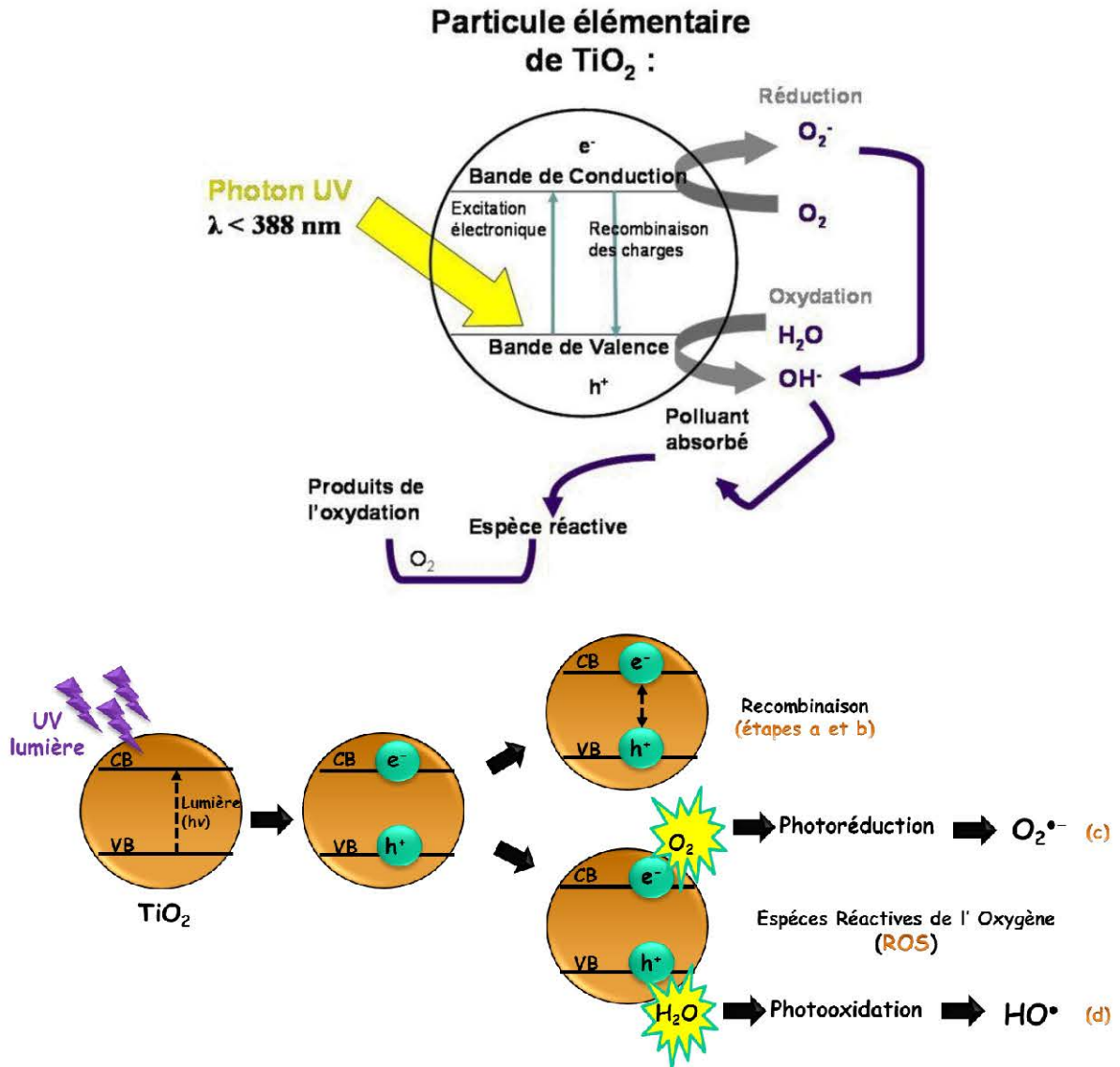


Fig. 1 : Schéma général de la photocatalyse avec TiO₂.

Le TiO_2 , est largement utilisé de nos jours dans les différents procédés industriels comme le composé commun du titane. Outre l'oxyde de titane (IV) et l'oxyde de titane, TiO_2 est également appelé E171 dans les colorants alimentaires et le blanc de titane ou le pigment blanc 6 dans les peintures de construction [13-15]. C'est un matériau blanc inodore. Le TiO_2 est insoluble dans l'eau et forme généralement des particules. De plus, la forme en poudre de TiO_2 possède un caractère hydrophile [15, 16]. Le titane possède de nombreuses qualités et des propriétés optiques, électroniques et physiochimiques particulières qui le rendent utile pour une large gamme d'application. Le TiO_2 est de faible coût, disponible, biologiquement et chimiquement inerte, stable et résistant à la corrosion. C'est un matériau de faible toxicité, de bonne biocompatibilité et de fort pouvoir oxydant. En outre, il est efficace en tant qu'agent antibactérien, dans la purification de l'environnement en raison de son activité photocatalytique élevée et de la protection UV [14-18].

Des études récentes ont montré qu'il existe une relation entre la stabilité des phases de TiO_2 et la taille des nanoparticules (NPs). Pour les NPs possédant une taille inférieure à 11 nm, la forme anatase semble être la plus stable. Cependant, avec des NPs dont la taille varie entre 11 et 35 nm, la phase de brookite semble être la plus stable. Pour les NPs d'une taille supérieure à 35 nm, le rutile est la phase la plus stable. Chacune de ces phases possède des caractéristiques physiques et chimiques distinctes, y compris une densité, une chimie et une structure de surface différente, une énergie de bande interdite, etc. Cependant, l'anatase et le rutile révèlent les différences les plus faibles et des caractéristiques physiques les plus similaires. En 1942, Earle a décrit les phases anatase et rutile du TiO_2 comme des semi-conducteurs de type n [19]. Les deux phases sont caractérisées par une large bande interdite. L'énergie de la bande interdite est comprise entre 3,2 eV pour l'anatase et 3,02 eV pour le rutile. Ces larges bandes de phases cristallographiques anatase et rutile permettent la réflexion de la lumière visible. Pourtant, l'anatase est capable de réfléchir une onde électromagnétique plus large constituant de la lumière ultraviolette aux UV [14]. Malgré le fait que les formes anatase et rutile soient catalytiquement photoactives, elles agissent différemment. Bien que les raisons exactes à l'origine de cette activité différente n'aient pas encore été complètement élucidées, il est possible qu'elles soient dûes à une structure cristalline différente. En terme de photoactivité, l'anatase est meilleur que le rutile. Plus de groupes hydroxyles occupent la surface de l'anatase TiO_2 par rapport à celle du rutile. Il est bien connu que la disponibilité des groupes OH induit une activité photocatalytique plus efficace [14, 20]. Il est également intéressant de discuter du cas particulier du catalyseur au TiO_2 connu sous le nom de Degussa P25. La poudre est constituée de phases cristallines anatase et rutile existant séparément dans ce composite. Bien que la composition

de phase précise ne soit pas encore définie, le rapport de l'anatase au rutile dans P25 serait compris entre 70:30 et 80:20 [21, 22]. Ce type de TiO_2 possède une surface spécifique relativement faible d'environ $49 \text{ m}^2 \text{ g}^{-1}$ [22]. P25 a été largement utilisé grâce à sa grande activité photocatalytique. En fait, il a été mentionné qu'il n'est pas facile de trouver un photocatalyseur de plus grande photoactivité par rapport à P25. Sur la base de ces informations, P25 est décrit comme le «photocatalyseur de titane standard *de facto*» et a été couramment utilisé comme «référence» pour les photocatalyseurs. Il a également été démontré que, dans plusieurs réactions, cet oxyde de titane en phase mixte présentait une photoactivité plus élevée que l'anatase pure. Plus de mille articles ont été publiés sur les réactions photocatalytiques impliquant Degussa P25 depuis 1990 [21-23].

Thérapie Photodynamique

Le cancer est la principale source de mortalité dans les pays à revenu faible, moyen et élevé (PRMF, CIH). Cette mortalité devrait augmenter au cours des prochaines décennies du fait des transitions démographiques et épidémiologiques mondiales en cours, telles que définies par l'OMS en 2011. Une étude mondiale sur la propagation du cancer réalisée en 2012 a estimé environ 14,1 millions de nouveaux cas de cancer et 8,2 millions de décès par cancer. Les cancers du poumon (1,82 million), du sein (1,67 million) et colorectal (1,36 million) étaient les types de cancer les plus souvent diagnostiqués. Cependant, les cancers du poumon (1,6 million), du foie (745000) et de l'estomac (723000) contribuent aux taux de mortalité par cancer les plus élevés. Dans les 50 pays sélectionnés dans cette enquête, des taux d'incidence et de mortalité plus élevés ont été observés chez les hommes que chez les femmes [24, 25].

La chirurgie reste le traitement de référence. Elle est suivie de près par la radiothérapie et la chimiothérapie. Un des inconvénients de ces techniques est leur non sélectivité, qui engendre la destruction des cellules malades mais également de certaines cellules saines.

La thérapie photodynamique est une méthode de traitement de certains cancers. Elle nécessite la présence simultanée de trois éléments : une molécule, de l'oxygène et de la lumière (**Fig. 2**). Elle consiste à exciter une molécule photo-activable, appelée photosensibilisateur (PS) qui va, en présence de lumière, transférer son énergie à l'oxygène environnant pour former des espèces chimiques très toxiques, principalement de l'oxygène singulet ($^1\text{O}_2$), responsable de la mort cellulaire

(réaction de type II). Les réactions de type I quant à elles produisent des espèces réactives de l'oxygène tels que des radicaux hydroxyles $\cdot\text{OH}$ ou $\text{R}\cdot$ par un transfert de protons ou d'électrons de l'état triplet du PS au milieu environnant. Pris séparément, chacun des 3 agents photosensibilisateur, lumière et oxygène ne sont pas nocifs.

Après injection du photosensibilisateur ou administration par voie topique pour les maladies de la peau, un intervalle drogue-lumière est respecté et permet de cibler soit la vascularisation (temps court), soit les cellules tumorales (temps long). La lumière est ensuite envoyée sur la zone à traiter, engendrant la formation de ROS responsables de la mort cellulaire. La **Fig. 2** résume le principe de la PDT.

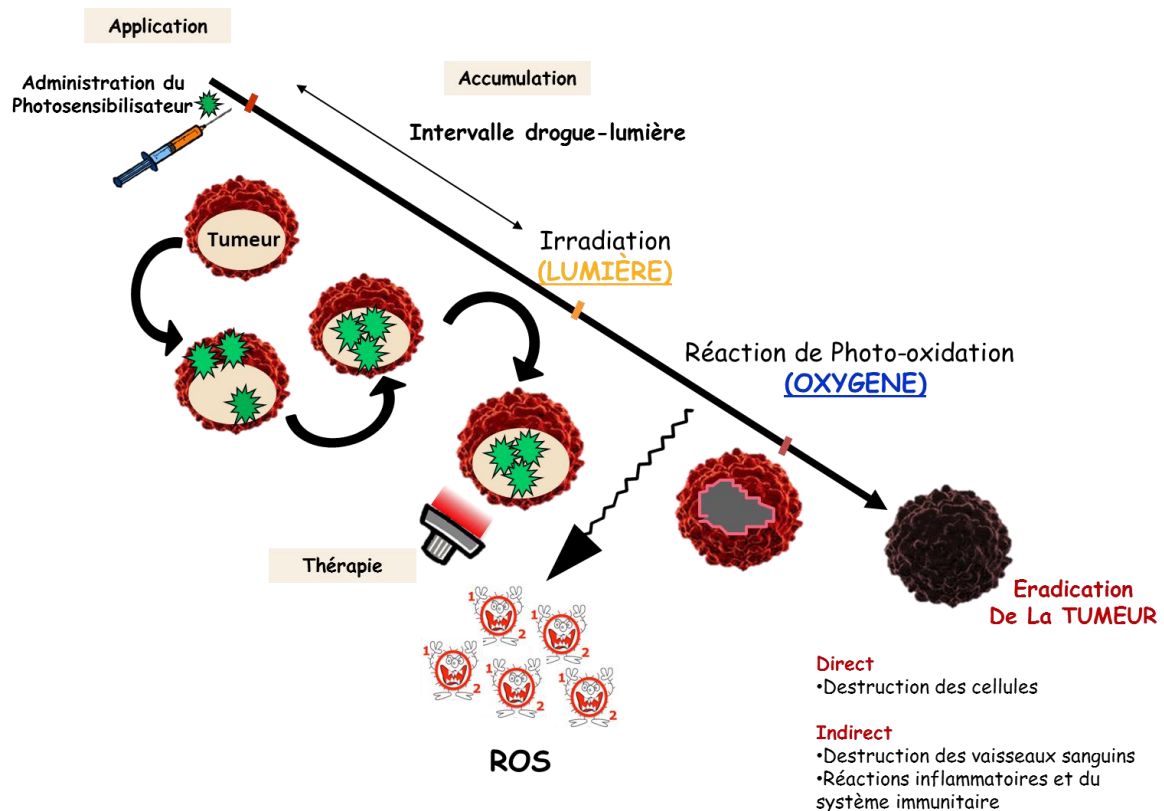


Fig. 2 : Protocole PDT.

La PDT a connu son heure de gloire médiatique dans les années 1980 lorsque plusieurs équipes cliniques, principalement aux Etats-Unis, au Canada et au Japon ont montré son efficacité dans la destruction de certaines tumeurs, généralement inopérables.

En ophtalmologie, la PDT avec la *Visudyne*[®] a connu un engouement important dans le traitement des patients atteints de la forme néovasculaire de la *dégénérescence maculaire* liée à l'âge [26].

En urologie, la société française Steba-Biotech a investi des sommes considérables pour développer un nouveau PS, le Tookad[®] (les résultats de la phase 3 seront disponibles cette année, et le traitement est autorisé depuis le 12 novembre 2015 au Mexique) pour le traitement du cancer de la prostate [27]. En gastroentérologie, la PDT bénéficie d'un regain d'intérêt en raison du développement des lasers à diode [28].

En gynécologie, l'intérêt de la PDT a pu être montré dans le traitement de lésions dysplasiques cervicales de bas et de haut grade après application cervicale d'une solution d'acide 5-aminolévulinique (5 ALA). Notre équipe a déposé récemment un brevet pour le traitement des métastases ovariennes par PDT [29].

En neurochirurgie, plusieurs études rapportent des résultats encourageant en clinique humaine en utilisant la PDT pour traiter des tumeurs cérébrales non opérables en première ligne ou bien en récurrence [30]. Des survies supérieures à 2 ans après traitement par PDT ont été rapportées. Depuis janvier 2017, un protocole clinique est mis en place à Lille, utilisant la PDT comme traitement de première intention. C'est une première mondiale.

En pneumologie, la PDT présente un réel intérêt dans le traitement du mésothéliome (cancer du poumon dû à l'amiante) [31]. Un protocole clinique a été mis en place en 2016 à Lille.

En dermatologie, la PDT devient progressivement le traitement de référence pour les kératoses actiniques (lésions pré-cancéreuses de la peau), les carcinomes baso-cellulaires superficiels et la maladie de Bowen (cancer intra-épidermique, *in situ*) [32].

Même si la thérapie photodynamique est appliquée cliniquement en France et dans le monde entier, peu de nouveaux PS sont mis sur le marché. L'un des verrous de la thérapie photodynamique est la formulation des photosensibilisateurs, souvent hydrophobes. Les nanoparticules de TiO₂ sont à

l'étude et une vingtaine de publications relatent du sujet, le premier papier ayant été publié en 1991 par l'équipe de Fujishima [33].

Verrou

Le principal verrou de la photocatalyse concerne les propriétés photochimiques des photocatalyseurs. Il s'agit donc de travailler sur cet aspect afin : (i) d'augmenter le rendement quantique du processus de photocatalyse et de (ii) développer des photocatalyseurs actifs dans le visible. En effet, la recombinaison des paires électron-trou est le facteur limitant de l'efficacité de la photocatalyse puisque la probabilité de recombinaison est de 99,9% (i). Cette recombinaison limite la production des radicaux hydroxyles impliqués dans les réactions de dégradation. Par conséquent, l'idée est de modifier la surface de TiO_2 par greffage d'une molécule photo-sensible de type porphyrine (photo-actif). L'idée est d'augmenter le rendement quantique du processus de photocatalyse. En effet, avec ce système, la conversion photon-électron et la séparation électron-trou est effectuée à la fois par les molécules fluorescentes et par les particules de TiO_2 . Des transferts de charge entre le ligand et le TiO_2 sont également anticipés. Cette configuration devrait permettre de limiter fortement le phénomène de recombinaison des excitons (paire électron-trou). L'autre verrou de la photocatalyse est de trouver des composés pouvant absorber dans le visible (ii). En effet, le TiO_2 n'absorbe qu'environ 3% du spectre solaire et de nombreuses études cherchent à élargir le domaine spectral vers le visible en modifiant le semi-conducteur par couplage avec un PS. L'association de TiO_2 avec un PS absorbant dans le visible offre ainsi plusieurs avantages.

L'un des verrous de la thérapie photodynamique est la vectorisation des photosensibilisateurs. A notre connaissance, seulement deux études ont été consacrées à l'emploi de TiO_2 modifié avec un photosensibilisateur pour des applications en thérapie photodynamique [34, 35]. Il semble donc naturel de mieux comprendre les propriétés photocatalytiques et photodynamiques de ces nanomatériaux hybrides à base de TiO_2 . L'originalité de ce projet est d'élaborer des nouvelles nanoparticules de composition judicieusement choisies, qui rendrait possible une production de ROS dont $^1\text{O}_2$ sous excitation UV-visible pour des efficacités photodynamique et photocatalytique maximales (Fig. 3).

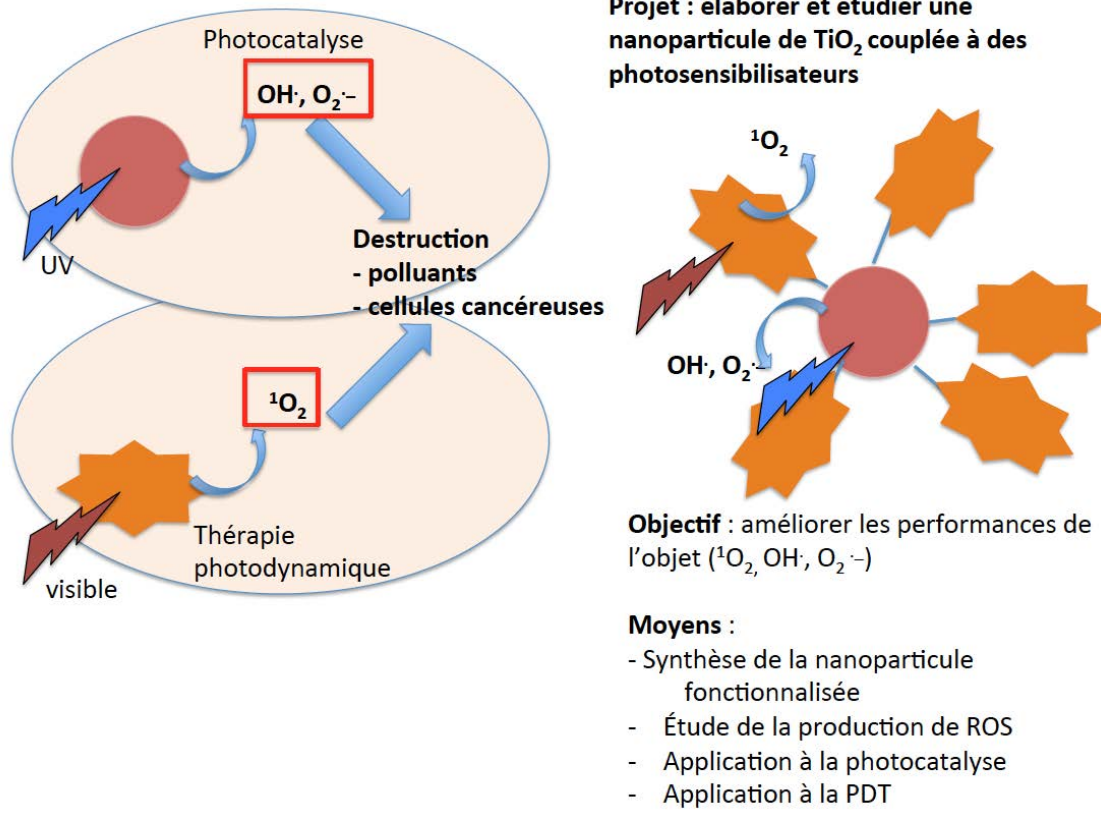


Fig. 3: Représentation schématique de la formation d'espèces réactives de l'oxygène (ROS) de TiO_2 couplé à un photosensibilisateur (PS).

L'objectif de la thèse est donc de synthétiser deux types de nanoparticules pour des applications en photocatalyse et PDT. La **Fig. 4** résume nos objectifs.

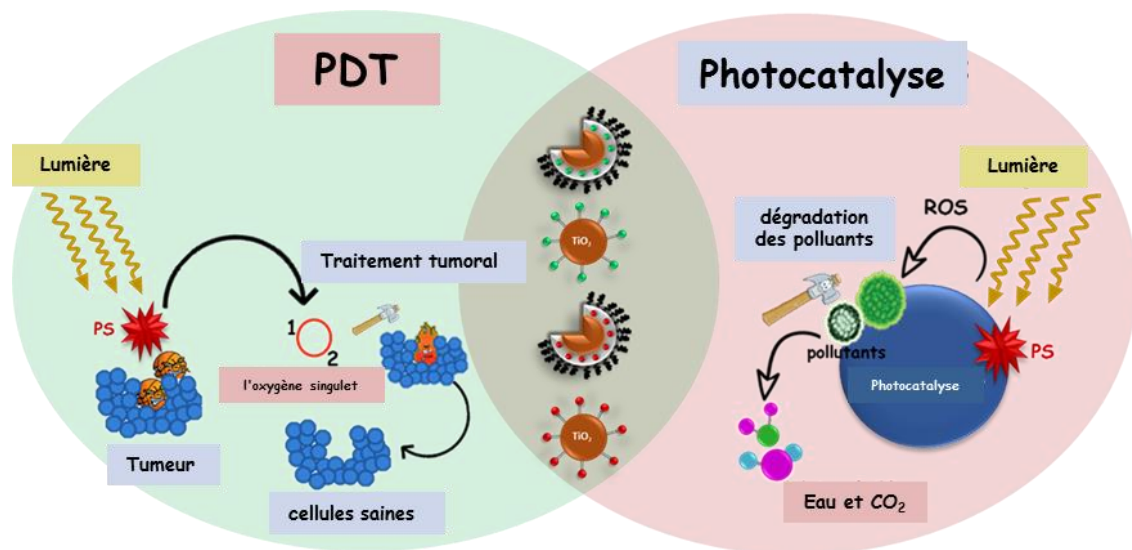


Fig. 4: Représentation schématique des objectifs la thèse.

Le travail de thèse concerne le développement de nanoparticules de TiO_2 et SiO_2 modifiées par des molécules photosensibles, de type porphyrine, greffées sur la surface pour des applications en photocatalyse pour le traitement des effluents et en thérapie photodynamique pour le traitement de certains cancers. Deux modes de modifications ont été envisagés. Le premier repose sur l'encapsulation des nanoparticules dans une couche d'organosilane composée de (3-aminopropyl) triéthoxysilane (APTES) et d'orthosilicate de tétraéthyle (TEOS) : $\text{TiO}_2@4\text{Si-PS-PEG}$ et $\text{SiO}_2@4\text{Si-PS-PEG}$. La deuxième concerne le greffage direct d'APTES sur la surface ($\text{TiO}_2\text{-APTES-PS}$ et $\text{SiO}_2\text{-APTES-PS}$). Ces deux modes sont représentés dans la **Fig. 5**. Pour ces deux systèmes le groupement APTES permet de relier le photosensibilisateur aux nanoparticules. Deux types de PSs ont été étudiés, à savoir la porphyrine tétraphényl monocarboxylique (P1-COOH) et la chlorine e6 (Ce6).

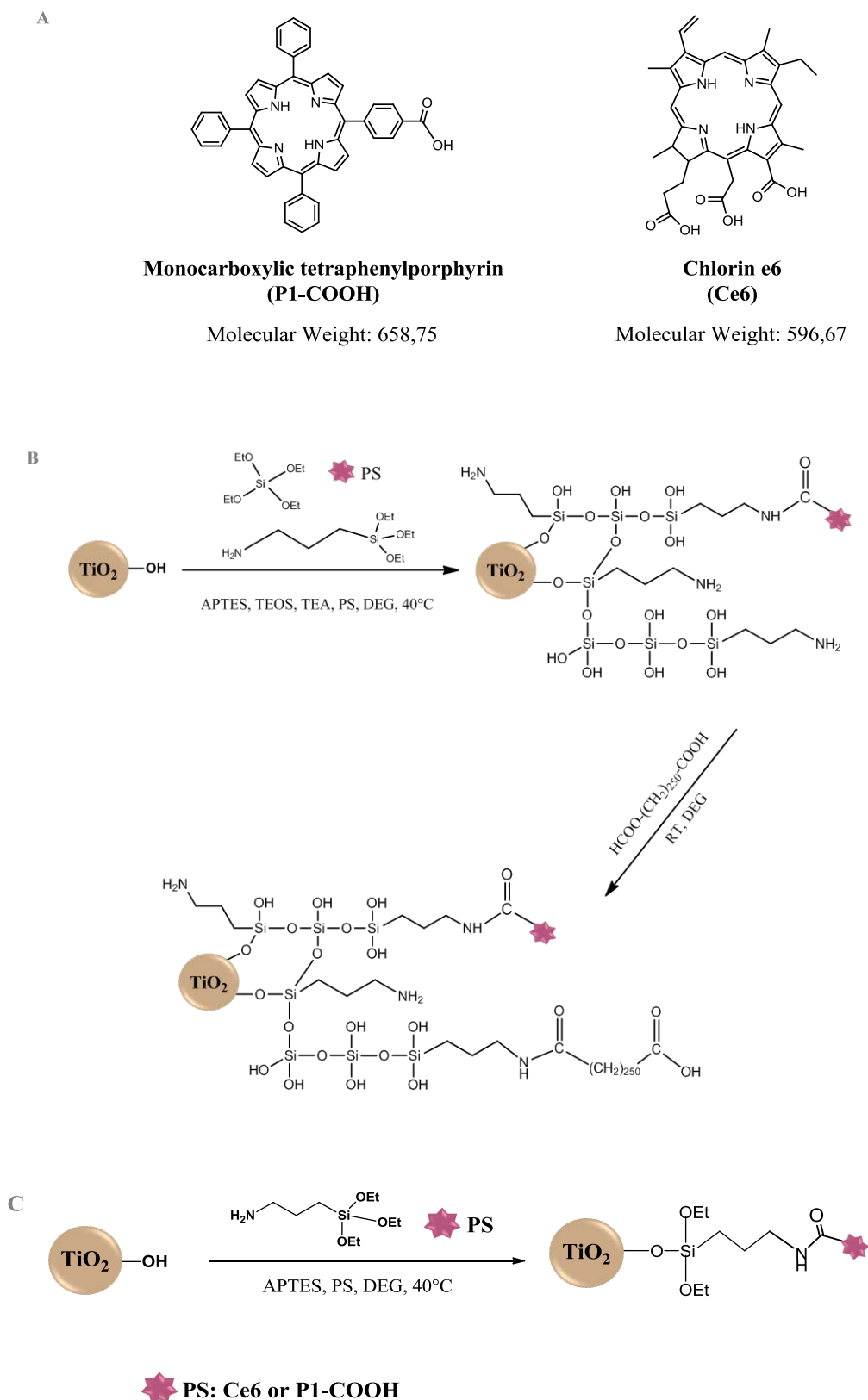


Fig. 5 : (A) Structure moléculaire des photosensibilisateurs. (B) Stratégie de préparation de système cœur/coquille $\text{TiO}_2@4\text{Si-PS-PEG}$ NPs. (C) Stratégie de préparation de système $\text{TiO}_2\text{-APTES-PS}$ NPs.

Le rapport de thèse est constitué de trois chapitres principaux qui assurent une description détaillée du travail effectué :

Chapitre I: Contexte biographique sur les NPs de TiO₂, photocatalyse et PDT.

Sous-chapitre I.1: C'est une revue détaillée de l'application de TiO₂ conjugué à un PS et d'autres matériaux, ZnO, fullerène et graphène, dans la photocatalyse.

Sous-chapitre I.2: C'est une revue détaillée sur l'application de TiO₂ conjugué à un PS et d'autres matériaux, ZnO, fullerène et graphène, dans PDT.

Chapitre II: La dégradation photocatalytique des polluants organiques modèles à partir de l'eau médiée par les NP TiO₂-PS et les SiO₂-PS modifiés par la couche d'APTES/TEOS et l'APTES seul sous effet d'irradiation de lumières UV et visible.

Chapitre III: Etude *in vitro* de l'efficacité photodynamique des NPs TiO₂-PS et SiO₂-PS vis-à-vis de l'éradication des cellules du glioblastome U87 sous irradiation de lumière visible.

Dans un premier temps, les propriétés morphologiques et photophysiques des nanoparticules couplées aux PSs ont été évaluées (**Fig. 6 et 7**). Les analyses de TEM haute résolution et de diffraction de rayons X ont permis de confirmer que la structure cristalline des particules demeure intacte après la silanisation et le greffage du PS (**Fig. 6**). Les mesures de spectrophotométrie UV-visible montrent que le comportement photochimique de toutes les nanoparticules hybrides a été étendu dans la région visible du spectre de lumière (**Fig. 7**). Les analyses de spectroscopie infra-rouge à transformée de Fourier ont prouvées que les PSs sont bien greffés de façon chimique (chimisorption) *via* des liaisons produites par des groupements amides. De plus, les nanoparticules de types TiO₂@4Si-PS-PEG, SiO₂@4Si-PS-PEG, TiO₂-APTES-PS et SiO₂-APTES-PS sont capables de fluorescer sous irradiation visible.

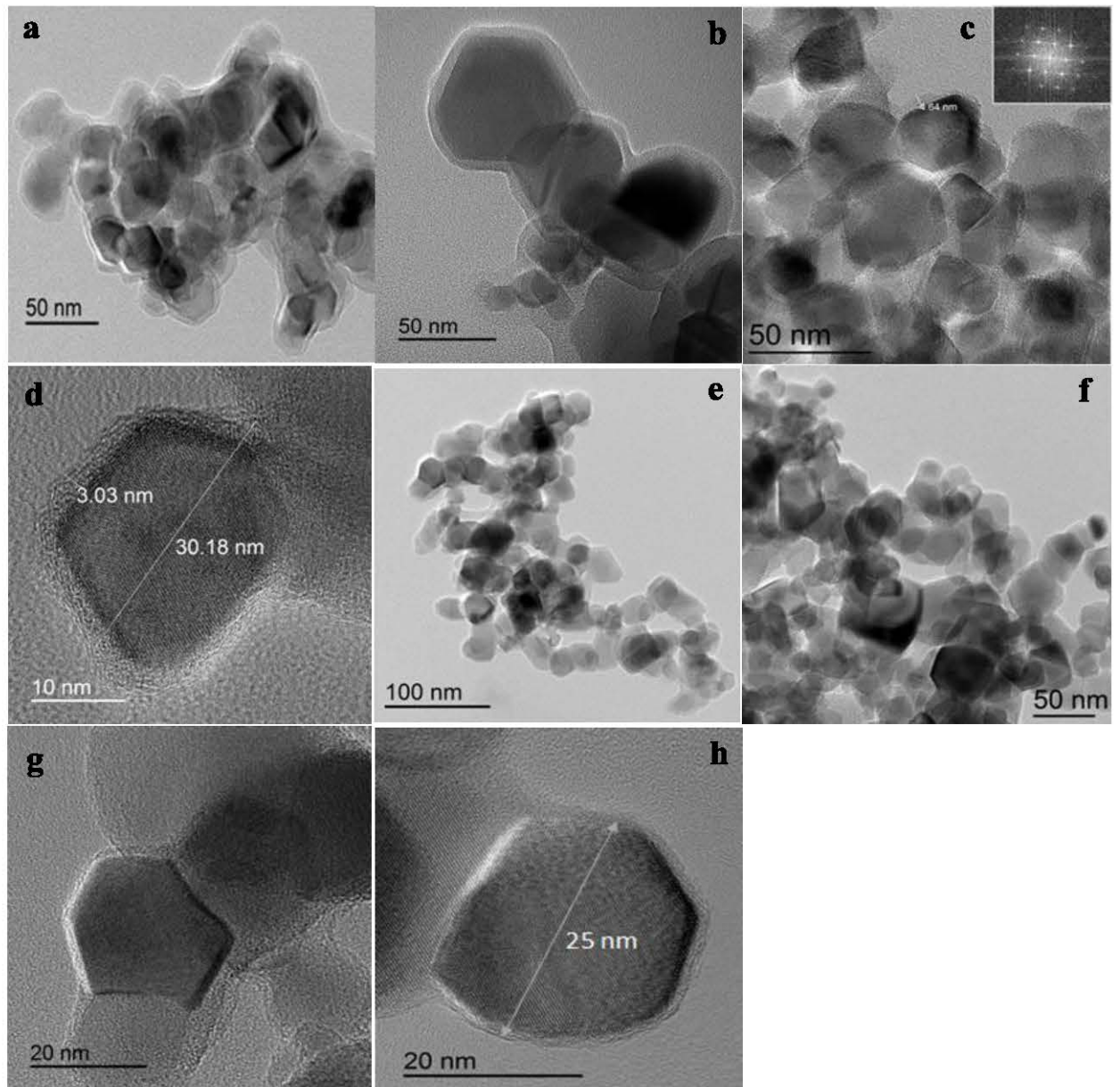


Fig. 6 : Images TEM et HRTEM (insets) de (a-d) $\text{TiO}_2@4\text{Si-Ce6-PEG}$ NPs, and (e-h) $\text{TiO}_2\text{-APTES-Ce6}$ NPs.

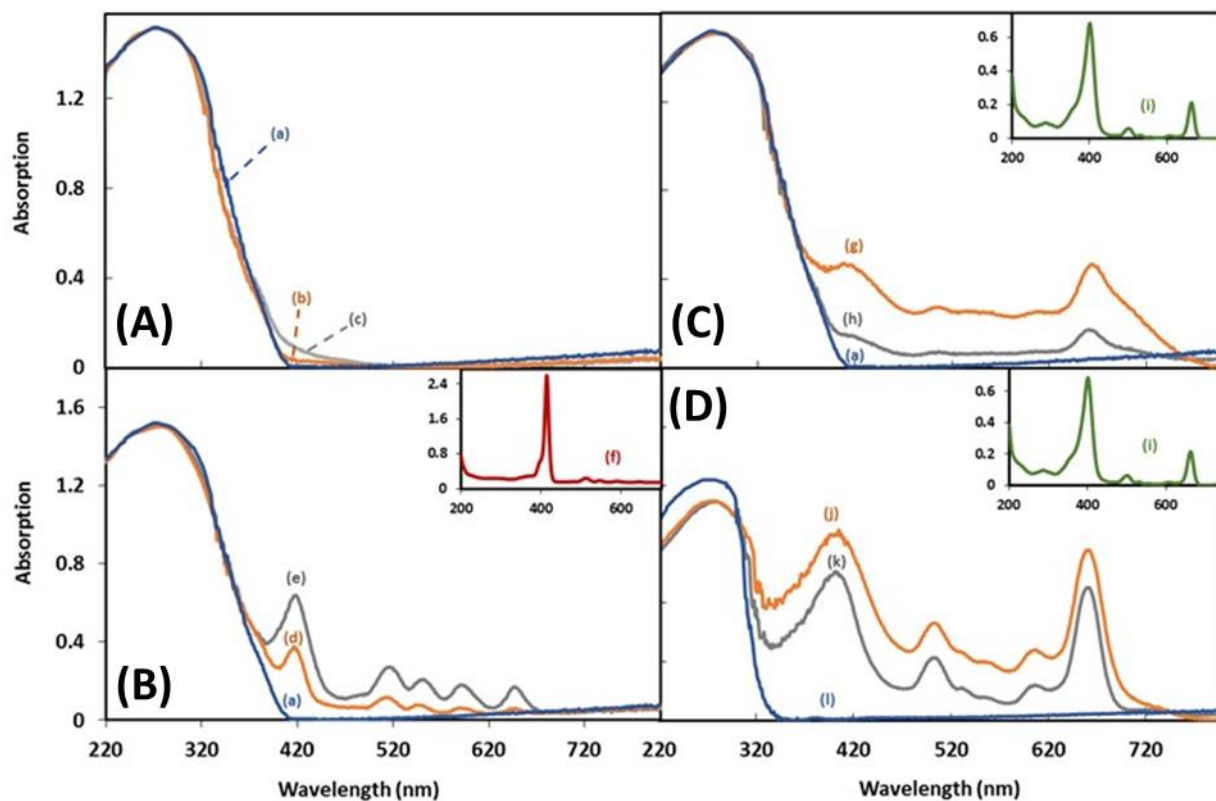


Fig. 7: Spectres d'absorption de (A) (a) TiO_2 , (b) TiO_2 -APTES, (c) $\text{TiO}_2@4\text{Si}$ -PEG; (B) (d) TiO_2 -APTES-P1, (e) $\text{TiO}_2@4\text{Si}$ -P1-PEG; (C) (g) TiO_2 -APTES-Ce6, (h) $\text{TiO}_2@4\text{Si}$ -Ce6-PEG; (D) (j) SiO_2 -APTES-Ce6, (k) $\text{SiO}_2@4\text{Si}$ -Ce6-PEG, et (l) SiO_2 NPs. Dans l'encart : (f) P1-COOH et (i) Ce6 PS dans l'éthanol.

L'activité photocatalytique de ces nanosystèmes a été évaluée en étudiant la dégradation de deux polluants modèles, à savoir l'orange de méthyle et le bleu de méthylène. Les expériences ont été conduites sous irradiation visible et solaire (**Fig. 8** et **9**). Le premier résultat important est que tous ces nanosystèmes hybrides ont permis d'étendre l'activité photocatalytique du dioxyde de titane et de la silice vers la lumière visible et solaire. Ils sont efficaces pour dégrader ces deux polluants modèles. Cependant, les propriétés photocatalytiques dépendent fortement du mode de greffage (cœur/coquille *vs* simple greffage), de la nature du PS (Ce6 *vs* P1-COOH), du type de lumière utilisée (solaire *vs* visible), et de la nature des particules (TiO_2 *vs* SiO_2). Les nanoparticules modifiées par de l'APTES en présence de photosensibilisateurs de type P1-COOH et Ce6 possèdent une

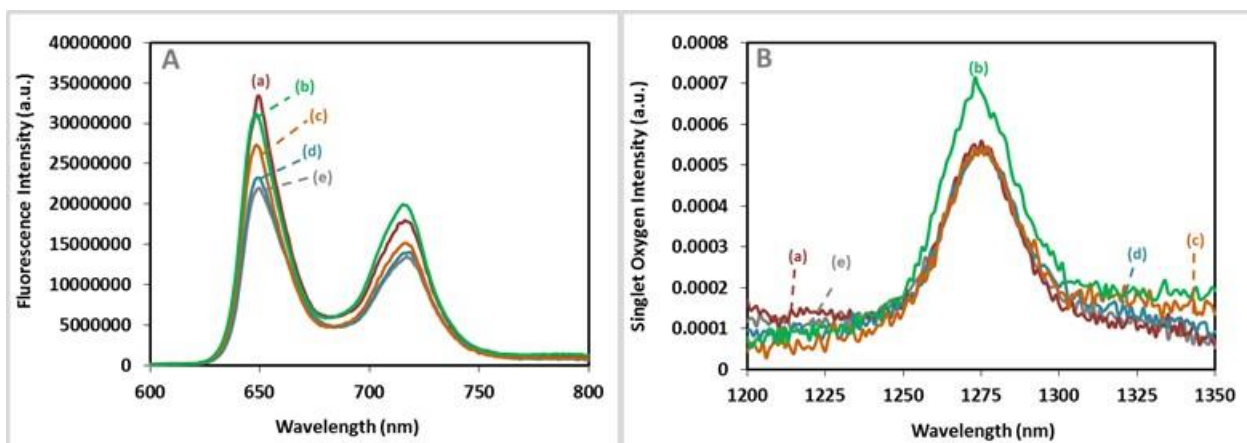
activité de photodégradation des polluants supérieure à celles des systèmes coeur/coquilles sous lumière visible et solaire.

Avec des NPs de TiO₂ couplés à P1-COOH, nous ne pouvons observer aucune altération de la forme des spectres d'émission de fluorescence entre le P1-COOH libre et celle greffée sur TiO₂ (Fig. 8iA). Les NP TiO₂ hybrides P1-COOH sont également capables de former de l'¹O₂.

Avec les NPs TiO₂ couplés à Ce6, la ligne de base des spectres d'absorption ne permettait pas la détection des bandes d'absorption de Ce6. En revanche, la bande de Soret autour de 400 nm et la bande Q1 à 660 nm peuvent être détectées pour les NPs SiO₂ couplés à Ce6. Tous les NPs présentent une émission de fluorescence même si elle est très faible pour TiO₂@4Si-Ce6-PEG. La durée de vie de fluorescence de Ce6 est similaire dans toutes les nanoparticules et proche de la durée de vie de Ce6 libre (4,8 ns). Néanmoins, une durée de vie plus courte apparaît dans TiO₂-APTES-Ce6 (0,6 ns), TiO₂@4Si-Ce6-PEG (1,5 ns), SiO₂-APTES-Ce6 (1,7 ns) mais pas dans SiO₂@4Si-Ce6-PEG. Ce6 pourrait être dans un environnement différent dans les NPs. Les PS qui sont plus à la surface des NPs sont principalement dans l'éthanol tandis que les Ce6 à l'intérieur de la coque sont entourés de silane. Cela pourrait expliquer les différentes durées de vie observées.

Tous les NPs produisent encore ¹O₂ par irradiation ($\lambda_{exc} = 420 \text{ nm}$) sauf TiO₂@4Si-Ce6-PEG. Comme attendu, la durée de vie de ¹O₂ ne change pas puisqu'elle a été mesurée tout le temps dans l'éthanol (entre 12 et 15 μs). Il semble, donc que ¹O₂ ne réagisse pas avec les PS.

(i)



(ii)

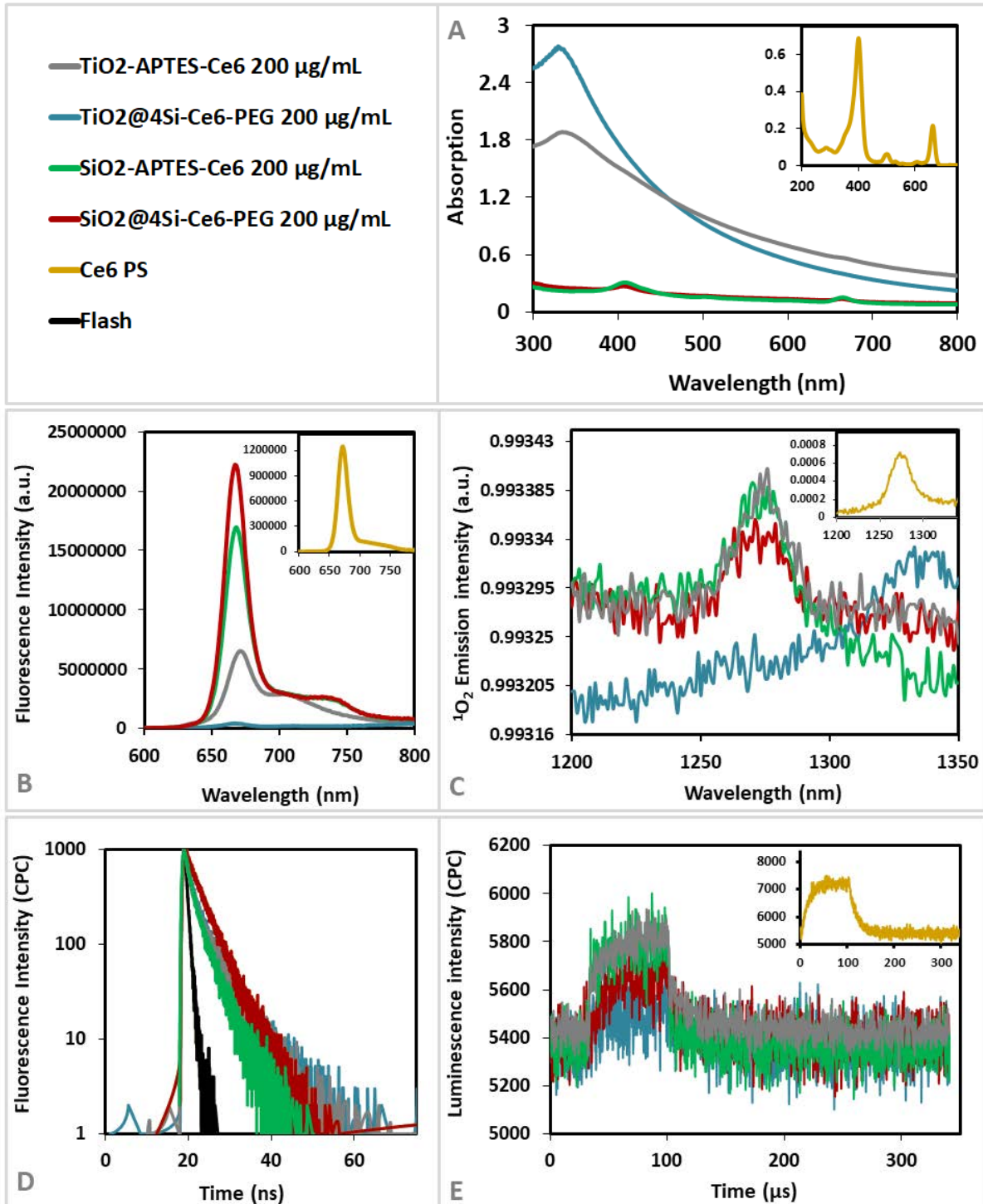


Fig. 8 : (i) Les spectres de fluorescence (A) et les spectres d'oxygène singulet (B) de (a) TiO₂-APTES-P1, (c) TiO₂-APTES-P1-PEG, (d) TiO₂@4Si-P1-PEG, (e) les nanotubes de TiO₂@4Si-P1-PEG, et (b) les PS P1-COOH libres (non fixés) à une densité optique d'environ 0,2 excités à 420 nm, (ii) les spectres d'absorption UV-visible (A), les spectres de fluorescence ($\lambda_{exc} = 420$ nm) (B), les spectres d'émission d'oxygène singulet ($\lambda_{exc} = 420$ nm) (C), la durée de vie de fluorescence ($\lambda_{exc} = 410$ nm) (D) et la durée de vie en oxygène singulet ($\lambda_{exc} = 410$ nm) (E) des NPs TiO₂@4Si-Ce6-

PEG, TiO_2 -APTES-Ce6, SiO_2 -APTES-Ce6 et $\text{SiO}_2 @ 4\text{Si}$ -Ce6-PEG à $200 \mu\text{g} / \text{mL}$ dans l'éthanol et dans les inserts Ce6 (densité optique de 0,2).

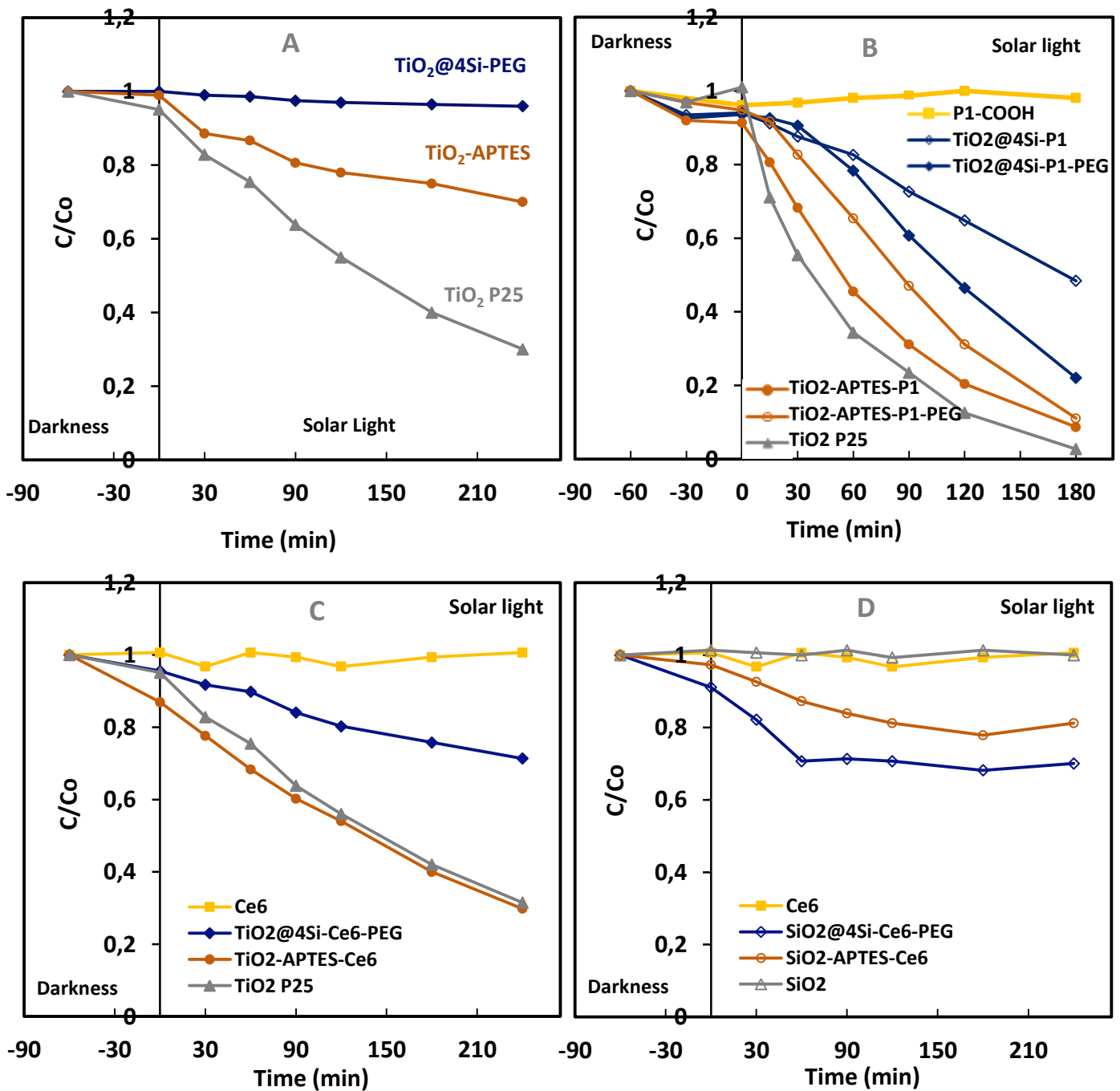


Fig. 9 : Activité photocatalytique sous lumière solaire. (A) Photodégradation de l'orange de méthyle (MO) par du TiO_2 pur et modifié en absence de PS. (B) Photodégradation du bleu de méthylène (MB) par du TiO_2 sensibilisé par P1-COOH, et P1-COOH non-attaché. (C) Photodégradation de MO

par du TiO₂ sensibilisé par Ce6, et Ce6 non-attaché. (D) Photodégradation de MO par de la silice seule et des nanoparticules de silice sensibilisée par Ce6.

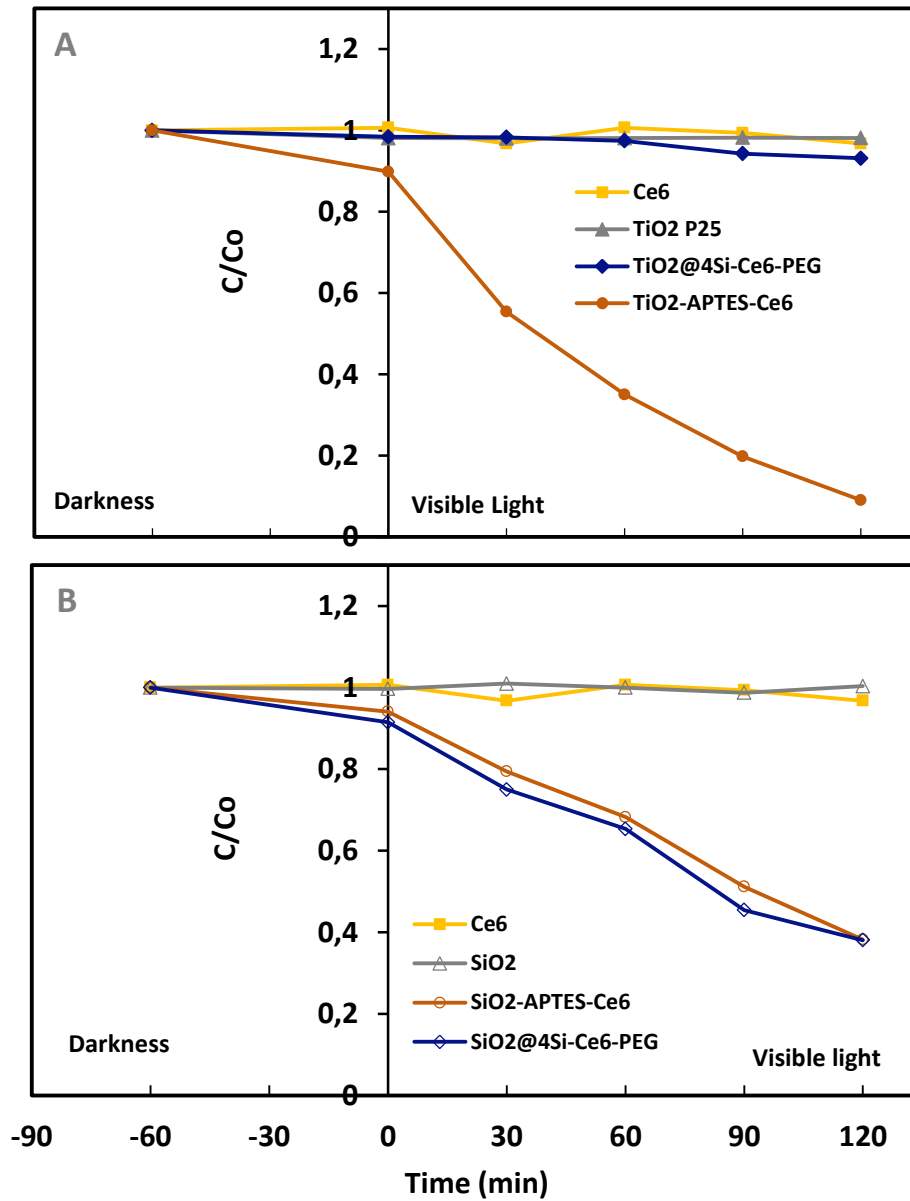


Fig. 10 : Dégradation photocatalytique de l'orange de méthyle (MO) sous lumière visible par (A) TiO₂, TiO₂-APTES-Ce6, TiO₂@4Si-Ce6-PEG NPs et Ce6 PS, (B) SiO₂, SiO₂-APTES-Ce6, SiO₂@4Si-Ce6-PEG NPs et Ce6 PS.

Parmi tous les systèmes étudiés, les meilleures performances sont obtenues avec des nanoparticules de TiO₂ modifiées par de l'APTES en présence de Ce6 sous lumière visible (91% de dégradation). Elles proviennent du faible taux de recouvrement de la surface par la couche de silane et du transfert de charge entre le PS photoactivé et le matériau semi-conducteur. De façon plus précise, le PS (Ce6) joue un double rôle. Il absorbe la lumière visible et devient excité pour produire de l'oxygène singulet (¹O₂) et des électrons. Ensuite, les électrons sont injectés dans la bande de conduction de TiO₂ pour produire une série de réactions permettant de produire des radicaux HO[•] très réactifs.

Pour comprendre ces résultats, nous avons suivi, par différentes techniques, la formation des différentes espèces réactives de l'oxygène (**Fig. 11**). Pour ce faire, les nanoparticules seules ont été étudiées (excitation à 420 nm), puis le PS seul (excitation 420 nm) et enfin, les nanoparticules greffées (excitation 420 nm). Différentes techniques ont été envisagées : détection de la luminescence directe de ¹O₂ à 1270 nm, et également l'utilisation de sondes chimiques telles que le singlet oxygen sensor green (SOSG) et l'hydroxyphényl fluorescéine (HPF) spécifiques des différents ROS (¹O₂ et HO[•]). La forte génération de radicaux HO[•] dans le cas du système TiO₂-APTES-Ce6 sous lumière visible a permis de valider l'hypothèse d'un transfert d'électrons du PS vers le matériau semi-conducteur. De plus, le double rôle joué par le PS Ce6 et le TiO₂ permet de produire une forte quantité de ROS. Pour les nanoparticules de silice, *i.e.* SiO₂-APTES-Ce6 NPs seule la production de ¹O₂ a été détectée. La source de ¹O₂ provient du ligand Ce6 tandis que la silice ne joue que le rôle de support pour l'adsorption des polluants mais ne contribue pas à la production de ROS. Les résultats obtenus avec la silice mettent également en avant le rôle fondamental du coeur de TiO₂ comme un composé fondamental dans le nanosystème TiO₂-APTES-Ce6 car il contribue à la fois à l'adsorption des contaminants et à la génération de ROS, particulièrement les radicaux HO[•] sous lumière solaire et visible.

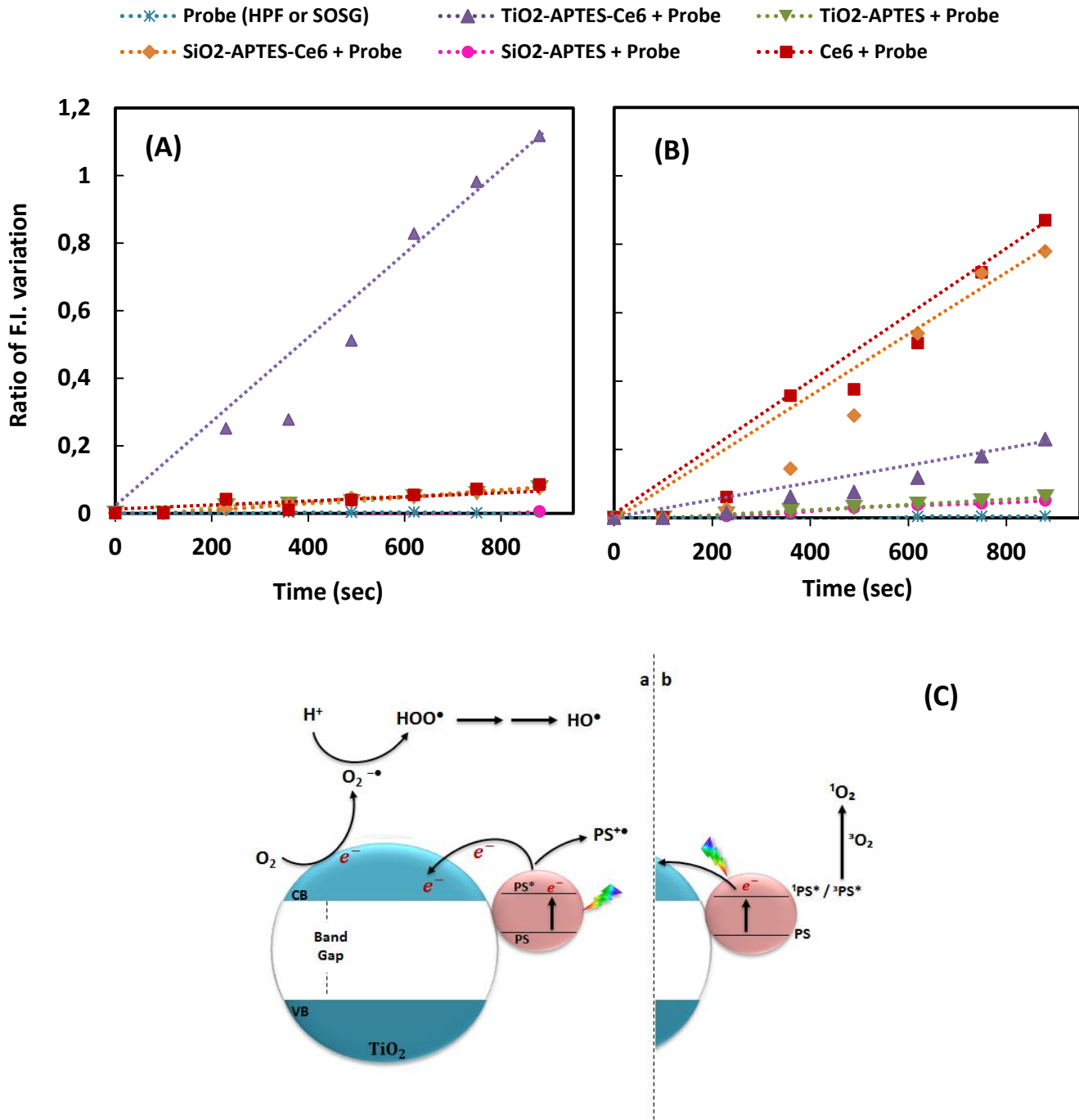


Fig. 11 : Evolution du rapport de fluorescence de (A) la sonde HPF à 514 nm dans le cas HPF seul, Ce6 PS, TiO₂-APTES, TiO₂-APTES-Ce6, SiO₂-APTES et SiO₂-APTES-Ce6 NPs toutes en présence de la sonde HPF dans l'eau ; et de (B) la sonde SOSG à 525 nm dans le cas de SOSG seul, Ce6, TiO₂-APTES, TiO₂-APTES-Ce6, SiO₂-APTES et SiO₂-APTES-Ce6 toutes en présence de sonde SOSG dans l'eau. Le rapport "ratio of F.I. variation" est défini comme le rapport entre la variation de l'intensité de fluorescence (F.I.) au temps t et l'intensité de fluorescence initiale au temps t₀

normalisée (ratio de F.I. variation = $(F.I.(t) - F.I.(t_0)) / F.I.(t_0)$). (C) Mécanismes de transfert se produisant avec des nanoparticules de TiO₂ photosensibilisés par Ce6.

En parallèle, nous avons étudié l'efficacité de ces nanosystèmes hybrides pour détruire des cellules cancéreuses par le procédé de thérapie photodynamique. Pour ce faire, les tests ont été réalisés *in vitro* sur des cellules de glioblastome U87 (tumeur cérébrale) en présence de différentes quantités de particules. Les cellules U87 ont été mises en contact avec les différentes nanoparticules pendant 24 heures et l'incorporation a été étudiée. Le signal de fluorescence des échantillons a été mesuré en double avec une longueur d'onde d'excitation de 405 nm et une longueur d'onde d'émission de 670 nm (spectrofluoromètre Tecan Infinite M200 Pro, Tecan) (Fig. 12). Les concentrations ont été déterminées à partir d'une courbe d'étalonnage standard obtenue en utilisant des concentrations diluées de Ce6 libre dans du DMSO.

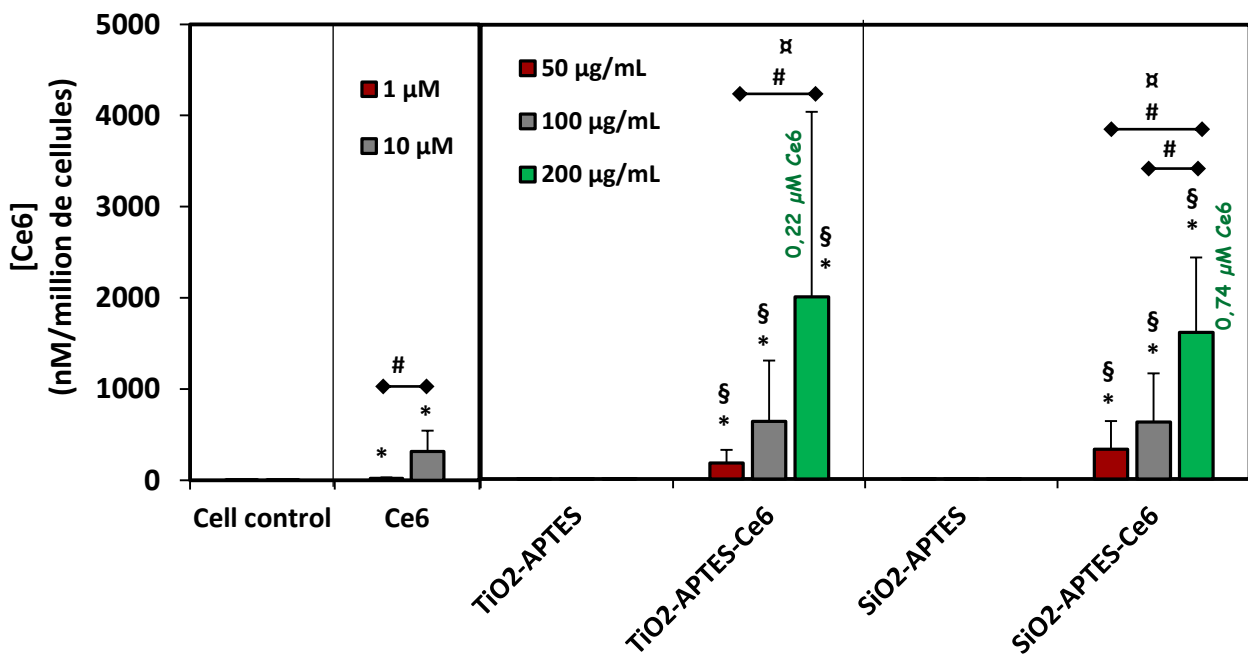


Fig. 12 : Incorporation dans des cellules U87 de Ce6 et Ce6 greffés sur des nanoparticules de TiO₂ et SiO₂ modifiées par l'APTES (Mean ± SD, n = 4, * versus cellules témoins, * p <0,05, § versus NPs-APTES sans Ce6, # versus NP-APTES -Ce6 200 μg /mL et α contre Ce6 10 μM).

La concentration de Ce6 retrouvées dans les cellules U87 augmente avec la concentration en NPs ou en Ce6.

La concentration en Ce6 des suspensions de NPs a été estimée à partir d'une gamme de qualibration en Ce6. Les suspensions à 200 $\mu\text{g/mL}$ de NPs $\text{TiO}_2\text{-APTES-Ce6}$ et NPs $\text{SiO}_2\text{-APTES-Ce6}$ correspondent respectivement à 0,22 et 0,74 μM de Ce6. Ainsi, l'incorporation de Ce6 est donc plus importante lorsqu'elle est greffée à des NPs que lorsqu'elle est libre en solution. Ce résultat est en accord avec la littérature indiquant que les NPs de petite taille peuvent permettre une forte accumulation du PS dans les cellules cancéreuses [36-40]. L'utilisation de NPs de dioxyde de titane et de silice en tant que vecteurs du PS améliore l'incorporation de Ce6 dans les cellules de U87.

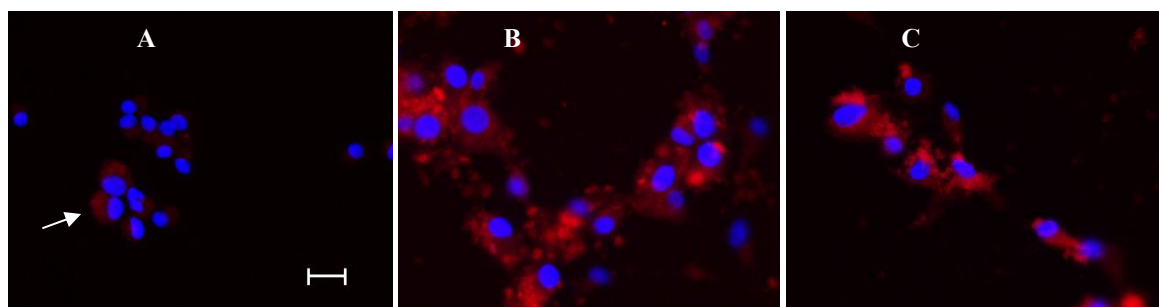


Fig. 13 : Microscopie de fluorescence de cellules U87 exposées à des NPs Ce6 (A), $\text{SiO}_2\text{-APTES-Ce6}$ (B) et $\text{TiO}_2\text{-APTES-Ce6}$ libres (C). La Ce6 ou Ce6 libre greffée sur les NP apparaît en rouge tandis que le noyau marqué au DAPI apparaît en bleu. Barre d'échelle : 20 μm .

Une étude en microscopie de fluorescence (**Fig. 13**) a permis de montrer que lorsque les cellules U87 ont été exposées à la Ce6 libre, le PS se retrouve dans le cytoplasme des cellules (**Fig. 13A**). Lorsque la Ce6 est greffée sur les NPs, le PS a été trouvé regroupé en vésicules quel que soit le type de NP utilisé (SiO_2 ou TiO_2) (**Fig. 13B, C**). Ces résultats indiquent que la localisation cellulaire de Ce6 est différente lorsque le PS est greffé sur les NPs ou s'il est libre. Cela peut expliquer la différence constatée dans l'efficacité de la PDT de la Ce6 seule et de la Ce6 greffée.

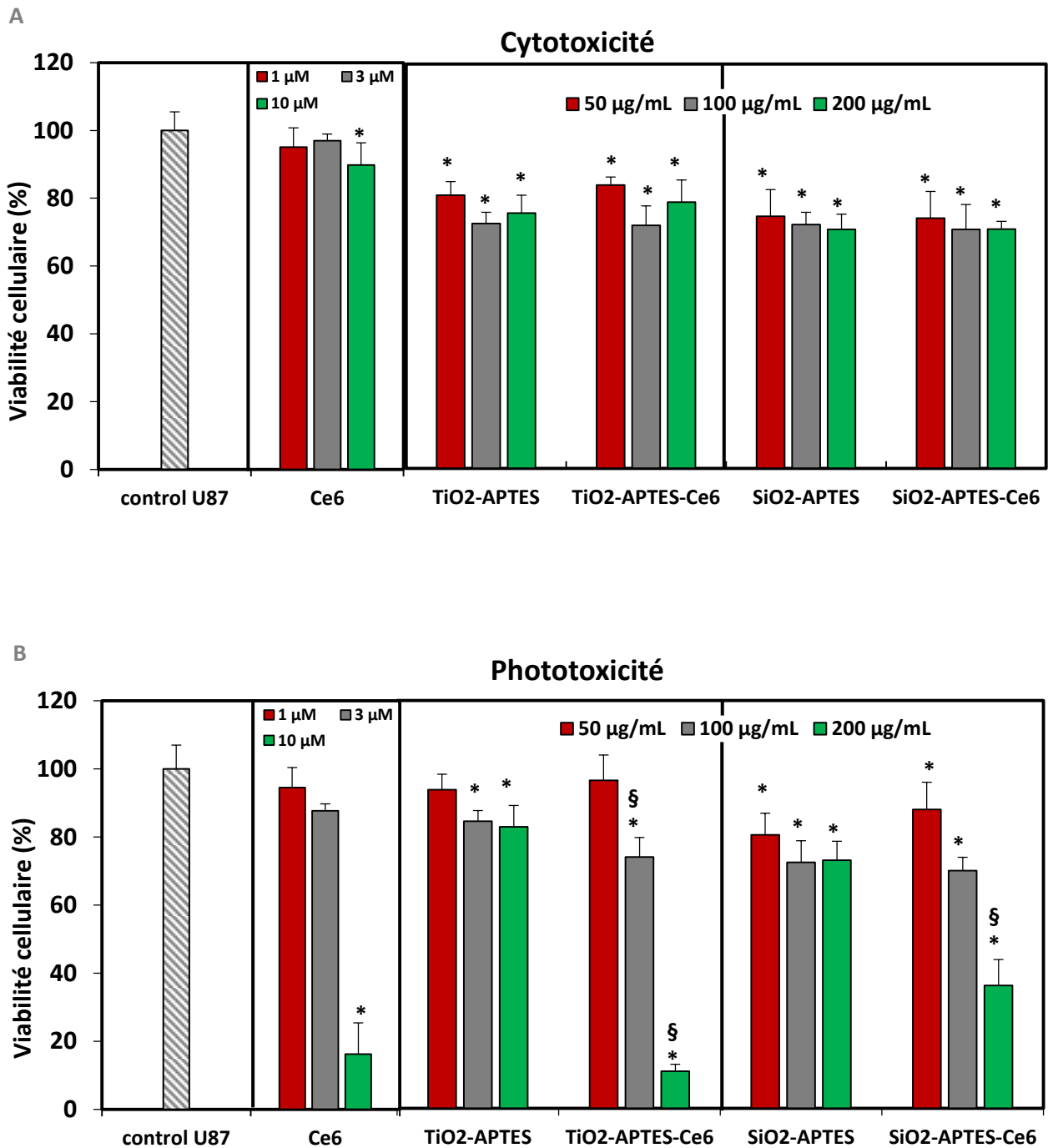


Fig. 14 : La viabilité cellulaire de cellules U87 traitées avec Ce6, TiO₂-APTES, TiO₂-APTES-Ce6, SiO₂-APTES et SiO₂-APTES-Ce6 NP et incubées dans l'obscurité (A, cytotoxicité) ou après irradiation avec une dose de lumière de 10 J/cm² (B, phototoxicité). Les résultats ont été exprimés en pourcentage de valeurs obtenues à partir de cellules non traitées et donnés par la moyenne ± SD, n = 3. * par rapport aux cellules témoins (control U87), * p < 0,05, § par rapport aux NPs sans PS.

La viabilité cellulaire de cellules U87 mises en contact avec Ce6, TiO₂-APTES, TiO₂-APTES-Ce6, SiO₂-APTES et SiO₂-APTES-Ce6 NPs et incubées dans l'obscurité ou après irradiation avec une dose de lumière de 10 J/cm² ($\lambda_{exc} = 652$ nm) est présentée respectivement dans la **Fig. 14A et B**.

Pour les NPs SiO₂-APTES-Ce6 (200 µg/mL), cette irradiation lumineuse a induit une diminution de 64% de la viabilité des cellules U87. Cependant, un effet photodynamique plus marquant a été trouvé en utilisant des NPs TiO₂-APTES-Ce6 (200 µg/mL), qui ont conduit à une diminution de 89% de la viabilité cellulaire. La Ce6 seule utilisée à 10 µM induit le même effet photodynamique que la Ce6 greffé sur les NPs TiO₂ (diminution de 84% de la viabilité cellulaire après exposition à la lumière). Comme mentionné précédemment, la concentration de la Ce6 greffée sur les NPs (200 µg/mL) de TiO₂-APTES-Ce6 et les NPs SiO₂-APTES-Ce6 correspond respectivement à 0,22 et 0,74 µM de Ce6.

Ces résultats indiquent que la Ce6 greffée sur les NPs est plus efficace que la Ce6 seule pour la PDT parce que plus CE6 est internalisé dans les cellules. Cela induit un niveau plus élevé de production de ROS. Par conséquent, des concentration plus faible en Ce6 peuvent être utilisés pour la PDT grâce au couplage du PS sur des systèmes de délivrance de médicaments à base de NPs.

La capacité des NPs TiO₂-APTES-Ce6 et SiO₂-APTES-Ce6 à produire des ROS lorsqu'ils sont irradiés à 652 nm a également été étudiée et comparée à celle de Ce6 libre. HPF et SOSG sont utilisés pour détecter la production de HO[•] et ¹O₂, respectivement. La **Fig. 15A, B** présente respectivement l'intensité de fluorescence de HPF et de SOSG, démontrant la production de ROS lors d'un traitement par PDT (10 J/cm², 652 nm) par des NPs TiO₂-APTES-Ce6, SiO₂-APTES-Ce6 (200 µg /mL) et Ce6 libre (10 µM).

En observant les spectres d'absorption des NPs TiO₂-APTES-Ce6 et SiO₂-APTES-Ce6 (**Fig. 7**), un pic relativement large localisé à environ 660 nm correspondant au pic d'absorption de la Ce6 greffée. Lors de l'irradiation, aucune évolution de l'intensité de fluorescence de SOSG n'est observée dans le cas de TiO₂-APTES et de SiO₂-APTES montrant qu'ils ne produisent pas de ROS. Cependant, l'intensité de fluorescence de SOSG augmente dans le cas des NP TiO₂-APTES-Ce6 et SiO₂-APTES-Ce6, signifiant la formation d'¹O₂. Les NPs de TiO₂-APTES-Ce6 produisent plus de ¹O₂ que les NPs de SiO₂-APTES-Ce6. La quantité de ¹O₂ produite par les deux types de NPs est

beaucoup plus faible que celle produite par la Ce6 libre à 10 μM , mais elle est encore détectable. Après l'addition de l'azoture de sodium, quencher de l' $^1\text{O}_2$, l'intensité de fluorescence de SOSG est diminuée à la fois pour les NPs et Ce6 libre. Ceci confirme que le ROS produit est bien l' $^1\text{O}_2$ (Fig. 15A).

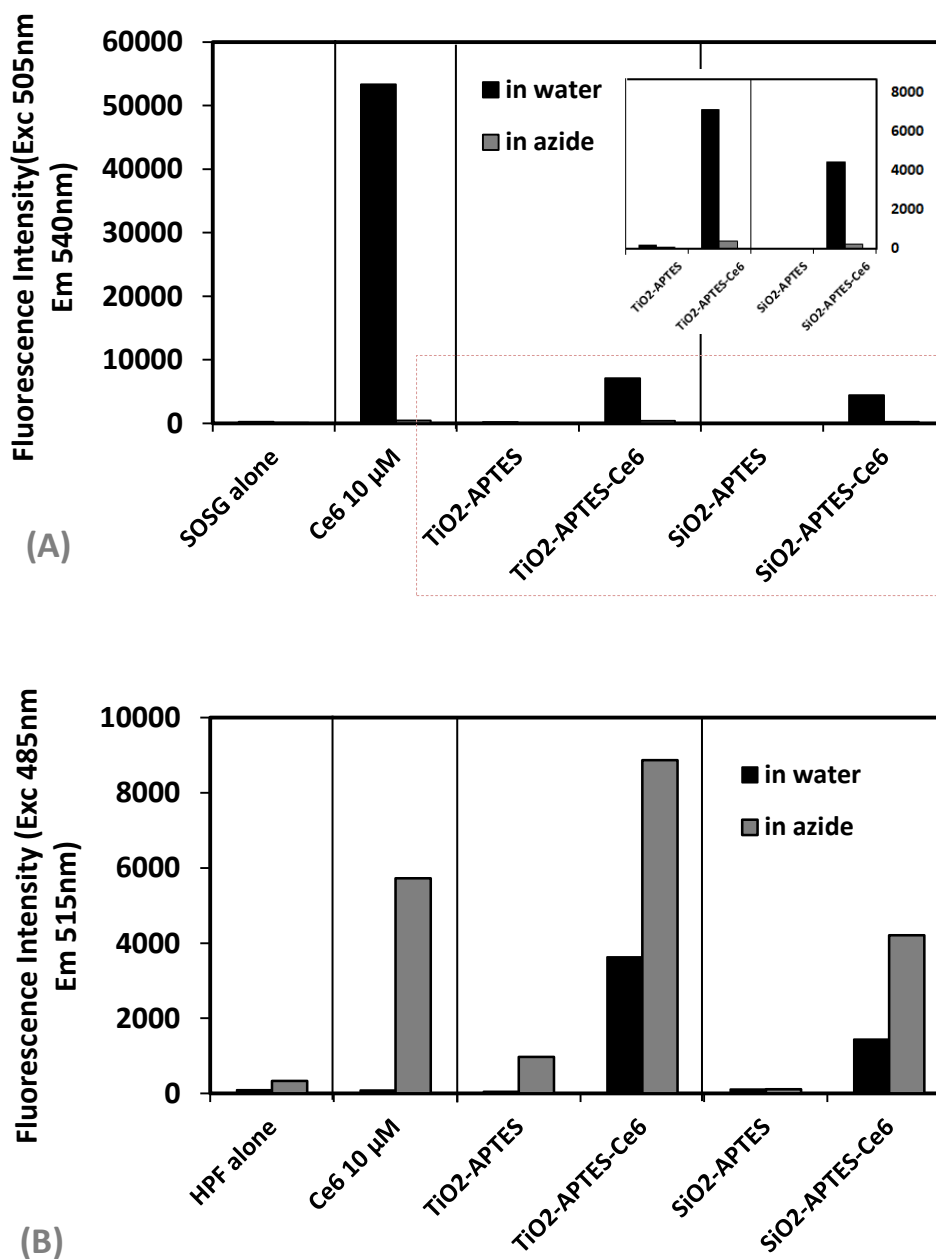


Fig. 15 : Détection d' $^1\text{O}_2$ (A) et $\text{HO}\cdot$ (B) par TiO₂-APTES, TiO₂-APTES-Ce6, SiO₂-APTES et SiO₂-APES-Ce6 NPs (200 $\mu\text{g}/\text{mL}$) et Ce6 libre (10 μM) après traitement par PDT, avec l'utilisation des sondes HPF et SOSG, respectivement.

La **Fig. 15B** présente l'évolution de l'intensité de fluorescence de HPF lors de l'irradiation des NPs et de Ce6 à 652 nm. Les témoins TiO₂-APTES, SiO₂-APTES NPs et Ce6 libre ne permettent pas une augmentation de l'intensité de fluorescence de HPF, ce qui indique qu'il n'y a pas de production de HO[•]. Cependant, les NPs TiO₂-APTES-Ce6 et SiO₂-APTES-Ce6 produisent des HO[•]. Les NPs TiO₂-APTES-Ce6 produisent environ 2,5 fois plus de HO[•] que les NPs SiO₂-APTES-Ce6. Les radicaux HO[•] peuvent être formés par l'activation indirecte des NPs par l'injection des électrons de la Ce6 excitée dans les NPs [41].

TiO₂ est un semi-conducteur possédant une large bande interdite. Dans le nanosystème TiO₂-APTES-Ce6, la Ce6 greffée absorbe la lumière visible plutôt que le TiO₂, limité à l'absorption dans les UV. Ainsi, la Ce6 est excitée dans des états singulet et triplet appropriés [42]. Par la suite, l'injection des électrons excités du Ce6 dans la bande de conduction (CB) de TiO₂ est favorisée par l'état d'énergie propre de ce PS par rapport à TiO₂ [43]. Les électrons réagissent avec l'oxygène moléculaire qui est pré-adsorbé sur la surface de TiO₂ et initient la production de ROS, en particulier les anions superoxydes et les radicaux hydroxyles [42]. Il est également indiqué que TiO₂ dans ses deux formes cristallines, anatase et rutile, pourrait interagir avec les composants cellulaires conduisant à la génération de ROS. Ainsi, la cytotoxicité induite par les ROS se produit lorsque la quantité générée de ROS surmonte la défense cellulaire antioxydante ou déclenche les mécanismes de l'apoptose mitochondriale [44].

Conclusion

Il est intéressant de constater que le système TiO₂-APTES-Ce6 présente les meilleures performances, parmi tous les systèmes étudiés, dans les deux types d'applications testées. Les propriétés d'usage recherchées dans ces deux procédés apparaissent similaires, à savoir la photogénération d'espèces réactives de l'oxygène (radicaux HO[•] et ¹O₂) sous lumière visible afin d'oxyder soit des cellules cancéreuses soit des polluants organiques. Le système TiO₂-APTES-Ce6 permet de produire à la fois des radicaux HO[•] et de ¹O₂.

Références

- [1] D. Fatta-Kassinos, S. Meric, A. Nikolaou, Pharmaceutical residues in environmental waters and wastewater: current state of knowledge and future research, *Anal. Bioanal. Chem.*, 399 (2011), 251–275.
- [2] M. Grassi, L. Rizzo, A. Farina, Endocrine disruptors compounds, pharmaceuticals and personal care products in urban wastewater: implications for agricultural reuse and their removal by adsorption process, *Environ. Sci. Pollut. Res.*, 20 (2013), 3616–3628.
- [3] S. D. Richardson, S. Y. Kimura, Water analysis: Emerging contaminants and current Issues, *Anal. Chem.*, 88 (2016), 546–582.
- [4] M. Trapido, I. Epold, J. Bolobajev, N. Dulova, Emerging micropollutants in water/wastewater: growing demand on removal technologies, *Environ. Sci. Pollut. Res.*, 21 (2014), 12217–12222.
- [5] Ghatak, H.R. (2014). Advanced oxidation processes for the treatment of biorecalcitrant organics in wastewater. *Crit Rev Environ Sci Technol* 44, 1167-1219.
- [6] Oturan, M.A. and Aaron, J.J. (2014). Advanced oxidation processes in water/wastewater treatment: Principles and applications. A review. *Crit Rev Environ Sci Technol* 44, 2577-2641.
- [7] de Witte, B., van Langenhove, H., Demeestere, K. and Dewulf, J. (2011). Advanced oxidation of pharmaceuticals: Chemical analysis and biological assessment of degradation products. *Crit Rev Environ Sci Technol* 41, 215-242.
- [8] Herrmann, J.M. (2005). Heterogeneous photocatalysis: State of the art and present applications. *Top Catal* 34, 49-65.
- [9] Herrmann, J.M. (2010). Photocatalysis fundamentals revisited to avoid several misconceptions. *Appl Catal, B* 99, 461-468.
- [10] Hoffmann, M.R., Martin, S.T., Choi, W.Y. and Bahnemann, D.W. (1995). Environmental applications of semiconductor photocatalysis. *Chem Rev* 95, 69-96.
- [11] Fujishima, A., Rao, T.N. and Tryk, D.A. (2000). Titanium dioxide photocatalysis. *J Photochem Photobiol C: Photochem Rev* 1, 1-21.
- [12] Gaya, U.I. and Abdullah, A.H. (2008). Heterogeneous photocatalytic degradation of organic contaminants over titanium dioxide: A review of fundamentals, progress and problems. *J Photochem Photobiol C: Photochem Rev* 9, 1-12.
- [13] M. J. Gázquez, J. P. Bolívar, R. Garcia-Tenorio, and F. Vaca, “A Review of the Production Cycle of Titanium Dioxide Pigment,” *Mater. Sci. Appl.*, vol. 05, no. 07, pp. 441–458, 2014.
- [14] Y. Lan, Y. Lu, and Z. Ren, “Mini review on photocatalysis of titanium dioxide nanoparticles and their solar applications,” *Nano Energy*, vol. 2, no. 5, pp. 1031–1045, Sep. 2013.
- [15] A. Karmakar, Q. Zhang, and Y. Zhang, “Neurotoxicity of nanoscale materials,” *J. Food Drug Anal.*, vol. 22, no. 1, pp. 147–160, Mar. 2014.
- [16] S. G. Kumar and L. G. Devi, “Review on Modified TiO₂ Photocatalysis under UV/Visible Light: Selected Results and Related Mechanisms on Interfacial Charge Carrier Transfer Dynamics,” *J. Phys. Chem. A*, vol. 115, no. 46, pp. 13211–13241, Nov. 2011.
- [17] G. Wang, L. Xu, J. Zhang, T. Yin, and D. Han, “Enhanced Photocatalytic Activity of Powders (P25) via Calcination Treatment,” *Int. J. Photoenergy*, vol. 2012, pp. 1–9, 2012.

- [18] J. Zhao, M. Milanova, M. M. C. G. Warmoeskerken, and V. Dutschk, "Surface modification of TiO₂ nanoparticles with silane coupling agents," *Colloids Surf. Physicochem. Eng. Asp.*, vol. 413, pp. 273–279, Nov. 2012.
- [19] A. Fujishima, X. Zhang, and D. Tryk, "TiO₂ photocatalysis and related surface phenomena," *Surf. Sci. Rep.*, vol. 63, no. 12, pp. 515–582, Dec. 2008.
- [20] M. Kassir et al., "Improvement of the photocatalytic activity of TiO₂ induced by organic pollutant enrichment at the surface of the organografted catalyst," *Colloids Surf. Physicochem. Eng. Asp.*, vol. 485, pp. 73–83, Nov. 2015.
- [21] B. Ohtani, O. O. Prieto-Mahaney, D. Li, and R. Abe, "What is Degussa (Evonik) P25? Crystalline composition analysis, reconstruction from isolated pure particles and photocatalytic activity test," *J. Photochem. Photobiol. Chem.*, vol. 216, no. 2–3, pp. 179–182, Dec. 2010.
- [22] T. Ohno, K. Sarukawa, K. Tokieda, and M. Matsumura, "Morphology of a TiO₂ Photocatalyst (Degussa, P-25) Consisting of Anatase and Rutile Crystalline Phases," *J. Catal.*, vol. 203, no. 1, pp. 82–86, Oct. 2001.
- [23] Z. Rui, S. Wu, C. Peng, and H. Ji, "Comparison of TiO₂ Degussa P25 with anatase and rutile crystalline phases for methane combustion," *Chem. Eng. J.*, vol. 243, pp. 254–264, May 2014.
- [24] L. A. Torre, R. L. Siegel, E. M. Ward, and A. Jemal, "Global Cancer Incidence and Mortality Rates and Trends--An Update," *Cancer Epidemiol. Biomarkers Prev.*, vol. 25, no. 1, pp. 16–27, Jan. 2016.
- [25] J. Ferlay et al., "Cancer incidence and mortality worldwide: Sources, methods and major patterns in GLOBOCAN 2012: Globocan 2012," *Int. J. Cancer*, vol. 136, no. 5, pp. E359–E386, Mar. 2015.
- [26] Brown G.C., Brown M.M., Campanella J., Beauchamp G.R. The costutility of photodynamic therapy in eyes with neovascular macular degeneration: a value-based reappraisal with 5-year data, *Am. J. Ophthalmol.*, 2005, 140, p. 679.
- [27] Azzouzi, A.R., Barret, E., Moore, C.M., Villers, A., Allen, C., Scherz, A., Muir, G., Wildt, M., Barber, N.J., Lebdai, S. and Emberton, M., 2013. TOOKAD® Soluble vascular- targeted photodynamic (VTP) therapy: determination of optimal treatment conditions and assessment of effects in patients with localised prostate cancer. *BJU international*, 112(6), pp.766-774.
- [28] Maunoury, V., S. Mordon, P. Bulois, D. Cochelard, J. Boyer, V. Quentin, M. Barthet et al. "La thérapie photodynamique en gastroentérologie: quoi de neuf en 2009?." *Acta endoscopica* 39, no. 5 (2009): 353.
- [29] Azaïs, H., C. Frochot, A. Grabarz, S. Khodja Bach, L. Colombeau, N. Delhem, S. Mordon, and P. Collinet. "Photosensibilisateur spécifique pour la thérapie photodynamique ciblée des métastases péritonéales des cancers ovariens." *Gynécologie Obstétrique Fertilité & Sénologie* 45, no. 4 (2017): 190-196.
- [30] Beck, T.J., Kreth, F.W., Beyer, W., Mehrkens, J.H., Obermeier, A., Stepp, H., Stummer, W. and Baumgartner, R., 2007. Interstitial photodynamic therapy of nonresectable malignant glioma recurrences using 5- aminolevulinic acid induced protoporphyrin IX. *Lasers in surgery and medicine*, 39(5), pp.386-393.
- [31] Du, K.L., Both, S., Friedberg, J.S., Rengan, R., Hahn, S.M. and Cengel, K.A., 2010. Extrapleural pneumonectomy, photodynamic therapy and intensity modulated radiation therapy for the treatment of malignant pleural mesothelioma. *Cancer biology & therapy*, 10(5), pp.425-429.

- [32] Morton, C.A., Szeimies, R.M., Sidoroff, A. and Braathen, L.R., 2013. European guidelines for topical photodynamic therapy part 1: treatment delivery and current indications—actinic keratoses, Bowen’s disease, basal cell carcinoma. *Journal of the European Academy of Dermatology and Venereology*, 27(5), pp.536-544.
- [33] A. Fujishima, X. Zhang, and D. Tryk, “TiO₂ photocatalysis and related surface phenomena,” *Surf. Sci. Rep.*, vol. 63, no. 12, pp. 515–582, Dec. 2008.
- [34] Ion R-M and Brezoi D-V. *New Nano-Sized Sensing Drug and Its Clinical Application Solid State Phenomena*. 2005;1006:79-82.
- [35] Ion RM. Porphyrinic nano-sensitizers encapsulated into colloidal carriers. *Rom. J. Phys.* 2004;49:867-71.
- [36] D. K. Chatterjee, L. S. Fong, and Y. Zhang, “Nanoparticles in photodynamic therapy: An emerging paradigm,” *Adv. Drug Deliv. Rev.*, vol. 60, no. 15, pp. 1627–1637, Dec. 2008.
- [37] N. Mehraban and H. Freeman, “Developments in PDT Sensitizers for Increased Selectivity and Singlet Oxygen Production,” *Materials*, vol. 8, no. 7, pp. 4421–4456, Jul. 2015.
- [38] X. Pan et al., “Enhancement of the photokilling effect of aluminum phthalocyanine in photodynamic therapy by conjugating with nitrogen-doped TiO₂ nanoparticles,” *Colloids*
- [39] J. H. Park and N. Oh, “Endocytosis and exocytosis of nanoparticles in mammalian cells,” *Int. J. Nanomedicine*, p. 51, May 2014.
- [40] A. M. Pekkanen, M. R. Dewitt, and M. N. Rylander, “Nanoparticle Enhanced Optical Imaging and Phototherapy of Cancer,” *J. Biomed. Nanotechnol.*, vol. 10, no. 9, pp. 1677–1712, Sep. 2014.
- [41] W. Lei, Q. Zhou, Z. Li, X. Wang, and B. Zhang, “Photodynamic Activity of Ascorbic Acid-modified TiO₂ Nanoparticles upon Visible Illumination (>550 nm),” *Chem. Lett.*, vol. 38, no. 12, pp. 1138–1139, Dec. 2009.
- [42] S. Rehman, R. Ullah, A. M. Butt, and N. D. Gohar, “Strategies of making TiO₂ and ZnO visible light active,” *J. Hazard. Mater.*, vol. 170, no. 2–3, pp. 560–569, Oct. 2009.
- [43] G. Granados-Oliveros, E. A. Páez-Mozo, F. M. Ortega, C. Ferronato, and J.-M. Chovelon, “Degradation of atrazine using metalloporphyrins supported on TiO₂ under visible light irradiation,” *Appl. Catal. B Environ.*, vol. 89, no. 3–4, pp. 448–454, Jul. 2009.
- [44] C. Jin et al., “Cellular Toxicity of TiO₂ Nanoparticles in Anatase and Rutile Crystal Phase,” *Biol. Trace Elem. Res.*, vol. 141, no. 1–3, pp. 3–15, Jun. 2011.

Chapter I: Bibliographic Background

In this part, we present the bibliographic background that highlights on the subject of our study. Firstly, TiO₂ NPs are described. The description includes the definition, origin, surface chemistry and photoreactivity of those nanoparticles. In addition, the production of ROS is thoroughly described. Then, the two targeted applications, photocatalytic water treatment and anti-cancer PDT, are then discussed. The contribution of TiO₂ NPs in those two applications is deliberated. This part also discusses the limitations of bare TiO₂ that require certain modifications especially the sensitization of titania with light-sensitive PS (Dye-sensitization: PS-TiO₂).

Furthermore, two detailed reviews about dye-sensitized nanoparticles in photocatalytic water treatment and anti-cancer PDT are presented. Beside TiO₂, those reviews include other materials such as zinc oxide, fullerene and graphene.

1. Titanium dioxide

1.1. Definition, origin and crystal forms

In 1791, the British clergyman and mineralogist William Gregor was credited with the first discovery of titanium from ilmenite, an iron-containing mineral (FeTiO_3), which he named menachite (**Fig. 1**). However, it was Klaproth, a German chemist, who termed it titanium after the giants of Greek mythology, few years later. ‘Ti’ symbolizes titanium which holds an atomic number of 22. It belongs to Group VIB of transition metals. Titanium originates from natural sources such as plants, waters and animals as well as in almost all sediments and rocks. Among the elements occupying the earth’s crust, Ti is the ninth most abundant one (0.63%). It is described as a silver-white metallic element. Titanium is a paramagnetic element that is immensely resistant to corrosion. It possesses a good strength and a scarce conductivity thermally and electrically [1–3].



Fig. 1: Ilmenite ore. Picture obtained from virtual museum of the University of Huelva [1].

The usual form of titanium in nature is metal oxide and not pure metal. Titanium embraces a forceful affinity towards oxygen, carbon and nitrogen. Such property of Ti produces the passivation of the surface of the metal through the deposition of an oxide layer, few nanometers thick. This form of titanium lies behind its superior corrosion resistance.

Titanium dioxide, TiO_2 , has been widely employed in our lives as the common compound of titanium. Besides titanium (IV) oxide and titania, TiO_2 is also termed E171 in food coloring and titanium white or pigment white 6 in building paints [1–3]. It is an odorless white material. TiO_2 is water insoluble and generally shape as particles. In addition, the powder form of TiO_2 possess a hydrophilic character [3, 4]. Titania embraces various merits and certain optical, electronic and physiochemical properties which makes it convenient for a wide range of applications. TiO_2 is of low cost, available, biologically and chemically inert, stable and corrosion resistant. It is a material of low toxicity, and strong oxidizing power. In addition, it is efficient as an anti-bacterial agent, in the environmental purification due to its high photocatalytic activity and in the UV protection [2–6].

Table 1: Properties of some minerals of titanium [1].

Name (Formula)	%TiO ₂	Color	Hardness (GPa)	Density (g cm ⁻³)	Crystal Form	Transparency
Ilmenite (FeTiO ₃)	52.6	Black	5-6	4.5-5.0	Hexagonal	Opaque
Perovskite (CaTiO ₃)	58	Black, brown, reddish-brown or yellow	5.5	4.48-4.26	Monoclinic (pseudocubic)	
Rutile, anatase, brookite (TiO ₂)	95	Reddish-brown, red, yellowish or black	6.0-6.5 (rutile) 5.5-6.0 (anatase and brookite)	4.23-5.5 (rutile) 3.82-3.97 (anatase) 4.08-4.18 (brookite)	Tetragonal (rutile, anatase) Orthorhombic (brookite)	Opaque or subtransparent
Titanite (sphene) (CaTiSiO ₅)	35-40	Brown, green, grey, yellow or black	5.0-5.5		Monoclinic	Transparent to opaque

In 1929, TiO₂, used as white pigment in buildings, was found to bleach under long solar illumination. This firstly shed light on the photoactive properties of TiO₂. Few years later, 1932-1934, the first scientific report on this topic was published. However, the photobleaching of dyes, PSs, by photoactive TiO₂ was reliably reported in 1938. In 1956, the term ‘TiO₂ photocatalyst’ was first considered [2]. The first demonstration of the photocatalytic activity of titania for water photolysis was reported by Akira Fujishima and Kenichi Honda [7]. Since 2000, the papers published on TiO₂ photocatalysts exceed 10,000 per year [2].

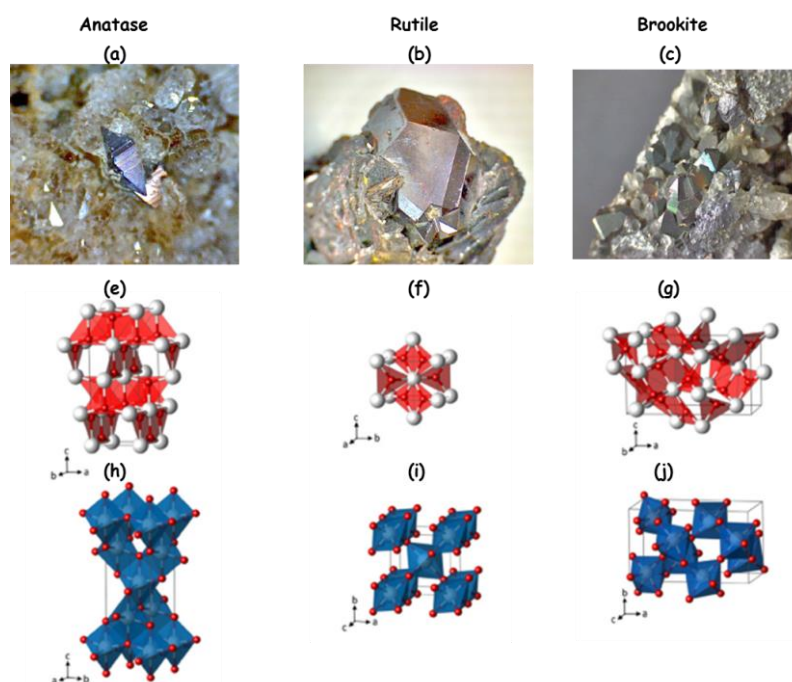


Fig. 2: The naturally occurring TiO₂ crystalline phases (a, b & c). The planar Ti₃O building-block representation (e, f & g) and TiO₆ polyhedra (h, i & j) for the TiO₂ phases anatase (a, e & h), rutile (b, f & i) and brookite (c, g & j) (Ti (white); O (red)). The experimental lattice parameters $a = b =$

4.5937 Å, $c = 2.9581$ Å for rutile, $a = b = 3.7842$ Å, $c = 9.5146$ Å for anatase and $a = 9.16$ Å, $b = 5.43$ Å, $c = 5.13$ Å for brookite have been used throughout this work [8].

Despite the fact that TiO_2 has many polymorphs, only three crystalline forms of titania are well-known. Those are naturally existing anatase, rutile and brookites discovered in 1801, 1803 and 1825, respectively. Anatase gained its name due to its extended crystallographic shape, while rutile's reddish color is the reason after its name. Brookite phase is named after a mineralogist. As pre-mentioned, the naturally occurring titanium ores are mainly found as ilmenite, FeTiO_3 (Fig. 2). However, it is frequently transformed, either as a sand or as rock, anatase (Fig. 2a), rutile (Fig. 2b), and brookite, (Fig. 2c). Those have the same formula but different crystalline structures [1].

Recent studies have elucidated the relationship between the stability of the TiO_2 phases and the size of nanoparticles (NPs). For NPs possessing a size below 11 nm, anatase form seems to be the most stable. Though, with NPs ranging between 11 and 35 nm in size, brookite phase seems to be the most stable. And as for NPs with a size exceeding 35 nm, rutile is the most stable phase. Each of those phases hold distinct physical and chemical features, including different density, surface chemistry and structure, band gap energy, etc. However, anatase and rutile reveal the bottommost differences and the most similar physical characteristics. In 1942, Earle described anatase and rutile phases of TiO_2 as n-type semiconductors [9]. Both phases are characterized by a wide band-gap. The energy of the band-gap ranges between 3.2 eV for anatase and 3.02 eV for rutile. Those wide band gaps of anatase and rutile crystallographic phases enable the reflection of visible light. Yet, anatase is capable of reflecting a wider electromagnetic wave constituting of long-wave ultraviolet light (UVA) beside the visible [2]. Despite that both anatase and rutile forms are proven to be catalytically photoactive, they act differently. Although the exact reasons causing such different activity have not been fully explicated yet, but the following explanation may give an idea. The difference in the catalytic activity and the physico-chemical characteristics between anatase and rutile is sometimes explained by their different crystalline structure. Such property gives rise to different TiO_2 supported catalysts which varies their photoactivity since the catalytic reactions involving heterogeneous catalysis mostly occur on the catalyst's surface or at the interface of the support and the active species [10]. In terms of photoactivity, it is said that anatase is superior to rutile. More hydroxyl groups occupy the surface of anatase TiO_2 as compared to that of rutile. The elevated number of OH groups results from the lower affinity to oxygen triggered by the higher fermi level of anatase (by 0.1 eV). It is well-known that the availability of OH groups prompts a more efficient photocatalytic activity [2, 11].

It seems also interesting to discuss the special case of the titania catalyst known as Degussa P25. The powder consists of anatase and rutile crystalline phases existing separately in this composite. Although the precise phase composition is not definite yet, the ratio of anatase to rutile in P25 is reported to range between 70:30 and 80:20 [12, 13]. This type of titania possesses a relatively low specific surface area of about $49 \text{ m}^2 \text{ g}^{-1}$ [13]. TiO_2 P25 has been extensively used thanks to its high photocatalytic activity. In fact it was mentioned that it is not easy to find a photocatalyst of greater photoactivity as compared to P25. Based on such information, P25 is described as the ‘de-facto standard titania photocatalyst’ and has been commonly employed as a ‘benchmark’ for photocatalysts. It has been also demonstrated that in several reactions, this mixed-phase titania exhibited a higher photoactivity than pure anatase. More than thousand papers have been issued on the photocatalytic reactions involving Degussa P25 TiO_2 since 1990 [10, 12, 13].

1.2. Surface chemistry: Chemical groups on the surface of TiO_2

On the surface of solid TiO_2 , Ti exists under two forms. Ti is either bonded to a hydroxyl group, Ti-OH, or to an oxygen atom, Ti-O-Ti. The presence of the former Ti-OH groups permits the grafting and the interaction of different species with TiO_2 , such as in the case of grafting surface modifying agents like organosilanes. Yet, Ti-O-Ti bridges can exhibit certain reactivity as it can be activated under certain conditions. Assessing the nature and the distribution of the metal-oxide bonds (M-O, Ti-O) and the amount of physisorbed water on the metal oxide allow to characterize the surface of titania. In general, on the surface of the metal oxides, several types of oxygen functions exist. The main functions are described in this context below and in Fig. 3 [14, 15]

- Isolated/free Titanol groups, $\equiv\text{Ti}-\text{OH}$: the titanium atom interacts through three covalent bonds with the core oxygen atoms and with a surface hydroxyl in a fourth bond.
- Geminal titanol groups, $=\text{Ti}(\text{OH})_2$: the titanium atom interacts through two covalent bonds with the core oxygen atoms and with two surface hydroxyl in additional two bonds.
- Vicinal titanol groups: two different titanium atoms are linked to two hydroxyl functions that are sufficiently close to interact by hydrogen bonds.
- Titoxane groups or Ti-O-Ti bridges: two titanium atoms are connected together by an oxygen atom on the surface.

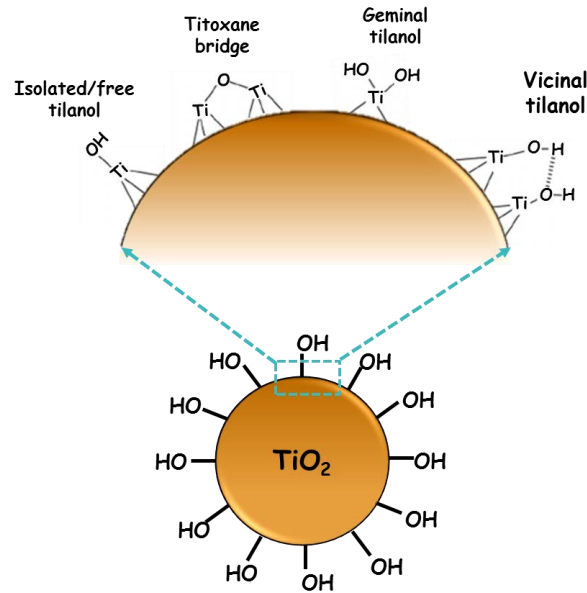


Fig. 3: Different surface groups of titanium. Reproduced from [15].

The pH of the medium greatly influences the surface charge of the titanium dioxide (**Fig. 4**). As the pH changes, between acidic and basic, the charge of the surface of titania passes through a point of zero charge (PZC). The PZC represents the pH at which the surface charge of the metal oxide becomes nul. As the nanoparticles become chargeless, their tendency to aggregate is at its maximum. The charge of the TiO₂ NPs becomes equal to zero at a pH between 6 and 7 (PZC = 6-7).

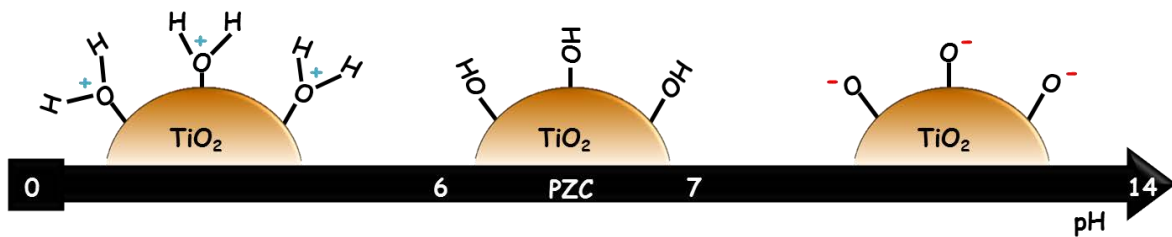
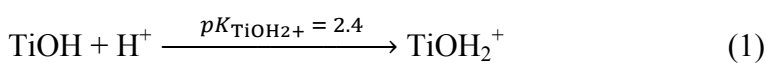


Fig. 4: Schematic presentation of the variation of the surface charge of TiO₂ as a function of pH.

In contrary to the point of zero charge, in both acidic (< 6) and basic (> 7) conditions, the surface hydroxyl groups carry a positive and a negative charge, respectively (**Fig. 4**). The surface charge is controlled by the following reactions [14, 16]:



1.3. Different applications of TiO₂

TiO₂ in all its nanostructural forms such as nanoparticles, nanowires, nanorods, nanotubes, nanofibers and nanowhiskers (Fig. 5) has been extensively used in a wide range of applications (Fig. 6) [17].

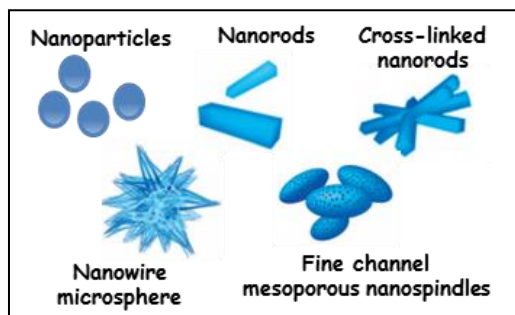


Fig. 5: Different nanostructural forms of TiO₂ [18].

In its nanoparticle form, TiO₂ has been ranked by the National Nanotechnology Initiative of America as one of the most globally manufactured nanoparticles [3]. The employment of TiO₂ in the industrial domain is fundamental. About 80% of TiO₂ in all its forms, especially the nanoparticle one, is extensively used in the manufacture of varnishes, plastics, rubber, papers and paints. TiO₂ is used as an ingredient in the development of sunscreen lotions, inks, toothpastes, cosmetics, cleaning merchandises, food products as in food coloring, and car materials. Besides, TiO₂ is also globally useful as white pigment in paints, catalyst supports, adsorbents, filters and as a dielectric and coating material [3, 19, 20]. One of the other important applications of this material is photocatalysis. Basically, in 1972, under UV light irradiation, TiO₂ electrode has been proved to be efficient in the photocatalytic water splitting. Since then, TiO₂ gained the spotlight as a significant photoactive candidate [7, 21]. It has been manufactured and used industrially in wide-ranging photocatalytic applications. Those applications include solar energy conversion, photocatalytic water splitting, photovoltaic cells, photosynthesis, electrochromic devices, self-cleaning glasses, photo-induced super hydrophilicity and photocatalytic anti-bacterial domain. Most importantly, TiO₂ possess photocatalytic self-cleaning properties, thus it has been broadly functional in the remediation techniques used to solve environmental issues. The environmental cleaning systems embrace the photocatalytic degradation of pollutants especially the organic matters in wastewater, the disposal of air contaminants and the decomposition of carbonic acid gas [2, 3, 17, 19–23].

Besides being active in the environmental applications, TiO₂ also gained an interest in the disinfection and the medical sections. In addition to the various advantageous properties, the outstanding photocatalytic efficiency of TiO₂ under UV excitation makes it attractive for other domains especially for the cancer treatment. In the recent years, TiO₂ NPs are functional in the field of phototherapy of malignant cells. It has been considered as a prospective photosensitizing agent for anti-cancerous PDT. This is due to its unique phototoxic effect under illumination. Moreover, titania

can also be competent in applications related to genetic engineering, for instance using TiO_2 as a nucleic acid endonuclease. Such titania-based systems can easily be tuned to suit other biomedical applications mainly for drug delivery, cell imaging and biological analysis [17, 20, 21, 24].

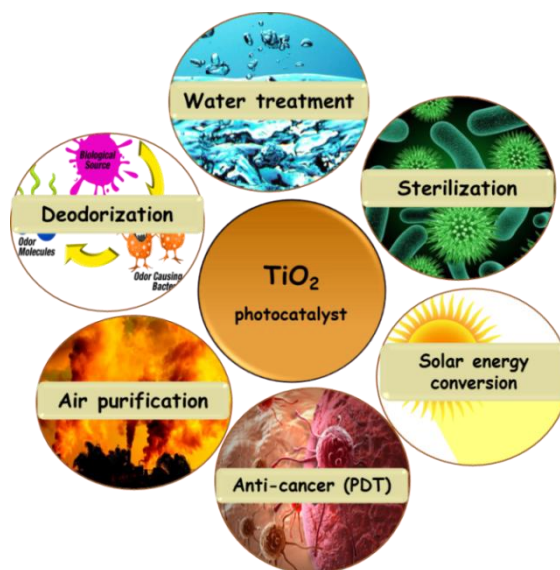
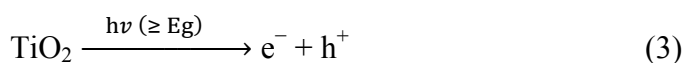


Fig. 6: Different applications involving TiO_2 photocatalyst.

1.4. Photoreactivity of TiO_2 and the production of reactive oxygen species (ROS)

As already mentioned TiO_2 possesses a wide band gap. Under ultraviolet illumination (280-400 nm) corresponding to energies between 3.10-4.43 eV that are equal to or exceed the energy of the band gap of nanoscaled TiO_2 semiconductor, the latter absorbs the photon. Consequently, an electron-hole (e^- , h^+) pair is photogenerated as an electron (e^-) is excited from the valence band (VB) of TiO_2 and occupies the conduction band (CB) leaving a positively charged hole (h^+) in the former (**Fig. 7**).

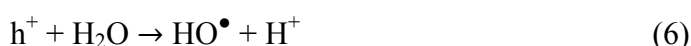


In the literature, it is described (**Fig. 7**) that the photogenerated electrons and holes ‘walk randomly’ towards the surface of the metal oxide where they get trapped. The formed electron-hole pairs are strong redox systems. However, the redox properties of those electrons and holes can be suppressed by their recombination (steps a and b in **Fig. 7**). They might recombine at trapping sites either at the surface or at the bulk with a heat release arising in the second case. The trapped electrons (e^-_{tr}) in the conduction band are good reduction mediators (+0.5 to -1.5 V vs. NHE), thus they interact with the electron acceptors, which are usually molecular oxygen pre-adsorbed on the

surface to TiO_2 , creating adsorbed superoxide anions ($\text{O}_2^{\bullet-}$) through photoreduction reactions (step c in Fig. 7).



As for the surface-trapped positive holes (h^+) (+1.0 to +3.5 V vs. NHE), they react with donor molecules which are usually pre-adsorbed HO^- and H_2O molecules through photooxidation reactions. Those reactions produce hydroxyl radicals (HO^\bullet) (step d in Fig. 7)



When the species are strongly adsorbed on the surface of the TiO_2 semiconductor, back-reactions can occur between the hole and the reduced acceptor molecules, and between the electron and the oxidized donor species after the charge transfer [25, 26]. It is noteworthy to mention that the quantity of ROS produced upon the UV illumination of the TiO_2 semiconductor seems to basically rely on the morphology and the size of the nanoparticles (*TiO2 ROS*).

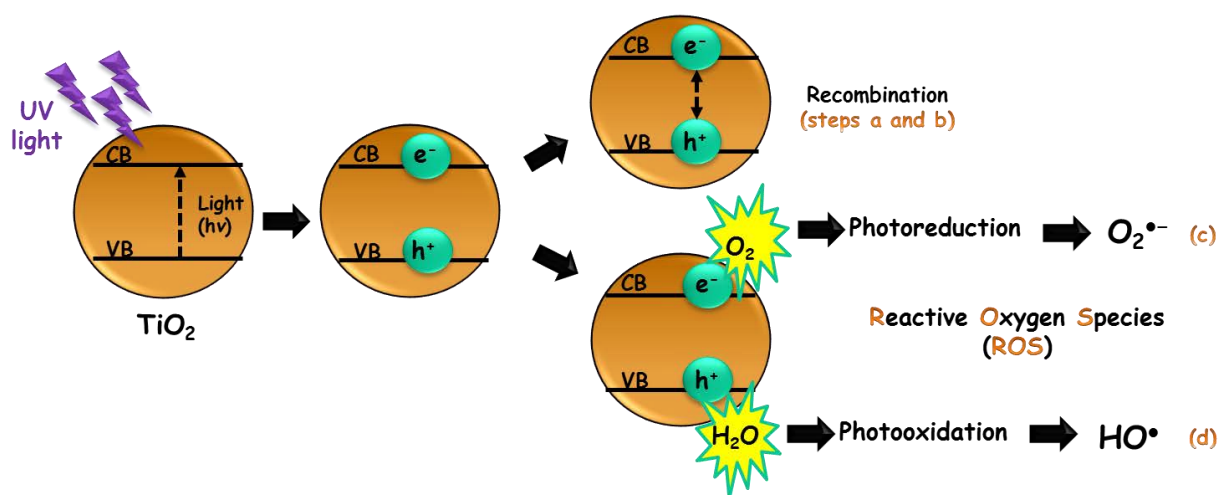


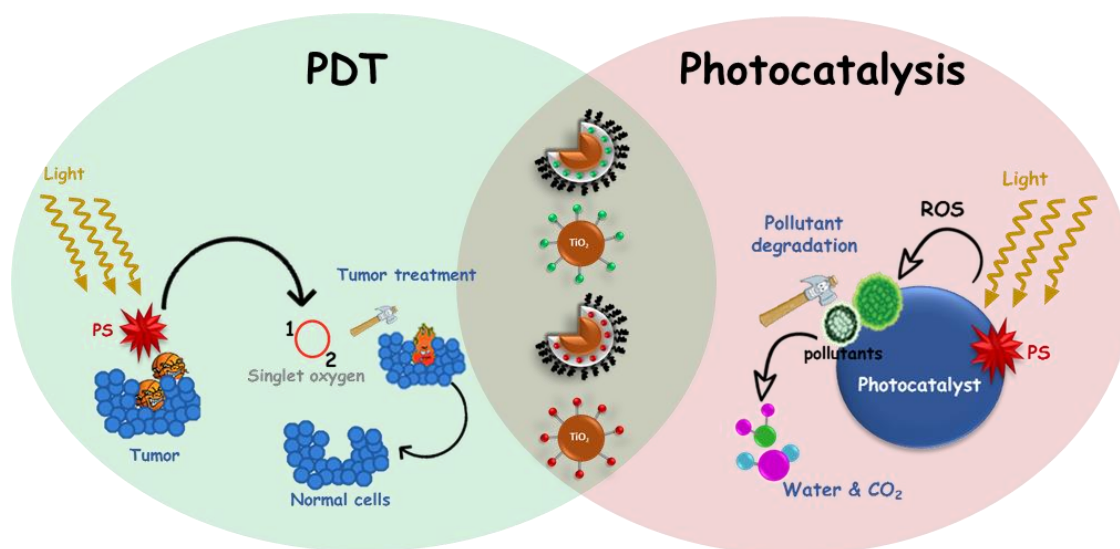
Fig. 7: The photoreactivity of TiO_2 under UV illumination: the fate of the generated ROS.

Reproduced from [2, 9].

The ROS elaborated from excited TiO_2 include the positively charged holes, either trapped or free, HO^\bullet and $\text{O}_2^{\bullet-}$, in addition to singlet oxygen ${}^1\text{O}_2$ produced in some cases (eq. 8) [27]. Alternatively, those radicals may also react to produce toxic hydrogen peroxide (H_2O_2) (eq. 7) [28].

The great photoactivity of TiO_2 in the wide range of applications especially the photocatalytic ones comprising the photodegradation and mineralization of almost all organic and polymeric constituents, microbial eradication is ascribed to the photoactivity of those species in the photocatalytic applications and its higher cytotoxic effect in terms of cells viability [27]. Those radicals also paved the way for applications targeting bacteria and viruses as the ROS are capable of reacting with the carbon in their cell walls [28]. The elaborated radicals and active species are adsorbed on the surface of the semiconductor, where the photocatalytic reactions occur onto or at the closest borders to this surface. It has been also shown that under UV illumination anatase form of TiO_2 is capable of elaborating more ROS than the rutile one. This might explain the former's superior activity in the photocatalytic applications and its higher cytotoxic effect in terms of cells viability [27].

This work targets on the use of modified TiO_2 in two applications which are the photocatalytic degradation of pollutants in water and the anti-cancer PDT (Scheme 1). On this basis, the two following sections (2 and 3) will shed light on those two applications and the involvement of TiO_2 in both of them.



Scheme 1: Illustration of the objective of the work.

2. Photocatalysis

2.1. Water pollution issue

Observed from space, the Earth seems like a 'magnificent blue marble'. This is due to the fact that over two thirds of the surface of this planet is water-covered leaving beneath a third as land. Water in its 'liquid form' exists as oceans, seas, rivers, lakes, ground water, etc. Humanity is witnessing a growth in the populations and life demands accompanied with a huge evolution in the

industrial, technological, medical, and agricultural sections. Such human activities are mostly the reason behind the decrease in the water quality as they are more and more pressurizing the aquatic resources of this planet. This poses the problem of water pollution [29, 30].

Water pollution is defined as the indirect and direct disposal or introduction of substances into the water to an extent that they threaten the human, animals including marine creatures and the whole ecosystem. Nature has its share in the water pollution problem through soil erosion and volcanic eruptions for example. However, human activities are the ever-leading source of the deteriorated water quality. This is achieved through the daily discharge of wastes from industrial, medical, pharmaceutical, municipal, residential and agricultural sources into the aquatic bodies (Fig. 8) [29–32]. Two million tons of industrial, agrarian and sewage waste are disposed into the water over the world every day [33]. Developing countries are the pioneer in the industrial advancement; however 70 % of their non-treated industrial refuses are discharged into the waterways [34]. On this basis, the treatment of wastewater and the degradation of liquid pollutants became the concern and the core of the studies of many researchers. This urges to seek for a practical, economical, energy-conserving and ecofriendly ‘green’ method [35].

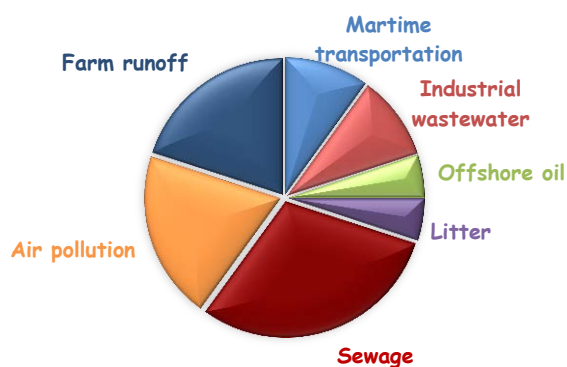


Fig. 8: The different types of pollutant sources entering the oceans [36].

2.2. Wastewater treatment methods

Various technologies and methods have been long-used for the treatment of polluted water. Conventional biological methods have been employed for the removal of wastewater toxic elements and molecules. Chemical coagulation/sedimentation is also used as the main process to discard suspended solids mainly natural particles such as clays and natural organic matter through the addition of coagulants that alter the electrostatic state of pollutants. For enhancing the efficiency of the removal of pollutants, other processes such as particle adsorption and sunlight photolysis can assist during this process. In addition, other common strategies include the removal of pollutants by adsorption on activated carbons. Besides, chlorination can contribute by the degradation of organic waste products through the oxidation of free chlorine. Chemical oxidation technologies and

advanced oxidation processes (AOPs) were also introduced and gained much spotlight. The chemical oxidation technologies include the employment of H_2O_2 and ozonation that are capable of oxidizing micropollutants either by a direct reaction with ozone or indirectly after formation of HO^\bullet . The advanced oxidation processes encompass cavitation, Fenton's process and photocatalysis [37].

Advanced oxidation processes are based on the formation of adequate quantities of highly reactive HO^\bullet capable of oxidizing a wide compass of water effluents especially the toxic organic ones. Those radicals can attack the aromatic rings of the organic pollutants degrading them into intermediate products and finally mineralizing them into water and CO_2 . AOPs display higher rates of pollutants' degradation as compared to the chemical oxidation methods due to the contribution of the highly reactive free radicals [37, 38].

Fenton process is the reaction occurring between the iron ions and H_2O_2 while photocatalysis is the oxidation of the pollutants requiring the utilization of a source of light that can be either UV, near UV or solar accompanied with the presence of a semiconductor catalyst (Fig. 9) [37].

- $\text{H}_2\text{O}_2/\text{Fe}^{2+}$	(Fenton)	- $\text{TiO}_2/\text{h}\nu/\text{O}_2$	(Photocatalysis)
- $\text{H}_2\text{O}_2/\text{Fe}^{3+}$	(Fenton-like)	- $\text{O}_3/\text{H}_2\text{O}_2$	
- $\text{H}_2\text{O}_2/\text{Fe}^{2+}(\text{Fe}^{3+})/\text{UV}$	(Photo-assisted Fenton)	- O_3/UV	
- $\text{H}_2\text{O}_2/\text{Fe}^{3+}$ - Oxalate		- $\text{H}_2\text{O}_2/\text{UV}$	
- $\text{Mn}^{2+}/\text{Oxalic acid}/\text{Ozone}$			

Fig. 9: Advanced oxidation processes [38].

2.3. Photocatalytic wastewater treatment

Catalysis, in general, is the acceleration in the rate of a chemical reaction owing to the participation of a substance termed catalyst. The catalytic processes are sub-divided into homogeneous and heterogeneous. In homogeneous catalysis, both the catalytic substance and the reactants form a monophasic solution. However, the heterogeneous photocatalysis is polyphasic since it involves a solid catalyst that forms a different phase than the reactants [39]. In photocatalysis, the substance is generally termed 'photocatalyst' and is capable of absorbing light at certain wavelengths [25].

Photocatalysis involves the use of photogenerated holes and electrons to initiate reactions described as 'back-to-back' or 'short-circuited' photoelectrochemical and electrochemical reactions. In the domain of water depollution, photocatalysis gains much attention. This is due to the capability of photocatalysis to achieve a complete degradation and further mineralization of a huge amount of organic species and bacteria at ambient pressure and temperature [37]. Photocatalysis presents a good alternative to the other methods since it does not involve the use of any oxidant, generates a lot

of highly reactive radicals and is relatively cheap as it utilizes only light which is inexpensive and accessible [40].

2.3.1. The use of semiconductors in photocatalysis

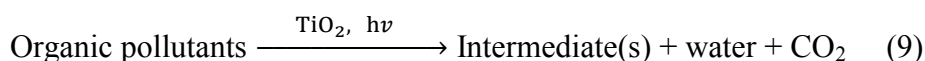
Nanostructured semiconductors are often employed as photocatalysts in the photodegradation applications of a broad variety of organic pollutants due to their outstanding physicochemical and optical characteristics. In addition, photo-activated semiconductors are considered attractive for the photocatalytic applications due to their unique electronic structure holding a vacant CB and an occupied VB. Chalcogenides are materials embracing as a minimum one chalcogen anion (Se^{2-} , S^{2-} , O^{2-} , etc.) bonded to at least one positively charged element. Those might be crystalline or amorphous; however, they are basically semiconductors and own a band gap ranging between 1 and 3 eV. Oxide chalcogenides mainly TiO_2 , ZnO , Fe_2O_3 , CeO_2 , ZrO_2 , MoO_3 and WO_3 in addition to sulfides including ZnS , CdS , etc., are frequently used as photocatalysts [4, 25, 41].

2.3.2. TiO_2 semiconductor in photocatalysis

TiO_2 is one of the most used and most efficient semiconductors in the photocatalytic decomposition of pollutants. TiO_2 is commercially accessible, easily synthesized and the dynamic phase-support interface boosts the photoactivity. Moreover, TiO_2 can be used in dispersion or fixed onto a substrate such as glass, activated carbon, inorganic materials, etc. for constant re-use [4, 10, 42].

Nano-scaled TiO_2 are characterized by a larger efficient surface area than bulk TiO_2 , light absorption is improved as the light band-gap is expanded and the rate of photoreduction is also improved. Nanosized TiO_2 induces an increase in the density of the surface photo-generated carriers. The absorption of H_2O and HO^- onto the surface of TiO_2 nanoparticles is enhanced by the elevated surface-volume ratio (A_0). Those properties of TiO_2 nanoparticles prompt more efficient photocatalytic reactions of increased rates [2, 6]. The photo-activation of TiO_2 as it absorbs a light of an energy exceeding that of the band gap and the production of ROS such as HO^\bullet , $\text{O}_2^{\bullet-}$, HOO^\bullet and H_2O_2 are thoroughly described in section 1.4.

In the photocatalytic system involving TiO_2 , the photo-generated holes and electrons and the ROS interact with the pollutants adsorbed on the surface of TiO_2 causing their degradation [25].



The overall photocatalytic reaction is schemed and detailed with all the steps involved [43] in

Fig. 10.

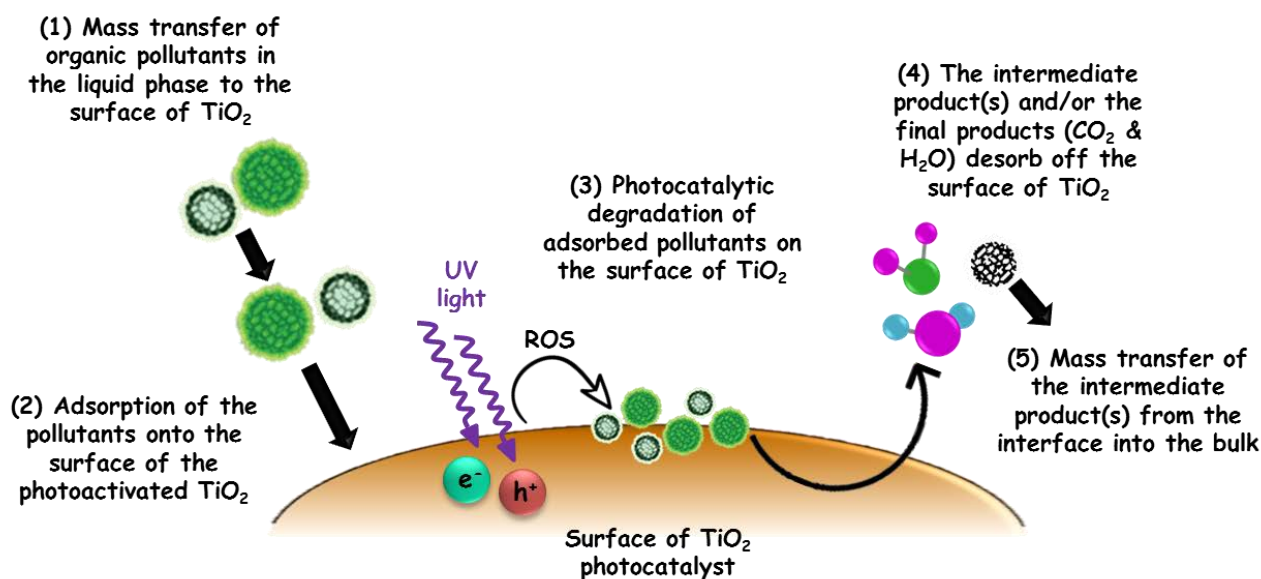


Fig. 10: The steps in photocatalytic reactions on heterogeneous TiO_2 catalyst.

For a photocatalytic reaction to be effectual, the photocatalyst should be capable of producing charge carriers (holes and electrons) with long lifetimes and a good rate of charge transfer on the interface leading to an efficient generation of ROS. Thus, the formation and the effective exploitation of the ROS is the key aspect in photocatalysis. Moreover, pollutants can adsorb onto the surface of the photocatalyst in different amounts depending on various factors especially the pH of the solution relative to their pKa. The concentration of the adsorbed pollutant affects the rate of its degradation. The more the pollutants adsorb onto the surface of TiO_2 , the more efficient the degradation is [25].

2.3.3. Limitations of TiO_2 in photocatalysis

Despite the advantageous properties of TiO_2 NPs that makes it this popular in the domain of photocatalytic water treatment, yet those NPs face some drawbacks that may limit their application and hence their commercialization.

The main drawback of TiO_2 limiting its practical applications is the fact that its photoactivity is restricted to the ultraviolet region of light ($\lambda \leq 390$ nm). This property is due to the wide band gap of TiO_2 in its anatase and rutile forms requiring an excitation wavelength belonging to the UV region. On condition that the solar light reaching the surface of the earth comprises about 5% UV

light, $\sim 43\%$ visible light and $\sim 52\%$ infrared, it appears that, for a practical photocatalytic application, a low proficiency in solar light exploitation by TiO_2 is witnessed. On this basis, the practical use and commercialization of TiO_2 -based photocatalysts for the environmental applications is undesirably affected [5, 9, 26, 44, 45].

As already mentioned, the separation, surface-trapping and interaction of the photogenerated holes and electrons with pre-adsorbed water and oxygen molecules to produce ROS are responsible for the high photoactivity of TiO_2 [2]. Adversely, the low separation efficiency and the fast and relatively high recombination rate of those charge carriers can largely diminish the photoactivity of TiO_2 and its efficient utilization in various practical applications especially the photocatalytic degradation of pollutants [23, 46]. In this recombination process, the excited electron occupying the CB of the semiconductor tends to fall back to the VB and recombines with the hole radiatively or non-radiatively. Defects, impurities and some crystal imperfections at the level of the bulk and/or the surface prompt the recombination of the charge carriers which can happen on the surface of the semiconductor or in the bulk. The recombination of electrons and holes happens in 10 ns, however, the elaborated electrons trapped by the surface through the reduction of Ti^{4+} ions to Ti^{3+} occurs in 30 ps [25].

The second application using TiO_2 to highlight on is the anti-cancer PDT. The following section (section 3) presents the bibliographic background of PDT and the involvement of TiO_2 in this domain.

3. Photodynamic therapy (PDT)

3.1. About cancer

In low-, middle- and high-income countries (LMIC, HIC) cancer is the leading source of mortality. Humanity is struggling with this burden which is expected to ever-increase over the next decades on both levels of cancer incidence and mortality due to the ongoing global demographic and epidemiologic transitions as elucidated by the WHO on 2011. A worldwide survey on the spread of cancer performed in 2012 showed the occurrence of about 14.1 million new cancer cases and 8.2 million cancer deaths. Lung (1.82 million), breast (1.67 million) and colorectal (1.36 million) cancers were the most commonly diagnosed cancer types. However, lung (1.6 million), liver (745000) and stomach (723000) cancers contribute to the highest cancer death rates (Fig. 11). In the 50 countries selected for this survey, higher incidence and mortality rates were revealed for men as compared to women [47, 48].

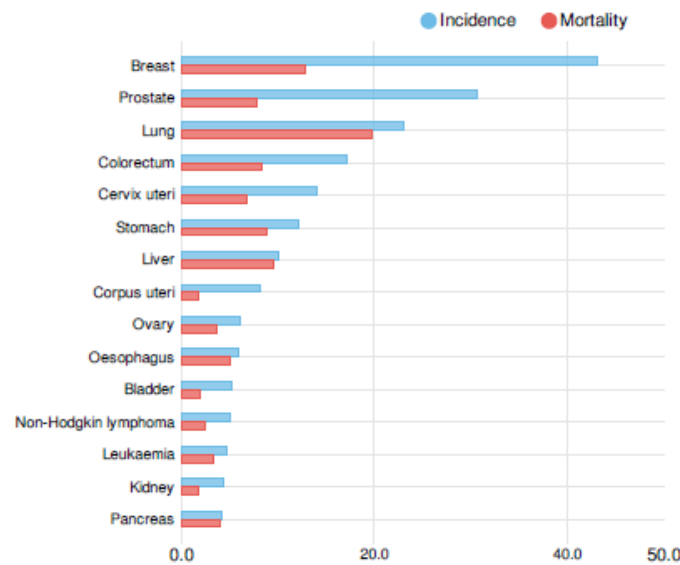


Fig. 11: Estimated age-standardized rate (world) incidence and mortality rates in both sexes. Data sources and methods: Incidence and mortality (Method: Population weighed average of the area-specific rates applied to the 2012 area population), prevalence (Sum of area-specific prevalent cases [49]).

In a more recent estimation performed by the American Cancer Society (ACS) (Fig. 12), it appears that there is an increase in the estimated new cancer cases and deaths. Prostate cancer in men and breast cancer in women witness the highest share of the new incidences [50].

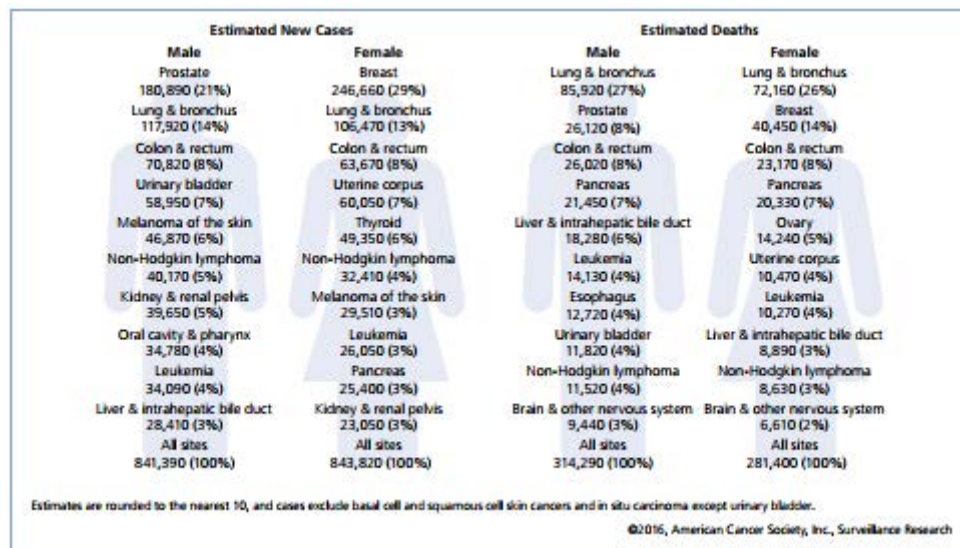


Fig. 12: Leading Sites of New Cancer Cases and Deaths – 2016 Estimates [50].

Scientists categorized cancer as a genetic disease that holds a distinct identity as compared to the most other genetic diseases. In general, the inherited genetic diseases are caused by genetic alterations, termed mutations, at the level of the germ cells (sperms, eggs). However, cancer, mostly, is caused by somatic not germ line mutations (Fig. 13) [51, 52].

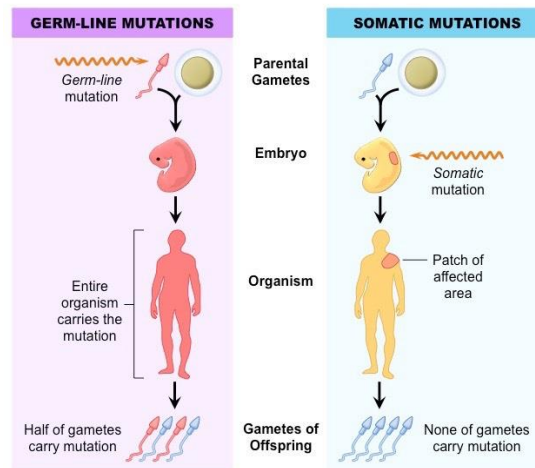


Fig. 13: Difference between germ-line and somatic mutations [53].

The occurring alterations hit the genes that govern the cell functioning particularly in terms of growth and division. Those mutations can be derived to the progeny of the mutated mother cell through cellular division. Besides this difference, tumorigenesis is a multi-step process arising from the accumulation of three to seven ‘hits’ and not a single mutation. Each single mutation induces an uncontrolled, disorganized and fast multiplication of the cells that evolve into a malignant neoplastic population holding some degree of autonomy [51, 52].

Generally, all types of tumors share a common feature, which is the successful breaking of the cellular defense against cancer. This target is achieved through inducing six massive mutations in the cell physiology. **Fig. 14** summarizes those physiologic alterations that collectively contribute to turning a normal cell into a malignant cancerous one [54].

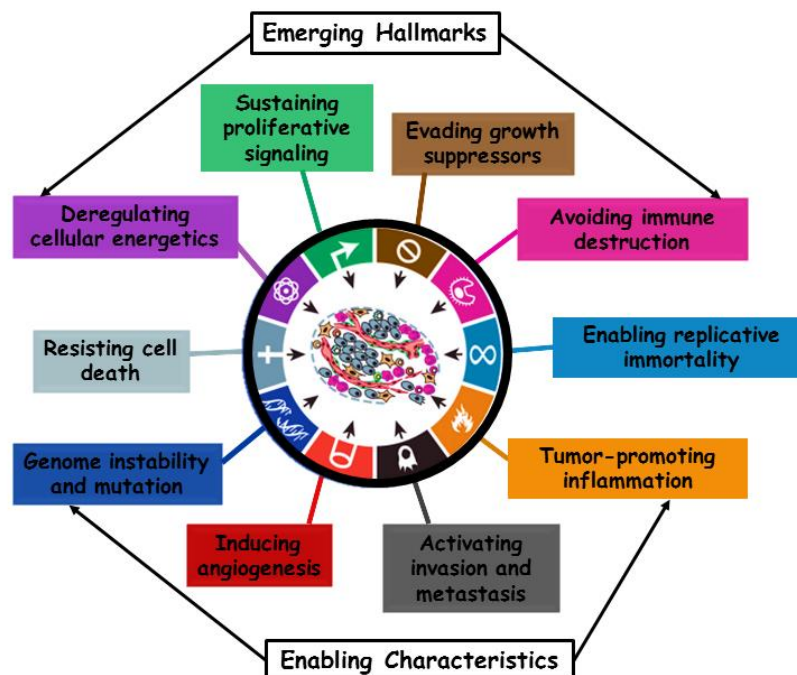


Fig. 14: The six essential physiological mutations exhibited by cancer [54].

Neoplasia emerges due to mutations in the cancer susceptibility genes in the mother cell and its progenies (**Fig. 15**). Those genes are categorized into gatekeepers, caretakers and landscapers, in which each group functions differently in the cell. Gatekeepers, including tumor-suppressor genes (TSG) and oncogenes, are responsible for the direct regulation of the cellular proliferation. Massive mutations in those genes suppress their capability of obstructing the tumor growth or inducing the cell death. Caretaker genes are in charge of preserving the genomic integrity of the cells in which their alteration can indirectly generate tumorigenesis [55, 56].

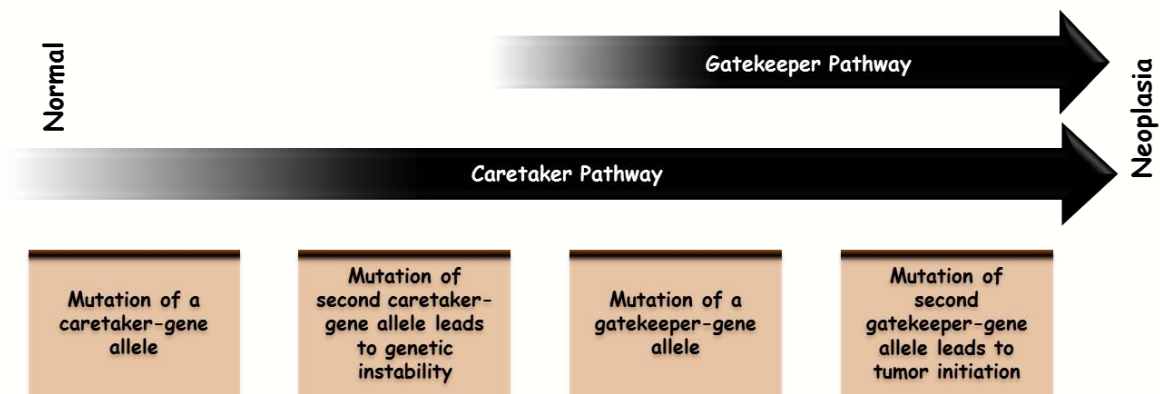


Fig. 15: Pathways to neoplasia [56].

Malignant human cancers evolve in a multistage process starting from the initiation of the tumor, its progression, up until angiogenesis and metastasis [55].

3.2. Angiogenesis: Growth of tumors

Angiogenesis is the physiologic process that fulfills the need of the tumor for vascular supply. This process is driven by interactions between vascular endothelial growth factors (VEGF) and three high-affinity VEGF receptors (VEGFR) (**Fig. 16**). Tumorigenesis is accompanied by high rates of cancer cells proliferation on the expense of the cellular nutrients and the healthy cells. Although it is a tough survivor, the growing tumor will face nutritional deficiency. A necrotic core inside the tumor is formed, which comprises the interior dead cancer cells with blocked access to the nutrients unlike the surviving edge-localized ones. Tumor cells takeover healthy ones and replace them as it attains a diffusion-limited maximal mass (2 mm^3). For the cancer cells to function and for the tumor to expand beyond the maximal size, acquiring the essential construction blocks such as oxygen, glucose and amino acids is a vital demand. Thus, the tumor tends to form new blood vessels called neovessels to get the access to the circulation and fuel the tumor that develops into an organ itself [57, 58].

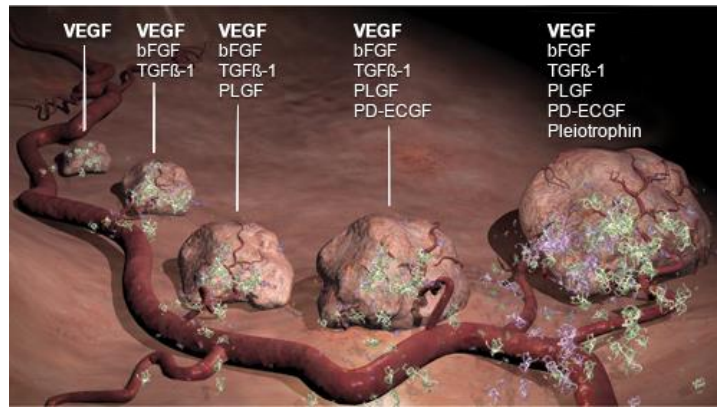


Fig. 16: Tumor angiogenesis [59].

3.3. Metastasis

Among cancer patients, metastasis is the main cause of mortality. Metastases are autonomously grown tumors created by motile malignant cancer cells that tend to shed and depart from the primary tumor, invade the surrounding tissues and implant secondary tumors in distant locations (Fig. 17) [60].

For metastasis to efficiently occur, various hurdles should be beaten. Circulating cancer cells should permeate through distant tissues and organs, escape the immune resistances, accustom to supportive niches, persist as dormant tumor-starting seeds and finally take over the host organ and replace it. Those obstacles limit the efficiency of the metastatic colonization, yet, once metastasis have been initiated, the condition cannot be effectively redeemed by the existing therapies [61, 62].

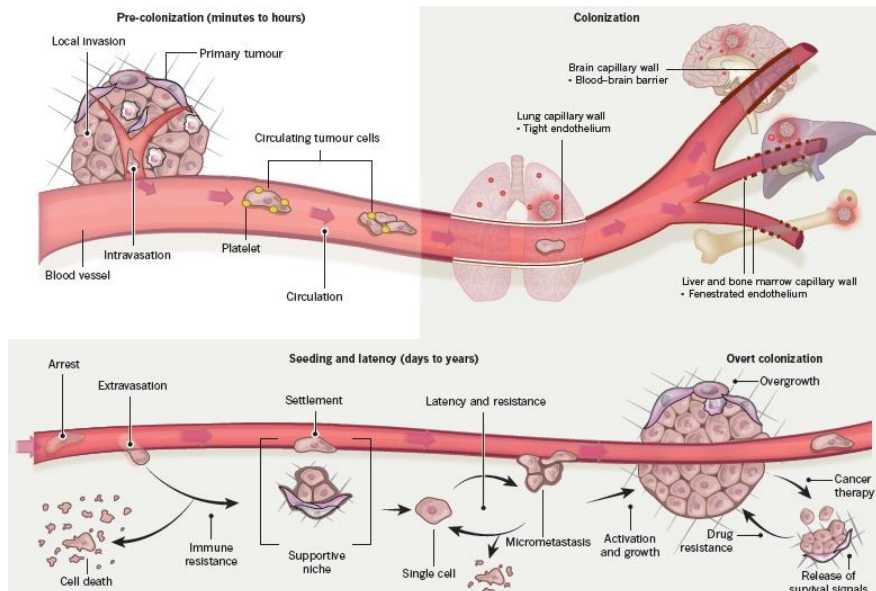


Fig. 17: The multiple steps and restrictive holdups involved in the metastatic colonization [61].

3.4. Types of cancer treatments

There exist various anti-cancer treatment methods. The intersection point that underlie the effectiveness of those treatments is their ability to destroy the cancer cells while leaving the healthy cells intact or at least distressing as few as possible of them. The choice of the most suitable treatment method depends on the type of cancer and its stage. Among the existing treatment approaches are the surgical resection, radiotherapy, medical treatments (chemotherapy, immunotherapy, and hormonotherapy), stem cell transplant, PDT, etc. It is noteworthy to mention the recent evolution in the field of the targeted-cancer treatment methods. A better knowledge in the molecular drivers of cancer paved the way for the development of ‘molecularly targeted therapies’ which are gaining interest [63].

3.4.1. Surgical resection

The surgical resection is the oldest and yet the main cancer therapeutic approach. It is an effectual treatment for various types of cancers especially in the case of small and localized solid tumors detected in their early stages. As a definition, the surgery is a resection operation used to eliminate the tumor with sometimes a margin of the healthy tissue surrounding it for guaranteeing the total removal of the malignant cells. Depending on the type and status of the tumor, surgery may be used against the tumor as the only treatment or can be combined with other conventional treatments such as chemotherapy and radiotherapy [64].

3.4.2. Radiotherapy

Radiotherapy is one of the most essential and well-known treatments for many cancer types. This therapeutic method is efficient in shrinking tumors, eradicating cancer cells and obstructing their proliferation and survival. Radiotherapy uses high-energy ionizing radiation comprising X-rays, gamma rays, electron beams and heavy ions, or charged particles to provoke damage in the DNA inside the cell. The disruption of the DNA triggers the activation of the DNA damage response (DDR) which leads to a temporary or permanent blockage of the cell cycle and a probable cell death depending on the degree of damage. Normal cells beneath the tumor may be adversely affected with the radiation; however most of them manage to restore their function. Beside the direct cytotoxic effect induced by the radiation therapy on the cellular DNA, it is recently evidenced that this therapy can also prompt, at least in part, some immune-stimulating functions capable of targeting radiation survivor cancer cells. This immune effect is demonstrated by the liberation of damage-associated molecular patterns (DAMPs) and tumor associated antigens (TAAs), together initiating a destructive immune response against the immunosuppressive tumor-supporting tissue or organ. Over half of people struggling with cancer receive radiation therapy either alone or with a prior or post contribution of chemotherapy or surgery [63, 65].

3.4.3. Chemotherapy

Chemotherapy involves the use of certain drugs to eradicate cancer cells. This therapeutic technique autonomously works on blocking the cells' growth and division by inducing a disorder in the DNA replication and cellular metabolism. Due to the fast uncontrollable multiplication of cancer cells as compared to healthy ones, it is assumed that the malignant cells are more susceptible to the actions of these drugs than the healthy ones. Besides acting on the DNA and the cellular division, it is recently suggested that the conventional chemotherapies may function through mechanisms that stimulate the immune system; *i.e.* 'immune-stimulatory'.

Since the early of the 20th century, chemotherapy was introduced as a treatment for cancer. **Fig. 18** describes briefly the history of chemotherapy since 1900. It is noteworthy to mention that Paul Ehrlich, the famous German chemist, was the one to term 'chemotherapy' and define it in the early 1900s. He greatly contributed to the field of cancer drug development. However, it was the four World War II-related programs and the effects of the drugs that emerged from them that inspired and motivated the foundation of the 'Cancer Chemotherapy National Service Center' in 1955 [66].

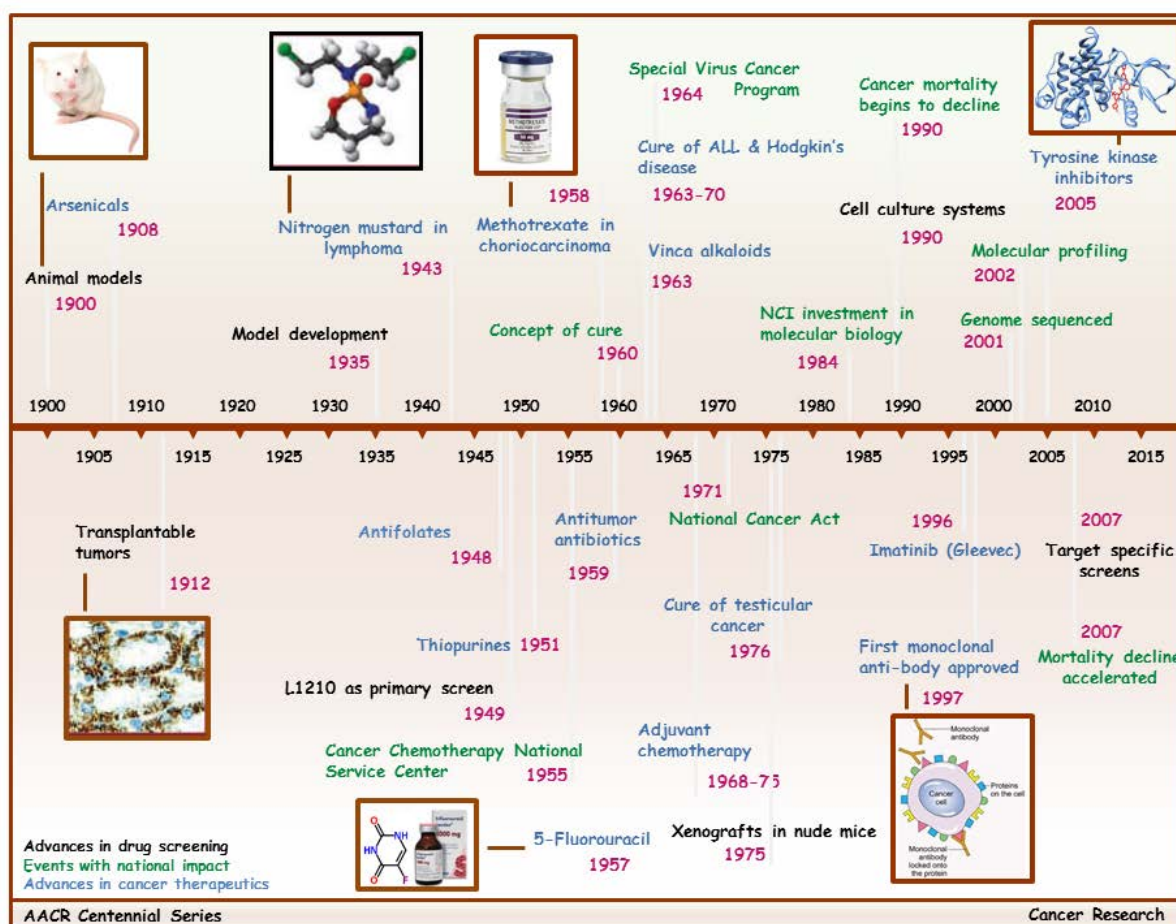


Fig. 18: Key advances in the history of cancer chemotherapy. Reproduced from [66].

Until 1960s, the surgical resection and the radiation therapy predominated the arena of anti-tumor treatments. Hindered by micrometastases, which was not appreciated and targeted as

nowadays, treatment with those methods provided static cure rates of about 33%. This outcome was in parallel with new researches concluding that a combination of chemo- with other therapies can contribute to a more effective destruction of several advanced tumor types.

The side effects of chemotherapy, mainly the lack of selective cell destruction, provoked more research efforts to overcome those obstacles. Advancement in this field, since 25 years ago, improved the survival rates in cancer patients [63, 66].

3.4.4. Immunotherapy

With its name derived from its targeted part of the human's body, immunotherapy is the treatment aiming to fight cancer, or other diseases, using certain part of the host's immune system. This goal can be achieved either by stimulating an enhanced self-immune response to fight tumor cells or through introducing certain synthesized immune system elements. Monoclonal antibodies, immune checkpoint drugs, cancer vaccines are the most common types of anti-cancer immunotherapy. This treatment modality is becoming of more importance in this field in the last few decades as newer immune treatment types are being investigated [67].

3.5. Anti-cancer PDT

3.5.1. Historical background on PDT

The idea of using light as a therapeutic tool against several diseases is not new. In fact, over 4000 years BC, ancient Egyptians used to ingest Amni Majus plant and expose themselves to sunlight as a successful healing method from a skin disorder disease called vitiligo. The successful effect attained was due to the active component in the plant; psoralen. Psoralen is currently engaged worldwide in the treatment of psoriasis (Fig. 19) [68].

As a definition, PDT is a minimally invasive treatment modality against malignant diseases. PDT can be used as an alternative to conventional cancer therapies. Moreover, PDT can also be combined with other therapeutic methods, as it can be applied before or after any of those treatments [69, 70].

Highlighting briefly on the historical background of PDT, in the early 1900s, Oscar Raab, Niels Finsen, Tappeiner and Jesionek contributed to this field through various studies and discoveries concerning the application of PDT against different diseases and the use of PSs (eosin). Yet, the first human PDT trial was performed by Meyer-Betz on himself using hematoporphyrin. In 1978, Dougherty succeeded to treat skin cancer using haematoporphyrin derivative (HpD) in patients, thus he was the first to elicit a modern demonstration of PDT as a technique for killing cancer cells (Fig. 19) [71].

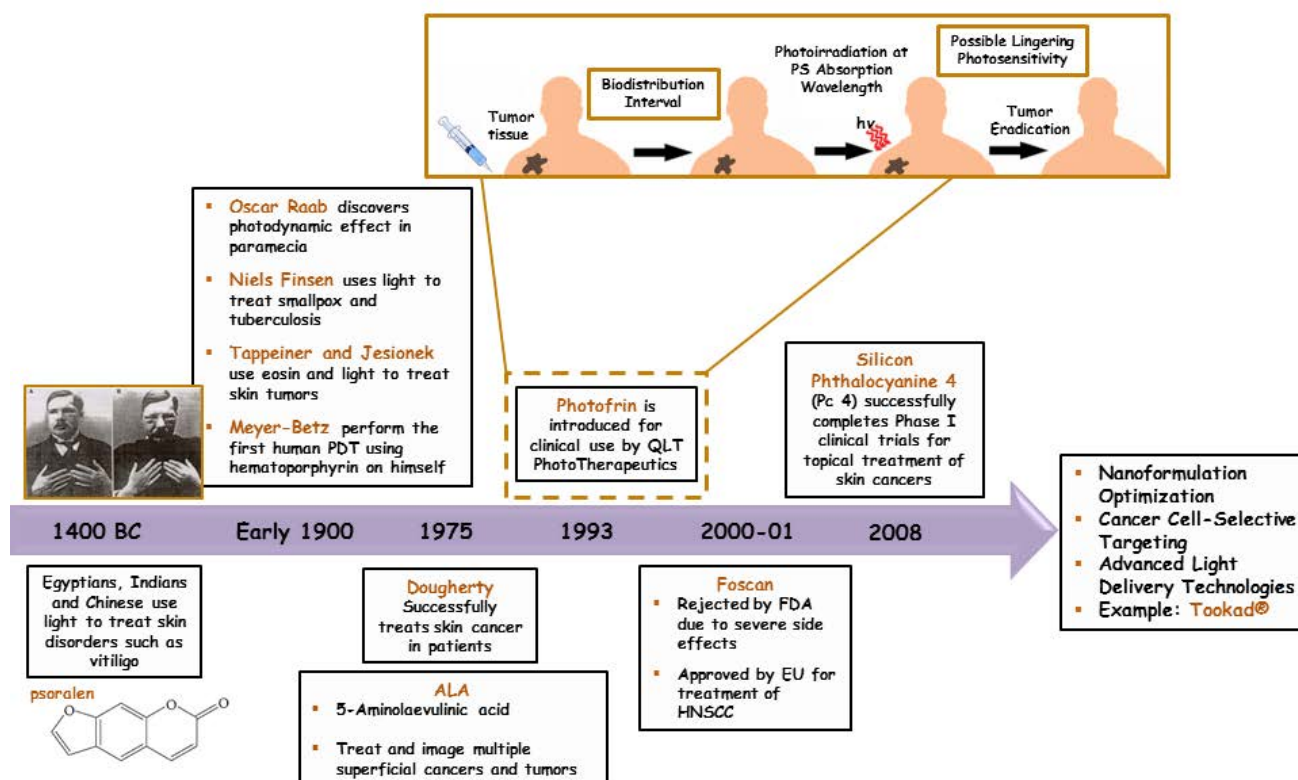


Fig. 19: The history, development and current state-of-the-art for PDT. Reproduced from reference [71].

In general, surgery, radiotherapy and chemotherapy proved to be efficient in the fight against cancer. However, resection surgeries are invalidating for patients and the latter two lack selectivity and jeopardize the viability of healthy tissues [70]. On this basis, PDT embraces various advantages as compared to those conventional treatments. PDT is a minimally invasive, precisely targeted, can be repeated several times onto the same location, and as compared to other locoregional therapeutic methods the rates and durability of the obtained response is as good or even better. PDT does not involve any tissue heating or connective tissues damaging. Additionally, from a cosmetic point, PDT leaves behind little or even no scarring. This reason made PDT suitable for the lesions of the skin, neck, head and oral cavity. The curative potential of PDT has been acknowledged about 25 years ago and it started to be used in clinics since 1993. PDT treats premalignant mucosal dysplasia and carcinoma-*in situ*, gastrointestinal cancers (oesophageal), lung cancer, etc [69, 72]. PDT is used in dermatology (actinic keratoses (KA)) [73], ophthalmology (Age-related macular degeneration, Visudyne®) [74], urology (prostate cancer, Tookad®) [75], gastroenterology (superficial cancers of the esophagus, dysplasia and inoperable cholangiocarcinoma) [76], gynecology (high grade cervical dysplastic lesions) [77], neurosurgery (glioblastoma) [78], pulmonology (malignant pleural mesothelioma (MPM)) [79], etc. A drawback of PDT is that only cancers that are reachable to the light can be treated.

3.5.2. Overview on PDT: Definition and principle

The anti-cancer PDT is a technique of treatment based on the association of a light-sensitive molecule termed photosensitizer (PS) capable of internalizing into the malignant cells and a locally focused light of a wavelength suitable for activating the PS. The exogenous PS and the received light photochemically react together. The light-activated PS interacts with the molecular oxygen to generate $^1\text{O}_2$ and ROS. The produced ROS are cytotoxic agents, hence, they can induce biochemical disorder in the cell when they toxically interact with the cellular components. Those localized photophysical processes and photochemical reactions lie at the core of PDT. Thus light, PS and oxygen are the essential building blocks of PDT. Separately, those components exhibit no toxicity and the absence of any of them, suppresses the photodynamic effect. It is the combination of all three at a well-regulated dosimetry of both light and PS that govern the overall efficiency of PDT [68, 70, 72, 80].

PDT is a multi-stage operation. This operation is illustrated in Fig. 20 and it comprises the following steps [68, 69]:

1. In the absence of light, the drug (PS) is systemically or topically delivered into the body of the patient and is left for a certain period of time (drug-light interval),
2. The drug selectively accumulates into the malignant neoplastic tissue or stays in the vessels,
3. Light at a proper wavelength and dose is strictly illuminated on the diseased tissue for specific time,
4. The tumor is eradicated as the cancer cells are damaged through induced apoptosis or necrosis (Fig. 22).

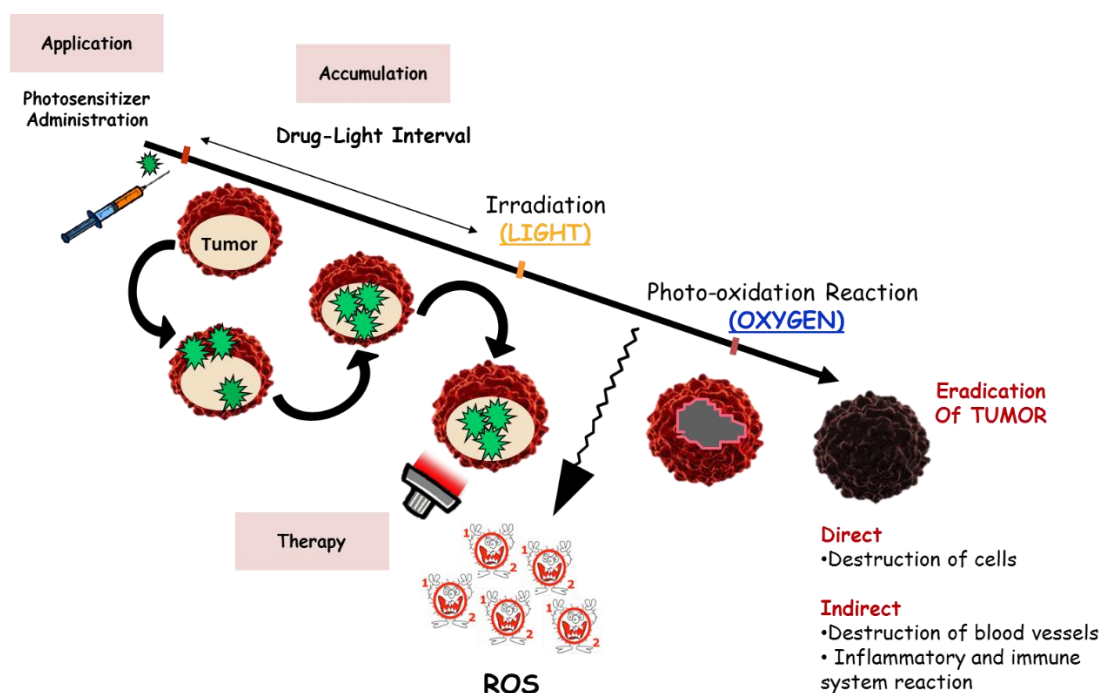


Fig. 20: The multi-stage process of PDT.

3.5.3. Mechanism of action

The photochemical and photophysical processes involved in PDT have been extensively studied and are illustrated by Perrin-Jablonski's diagram and the equations (eq. 10-23) (Fig. 21) [80, 81]. Irradiating at a wavelength appropriate to the PS enables this light-sensitive molecule to absorb a photon ($h\nu$) and get excited from its ground state (S_0) to singlet excited state (S_n) (eq. 10). The excited PS relaxes then to the lowest excited singlet state of the sensitizer S_1 (eq. 11), followed by i) conversion to the sensitizer triplet state (T_1) generated by the non-radiative intersystem crossing process (eq. 14), ii) back to S_0 with emission of light (Fluorescence) (eq. 12), iii) back to S_0 without emission of light (eq. 13). The lifetime of the triplet state (μs) is longer than that of the singlet state S_1 (ns). The interaction of the PS in its T_1 excited state with the other nearby molecules is enhanced with longer T_1 lifetimes. Consequently, the T_1 state is capable of reacting in two ways, classified as Types I and II mechanisms. Type I mechanism produces ROS such as HO^\bullet , $\text{O}_2^{\bullet-}$, HOO^\bullet , etc. This mechanism is based on hydrogen-atom abstraction or electron-transfer reactions usually occurring between the PS in its excited T_1 state and another substrate; *i.e.* a solvent, another PS, etc. Type I reaction is favored in polar and oxygen-deficient environments and the produced ROS are highly reactive and can induce a great damage to the cell. Type II photochemical mechanism involves a process of energy transfer mediated by the collision between the excited PS and oxygen in its triplet state. This energy transfer generates $^1\text{O}_2$ which is believed to be the major cytotoxic agent responsible for photobiological activity. Both Types I and II reactions can occur concurrently with a ratio relying on the type of the PS and its surrounding environment. Both reactions exhibit analogous oxidative damage [68, 80–82].

In vivo, any cellular constituent, such as nuclei, mitochondria, cytoplasmic membrane, lysosomes, etc., represents a target for the cytotoxic ROS. The neoplastic cell is eradicated either *via* apoptosis or *via* necrosis (Fig. 22) depending on the attacked target, the type and amount of the used PS and the light dose implemented. PDT has been recognized to cause cell death by prompting inflammations and some tumor-specific immune responses [80].

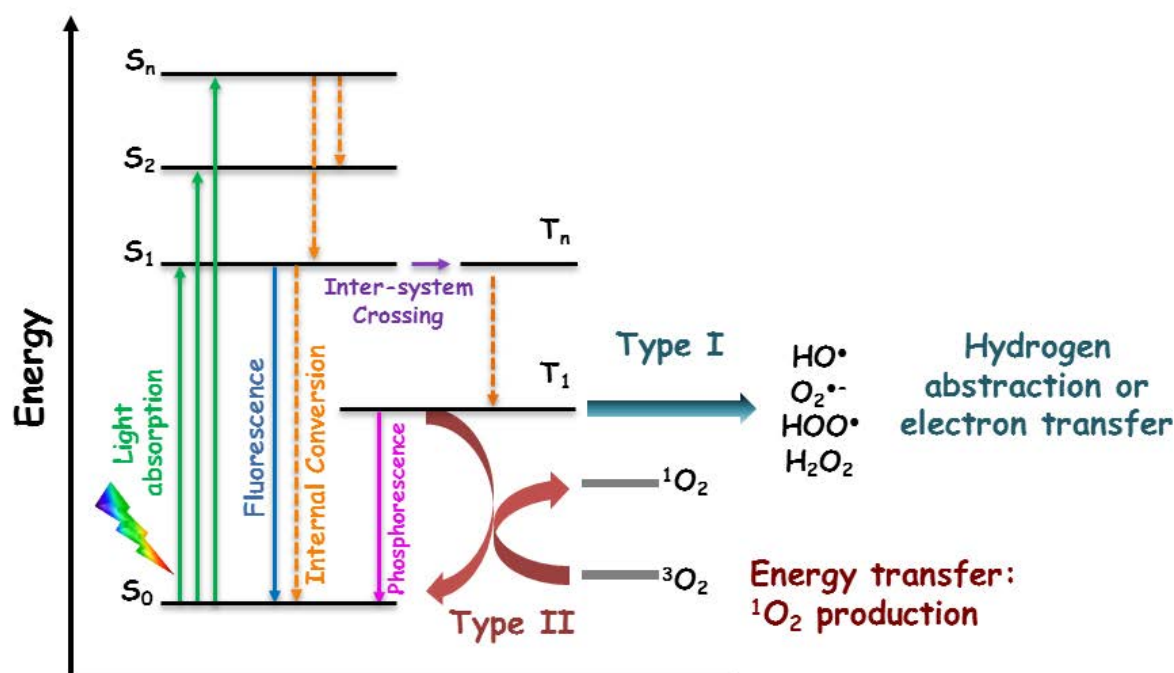
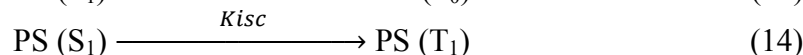
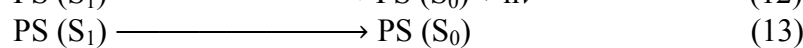
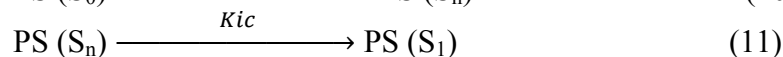
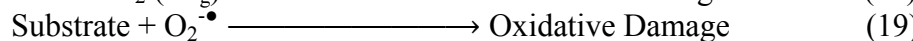
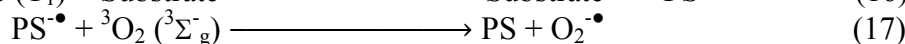


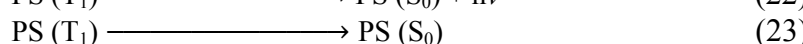
Fig. 21: Modified Perrin-Jablonski's diagram illustrating the principle of PDT. Where S_0 , S_1 and T_1 are respectively, the singlet ground state, first excited singlet state and first excited triplet state of the PS. 3O_2 ($^3\Sigma_g^-$) and 1O_2 ($^1\Delta_g$) denote, respectively, to the ground triplet and excited singlet states of oxygen [80, 81].



Type I Photoprocess



Type II Photoprocess



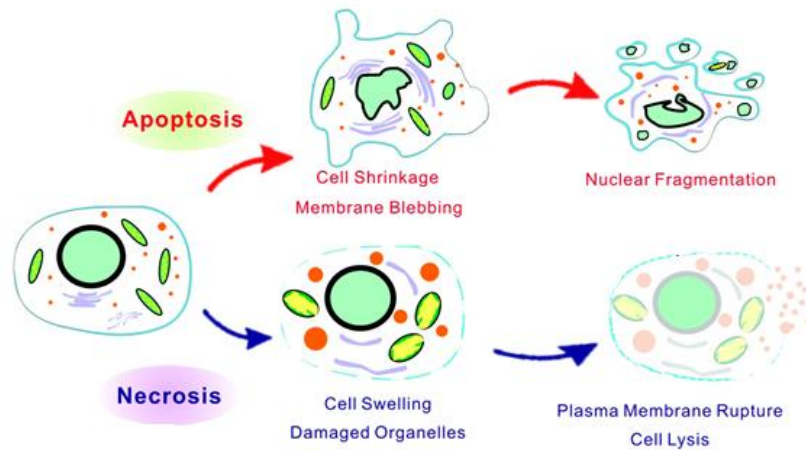


Fig. 22: Illustration of the apoptotic and necrotic cell death. Reproduced from [83].

3.5.4. Main components in PDT

For PDT to be better implemented in clinics there should exist a well-planned combination of a suitable light delivery system and an adequate concentration of the PS in the presence of molecular oxygen.

3.5.4.1. Light

Carrying the PDT treatment technique from the bench of the lab to the clinical practice required the development of new and more advanced light sources and light delivery devices.

The depth of the penetration of light into the tissue relies on the wavelength of the delivered light. **Fig. 23a** reveals that longer light wavelengths are capable to penetrate the tissue more efficiently. Hence, the penetration of the blue light (400-450 nm) into the tissue is superficial with < 1 mm depth, unlike orange light (590-620 nm) and red light (600-720 nm) penetrating about 1.5 and 3 mm deep, respectively. On this basis, treating deep tissue tumors requires a light source of high tissue-penetration capability mediated through proper light delivery devices capable of transferring light through interstitial and intra-tumoral tissues [71, 84].

Lasers are considered the most coherent light sources for PDT. The development of more advanced light delivery systems have been a challenge, those systems include Argon/dye lasers, Metal vapor lasers, KTP:YAG/dye lasers, Diode lasers, Nonlaser light sources, Fiber optic delivery devices, Cylindrical fibers, Balloon catheters and Lens fiberoptics. **Fig. 23b** shows the penetration depth in the tissues for various laser types used [84]. More recently, researchers are developing devices based on fibers and textiles; Woven-based light emitting fabric, for a more efficient, flexible, selective and homogeneous light transmittance (**Fig. 24**) [87].

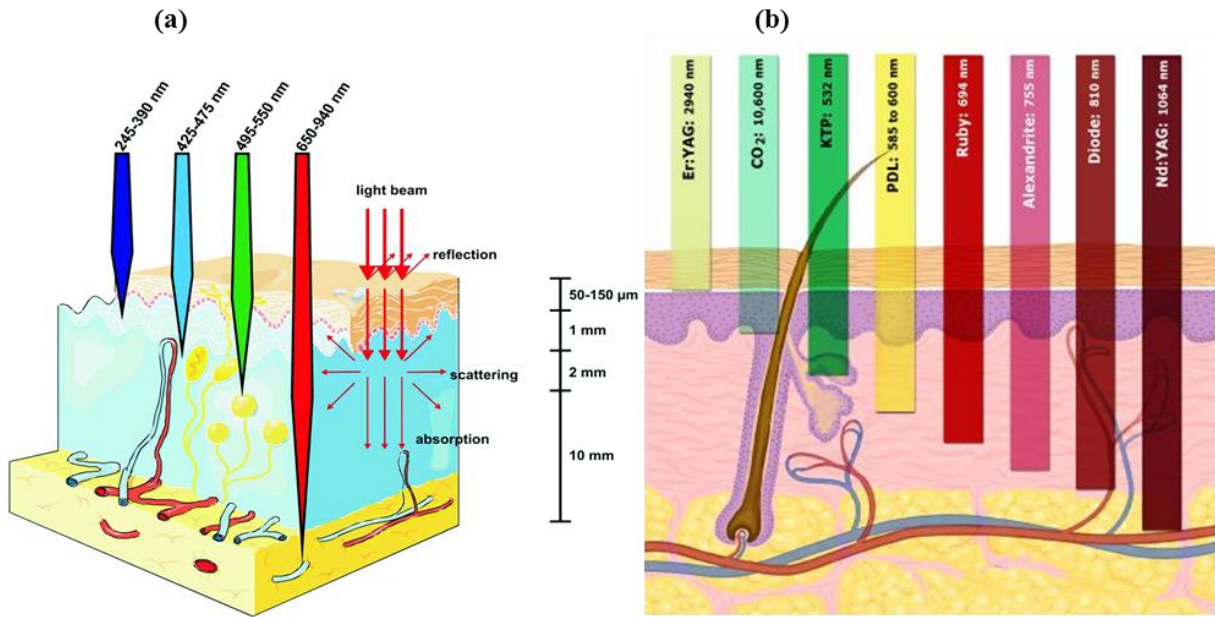


Fig. 23: The depth of light penetration into the tissues [85, 86].

In PDT, the term “phototherapeutic window” refers to the range of wavelengths mostly used in PDT which is between 650-850 nm. In general, this range is appropriate for exciting a wide series of PSs used for PDT and at the same time assures a maximum tissue penetration. However, the wavelength and type of light used depends on the type of cancer and the application. For example, treating skin cancers requires sunlight or blue light, while treating tumors in esophagus necessitates green light. Hence, optimizing an ideal light dosage that is strong enough to activate the PS and kill the neoplastic cells without damaging the healthy ones is compulsory [84].



Fig. 24: Example on tissue-based light emitting fabric [87].

3.5.4.2. Photosensitizers (PS)

The term photosensitizer (PS) describes the molecules or compounds that are proficient in absorbing the light at specific wavelengths and converting it into valuable energy. PSs can either occur naturally as in plants or synthesized. For a PS to be efficient in PDT, it should produce lethal cytotoxic agents that are the ROS [80].

In 1960, the first PS to attract the attention of the scientific society towards PDT was hematoporphyrin derivative (HpD), discovered and studied by Lipson and Schwartz at the Mayo Clinic. The development of Photofrin (porfimer sodium), which is a partially purified form of HpD belonging to the porphyrin family, boosted the chance of popularity of PDT as it was the first FDA approved PDT sensitizer.

An ideal PS in PDT should embrace the following properties [82, 88]:

- High absorption and extinction coefficients in the spectral region of the excitation light mostly but not always in the “phototherapeutic window” (680-800 nm) depending on the application
- Synthesizable from available precursors, easily reproduced and chemically pure with known chemical composition
- The efficacy of the PS relies on the photophysical characteristics of its lowest excited triplet state, thus this triplet state should possess a high quantum yield (> 0.4), long lifetime ($> 1 \mu\text{s}$) and of appropriate energy ($\geq 95 \text{ kJ mol}^{-1}$) allowing an efficient energy transfer to the oxygen in its ground state
- Effectively generates $^1\text{O}_2$ and/or other ROS
- Easily administrated into the patient’s body and shows good stability and solubility in the body’s tissue fluids
- Possessing a minimal dark toxicity (the PS and its metabolites)
- Effectively and selectively accumulating in the malignant tissues with a fast selective metabolism and/or clearance from the healthy tissues until reaching the optimum concentration in tumor tissues. Cancer tissues are characterized by a leaky vasculature and a poor lymphatic drainage, which normally helps in achieving this process. This fact lies behind the larger uptake of the intravenously delivered PS by malignant tissues as compared to healthy ones
- The PS should excrete from the patient’s body after finishing the treatment

PSs can be classified into various categories [89]:

- ***Organic dyes and aromatic hydrocarbons***

This category includes dyes such as rose bengal, eosin, and methylene blue which are very effective PSs (Fig. 25). Those PSs possess a proper energy of triplet states for the sensitization of oxygen. In addition, aromatic hydrocarbons such as biphenyls, quinones and anthraquinone derivatives are good PSs for $^1\text{O}_2$ production.

- ***Porphyrins and related photosensitizers***

Such as octaethylporphine, tetraphenylporphine, phthalocyanines, metallophthalocyanines, naphthalocyanines, chlorins, bacteriochlorins, texaphyrins, etc (Fig. 25). Those PSs are considered good candidates for the use in biological $^1\text{O}_2$ generation due to their occurrence in natural

systems. They are capable to absorb at several wavelengths in the UV-visible range. Their properties are tunable mainly through adding macrocycle substituents. High quantum yields can be attained due to the long-lived triplet states of many porphyrins.

- ***Transition metal complexes***

Many of the ruthenium-based PSs are efficient $^1\text{O}_2$ producers, especially Ru(II) tris-bipyridine, $[\text{Ru}(\text{bpy})_3]^{2+}$. Many others have been complexed with platinum and palladium where Pt(II) revealed superior efficiency as compared to Pd(II).

- ***Semiconductors***

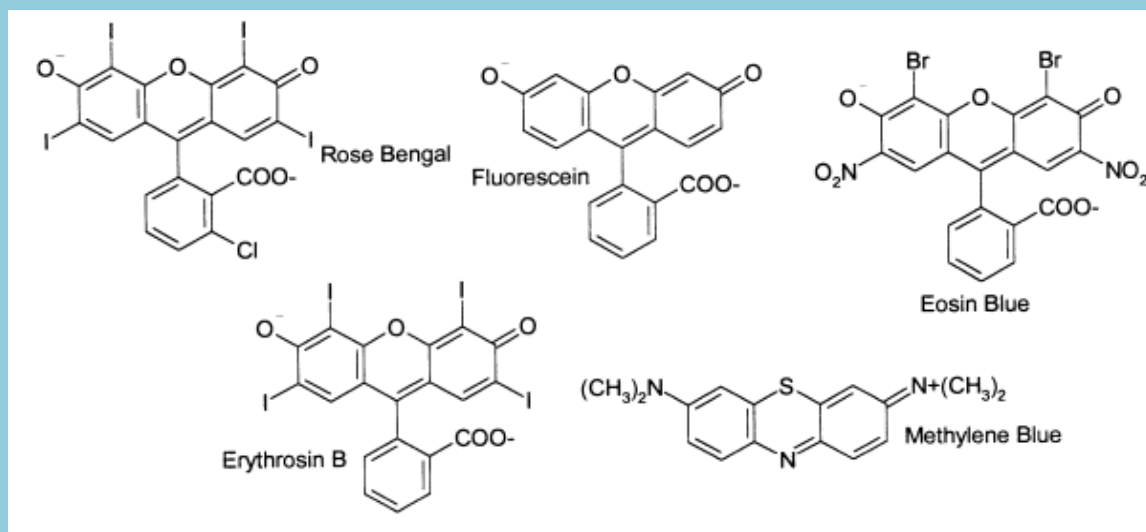
Such as TiO_2 and ZnO that induce photosensitized production of $^1\text{O}_2$ under UV irradiation.

- ***Immobilized heterogeneous photosensitizers***

They are attained by fixing the PS on a substrate. Those PSs possess several advantages, where their ability of recovery and reuse in water purification make it economically and environmentally feasible in addition to their ease of isolation from the reaction products in case of photochemical synthesis. These advantages compensate the disadvantage of reduced quantum yields of these PSs.

Concerning PDT, to date, there exist four generations of PSs. The first generation of PSs comprises those of natural sources, namely, hematoporphyrin derivative (HpD) and its famous purified version; Photofrin[®]. Although proved a good PDT efficacy, those PSs encounter certain inconveniences that confine their application (see **Table 2**). Thus, seeking for a second generation PSs designed to minimize the adverse drawbacks of their ancestors was the strategic plan towards more developed PDT applications. The second generation PSs constitute of an extensive group of new PSs employed in a broad range of applications (**Table 3**) [68, 82].

Organic dyes and aromatic hydrocarbons (non-porphyrinic photosensitizers)



Porphyrioid photosensitizers

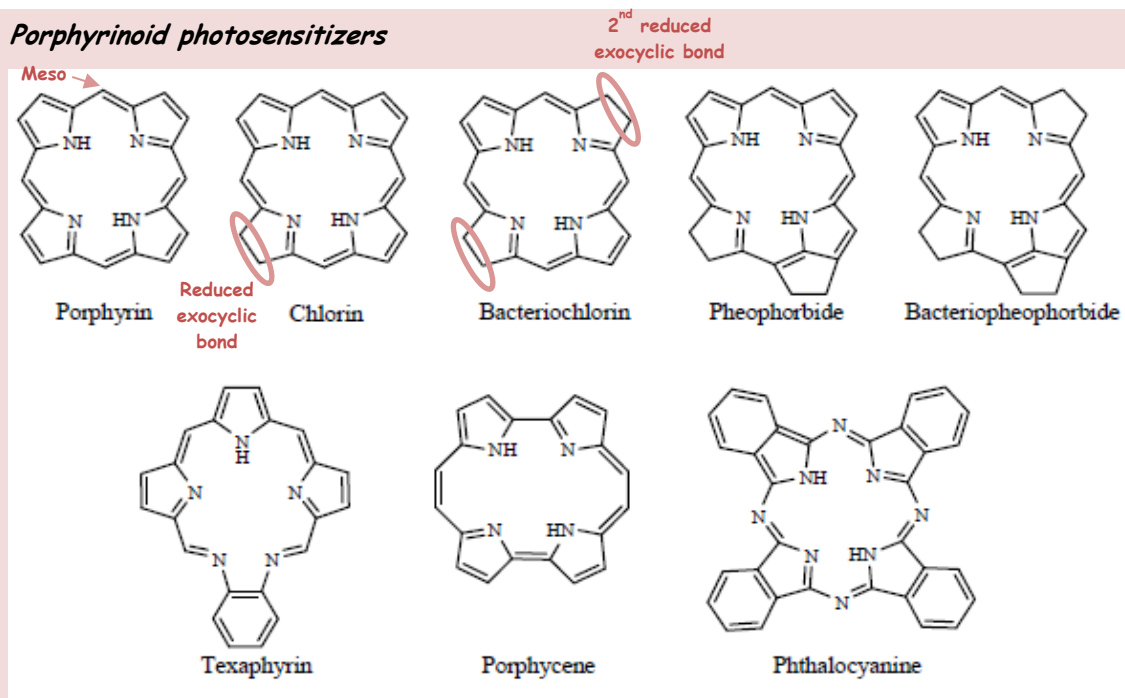
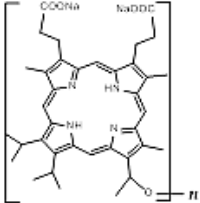
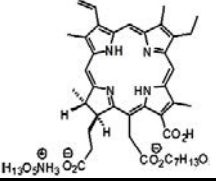


Fig. 25: Different types of photosensitizers.

Table 2: First generation PSs.

	PS	Application	Disadvantages	Scheme
First generation: Haematoporphyrin derivative (HpD) and its analogues	Photofrin® (Porfimer Sodium)	First FDA approved PDT sensitizer, safe, high Φ_{Δ} Approved for: Canada (1993)—bladder cancer, USA (1995)—esophageal Cancer, USA (1998)—lung cancer, USA (2003)—Barrett's esophagus, Japan—cervical cancer, Europe, Canada, Japan, USA, UK, endobroncheal cancer, extend to head, neck, abdominal, thoracic, brain, intestinal, skin, breast, and cervical cancer	Poor selectivity, only 0.1-3% of injected PS are found in tumor tissue Slow clearance from cutaneous tissue (~10 weeks), skin sensitivity Low absorption in the red (shallow light penetration)	 Photofrin
	Photogem®	Approved for use in clinical applications in Russia and Brazil		
	Photosan-3®	Approved for clinical use in the EU		

The second generation PSs for PDT are classified into six groups, mainly porphyrins and chlorins:

- Porphyrins

Porphyrin derivatives (**Fig. 25**) are a major class of PSs. Inspired by their vital biological roles in natural systems such as photosynthesis and oxygen transport, porphyrins paved their way into the medicinal field. It has been widely employed in arenas of fluorescence imaging to medications, etc. Porphyrins constitute of a group of naturally existing compounds characterized by an intensive purple color, from which their name was derived (porphura = purple in Greek language). Chlorophyll and heme, which are metalloporphyrins due to the presence of a metal occupying the center of their porphyrin ring, are the natural representatives of porphyrin. Porphyrins are tetrapyrrolic molecules with a heterocyclic core termed porphine (**Fig. 25, 26**) [90].

- Chlorins

Chlorins are chlorophyll derivatives which are also considered a major category of PSs evaluated for PDT. Generally, chlorophyll derivatives, especially chlorin e6 (Ce6) are good applicants for PDT, due to their better selectivity in microorganisms compared to mammalian cell, especially under low incubation times. Chlorins possess a chemical structure similar to chlorophyll. Compared to porphyrins, the structure of chlorins differs by a reduced exocyclic bond with the presence of two extra hydrogens in one pyrrole ring (**Fig. 25, 26**). This structural alteration lies behind the bathochromic red shift in the absorption band of chlorins [88, 91].

- Pheophorbides

Can be derived from chlorophyll and possess two extra hydrogens in one pyrrole unit (**Fig. 25**).

- Bacteriopheophorbides

Are analogous to bacteriochlorins in structure, however, they possess four more hydrogens than the corresponding porphyrins (Fig. 25). Their λ_{\max} is red-shifted to 740–800 nm (Fig. 26).

- Texaphyrins

A porphyrinoid analog with a pentaaza core (Fig. 25). It is water soluble. Texaphyrins absorb light at 732 nm.

- Phthalocyanines

It necessitates metal complex formation to display PDT characteristics since transition metals allow the occurrence of intersystem crossing. ($\lambda_{\max} \sim 670\text{--}700\text{ nm}$) (Fig. 25, 26) [88].

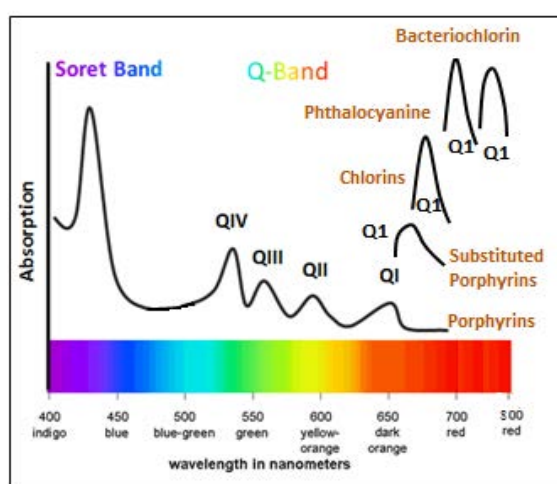


Fig. 26: Absorption spectra of different PSs [92].

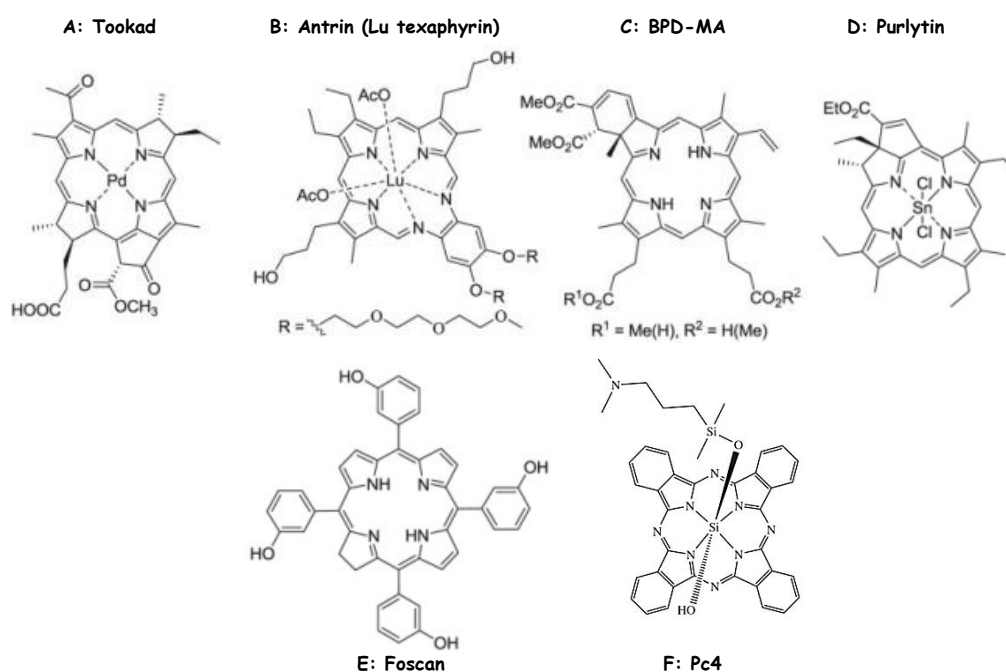


Fig. 27: Examples on second generation PSs.

Table 3: Second generation photosensitizers (see Fig. 27 for structures) [88].

Compound	Trademark	λ_{\max} (nm) ϵ_{\max} ($M^{-1} \text{ cm}^{-1}$)	Φ_{Δ} (solvent not mentioned)	Application (First approved)
Second Generation: Porphyrins				
5-Aminolevulinic acid (ALA)	Levulan	632 (5000)	0.56	USA (1999)—actinic keratosis
Methyl aminolevulinate (MAL)	Metvixia	-	-	USA (2004)—actinic keratosis
Hexaminolevulinate (HAL)	Cysview	-	-	USA (2010)—bladder cancer diagnosis
Second Generation: Chlorins				
Meta-tetra(hydroxyphenyl)chlorin (m-THPC)	Foscan	652 (35,000)	0.87	Europe-neck and head cancer
Tin ethyl etiopurpurin	Purlytin	664 (30,000)	-	Clinical trials—breast adenocarcinoma, basal cell carcinoma, Kaposi's sarcoma, age-related macular degeneration
N-aspartyl chlorin e6 (NPe6)	Laserphyrin, Litx	664 (40,000)	0.77	Japan (2003)-lung cancer
Second Generation: Pheophorbides				
2-(1-Hexyloxyethyl)-2-devinyl pyropheophorbide (HPPH)	Photochlor	665 (47,000)	-	Clinical trials—esophageal cancer, basal cell carcinoma, lung cancer, Barrett's esophagus
Second Generation: Bacteriopheophorbides				
Palladium bacteriopheophorbide (WST09)	Tookad	763 (88,000)	0.5	Clinical trials—prostate cancer
WST11	Stakel	-	-	Clinical trials—prostate cancer
Second Generation: Texaphyrins				
Motexafin lutetium (Lu-Tex)	Lutrin, Optrin, Antrin	732 (42,000)	-	Clinical trials—prostate cancer, age-related macular degeneration, breast cancer, cervical cancer, arterial disease
Second Generation: Phthalocyanines				
Aluminum phthalocyanine tetrasulfonate (AlPcS4)	Photosens	676 (200,000)	0.38	Russia (2001)—stomach, skin, lips, oral cavity, tongue, breast cancer
Silicon phthalocyanine (Pc4)	-	675 (200,000)	-	Clinical trials—actinic keratosis, Bowen's disease, skin cancer, mycosis fungoides
Third Generation: Visudyne (PS encapsulated into liposomes)				
Benzoporphyrin derivative monoacid ring A (BPD-MA)	Visudyne	689 (34,000)	0.84	USA (1999)—age-related macular degeneration

Various PS face hindrances in terms of the direct intravenous delivery into the blood flow due to their scarce solubility in aqueous media specifically at physiological pH. Thus, the development of a third generation of PSs to overcome this obstacle was necessary. Those are second generation PSs encapsulated into or conjugated to NPs, or attached carrier molecules to assure better targeting, recognition and selective accumulation into the tumor tissues. Those targeting molecules

include antibodies, peptides, LDLs, monosaccharides, polymers, polymeric nanoparticles, etc. It is noteworthy to mention that only Visudyne[®] is used for clinical applications. [93].

3.5.5. The use of nanoparticles in PDT

The use of NPs as vehicles for the efficient delivery of water-insoluble PSs is interesting due to the capability of the former to employ passive and active targeting strategies. Those strategies enhance the selective intracellular accumulation of the PSs in neoplastic cells while inducing no toxicity in healthy cells. Beside the PS, specific receptors or ligands can be bound to the NPs for better NP-cancer cell selective recognition and internalization.

NPs applicable in PDT for drug-delivery purposes are devices or systems that possess a size ranging from 3-200 nm (submicron-sized) and are synthesized on the basis of certain materials. Those NPs include (Figure 28, 30) [94, 95]:

- Dendrimers, polymeric nanoparticles or micelles (Polymeric)
- Liposomes (Lipidic)
- Viral NPs (Viruses)
- Nanotubes (Organometallics)
- Silicon or carbon materials
- Magnetic nanoparticles
- ...

NPs profit from their small size by retaining certain favorable and unique physicochemical and biological properties making them good candidates for biomedical applications. Those properties include the improved reactive area and the more facilitated uptake by the cells than other larger molecules and the capability to traverse the cell-tissue borders.

The conjugation of the drug (PS) to the nanoparticles can be achieved through adsorption, covalent linkage or encapsulation. The stable covalent bonding appears to be more advantageous over the other methods as it permits to control the amount of PS grafted onto the nanocarriers [94]

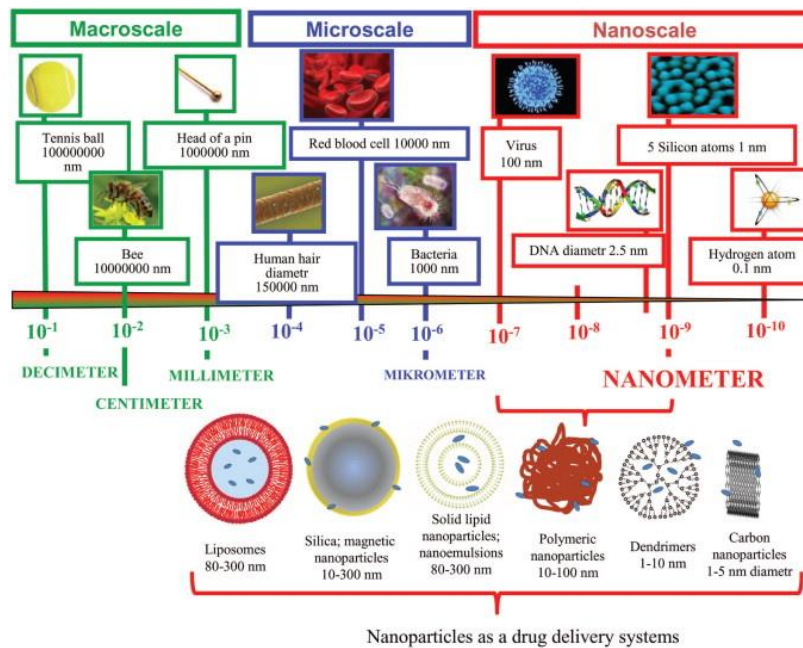


Fig. 28: Nanoparticle drug-delivery systems with respect to other scales [94].

As pre-mentioned, nanocarriers are capable of better cell-specific targeting through active or passive strategies (Fig. 29) [93]:

- **Active targeting**

Is achieved through the inclusion of a cell-specific recognition ligands, antibodies or low molecular ligands (folic acids, peptides) to the PS-NP conjugates. Such systems allow specific binding to cancer cells and are internalized through endocytosis. The manipulation of the physical stimuli such as the pH and temperature can also accomplish active targeting.

- **Passive targeting**

Tumors differ from normal cells by their leaky vasculature the fact that facilitates a targeted delivery of the anti-cancer agents. This is termed ‘enhanced permeation and retention (EPR)’ effect. EPR lies at the core of passive targeting. The NPs must satisfy the size and surface characteristics requirements for the EPR effect to take place.

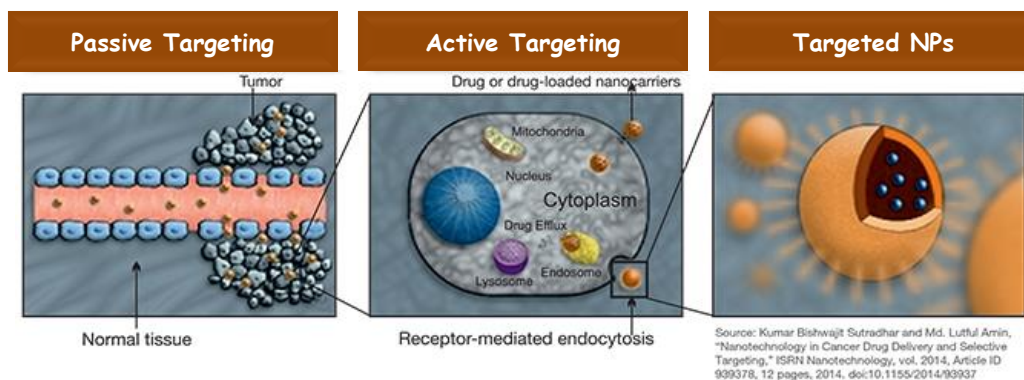
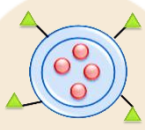


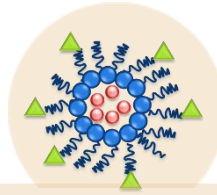
Fig. 29: Targeting tumor cells by nanoparticles [96].

Polymeric nanoparticles (polymer-drug conjugates)



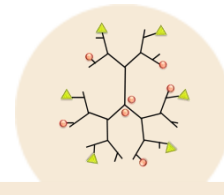
Polymers such as albumin, chitosan, and heparin occur naturally and have been a material of choice for the delivery of oligonucleotides, DNA, protein and drugs

Polymeric micelles



Hydrophobic core region: reservoir for hydrophobic drugs
Hydrophilic shell region: stabilizes the hydrophobic core and renders the polymers water-soluble

Dendrimers



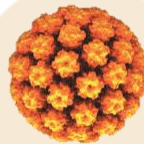
Composition: multiple highly branched monomers that emerge radially from the central core
Favorable properties: monodisperse size, modifiable surface functionality, water solubility, multivalency, and available internal cavity

Liposomes



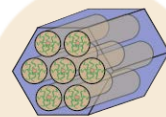
Spherical vesicles composed of phospholipids and steroids (e.g., cholesterol), bilayers, or other surfactants reported to increase the solubility of drugs and improve their pharmacokinetic properties

Viral based nanoparticles



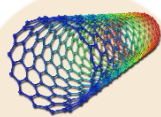
Ex: cowpea mosaic virus, cowpea chlorotic mottle virus, and bacteriophages: used in tissue targeting and drug delivery
Canine parvovirus: Natural affinity for receptors on cancer cells, such as transferrin receptors

Silica materials



Xerogels & mesoporous silica nanoparticles: used in controlled drug delivery systems
Advantages: biocompatibility, highly porous framework and an ease in terms of functionalization

Carbon nanotubes



Carbon cylinders

Applications: sensors for detecting DNA and protein, carriers to deliver vaccine or protein, etc.
Need to be modified since alone they're insoluble

Magnetic nanoparticles



Advantages: Easy handling with external magnet, possible active and passive targeting, MRI, enhanced uptake
Main disadvantages: formation of large aggregates

Fig. 30: The basic properties of the main types of drug nanocarriers used in PDT [94].

Our team developed multifunctional core-shell nanoparticles with a combined action in both magnetic resonance imaging (MRI) and Vascular-targeted PDT (VTP). Those actions were achieved thanks to the design of those nanoparticles that is composed of a gadolinium oxide (Gd_2O_3) functioning as a contrasting image for MRI, a hybrid shell carrying the targeting peptide for VTP, hydrophilic polyethylene glycol (PEG) and a covalently linked PS onto the matrix (**Fig. 31a**). Another interest of our team was the development of X-ray excitable nanoparticles. This therapeutic approach associates radiotherapy with the PDT principle for the treatment of deep tumors previously untreated by PDT. In this approach, the PS is linked to NPs containing Gd_2O_3 or Tb_2O_3 (**Fig. 31b**). Upon X-ray excitation (radiotherapy), the particles generate photons that induce photo-oxidation reactions of the coupled PS. It was demonstrated that upon X-ray illumination, the NPs emit scintillation or persistent luminescence that was capable of activating the PS once converted. Nanoparticles-PS systems containing scintillators ($BaFBr:Eu^{2+},Mn^{2+}$ and $LaF_3:Tb^{3+}$) is considered interesting since they are capable of generating a photodynamic effect after X-ray excitation [97, 98].

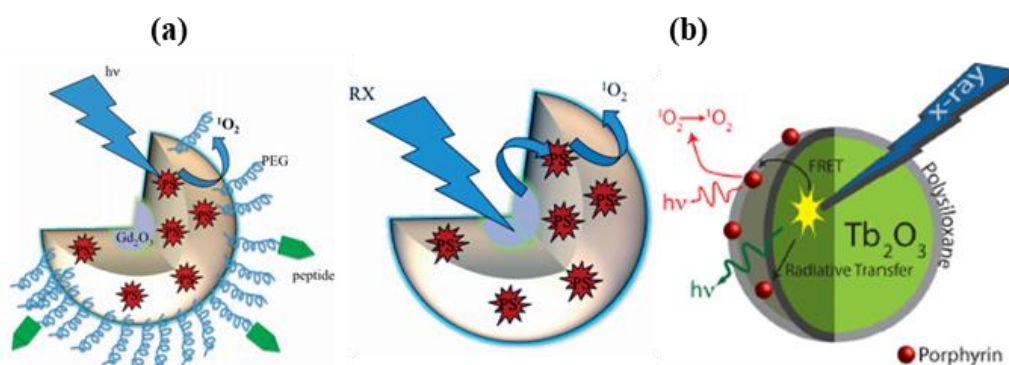


Fig. 31: (a) Multifunctional core-shell nanoparticles and (b) X-ray excitable nanoparticles [97, 98].

3.5.6. The use of TiO_2 in PDT

NPs used in PDT can be classified into organic and inorganic. Usually the pre-described organic NPs comprising liposomes, micelles, microspheres (**Fig. 30**), etc., require the encapsulation of the drug and its release for the PDT application to occur. Beside this class, a varied array of inorganic NPs used for PDT exists. From those we may mention the carbon nanotubes, silica NPs, iron oxide (**Fig. 32**), gold NPs, quantum dots (QDs), up conversion NPs, core-shell NPs, Zinc Oxide (ZnO), TiO_2 , etc. The PS is rather coupled to than encapsulated into those NPs, thus it can be photo-activable without the need to being released. As the PSs are not released into the targeted cells, the molecular oxygen should diffuse into the NPs and then the generated 1O_2 should diffuse out of those NPs. Various aspects govern the production and the expenditure of 1O_2 . The first is related to the accessibility to oxygen so that the matrix of the NPs should be porous and permeable enough to both

molecular and singlet oxygen. Secondly, the efficiency of $^1\text{O}_2$ may be jeopardized since it may be quenched by the NPs themselves or by the surface agents prior reaching the targeted cells.

Among the inorganic NPs, gold NPs are capable of enhancing the $^1\text{O}_2$ production by the surface plasmon resonance effect. In addition, ZnO and TiO_2 are regarded as NPs that can produce ROS by themselves. Those are UV-activated semiconductors capable of generating ROS through redox reactions mediated by their photogenerated holes and electrons (the photoactivation of TiO_2 is already discussed in [Section 1.4](#)). ZnO NPs are of interest in PDT due to their low toxicity and good optical and electronic properties. In recent years, TiO_2 NPs were regarded for their therapeutic competences as potential photosensitizing agents for PDT of malignant cells due to their pre-discussed distinctive phototoxic effect under UV irradiation ([Section 1.4](#)). In 1991, Fujishima's team was the first to report about the application of TiO_2 NPs in PDT. Until 2016, around 20 publications illustrated the importance of TiO_2 in PDT ([Fig. 31](#)) and TiO_2 NPs are proved to possess a good potential as photosensitizers for PDT ([Table 4](#)) [99–101].

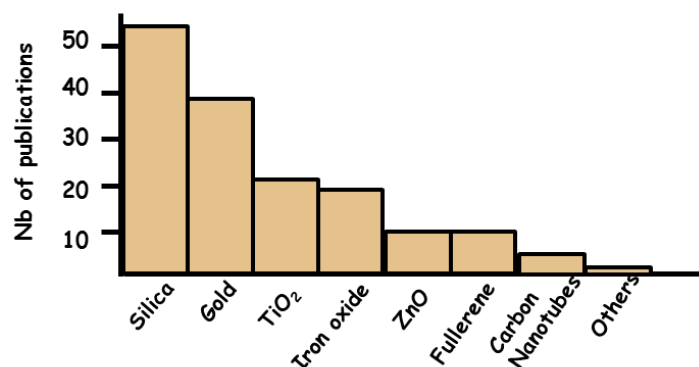


Fig. 32: Number of overall publications of each type of NPs in PDT applications until 2016 [100].

Table 4: Series of TiO_2 NPs with killing cancer cell properties.

Type of TiO_2	Killing cell ability
TiO_2 -Pt	Microbial cells in water can be destroyed by TiO_2 -Pt catalyst irradiated by near UV light for 1-2 h
TiO_2 -acetylcellulose membrane	<i>E-coli</i> suspension flowing through was completely killed Create new avenues for sterilization, disinfecting drinking water and eliminating bio aerosols from indoor environments
TiO_2	Killing of polyunsaturated phospholipids as integral component of the bacterial cell membrane
TiO_2	nanoparticle Lipid peroxidation reaction
TiO_2	The surviving fraction of <i>S.mutans</i> cells up to 58 % under white fluorescent light The analysis based on second order kinetics with respect to the concentrations of microbial cell and oxidative radicals
Ultra-fine TiO_2	Can cause plasmid DNA breakage at the concentration range of 0.05 to 0.15 mg/mL after incubation for 8 hours at 37°C

However, the application of TiO₂ in PDT especially in clinics is limited by its main drawback which is the UV-limited photoresponse. TiO₂ possess a wide band gap that requires an irradiation that falls in the ultraviolet region of light ($\lambda \leq 390$ nm). In terms of PDT, UV light appears to be harmful to the human body and cannot deeply penetrate into the tissues. Being mostly absorbed by the skin, the UV light can only reach few millimeters into the human tissues. Thus UV light is not capable of reaching the tissues embracing the cancer for applications in biological anti-cancer therapies. However, the visible light irradiation, especially of a wavelength that falls in the region between 600 and 700 nm, can efficiently penetrate into the tissues. On this basis, the application and the commercialization of TiO₂-based NPs in the biological field is unfavorably affected. In addition, TiO₂ is not adequately selective to cancer cells due to the absence of cell-specific targeting groups [20, 24–26, 102].

4. Strategies to modify TiO₂ for enhancing its efficiency

4.1. How to extend the absorption of TiO₂ to visible and limit electron-hole recombination?

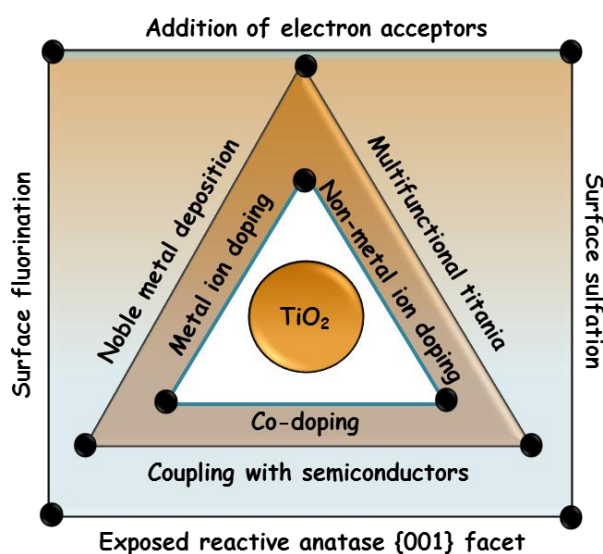


Fig. 33: Presentation of the strategies employed for modifying TiO₂ [4].

On the basis of the pre-mentioned parameters especially the UV-limited photoresponse that restrains the efficacy and commercialization of bare TiO₂, it appears crucial to seek for a solution. Fortunately, the physicochemical and optical characteristics of TiO₂ can be tuned for the sake of designing efficient TiO₂-based systems with a photoresponse extended towards the visible light region that guarantees a more competent solar light utilization. For the action to serve this goal, efforts have been dedicated about one decade ago. The modification methods are various (**Fig. 33**) and embrace doping with metal, non-metal atoms (anion doping), coupling with narrow band-gap semiconductor, co-doping with two or more foreign ions, designing oxygen-deficient titanium

dioxide, surface fluorination or sulfation, deposition of noble metals, dye sensitization (by organic dyes or metal complexes), etc.

Those strategies contribute to the target through modifying the electronic band structure making it more favorable and suitable especially for fulfilling the applications requiring visible and solar irradiations accompanied with retaining the same or greater efficiencies.

4.1.1. Semiconductor-semiconductor coupling: Heterojunction

This method is based on coupling TiO_2 to other semiconductors holding different band gap energies. Thus, to accomplish a better electron-hole separation, TiO_2 has been coupled to a varied array of wide gap semiconductors such as ZnO , SnO_2 , WO_3 , In_2O_3 , V_2O_5 , iron oxides, Bi_2S_3 and CdS or to quantum dots including CdSe , CdTe , CdS , Cu_2O , MoS_2 , PbS , CuInS_2 , InP and WS_2 . The coupled semiconductor should be on a proper band edge position with respect to the other semiconductor to favor the charge transfer process. Basically, the level of the CB of one semiconductor should possess a more negative value with respect to the other semiconductor. Some examples of semiconductor heterojunctions describing the charge transfer mechanism is schematized in Fig. 34. This charge transfer yields longer lifetimes of the holes and electrons and limits the charge recombination issue. Consequently, as a better charge segregation is achieved, an improved photocatalytic efficacy can be reached. Despite its advantages, such systems possess low energy conversion efficiencies [4, 25].

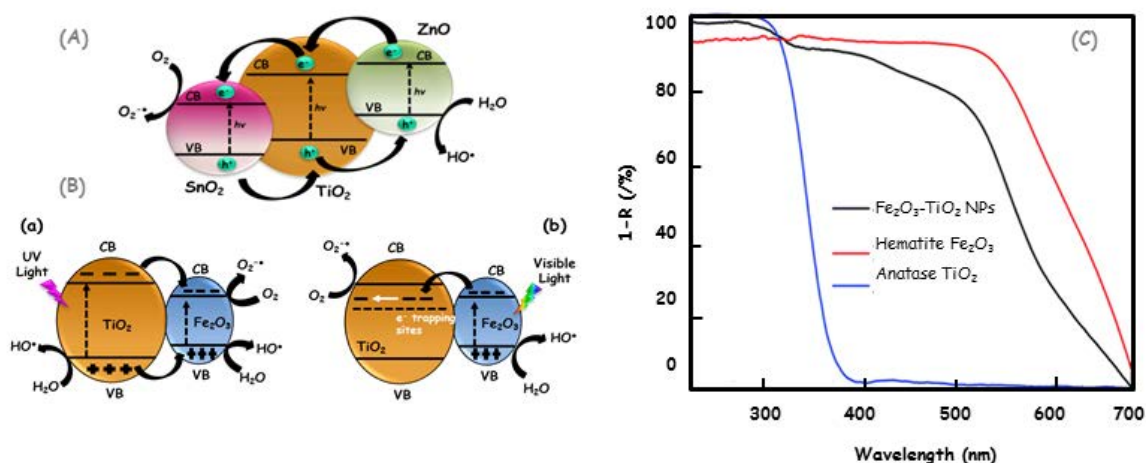


Fig. 34: Electron transfer mechanism in (A) composite semiconductor, (B) $\text{Fe}_2\text{O}_3/\text{TiO}_2$ semiconductor heterojunction system under (a) UV and (b) visible light and (C) absorption spectra of bare TiO_2 and $\text{TiO}_2\text{-Fe}_2\text{O}_3$ NPs. Reproduced from [25].

4.1.2. Metal ion doping

Another extensively applied strategy for visible light photocatalysis by TiO_2 is the doping of the semiconductor with metals. More oxygen defects result from doping the transition metals into the TiO_2 matrix which triggers more facile oxygen chemisorption leading to enhanced O_2^- generation. Since the redox energy state of the dopant is localized within the band gap of TiO_2 either neighboring the CB or the VB, it acts as an ‘intrapand’ state inducing impurity energy levels. As a result, the visible light can be efficiently harvested. The charge transfer process occurring between the d electrons of the transition metal and the CB or VB of TiO_2 prompts an enhanced photocatalytic efficacy (**Fig. 35**). Examples on transition metals used as TiO_2 dopants are Fe, V, Zn, Ni, Re, Ru, Rh, and Os [4, 25]. In addition noble metals such as Ag, Au, Pd and Pt have been recommended as efficient dopants for TiO_2 . Those metals possess fermi levels inferior to that of TiO_2 thus are proper for efficient charge transfer [25, 28].

Although the visible light photocatalysis by metal-doped- TiO_2 was enhanced, but some limitations still exist. The photogenerated electrons and holes tend to recombine together lowering the quantum efficiency and, thus, limiting the photocatalytic application by those NPs. Additionally, the active reaction sites occupying the surface of the TiO_2 are masked by those transition metals [1, 25].

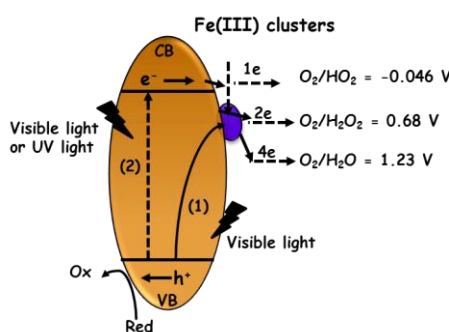


Fig. 35: Schematic diagram illustrating the possible photocatalytic mechanism of Fe(III)/ TiO_2 involving interfacial electron transfer and multielectron oxygen reduction [25].

4.1.3. Non-metal ion doping

Doping TiO_2 semiconductor with non-metal ions and elements such as N, S, C, F, I, P, etc. appeared to improve the photocatalytic application of TiO_2 under visible light. Non-metal TiO_2 doping seems to be more efficient than metal doping technique as it can induce less charge recombination and helps to avoid the weakening thermal stability of the semiconductor. N- TiO_2 doped systems are the most investigated among all other non-metal elements [4, 25, 28].

4.1.4. Non-metal codoping

Codoping represents the combination of multiple non-metal dopants for shifting the photoresponse of TiO₂ to visible. As compared to bare and single-metal doped titania, this technique seems to produce important synergetic effects. Non-metal codoping induces a drop in the electron-hole recombination and allows improved harvesting of visible light. F-N-TiO₂, S-N-TiO₂, C-N-TiO₂, B-N-TiO₂ are some examples of the commonly used co-doped-TiO₂ NPs [4, 25].

4.1.5. Mixed-Phase Titania

The effect of the mixed-phase structured TiO₂ on its photocatalytic efficiency is debatable. Titania can be biphasic such as in the composites holding an anatase-rutile, rutile-brookite or anatase-brookite structures or triphasic constituting of all the three pre-mentioned phases. Superior photocatalytic efficiency is accomplished by those mixed-phase TiO₂ NPs over monophasic TiO₂ NPs [4]. The most common example is the commercial TiO₂ Evonik Degussa P25. TiO₂ P25 is a biphasic composite constituting of 20-30 % rutile and 70-80 % anatase. The enhancement in the photocatalytic activity of to the latter biphasic TiO₂ is attributed to lower electron-hole recombination achieved by the electron transfer occurring from the conduction band of the anatase phase into that of rutile [4, 5, 12].

4.1.6. Sensitization of titania with organic compounds/inorganic metal complexes

Dye sensitization technique is based on the attachment of an organic molecule to the surface of the wide band gap TiO₂ semiconductor. This process can be accomplished either by physical adsorption of the dye (through weak Van der Waals interaction) or by establishing a covalent chemical bond between the dye and the surface of TiO₂ [103].

Dye-sensitization is considered as a widely used technique for the visible-light activation of UV-limited TiO₂. It induces an indirect activation of TiO₂. Under visible light irradiation, the dye or photosensitizer absorbs the visible light unlike TiO₂. The PS is excited to suitable singlet and triplet states and then converted into cationic PS radicals. The generated electrons are transferred into the CB of the host TiO₂ semiconductor (Fig. 36b) [4]. This electron injections process is very fast and occurs in a femtosecond scale with a slow backwards reaction. However, the recombination of the electrons and holes occurs in nanoseconds to milliseconds scale [25]. Molecular oxygen pre-adsorbed on the surface of the semiconductor scavenges the injected electrons, thus generating ROS mainly HO[•], O₂^{•-} and H₂O₂, etc.

In such systems TiO_2 does not only play the role of the support but also is active through indirect excitation mediated by the electron transfer process [4, 25, 103]. The production of $^1\text{O}_2$ by the excited PS is rarely reported but it exists [4]. The formed ROS are the source of activity of TiO_2 in a vast range of applications mainly photocatalytic degradation of pollutants, anti-cancer PDT, photovoltaics, etc.

The electron-transfer process is the fundamental factor in the dye-sensitized systems. In general, the potential of the lowest unoccupied molecular orbitals (LUMO) of the PS is more negative than that of the CB of titania which renders a favored electron transfer. Only the PS molecules linked to TiO_2 contribute in the photoactivation process rather than the PS in the bulk [103].

TiO_2 has been sensitized by diverse types of PSs including MB, acid red 44, Acid Orange 7 (AO7), eosin-Y, rhodamine B, phthalocyanines, porphyrins and their derivatives and metallated analogues, etc. [4, 104]. Subchapters I.1 and I.2 will highlight more on the PSs linked to TiO_2 for photocatalytic and PDT applications.

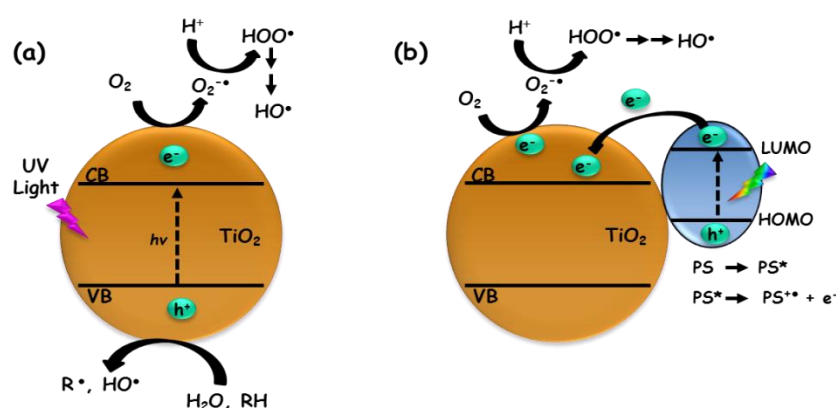


Fig. 35: The photoactivation mechanism of (a) Bare TiO_2 irradiated by UV light and (b) dye-sensitized TiO_2 irradiated by visible light [4, 104].

4.2. How to increase its selectivity in PDT?

Nanotechnology has induced an enormous revolution in the selective cancer targeting. Nanoparticles are tunable in terms of their size, surface chemistry, shape, physico-chemical and photophysical properties. This advantage of NPs enables certain modifications that guarantee an enhanced targeting of the desired cancer cells. Selective cancer targeting may be achieved either through active or passive targeting.

Active targeting relies on the molecular recognition. In this targeting process, the conjugated NP-PS system is designed and modified to directly target the neoplastic cells and interact with them.

This is achieved through attaching cell-specific targeting agents by ligand-receptor or antibody-antigen interaction. The targeting agents include peptides, specific receptors, antibodies, folic acid, etc.

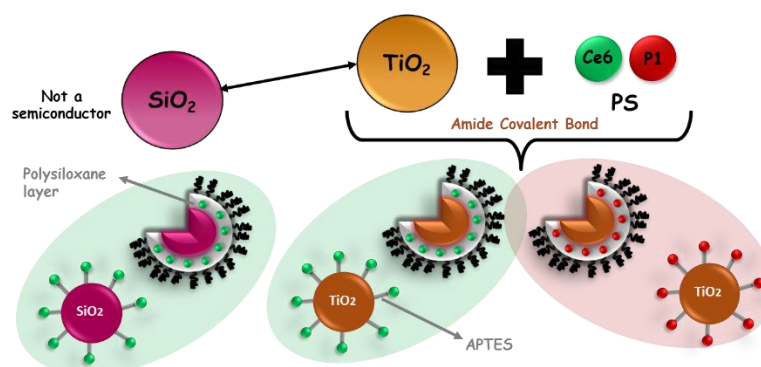
In passive targeting, thanks to EPR effect, the NPs can easily and selectively accumulate and then diffuse into the cancer cells. However to minimize the effect of opsonization and the removal by macrophages, certain stabilizing molecules such as deoxyribonucleic acid (DNA), albumin and polyethylene glycol (PEG) have been used to functionalize the surface of the NPs. Those molecules can decrease the ionic strength and enhance the dispersion of the NPs by preventing their aggregation in the biological media. Grafting PEG onto the surface of the NPs also reduces the probable uptake by the macrophages and accordingly increases the time of NPs' circulation in blood.

Another example is the core-shell NPs. Those are constituted of a core NP encapsulated in a silica shell formed from APTES and TEOS. Silica shell act as a protector and improves the dispersion of NPs mediating longer duration in blood thus a more efficient passive targeting. Thus beside mediating the formation of durable bonds between organic and inorganic materials, silane reagents can help better disperse the NPs in aqueous media [97, 98, 105–107].

The use of TiO_2 -PS systems in both photocatalysis and PDT is thoroughly discussed in the following two reviews (subchapters 1.1 and 1.2 for photocatalysis and PDT, respectively). The employed TiO_2 -PS systems are described on the basis of the type of TiO_2 used, the type PS linked to TiO_2 , the linking mode either physical adsorption or covalent grafting and the number of linked PS when possible.

Besides TiO_2 , an overview regarding ZnO-PS, fullerene-PS and graphene-PS nanosystems that have shown a good potential in both photocatalysis and PDT is also reflected in subchapters 1.1 and 1.2, respectively.

The goal of this work is to design new TiO_2 NPs that can be used in both photocatalysis and PDT. Amorphous SiO_2 analogues were also designed for comparative reasons.



Scheme 2: Illustration of the composition of the NPs synthesized in this study.

References for the bibliographic part

- [1] M. J. Gázquez, J. P. Bolívar, R. Garcia-Tenorio, and F. Vaca, "A Review of the Production Cycle of Titanium Dioxide Pigment," *Mater. Sci. Appl.*, vol. 05, no. 07, pp. 441–458, 2014.
- [2] Y. Lan, Y. Lu, and Z. Ren, "Mini review on photocatalysis of titanium dioxide nanoparticles and their solar applications," *Nano Energy*, vol. 2, no. 5, pp. 1031–1045, Sep. 2013.
- [3] A. Karmakar, Q. Zhang, and Y. Zhang, "Neurotoxicity of nanoscale materials," *J. Food Drug Anal.*, vol. 22, no. 1, pp. 147–160, Mar. 2014.
- [4] S. G. Kumar and L. G. Devi, "Review on Modified TiO₂ Photocatalysis under UV/Visible Light: Selected Results and Related Mechanisms on Interfacial Charge Carrier Transfer Dynamics," *J. Phys. Chem. A*, vol. 115, no. 46, pp. 13211–13241, Nov. 2011.
- [5] G. Wang, L. Xu, J. Zhang, T. Yin, and D. Han, "Enhanced Photocatalytic Activity of Powders (P25) via Calcination Treatment," *Int. J. Photoenergy*, vol. 2012, pp. 1–9, 2012.
- [6] J. Zhao, M. Milanova, M. M. C. G. Warmoeskerken, and V. Dutschk, "Surface modification of TiO₂ nanoparticles with silane coupling agents," *Colloids Surf. Physicochem. Eng. Asp.*, vol. 413, pp. 273–279, Nov. 2012.
- [7] A. Fujishima and K. Honda, "Electrochemical Photolysis of Water at a Semiconductor Electrode," *Nature*, vol. 238, no. 5358, pp. 37–38, Jul. 1972.
- [8] M. Landmann, E. Rauls, and W. G. Schmidt, "The electronic structure and optical response of rutile, anatase and brookite TiO₂," *J. Phys. Condens. Matter*, vol. 24, no. 19, p. 195503, May 2012.
- [9] A. Fujishima, X. Zhang, and D. Tryk, "TiO₂ photocatalysis and related surface phenomena," *Surf. Sci. Rep.*, vol. 63, no. 12, pp. 515–582, Dec. 2008.
- [10] Z. Rui, S. Wu, C. Peng, and H. Ji, "Comparison of TiO₂ Degussa P25 with anatase and rutile crystalline phases for methane combustion," *Chem. Eng. J.*, vol. 243, pp. 254–264, May 2014.
- [11] M. Kassir *et al.*, "Improvement of the photocatalytic activity of TiO₂ induced by organic pollutant enrichment at the surface of the organografted catalyst," *Colloids Surf. Physicochem. Eng. Asp.*, vol. 485, pp. 73–83, Nov. 2015.
- [12] B. Ohtani, O. O. Prieto-Mahaney, D. Li, and R. Abe, "What is Degussa (Evonik) P25? Crystalline composition analysis, reconstruction from isolated pure particles and photocatalytic activity test," *J. Photochem. Photobiol. Chem.*, vol. 216, no. 2–3, pp. 179–182, Dec. 2010.
- [13] T. Ohno, K. Sarukawa, K. Tokieda, and M. Matsumura, "Morphology of a TiO₂ Photocatalyst (Degussa, P-25) Consisting of Anatase and Rutile Crystalline Phases," *J. Catal.*, vol. 203, no. 1, pp. 82–86, Oct. 2001.
- [14] M. Kassir, "Modification contrôlée des propriétés cristallographiques et physico-chimiques de matériaux nanostructurés à base de TiO₂ pour la maîtrise des propriétés photocatalytiques," Université de Lorraine et Université Libanaise, 2013.
- [15] L. T. Zhuravlev, "The surface chemistry of amorphous silica. Zhuravlev model," *Colloids Surf. Physicochem. Eng. Asp.*, vol. 173, no. 1–3, pp. 1–38, Nov. 2000.
- [16] C. Kormann, D. W. Bahnemann, and M. R. Hoffmann, "Photolysis of chloroform and other organic molecules in aqueous titanium dioxide suspensions," *Environ. Sci. Technol.*, vol. 25, no. 3, pp. 494–500, Mar. 1991.
- [17] M. J. Uddin, M. A. Islam, S. A. Haque, S. Hasan, M. S. A. Amin, and M. M. Rahman, "Preparation of nanostructured TiO₂-based photocatalyst by controlling the calcining temperature and pH," *Int. Nano Lett.*, vol. 2, no. 1, Dec. 2012.
- [18] Z. Sun, T. Liao, L. Sheng, L. Kou, J. H. Kim, and S. X. Dou, "Deliberate Design of TiO₂ Nanostructures towards Superior Photovoltaic Cells," *Chem. - Eur. J.*, vol. 22, no. 32, pp. 11357–11364, Aug. 2016.
- [19] S. Valencia, J. M. Marín, and G. Restrepo, "Study of the Bandgap of Synthesized Titanium Dioxide Nanoparticles Using the Sol-Gel Method and a Hydrothermal Treatment," *Open Mater. Sci. J.*, vol. 4, no. 1, pp. 9–14, Feb. 2010.

- [20] Y. Tokuoka, M. Yamada, N. Kawashima, and T. Miyasaka, "Anticancer Effect of Dye-sensitized TiO₂ Nanocrystals by Polychromatic Visible Light Irradiation," *Chem. Lett.*, vol. 35, no. 5, pp. 496–497, May 2006.
- [21] Z. Fei Yin, L. Wu, H. Gui Yang, and Y. Hua Su, "Recent progress in biomedical applications of titanium dioxide," *Phys. Chem. Chem. Phys.*, vol. 15, no. 14, p. 4844, 2013.
- [22] S. Xu, J. Shen, S. Chen, M. Zhang, and T. Shen, "Active oxygen species (1O₂, O₂⁻) generation in the system of TiO₂ colloid sensitized by hypocrellin B," *J. Photochem. Photobiol. B*, vol. 67, no. 1, pp. 64–70, May 2002.
- [23] K. Huang, L. Chen, J. Xiong, and M. Liao, "Preparation and Characterization of Visible-Light-Activated Fe-N Co-Doped TiO₂ and Its Photocatalytic Inactivation Effect on Leukemia Tumors," *Int. J. Photoenergy*, vol. 2012, pp. 1–9, 2012.
- [24] J. Xu *et al.*, "Photokilling cancer cells using highly cell-specific antibody–TiO₂ bioconjugates and electroporation," *Bioelectrochemistry*, vol. 71, no. 2, pp. 217–222, Nov. 2007.
- [25] V. Etacheri, C. Di Valentin, J. Schneider, D. Bahnemann, and S. C. Pillai, "Visible-light activation of TiO₂ photocatalysts: Advances in theory and experiments," *J. Photochem. Photobiol. C Photochem. Rev.*, vol. 25, pp. 1–29, Dec. 2015.
- [26] Z. Li, X. Pan, T. Wang, P.-N. Wang, J.-Y. Chen, and L. Mi, "Comparison of the killing effects between nitrogen-doped and pure TiO₂ on HeLa cells with visible light irradiation," *Nanoscale Res. Lett.*, vol. 8, no. 1, p. 96, 2013.
- [27] B. Geiseler, M. Miljevic, P. Müller, and L. Fruk, "Phototriggered Production of Reactive Oxygen Species by TiO₂ Nanospheres and Rods," *J. Nanomater.*, vol. 2012, pp. 1–9, 2012.
- [28] S. Noimark, C. W. Dunnill, and I. P. Parkin, "Shining light on materials — A self-sterilising revolution," *Adv. Drug Deliv. Rev.*, vol. 65, no. 4, pp. 570–580, Apr. 2013.
- [29] D. Fatta-Kassinos, S. Meric, and A. Nikolaou, "Pharmaceutical residues in environmental waters and wastewater: current state of knowledge and future research," *Anal. Bioanal. Chem.*, vol. 399, no. 1, pp. 251–275, Jan. 2011.
- [30] M. Grassi, L. Rizzo, and A. Farina, "Endocrine disruptors compounds, pharmaceuticals and personal care products in urban wastewater: implications for agricultural reuse and their removal by adsorption process," *Environ. Sci. Pollut. Res.*, vol. 20, no. 6, pp. 3616–3628, Jun. 2013.
- [31] S. D. Richardson and S. Y. Kimura, "Water Analysis: Emerging Contaminants and Current Issues," *Anal. Chem.*, vol. 88, no. 1, pp. 546–582, Jan. 2016.
- [32] M. Trapido, I. Epold, J. Bolobajev, and N. Dulova, "Emerging micropollutants in water/wastewater: growing demand on removal technologies," *Environ. Sci. Pollut. Res.*, vol. 21, no. 21, pp. 12217–12222, Nov. 2014.
- [33] "United Nations World Water Assessment Programme. The World Water Development Report 1: Water for People, Water for Life. UNESCO: Paris, France."
- [34] "<http://www.unwater.org/worldwaterday/downloads/wwd09brochureenLOW.pdf>."
- [35] Y. Su *et al.*, "Enhanced photodegradation of methyl orange with TiO₂ nanoparticles using a triboelectric nanogenerator," *Nanotechnology*, vol. 24, no. 29, p. 295401, Jul. 2013.
- [36] "<https://waterstse.wordpress.com/world-impact/>."
- [37] P. R. Gogate and A. B. Pandit, "A review of imperative technologies for wastewater treatment I: oxidation technologies at ambient conditions," *Adv. Environ. Res.*, vol. 8, no. 3–4, pp. 501–551, Mar. 2004.
- [38] R. Andreozzi, "Advanced oxidation processes (AOP) for water purification and recovery," *Catal. Today*, vol. 53, no. 1, pp. 51–59, Oct. 1999.
- [39] A. Baiker, "Supercritical Fluids in Heterogeneous Catalysis," *Chem. Rev.*, vol. 99, no. 2, pp. 453–474, Feb. 1999.
- [40] J.-M. Herrmann, "Photocatalysis fundamentals revisited to avoid several misconceptions," *Appl. Catal. B Environ.*, vol. 99, no. 3–4, pp. 461–468, Sep. 2010.
- [41] V. K. Gupta, I. Ali, T. A. Saleh, A. Nayak, and S. Agarwal, "Chemical treatment technologies for waste-water recycling—an overview," *RSC Adv.*, vol. 2, no. 16, p. 6380, 2012.

- [42] G. Charles, T. Roques-Carmes, N. Becheikh, L. Falk, J.-M. Commenge, and S. Corbel, "Determination of kinetic constants of a photocatalytic reaction in micro-channel reactors in the presence of mass-transfer limitation and axial dispersion," *J. Photochem. Photobiol. Chem.*, vol. 223, no. 2–3, pp. 202–211, Sep. 2011.
- [43] M. N. Chong, B. Jin, C. W. K. Chow, and C. Saint, "Recent developments in photocatalytic water treatment technology: A review," *Water Res.*, vol. 44, no. 10, pp. 2997–3027, May 2010.
- [44] T. Lopez *et al.*, "Study of the stabilization of zinc phthalocyanine in sol-gel TiO₂ for photodynamic therapy applications," *Nanomedicine Nanotechnol. Biol. Med.*, vol. 6, no. 6, pp. 777–785, Dec. 2010.
- [45] A. Jańczyk, A. Wolnicka-Głubisz, K. Urbanska, H. Kisch, G. Stochel, and W. Macyk, "Photodynamic activity of platinum(IV) chloride surface-modified TiO₂ irradiated with visible light," *Free Radic. Biol. Med.*, vol. 44, no. 6, pp. 1120–1130, Mar. 2008.
- [46] W. A. Herrmann, M. Elison, J. Fischer, C. Köcher, and G. R. J. Artus, "Metal Complexes of N-Heterocyclic Carbenes—A New Structural Principle for Catalysts in Homogeneous Catalysis," *Angew. Chem. Int. Ed. Engl.*, vol. 34, no. 21, pp. 2371–2374, Nov. 1995.
- [47] L. A. Torre, R. L. Siegel, E. M. Ward, and A. Jemal, "Global Cancer Incidence and Mortality Rates and Trends--An Update," *Cancer Epidemiol. Biomarkers Prev.*, vol. 25, no. 1, pp. 16–27, Jan. 2016.
- [48] J. Ferlay *et al.*, "Cancer incidence and mortality worldwide: Sources, methods and major patterns in GLOBOCAN 2012: Globocan 2012," *Int. J. Cancer*, vol. 136, no. 5, pp. E359–E386, Mar. 2015.
- [49] "http://globocan.iarc.fr/Pages/fact_sheets_population.aspx."
- [50] "<https://www.cancer.org/content/dam/cancer-org/research/cancer-facts-and-statistics/annual-cancer-facts-and-figures/2016/cancer-facts-and-figures-2016.pdf>."
- [51] B. Vogelstein and K. W. Kinzler, "The multistep nature of cancer," *Trends Genet.*, vol. 9, no. 4, pp. 138–141, Apr. 1993.
- [52] E. Farber, "'The multistep nature of cancer development.' *Cancer Res* 44, no. 10," pp. 4217–4223, 1984.
- [53] "<http://ib.bioninja.com.au/standard-level/topic-3-genetics/33-meiosis/somatic-vs-germline-mutatio.html>."
- [54] D. Hanahan and R. A. Weinberg, "The Hallmarks of Cancer," *Cell*, vol. 100, no. 1, pp. 57–70, Jan. 2000.
- [55] F. Michor, Y. Iwasa, and M. A. Nowak, "Dynamics of cancer progression," *Nat. Rev. Cancer*, vol. 4, no. 3, pp. 197–205, Mar. 2004.
- [56] K. W. Kinzler and B. Vogelstein, "Gatekeepers and caretakers, *Nature*," pp. 761–763, 1997.
- [57] L. Brannon-Peppas and J. O. Blanchette, "Nanoparticle and targeted systems for cancer therapy," *Adv. Drug Deliv. Rev.*, vol. 56, no. 11, pp. 1649–1659, Sep. 2004.
- [58] M. J. Bissell and D. Radisky, "Putting tumours in context," *Nat. Rev. Cancer*, vol. 1, no. 1, pp. 46–54, Oct. 2001.
- [59] "www.biooncology.com/pathways/cancer-tumor-targets/vegf.html."
- [60] A. Schroeder *et al.*, "Treating metastatic cancer with nanotechnology," *Nat. Rev. Cancer*, vol. 12, no. 1, pp. 39–50, Dec. 2011.
- [61] J. Massagué and A. C. Obenauf, "Metastatic colonization by circulating tumour cells," *Nature*, vol. 529, no. 7586, pp. 298–306, Jan. 2016.
- [62] L. Hanin and M. Zaider, "Effects of Surgery and Chemotherapy on Metastatic Progression of Prostate Cancer: Evidence from the Natural History of the Disease Reconstructed through Mathematical Modeling," *Cancers*, vol. 3, no. 4, pp. 3632–3660, Sep. 2011.
- [63] P. Gotwals *et al.*, "Prospects for combining targeted and conventional cancer therapy with immunotherapy," *Nat. Rev. Cancer*, vol. 17, no. 5, pp. 286–301, Mar. 2017.
- [64] "<https://www.cancer.gov/about-cancer/treatment/types/surgery>."
- [65] K. Lauber, A. Ernst, M. Orth, M. Herrmann, and C. Belka, "Dying cell clearance and its impact on the outcome of tumor radiotherapy," *Front. Oncol.*, vol. 2, 2012.
- [66] V. T. DeVita and E. Chu, "A History of Cancer Chemotherapy," *Cancer Res.*, vol. 68, no. 21, pp. 8643–8653, Nov. 2008.

- [67] “<https://www.cancer.org/treatment/treatments-and-side-effects/treatment-types/immunotherapy/what-is-immunotherapy.html>.”
- [68] L. B. Josefsen and R. W. Boyle, “Photodynamic Therapy and the Development of Metal-Based Photosensitisers,” *Met.-Based Drugs*, vol. 2008, pp. 1–23, 2008.
- [69] C. Hopper, “Photodynamic therapy: a clinical reality in the treatment of cancer,” *Lancet Oncol.*, vol. 1, no. 4, pp. 212–219, Dec. 2000.
- [70] “Frochot C, Barberi-Heyob M, Blanchard-Desce M, Bolotine L, Bonneau S, Chiara M, Durand JO, Lassalle HP, Lemercier G, Mordon S, Maillard P. La thérapie photodynamique: état de l’art et perspectives. *L’Actualité Chimique*. 2015 Jun(397-398):46-50.”
- [71] A. Master, M. Livingston, and A. Sen Gupta, “Photodynamic nanomedicine in the treatment of solid tumors: Perspectives and challenges,” *J. Controlled Release*, vol. 168, no. 1, pp. 88–102, May 2013.
- [72] S. B. Brown, E. A. Brown, and I. Walker, “The present and future role of photodynamic therapy in cancer treatment,” *Lancet Oncol.*, vol. 5, no. 8, pp. 497–508, Aug. 2004.
- [73] K. L. Du, S. Both, J. S. Friedberg, R. Rengan, S. M. Hahn, and K. A. Cengel, “Extrapleural pneumonectomy, photodynamic therapy and intensity modulated radiation therapy for the treatment of malignant pleural mesothelioma,” *Cancer Biol. Ther.*, vol. 10, no. 5, pp. 425–429, Sep. 2010.
- [74] G. C. Brown, M. M. Brown, J. Campanella, and G. R. Beauchamp, “The Cost-Utility of Photodynamic Therapy in Eyes With Neovascular Macular Degeneration—A Value-Based Reappraisal With 5-Year Data,” *Am. J. Ophthalmol.*, vol. 140, no. 4, p. 679.e1-679.e10, Oct. 2005.
- [75] A.-R. Azzouzi *et al.*, “TOOKAD[®] Soluble vascular-targeted photodynamic (VTP) therapy: determination of optimal treatment conditions and assessment of effects in patients with localised prostate cancer: TOOKAD[®] soluble vascular targeted photodynamic (VTP) therapy in patients with localised prostate cancer,” *BJU Int.*, vol. 112, no. 6, pp. 766–774, Oct. 2013.
- [76] H. Moole *et al.*, “Success of photodynamic therapy in palliating patients with nonresectable cholangiocarcinoma: A systematic review and meta-analysis,” *World J. Gastroenterol.*, vol. 23, no. 7, p. 1278, 2017.
- [77] P. Soergel, M. Loning, I. Staboulidou, C. Schippert, and P. Hillemanns, “Photodynamic Diagnosis and Therapy in Gynecology,” *J. Environ. Pathol. Toxicol. Oncol.*, vol. 27, no. 4, pp. 307–320, 2008.
- [78] A. F. Degen *et al.*, “Photodynamic endometrial ablation for the treatment of dysfunctional uterine bleeding: A preliminary report: PHOTODYNAMIC ENDOMETRIAL ABLATION,” *Lasers Surg. Med.*, vol. 34, no. 1, pp. 1–4, Jan. 2004.
- [79] K. Moghissi and K. Dixon, “Is bronchoscopic photodynamic therapy a therapeutic option in lung cancer?,” *Eur. Respir. J.*, vol. 22, no. 3, pp. 535–541, Sep. 2003.
- [80] W. M. Sharman, C. M. Allen, and J. E. van Lier, “Photodynamic therapeutics: basic principles and clinical applications,” *Drug Discov. Today*, vol. 4, no. 11, pp. 507–517, Nov. 1999.
- [81] E. D. Sternberg, D. Dolphin, and C. Brückner, “Porphyrin-based photosensitizers for use in photodynamic therapy,” *Tetrahedron*, vol. 54, no. 17, pp. 4151–4202, Apr. 1998.
- [82] S. M. Banerjee, A. J. MacRobert, C. A. Mosse, B. Periera, S. G. Bown, and M. R. S. Keshtgar, “Photodynamic therapy: Inception to application in breast cancer,” *The Breast*, vol. 31, pp. 105–113, Feb. 2017.
- [83] C.-P. Tan, Y.-Y. Lu, L.-N. Ji, and Z.-W. Mao, “Metallomics insights into the programmed cell death induced by metal-based anticancer compounds,” *Metallomics*, vol. 6, no. 5, p. 978, 2014.
- [84] I. Yoon, J. Z. Li, and Y. K. Shim, “Advance in Photosensitizers and Light Delivery for Photodynamic Therapy,” *Clin. Endosc.*, vol. 46, no. 1, p. 7, 2013.
- [85] “<http://cursoenarm.net/UPTODATE/contents/mobipreview.htm?31/19/>.”
- [86] Z. Zhou, J. Song, L. Nie, and X. Chen, “Reactive oxygen species generating systems meeting challenges of photodynamic cancer therapy,” *Chem Soc Rev*, vol. 45, no. 23, pp. 6597–6626, 2016.
- [87] C. Cochrane, S. R. Mordon, J. C. Lesage, and V. Koncar, “New design of textile light diffusers for photodynamic therapy,” *Mater. Sci. Eng. C*, vol. 33, no. 3, pp. 1170–1175, Apr. 2013.
- [88] A. Ormond and H. Freeman, “Dye Sensitizers for Photodynamic Therapy,” *Materials*, vol. 6, no. 3, pp. 817–840, Mar. 2013.

- [89] M. DeRosa, "Photosensitized singlet oxygen and its applications," *Coord. Chem. Rev.*, vol. 233–234, pp. 351–371, Nov. 2002.
- [90] L. B. Josefsen and R. W. Boyle, "Unique Diagnostic and Therapeutic Roles of Porphyrins and Phthalocyanines in Photodynamic Therapy, Imaging and Theranostics," *Theranostics*, vol. 2, no. 9, pp. 916–966, 2012.
- [91] M. P. Uliana *et al.*, "Photobiological characteristics of chlorophyll a derivatives as microbial PDT agents," *Photochem Photobiol Sci*, vol. 13, no. 8, pp. 1137–1145, 2014.
- [92] "<http://photobiology.info/Berg.html>."
- [93] K. Cho, X. Wang, S. Nie, Z. Chen, and D. M. Shin, "Therapeutic Nanoparticles for Drug Delivery in Cancer," *Clin. Cancer Res.*, vol. 14, no. 5, pp. 1310–1316, Mar. 2008.
- [94] A. Z. Wilczewska, K. Niemirowicz, K. H. Markiewicz, and H. Car, "Nanoparticles as drug delivery systems," *Pharmacol. Rep.*, vol. 64, no. 5, pp. 1020–1037, Sep. 2012.
- [95] L. Zhang, F. Gu, J. Chan, A. Wang, R. Langer, and O. Farokhzad, "Nanoparticles in Medicine: Therapeutic Applications and Developments," *Clin. Pharmacol. Ther.*, vol. 83, no. 5, pp. 761–769, May 2008.
- [96] "<https://www.slideshare.net/arancaresearch/mechanism-of-targeting-tumor-cells-using-nanoparticles>."
- [97] C. Frochot and M. Barberi-Heyob, "CHAPTER 6. Multifunctional Nanoparticles for Theranostic or X-Ray-Induced Photodynamic Therapy," in *Comprehensive Series in Photochemical & Photobiological Sciences*, H. Kostron and T. Hasan, Eds. Cambridge: Royal Society of Chemistry, 2016, pp. 101–112.
- [98] A.-L. Bulin *et al.*, "X-ray-Induced Singlet Oxygen Activation with Nanoscintillator-Coupled Porphyrins," *J. Phys. Chem. C*, vol. 117, no. 41, pp. 21583–21589, Oct. 2013.
- [99] R. Vanderesse, C. Frochot, M. Barberi-Heyob, S. Richeter, L. Raehm, and J.-O. Durand, "Nanoparticles for Photodynamic Therapy Applications," in *Intracellular Delivery*, vol. 5, A. Prokop, Ed. Dordrecht: Springer Netherlands, 2011, pp. 511–565.
- [100] L. Colombeau *et al.*, "Inorganic Nanoparticles for Photodynamic Therapy," in *Light-Responsive Nanostructured Systems for Applications in Nanomedicine*, vol. 370, S. Sortino, Ed. Cham: Springer International Publishing, 2016, pp. 113–134.
- [101] "Stallivieri, A., Baros, F., Arnoux, P., Vanderesse, R., Barberi-Heyob, M. and Frochot, C., 2016. Production of singlet Oxygen by nanoparticle-bound photosensitizers. In Singlet Oxygen (pp. 209-223).," .
- [102] X. Feng, S. Zhang, and X. Lou, "Controlling silica coating thickness on TiO₂ nanoparticles for effective photodynamic therapy," *Colloids Surf. B Biointerfaces*, vol. 107, pp. 220–226, Jul. 2013.
- [103] S. Rehman, R. Ullah, A. M. Butt, and N. D. Gohar, "Strategies of making TiO₂ and ZnO visible light active," *J. Hazard. Mater.*, vol. 170, no. 2–3, pp. 560–569, Oct. 2009.
- [104] B. U. Jang, J. H. Choi, S. J. Lee, and S. G. Lee, "Synthesis and characterization of Cu -phthalocyanine hybrid TiO₂ sol," *J. Porphyr. Phthalocyanines*, vol. 13, no. 07, pp. 779–786, Jul. 2009.
- [105] X. Feng, S. Zhang, H. Wu, and X. Lou, "A novel folic acid-conjugated TiO₂–SiO₂ photosensitizer for cancer targeting in photodynamic therapy," *Colloids Surf. B Biointerfaces*, vol. 125, pp. 197–205, Jan. 2015.
- [106] F. Cheng, S. M. Sajedin, S. M. Kelly, A. F. Lee, and A. Kornherr, "UV-stable paper coated with APTES-modified P25 TiO₂ nanoparticles," *Carbohydr. Polym.*, vol. 114, pp. 246–252, Dec. 2014.
- [107] P. Couleaud *et al.*, "Functionalized silica-based nanoparticles for photodynamic therapy," *Nanomed.*, vol. 6, no. 6, pp. 995–1009, Aug. 2011.

Subchapter I.1:

Dye-sensitized nanoparticles for heterogeneous photocatalysis: Cases Studies with TiO₂, ZnO, Fullerene and Graphene for water purification

Zahraa Youssef^{a,b}, Ludovic Colombeau,^{a,c} Nurlykyz Yesmurzayeva^a, Francis Baros^a, Régis Vanderesse,^c Tayssir Hamieh,^b Céline Frochot,^a Thibault Roques-Carnes^{a,*}

^a Université de Lorraine, Laboratoire Réactions et Génie des Procédés, UMR 7274 CNRS, 54000 Nancy, France

^b Laboratory of Materials, Catalysis, Environment and Analytical Methods, Faculty of Sciences I, Lebanese University, Campus Rafic Hariri, Beyrouth, Lebanon

^c Université de Lorraine, Laboratoire de Chimie Physique Macromoléculaire, UMR 7375 CNRS 54000 Nancy, France

Review to be submitted to Pigments and Dyes Journal

Dye-sensitized nanoparticles for heterogeneous photocatalysis: Cases Studies with TiO₂, ZnO, Fullerene and Graphene for water purification

Abstract

In this review, the use of dye-sensitized nanoparticles (NPs) for heterogeneous photocatalysis related to water purification is considered. The dye sensitization by the mean of a photosensitizer (PS) appears as a relevant alternative method used to enhance the photocatalytic efficiency and, particularly, to extend the activity towards visible light domain. The discussion covers the impact of the type of nanoparticles, the nature and the content of the PS, the linkage mode between the PS and the surface of the NPs (physisorption, covalent grafting), the presence of a heavy-metal atom coordinated to the ring of the PS, the type of light used for the activation (UV, visible or solar), and the presence or absence of an oxidant (H₂O₂) on the photocatalytic performances. These processes have been conducted principally with TiO₂ coupled with organic dyes (porphyrin and phthalocyanine) photosensitizers. The main trends in terms of PS nature, linkage mode, PS content, presence of metallic heavy atoms are extracted by studying the TiO₂/PS materials. In the research of alternative photocatalysts, ZnO/PS systems appear attractive since ZnO displays a lot of similarities with titania. Recent photocatalysts based on carbon materials such as fullerene/PS and graphene/PS are also discussed. For each system and under each irradiation source, the mechanism of the light-induced charge transfer and the nature of the radicals generated is also described.

Keywords: Photocatalysis; water treatment; photosensitizers; organic dyes; semiconductor; titanium dioxide; zinc oxide; carbon materials

1. Introduction

Water scarcity in parallel to the increase of the water demand appears as one of the greatest worldwide challenge of the century. At the same time, the release of hazardous compounds into the water from the urban and the industrial sectors remains an issue because of the presence of a large variety of chemical species at various concentrations. It becomes also well established that the current wastewater treatment technologies are reaching their limits. As an example, they are not well suited to remove the emerging micropollutants which are present at very low concentrations in a

range of $\mu\text{g/L}$ and ng/L .^[1,2] Pharmaceuticals, personal care products, industrial chemicals and pesticides, are some examples.^[3] In this context, nanomaterials and, particularly, nanoparticles appear as a very promising alternative for the next-generation of water treatment processes.^[4-8] Nanomaterials offer several advantages compared to bulk materials. For instance, they display larger surface area, higher reactive sites, and greater light absorption capacity. The potential applications of nanoparticles in wastewater treatment include adsorption,^[9-12] membrane,^[13,14] heterogeneous photocatalysis,^[15-17] heterogeneous photo-Fenton,^[18,19] disinfection and microbial control.^[20,21]

Among them, heterogeneous photocatalysis emerges as a promising wastewater treatment technology.^[15-17] In particular, it is well suited to degrade the aromatic compounds which present a potential hazard to the environment,^[15-17,22-25] and also for the inactivation of bacteria.^[26-28] The most commonly used semiconductor photocatalyst remains titanium dioxide (TiO_2) due to its unique photochemical properties and low cost.^[29-32] Zinc oxide (ZnO) nanoparticles become also very popular in spite of the possible photocorrosion under irradiation.^[33-35] Due to their wide band gap (eg = 3.2, 3.2 and 3.0 eV for ZnO , TiO_2 anatase and rutile phases, respectively), these photocatalysts can be activated only under ultraviolet light irradiation. These two materials work very efficiently under UV light irradiation. However, they face severe issues that hinder their industrialization to large-scale systems. On one hand, their activity under visible and solar light is restricted since the solar light reaching earth is constituted of about 4-6 % of UV light and of approximately 45 % of visible light.^[36-38] On the other hand, they suffer from the high electron-hole recombinations which reduce significantly the photonic efficiency.^[15-17] In order to overcome these drawbacks, and principally to extend their light absorption profile towards the visible light, several strategies have been developed. One of those strategies is to dope the semiconductor with metal ions, including Fe, Au, Gd, Ag, etc... or non-metallic ions such as C, N and S.^[36,38-40] In spite of the difficult multi-steps preparation process, the doping methods succeeded to improve the photocatalytic activity of TiO_2 under visible light to a certain extent. However, the doped-semiconductor photocatalytic systems presented a limited photocatalytic activity and quantum efficiency. This is due to the low carriers' mobility of the photo-excited electron-hole pairs (e^- - h^+) in addition to the relatively high recombination rate of those electrons and holes.^[40,41] The problem of e^- - h^+ recombination can be somehow solved through coupling the photocatalyst (TiO_2 or ZnO) with other semiconductors such as SnO_2 , WO_3 , iron oxides or quantum dots (CdS , Cu_2O , CdTe),^[42-45] yielding an enhanced activity. Unfortunately, this latter system encountered low energy conversion efficiency.^[40]

Other possibilities involve the use of photosensitizers (PS) or dyes. The concept of coupling a PS with a semiconductor material is deliberately inspired from the Gratzel cells in photovoltaic applications^[46,47] and also from photodynamic therapy^[48,49] in medical applications related to cancer treatment. In fact, dye-sensitization of semiconductor photocatalysts leads to a larger than or equal photocatalytic activity in comparison with the other methods (doping, etc). For these reasons, it

becomes a substitute approach in the domain of visible-light photocatalysis.^[36,38] Upon sensitization, the hybrid TiO₂/PS system displays both absorption peaks of TiO₂ and the PS, thus broadening the range of the NP's excitation (**Fig. 1**).

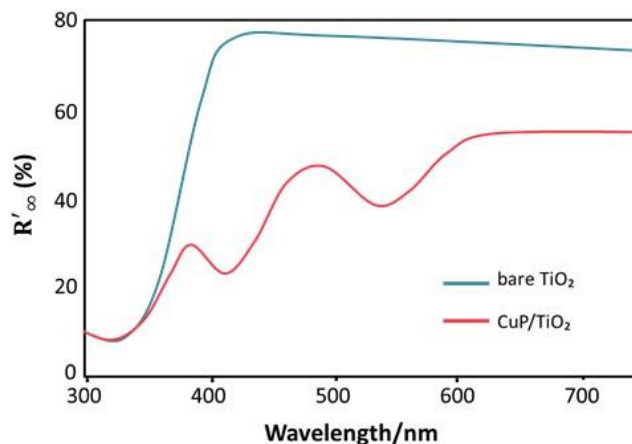


Fig. 1: The diffuse reflectance spectra displayed by bare TiO₂ and Cu-Porphyrin/TiO₂. Taken from reference ^[50].

However, for photocatalytic applications, it remains a challenge to develop a NPs/sensitized system with a good stability, intensive visible light harvesting capability and efficient photocatalytic activity. For the sake of fulfilling this goal, several parameters have to be optimized. The type of nanoparticles (TiO₂, ZnO, fullerene, graphene), the nature and the content of the PS, the presence or absence of metallic atoms, the linkage mode between the PS and the surface of the NPs (physisorption, covalent grafting), the type of light used for the photocatalytic application (UV, visible or solar) and the presence or absence of an oxidant (H₂O₂). All those parameters and their effects on the photocatalytic efficiency of the NPs are discussed in this review.

This paper specifically addresses the NPs/PS systems mainly devoted to water treatment applications. The review is organized as follows. First, the main part of the review is dedicated to the TiO₂/PS materials. Actually, a huge amount of data are available with these systems. We extract the main trends in terms of the nature of the PS, linkage mode, PS content, presence of metallic heavy atoms, etc. In the second part, the effect of the PS when it is used with ZnO semiconductor will be investigated. ZnO/PS systems appear attractive for water purification since ZnO displays a lot of similarities with TiO₂. Then, carbon materials such as fullerene and graphene are discussed. They have recently emerged as promising candidates for photocatalysis. They can be seen as “hot topic” and will certainly induce major changes in the fields of photocatalysis and water treatment.

2. Titania/PS systems

Several kinds of titania are utilized for photocatalytic applications. Nanoparticles include commercial Degussa P25 (80% anatase and 20% rutile),^[40,51-60] pure anatase either prepared by sol-

gel method or commercial.^[36,50,61-72] In some special case, TiO₂ nanotubes^[73] and TiO₂ nanofibers^[74] are also employed. The impact of the nature of titania will not be investigated in this review since it is already discussed in a lot of reports and reviews.^[29-32] However, the nature of the titanium dioxide nanoparticles will be mentioned in all the examples presented below. In addition, **Table 1** summarizes the PS/TiO₂ systems reported in the literature along with the photodegradation parameters and pollutants.

Table 1: Summary of the literature on PS/TiO₂ systems along with the photocatalytic degradation parameters and pollutants.

Type of TiO ₂	Size of nanoparticle	PS	Amount of PS	Adsorbed or grafted	Type of covalent bond	H ₂ O ₂	Pollutant/Photocatalytic application	Light used (wavelength range)	Type of ROS involved	Ref
Commercial Anatase	3.5 nm	CuPc	1.5% of CuPc loading mass fraction	Adsorbed	-	no	furfural pollutant	Simulated solar light (Visible + small % UV)	ns	[63]
Sol-gel	100-200 nm	CuPcTs	-	Adsorption (Direct complexation)	-	no	AO7	Simulated solar light (Visible + small % UV) ($\lambda > 295$ nm)	¹ O ₂ and other ROS from TiO ₂	[75]
As-prepared anatase	-	P FeP	-	Adsorption (Chemisorption)	-	Yes	RhB	Pure visible light and UV light	O ₂ ^{•-} and HO [•]	[62]
Anatase polycrystalline	-	Cu(II)TCPP with different peripheral substituents	6-10 μ mol PS/g-TiO ₂	Adsorption (impregnation)	-	no	4-NP	Simulated solar light (Visible + small % UV)	ns	[69]
TiO ₂ P25	~30 nm	MTCPP (M=Fe, Cu, Zn) HTCPP	~4-6 μ mol PS/g-TiO ₂	Adsorption	-	Yes	Atrazine	Pure visible light ($\lambda > 420$ nm)	Mainly HO [•]	[51]
TiO ₂ polycrystalline (80% anatase & 20% rutile)	~ 30 nm	H ₂ TPP CuTPP	18 μ mol PS/g-TiO ₂	Adsorption	-	no	4-NP	Pure visible light	Mainly O ₂ ^{•-}	[38]
Anatase sol-gel TiO ₂ coated on a cotton fabric	~ 10 nm	TCPP		Adsorption	-	no	MB Coffee and red wine stains	Simulated solar light (Visible + small % UV)	O ₂ ^{•-}	[36]
Anatase sol-gel TiO ₂ coated on a cotton fabric	-	CuTCPP		Adsorption	-	no	MB Coffee and red wine stains	Simulated solar light (Visible + small % UV)	¹ O ₂ and O ₂ ^{•-}	[76]
Anatase TiO ₂	-	CuTCPP with different peripheral substituents (-OH, -CO ₂ C ₂ H ₅ , -COOH)	6 μ mol PS/g-TiO ₂	Adsorption	-	no	4-NP	Simulated solar light (Visible + small % UV) (λ : 380-780 nm)	HO [•] , O ₂ ^{•-} as well as h ⁺	[65]
TiO ₂ P25	-	TCPP	0.015-0.025 g PS/g-TiO ₂	Adsorption	-	no	Pharmaceutical famotidine	Pure visible light and Real sunlight	¹ O ₂ and O ₂ ^{•-}	[54]

Anatase Sol-gel	4-10 μm	CuAPTPP	-	Grafting	Covalent bond <i>via</i> TDI	no	MB	Pure visible light	ns	[66]
TiO ₂ P25	~ 100 nm in diameter	FeTCPP	-	Grafting	Covalent bond <i>via</i> SA or SSA	no	MB	Pure visible light (λ : 400-800 nm)	ns	[40]
Degussa P25	Aggregates > 20nm	MTPP (M= Fe, Co, Mn & Cu)	6 μmol PS/g-TiO ₂	Adsorption	-	no	MO	Pure visible light (λ >400 nm) and UV light	HO [•] and O ₂ ^{•-}	[59]
TiO ₂ P25	21 nm	TCPP	0.05 mmol PS/g-TiO ₂	Adsorption	-	no	MB	Pure visible light (λ >420 nm)	HO [•] , O ₂ ^{•-} and h ⁺	[57]
Anatase TiO ₂	-	MTPP (M=Cu, Zn & Ni)	6 μmol PS/g-TiO ₂	Adsorption	-	no	4-NP	Simulated solar light (Visible + small % UV)	HO [•] and O ₂ ^{•-}	[68]
Sol-gel TiO ₂ (mesoporous anatase)	-	H ₂ EtPp MCPp (M=Zn, Cu & Co)	-	Adsorption (one-pot solvothermal condition <i>via</i> a one-step method)	-	no	4-NP	Simulated solar light (Visible + small % UV)	HO [•] and O ₂ ^{•-}	[71]
Degussa P25	-	HTPP ZnHTPP SnHTPP	10 mg PS/g-TiO ₂	Adsorption (<i>via</i> phenol hydroxyl bonding mode)	-	no	MO	Pure visible light	HO [•] , O ₂ ^{•-} and ¹ O ₂	[52]
Commercial pure anatase Polycrystalline TiO ₂ (Sol-gel)	-	CuTCPP with different peripheral substituents (-OH, -CO ₂ C ₂ H ₅ , -COOH)	6 μmol PS/g-TiO ₂	Adsorption	-	no	4-NP	Simulated solar light (Visible + small % UV) (λ : 340-780 nm)	ns	[64]
Anatase TiO ₂	-	CuTCPP with different peripheral substituents (-CO ₂ C ₂ H ₅ , -COOH)	6 μmol PS/g-TiO ₂	Adsorption	-	no	4-NP	Simulated solar light (Visible + small % UV)	ns	[67]
Degussa P25	-	NiTCPP	0.002-0.0855 mmol PS/g-TiO ₂	Adsorption (Chemisorption)	-	no	Decomposition of H ₂ O ₂	Simulated solar light (Visible + small % UV)	HO [•]	[55]
TiO ₂ P25 coated on stainless steel mesh	~25 nm (SEM)	CuPc	0.005-1 g PS/g-TiO ₂	Adsorption	-	no	Photocatalytic conversion of CH ₄ and CO ₂	Pure visible light and UV light	[•] CO ₂ ⁻ and [•] CH ₃	[58]
TiO ₂ P25	12.47 nm (XRD) 15-20 nm (TEM)	ZnPc	0.001 g PS/g-TiO ₂	Adsorption (Chemical impregnation)	-	no	Erythromycin pharmaceutical antibiotic	Pure visible light (λ >400 nm)	HO [•] and O ₂ ^{•-}	[56]
Anatase (main phase)/brookite mixed crystal TiO ₂	~10 nm	Assymmetric ZnP containing three pyridine and one COOH groups	1.0% ZnP/TiO ₂	Adsorption	-	no	Photoreduction of CO ₂ into CO/CH ₄	Pure visible light (λ ≥420 nm)	-	[77]
Anatase TiO ₂	-	Substituted CuTPP	6 μmol PS/g-TiO ₂	Adsorption	-	Yes	4-NP	Pure visible light (λ >400 nm)	O ₂ ^{•-} and mainly HO [•]	[50]

Thin film of nanocrystal line sol-gel TiO ₂	~80 nm	substituted-Ru(bpy) ₃ ²⁺	-	Adsorption	-	no	MB	Pure visible light ($\lambda > 425$ nm)	Not mentioned	[78]
Degussa P25	-	Silylated [Ru ^{II} (py-pzH) ₃] ²⁺ : Ru(py-pz-Si≡) ₃	2.23 μ mol PS/g-TiO ₂	Grafting	Covalent bond via the silyl group of PS	no	Perhalogenated organics (CCl ₄)	Pure visible light ($\lambda > 450$ nm)	-	[60]
TiO ₂ P25	-	Xanthene dyes (rose Bengal, rhodamine B, eosin Y and erythrosine)	0.05 mmol PS/g-TiO ₂	Adsorption	-	no	2,4-DCP	Pure visible light ($\lambda > 420$ nm)	¹ O ₂ , HO [•] and O ₂ ^{•-}	[53]
Commercial Anatase TiO ₂	-	imidazolyl-linked CuP	6 μ mol PS/g-TiO ₂	Adsorption	-	Yes	4-NP	Pure visible light ($\lambda > 400$ nm)	HO [•] from H ₂ O ₂	[70]
TiO ₂ nanotubes	Internal diameter of 100nm and wall thicknesses of 15nm	H ₂ TCIPP	2.5 mmol/L H ₂ TCIPP	Adsorption (Impregnation)	-	no	RhB	Pure visible light	O ₂ ^{•-} and mainly HO [•]	[73]
TiO ₂ nanofibers	Nanorods: diameters of 30-60 nm and lengths of 80-120 nm	TNCuPc	-	Adsorption (solvothetmal processing)	-	no	RhB	Pure visible light ($\lambda > 400$ nm)	HO [•]	[74]
TiO ₂ paste containing polyethylene glycol	-	Azo-bridged ZnP	1 mmol/L	Grafting	Covalent bond via hydroxybenzoic acid	no	Photovoltaics (DSSC: Dye Sensitized Solar Cells)	-	-	[79]
Commercial Anatase TiO ₂	-	Chloro-and hydroxo-Sn(IV)P	6 μ mol PS/g-TiO ₂	Adsorption (impregnation)	-	no	4-NP	Pure visible light and simulated solar light	¹ O ₂	[61]
Sol-gel TiO ₂ film	-	Substituted ZnTPP	-	Adsorption	-	no	-	-	-	[80]
TiO ₂ P25 Sol-gel TiO ₂	~ 30 nm	Co ^{II} TSP	7.7mg PS/1g TiO ₂ -APTES 30% coverage (6.4 x 10 ⁻⁴ : 1)	Grafting	Covalent bond via APTES	-	Photocatalytic formation and depletion of H ₂ O ₂	Pure visible light	O ₂ ^{•-} , HO [•] and HOO [•]	[81]
Sol-gel TiO ₂ (anatase)	80-100 nm	NiTPP	1% (w/w) porphyrin/TiO ₂	Adsorption	-	no	2,4-DCP	Visible light ($\lambda = 419$ nm)	HO [•] (increases with pH)	[82]
TiO ₂ P25	-	C.I. Pigment Yellow 154 (PY) C.I. Pigment Red 254 (PR)	1.1 mmol PS/51.8 mmol TiO ₂ PS adsorbed: 5.5% (PY/TiO ₂) 4.4% (PR/TiO ₂)	Adsorption (solvothetmal method)	-	no	MO	Visible light ($\lambda > 420$ nm)	O ₂ ^{•-}	[83]

2.1. Nature of the PS

Various types of PSs were utilized as photosensitizers with TiO₂.^[69, 78] Three main classes can be distinguished: xanthene dyes, transition metal based dyes and organic dyes.

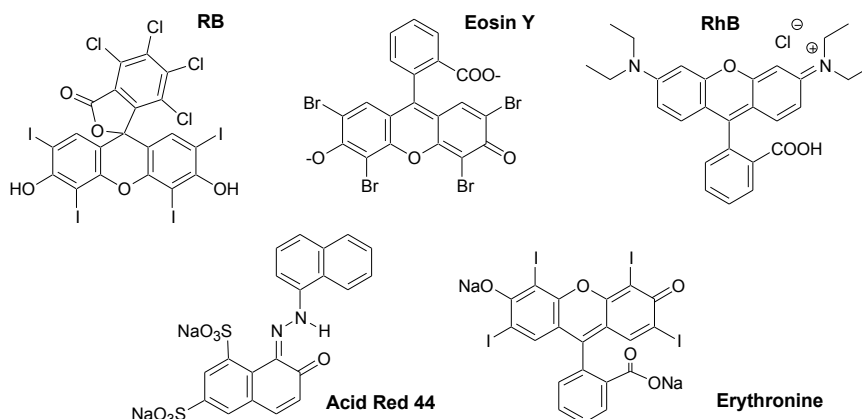
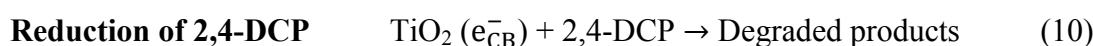
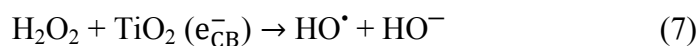
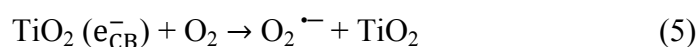
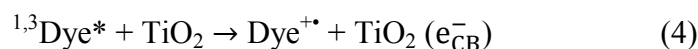


Fig. 2: Schematic presentation of various types of Xanthene dyes: Rose bengal (RB), Eosin Y, Rhodamine B (RhB), Acid Red 44, and Erythrosine

The first class of PSs concerns the xanthene dyes (Fig. 3). As an example, Li *et al.* used Rose bengal, rhodamine B, eosin Y and erythrosine for sensitizing TiO₂ P25.^[53] Note that the PS was linked by adsorption in both monomer and dimer forms. The carboxyl groups of the dyes render possible to link the PS to TiO₂ surface through the valence-unfilled Ti(IV). The photocatalytic activity towards the degradation of 2,4-dichlorophenol (2,4-DCP) under visible light was scarce in the cases of free (non linked to the NP) Rose bengal, erythrosine, eosin Y, but null in the case of Rhodamine B (RhB). This effect was attributed to the singlet oxygen (¹O₂) production of Rose bengal (ϕ_{Δ} : 0.76), erythrosine (ϕ_{Δ} : 0.60) and eosin Y (ϕ_{Δ} : 0.40) triggering this pollutant's photodecomposition. Rhodamine B was unable to produce ¹O₂. More interestingly, when adsorbed onto TiO₂, the photocatalytic degradation of 2,4-dichlorophenol (2,4-DCP) under visible light was significantly enhanced for all the four PSs. The greater performances of the PS/TiO₂ systems is attributed to the fact that the tested PSs possess oxidation potentials higher than that of TiO₂, making possible the electron transfer from the excited PS to the conduction band (CB) of TiO₂. Thus, besides ¹O₂ mainly elaborated by PS, other reactive oxygen species (ROS) especially HO[•] and O₂^{-•} result from this electron transfer. The authors also demonstrated that even in the absence of molecular oxygen, the PS/TiO₂ system can photodegrade the organic pollutant *via* the direct scavenging of the electron from the CB of TiO₂. The photo-degradation of 2,4-DCP has the following order: eosin Y \approx Rose bengal > erythrosine B > Rhodamine B.^[53] The proposed mechanism of the photodegradation of the organic pollutants by the dye/titania system under visible light irradiation is mentioned because it is roughly similar for all the PS/titania systems regardless of the nature of the PS.^[53]



It appears that these xanthene dyes including Rose bengal, erythrosine, eosin Y and Acid Red 44 have the capacity to degrade organic pollutants. They are attractive due to their low cost, large visible light absorption and moderate oxidation-reduction aptitude as compared to the other organic dyes and transition metal based dyes. However, they possess lower photo-conversion efficiency and lack good stability.^[53,76] For these reasons, these systems are not the most used dyes in practice to sensitize titania.

The other category of PS is related to the d^6 transition metal based dyes such as ruthenium Ru(II)- or iridium Ir(III) complexes.^[37,53] As an example, substituted Tris(bipyridine)ruthenium(II) dyes $[\text{Ru}(\text{bpy})_3^{2+}]$ (Fig. 3) were adsorbed onto a thin film of nanocrystalline sol-gel TiO_2 spin-coated on indium tin oxide plates (ITO).^[78]

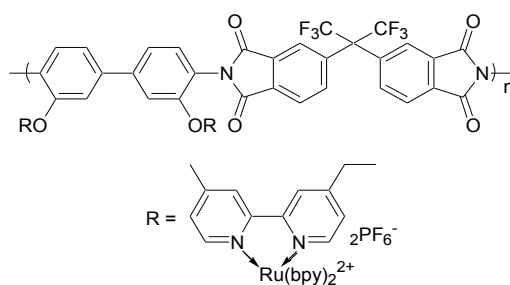


Fig. 3: Formula of substituted Tris(bipyridine)ruthenium(II) dyes $[\text{Ru}(\text{bpy})_3^{2+}]$. Taken from reference ^[78]

Beside the high light absorptivity of this dye, it was of interest because it can yield an efficient and stabilized adsorption onto TiO_2 thanks to its polyimide backbone. Hence, the combination of the good thermal and mechanical stabilities of the pre-stated polyimide backbone and the elevated local density of the dye, made it a good candidate for TiO_2 photosensitization. Under visible light, the photoactivity of the obtained catalytic system was evaluated in terms of methylene blue (MB) degradation. The $\text{Ru}/\text{TiO}_2/\text{ITO}$ system prompted a small level of photooxidative degradation of MB under the adopted experimental conditions while no activity was reported in the case of TiO_2 alone

(neither sol-gel nor commercial P25). This outcome proved that the photoactive range of TiO₂ was extended efficiently from the ultraviolet into the visible light region and that the dye-sensitized hybrid catalyst had a potential photocatalytic activity.

However, this PS remains quite expensive. This is due to the large cost of the synthesis as well as the purification operations. For instance, one gram of terpyridine ruthenium-based black dye costs around 3300 euros.^[84] In addition, the phototoxicity of these dyes cannot be excluded.^[85] For all these reasons, it appears yet impossible to implement these dyes in large-scale water treatment systems.

The organic dyes represent the most used category of PS in photocatalysis applications for water treatment. The two most popular are porphyrins and phthalocyanines. Phthalocyanines are interesting as they are photoactive in the visible and the IR light zones. The majority of phthalocyanines are solubilized in ethanol but encounter a scarce solubility and high aggregation in aqueous solutions.^[75] However, tetrasulfonated (Ts) phthalocyanines (Pc), named as PcTs, are better solubilized in water (**Fig. 4**). This property is credited to the occurrence of the four sulfonated functional groups. Besides, the latter groups can also enable a facile linkage of this PS to the TiO₂ NPs surface.^[75,86] The ¹O₂ generation by PcTs is pH dependent. Thus, ¹O₂ is efficiently generated at pH of 0.6 unlike at pH 8 at which the dispersion of the PS lacks good stability.^[75] These PSs are considered as good candidates to sensitize TiO₂ for various reasons. When phthalocyanines absorb the visible light, the injection of the excited electrons from the PS to the conduction band of TiO₂ is favored due to the proper energy state of this PS regarding TiO₂.^[86]

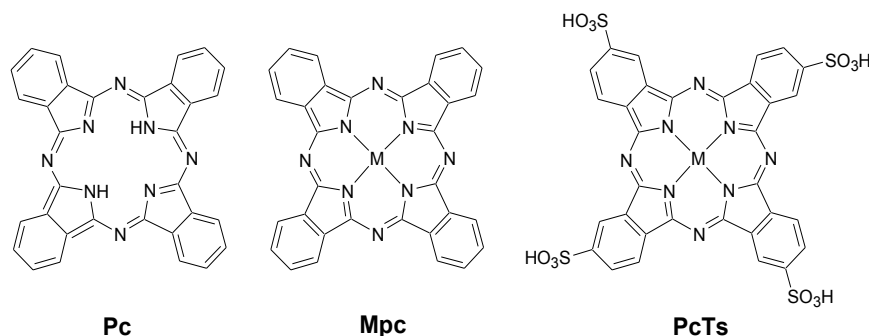


Fig. 4: Schematic presentation of phthalocyanine, metallo-phthalocyanine and tetra-sulfonated metallo-phthalocyanine (PcTs)

Porphyrins and their analogues including metal-free, metallated and supramolecular porphyrins, already exist in natural systems and are involved in many vital processes. In plants, porphyrin-based chlorophyll chromophores maintain superior absorption of light which generates an efficient harvesting of the solar energy serving for photosynthesis. Such role of porphyrins in photosynthesis grew a lot of curiosity around it for researchers aiming to mimic nature and implement its systems. Based on this, porphyrins were considered as efficient candidates for visible-light sensitization of the

TiO₂ matrix targeting enhanced photocatalytic activity.^[36,38,51,69,76] In details, porphyrins are macrocyclic molecules holding a large delocalized π electrons system (**Fig. 5**).^[51,76] Due to this structure, porphyrins possess a large light absorption coefficient. They absorb intensively in the visible range of light, precisely in the 400–450 nm region referring to the Soret band (blue) as well as in the 500–700 nm region corresponding to the Q-bands (red), all representing major constituents of the solar light.^[36,38,51,76] Similar to phthalocyanines, the energy of the excited state of the porphyrin PS favors the electron injection into the CB of TiO₂.^[51] Likewise, most of the porphyrins have poor solubility in aqueous media.^[38] Furthermore, porphyrins embrace a wide range of redox, photochemical and photophysical properties and a high chemical- and photo-stability.^[36,51,52,76] Sensitizing TiO₂ semiconductor with porphyrins produces a highly effective TiO₂/porphyrin photocatalytic system. Similar to other PS/TiO₂ systems, the latter benefits from the electron transfer from excited porphyrin to the CB of TiO₂ or pre-adsorbed molecular oxygen. Nevertheless, another interesting feature is that some porphyrins are capable of direct O₂ activation without the aid of TiO₂, thus cooperating with TiO₂ in the photooxidation reactions.^[38]

In the following, we will mainly concentrate on the organic dyes, *i.e.* phthalocyanine and porphyrins.

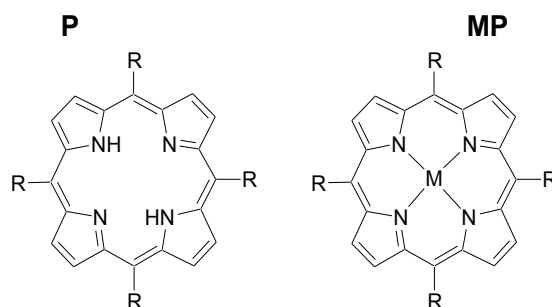


Fig. 5: Schematic presentation of porphyrin (P) and metallo-porphyrin (MP)

2.2. Metallo-PS

The photophysical characteristics of the organic dyes can be easily altered by inserting a metal into the central cavity of the PS. The coordination of a central metal, such as Cu, Fe, Zn, etc, into these PSs generates metalloporphyrins and metallophthalocyanines, that share many common properties with metal-free PSs but with more extensive and stronger photoresponse in the visible light range.^[38,51,62,69,71,76]

2.2.1. Metallo-porphyrins

Many studies investigated the influence of introducing a metal into the inner cavity of the porphyrin on the photocatalytic performance of the hybrid organic/inorganic PS/TiO₂ composites. Also, various attempts were made to explore the type of metal that can harvest the best photocatalytic efficacy. As an example, Wang *et al.* chose Cu metal to occupy their substituted-

tetrakis(4-carboxyphenyl)porphyrin (TCPP) rings.^[38] The metal-free and the copper porphyrin PSs were impregnated onto polycrystalline TiO₂ to conduct the degradation of 4-nitrophenol (4-NP) when irradiated with visible light. It was demonstrated that the photoactivity of the sensitized TiO₂ in the presence of Cu was more elevated than that involving metal-free porphyrin. Thus, the coordination of Cu to the porphyrin ring enhanced the photocatalytic activity of the NP composites due to its significant role in the electron transfer process mainly generating superoxide anions as revealed in this mechanism.^[38]



In general, the introduction of the metal ion enhanced the adsorption of the pollutant and rendered an easier charge-transfer process between the pollutant and TiO₂. As for CuTCPP/TiO₂, Cu(II) ions own partially filled d-orbitals enabling fluorescence quenching by electron or energy transfer.^[59] To support this hypothesis, it appears interesting to mention the work of Huang *et al.* They used non-metallated porphyrins, zinc- and tin- metallated porphyrins to sensitize TiO₂ NPs by a phenol hydroxyl bonding mode. It was observed that the fluorescence normally displayed by all the above mentioned PS was quenched after the adsorption of those PS onto TiO₂ (**Fig. 6**). This seems to imply that the photogenerated electrons are effectively injected into the CB of TiO₂.^[52]

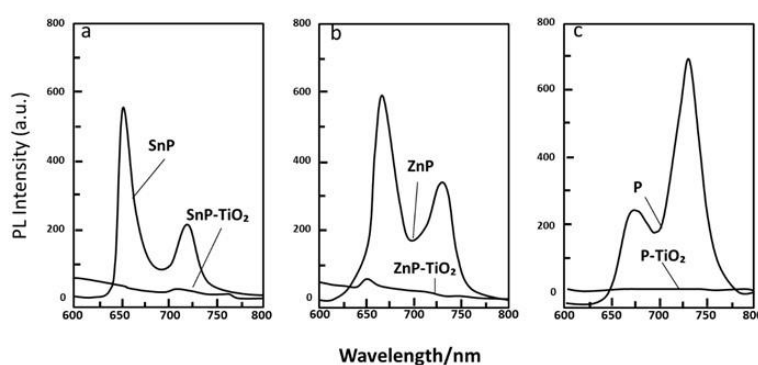


Fig. 6: Fluorescence spectra of porphyrin (P), Sn and Zn porphyrins (SnP and ZnP) and TiO₂ NPs linked with porphyrins ($\lambda_{\text{ex}} = 549 \text{ nm}$). Taken from reference ^[52]

To confirm the role of different ROS produced by PS/TiO₂ systems, it seems relevant to discuss the results of Granados-Oliveros and coworkers.^[51] In their trial to photodegrade atrazine pollutant under visible light, Granados-Oliveros and coworkers employed metal-free TCPP and its metal

analogues with different metal centers (MTCPP, M = Fe(III), Cu(II), Zn(II)) adsorbed onto TiO₂ P25 NPs. In such reacting systems involving those types of nanoparticle composites, it seems that superoxide anions (O₂^{•-}) are the most generated ROS. Though, the photocatalytic experiments using CuTCPP/TiO₂ targeting the degradation of atrazine under visible light and in the presence of molecular oxygen was conducted but no effect was observed.^[51] Thus, it was concluded that O₂^{•-} species are not capable of interacting with atrazine unlike in the case of nitrophenol.^[38] This sheds light on the relation between the nature of the targeted pollutant and the type of ROS required to degrade them when assessing the photoactivity of certain catalysts. So just like the degradation of atrazine requires HO[•] more likely than O₂^{•-}, other organic pollutants such as cyanuric acid and chlorofluorocarbons cannot be degraded by HO[•]. The authors used the same systems but in the presence of an optimized quantity of H₂O₂ which gave good results in photodegradation of atrazine.^[51] The precise mechanism involved in the presence of H₂O₂ will be discussed in details in the section 2.3.4. of the review.

Coming back to the metalloporphyrins discussed by Granados-Oliveros and coworkers, *i.e.* metal-free TCPP and MTCPP with different metal centers, Fe(III), Cu(II) and Zn(II), adsorbed onto TiO₂ P25 NPs, the effect of the central metal can be described. All the NPs with Zn, Fe and Cu metals possess better efficiency in photocatalysis than metal-free hybrid NPs under the tested conditions. As comparing between the metal ions, Cu evidenced the best among them all according to the following order: CuTCPP/TiO₂ > FeTCPP/TiO₂ > ZnTCPP/TiO₂. It was concluded that the metal ions with unfilled d-orbitals (Cu) induced a superior photoreactivity compared to those with filled electron shells or metal-free ones.^[51]

The greater positive impact in photocatalysis displayed by the presence of Cu in the ring of the porphyrin was also confirmed by Sun *et al.*^[68] This research team synthesized a mono-functionalized porphyrin derivative, 5-mono-[4-(2-(4-hydroxy)-phenoxy)ethoxy]10,15,20-triphenyl porphyrin, and its Cu(II), Zn(II) and Ni(II) metalloporphyrins, which were adsorbed onto anatase TiO₂. The assessment of the photocatalytic efficiency of all those MP/TiO₂ composites through the degradation of 4-NP under simulated solar light revealed much better effect than with bare TiO₂. However, as shown by previous studies, CuP/TiO₂ lead to the best performance followed by ZnP/TiO₂, and then NiP/TiO₂. This result was explained by the compatibility between the excited potential of CuP with the potential of the CB of TiO₂.^[68]

In a similar approach, Zhou *et al.* also demonstrated that in terms of photocatalysis efficiency, CuP/TiO₂ dominated the other metalloporphyrin(MP)/TiO₂(P25) systems including those involving Fe, Co and Mn metals either under pure visible or under UV light. Under both light sources, all the stated MP have better activity than pure TiO₂. In addition, the greater improvement in the photocatalytic efficiency was witnessed under UV light.

The pre-listed results obtained by the researchers were also validated and further explained by Zhao *et al.*^[71] Their metalloporphyrins (MP, M= Zn, Cu and Co) were linked to TiO₂ under a one-pot solvothermal condition involving a one-step method. The hybrid MPs gave the same trend in photocatalysis under simulated solar light assuring the earlier results. Thus, again CuP/TiO₂ possessed the best efficiency among all following this order: CuP-TiO₂ > CoP-TiO₂ > ZnP-TiO₂ > bare TiO₂ (Fig. 7).

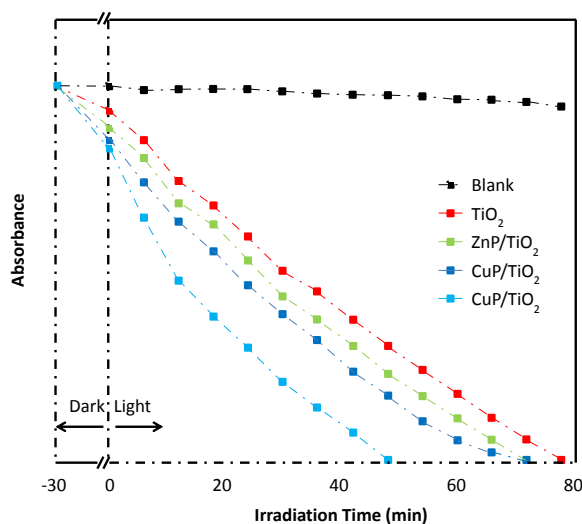


Fig. 7: Photocatalytic degradation of 4-NP as a function of the time of irradiation for CuP/TiO₂, CoP/TiO₂, ZnP/TiO₂ and bare TiO₂. Taken from reference^[71]

Comparing the metals, Zn(II) holds a completely filled d-orbital maintaining its stability and hindering any further acceptance or transfer of external electrons. Conversely, Co(II) holds a d⁷ orbital. Consequently, it is possible for Co(II) to gain electrons but the potentials of the PS and the CB of TiO₂ do not match. Cu(II) needs to gain only one electron to reach steady state. Thus, in combination of the CB of TiO₂, the electron transfer is improved since the holes and electrons are efficiently separated generating a better photocatalytic performance.^[71]

At the same time, Afzal *et al.* inaugurated the work on ‘visible-light-active self-cleaning’ fabrics based on dye-sensitization (Fig. 8).^[36] They also utilized TCPP to sensitize anatase TiO₂ coated on a cotton fabric for self-cleaning purposes. This system showed very good efficiency for self-cleaning revealed by its significant photodegradation of MB, coffee and red wine stains under simulated sunlight. As their systems encountered photostability issues, this research team introduced a Cu metal into the previously-used porphyrin’s core. Their choice of Cu was based on its superior photocatalytic efficiency under visible light over the other metals (Zn, Fe, Ni and Co) which is compatible with the previous illustration in this review.

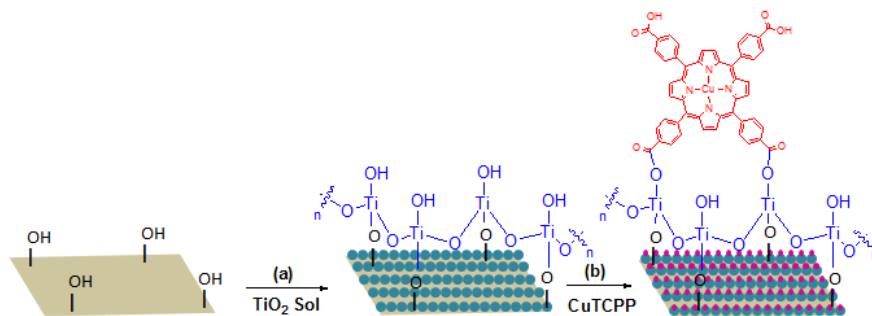


Fig. 8: Schematic presentation of the formation of self-assembled monolayer of CuTCPP molecules on TiO₂-coated cotton. (a) Treatment of pristine cotton with TiO₂ colloid. (b) Treatment of TiO₂-coated cotton with CuTCPP solution in DMF to form CuTCPP/TiO₂-coated cotton. Taken from reference [76]

Assessing their photocatalytic activity, the TiO₂ system functionalized with TCPP alone possessed faster degradation rate than that with CuTCPP. Indeed, it is twice faster for TCPP in the degradation of MB under visible light than for CuTCPP. This result appeared to be contradictory with the other results involving copper porphyrins. The authors explained that the slower rate in photocatalysis employing CuTCPP, possessing unpaired electrons in d orbital, may be due to the short lifetime of the excited state and the lack of fluorescence emission as compared to TCPP. Free-base porphyrins, for instance TCPP, with no unpaired electrons displayed long excited state lifetime and are intensely fluorescent, causing an efficient electron injection into the CB of TiO₂. Yet, the authors improved the photostability and the reproducibility after the incorporation of Cu (**Fig. 9**). The authors considered that Cu in Cu(II)TCPP is paramagnetic with partially filled d orbitals which causes the deactivation of TCPP excited state. This results in larger recombination with no fluorescence emission, and thus, making Cu(II)TCPP less susceptible to photobleach. [76]

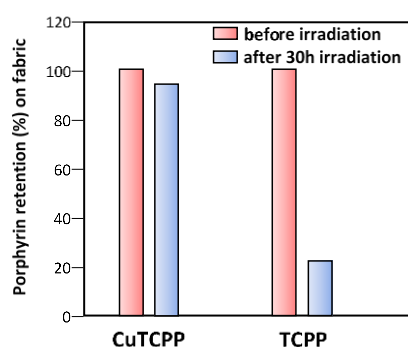


Fig. 9: Percentage retention of CuTCPP and TCPP on TiO₂-coated cotton fabrics after 30 h of visible light irradiation. Taken from reference [76]

Tin (Sn) appears also as a good candidate for metallo-porphyrin/TiO₂ systems. Huang *et al.* used non-metallated (P), zinc- and tin- metallated (ZnP, SnP) porphyrins to sensitize TiO₂ NPs *via* a phenol hydroxyl bonding mode. It was observed that the fluorescence normally displayed by all the above mentioned PS was quenched after the adsorption of those PS onto TiO₂ (**Fig. 6**). This seems to

imply that the photogenerated electrons are effectively injected into the CB of TiO₂. Under visible light irradiation, all the sensitized NPs showed better photocatalytic activity towards the degradation of methyl orange (MO) than pure TiO₂, with SnP/TiO₂ being the most efficient followed by P/TiO₂ then ZnP/TiO₂ (Fig. 10). This effect was possible due to the ROS and ¹O₂ by the reaction between the produced electrons and the pre-adsorbed oxygen molecules.

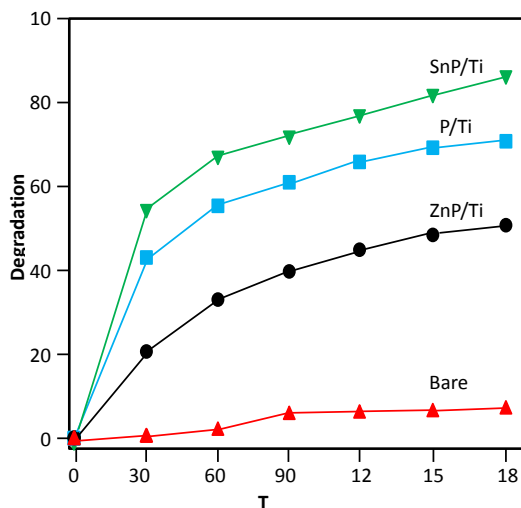
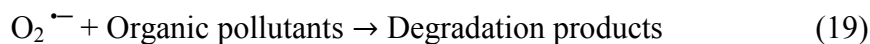
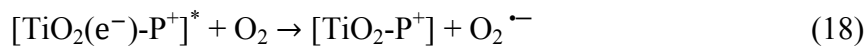


Fig. 10: Kinetic curves of the degradation of MO by bare TiO₂, P/TiO₂, SnP/TiO₂ and ZnP/TiO₂ nanoparticles. Taken from reference [52]

The higher efficiency of Sn may be ascribed to the fact that Sn(IV) possesses a d⁶-orbital with trans-diaxial ligands. In addition to the phenol hydroxyls linking of the SnP to TiO₂ by the hydroxyl group of TiO₂, Sn⁴⁺ ions may interact also with those hydroxyl groups. This type of interaction may enhance the electron transfer process between the PS and titania. As for ZnP having the lowest efficiency, Zn²⁺ exhibits no interaction with the hydroxyl groups of TiO₂ and its charge remains unfavorable for the electron transfer process to occur. It should be also stressed that SnP is stable against the acid-induced demetallation and that the high charge on Sn⁴⁺ ion makes it the most easily ring-reduced among all metalloporphyrins. [52]

On the contrary, Fe seems less appropriate for photocatalytic applications. Porphyrin (P) and Fe(III)P were adsorbed onto TiO₂ surface *via* their carboxyl group by Huang and coworkers. [62] The absorption spectrum of TiO₂ after sensitization displayed the profile of porphyrin. However, a blue shift of the Soret and Q-bands is witnessed in the case of hybrid TiO₂ linked to the metal-P as compared to TiO₂ sensitized with free P. The photocatalytic activity of those composites and bare TiO₂ towards the degradation of RhB under both UV and visible light indicated that the sensitization of TiO₂ improved its photocatalytic activity by 20-26 % under UV light. Unexpectedly, although both TiO₂-P and TiO₂-Fe(III)P displayed almost same absorption bands in the visible light range, only the former was capable of degrading RhB under visible light with lower rate as compared to its activity under pure UV. The authors thus declared that unlike TiO₂-P, TiO₂-Fe(III)P is not being excited under visible light. As a result, no electron transfer from the excited PS into the CB of TiO₂

existed leading to the suppression of the RhB degradation. Further addition of H₂O₂ to the TiO₂-Fe(III)P system provoked better results in terms of photocatalysis performance.^[62] The involvement of H₂O₂ is to be discussed in another part of this review.



2.2.2. Metallo-phthalocyanines

The insertion of a metal in the central cavity of the organic PS is a useful way to enhance the visible light sensitivity of TiO₂ in dye-sensitized systems. Metallophthalocyanines (MPc, M = Zn,^[56] Cu) (**Fig. 4**),^[58,63,74,75] tend to absorb intensively in the blue-green light zone. They are proficient of accumulating up to 50 % of the sunlight energy and retain a superior stability and resistance over chemical degradation.

Metallophthalocyanines, particularly with copper as the coordinated metal (CuPc), have been selected for prolonging the visible light sensitivity of TiO₂ in several studies. For example, in 2007, Kang *et al.* synthesized CuPc/TiO₂ composites through adsorption method.^[63] The introduction of this PS onto TiO₂ was proved to leave the crystal structure of the NPs intact since the PS occupies only the surface of TiO₂. The evolution of new peaks in the absorption profile of TiO₂ in the 500-600 nm region was witnessed. Thus, the photoresponse of those NPs was said to be shifted to visible light region. This composite system, at an optimal amount of CuPc adsorbed, showed good photocatalytic efficiency towards the degradation of furfural pollutant under simulated solar light.^[63]

In another study, copper(II) phthalocyanine tetrasulfonate (CuPcTs) was utilized to sensitize bare sol-gel TiO₂ by direct complexation.^[75] The yielded hybrid NPs succeeded in photodegrading Acid Orange 7 (AO7) under simulated solar light. This effect was attributed to both ¹O₂ generated from this PS upon excitation beside other ROS produced from the indirect photo-activation of TiO₂.

On the same pattern, the photocatalytic properties of TiO₂ were enhanced through the coupling of copper tetranitrophthalocyanine (TNCuPc) (**Fig. 11**) with TiO₂ nanofibers using solvothermal processing.^[74] Bare TiO₂ had negligible photocatalytic activity when the degradation of RhB was investigated under pure visible light. However, and under the same experimental conditions, introducing large loadings of TNCuPc onto TiO₂ contributed to better photocatalytic degradation efficiency towards RhB (**Fig. 11**).^[74]

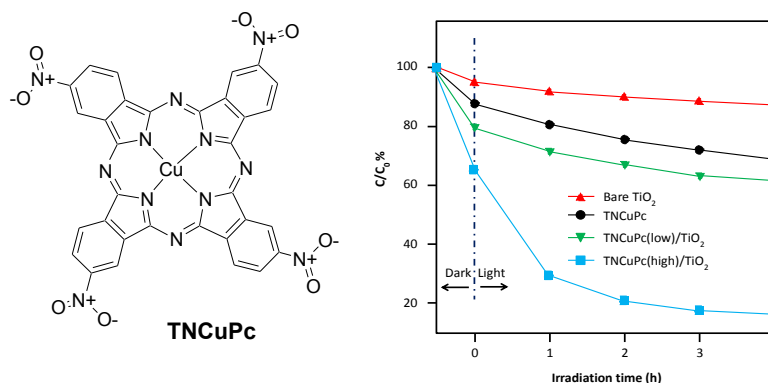


Fig. 11: Schematic presentation of copper(II) 2,9,16,23-tetranitrophthalocyanine) (TNCuPc) and the degradation rate of RhB in the presence of bare TiO₂, pure TNCuPc and TNCuPc/TiO₂ with lower and higher concentrations of Cu. Taken from reference [74].

In a more recent approach, CuPc was also chosen by Yazdanpour and coworkers to sensitize TiO₂ P25. CuPc/TiO₂ was coated on a stainless steel mesh. The proficiency of this catalyst was assessed through the photocatalytic conversion of methane and carbon dioxide gases under visible light where it appeared to be efficient. [58] However, Vignesh *et al.* investigated zinc phthalocyanine ZnPc coupled to TiO₂ (ZnPc/TiO₂) *via* chemical impregnation. The modified NPs were employed in the photocatalytic degradation of erythromycin pharmaceutical antibiotic under visible light irradiation. Those NPs showed superior photoactivity as compared to bare TiO₂. It should be noted that the authors shed light on the importance of a moderate PS/TiO₂ catalyst amount used in the photocatalytic test, since an optimal increase in the amount of ZnPc/TiO₂ triggered better photodegradation. This is attributed to the increase of the number of active sites on the surface of the catalyst, inducing more photoreduction. Otherwise, with higher amounts of the catalyst, the NPs tend to agglomerate which decrease its accessible surface area and hence lessens its photoactivity. [56] This aspect will be discussed thoroughly in the section 2.4.

2.3. Photocatalytic mechanisms under UV, solar and visible light

It is well-established that the efficient photocatalytic degradation of different types of pollutants by the dye-sensitized TiO₂ systems is attributed to the concomitant effect of both the semiconductor and the PS. The key factor in this cooperation is the electron-transfer.

However, the excitation of TiO₂ necessitates the availability of UV light while the PS is visible-light sensitive. Such characteristics compel a different performance in the degradation of pollutants when the type of light is changed. The light source may be pure visible ($\lambda \geq 400$ nm), simulated solar light or UV light. The mechanism of charge transfer provoked by each type of irradiation source onto the dye-sensitized TiO₂ system is further explained. In addition, the nature of the additional radicals generated in the presence of H₂O₂ is also described.

2.3.1. Visible light

In general, upon visible light irradiation of the PS/TiO₂ catalytic system, only the PS is excited to generate an electron (e⁻) in the singlet excited state of the PS. The produced electrons are injected into the conduction band (CB) of the semiconductor while the valence band remains intact. The transferred electrons react with the adsorbed oxygen molecules prompting a series of oxidation-reduction reactions that generate reactive oxygen species (ROS, O₂^{•-} and HO[•]) leading to the degradation of the pollutants (Fig. 12a).^[51,53,57,58] In the majority of the studies, the PS is employed to indirectly induce the activation of TiO₂ to initiate the production of O₂^{•-} and HO[•] that seem to be the dominant ROS involved in the catalytic process. However, the contribution of ¹O₂ produced by the PS is barely mentioned but may not be excluded.^[76] This ¹O₂ is formed in a type II mechanism which occurs by an energy transfer between the PS in its excited triplet state and the oxygen in its fundamental triplet state upon collision (Fig. 12b).^[38]

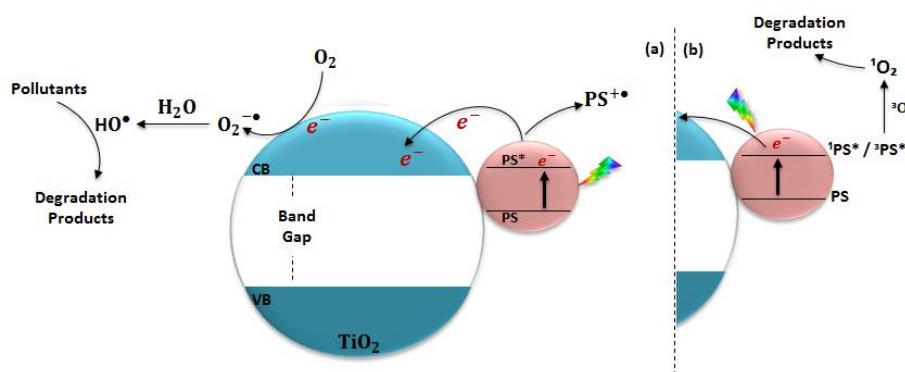


Fig. 12: Scheme of the mechanism of the light-induced charge transfer and the nature of the radicals generated under visible light activation.

2.3.2. Simulated solar light

Simulated solar light mimics the real sunlight, which is constituted of a 4-6 % of UV and a majority of visible light. Hence, the mechanism of the photocatalytic degradation of contaminants under such light can be described as a ‘give-and-take’ electron exchange process between both poles of the nanosystem: TiO₂ and PS (Fig. 13).^[40] On one hand, the UV portion of light is sufficient to activate the semiconductor generating mobile electrons in its CB and positively charged holes in its valence band (VB). On the other hand, the PS is excited as it absorbs the visible light, also producing electrons that are rapidly injected into the CB of TiO₂. The electrons occupying the CB of TiO₂ tend to react with the molecular oxygen adsorbed onto the surface of this semiconductor elaborating various ROS especially O₂^{•-} and HO[•] that are highly reactive towards the degradation of pollutants. In addition to that, and to fulfill the ‘give-and-take’ process, the holes occupying the VB of TiO₂ are transferred to the PS, efficiently suppressing the electrons-holes recombination. Those holes oxidize

adsorbed water into hydroxyl radicals, which assist in the degradation and further mineralization of pollutants.^[68,71]

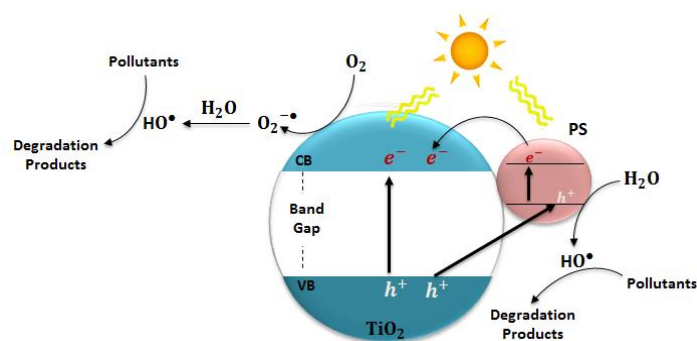


Fig. 13: Scheme of the mechanism of the light-induced charge transfer and the nature of the radicals generated under simulated solar light activation.

2.3.3. Ultra-violet light

The UV light is the field of activation of TiO_2 . Thus, in contrast to pure visible light, TiO_2 plays the major role under UV irradiation. The well-known procedure takes place as TiO_2 absorbs the UV light leading to the production and migration of electron to the CB band and the abundance of positive holes in the VB. The electrons are involved in the reduction of pre-adsorbed oxygen into ROS. In parallel, the holes are injected into the PS, preventing $e^- - h^+$ recombination and creating water oxidative sites that produce reactive HO^\bullet . All the elaborated ROS degrade and mineralize the adsorbed pollutants (**Fig. 14**).

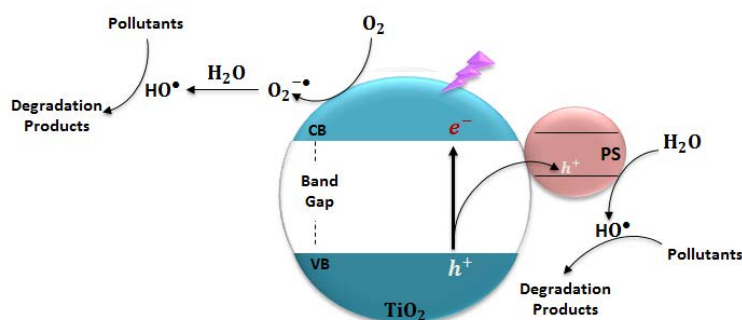


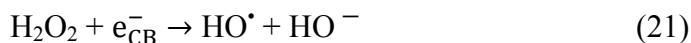
Fig. 14: Scheme of the mechanism of the light-induced charge transfer and the nature of the radicals generated under UV light activation.

However, it is noteworthy to discuss the superior activity of hybrid TiO_2 NPs functionalized with metallo-porphyrins or metallo-phthalocyanines under UV light as compared to its activity under pure visible irradiation. Under visible light, the PS is playing the major role. However, under UV light, TiO_2 is playing in its strength field where it is activated and produces its own electrons. The electrons from the CB of TiO_2 activate the role of the metallo-PS in the degradation process. Those electrons reduce the metal in the PS, which tends to re-oxidize by oxygen producing ROS. Therefore,

the cooperative role of both TiO₂ and the metal coordinated to the PS are responsible for the enhancement of the photocatalytic activity of the hybrid nanosystem under UV light irradiation.^[59,62]

2.3.4. Presence of H₂O₂

As previously stated, the hybridization of TiO₂ NPs with a PS aims to extend its absorption response to the visible region in order to better utilize the sunlight as an advantage accompanied with improving, or at least, retaining the good photocatalytic activity of TiO₂ NPs towards the wide range of pollutants. However, displaying an improved absorption of light in the visible range does not always enhance the photoreactivity rate. Therefore, there are other factors besides introducing an excess of PS onto TiO₂ NPs that have adverse effect on the system's photoreactivity. The type of ROS produced by the hybrid system upon illumination should be specific for degrading the targeted pollutant. Thus if the system produces predominately superoxide anions while the degradation of the present pollutants requires hydroxyl radicals, no photocatalytic effect will be detected. In such cases, an optimized amount of hydrogen peroxide can help in the production of hydroxyl radicals required for the photocatalytic degradation process.^[51] The production of HO• radicals is generally attributed to the following mechanisms:^[51]



In some other cases, H₂O₂ can initiate the photocatalytic process in hybridized nanosystems which are inactive under visible light. For instance, the Fe(III)P/TiO₂ hybrid system described by Huang *et al.* lacked any photocatalytic activity under visible light towards the degradation of RhB.^[62] However, when H₂O₂ was introduced, the Fe(III)P photosensitizer induced the photooxidation of H₂O₂ into HO₂•. In parallel, the hydrogen peroxide oxidized Fe(III)P in Fe(II)P generating HO•. As a result, an efficient photo-degradation of RhB was obtained under visible light irradiation.^[62]

2.4. Bonds between PS and TiO₂ surface

Regardless of their nature, photosensitizers have been attached to the surface of titania NPs through various bonds. Those linking modes fluctuate between covalent bonding, hydrogen bonding, hydrophobic interactions, physical entrapment and electrostatic interactions.^[57,60]

2.4.1. Physical adsorption

The majority of the published dye-sensitized TiO₂ systems for photocatalytic applications seem to rely on physical adsorption, *i.e.* physisorption. Copper phthalocyanines,^[58,63,74,75] a wide variety of porphyrins such as metal-free and Cu, Fe, Zn, Ni, Mn and Co tetra(4-carboxyphenyl)porphyrins

(TCPP),^[51,59,76] 5,10,15,20-tetra-[4-(3-phenoxy) propoxy]phenyl porphyrin,^[38] 5-mono-[4-(2-(4-hydroxy)-phenoxy)ethoxy]-10,15,20-triphenylporphyrin and its Cu, Zn and Ni metalloporphyrins,^[68] 5,10,15,20-tetrakis(4-chlorophenyl)porphyrin (H₂TCIPP) are some examples of PSs adsorbed on TiO₂.^[73] All of those PS/TiO₂ systems showed good photocatalytic efficiencies towards the degradation of many model pollutants and pharmaceutical wastes under pure visible or simulated solar light irradiation.^[51,75,76] The physical interactions between the PS and the surface involve different groups mainly hydroxyl, carboxyl, sulfonyl and phosphate. Those are the most frequently used anchoring group.^[52,71]

Although adsorption has been widely adopted in the domain of TiO₂ sensitization, this mode of linkage presents a lot of disadvantages. Mainly, it should be noted that the link established between the dye and the surface of the NP is just a weak physical adsorption with scarce strength and long-term stability instead of a stable chemical bond. As a result, the PS would be susceptible to desorb from the surface of TiO₂. Consequently, the efficiency of the sensitization process and the photocatalytic application might be jeopardized.^[40,52,66] An example of this is the broadly used 'ester' linking bonds resulting from the reaction between the hydroxyl groups present on the surface of the semiconductor and the carboxyl groups of the PS. This ester-anchoring bond revealed an auspicious electronic coupling but a tendency to hydrolyze under the photochemical reaction conditions as well. Consequently, its efficiency in photocatalysis is diminished.^[37]

However, Huang *et al.* assumed that the efficiency of the linkage established by carboxyl, sulfonyl and phosphate groups would be hindered by its deficient long-term stability. According to the authors, this anchorage between the PS and TiO₂ lacks enough strength to prevent the slow desorption of the PS often arising in aqueous media. To overcome this, and encouraged by the good photocatalytic results realized by Lu *et al.* upon employing a copper porphyrin with hydroxyl group,^[65] this research team utilized the phenol hydroxyl bonding mode with greater affinity. Involving phenol hydroxyl groups enables a robust grating with the surface of TiO₂ and, hence, an efficient electron transfer and good photocatalytic activity.^[52]

Those limitations of adsorption rise the urge to seek a mode that guarantees a stronger and more energetically favored coupling of the dye molecule onto the surface of TiO₂ semiconductor.^[37] This aspect is discussed in the next part.

2.4.2. Grafting

The covalent bonding of PSs to TiO₂ by carboxyl, phosphonato, amido and silyl functionalities have been already established (**Fig. 15**).^[60]

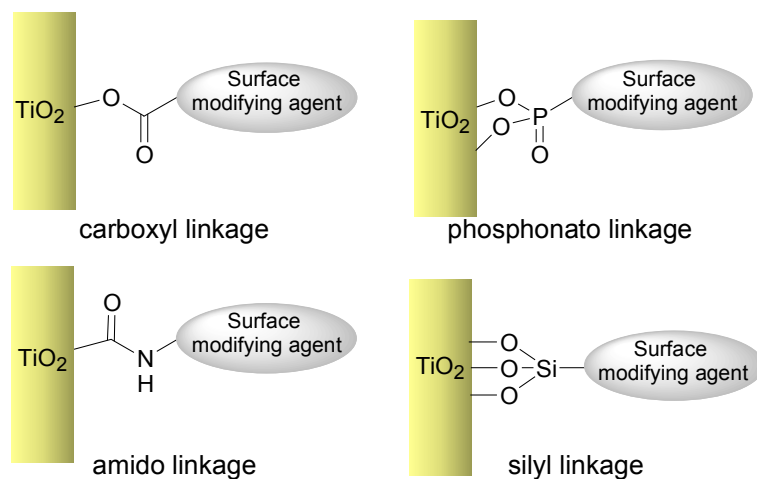


Fig. 15: Some of the most common covalent anchoring groups for surface modification of TiO₂ photocatalysts and TiO₂ nanocrystalline electrodes. Taken from reference [60]

Those functionalities do not share the same stability behavior. Bonding groups such as carboxyl and phosphonate-esters retain their stability under certain pH conditions in aqueous media. However, their stability becomes weakened in organic or aqueous-organic solvents. [60] It appears that silyl anchoring groups attract much interest because they seem to be the only group maintaining a covalent linkage that exhibits no dissociation or de-chelation. Moreover, the modification of the surface of TiO₂ involving a silyl anchoring group is favored. This is due to the high affinity between the silyl functionalities and the OH groups that occupy the surface of TiO₂ leading to the formation of chemically inert Ti-O-Si bonds. [60, 87-90] It is interesting to note that the anchoring group can occur either on the surface of the TiO₂ semiconductor or on the photosensitizer itself. [40]

In 1987, Hong *et al.* synthesized the first ‘extremely stable’ hybrid PS/TiO₂ nanosystem for photocatalysis application in water treatment. Those researchers grafted cobalt(II) tetrasulfophthalocyanine CoPcTS, onto the surface of TiO₂ P25 *via* a silane reagent, *i.e.* 3-aminopropyl triethoxysilane (APTES). The latter acted as an anchoring group between the PS and the titania surface. First, the surface of TiO₂ was modified by APTES organosilane. Then, the PS was attached to this silane by reacting with the latter’s amine group. Consequently, the PS was attached to TiO₂ through a silane linkage connecting the surface oxygen of TiO₂ and a sulfonyl peripheral group of phthalocyanine creating a very stable bond (Fig. 16). The established chemical covalent bond proved to be robust in strongly acidic and alkaline media. In contrast, in the case of adsorption and at alkaline pH, the weak reversible interaction and the electrostatic forces trigger the repulsion of the negatively charged CoPcTS from the surface of TiO₂. This hybrid catalyst showed high efficiency in the production of very high quantum yields of hydrogen peroxide under UV irradiation through the reduction of dioxygen. The good efficiency of TiO₂-APTES-CoPcTS NPs was attributed

to the very strong covalent bond between the PS and the semiconductor permitting an efficient electron transfer process.^[81]

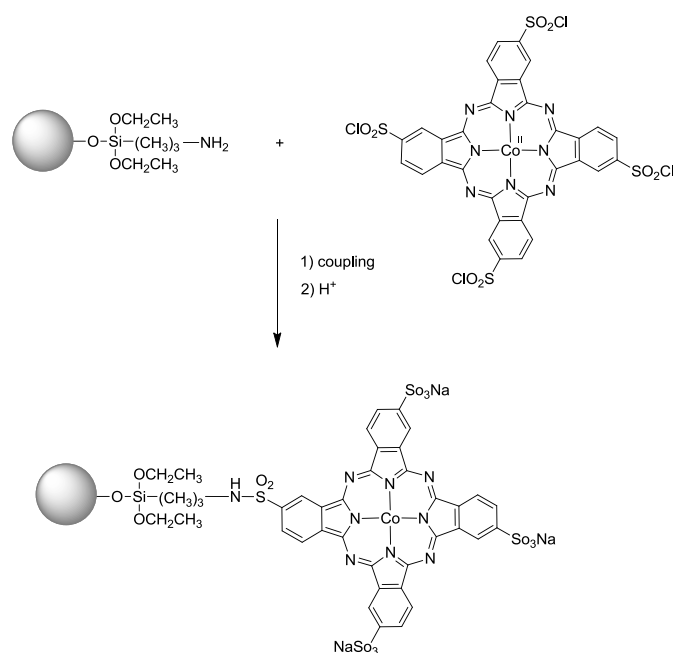


Fig. 16: Schematic diagram summarizing the steps of the synthesis of CoPcTS chemically bonded to the surface of TiO_2 (TiO_2 -APTES- CoPcTS). Taken from reference ^[81]

The efficient contribution of the silyl anchoring groups in mediating a stable PS/ TiO_2 system was further confirmed by Fung *et al.*^[60] However, instead of the silanization of the surface of TiO_2 , the authors tend to modify the PS itself. The PS is a ruthenium(II) polypyridyl complex, $[\text{RuII}(3-(20\text{-pyridyl})\text{pyrazole})_3]^{2+}$, which was silylated by SiCl_4 . The silyl group of the generated silyl Ru(II) PS initiates an excellent covalent bonding and electronic linkage between this PS and the surface of the TiO_2 NPs (**Fig. 17**). Assessing its photocatalytic activity under visible light, this catalyst evidenced a superior reductive photodegradation of perhalogenated organics (CCl_4) in the presence of an electron donor compared to that of bare TiO_2 NPs. Hence, this enhanced photoactivity can be ascribed to the silyl bonding group which enhances the driving force for photo-induced electron injection from the PS into the CB of TiO_2 .^[60]

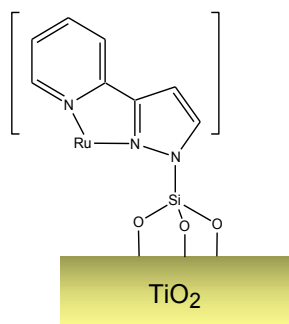


Fig. 17: TiO_2 modified by a ruthenium(II) polypyridyl complex by silyl-linkage. Taken from reference ^[60]

It becomes necessary to discuss the effect of the nature of the anchoring group between the PS and TiO_2 on the electron transfer process. To this aim, Peng *et al.* established a strong covalent bond between copper 5-(4-aminophenyl)-10,15,20-triphenylporphyrin (CuAPTPP) and TiO_2 modified by toluene diisocyanate (TDI) bridging molecule. TDI possesses two highly reactive $-\text{NCO}$ groups that makes it possible to react with both the hydroxyl ($-\text{OH}$) and the amino ($-\text{NH}_2$) groups of TiO_2 and the PS, respectively (Fig. 18). Compared to CuAPTPP/ TiO_2 NPs prepared by adsorption, those CuAPTPP-TDI/ TiO_2 NPs showed superior photocatalytic activity towards the degradation of MB under visible light in addition to their photostability and recyclability. This could be credited to the firm linkage between TDI and TiO_2 that enhanced the sensitization efficacy, amplified the hydrophobicity of the catalyst and strengthened its capability of adsorbing the hydrophobic MB pollutant and, most importantly, prevented the $e^- - h^+$ recombination through efficient electron transfer.^[66]

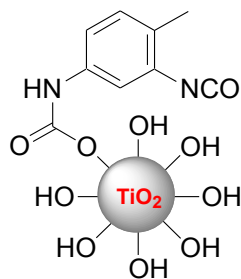


Fig. 18: Structure of TDI-modified TiO_2 . Taken from reference ^[66]

However, the use of TDI was hindered due to its toxicity and low stability. As a matter of fact, this team used the same approach but with different types of bridging molecules, *i.e.* 2-hydroxy-5-sulfosalicylic acid (SSA) and salicylic acid (SA). Those molecules were used to anchor iron tetracarboxyphenyl-porphyrin (FeTCPP) onto TiO_2 P25 nanoparticles (Fig. 19a,b). In terms of MB photodegradation under visible light, both FeTCPP-SSA/ TiO_2 and FeTCPP-SA/ TiO_2 displayed greater activity than both FeTCPP- TiO_2 (adsorption) and bare TiO_2 with FeTCPP-SSA/ TiO_2 being the best (Fig. 19c). Linking the PS to TiO_2 by SSA and SA prohibited its desorption and triggered good photostability. Due to the multi-functional groups that SSA holds, the links between SSA- TiO_2 and FeTCPP was reinforced, which enabled higher sensitizer content bonded to SSA- TiO_2 and easier electron transfer. In addition, grafting SSA anchoring groups onto TiO_2 seems to increase the specific surface area and the average pore size of the catalyst, thus forming more active sites prompting better adsorption and degradation of organic pollutants.^[40]

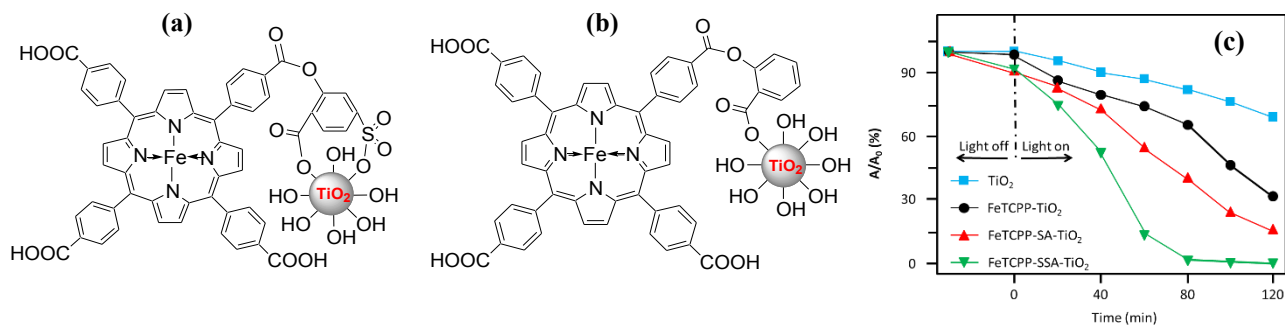


Fig. 19: Formulas of (a) FeTCPP-SSA-TiO₂ and (b) FeTCPP-SA-TiO₂. (c) The photocatalytic performance of those catalysts, bare TiO₂ and FeTCPP-TiO₂ towards the degradation of MB. Taken from ref [40]

Guo and coworkers modified 5,10,15,20-tetra-(pamminophenyl) porphyrin (TAPP) either by *meta*-hydroxybenzoic acid or *ortho*-hydroxybenzoic acid (salicylic acid) in the presence of NaNO₂, eventually forming azo-bridged zinc porphyrin (ZnP) dyes holding carboxyl and hydroxyl anchoring groups.^[79] Those two dyes in addition to free ZnTCPP were coupled to TiO₂ film (**Fig. 20**).



Fig. 20: Schematic presentation of the binding modes. Taken from reference [79]

In the azo-bridged ZnP system involving *ortho*-hydroxybenzoic acid (salicylic acid) as an anchoring group, the hydroxyl and the carboxyl groups were situated in the *para*- and *meta*-position relative to azo group. Thanks to such configuration, when anchored onto TiO₂, this dye can bind through the hydroxyl group and through both the oxygen and the OH functions of the carboxyl group, resulting in a ‘tridentate’ binding mode. However, for the azo-bridged ZnP system involving *meta*-hydroxybenzoic acid as the anchoring group, a bidentate binding mode involving only the carboxyl group is initiated with TiO₂. The involvement of the hydroxyl group in the binding with TiO₂ was inhibited by the steric effect. Thus, it was established that the intimacy between the salicylic anchoring group and the surface of TiO₂ semi-conductor mediated by the tridentate binding boosts the efficiency of the electron transfer from the PS to TiO₂.^[79]

2.4.3. Different peripheral substituents and PS orientation

We already stated that the wide range of photophysical properties of porphyrins can be easily tuned by various methods including the alteration of the peripheral substituents on the porphyrin ring. Various efforts were devoted for studying the effect of modifying those peripheral groups on the photocatalytic effectiveness of the porphyrin/TiO₂ system. Those groups normally establish the

linkage between the PS and the surface of the NPs. Note that, in the examples mentioned below, the PS is adsorbed or physisorbed onto the titania surface.

Besides investigating the effect of copper metalation on the efficacy of the PS/TiO₂ system, Wang *et al.*^[38] attached lipophilic ether-chain groups as exterior substituents onto the porphyrin ring of the metallated and metal-free PS in *para*- (a) or *ortho*- (b) positions (**Fig. 21**). This study aimed to figure out the effect of such modification on the photocatalytic capability of the sensitized NPs.

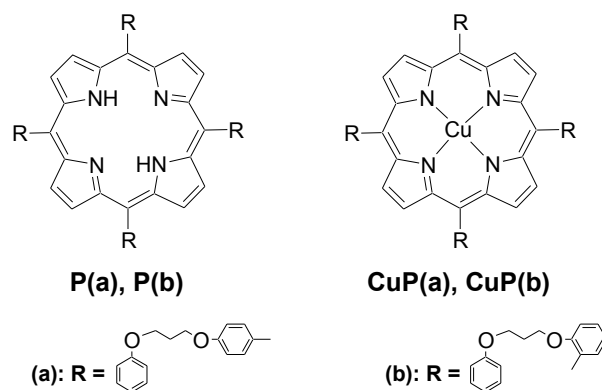


Fig. 21: Molecular structures of metal-free porphyrin (P) and Cu-porphyrin (CuP) holding (a) *para*- and (b) *ortho*- positioned peripheral groups. Taken from^[38]

Despite the effect of Cu coordination, comparing the activity of all four composites: P/TiO₂ (a & b) and CuP/TiO₂ (a & b) towards the photodegradation of 4-NP under visible light gave the following order: CuP/TiO₂ (b) > CuP/TiO₂ (a) > P/TiO₂ (b) > P/TiO₂ (a). The difference in the percentage of 4-NP degradation between *para*- and *ortho*-substituted PS-TiO₂ systems was about 1.13 % and 5.28 % in the case of CuP/TiO₂ and P/TiO₂, respectively. Thus it seems that *ortho*- (b) and *para*- (a) substituted porphyrins exhibit a slight difference in terms of photoactivity. The relatively higher photoactivity of the NPs with *ortho*-substituted porphyrins was ascribed to their ability to trap and activate more O₂ due to their lower symmetry inducing lower aggregation and less intermolecular π - π interactions.^[38]

The synthesis of TiO₂ loaded with hydroxo-tin porphyrins holding four phenoxy propoxy peripheral groups attached in *ortho*- (a), *meta*- (b) and *para*- (c) positions was conducted by Duan *et al* (**Fig. 22**).^[61]

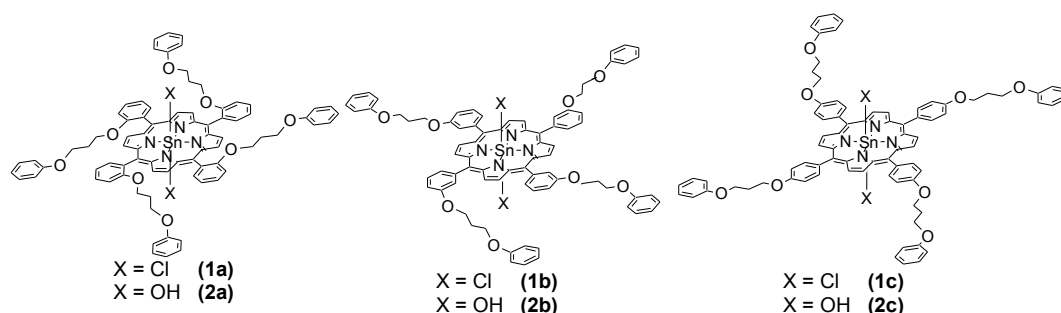


Fig. 22: Molecular structures of Cl₂SnP and (OH)₂SnP holding (a) *ortho*-, (b) *meta*- and (c) *para*- positioned peripheral substituents. Taken from reference^[61]

All those hybrid composites displayed better photocatalytic efficiency in the decomposition of 4-NP than bare TiO_2 under both pure visible and simulated solar light with *para*-substituted porphyrin being the best followed by *meta*-, and then *ortho*- (Fig. 23). Passing from *ortho*- to *meta*- up till *para*- positioned substituents, the molecular structures tend to become less stressed and stereochemically less complicated. The strong steric effect dominating in the case of *ortho* substituents compels it to adopt a somehow perpendicular position relative to the porphyrin planes, while in the less stressed *para* substituents, those tend to stretch out well adopting the most planar conformation among all three. This position renders the *para*-porphyrin easily accessible which enhances its interaction with the surface of TiO_2 . Consequently, the electron transfer process can be improved ensuring higher activity of the hybrid composite catalyst.^[61]

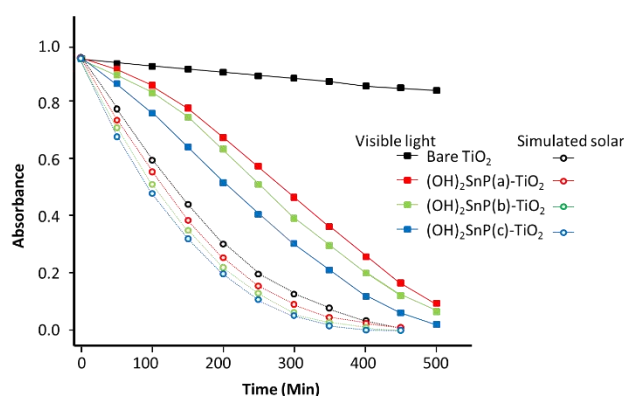


Fig. 23: The degradation of 4-NP in the presence of different $(\text{OH})_2\text{SnP}-\text{TiO}_2$ photocatalysts under pure visible and simulated solar irradiations from Taken from reference ^[61]

Complementary studies were performed by the same team to investigate in more details the effect of the nature of the substituted porphyrin on the photocatalytic activity of the composite. For this goal, CuTCPP PS possessing one, two, three or four phenoxy propoxy exterior substituents were synthesized, and the same amount of each was impregnated onto TiO_2 to exclude the effect of other factors on the efficiency of the porphyrin/ TiO_2 composites (Fig. 24a). Those catalysts were tested for their photocatalytic viability against 4-NP degradation under simulated solar light (Fig. 24b).

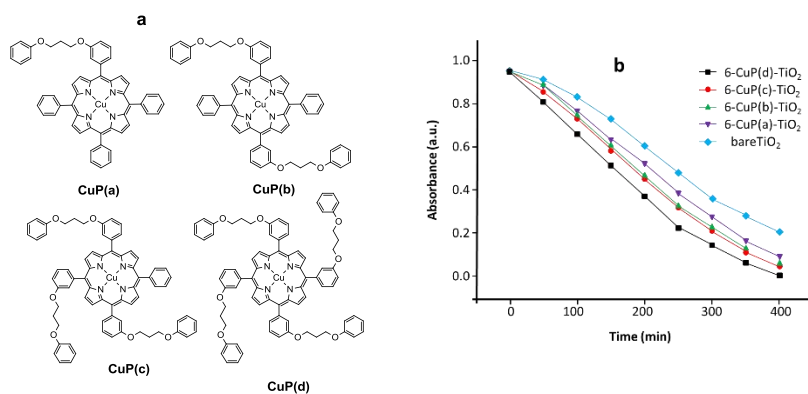


Fig. 24: (a) Molecular structures of CuP(a), CuP(b), CuP(c) and CuP(d) functionalized by one, two, three and four substituents respectively. (b) The photocatalytic degradation of 4-NP in the presence of different CuP- TiO_2 photocatalysts. Taken from reference ^[69]

peripheral phenyl rings of their CuP with different functional groups including $-\text{OH}$, $-\text{OCH}_2\text{CO}_2\text{C}_2\text{H}_5$ and $-\text{OCH}_2\text{COOH}$ groups (**Fig. 26a**). In their photocatalytic competency assessment, all the porphyrin- TiO_2 systems were efficient in the photo-decomposition of 4-NP under simulated solar light (**Fig. 26b**). They exhibited the following trend: $\text{CuP}(-\text{OCH}_2\text{COOH})/\text{TiO}_2 > \text{CuP}(-\text{OH})/\text{TiO}_2 > \text{CuP}(-\text{OCH}_2\text{CO}_2\text{C}_2\text{H}_5)/\text{TiO}_2 > \text{bare TiO}_2$.^[64, 65]

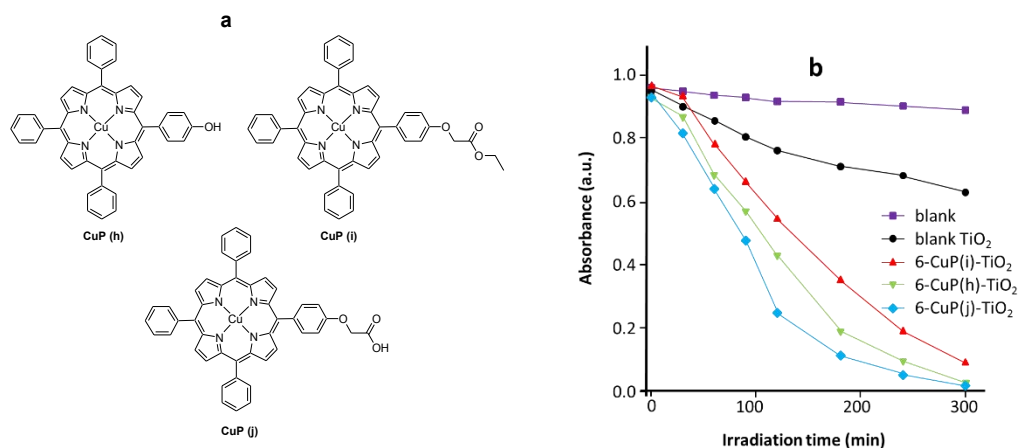


Fig. 26: (a) Molecular structures of CuP functionalized with $-\text{OH}$ [CuP(h)], $-\text{OCH}_2\text{CO}_2\text{C}_2\text{H}_5$ [CuP(i)] and $-\text{OCH}_2\text{COOH}$ [CuP(j)] groups. (b) The photocatalytic performance of each after adsorption onto TiO_2 under visible light. Taken from reference ^[65]

Su *et al.* followed a similar approach but they functionalized the four peripheral rings of their CuP by $-\text{OCH}_2\text{CO}_2\text{C}_2\text{H}_5$ (k) and $-\text{OCH}_2\text{COOH}$ (l) substituents before adsorbing them onto TiO_2 (**Fig. 27a**). The photocatalytic efficacy results confirmed the higher activity of the hybrid TiO_2 composites holding carboxyl groups on their PS over the others with ester groups (**Fig. 27b**).^[67]

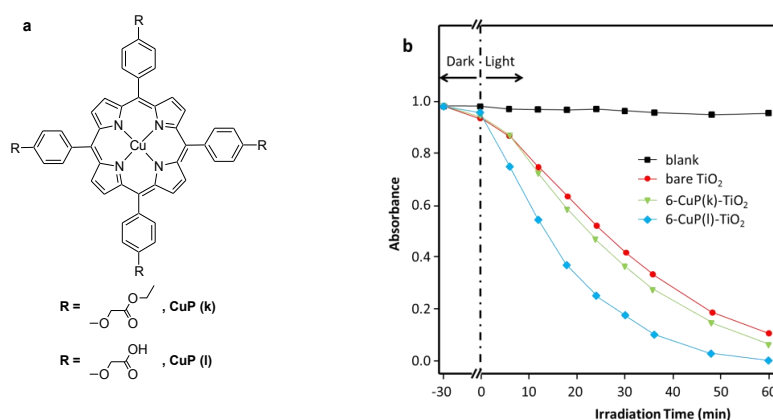


Fig. 27: (a) Molecular structures of CuP with all peripheral rings functionalized with $-\text{OCH}_2\text{CO}_2\text{C}_2\text{H}_5$ [CuP(k)] and $-\text{OCH}_2\text{COOH}$ [CuP(l)] groups. (b) The photocatalytic performance of each after adsorption onto TiO_2 under visible light. Taken from reference ^[67]

It is noteworthy to mention that the stronger interaction displayed by the PS holding polar COOH group with the surface of TiO_2 enables the formation of a denser organic layer onto TiO_2 as

compared to that involving the less polar PS being proved through high-resolution transmission electron microscopy (HRTEM) (**Fig. 28**).^[67]

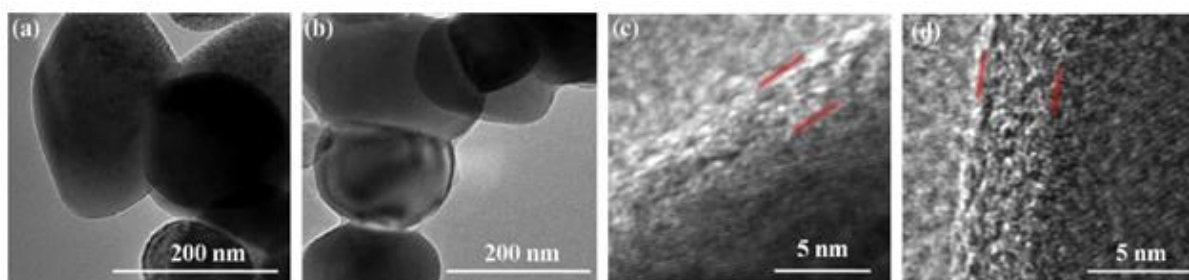


Fig. 28: TEM and HRTEM images of (a,c) CuP(k)-TiO₂, and (b,d) CuP(l)-TiO₂. Taken from reference.^[67] With permission of Elsevier

All the previous results followed the same logical trend which is interesting to summarize here. The influence of the different substituent groups on CuP appeared to be a matter of polarity. Hence, as the polarity increases, such as in the case of carboxyl and hydroxyl groups, stronger chemical interaction is achieved between the PS and the titania surface. Consequently, a direct linkage is created between the polar carboxyl (–COOH) groups of the porphyrin and the HO[–] polar surface groups of TiO₂. Conversely, a weak physical interaction only takes place between TiO₂ and the ester group of the PS. As a matter of fact, a stronger PS-NP interaction prompts a faster electron transfer process, leading to improved e[–]-h⁺ separation inducing better photocatalytic activity. Therefore, it was demonstrated that the functional groups contribute in the adsorption phenomena as well as in the electron transfer.^[64, 65, 67]

When the functional groups of the PS are altered between polar and non-polar, they exhibit different stacking modes on the surface. Such factor plays an important role in specifying the mode of orientation and the accumulation pattern of those PS onto the titania surface. This orientation or binding conformation can be flat, vertical to the surface of TiO₂ such as in the case of the ester group (**Fig. 29a**), or tilt as established in the case of the carboxyl group (b) where the PS bind to the surface of the semiconductor through two carboxylic groups (**Fig. 29b**).^[64, 67] Based on this description, the distance ‘R’ between the surface of the TiO₂ NPs and the bottom of the PS ring, particularly the porphyrin ring, changes in parallel to the variation of the binding mode. It is important to note that the electron transfer process between the excited porphyrin and the CB of TiO₂ occurs mostly through space not through the linker group. As a consequence, R may represent the distance of electron transfer. The distance R is shorter in the case of porphyrins/TiO₂ systems with tilt (**Fig. 29b**) binding mode than that of the vertically linked system (a) (**Fig. 29a**). This influences the rate of the ‘through-space’ electron transfer which will be more efficient for hybrid systems displaying tilt binding mode.^[67]

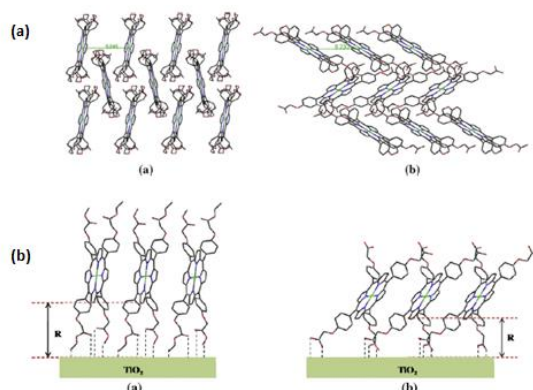


Fig. 29: (a) Stacking structures of CuP holding ester ‘a’ and carboxyl ‘b’ substituent groups. (b) The accumulation pattern of those porphyrins onto TiO₂. Taken from reference [67] With permission of Elsevier.

Various authors have previously discussed the effect of binding orientation and the resulting distance displayed between the PS and the surface of the semiconductor. For instance, *para*-ZnTCPP can bind through two dominantly possible modes onto titania depending on its orientation relative to the surface of the semiconductor. The PS can be linked to the surface of the metal oxide either by one or two carboxyl groups (**Fig. 30**). Consequently, the distance between the PS and the surface of the semiconductor change with the binding mode, and thus, affects the photophysical properties of the fixed dye as well as the efficiency of the electron transfer process. [78,80]

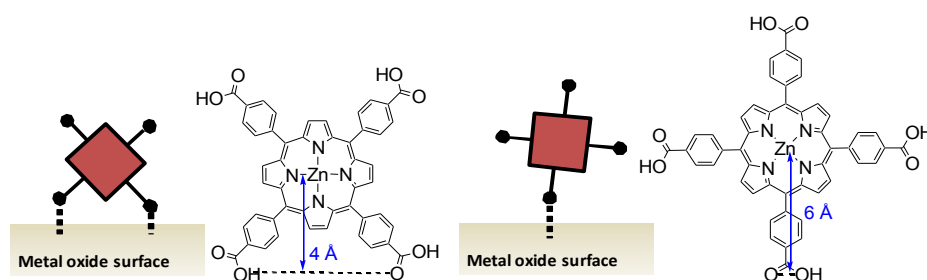


Fig. 30: The two possible binding modes of *para*-ZnTCPP onto the metal oxide surface. Taken from reference [80]

2.5. PS loadings and different geometries

The amount of PS deposited onto the surface makes a significant contribution in the photocatalytic activity of the PS/TiO₂ systems. In order to extract the general trends, it seems pertinent to discuss the results of **Fig. 31** which is extracted from the reference. [69] The figure displays the evolution of the absorbance of 4-nitrophenol, related to its concentration, with respect to the amount of each substituted porphyrins impregnated onto titania. Relying on this graph, and putting aside the less affecting factor which is the number of substituents, the influence of the loaded porphyrin amount becomes quite clear. The photocatalytic behavior for all the four composites follows the same trend. When the amount of the PS remains low, it remains insufficient to extend

efficiently the photo-response of TiO_2 into the visible range of light. On the opposite, adding an excess of porphyrin results in a multi-layered aggregate deposition of the PS onto the surface of TiO_2 . Both are the extreme cases leading to the drop of the photocatalytic activity of the NP system. Based on this result, a moderate optimized amount of PS is always the target. It should display minimal aggregation and should be adequate for allowing efficient photo-induced excitation of TiO_2 without crowding and masking totally its surface. In this study, it is observed that the ideal amount to be linked on TiO_2 for attaining the best photoactivity differs between the four substituted porphyrins. This optimal PS loading is the amount needed to accomplish a monolayer of the least aggregated PS onto the surface of TiO_2 . Thus, the area covered by the PS to achieve the monolayer is dependent on the size of this PS. Yet, as the number of substituents increases, the size of PS increases, thus lower the optimal amount of the PS required for the monolayer formation reference.^[69] For the chemical structures of CuP(a-d) see Fig. 24.

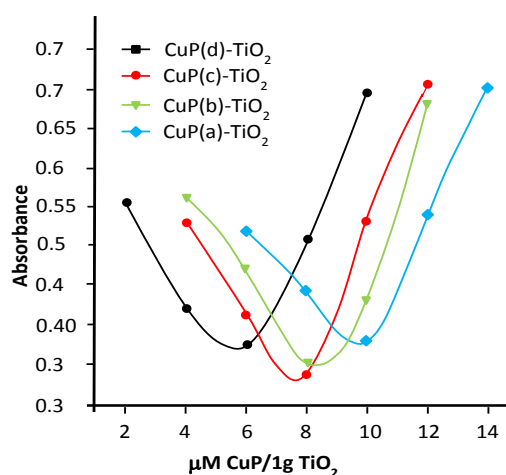


Fig. 31: Comparison of the photocatalytic activities in terms of 4-NP concentration vs. different impregnation ratio CuP(a)- TiO_2 -CuP(d)- TiO_2 after 200 min of irradiation. Taken from reference ^[69]

The previous outcomes were confirmed by various studies. For instance, Afzal and coworkers highlighted the importance of an optimal amount of PS. They introduced different PS loadings onto TiO_2 to figure out the best suiting amount for photocatalysis which was 20 and $2\mu\text{M/g}$ of TiO_2 for TCPP and CuTCPP respectively.^[76]

Kang *et al.* reported on the photooxidation of furfural pollutant in the presence of TiO_2/CuPc catalyst composite.^[63] This catalyst is constituted of commercial anatase TiO_2 sensitized by different loadings of copper phthalocyanine through adsorption. Introducing larger amounts of CuPc PS onto the titania surface induces relatively broader and higher absorption peaks in visible light range and larger capability of adsorbing furfural pollutant. Thus, up to 1.5 % of CuPc loading mass fraction, the PS is assumed to remain in monomeric form, causing the photocatalytic degradation of furfural to be proportionally enhanced up to 90 % with a total organic carbon (TOC) eliminate rate about 70 % under simulated solar light. The authors emphasized that a CuPc loading above 1.5% mass fraction

may hinder the penetration of the light on the TiO₂ surface, thus, decreasing the photocatalytic activity of the catalyst composites.

Wang *et al.* aimed also to address the effect induced by the amount of PS loaded onto TiO₂.^[69] Different contents of copper and metal-free TCPP with *ortho*- or *para*-attached lipophilic ether-chain groups were impregnated onto TiO₂ polycrystalline. It is confirmed that an optimal loading is the target, where the NPs overcome their UV-restricted photoresponse towards visible. It is also important to avoid the deposition of multilayer of PS, at larger PS content, that hampers the accessibility of light into the semiconductor thus diminishing the photoactivity of the composite.^[38]

The same trend was also reported for a slightly different photocatalytic application. In order to achieve the photoreduction of CO₂ into methane and carbon monoxide, Li *et al.* sensitized TiO₂ nanoparticles with different loading levels of asymmetric zinc porphyrin (ZnP) possessing three pyridine and one phenyl-COOH group. The spectrum of the functionalized NPs displays the absorption profile of the PS adsorbed but with an enhanced absorption in the Q-bands. From the authors' point of view, this augmentation is ascribed to the electron transfer from the ZnP PS into TiO₂. Those ZnP/TiO₂ NPs showed potential CO₂ photoreduction under visible light irradiation. Through their study, the authors emphasized the significance of an optimum loading of PS. PS amounts higher than 1 % of ZnP/TiO₂ induced lower activity due to hindered light harvesting and less electron injection caused by the $\pi - \pi$ stacking of the PS on the titania surface.^[77]

Logically, the amount of PSs can be correlated to their conformation onto titania's surface. Tasseroul and coworkers used NiTCPP PS to functionalize TiO₂ P25 by chemisorption. The authors emphasized the occurrence of different geometries of the functionalized NPs corresponding to different linkage modes, all depending on the PS loading. NiTCPP possesses four carboxylic groups, through which the PS is linked to the NP's surface. This linkage can be achieved through one, two, three or all four carboxyl groups. The area occupied by this PS on the semiconductor's surface depends on the number of carboxyl groups involved in the linkage. It was proved that lower loadings of NiTCPP yields a flat geometry (**Fig. 32**) of the porphyrin with the four carboxyl groups being linked to TiO₂. This geometry permits a full coverage of TiO₂ NPs (monolayer). On the opposite, a partial TiO₂ coverage and an edgewise stacking geometry (**Fig. 32a**) resulted from the linkage of NiTCPP to TiO₂ through one or two carboxylic groups at higher PS contents. The decomposition of H₂O₂ under simulated solar light irradiation was employed to figure out the optimal amount of PS required to generate the best photoactive hybrid NPs. It seemed that there should be average conditions of partial coverage of TiO₂ with NiTCPP involving four carboxylic groups. Under such conditions, TiO₂ can still be photo-excited and a strong linkage between the PS and TiO₂ can be created. Thus the porphyrin adopts a flat geometry that leaves the Ni center accessible to H₂O₂ enabling higher levels of decomposition. Those conditions can only be achieved by adsorbing an optimum loading of PS into the surface of the TiO₂ semiconductor.^[55]

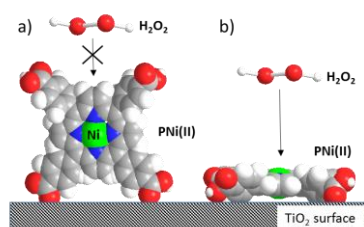


Fig. 32: NiTCPP geometry and interaction with TiO_2 surface and H_2O_2 . Taken from reference [55]

3. PS/ZnO systems

ZnO/PS systems appear attractive for water treatment applications. However, few work has been reported with these systems in comparison to those with PS/titania hybrid materials. Nevertheless, ZnO is a semiconductor which displays a lot of similarities with TiO_2 . The bandgap is equal to 3.2 eV while it reads as 3.2 and 3.0 eV for anatase and rutile TiO_2 , respectively. Similarly to titanium dioxide, the ZnO suffers from a low activity under visible light. In other words, the ZnO band gap remains too large to absorb efficiently the visible light. In addition, the other drawback comes from the photocorrosion of the surface of the material under UV light. This corrosion produces a leaching of zinc ions in solution which is detrimental for the water treatment process. In order to overcome these issues, it seems appealing to couple photosensitizers to ZnO NPs. The presence of the PS reduces the photocorrosion, shifts the photocatalytic activity towards solar and also visible light, and can also lead to charge transfer from the PS to ZnO. **Table 2** summarizes the literature reporting PS/ZnO systems along with the photodegradation parameters and pollutants.

Phthalocyanines^[91-93] and porphyrins^[94,95] remain the most widely used photosensitizers linked to zinc oxide. In practically all the studies, the authors utilized PS-heavy metal complexes with visible light (**Fig. 33**). As already discussed, the role of the complexed heavy atoms is to enhance the population of the triplet photoexcited state of the PS and also to prolong the visible light sensitivity of the ZnO.

As far as the linkage of the PS onto ZnO is concerned, it appears that the physisorption^[58,91,95] and the grafting^[92,94,96] are employed regardless of the PS nature. The covalent attachment of the porphyrin onto ZnO takes place *via* Zn-OOC link^[96] while the phthalocyanines are chemisorbed thanks to carboxylic groups. For the latter case, Seddigi *et al.*^[92] reported a bidentate mode of binding by tartrate linking agent between the semiconductor and the phthalocyanine (**Fig. 33a**). The efficiency of the electron transfer from the PS to the conduction band of ZnO seems to not depend on the mode of linkage (adsorption vs grafting). The nature of the metal coupled to the PS plays a role on the photocatalytic activity. Yarahmadi and Sharifna^[93] emphasized that Cu phthalocyanine (CuPc) is more efficient than Ni (NiPc) and Co (CoPc) phthalocyanine for the photocatalytic conversion of

CO₂ in the presence of CH₄ as reductant under visible light. However, in that particular case, the change in conversion was attributed to the surface coverage. CuPc had a uniform surface coverage while the NiPc and CoPc uptakes were lower. In another work, Kar *et al.*^[96] used iron and copper porphyrin based ZnO. Note that the metal ions were present in the aqueous solution during the experiments. The complexation rate of copper with the PS (4.9 %) was higher than that of Fe (1.5 %). Under visible light irradiation, the photodegradation performance of CuP/ZnO towards MB was significantly greater than that of FeP/ZnO. Using UV light, the two photocatalysts displayed the same activity (**Fig. 34**).

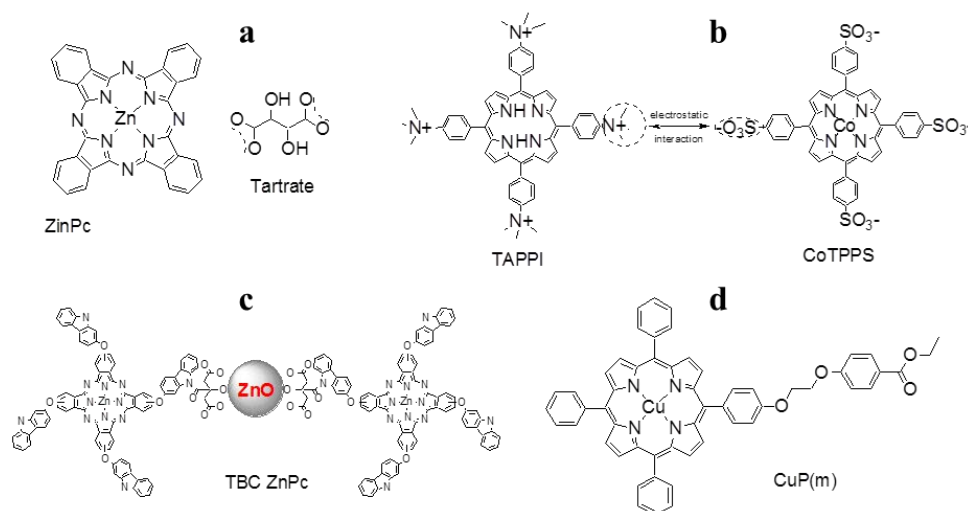


Fig. 33: Molecular structure of some photosensitizers. (a) ZnPc: Zinc phthalocyanine, (b) TAPPI-CoTPPS porphyrin heteroaggregates: heteroaggregate containing tetrakis(4-trimethyl aminophenyl) porphyrin (TAPPI) and tetrakis (4-sulfonatophenyl) porphyrin cobalt II (CoTPPS), (c) TCB ZnPc: 2,3 tetra(carbazol-2-yloxy) phthalocyaninate Zinc (II), and (d) CuPm : Copper(II) 5-mono-[4-(2-ethyl-p-hydroxy benzoate ethoxyl)]-10,15,20-triphenyl porphyrin. Taken from reference ^[91-95]

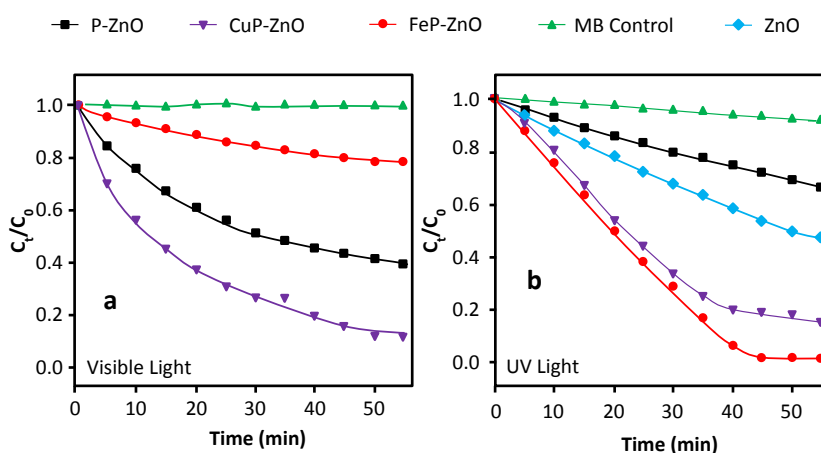


Fig. 34: Comparison between the photocatalytic activity of ZnO-PS under visible and UV light. Photocatalytic degradation of MB in the presence of iron and copper porphyrin based ZnO, FeP/ZnO and CuP/ZnO Taken from reference ^[96]

The wavelength of excitation depends on the nature of the PS-metal system. Irradiation in the near-IR region might be appealing since it represents 49 % of the solar spectrum. The classical systems do not absorb in the red region of the solar spectrum ($\lambda = 620$ nm). Seddigi and coworkers^[92] designed a zinc phthalocyanine grafted onto ZnO (**Fig. 33a**). The hybrid catalyst absorbs the red light at 620 nm and the presence of ROS ($O_2^{\cdot-}$ and electron) was detected. The degradation of MO occurs by the generation of ROS as a result of the photo-induced charge separation in the composite. The photocatalytic activity is also affected by the amount of PS. Li *et al.*^[94] developed an interesting hybrid ZnO system bearing two PSs instead of one. They elaborated a porphyrin heteroaggregate composed of positively charged tetrakis(4-trimethyl aminophenyl) porphyrin (TAPPI) and negatively charged tetrakis(4-sulfonatophenyl) porphyrin (CoTPPS). The two PSs bear opposite charge and are linked *via* electrostatic interaction (**Fig. 33b**). The porphyrin heteroaggregate is then linked onto the ZnO. The photocatalytic efficiency of the degradation of RhB under visible light was better with ZnO/TAPPI-CoTPPS photocatalyst than with ZnO/CoTPPS (**Fig. 35**).

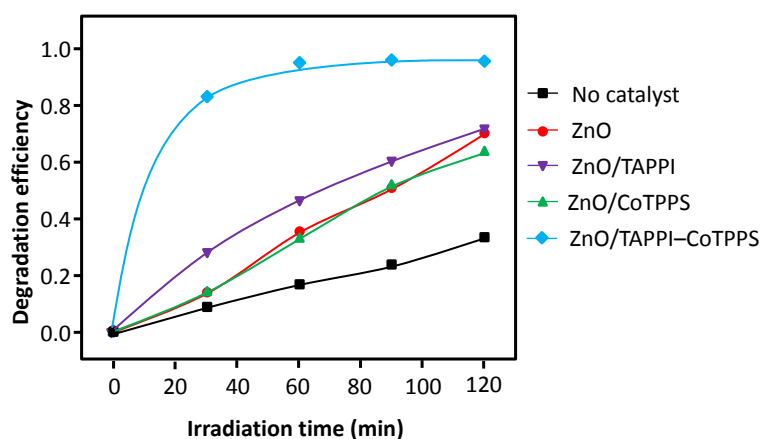


Fig. 35: Effect of the amount of PS. Photocatalytic degradation of RhB under visible light using ZnO/TAPPI-CoTPPS, ZnO/CoTPPS and ZnO photocatalysts. Taken from reference^[94]

In all the cases, the photochemical mechanism of degradation of the pollutants depends on the nature of the light used to activate the system. Under visible irradiation, the PS acts as a sensitizer while the ZnO acts as a catalyst (**Fig. 36a**). The photosensitization of the material proceeds with the initial excitation of the PS. Then, the electron injection takes place from the PS to the CB of the semiconductor. The degradation of the contaminants (MB, MO, RhB) proceeds through ROS generated onto the ZnO. For instance, Sun *et al.*^[95] confirmed that $O_2^{\cdot-}$ is the dominant active species under visible light through ROS measurements. The same conclusion was reached by Seddigi *et al.*^[92] Note that in addition to $O_2^{\cdot-}$, 1O_2 was detected by Khoza and Nyokong^[91] when using tetracarbazole zinc phthalocyanine conjugated with ZnO for the photocatalytic degradation of RhG (**Fig. 33c**). However, the 1O_2 quantum yield was quite low (0.2). In addition, in order to enhance the photocatalytic activity under visible light, the use of H_2O_2 can be recommended. Sun and

coworkers^[95] reported a substantial enhancement of the photodegradation of RhB by ZnO coupled with copper(II) 5-mono-[4-(2-ethyl-*para*-hydroxy benzoate ethoxyl)]-10,15,20 triphenyl porphyrin in the presence of hydrogen peroxide (**Fig. 33d**). In that case, in addition to the $O_2^{\cdot-}$ ROS, the reaction of H_2O_2 with the photoinduced electrons leads to the production of hydroxyl radicals HO^{\cdot} :

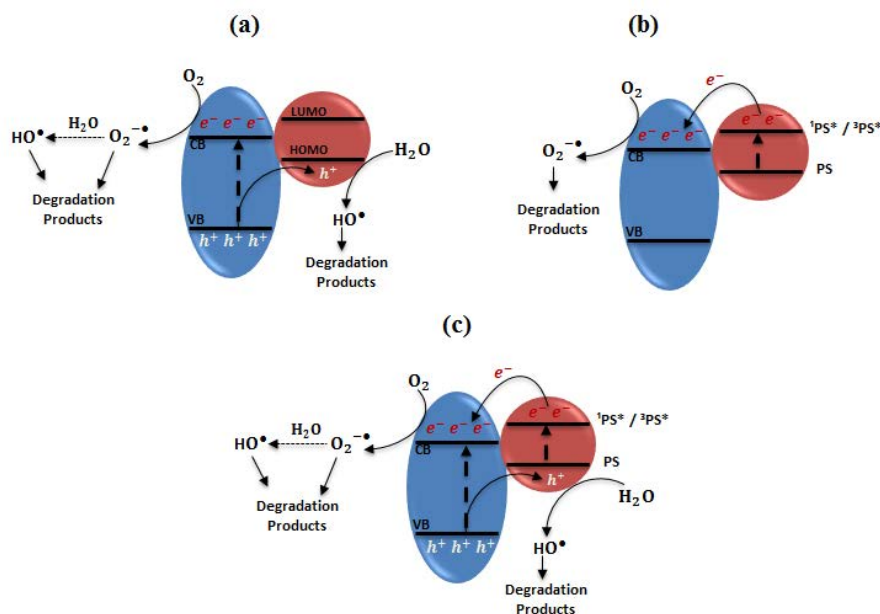


Fig. 36: Schematic representation of the formation of ROS from PS/ZnO NPs under (a) UV, (b) visible and (c) solar light irradiation.

Conversely, the holes h^+ in the valence band of the ZnO play the dominant role on the photodegradation when the catalyst is illuminated with UV light (**Fig. 36b**). The PS improved the separation of the photogenerated electrons and holes. The hybrid system displays a lower recombination of electrons and holes of the semiconductor.^[95] In fact, the UV light activated the ZnO *via* the production of electrons and holes. The photogenerated electron becomes trapped in the PS which produces an enhancement of the excitation lifetime of the hole. The latter can then produce radicals like HO^{\cdot} which degrade the pollutants. The presence of h^+ and HO^{\cdot} were detected using several types of species scavenger.^[95]

It becomes also interesting to compare the photocatalytic activity of the hybrid materials under UV and visible light. This aspect was mentioned by Kar *et al.*^[96] First of all, regardless of the light used, greater photocatalytic degradation of MB occurs with the Cu-porphyrin/ZnO composite compared to that of pure ZnO (**Fig. 34**). Second, similar photodegradation takes place with the hybrid catalyst under UV and visible light. Note that the UV light intensity was larger than for visible irradiation since they used the same lamp but a high-pass optical filter was utilized for visible light.

The reusability and the long-term stability of the photocatalytic properties of the hybrid catalyst is an important parameter for future industrial applications. This aspect has been evaluated with Copper(II) 5-mono-[4-(2-ethyl-*p*-hydroxy benzoate ethoxyl)]-10,15,20-triphenyl porphyrin/ZnO towards the degradation of RhB under UV and visible light irradiations.^[95] No significant decrease in the performance of the catalyst was detected during the first five cycles. This suggests that the catalyst retains a high photocatalytic activity and attests to the long-term stability of the material. Similarly, Kar *et al.*^[96] pointed out that the presence of copper on the porphyrin-based ZnO enhanced the stability against photobleaching.

To summarize, a lot of similarities exist between the PS/TiO₂ and PS/ZnO nanomaterials. As an example, their mechanisms of photo-degradation are similar. However, it appears difficult to directly compare the efficiency of the PS/ZnO catalyst with those of PS/TiO₂. Sun and coworkers already make this tentative.^[95] Note that they used TiO₂ without giving more precision on the nature of titania. The system was composed of semiconductor coupled with Copper(II) 5-mono-[4-(2-ethyl-*p*-hydroxy benzoate ethoxyl)]-10,15,20-triphenyl porphyrin and was utilized for the photodegradation of RhB using both UV and visible light irradiation. Under visible light irradiation the CuP/ZnO system was more efficient than CuP/TiO₂. Conversely, UV light leads to a better photocatalytic activity of CuP/TiO₂ (Fig. 37).

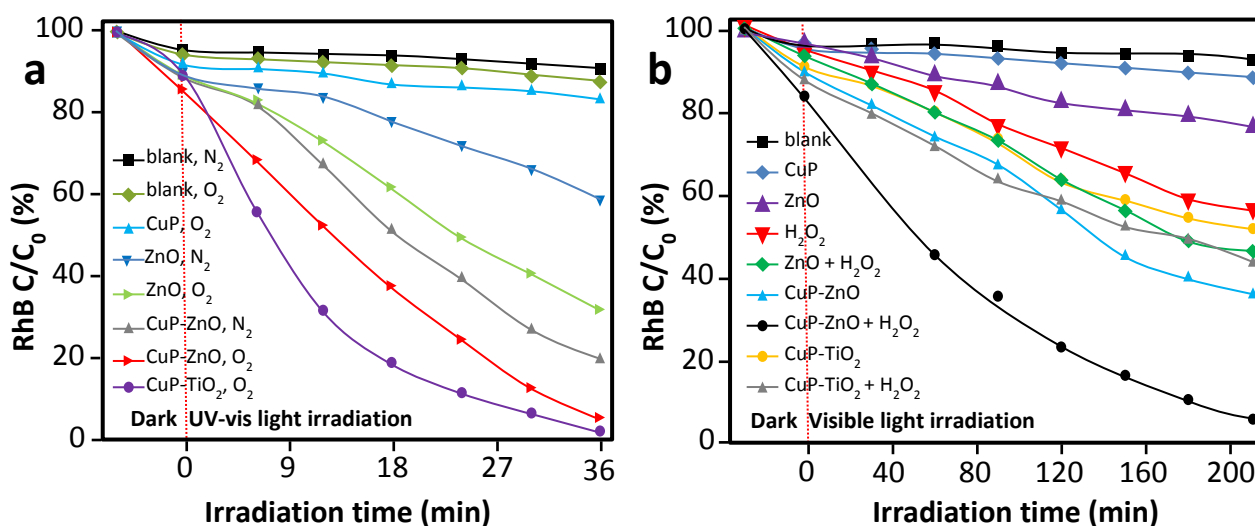


Fig. 37: Comparison between ZnO/PS and TiO₂/PS photocatalytic activity. Photodegradation of RhB as a function of the irradiation time with CuP/ZnO under (a) UV-Vis light irradiation, and (b) visible light irradiation. Taken from reference ^[95]

Table 2: Summary of the literature on PS/ZnO systems along with the photocatalytic degradation parameters and pollutants.

Type of ZnO	Size of nanoparticle	PS	Amount of PS	Adsorbed or grafted	Type of covalent bond	H ₂ O ₂	Pollutant/Photocatalytic application	Light used (wavelength range)	Type of ROS involved	Ref
Electrospun fibers	Fibers d = 3 – 19 μ m	TCB-ZnPc	-	Grafting	-	no	RhG	Visible	¹ O ₂	[91]
Hydrothermal synthesis	d = 28 nm	ZnPc	-	Grafting	Grafted via two carboxyl groups (from tartaric acid)	no	MO	Visible (λ = 620 nm)	ROS	[92]
Commercial (Aldrich)	d = 35 nm	CuP	-	Physisorption (impregnation)	Physical interaction	Yes	RhB	Simulated solar light (λ : 380-780 nm) and Visible (λ \geq 420 nm)	h ⁺ , O ₂ ^{•-} and HO [•]	[95]
Commercial (Merck)	ZnO coated on stainless steel mesh	CuPc NiPc CoPc	-	Physisorption	-	no	Conversion of CO ₂ in the presence of CH ₄ as the reductant	Visible light	Not mentioned	[93]
Commercial (Aldrich)	d = 50 nm	Protoporphyrin in the presence of iron(II) and copper(II) ions in solutions	Complexation rate copper : 4.95 % Iron : 1.52 %	Grafting	Zn(OOC) ₂ -PS	no	MB in water In the presence of iron and copper ions	Visible light 8 W UV source A + high-pass optical filter (395 nm)	Not mentioned	[96]
ZnO Microrods	d = 2 μ m	TAPPI-CoTPPS Porphyrin heteroaggregates	1.4 μ mol PS/g-ZnO		-	no	RhB	Visible light (λ \geq 420 nm)	Not mentioned	[94]

4. PS/Fullerene systems

Carbon materials such as fullerene (C₆₀) have recently emerged as promising candidates for photocatalysis. These materials possess the ability to efficiently produce ¹O₂ under UV irradiation in organic media and in aqueous solvent.^[97] The quantum yield of ¹O₂ production is close to 1.^[98] Fullerene absorbs strongly in UV and moderately in visible due to its band gap of 1.7 eV. The efficiency of C₆₀ to absorb the visible light is substantially enhanced compared to that of TiO₂ and ZnO. Nevertheless, fullerene powders are highly hydrophobic since they possess a low surface energy (41.7 mJ/m²) with a dominant non-polar Lifshitz–van der Waals component.^[99] In aqueous

systems, C_{60} particles cannot be well dispersed and they produce large aggregates. It is now well established that the hydrophobic attraction due to the high cohesion of water is the driving force for C_{60} aggregation.^[99] This coalescence leads to a significant diminution of the available catalyst surface for the light and the pollutants. Consequently, it reduces the contaminant adsorbed amount and the light absorption. In addition, self-quenching mechanisms occur inside the aggregates reducing the photochemical properties and the 1O_2 production.^[100] For these reasons, bare C_{60} particles cannot be directly utilized for water treatment applications. In an attempt to overcome the C_{60} aggregation in water, two major options have been studied.

On one hand, the immobilization of the C_{60} on a convenient support could be advantageous and seems to be the most preferred solution.^[98,101-107] Silica and titania particles appear as interesting supports for C_{60} and are the most used supports for fullerene. The C_{60}/SiO_2 systems were very efficient for the production of 1O_2 under UV light in water.^[102] As a consequence, a fast photodegradation of phenolates by $C_{60}/silica$ was obtained at basic pH. Under visible light irradiation, in spite of the moderate light absorption of the C_{60} , 1O_2 formation was highlighted.^[98,106] For instance, Moor and Kim^[106] demonstrated that the supported C_{60} composite produced the inactivation of MS₂ bacteriophages in water. However, it appears that 1O_2 remains less efficient than HO^\bullet radicals to remove the pollutants from the water. In details, electrophilic 1O_2 oxidizes preferentially electron-rich species such as olefins, dienes, and sulfides while HO^\bullet is a non-selective oxidant more adapted to degrade the majority of the organic species.^[102] As previously mentioned, HO^\bullet radicals can be generated in the presence of TiO_2 . For this reason, the immobilization of C_{60} onto titania is the most preferred solution. In that case, the C_{60} plays the role of the photosensitizer. The high electron affinity of the fullerene is employed to scavenge the photogenerated electrons from the TiO_2 particles, and, thus, to increase the photocatalytic activity by reducing the rate of e^-h^+ recombinations of titania.^[103,105] It is interesting to note that fullerene is capable of accepting as many as six electrons.^[101] Consequently, the number of available HO^\bullet radicals onto TiO_2 is enhanced in the presence of C_{60} . As an example, Krishan *et al.* have shown that the concentration of HO^\bullet radicals generated by a $C_{60}/titania$ mixture is up to 60% larger than that obtained without C_{60} under UV light illumination.^[104] As a consequence, the degradation of Procion red MX-5B dye and the inactivation of *Escherichia coli* are greatly improved in the presence of fullerene deposited onto titania. Despite the moderate absorption of the visible light by the fullerene, it was emphasized that the presence of C_{60} onto titania promotes the visible light response of the composite.^[101,104,107]

On the other hand, to avoid the aggregation of the fullerene in water the C_{60} surface can be modified. Previous reports have employed surfactants,^[108,109] cyclodextrins, polymers, and liposomes.^[110] However, a high degree of functionalization on C_{60} results in a reduction of the 1O_2 production quantum yield.^[109] In addition, due to the moderate absorption of the visible light by C_{60} , it appears more relevant to functionalize the fullerene surface with organic PSs. More interestingly,

the C_{60}/PS becomes an electron donor-acceptor system.^[111,112] Obviously, the PS is the electron donor while the C_{60} is the electron acceptor. The PS acts as both a chromophore and an electron donor.^[111] Nevertheless, up until now only a small amount of studies reported on the photocatalytic water purification with C_{60}/PS systems. **Table 3** summarizes the literature reporting PS/ C_{60} systems along with the photodegradation parameters and pollutants. The most interesting study was published in 2016^[113] The authors described a visible-light responsive cobalt phthalocyanine coupled with fullerene as photocatalyst ($CoPc/C_{60}$). The composite was able to oxidized various organic substances (trimethylamine, acetaldehyde and 2-mercaptoethanol) under relatively low visible light irradiation ($1\text{ mW}/\text{cm}^2$). Complete mineralization of the pollutants was obtained (**Fig. 38a,b**). In addition, the reusability and the long-term stability of the photocatalytic properties of the hybrid catalyst was maintained during five cycles (**Fig. 38c**). The photocatalytic activity was greatly improved in comparison to those of bare $CoPc$, bare C_{60} , and $AlPc/C_{60}$ composite. This latter result confirms that the nature of the metal coupled to the PS is an important parameter. The larger oxidation power of the $CoPc/C_{60}$ composite is attributed to the holes generated at the $CoPc/C_{60}$ interface resulting from the electron transfer at the p/n junction.^[113]

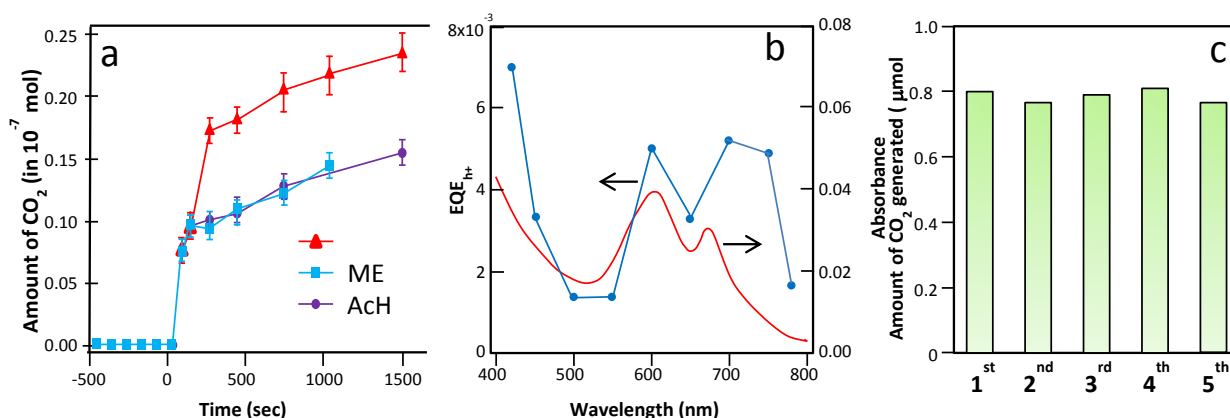


Fig. 38: (a) Time course of CO_2 evolution from aqueous trimethylamine (TMA), acetaldehyde (AcH) and 2-mercaptoethanol (ME) decomposition under visible light illumination using $CoPc/C_{60}$ as photocatalyst ($CoPc$: cobalt phthalocyanine). (b) Parallel evolution of the external quantum efficiency (EQE) and the light absorption during the photodegradation of TMA with the $CoPc/C_{60}$ composite. (c) Repetitive use of the photocatalyst: Amount of CO_2 photogenerated during the several runs of the photocatalytic degradation of AcH with the $CoPc/C_{60}$ composite. Taken from reference [113]

A demonstration of the electron transfer from the PS to fullerene was given by Abe *et al.*^[114] They photoelectrochemically split the water into H_2 and O_2 using an organic photodevice responsive to the visible light. The organic p/n layer was composed of metal free phthalocyanine (Pc, p-type semiconductor) deposited onto fullerene (n-type semiconductor) and was applied as photocathode after deposition onto an indium-tin-oxide ITO substrate. The proposed mechanism involved the

formation of C_{60}^{2-} active species originating from the charge separation of the excitons at the p/n interfaces, *i.e.* the electron transfer from the PS to the C_{60} (Fig. 39). The same system was also utilized for the decomposition of hydrazine in N_2 and H_2 under visible light.^[115] As previously reported with titania/PS, the molecular organization of the PS at the surface of the fullerene has a strong impact on the efficiency of the photoinduced electron transfer.^[111]

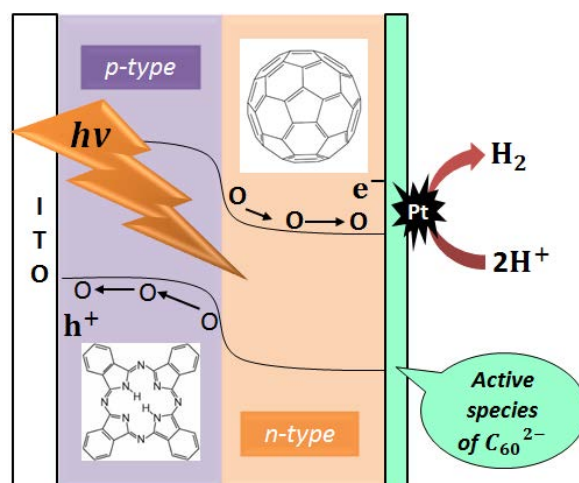


Fig. 39: Schematic diagram for H_2 evolution at the ITO/Pc/ C_{60} /Pt electrode under visible light irradiation. Taken from reference ^[114]

While the PS is generally grafted onto the fullerene, one study explored the formation of ionically-bound aggregates of oppositely charged phthalocyanine and fullerene derivative in aqueous solution.^[116] The composite displays a large photocatalytic activity in the oxidation of 3-mercaptopropanol by molecular oxygen using visible light. The activity is in the same order than that with grafted phthalocyanine since the photoelectron transfer mechanism is maintained with the physisorbed system.

Due to the low dispersability of C_{60} in water coupled to the lower amount of 1O_2 generated, the field of PS/ C_{60} has been the focus of increased experimental activity in non-polar media. A special attention has been given to the development of new PSs. Strong absorption of visible light and long-lived triplet photoexcited state are required for intermolecular electron transfer between the PS and the C_{60} particles. Actually, PSs usually contain heavy atoms which facilitate intersystem crossing to produce a triplet state.^[117] One of the objective of these researches is the development of molecular structures for heavy-atom free organic PS. In addition, all the current PSs are based on a monochromophore and they possess one main absorption band in the visible region. Consequently, they cover only a small range of the visible spectrum. Huang *et al.* have developed C_{60} coupled with new PSs, namely bodipy triads and tetrads, based on energy tunneling effect that display a broad-band absorption in the visible region (Fig. 40a,b).^[117] The new PSs contain two and three different light harvesting antennas associated with different absorption wavelengths that result in a broad

absorption band from 450 to 650 nm. These PSs are based on a multiple intramolecular energy tunneling effect from the antenna (PS) to the C₆₀ unit without the presence of any heavy metallic atom. Here, the excited state of the triads and tetrads are populated upon visible light excitation. The production of ¹O₂ is larger with the triads than with the dyads PS. Following the same idea, Huang and Zhao^[118] have synthesized metal free C₆₀/bodipy hybrids materials exhibiting strong absorption of visible light coupled with long-lived triplet excited state (**Fig. 40c**). The composites were used as photocatalyst for photocatalytic organic reactions. The tandem oxidation/[3+2] cycloaddition of tetrahydroisoquinoline with *N*-phenylmaleimide to produce pyrrole isoquinoline was successively achieved under visible light illumination. Fullerene derivatives bearing five-membered heterocyclic wings were also developed and appeared efficient in the ¹O₂ production (**Fig. 40d**).^[119] In parallel, the two photons absorption process has been explored as a new way to excite the PS. Collini *et al.* have developed a fullerene/distyrylbenzene PS with a high two photons absorption cross-section which presents a high ¹O₂ quantum yield (**Fig. 40e**).^[97] They point out that the PS antenna transfers its exciton *via* electron transfer to the fullerene, where inter-system crossing and ¹O₂ production takes place.

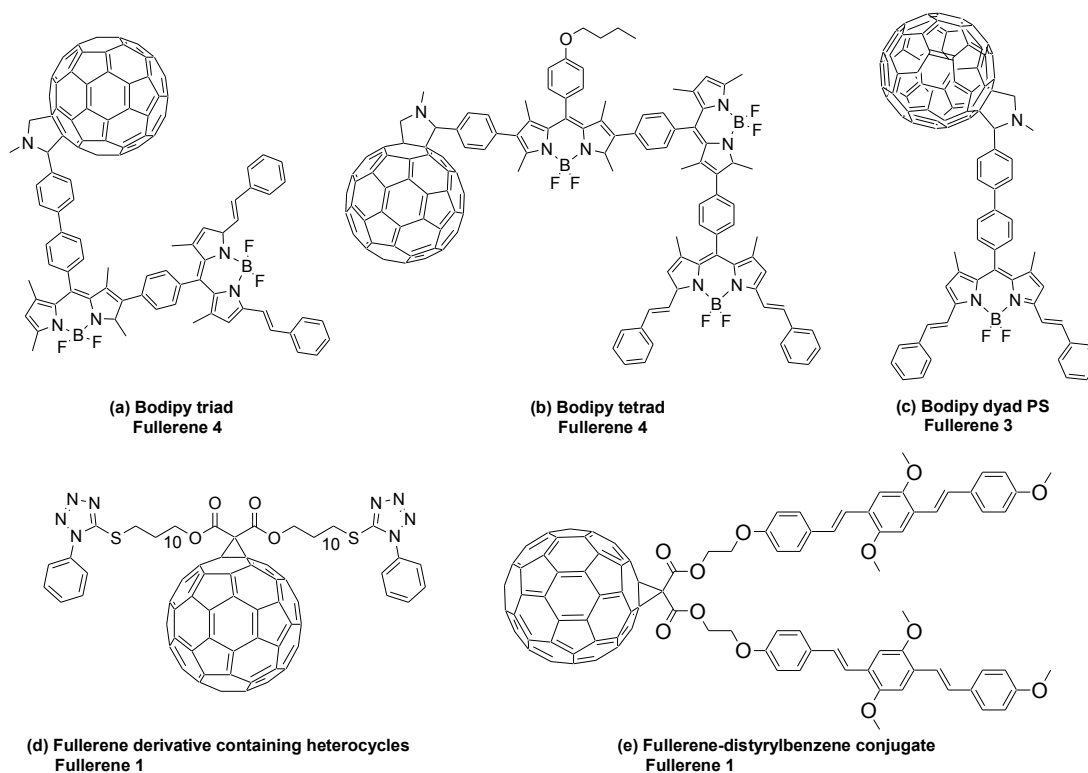


Fig. 40: Molecular structure of some new PSs. (a) Bodipy triad, (b) Bodipy tetrad, (c) Bodipy dyad PS, (d) Fullerene derivative containing heterocycles, and (e) fullerene-distyrylbenzene conjugate. Taken from reference ^[97,117-119]

Table 3: Summary of the literature on PS/Fullerene systems along with the photocatalytic degradation parameters and pollutants.

Type of Fullerene	Size of nanoparticle	PS	Adsorbed or grafted	Type of covalent bond	Pollutant/ Photocatalytic application	Light used (wavelength range)	Type of ROS involved	Ref	
Commercial C ₆₀	d = 38-41 nm	CoPc	Physisorption		TMA AcH ME	Visible light ($\lambda = 420 - 800$ nm)	Photogenerated holes h^+	[113]	
	H ₂ Pc/C ₆₀ used as photocathode ITO/H ₂ Pc/C ₆₀ /Pt	H ₂ Pc	Vapor deposition		Water photoelectrochemically splitted into H ₂ and O ₂	Visible light ($\lambda < 750$ nm)	Formation of C ₆₀ ²⁻ species	[114]	
	-	Five heterocycles	Grafting	C-C bond	-	UVA Solid state laser ($\lambda = 375$ nm)	¹ O ₂ and O ₂ ^{•-}	[119]	
	-	Distyrylbenzene Dimer	Grafting	C-C bond	-	Visible Near-IR region ($\lambda = 710 - 750$ nm)	¹ O ₂	[97]	
	-	Bodipy dyad	Grafting	C-C bond	Tandem oxidation/[3+2] cycloaddition of tetrahydro isoquinoline with N-phenyl maleimide In CH ₂ Cl ₂	Visible light ($\lambda > 385$ nm)	¹ O ₂ and O ₂ ^{•-}	[118]	
		Bodipy triads and tetrads	Grafting	C-C bond	Photooxidation of naphthol to juglone Aerobic oxidation of aromatic boronic acid to produce phenol	Visible light ($\lambda > 385$ nm)	¹ O ₂ and O ₂ ^{•-}	[117]	
		PdP PtP	Grafting	C-C bond		Visible light		[112]	
		ZnPc	Physisorption Positively and negatively charged ZnPc Ionic interaction with C ₆₀			Photooxidation of 2-mercaptoethanol by molecular oxygen	Visible light	¹ O ₂	[116]
		ITO/C60/ZnPc	ZnPc	ZnPc coated on top of the C ₆₀ layer		Decomposition of hydrazine (N ₂ H ₄) to H ₂ product	Visible light	-	[115]

5. PS/Graphene systems

Based on the literature and the research efforts performed on graphene (GR), it appears that this material is not employed alone in photocatalysis. Graphene, as a two-dimensional network constituted of a single layer of sp^2 -bound carbon atoms, possesses a wide range of valuable properties. Those include mainly the large specific surface area, outstanding optical transmittance and outstanding electron conductivity.^[120,121] Such properties paved the way for graphene to be used mostly for ‘assisting’ roles in the UV- and visible-light driven photocatalytic applications.

In visible/solar light photocatalysis, and precisely, in the dye-sensitized nanosystems, graphene is rarely used as an independent photocatalyst functionalized with a dye as it is familiar in the case of TiO_2 and ZnO . However, graphene (GR) and graphene oxide (GO) are mostly used as photosensitizers or electron mediators in photocatalytic systems involving semiconductors or other types of co-catalysts. GR and GO are used in dye-sensitized systems as electron mediators. GR matrix has been immobilized by the PS (Eosin Y, Ru-tris(dicarboxybipyridine), 5,10,15,20-tetrakis(4-(hydroxyl)-phenyl)porphyrin, tin(IV) porphyrin, etc...) together with a co-catalyst nanoparticles such as Pt and Ag. Thus, the PS can be excited upon visible light absorption generating electrons. The produced electrons are then transferred to the graphene matrix, that transfers the electrons to the co-catalyst (**Fig. 41a**). Other possibilities are to immobilize the GR by an electron acceptor (fullerene C_{60} , etc...) beside the PS. A similar electron transfer mechanism as the pre-mentioned takes place, in which the electrons produced by the excited PS are transferred indirectly to the electron acceptor through the GR matrix (**Fig. 41c**). However, dye-sensitized semiconductors mainly with TiO_2 and ZnO nanosystems (**Fig. 41b**) have also occupied the GR matrix. The generated electrons from the visible light activated PS are injected into the semiconductor to be finally destined onto GR (**Fig. 41b**). The low-lying Fermi level of GR enables the capture of the electrons generated by the excited dye upon visible-light irradiation and their transfer to the catalysts, limiting the e^-h^+ recombination, and hence enhancing the photocatalytic activity.^[121-128]

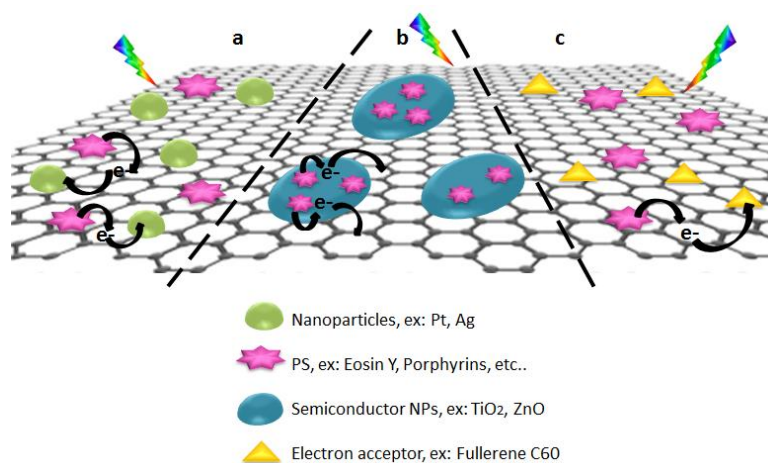


Fig. 41: The mechanism of electron transfer on GR matrix immobilized by (a) NP and PS, (b) dye-sensitized semiconductor NP, and (c) electron acceptor and PS.

In other research efforts, GR has also been used as a PS to extend the light activation range of some semiconductors encountering UV-limited activity. As one of the many examples in this domain, Yang *et al* proposed a GR–ZnO composite with different weight addition ratios of GR (1–30 %). When the composite is irradiated by visible light ($\lambda > 400$ nm), graphene absorbs this light and is excited from its ground state GR* generating electrons. Those electrons are injected into the CB of ZnO and consequently can cause the reduction of Cr(VI) to Cr(III) (Fig. 42a,b).^[129]

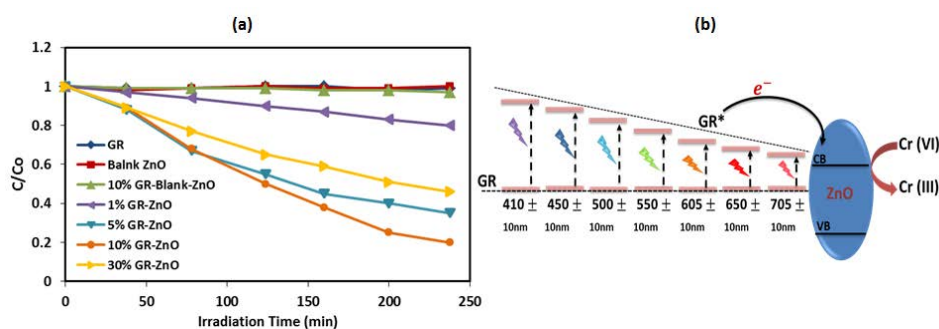


Fig. 42: (a) Photocatalytic performance of bare GR, blank ZnO, GR–ZnO with different weight addition ratios of GR, and 10% GR–Blank–ZnO in the reduction of Cr(VI) aqueous solution under visible light irradiation ($\lambda > 400$ nm). (b) Illustration of the proposed reaction mechanism for photocatalytic reduction of Cr(VI) in aqueous solution over the 10% GR–ZnO nanocomposite under the irradiation of different monochromatic light in the wavelength range of 400–700 nm. Taken from reference ^[129]

GR and especially reduced graphene oxide (RGO) also served as a semiconductor that plays a crucial role in the visible light activity of other nanocomposites. An example is the use of RGO to hybridize BiOIO₃ by Xiong and coworkers. RGO is employed to assist in overcoming the deficiency of BiOIO₃ in utilizing solar light due to their wide band gap to consequently improve the latter's photocatalytic efficiency. The authors insist that RGO acts mainly as a semiconductor instead of a PS or an electron reservoir.^[120]

6. Conclusions

The most important developments in the last 10 years in the area of heterogeneous photocatalysis concern the efficient shift of the light absorption towards visible in order to accelerate the industrialization to large-scale systems. Among them, the development of dye-sensitized nanoparticles is promising to enhance the photocatalytic efficiency and, particularly, to extend the activity towards the visible light domain.

The TiO₂/organic dye or PS (porphyrin and phthalocyanine) remain the most widely employed hybrid systems. It was useful in order to obtain general trends and to extract different parameters to optimize the photocatalytic activity. In all the cases, the TiO₂/PS systems succeed in extending the photocatalytic activity towards solar and visible light domain. The efficiency of the process depends on the content of PS, the linkage mode between the PS and the surface of the semiconductor, the presence of a heavy-metal atom coordinated to the PS's ring, the type of light used to activate the catalyst and the presence or absence of an oxidant. The optimal conditions are obtained with grafted metallo-PS modified on its periphery with an optimum loading around 1-10 μmol PS/1 g TiO₂. The mechanism of the light-induced charge transfer and the nature of the radicals generated are affected by the wavelength of the incident light. Upon visible light irradiation, the photo-excited PS injects electrons to the conduction band of the semiconductor, and, then reacts with the adsorbed oxygen molecules to generate O₂^{•-} and HO[•] radicals. Under simulated solar light, the electrons occupying the CB of TiO₂ react with the adsorbed molecular oxygen elaborating various ROS especially O₂^{•-} and HO[•]. At the same time, the holes occupying the valence band of TiO₂ are transferred to the PS, preventing e⁻ - h⁺ recombination and creating water oxidative sites that produce reactive HO[•]. In the presence of UV light, the electrons from titania are involved in the reduction of pre-adsorbed oxygen into ROS while the holes are injected into the PS. The same conclusions can be drawn with ZnO/PS hybrid nanomaterials due to the similarities between titania and zinc oxide nanoparticles. As an example, their mechanisms of photo-degradation, including the light-induced charge transfer and the nature of the radicals generated, are similar. However, it appears difficult to safely compare the efficiency of the PS/ZnO catalysts with that of PS/TiO₂ catalysts.

While they are not yet used in water purification, new hybrid photocatalysts based on carbon materials such as fullerene and graphene will certainly open the way to more innovative possibilities in this area. On the one hand, due to its efficient production of ¹O₂, high electron affinity, and fair visible light absorption (larger than that of TiO₂ and ZnO), C₆₀ was used, at the beginning as PS to sensitize titania catalysts. More recently, C₆₀ was coupled to PS to produce an electron-acceptor system where the C₆₀ is the electron acceptor while the PS acts as both chromophore and electron donor. The field of PS/C₆₀ is currently the focus of increased experimental activity with a special emphasize on the development of new kinds of efficient PSs in order to avoid the utilization of heavy atoms. On the other hand, graphene/PS systems are not used directly. The graphene is employed as a catalyst scaffold and efficient electron mediator between the PS and the other photocatalysts including titania, zinc oxide and fullerene.

References of Subchapter I.1

- [1] Fatta-Kassinos, D., Meric, S. and Nikolaou, A. (2011). Pharmaceutical residues in environmental waters and wastewater: current state of knowledge and future research. *Anal Bioanal Chem* 399, 251-275.
- [2] Igos, E., Benetto, E., Venditti, S., Kohler, C., Cornelissen, A., Moeller, R. and Biwer, A. (2012). Is it better to remove pharmaceuticals in decentralized or conventional wastewater treatment plants? A life cycle assessment comparison. *Sci Total Environ* 438, 533-540.
- [3] Richardson, S.D. and Ternes, T.A. (2014). Water analysis: Emerging contaminants and current issues. *Anal Chem* 86, 2813-2848.
- [4] Ahmed, T., Imdad, S., Yaldram, K., Butt, N.M. and Pervez, A. (2014). Emerging nanotechnology-based methods for water purification: a review. *Desalin Water Treat* 52, 4089-4101.
- [5] Chen, H.J. and Wang, L.Z. (2014). Nanostructure sensitization of transition metal oxides for visible-light photocatalysis. *Beilstein J Nanotechnol* 5, 696-710.
- [6] Kwon, S., Fan, M., Cooper, A.T. and Yang, H.Q. (2008). Photocatalytic applications of micro- and nano-TiO₂ in environmental engineering. *Crit Rev Environ Sci Technol* 38, 197-226.
- [7] Qu, X.L., Alvarez, P.J.J. and Li, Q.L. (2013). Applications of nanotechnology in water and wastewater treatment. *Water Res* 47, 3931-3946.
- [8] Qu, X.L., Brame, J., Li, Q.L. and Alvarez, P.J.J. (2013). Nanotechnology for a safe and sustainable water supply: Enabling integrated water treatment and reuse. *Acc Chem Res* 46, 834-843.
- [9] Kurniawan, T.A., Sillanpaa, M.E.T. and Sillanpaa, M. (2012). Nanoadsorbents for remediation of aquatic environment: Local and practical solutions for global water pollution problems. *Crit Rev Environ Sci Technol* 42, 1233-1295.
- [10] Kuwahara, Y., Aoyama, J., Miyakubo, K., Eguchi, T., Kamegawa, T., Mori, K. and Yamashita, H. (2012). TiO₂ photocatalyst for degradation of organic compounds in water and air supported on highly hydrophobic FAU zeolite: Structural, sorptive, and photocatalytic studies. *J Catal* 285, 223-234.
- [11] Sakai, T., Da Loves, A., Okada, T. and Mishima, S. (2013). Titania/C-n TAB Nanoskeleton as adsorbent and photocatalyst for removal of alkylphenols dissolved in water. *J Hazard Mater* 248, 487-495.
- [12] Yang, K. and Xing, B.S. (2010). Adsorption of organic compounds by carbon nanomaterials in aqueous phase: Polanyi theory and Its application. *Chem Rev* 110, 5989-6008.
- [13] Pendergast, M.M. and Hoek, E.M.V. (2011). A review of water treatment membrane nanotechnologies. *Energy Environ Sci* 4, 1946-1971.
- [14] Wei, Q., Yang, D.L., Fan, M.H. and Harris, H.G. (2013). Applications of nanomaterial-based membranes in pollution control. *Crit Rev Environ Sci Technol* 43, 2389-2438.
- [15] Herrmann, J.M. (2005). Heterogeneous photocatalysis: State of the art and present applications. *Top Catal* 34, 49-65.
- [16] Herrmann, J.M. (2010). Photocatalysis fundamentals revisited to avoid several misconceptions. *Appl Catal, B* 99, 461-468.
- [17] Hoffmann, M.R., Martin, S.T., Choi, W.Y. and Bahnemann, D.W. (1995). Environmental applications of semiconductor photocatalysis. *Chem Rev* 95, 69-96.
- [18] Kim, S., Durand, P., Roques-Carmes, T., Eastoe, J. and Pasc, A. (2015). Metallo-solid lipid nanoparticles as colloidal tools for meso-macroporous supported catalysts. *Langmuir* 31, 1842-1849.
- [19] Pouran, S.R., Aziz, A.R.A. and Daud, W. (2015). Review on the main advances in photo-Fenton oxidation system for recalcitrant wastewaters. *J Ind Engin Chem* 21, 53-69.
- [20] Goli, K.K., Gera, N., Liu, X.M., Rao, B.M., Rojas, O.J. and Genzer, J. (2013). Generation and properties of antibacterial coatings based on electrostatic attachment of silver nanoparticles to protein-coated polypropylene fibers. *ACS Appl Mater Interfaces* 5, 5298-5306.
- [21] Noimark, S., Dunnill, C.W. and Parkin, I.P. (2013). Shining light on materials - A self-sterilising revolution. *Adv Drug Del Rev* 65, 570-580.
- [22] Ghatak, H.R. (2014). Advanced oxidation processes for the treatment of biorecalcitrant organics in wastewater. *Crit Rev Environ Sci Technol* 44, 1167-1219.
- [23] Oturan, M.A. and Aaron, J.J. (2014). Advanced oxidation processes in water/wastewater treatment: Principles and applications. A review. *Crit Rev Environ Sci Technol* 44, 2577-2641.
- [24] Sud, D. and Kaur, P. (2012). Heterogeneous photocatalytic degradation of selected organophosphate pesticides: A review. *Crit Rev Environ Sci Technol* 42, 2365-2407.
- [25] Yang, W.B., Zhou, H.D. and Cicek, N. (2014). Treatment of organic micropollutants in water and wastewater by UV-based processes: A literature review. *Crit Rev Environ Sci Technol* 44, 1443-1476.
- [26] Aponiene, K. and Luksiene, Z. (2015). Effective combination of LED-based visible light, photosensitizer and photocatalyst to combat Gram (-) bacteria. *J Photochem Photobiol B: Biol* 142, 257-263.

- [27] de Witte, B., van Langenhove, H., Demeestere, K. and Dewulf, J. (2011). Advanced oxidation of pharmaceuticals: Chemical analysis and biological assessment of degradation products. *Crit Rev Environ Sci Technol* 41, 215-242.
- [28] Rahal, R., Le Behec, M., Guyoneaud, R., Pigot, T., Paolacci, H. and Lacombe, S. (2012). Bactericidal activity under UV and visible light of cotton fabrics coated with anthraquinone-sensitized TiO₂. *Catal Today* 209, 134-139.
- [29] Blin, J.L., Stebe, M.J. and Roques-Carmes, T. (2012). Use of ordered mesoporous titania with semi-crystalline framework as photocatalyst. *Colloids Surf Physicochem Eng Aspects* 407, 177-185.
- [30] Charles, G., Roques-Carmes, T., Becheikh, N., Falk, L. and Corbel, S. (2012). Impact of the design and the materials of rectangular microchannel reactors on the photocatalytic decomposition of organic pollutant *Green Process Synth*, 363).
- [31] Fujishima, A., Rao, T.N. and Tryk, D.A. (2000). Titanium dioxide photocatalysis. *J Photochem Photobiol C: Photochem Rev* 1, 1-21.
- [32] Gaya, U.I. and Abdullah, A.H. (2008). Heterogeneous photocatalytic degradation of organic contaminants over titanium dioxide: A review of fundamentals, progress and problems. *J Photochem Photobiol C: Photochem Rev* 9, 1-12.
- [33] Daneshvar, N., Salari, D. and Khataee, A.R. (2004). Photocatalytic degradation of azo dye acid red 14 in water on ZnO as an alternative catalyst to TiO₂. *J Photochem Photobiol A: Chem* 162, 317-322.
- [34] Gaya, U.I., Abdullah, A.H., Hussein, M.Z. and Zainal, Z. (2010). Photocatalytic removal of 2,4,6-trichlorophenol from water exploiting commercial ZnO powder. *Desalination* 263, 176-182.
- [35] Rao, A.N., Sivasankar, B. and Sadasivam, V. (2009). Kinetic study on the photocatalytic degradation of salicylic acid using ZnO catalyst. *J Hazard Mater* 166, 1357-1361.
- [36] Afzal, S., Daoud, W.A. and Langford, S.J. (2012). Self-cleaning cotton by porphyrin-sensitized visible-light photocatalysis. *J Mater Chem* 22, 4083-4088.
- [37] Kruth, A., Peglow, S., Rockstroh, N., Junge, H., Bruser, V. and Weltmann, K.D. (2014). Enhancement of photocatalytic activity of dye sensitised anatase layers by application of a plasma-polymerized allylamine encapsulation. *Journal of Photochemistry and Photobiology a-Chemistry* 290, 31-37.
- [38] Wang, C., Li, J., Mele, G., Yang, G.M., Zhang, F.X., Palmisano, L. and Vasapollo, G. (2007). Efficient degradation of 4-nitrophenol by using functionalized porphyrin-TiO₂ photocatalysts under visible irradiation. *Appl Catal, B* 76, 218-226.
- [39] Assaker, K., Carteret, C., Roques-Carmes, T., Ghanbaja, J., Stebe, M.J. and Blin, J.L. (2014). Influence of Zn ion addition on the properties of ordered mesoporous TiO₂. *New J Chem* 38, 2081-2089.
- [40] Yao, B.H., Peng, C., Zhang, W., Zhang, Q.K., Niu, J.F. and Zhao, J.E. (2015). A novel Fe(III) porphyrin-conjugated TiO₂ visible-light photocatalyst. *Appl Catal, B* 174, 77-84.
- [41] Niu, M., Cheng, D. and Cao, D. (2014). Understanding the mechanism of photocatalysis enhancements in the graphene-like semiconductor sheet/TiO₂ composites. *J. Phys. Chem. C* 118, 5954-5960.
- [42] Carcel, R.A., Andronic, L. and Duta, A. (2010). Photocatalytic degradation of methylorange using TiO₂, WO₃ and mixed thin films under controlled pH and H₂O₂. *J Nanosci Nanotechnol* 11, 9095-9101.
- [43] Senevirathna, M.K.I., Pitigala, P. and Tennakone, K. (2005). Water photoreduction with Cu₂O quantum dots on TiO₂ nano-particles. *J Photochem Photobiol A: Chem* 171, 257-259.
- [44] Sun, W.T., Yu, Y., Pan, H.Y., Gao, X.F., Chen, Q. and Peng, L.M. (2008). CdS quantum dots sensitized TiO₂ nanotube-array photoelectrodes. *J Am Chem Soc* 130, 1124-+.
- [45] Yu, C.L., Yu, J.C., Zhou, W.Q. and Yang, K. (2010). WO₃ coupled P-TiO₂ photocatalysts with mesoporous structure. *Catal Lett* 140, 172-183.
- [46] Cahen, D., Hodes, G., Gratzel, M., Guillemoles, J.F. and Riess, I. (2000). Nature of photovoltaic action in dye-sensitized solar cells. *J Phys Chem B* 104, 2053-2059.
- [47] Gratzel, M. (2003). Dye-sensitized solar cells. *J Photochem Photobiol C: Photochem Rev* 4, 145-153.
- [48] Feng, X.H., Zhang, S.K., Wu, H. and Lou, X. (2015). A novel folic acid-conjugated TiO₂-SiO₂ photosensitizer for cancer targeting in photodynamic therapy. *Colloids Surf B Biointerfaces* 125, 197-205.
- [49] Lux, F., Mignot, A., Mowat, P., Louis, C., Dufort, S., Bernhard, C., Denat, F., Boschetti, F., Brunet, C., Antoine, R., Dugourd, P., Laurent, S., Vander Elst, L., Muller, R., Sancey, L., Josserand, V., Coll, J.L., Stupar, V., Barbier, E., Remy, C., Broisat, A., Ghezzi, C., Le Duc, G., Roux, S., Perriat, P. and Tillement, O. (2011). Ultrasmall rigid particles as multimodal probes for medical applications. *Angew Chem Int Ed* 50, 12299-12303.
- [50] Sun, W.J., Li, J., Yao, G.P., Jiang, M. and Zhang, F.X. (2011). Efficient photo-degradation of 4-nitrophenol by using new CuPp-TiO₂ photocatalyst under visible light irradiation. *Catal Commun* 16, 90-93.
- [51] Granados-Oliveros, G., Paez-Mozo, E.A., Ortega, F.M., Ferronato, C. and Chovelon, J.M. (2009). Degradation of atrazine using metalloporphyrins supported on TiO₂ under visible light irradiation. *Appl Catal, B* 89, 448-454.

- [52] Huang, C., Lv, Y., Zhou, Q., Kang, S.Z., Li, X.Q. and Mu, J. (2014). Visible photocatalytic activity and photoelectrochemical behavior of TiO₂ nanoparticles modified with metal porphyrins containing hydroxyl group. *Ceram Int* 40, 7093-7098.
- [53] Li, X.Z., Zhao, W. and Zhao, J.C. (2002). Visible light-sensitized semiconductor photocatalytic degradation of 2,4-dichlorophenol. *Sci China, Ser B* 45, 421-425.
- [54] Murphy, S., Saurel, C., Morrissey, A., Tobin, J., Oelgemoller, M. and Nolan, K. (2012). Photocatalytic activity of a porphyrin/TiO₂ composite in the degradation of pharmaceuticals. *Appl Catal, B* 119, 156-165.
- [55] Tasserou, L., Paez, C.A., Lambert, S.D., Eskenazi, D. and Heinrichs, B. (2016). Photocatalytic decomposition of hydrogen peroxide over nanoparticles of TiO₂ and Ni(II)-porphyrin-doped TiO₂: A relationship between activity and porphyrin anchoring mode. *Appl Catal, B* 182, 405-413.
- [56] Vignesh, K., Rajarajan, M. and Suganthi, A. (2014). Photocatalytic degradation of erythromycin under visible light by zinc phthalocyanine-modified titania nanoparticles. *Mater Sci Semicond Process* 23, 98-103.
- [57] Wang, H.G., Zhou, D.M., Wu, Z.Z., Wan, J.M., Zheng, X.M., Yu, L.H. and Phillips, D.L. (2014). The visible light degradation activity and the photocatalytic mechanism of tetra(4-carboxyphenyl) porphyrin sensitized TiO₂. *Mater Res Bull* 57, 311-319.
- [58] Yazdanpour, N. and Sharifnia, S. (2013). Photocatalytic conversion of greenhouse gases (CO₂ and CH₄) using copper phthalocyanine modified TiO₂. *Sol Energy Mater Sol Cells* 118, 1-8.
- [59] Zhou, X.T., Ji, H.B. and Huang, X.J. (2012). Photocatalytic degradation of methyl orange over metalloporphyrins supported on TiO₂ Degussa P25. *Molecules* 17, 1149-1158.
- [60] Fung, A.K.M., Chiu, B.K.W. and Lam, M.H.W. (2003). Surface modification of TiO₂ by a ruthenium(II) polypyridyl complex via silyl-linkage for the sensitized photocatalytic degradation of carbon tetrachloride by visible irradiation. *Water Res* 37, 1939-1947.
- [61] Duan, M.Y., Li, J., Mele, G., Wang, C., Lu, X.F., Vasapollo, G. and Zhang, F.X. (2010). Photocatalytic activity of novel tin porphyrin/TiO₂ based composites. *J Phys Chem C* 114, 7857-7862.
- [62] Huang, H.Y., Gu, X.T., Zhou, J.H., Ji, K., Liu, H.L. and Feng, Y.Y. (2009). Photocatalytic degradation of Rhodamine B on TiO₂ nanoparticles modified with porphyrin and iron-porphyrin. *Catal Commun* 11, 58-61.
- [63] Kang, C.L., Lu, Y., Guo, P., Zhang, F., Yu, H.B. and Lin, X.Y. (2007). Photooxidation of furfural with phthalocyanine-sensitized TiO₂ particle under xenon lamp. *Chemical Research in Chinese Universities* 23, 154-158.
- [64] Lu, X.F., Qian, H., Mele, G., De Riccardis, A., Zhao, R., Chen, J., Wu, H. and Hu, N.J. (2017). Impact of different TiO₂ samples and porphyrin substituents on the photocatalytic performance of TiO₂@copper porphyrin composites. *Catal Today* 281, 45-52.
- [65] Lu, X.F., Sun, W.J., Li, J., Xu, W.X. and Zhang, F.X. (2013). Spectroscopic investigations on the simulated solar light induced photodegradation of 4-nitrophenol by using three novel copper(II) porphyrin-TiO₂ photocatalysts. *Spectrochim Acta, Part A* 111, 161-168.
- [66] Peng, C., Yao, B.H., Zhang, W., Niu, J.F. and Zhao, J. (2014). Synthesis of CuAPTPP-TDI-TiO₂ conjugated microspheres and its photocatalytic activity. *Chin J Chem Phys* 27, 200-208.
- [67] Su, X.Q., Li, J., Zhang, Z.Q., Yu, M.M. and Yuan, L. (2015). Cu(II) porphyrins modified TiO₂ photocatalysts: Accumulated patterns of Cu(II) porphyrin molecules on the surface of TiO₂ and influence on photocatalytic activity. *J Alloys Compd* 626, 252-259.
- [68] Sun, W.J., Li, J., Yao, G.P., Zhang, F.X. and Wang, J.L. (2011). Surface-modification of TiO₂ with new metalloporphyrins and their photocatalytic activity in the degradation of 4-nitrophenol. *Appl Surf Sci* 258, 940-945.
- [69] Wang, C., Li, J., Mele, G., Duan, M.Y., Lu, X.F., Palmisano, L., Vasapollo, G. and Zhang, F.X. (2010). The photocatalytic activity of novel, substituted porphyrin/TiO₂-based composites. *Dyes Pigm* 84, 183-189.
- [70] Yao, G.P., Li, J., Luo, Y. and Sun, W.J. (2012). Efficient visible photodegradation of 4-nitrophenol in the presence of H₂O₂ by using a new copper(II) porphyrin-TiO₂ photocatalyst. *J Mol Catal A: Chem* 361, 29-35.
- [71] Zhao, X., Liu, X., Yu, M.M., Wang, C. and Li, J. (2017). The highly efficient and stable Cu, Co, Zn-porphyrin-TiO₂ photocatalysts with heterojunction by using fashioned one-step method. *Dyes Pigm* 136, 648-656.
- [72] Zimny, K., Roques-Carmes, T., Carteret, C., Stébé, M.J. and Blin, J.L. (2012). Synthesis and photoactivity of ordered mesoporous titania with a semicrystalline framework. *J Phys Chem C* 116, 6585-6594.

- [73] Han, C., Shao, Q., Liu, M., Ge, S.S., Liu, Q.Y. and Lei, J. (2016). 5,10,15,20-tetrakis(4-chlorophenyl)porphyrin decorated TiO₂ nanotube arrays: Composite photoelectrodes for visible photocurrent generation and simultaneous degradation of organic pollutant. *Mater Sci Semicond Process* 56, 166-173.
- [74] Zhang, M.Y., Shao, C.L., Guo, Z.C., Zhang, Z.Y., Mu, J.B., Cao, T.P. and Liu, Y.C. (2011). Hierarchical nanostructures of copper(II) phthalocyanine on electrospun TiO₂ nanofibers: Controllable solvothermal-fabrication and enhanced visible photocatalytic properties. *ACS Appl Mater Interfaces* 3, 369-377.
- [75] Jang, B.U., Choi, J.H., Lee, S.J. and Lee, S.G. (2009). Synthesis and characterization of Cu-phthalocyanine hybrid TiO₂ sol. *J Porphyrins Phthalocyanines* 13, 779-786.
- [76] Afzal, S., Daoud, W.A. and Langford, S.J. (2013). Photostable self-cleaning cotton by a copper(II) porphyrin/TiO₂ visible-light photocatalytic system. *ACS Appl Mater Interfaces* 5, 4753-4759.
- [77] Li, K., Lin, L., Peng, T.Y., Guo, Y.Y., Li, R.J. and Zhang, J. (2015). Asymmetric zinc porphyrin-sensitized nanosized TiO₂ for efficient visible-light-driven CO₂ photoreduction to CO/CH₄. *Chem Commun* 51, 12443-12446.
- [78] Osora, H., Li, W.J., Otero, L. and Fox, M.A. (1998). Photosensitization of nanocrystalline TiO₂ thin films by a polyimide bearing pendent substituted-Ru(bpy)(3)(+2) groups. *J Photochem Photobiol B: Biol* 43, 232-238.
- [79] Gou, F.L., Jiang, X., Li, B., Jing, H.W. and Zhu, Z.P. (2010). Salicylic acid as a tridentate anchoring group for azo-bridged zinc porphyrin in dye-sensitized solar cells. *ACS Appl Mater Interfaces* 5, 12631-12637.
- [80] Rochford, J. and Galoppini, E. (2008). Zinc(II) tetraarylporphyrins anchored to TiO₂, ZnO, and ZrO₂ nanoparticle films through rigid-rod linkers. *Langmuir* 24, 5366-5374.
- [81] Hong, A.P., Bahnemann, D.W. and Hoffmann, M.R. (1987). Cobalt(II) tetrasulfophthalocyanine on titanium-dioxide - a new efficient electron relay for the photocatalytic formation and depletion of hydrogen-peroxide in aqueous suspensions. *Journal of Physical Chemistry* 91, 2109-2117.
- [82] Chang, M.Y., Hsieh, Y.H., Cheng, T.C., Yao, K.S., Wei, M.C. and Chang, C.Y. (2009). Photocatalytic degradation of 2,4-dichlorophenol wastewater using porphyrin/TiO₂ complexes activated by visible light. *Thin Solid Films* 517, 3888-3891.
- [83] Shang, X.L., Li, B., Zhang, T.Y., Li, C.H. and Wang, X. (2013). Photocatalytic degradation of methyl orange with commercial organic pigment sensitized TiO₂. *2013 International Symposium on Environmental Science and Technology* (Procedia Environmental Sciences, 478-485).
- [84] Peter, L.M. (2011). The Gratzel Cell: Where next? *J Phys Chem Lett* 2, 1861-1867.
- [85] Dobrucki, J.W. (2001). Interaction of oxygen-sensitive luminescent probes Ru(phen)₃²⁺ and Ru(bipy)₃²⁺ with animal and plant cells in vitro - Mechanism of phototoxicity and conditions for non-invasive oxygen measurements. *J Photochem Photobiol B: Biol* 65, 136-144.
- [86] Ding, H.M., Zhang, X.Q., Ram, M.K. and Nicolini, C. (2005). Ultrathin films of tetrasulfonated copper phthalocyanine-capped titanium dioxide nanoparticles: Fabrication, characterization, and photovoltaic effect. *J Colloid Interface Sci* 290, 166-171.
- [87] Alloul, H., Roques-Carmes, T., Hamieh, T., Razafitianamaharavo, A., Barres, O., Toufaily, J. and Villieras, F. (2013). Effect of chemical modification on surface free energy components of Aerosil silica powders determined with capillary rise technique. *Powder Technol* 246, 575-582.
- [88] Alloul, H., Roques-Carmes, T., Toufaily, J., Kassir, M., Pelletier, M., Razafitianamaharavo, A., Hamieh, T. and Villieras, F. (2016). Towards a better description of organosilane grafting onto silica particles using volumetric techniques based on molecular probing. *Adsorption* 22, 923-937.
- [89] Kassir, M., Roques-Carmes, T., Hamieh, T., Razafitianamaharavo, A., Barres, O., Toufaily, J. and Villieras, F. (2013). Surface modification of TiO₂ nanoparticles with AHAPS aminosilane: distinction between physisorption and chemisorption. *Adsorption* 19, 1197-1209.
- [90] Kassir, M., Roques-Carmes, T., Hamieh, T., Toufaily, J., Akil, M., Barres, O. and Villieras, F. (2015). Improvement of the photocatalytic activity of TiO₂ induced by organic pollutant enrichment at the surface of the organografted catalyst. *Colloids and Surfaces a-Physicochemical and Engineering Aspects* 485, 73-83.
- [91] Khoza, P. and Nyokong, T. (2015). Visible light transformation of Rhodamine 6G using tetracarbazole zinc phthalocyanine when embedded in electrospun fibers and in the presence of ZnO and Ag particles. *J Coord Chem* 68, 1117-1131.
- [92] Seddigi, Z.S., Ahmed, S.A., Sardar, S. and Pal, S.K. (2015). Ultrafast dynamics at the zinc phthalocyanine/zinc oxide nanohybrid interface for efficient solar light harvesting in the near red region. *Sol Energy Mater Sol Cells* 143, 63-71.
- [93] Yarahmadi, A. and Sharifnia, S. (2014). Dye photosensitization of ZnO with metallophthalocyanines (Co, Ni and Cu) in photocatalytic conversion of greenhouse gases. *Dyes Pigm* 107, 140-145.

- [94] Li, X.Q., Cheng, Y., Kang, S.Z. and Mu, J. (2010). Preparation and enhanced visible light-driven catalytic activity of ZnO microrods sensitized by porphyrin heteroaggregate. *Appl Surf Sci* 256, 6705-6709.
- [95] Sun, W.J., Li, J., Mele, G., Zhang, Z.Q. and Zhang, F.X. (2013). Enhanced photocatalytic degradation of rhodamine B by surface modification of ZnO with copper (II) porphyrin under both UV-vis and visible light irradiation. *J Mol Catal A: Chem* 366, 84-91.
- [96] Kar, P., Sardar, S., Alarousu, E., Sun, J.Y., Seddigi, Z.S., Ahmed, S.A., Danish, E.Y., Mohammed, O.F. and Pal, S.K. (2014). Impact of metal ions in porphyrin-based applied materials for visible-light photocatalysis: Key information from ultrafast electronic spectroscopy. *Chemistry-a European Journal* 20, 10475-10483.
- [97] Collini, E., Fortunati, I., Scolaro, S., Signorini, R., Ferrante, C., Bozio, R., Fabbrini, G., Maggini, M., Rossi, E. and Silvestrini, S. (2010). A fullerene-distyrylbenzene photosensitizer for two-photon promoted singlet oxygen production. *PCCP* 12, 4656-4666.
- [98] Panagiotou, G.D., Tzirakis, M.D., Vakros, J., Loukatzikou, L., Orfanopoulos, M., Kordulis, C. and Lycourghiotis, A. (2010). Development of [60] fullerene supported on silica catalysts for the photo-oxidation of alkenes. *Appl Catal, A* 372, 16-25.
- [99] Ma, X., Wigington, B. and Bouchard, D. (2010). Fullerene C60: Surface energy and interfacial interactions in aqueous systems. *Langmuir* 26, 11886-11893.
- [100] Hotze, E.M., Labille, J., Alvarez, P. and Wiesner, M.R. (2008). Mechanisms of photochemistry and reactive oxygen production by fullerene suspensions in water. *Environ Sci Technol* 42, 4175-4180.
- [101] Apostolopoulou, V., Vakros, J., Kordulis, C. and Lycourghiotis, A. (2009). Preparation and characterization of [60] fullerene nanoparticles supported on titania used as a photocatalyst. *Colloids Surf Physicochem Eng Aspects* 349, 189-194.
- [102] Kim, H., Kim, W., Mackeyev, Y., Lee, G.S., Kim, H.J., Tachikawa, T., Hong, S., Lee, S., Kim, J., Wilson, L.J., Majima, T., Alvarez, P.J.J., Choi, W. and Lee, J. (2012). Selective oxidative degradation of organic pollutants by singlet oxygen-mediated photosensitization: Tin porphyrin versus C-60 aminofullerene Systems. *Environ Sci Technol* 46, 9606-9613.
- [103] Krishna, V., Noguchi, N., Koopman, B. and Moudgil, B. (2006). Enhancement of titanium dioxide photocatalysis by water-soluble fullerenes. *J Colloid Interface Sci* 304, 166-171.
- [104] Krishna, V., Yanes, D., Imaram, W., Angerhofer, A., Koopman, B. and Moudgil, B. (2008). Mechanism of enhanced photocatalysis with polyhydroxy fullerenes. *Applied Catalysis B-Environmental* 79, 376-381.
- [105] Meng, Z.D., Choi, J.G., Park, J.Y., Zhu, L. and Oh, W.C. (2011). Review for fullerene materials enhanced TiO₂ photocatalysis. *J Photocatal Sci* 2, 29-38.
- [106] Moor, K.J. and Kim, J.H. (2014). Simple synthetic method toward solid supported c60 visible light-activated photocatalysts. *Environ Sci Technol* 48, 2785-2791.
- [107] Yang, M.Q., Zhang, N. and Xu, Y.J. (2013). Synthesis of fullerene-, carbon nanotube-, and graphene-TiO₂ nanocomposite photocatalysts for selective oxidation: A comparative study. *ACS Appl Mater Interfaces* 5, 1156-1164.
- [108] Lee, J. and Kim, J.-H. (2008). Effect of encapsulating agents on dispersion status and photochemical reactivity of C60 in the aqueous phase. *Environ Sci Technol* 42, 1552-1557.
- [109] Yu, C., Canteenwala, T., El-Khouly, M.E., Araki, Y., Pritzker, K., Ito, O., Wilson, B.C. and Chiang, L.Y. (2005). Efficiency of singlet oxygen production from self-assembled nanospheres of molecular micelle-like photosensitizers FC4S. *J Mater Chem* 15, 1857-1864.
- [110] Ikeda, A. (2013). Water-soluble fullerenes using solubilizing agents, and their applications. *Journal of Inclusion Phenomena and Macrocyclic Chemistry* 77, 49-65.
- [111] Hasobe, T. (2013). Porphyrin-based supramolecular nanoarchitectures for solar energy conversion. *J Phys Chem Lett* 4, 1771-1780.
- [112] Obondi, C.O., Lim, G.N. and D'Souza, F. (2015). Triplet-triplet excitation transfer in palladium porphyrin fullerene and platinum porphyrin -fullerene dyads. *J Phys Chem C* 119, 176-185.
- [113] Arunachalam, P., Zhang, S., Abe, T., Komura, M., Iyoda, T. and Nagai, K. (2016). Weak visible light (mW/cm²) organophotocatalysis for mineralization of amine, thiol and aldehyde by biphasic cobalt phthalocyanine/fullerene nanocomposites prepared by wet process. *Appl Catal, B* 193, 240-247.
- [114] Abe, T., Tobinai, S., Taira, N., Chiba, J., Itoh, T. and Nagai, K. (2011). Molecular hydrogen evolution by organic p/n bilayer film of phthalocyanine/fullerene in the entire visible-light energy region. *J Phys Chem C* 115, 7701-7705.
- [115] Abe, T., Taira, N., Tanno, Y., Kikuchi, Y. and Nagai, K. (2014). Decomposition of hydrazine by an organic fullerene-phthalocyanine p-n bilayer photocatalysis system over the entire visible-light region. *Chem Commun* 50, 1950-1952.

- [116] Makarov, S.G., Kazarin, A.S., Suvorova, O.N., Ketkov, S.Y., Lopatin, M.A. and Wohrle, D. (2014). Ionic interactions between charged phthalocyanine and fullerene derivatives. *Macroheterocycles* 7, 145-152.
- [117] Huang, L., Cui, X., Therrien, B. and Zhao, J. (2013). Energy-funneling-based broadband visible-light-absorbing bodipy-C60 triads and tetrads as dual functional heavy-atom-free organic triplet photosensitizers for photocatalytic organic reactions. *Chemistry* 19, 17472-17482.
- [118] Huang, L. and Zhao, J. (2013). C(60)-Bodipy dyad triplet photosensitizers as organic photocatalysts for photocatalytic tandem oxidation/[3+2] cycloaddition reactions to prepare pyrrolo[2,1-a]isoquinoline. *Chem Commun (Camb)* 49, 3751-3753.
- [119] Santos, L.J., Goncalves, A.S.P., Krambrock, K., Pinheiro, M.V.B., Eberlin, M.N., Vaz, B.G., de Freitas, R.P. and Alves, R.B. (2011). Synthesis of [60]fullerene derivatives bearing five-membered heterocyclic wings and an investigation of their photophysical kinetic properties. *J Photochem Photobiol A: Chem* 217, 184-190.
- [120] Xiong, T., Dong, F., Zhou, Y., Fu, M. and Ho, W.K. (2015). New insights into how RGO influences the photocatalytic performance of BiOIO₃/RGO nanocomposites under visible and UV irradiation. *J Colloid Interface Sci* 447, 16-24.
- [121] Zhu, M.S., Li, Z., Xiao, B., Lu, Y.T., Du, Y.K., Yang, P. and Wang, X.M. (2013). Surfactant assistance in improvement of photocatalytic hydrogen production with the porphyrin noncovalently functionalized graphene nanocomposite. *ACS Appl Mater Interfaces* 5, 1732-1740.
- [122] Das, S.K., Chandra, B.K.C. and D'Souza, F. (2014). Studies on the photocatalytic electron pooling of graphene oxide hybrids decorated with electron donor and electron acceptor molecules. *Fuller Nanotub and Carb N* 22, 128-137.
- [123] Li, H.Y., Zhang, Y.W., Chang, G.H., Liu, S., Tian, J.Q., Luo, Y.L., Asiri, A.M., Al-Youbi, A.O. and Sun, X.P. (2012). Environmentally friendly photocatalytic synthesis of porphyrin/Ag nanoparticles/reduced graphene oxide ternary nanohybrids having superior catalytic activity. *Chempluschem* 77, 545-550.
- [124] Liu, Y., Hu, Y., Zhou, M.J., Qian, H.S. and Hu, X. (2012). Microwave-assisted non-aqueous route to deposit well-dispersed ZnO nanocrystals on reduced graphene oxide sheets with improved photoactivity for the decolorization of dyes under visible light. *Appl Catal, B* 125, 425-431.
- [125] Meng, Q.Y., Zhong, J.J., Liu, Q., Gao, X.W., Zhang, H.H., Lei, T., Li, Z.J., Feng, K., Chen, B., Tung, C.H. and Wu, L.Z. (2013). A cascade cross-coupling hydrogen evolution reaction by visible light catalysis. *J Am Chem Soc* 135, 19052-19055.
- [126] Min, S.X. and Lu, G.X. (2011). Dye-sensitized reduced graphene oxide photocatalysts for highly efficient visible-light-driven water reduction. *J Phys Chem C* 115, 13938-13945.
- [127] Mondal, I. and Pal, U. (2015). Noble metal free naphthylbisimide/TiO₂/graphene: an efficient H₂ evolution photocatalyst. *New J Chem* 39, 6925-6934.
- [128] Zhu, M.S., Dong, Y.P., Xiao, B., Du, Y.K., Yang, P. and Wang, X.M. (2012). Enhanced photocatalytic hydrogen evolution performance based on Ru-tris(dicarboxy)pyridine-reduced graphene oxide hybrid. *J Mater Chem* 22, 23773-23779.
- [129] Yang, M.Q. and Xu, Y.J. (2013). Basic principles for observing the photosensitizer role of graphene in the graphene-semiconductor composite photocatalyst from a case study on graphene-ZnO. *J Phys Chem C* 117, 21724-21734.

Subchapter I.2:

The application of titanium dioxide, zinc oxide, fullerene and graphene nanoparticles in photodynamic therapy

Zahraa Youssef^{1,4}, Régis Vanderesse², Ludovic Colombeau¹, Francis Baros¹, Thibault Roques-Carnes¹, Céline Frochot¹, Habibah Wahab³, Joumana Toufaily⁴, Tayssir Hamieh⁴, Samir Acherar^{2*},
Amirah Mohd Gazzali^{2,3}

¹Laboratoire Réactions et Génie des Procédés, Université de Lorraine-CNRS, UMR 7274, 1 rue Grandville, BP 20451, 54001 Nancy cedex, France

²Laboratoire de Chimie Physique Macromoléculaire, Université de Lorraine-CNRS, UMR 7375, 1 rue Grandville, BP 20451, 54001 Nancy cedex, France

³School of Pharmaceutical Sciences, Universiti Sains Malaysia, 11800 Penang, Malaysia

⁴Laboratory of Materials, Catalysis, Environment and Analytical Methods, Faculty of Sciences I, Lebanese University, Campus Rafic Hariri, Beyrouth, Lebanon

The review is published in Cancer Nanotechnology
(Youssef *et al.* *Cancer Nano* (2017) 8:6
DOI 10.1186/s12645-017-0032-2)

The application of titanium dioxide, zinc oxide, fullerene and graphene nanoparticles in photodynamic therapy

Abstract

Nanoparticles (NPs) have been shown to have good ability to improve the targeting and delivery of therapeutics. In the field of photodynamic therapy (PDT), this targeting advantage of NPs could help for ensuring drug delivery at specific sites. Among the commonly reported NPs for PDT applications, NPs from zinc oxide (ZnO), titanium dioxide (TiO₂), and fullerene are commonly reported. In addition, graphene has also been reported to be used as NPs albeit being relatively newer in this field. In this context, the present review is organized by these different NPs and contains numerous research works related to PDT applications. The effectiveness of these NPs for PDT is discussed in detail by collecting all essential information described in the literature. The information thus assembled could be useful in designing new NPs specific for PDT and/or PTT applications in the future.

Keywords: Nanoparticles; Photodynamic therapy; Titanium dioxide; Zinc oxide; Fullerene; Graphene

1. Background

In current era, the explosion of advancement in nanotechnology has opened up different possibilities of its applications, examples being in drug delivery systems, cosmetics, sunscreens and electronics. The European Union in 2011 has defined nanomaterials as natural, incidental or manufactured materials containing particles, in an unbound state, as an aggregate or agglomerate, in which at least 50% of the particles exhibit an external size dimension of between 1 to 100 nm (De Jong and Borm 2008; Shi et al. 2013).

In general, nanomaterials such as nanoparticles (NPs) include polymeric NPs, liposomes (multilayer), lipidic micelles (unilayer), quantum dots and metallic NPs (made from different types of metals such as Au, Fe₂O₃, ZnO, TiO₂...), and graphene (Huang et al. 2012). In addition to these groups of NPs, certain specific structures have also been developed and included NPs such as dendrimers, fullerenes, cubosomes and niosomes (Lohani et al. 2014; Voon et al. 2014). The

preparation technique of the NPs differs depending on their structures and need, the most common being nano-precipitation technique, solvent evaporation and lithography technique, to name a few.

The vast diversified types of NPs available to date gave a possibility to pick and choose the most suitable NPs for specific applications. Indeed, the application of NPs is very wide ranging from cosmetics, engineering, medicals and pharmaceuticals, among other. In the interest of our research, NPs are being used in the delivery of photosensitizers (PSs) for photodynamic therapy (PDT), which is a good approach in improving their specific site delivery.

PDT is a relatively new treatment modality that has attracted attention since the past 30 years (Yano et al. 2011). Its principal of treatment necessitates the presence of a PS, light of an appropriate wavelength and molecular oxygen. Among these three components, PS and light are two modifiable factors, and the development of tumor specific PS is of interest to many researchers in chemistry and pharmaceutical fields (Olivo et al. 2010).

The modification of PS could be performed by conjugation with targeting moieties or by using advanced drug delivery systems such as NPs (Huang et al. 2012; Wang et al. 2004). The PS in this kind of conjugate or system is known as the third generation PS, which has good potential to improve the targeting and delivery of PS towards the diseased tissues. NPs in particular have showed good ability to enhance the delivery of therapeutics through passive targeting by the enhanced permeability and retention (EPR) effect (Blanco et al. 2015). In PDT, the application of NPs has already been used in the formulation of Visudyne[®], which is a third generation PS. In this formulation, its delivery has been shown to be significantly improved (Chang and Yeh 2012).

In the development of third generation PS, several types of NPs were already being reported in the literature with good potential and positive effect on PDT efficacy. Some representative examples on the use of NPs as anticancer agents are given in the following reviews and can be of interest for the readers (Benachour et al. 2012; Calixto et al. 2016; Chouikrat et al. 2012; Colombeau et al. 2016; Couleaud et al. 2011; Monge-Fuentes et al. 2014; Roblero-Bartolon and Ramon-Gallegos 2015; Shen et al. 2016; Stallivieri et al. 2016; Vanderesse et al. 2011). The nano-range size of NPs is indeed very advantageous because they could penetrate through the fenestration presence at the cell junction. Among the different NPs, there are also specific types of particles that have found application in photo-catalysis besides being useful in PDT. As examples, the NPs formed by zinc oxide (ZnO), titanium dioxide (TiO₂), fullerene and graphene have showed this dual ability based on huge number of papers published up to this date. A review by Lucky et al. in 2015 has given in detail the different types of biodegradable and non-biodegradable NPs currently available (Lucky et al. 2015). They have also mentioned the works reported on the development of TiO₂, ZnO and fullerene NPs as downconverting PSs, but the information gathered were briefly described.

Beside PDT, hyperthermia (and particularly photothermal therapy, PTT) refers to the use in medicine of heat to increase the temperature of human tissues for therapeutic purposes. For example,

it has been used for the treatment of cancer tumors, for more rapidly delivering drugs to cancer tissues by increasing blood flow or radiotherapy by sensitizing cancer cells by radiation. Cancer cells are naturally more sensitive to radiation than normal cells. This is why a number of protocols, based on hyperthermia, have been developed to destroy tumor cells irreversibly. Indeed, temperatures ranging from 41 to 47°C can break the membrane of the cells and denature the proteins. Various laser, microwave, radio frequency and ultrasonic methods have been tested to localize and destroy tumors. The main drawbacks are the destruction of healthy tissues close to the tumor and the difficulty in obtaining a uniform temperature in the tumor. In order to better targeting of cancer tissues, some authors have proposed to place photo-absorbing agents in the desired region before irradiation by laser radiation. It has been called photothermal therapy (PTT) because photo-absorbing agents convert light into heat. PTT is a minimally invasive, controllable and efficient sterilization method. In the presence of an external NIR light source, PTT materials convert light energy into heat energy to kill cells. The most commonly used PTT materials include metal nanoscale materials, such as gold, silver, palladium, copper NPs, graphene and carbon nanotubes, and polymeric nanoparticles.

Dual-modal phototherapeutics that combine PDT and PTT can have synergistic effects that enhance therapeutic efficacy compared to PDT or PTT alone.

Poor light penetration could be a limitation to treat deep tumors in the field of research in PDT. A solution that has been related first by the Chen's team (Chen and Zhang 2006) in 2006 is the use of X-rays, instead of light, combined with NPs as a new PDT modality. Since this date, other teams developed different kind of NPs to perform X-ray PDT. Our team (Bulin et al. 2013) synthesized terbium oxide NPs coupled to a porphyrin and showed the formation of $^1\text{O}_2$ upon X-ray excitation. Wang et al. (2016) demonstrated the efficiency of $\text{SrAl}_2\text{O}_4:\text{Eu}^{2+}$ NPs with MC540 as a Ps co-loaded in mesoporous silica in vivo with a subcutaneous tumor model or H1299 cells into the lung. The use of microwave appears also as a promising alternative as source of excitation. The microwaves penetrate deeper than UV and visible light, and propagate through all kind of tissues. This kind of electromagnetic wave can be useful in order to tackle the issue of the small penetration of light. Only recently, microwave induced photodynamic therapy has emerged as a new and interesting phenomenon (Gu 2013). The proof of concept for this process was given by Yao et al. using copper cysteamine NPs to destroy rat osteosarcoma cells (Yao et al. 2016). In parallel, graphitic-phase carbon nitride quantum dots has been explored by the same team (Chu et al. 2017) as a new agent for microwave induced photodynamic therapy. The singlet oxygen production under microwave irradiation was assessed and the NPs were efficient to kill cancer cells and promote tumor cell death.

This review is hence dedicated to bring together all the reported literature to date on the development of ZnO, TiO₂, fullerene and graphene NPs in the specific field of PDT and/or photothermal therapy (PTT) applications.

2. Zinc oxide Nanoparticles (ZnO NPs)

ZnO NPs have long been discovered to have excellent physico-chemical properties as drug delivery vehicles. The Food and Drug Administration (FDA) has recognized ZnO as safe due to its lack or very weak dark toxicity *in vitro* and *in vivo* (Hu et al. 2013).

The advantage that could be firmly associated with ZnO NPs in PDT is their ability to generate visible light upon X-ray radiation. Due to the fact that most currently available PSs absorb light at low wavelength, ZnO NP is a good candidate in improving PDT efficiency because its UV emission upon X-ray excitation more or less matches the UV absorption of most PSs, and hence has a good potential to serve as irradiation source for PDT on deep-seated tumors. This concept is called Self-Lighting Photodynamic Therapy (SLPDT) which was first described by Chen et al. in 2006 (Chen and Zhang 2006) and updated by Sadjadpour in 2016 (Sadjadpour et al. 2016).

NPs, due to its small size have the ability to reach internal organs and tissues through small arteries, veins and blood capillaries. In the case of ZnO NPs, the unique property described above also allows the NPs to act as a PS themselves in the presence of suitable light dose, hence opening an excellent chance of delivering PDT application to the tumor areas that are difficult to reach by conventional PSs. For the purpose of this review however, we will only focus on the application of ZnO NPs as a carrier for the delivery of second generation PS. Three types of excitation can be applied: a) UV-A to excite ZnO NPs, b) UV-visible to excite PS and c) X-ray for fluorescence resonance energy transfer (FRET) between ZnO NPs and PS.

In a work reported Liu et al. (Liu et al. 2008), a conjugate of ZnO-MTAP (*meso*-tetra(*o*-amino phenyl) porphyrin) was prepared. Its PDT effects were investigated on human ovarian carcinoma cell line (NIH:OVCAR-3) and compared with ZnO NPs and MTAP as free molecules. It was showed that the conjugate has significant photocytotoxicity on the cell lines as compared to ZnO NPs or MTAP alone, in which only 10% cells were viable after UV irradiation (365 nm, 30 minutes) as compared to 98% and 75% for ZnO NPs and MTAP respectively (Fig.1). These results suggested that ZnO NP is not cytotoxic in NIH:OVCAR-3 cell lines both in dark and under UV irradiation whilst the ZnO-MTAP conjugate showed significant improvement of photocytotoxicity in the presence of light. The authors estimated to 83% the energy transfer efficiency from ZnO to MTAP.

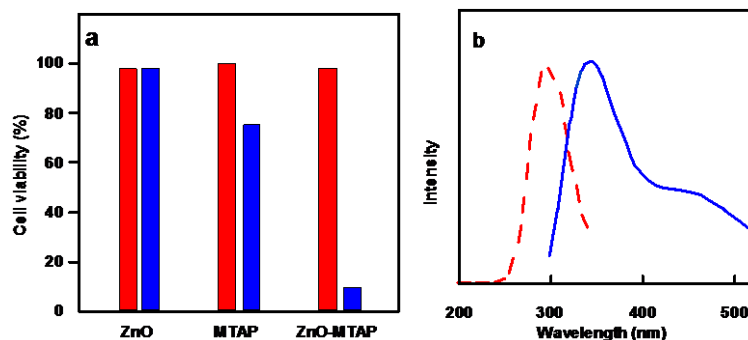


Fig.1: (a) Cell viability in NIH:OVCAR-3 cells exposed to either ZnO NPs alone (0.3 μM), MTAP alone (0.075 μM) or ZnO-MTAP conjugates (0.3 μM , ZnO/MTAP \approx 4/1) under dark conditions (red) or UV illumination (light gray, 365 nm, 30 min, blue). (b) Excitation (red) and emission (blue) spectra of ZnO NPs. Taken from reference (Liu et al. 2008)

They also reported the photophysical properties of the ZnO NPs. The NPs present excitation peak at 300 nm and two emission peaks at 345 nm and 445 nm, hence the emission of ZnO NP is over-lapping with the absorption band of porphyrin and many other PSs. They proposed that this property could be utilized for SLPDT concept as mentioned earlier.

In a subsequent study by Zhang et al. reported singlet oxygen ($^1\text{O}_2$) production and *in vitro* cytotoxic effects of the water soluble ZnO-MTAP conjugate (Zhang et al. 2008). They used 2,7-dichlorodihydrofluorescein diacetate acetyl ester (CM-H₂DCFDA) as molecular probe and subsequently the fluorescence intensity was determined by using a microplate reader under excitation/emission at 485/530 nm. The production of reactive oxygen species (ROS) was concentration- and irradiation-dose dependent. Cell viability was estimated through MTT assay, which has a direct link to mitochondrial enzymes. A reduction in MTT assay was observed in cells which were loaded with ZnO-MTAP conjugate and subsequently irradiated, suggesting that the conjugate were photoactivated, generating ROS and leading to mitochondrial damage and hence reduced cell viability. Only 8% of cells are viable after a co-treatment of UVA and a higher dose of ZnO-MTAP conjugate (treatment II + IV, Fig. 2).

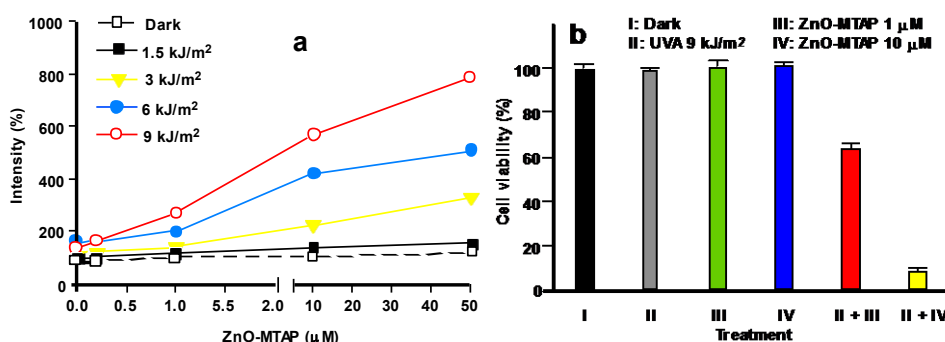


Fig. 2: (a) ROS generation by ZnO-MTAP conjugates in the presence or absence of UVA light. (b) OVCAR-3 cell viability (20 hours later) exposed to ZnO-MTAP conjugates (1 or 10 μM) under dark or UVA conditions (0 or 9 kJ/cm^2 after 4 hours exposure). Taken from reference (Zhang et al. 2008)

ZnO nanorods (NRs) conjugated with Photofrin[®] was investigated by Atif et al. in 2011 (Atif et al. 2011). Hepatocellular carcinoma (HepG2) cells viability was investigated upon exposure to the conjugates and UV light at 240nm. Even in the absence of UV irradiation the cell viability in HepG2 cells was found to decrease, although slowly, with increasing conjugate concentration administered from 0 to 800 $\mu\text{g}/\text{mL}$. Around 80% cells remained viable at the highest concentration (Fig. 3a). In the presence of UV light from diode laser light (240 nm), the white light emitted by ZnO NRs activated the Photofrin[®], which subsequently produced ROS and cell necrosis within few minutes. Hence 77% in cell viability could be observed (Fig.3b).

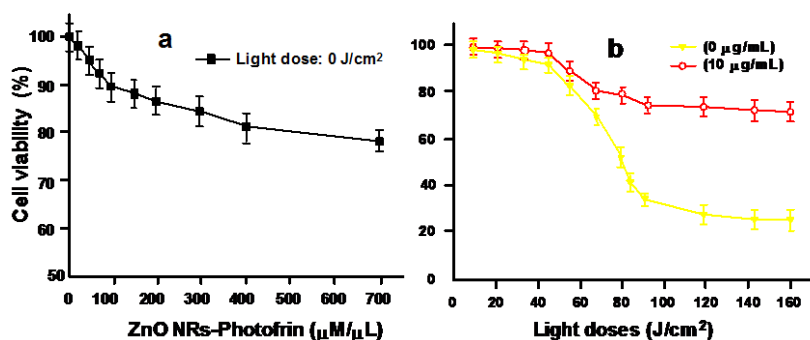


Fig. 3: HepG2 cells viability exposed to ZnO NRs conjugated to Photofrin[®]. (a) In the absence of light. (b) In the presence of diode laser light (240 nm). Taken from reference (Atif et al. 2011)

The same year, Fakhar-e-Alam et al. also reported the application of ZnO NPs conjugated with Photofrin[®] and 5-ALA (5-aminolevulinic acid) for PDT on HepG2 cells (Fakhar-e-Alam et al. 2011a). They observed that both conjugates of ZnO NPs showed minimal toxicity in the absence of light, but they can enhance the fluorescence in the cells due to the Photofrin[®] or protoporphyrin IX (PpIX). ZnO NPs conjugated to 5-ALA were found to better enhance the endogenous fluorescence in the HepG2 cells, as compared to ZnO NPs conjugated to Photofrin[®]. However they reported that upon irradiation with visible light at 635 nm, no significant difference on the viability of the cells treated with the two conjugates was observed as compared to ZnO NPs alone, implying the inability of the presence of PS on NPs to induce cell death in the HepG2 cells.

In another publication in 2011, Fakhar-e-Alam et al. tested the cytotoxicity of ZnO NPs in the form of NRs as bare and in conjugation with different PSs which were 5-ALA, Photofrin[®] or PPDME (protoporphyrin dimethyl ester) under irradiation at 635 nm on HeLa cells (Fakhar-e-Alam et al. 2011b). They reported that the treatment with bare ZnO reduced cell viability by 75%, and the conjugation with PSs showed further reduction of cell viability, 90% reduction for ZnO NPs conjugated to 5-ALA and 80% reduction for ZnO NPs conjugated to Photofrin[®]. As in the case of PPDME, there was an increase of cell viability at higher conjugate concentrations as compared to lower ones (Fig. 4). Hence, ZnO-5-ALA and ZnO-Photofrin[®] conjugates are photocytotoxic on HeLa cells at 635 nm but are less efficient on HepG2 cells in the same conditions.

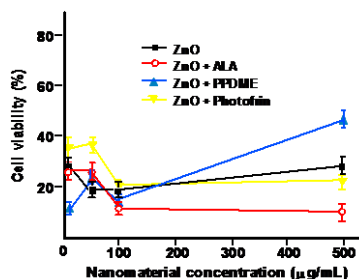


Fig. 4: Cell viability of HeLa cells treated with different concentration of ZnO NRs and their ligands with PSs. Taken from reference (Fakhar-e-Alam et al. 2011b)

In 2012, the same team published a study on the effect of nanoporous ZnO NPs conjugated with Photofrin[®] on human lung cancer cells (A549 cells) (Fakhar-e-Alam et al. 2012). They found that upon UV irradiation, ZnO-Photofrin[®] conjugate displayed valuable reduction in cell viability as compared to Photofrin[®] alone. Significant ROS production was observed and about 92% of cells were killed. They also established that the acceptable incubation period for PDT effect is 10-18 hours with the optimal time being 12 hours. They concluded that ZnO NP has a synergistic effect with Photofrin[®] and hence a good potential for PDT application on A549 cancer cells.

Fakhar-e-Alam et al. explored the application of ZnO NPs in PDT from different angles and application methods, in which ZnO NPs were investigated as a drug delivery vehicle for PSs (Fakhar-e-Alam et al. 2014b). Bare ZnO NPs and ZnO NPs PEGylated PpIX were prepared as the model PS and the cell killing effect on human muscle carcinoma RD cells was tested. In the absence of laser light, ZnO NPs at 1 mM concentration has very low cytotoxicity; 98% of RD cells are viable after a 12 hours incubation period, in comparison to the ZnO NPs PEGylated PPIX in which only 85% of cells are viable at a much lower concentration, 0.2 mM. In the presence of laser light (630 nm, 80 J/cm²), the cytotoxicity of ZnO NPs PEGylated PPIX was very evident and the complex induced cell damage. Besides, good localization of the drug was obtained in the tumor area, showing that ZnO NPs are indeed a good drug delivery system.

D'Souza et al. studied the photophysical properties of phthalocyanines (Pcs) in the presence of ZnO NPs (D'Souza et al. 2015). They proposed that Pc adsorbed on the surface of ZnO NPs spontaneously at an average ratio of 12:1 and subsequent changes in the photophysical properties of the Pcs could be observed. The fluorescence quantum yield of Pc was lower and the fluorescence lifetime is shorter in the presence of ZnO NPs. They concluded that the presence of ZnO NPs influences on the fluorescence behaviour of Pcs and this could serve as good information in the application of ZnO NPs with Pcs for PDT.

Besides anticancer PDT application, PDT is also effective in antimicrobial therapy. Senthilkumar et al. investigated in 2013 the action of ZnO NPs encapsulated TSPP (*meso*-tetra (4-sulfonatophenyl) porphyrin, **Fig. 5a**) for antipathogen PDT (Senthilkumar et al. 2013). It was already known that ZnO NP has the ability to inhibit the growth of different pathogenic bacteria under

normal visible light. TSPP which is an anionic PS has low photoinactivation of gram negative bacteria such as *E. coli*. The encapsulation of TSPP in ZnO NPs was believed to be able to increase the photoinactivation of *E. coli* through increase cellular delivery and improve $^1\text{O}_2$ production. They indeed showed that under visible light (400-800 nm), ZnO NPs encapsulated TSPP have significantly higher antibacterial activity as compared to TSPP or ZnO NPs alone (98% activity as compared to 30%). The activity of TSPP alone was negligible on *E. coli* under visible light (Fig. 5b).

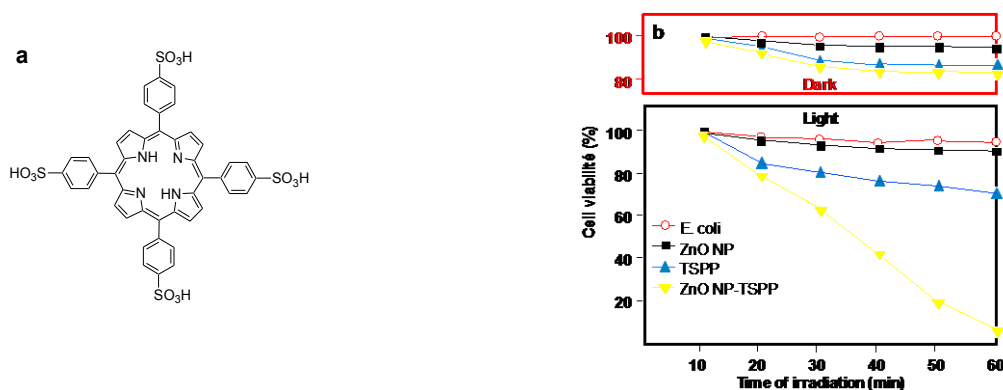


Fig. 5: (a) Chemical structure of TSPP. (b) Antimicrobial activity of ZnO, TSPP and ZnO NPs encapsulated TSPP on *E. coli* bacterial cells under dark and visible light irradiation. Taken from reference (Senthilkumar et al. 2013)

In 2016, Sadjadpour et al. studied the synthesis and conjugation of ZnO NPs with two different porphyrins, *meso*-tetra (4-carboxyphenyl) porphyrin (MTCP) and CuMTCP (Fig. 5a) and their PDT effects on prostate DU145 and breast T-47D cancer cells (Sadjadpour et al. 2016). The conjugation was performed by first coating the surface of ZnO NPs with L-cysteine and subsequently it was conjugated with the porphyrin. The fluorescence intensity of ZnO NPs coated L-cystein was mostly quenched at 370 nm after conjugation with porphyrin and a new peak corresponding to the energy transfer between ZnO NPs coated L-cystein and the conjugated porphyrin molecules appeared. The T-47D cells were more resistant towards PDT treatment by the conjugates as compared to the DU145 cells, and this could be due to the presence of a defense mechanism against NPs uptake by the T-47D cells. Between the two conjugates (ZnO-MTCP and ZnO-CuMTCP), ZnO-MTCP showed higher photocytotoxicity under UV irradiation (UV-A/B, $100 \mu\text{W}/\text{cm}^2$ for 3 minutes) towards the two selected cell lines as compared to ZnO NPs alone, which indicated an efficient FRET between ZnO and PS (Fig. 6b). In contrast under X-ray irradiation (0.94 Gy, 30 seconds), ZnO NPs alone gave a significant cytotoxicity on both T-47D and DU145 cell lines, while no cytotoxic effect was observed when the cells were treated with the two conjugates (Fig. 6b). The authors are of the opinion that this may be due to a lack of FRET between ZnO and PS in the conjugated compounds.

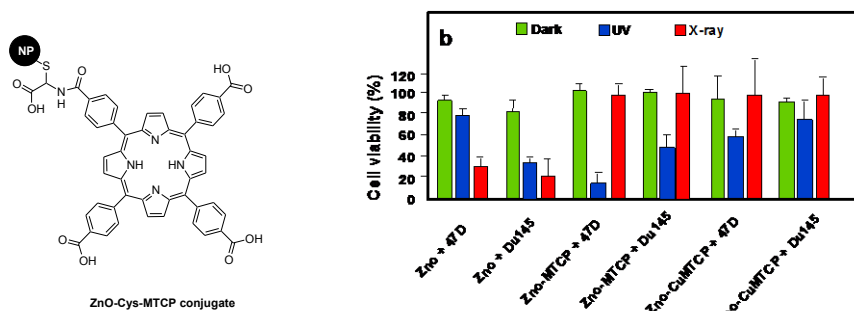


Fig.6: (a) Chemical structure of ZnO-MTCP conjugate. (b) T-47D and DU145 cells viability incubated with ZnO, ZnO-MTCP, and ZnO-CuMTCP at 60 μ M concentration under dark condition, UV irradiation (UV-A/B, 100 μ W/cm² for 3 min) and X-ray irradiation (0.94 Gy, 30 sec). Taken from reference (Sadjadpour et al. 2016)

Table 1 below summarized the data available from literature on the application of ZnO NPs in PDT.

Table 1: Application of ZnO NPs in PDT

Type of NPs (size, nm)	PS (amount)	NPs-PS interactions	Irradiation conditions	Type of ROS	Cancer cell line		Refs.
					In vitro	In vivo	
NPs (5)	MTAP (4/ ZnO)	Conjugated by coupling reaction	UV light 365 nm, 0.51 W/cm ² , 30 min	nd	NIH-OVCAR-3	-	Liu et al. (2008)
NPs (5)	MTAP (4/ ZnO)	Conjugated by coupling reaction	UV-A lamp 365 nm, 0.50 W/cm ² , 30-120 min	ROS	NIH-OVCAR-3	-	Zhang et al. (2008)
Nanorods (130-150)	Photofrin and 5-ALA (nd)	Conjugated	Diode laser 630 nm along with UV light of 240 nm, 0-160 J/cm ² , 0-20 min	ROS	HepG2	SD rats	Atif et al. (2011)
NPs (80-120)	Photofrin and 5-ALA (nd)	Conjugated	Diode laser 635 nm, 80 J/cm ²	nd	HepG2	-	Fakhar-e-Alam et al. (2011a)
Nanorods (150-200)	Photofrin, 5-ALA and PPDME (nd)	Conjugated	Diode laser 635 nm, 30 J/cm ² , 6.5 min	ROS	HeLa	-	Fakhar-e-Alam et al. (2011b)
Nanoporous (200-600)	Photofrin (nd)	Conjugated	Diode laser, 80 J/cm ²	ROS	RD	-	Fakhar-e-Alam et al. (2012)
NPs (35)	PpIX (nd)	Encapsulated	Laser 630 nm, 80 J/cm ²	ROS	A549	-	Fakhar-e-Alam et al. (2014b)
Nanowires (150-170)	PpXI (nd)	Conjugated	UV-A illumination, light dose 10 J/cm ²	ROS	FM5SP AG01518	-	Fakhar-e-Alam et al. (2014a)
NPs (3-26)	MTCP and CuMTCP (nd)	Conjugated by coupling reaction	UV-A/B (100 μ W/cm ² , 3 min) or X-ray (0.94 Gy, 30 s) irradiation	ROS	DU145 T-47D	-	Sadjadpour et al. (2016)
Nanohexagons Nanorods (25-90)	ZnPc ZnTMAAPc ZnTMPAPc (OH)AlPc-Smix (Pc ZnO NPs, 12:1)	Conjugated by coupling reaction	669-690 nm	nd	-	-	D'Souza et al. (2015)
NPs (25-40)	TSPP (nd)	Encapsulated	Visible light irradiation	¹ O ₂	<i>S. aureus</i> <i>E. coli</i> KCCM 12234	-	Senthilkumar et al. (2013)

*NP*s nanoparticles
PS photosensitizer
ROS reactive oxygen species
nd not disclosed
MTAP meso-tetra(*o*-aminophenyl) porphyrin
UV ultraviolet
5-ALA 5-aminolevulinic acid
SD Sprague Dawley
PPDME protoporphyrin dimethyl ester
PpIX protoporphyrin IX
MTCP meso-tetra(4-carboxyphenyl)porphyrin, *ZnPc* zinc phthalocyanine
ZnTMAAPc 2,(3),9(10),16(17),23(24)-tetrakis-(mercaptoacetic acid phthalocyaninato) zinc(II)
ZnTMPAPc 2,(3),9(10),16(17),23(24)-tetrakis-(mercaptoacetic acid phthalocyaninato) zinc(II)
(OH)AlPcSmix mixture of the di-, tri-, and tetra-sulfonated phthalocyanine derivatives
ZnO zinc oxide
TSPP meso-tetra(4-sulfonatophenyl)porphyrin

It is also important to note that although ZnO NP is regarded as having the necessary bio-safety and biocompatibility profiles and recently its toxicology profile has gained more attention. The toxicity of ZnO NP is regarded due to its dispersibility. The solubility of ZnO in the extracellular region could lead to an increase in the intracellular Zn^{2+} level and this might subsequently induce cytotoxicity through certain mechanisms that are still unclear (Pandurangan and Kim 2015). Interestingly, research has shown that surface modification technique such as PEGylation could reduce its cytotoxicity by reducing its cellular intake (Luo et al. 2014). Surface coating with polymers has also shown to reduced cytotoxicity as reported by Osmond-McLeod et al. (Osmond-McLeod et al. 2014) Another technique called “ion-doping” was also found to have reduction effect on the cytotoxicity of this particle, example being on lung toxicity as reported by several papers (Cho et al. 2012; Xia et al. 2011). Nevertheless, more studies are needed to determine specifically the mechanism of toxicity and the exact safety conditions of ZnO application as NPs.

In summary, ZnO is a semiconductor material already used for the water treatment. More recently, ZnO NPs appear like a good candidate for PDT or antimicrobial therapy. Thanks to its small size and the various forms which they can adopt (nanoparticles or nanorods), ZnO-PS systems are good drug delivery systems. Conjugated ZnO-PS systems possess great photophysical properties to obtain a good PDT efficiency and have also evidenced a good ROS production (1O_2 and other radicals). Biologically, ZnO-PS systems present good phototoxicities and, more recently, their toxicity have been investigated and some studies showed that the solubility of ZnO in the extracellular region could lead to an increase in the intracellular Zn^{2+} level inducing cytotoxicity. Other studies are led to determine the safety conditions of ZnO NPs utilizations.

3. Titanium dioxide nanoparticles (TiO_2 NPs)

Titanium dioxide fine particles (TiO_2 FPs) has long been manufactured and used worldwide for different applications. In the past, they were considered to have very low toxicity. However, a finding reported in 1985 has given a new perspective on its safety. It was found that a chronic exposure of this FPs in mice at a high concentration of 250 mg/m^3 for two years (6 hours/day for 5 days/week) could lead to bronchioloalveolar adenomas and cystic keratinizing squamous cell carcinomas (Lee et al. 1985). However, the detected tumors were different from the common human lung tumors and has no metastases could be observed. In the opinion of the researchers, this finding has no biological relevance for human and it is also possible that the tumour was due to overloaded TiO_2 FPs instead of specific carcinogenicity of the particles (Lee et al. 1985; Shi et al. 2013).

TiO_2 NPs are found to have different physico-chemical properties which may lead to changes in their bioactivity. This NP has been used widely in industrial and consumer products due to their strong catalytic activity (Shi et al. 2013). TiO_2 is also known as a wide-band gap semiconductor, and

is photoactive in the presence of UV light against microorganisms and cancer cells. Approach has been taken to use TiO_2 in the form of NP as a support in PDT, by grafting PSs onto the TiO_2 NP surface. This grafting enables the use of visible light, instead of UV light for TiO_2 alone, in the activation of TiO_2 NPs conjugated PS (Jia and Jia 2012). Several studies have shown promising results in the application of these TiO_2 NPs conjugated to PS and will be described below.

In the early 2000s, Ion and Brezoi described the synthesis of a new conjugate TiO_2 -Sil-TSPP consisting of a coupling between *meso*-tetra (4-sulfonatophenyl) porphyrin (TSPP) bearing a silane arm (Sil) with a TiO_2 NP (Fig. 7) (Ion and Brezoi 2005a; Ion 2005). Electronic absorption spectra confirmed the binding of Sil-TSPP to the TiO_2 NPs. Atomic force microscopy (AFM) images taken has enabled determination of the conjugated NP size which was around 39 nm. The *in vivo* study of this TiO_2 -Sil-TSPP conjugate on animal model (mice with underskin implanted cancer cells) showed that the conjugate inhibited tumor growth after a laser irradiation (Fig. 8). No further details are given.

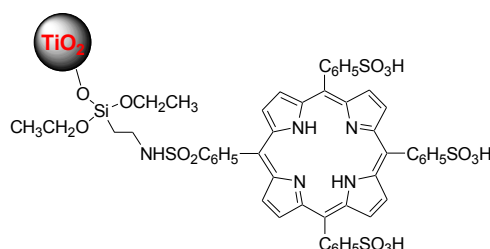


Fig. 7: Chemical structure of TiO_2 -Sil-TSPP conjugate. Taken from reference (Ion and Brezoi 2005b)

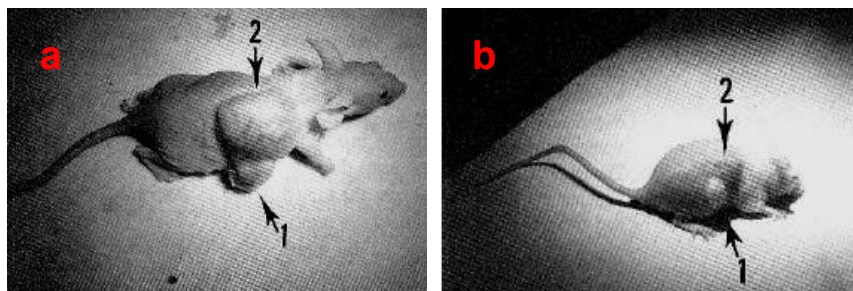


Fig. 8: Effect of laser before (a) and after (b) illumination (no detail given). Reused with permission from reference (Ion 2005)

In 2010, Lopez et al. (Lopez et al. 2010) synthesized *via* the sol-gel method a TiO_2 -ZnPc conjugate by the incorporation of ZnPc into the porous network of TiO_2 NPs. The different techniques (IR, UV-Vis, Raman spectroscopies) proved that Pc and NPs were linked covalently by the N-pyrrole. The photosensitizing effects of ZnPc, TiO_2 NPs, and TiO_2 -ZnPc conjugate have been studied against four mammalian cells and on two forms of *Leishmania* parasites (Table 2). Under light irradiation (670 nm), TiO_2 NPs were not phototoxic for the cells, as expected. In the same conditions, the treatment with ZnPc was photoactive for all the mammalian cells and a higher

phototoxic effect was observed using 597-752 nm irradiation compared to 670 nm irradiation. Nevertheless the activity against mammalian cells of TiO₂-ZnPc conjugate was lower than that of the ZnPc alone. TiO₂-ZnPc conjugate had no phototoxicity for *Leishmania* parasites. The internalization of TiO₂-ZnPc conjugate by the cells was lower than for ZnPc alone. The localization of TiO₂-ZnPc conjugate and ZnPc alone were observed in mitochondrial cytoplasm. Finally the authors concluded that TiO₂-ZnPc conjugate could be a potential PS for PDT treatment.

Table 2: Photoactivity of ZnPc and ZnPc-TiO₂ on *Leishmania* promastigotes and different mammalian cell lines

	Fluency (J/cm ²)	IC ₅₀ (μM)		CC ₅₀ (μM)			
		<i>Leishmania</i> parasites		Mammalian cell lines			
		<i>chagasi</i>	<i>panamensis</i>	HDFs	THP-1	HepG2	Vero
ZnPc	0	>15	14.76	9.21	7.74	10.70	0.78
	2.5 ^a	12.86	6.63	1.08	0.14	0.28	0.24
	2.5 ^b	0.19	0.39	0.15	0.02	0.035	0.09
	10 ^a	5.63	5.63	0.05	0.17	0.086	0.038
ZnPc-TiO₂	0	>10	>10	>10	>10	>10	0.087
	2.5 ^a	>10	>10	5.51	7.45	>10	0.079
	2.5 ^b	>10	>10	3.54	0.28	0.43	0.023
	10 ^a	>10	>10	nd	2.00	5.50	0.001

^a laser light irradiation (670 nm), ^b biological photoreactor irradiation (597-752 nm), ZnPc zinc phthalocyanine, IC₅₀ concentration that induces 50% of parasite inhibition, CC₅₀ cytotoxic concentration that induces 50% of cell death, HDFs human-derived fibroblasts, THP-1 human macrophages, HepG2 human hepatocellular carcinoma cells

In 2015, Gangopadhyay et al. described the use of TiO₂ NPs loaded with 7,8-dihydroxy-4-bromomethylcoumarin-chlorambucil (Ti-DBMC-Cmbl NPs, Fig. 9a) as a targeted combination therapeutic system for MDA-MB-231 breast cancer cells (Gangopadhyay et al. 2015). This conjugate combines the PDT *via* the coumarin chromophore and the chemotherapy by the chlorambucil drug. Spectroscopic characterizations (IR, UV-Vis and fluorescence) confirmed the binding of DBMC-Cmbl to TiO₂ NPs. The conjugate possess three absorption peaks at 250, 330 and 500 nm. The authors found that the Ti-DBMC-Cmbl NPs have a size of 164.18 nm with good PDT efficiency and ¹O₂ quantum yield of 0.29 when excited at 425 nm.

The *in vitro* studies on MDA-MB-231 breast cancer cells showed a good uptake of the conjugate in tumor cells, an inhibited proliferation and a significant induction of apoptosis (Fig. 9b). Furthermore, for a better tumor targeting, they functionalized the Ti-DBMC-Cmbl NPs with folic acid (FA) to target folic acid receptor which is overexpressed on the surface of certain cancer cells (Reddy et al. 2005; Segal and Low 2008). The resulting Ti-FA-DBMC-Cmbl NPs appeared much more efficient than Ti-DBMC-Cmbl NPs after 1 hour of irradiation (≥ 410 nm) and the authors

observed only ~ 19% cell viability compared to ~ 35% cell viability in the case of the conjugate without FA (Fig.9b).

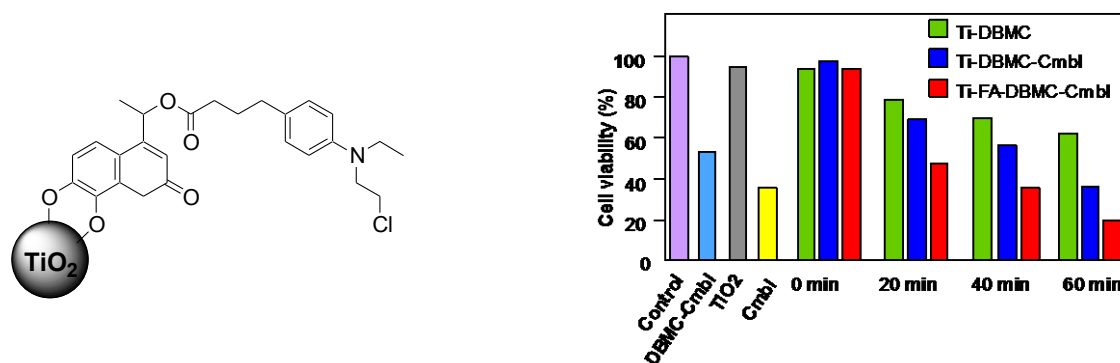


Fig. 9: (a) Chemical structure of Ti-DBMC-Cmbl NPs. (b) Cell viability of MDA-MB-231 cells treated with Ti-DMC, Ti-DBMC-Cmbl NPs and Ti-FA-DBMC-Cmbl NPs (250 µg/mL). Taken from reference

To improve the cellular uptake of aluminum phthalocyanine chloride tetrasulfonate (AlPcS₄, named Pc), Pan et al. (Pan et al. 2015) used Nitrogen-doped TiO₂ NPs (N-TiO₂ NPs) to carrier Pc. They obtained the N-TiO₂-Pc conjugate by a two-step synthesis: the first step consisted in a silanization reaction of N-TiO₂ with APTES to obtain N-TiO₂-NH₂ following by the conjugation of Pc. A transmission electron microscopy (TEM) analysis allowed to determine that the size was around 25-40 nm for the conjugate. The authors compared the absorption spectra of Pc alone and N-TiO₂-Pc conjugate, which expands from 400 to 800 nm region, resulting in a 2.6 times better production of ROS under visible light irradiation compared to Pc alone. *In vitro* studies on HeLa cells (Fig. 10a) and KB cells (Fig. 10b) showed that the cellular uptake of the conjugate was enhanced as much as 6.0 times than Pc alone and its phototoxicity was low. Confocal microscopy allowed to detect N-TiO₂-Pc conjugate in the nucleus area. The photokilling effect was also evaluated (Fig. 10) and the results suggested that N-TiO₂-Pc conjugate could be an excellent candidate as PS in PDT.

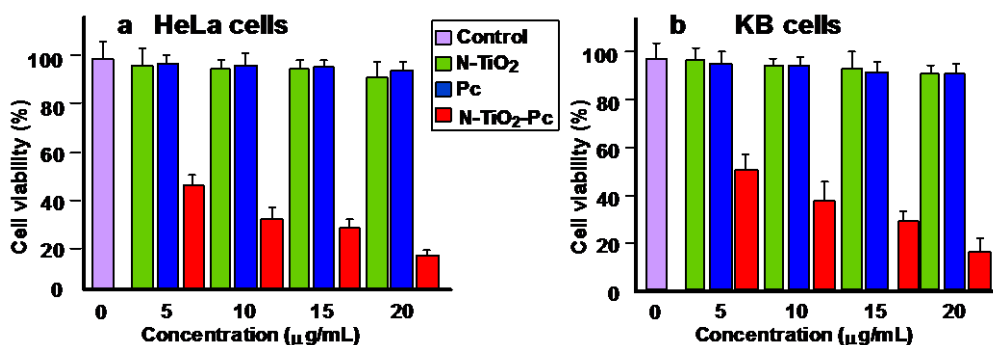


Fig. 10: Comparative cell viability on (a) HeLa cells and (b) KB cells treated with Pc, N-TiO₂ NPs and N-TiO₂-Pc NPs (250 µg/mL). Taken from reference (Pan et al. 2015)

It is well known that TSPP (see Fig. 6a) possesses adverse effects hampering its potential use in PDT. TSPP enters the cell *via* endocytosis and localizes in cellular organelle (lysosomes, endosomes and endoplasmic reticulum) where it interferes with cellular signal pathways, thus producing apoptosis or necrosis (Berg et al. 2011; Høgset et al. 2004). Rehman et al. studied the protective effect of TiO₂ nanowhiskers (TiO₂ NWs) complexed with TSPP *in vitro* and *in vivo* (Rehman et al. 2016b; Rehman et al. 2015). TSPP-TiO₂ NWs were prepared by mixing TSPP and TiO₂ together. Various concentrations of TiO₂ NWs, TSPP and TiO₂-TSPP NWs were injected to four different rat groups (the fourth group is the group control). Histopathology, complete blood cells count (CBC) and fluorescent microscopy were used to evaluate the toxic effects on excretory and circulatory system. The CBC, histopathology, and fluorescent microscopic studies also showed that low concentration TSPP-TiO₂ NWs was the more secure. The *in vitro* cytotoxicity was evaluated and a maximum viability was showed for illuminated TSPP-TiO₂ NWs group. To conclude the authors proposed that the use of these TSPP-TiO₂ NWs would be adapted for the PDT, bio-imaging of cancer or other diseases.

The same team (Zhao et al. 2016; Zhao et al. 2015) was interested in the target cellular bio-imaging and treatment of rheumatoid arthritis by using TiO₂-TSSP NPs, which were obtained by mixing a solution of TSPP in PBS to a suspension of TiO₂ in an acetic acid/sodium acetate buffer. The TiO₂-TSSP NPs were characterized by UV-Vis, fluorescence, zeta potential and IR showing that the porphyrin is covalently linked to TiO₂ NPs by the NH-pyrrole. The TSPP loading capacity on TiO₂ NPs was about 17.4 wt%. The SEM (Scanning Electron Microscope) images showed that the TSSP-TiO₂ NPs were agglomerated whereas TiO₂ alone had a 30 nm diameter. Fig. 11 shows the capability of NPs to produce enough ¹O₂ and guarantee a good PDT effect. The *in vitro* studies on the HSC (Human rheumatoid arthritis synovial fibroblast cells) and the RSC (Murine rheumatoid arthritis synovial fibroblast cells) showed that the TSSP-TiO₂ NPs were less cytotoxic than the TSSP alone and demonstrated a good inhibition of the cellular growth of the synovial fibroblast. These NPs appear like good candidates for the theranostic of rheumatoid arthritis.

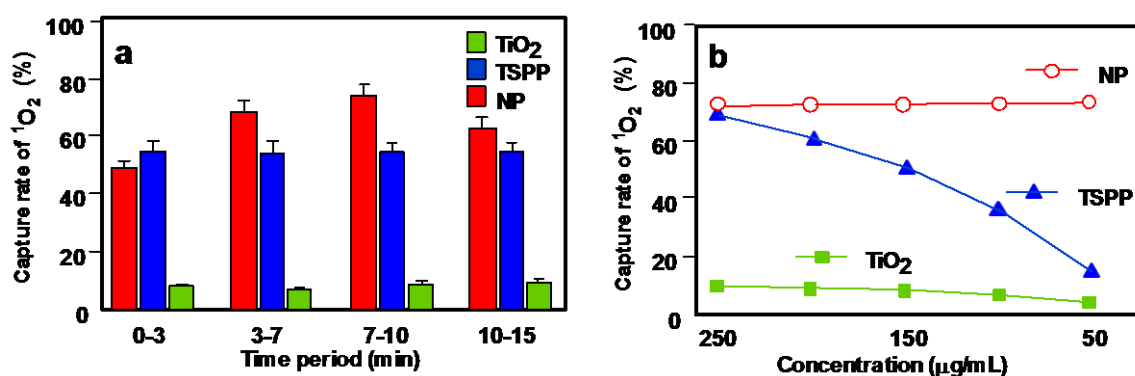


Fig. 11: ¹O₂ quantum yields determination (a) in different time periods and (b) at various concentrations for TSSP-TiO₂ NP, TSPP and TiO₂ alone. The ¹O₂ quantum yields are corresponding

to the 1,3-diphenylisobenzofuran (DPBF) capture rate of $^1\text{O}_2$. Taken from references (Zhao et al. 2016; Zhao et al. 2015)

In 2015, Lu et al. studied the PDT effect of Fe and 5-ALA modified TiO_2 NPs, *i.e.* Fe/ TiO_2 and 5-ALA/ TiO_2 NPs (Lu et al. 2015). Fe/ TiO_2 (2 wt%) and Fe/ TiO_2 (5 wt%) NPs were synthesized by precipitation method, while 5-ALA/ TiO_2 NPs were synthesized by ultrasonic method. All the modified TiO_2 NPs were characterized by X-ray diffraction and UV-Vis spectroscopy. The characteristic peaks at 1430 cm^{-1} and 1730 cm^{-1} observed on FTIR spectra of 5-ALA/ TiO_2 NPs proved that 5-ALA was covalently bound to TiO_2 NPs by an ester link. All the modified TiO_2 NPs possess an enhanced absorption in visible light region. Fig. 12 presents the dark toxicity of modified TiO_2 NPs on HL60 cells at different concentrations (Fig. 12a). 5-ALA/ TiO_2 NPs were less toxic to HL60 cells than Fe/ TiO_2 NPs, but more than TiO_2 NPs alone. The PDT effect of modified TiO_2 NPs was evaluated on HL60 cells after 1 hour light exposure at 403 nm. Cell viability with 5-ALA/ TiO_2 , Fe/ TiO_2 (2 wt%), and Fe/ TiO_2 (5 wt%) was 19.4%, 28.4%, and 28.0% respectively (Fig. 12b). 5-ALA/ TiO_2 NPs present a promising PDT effect as assessed by the ultrastructural morphology of HL60 cells before and after PDT treatment (Fig. 13).

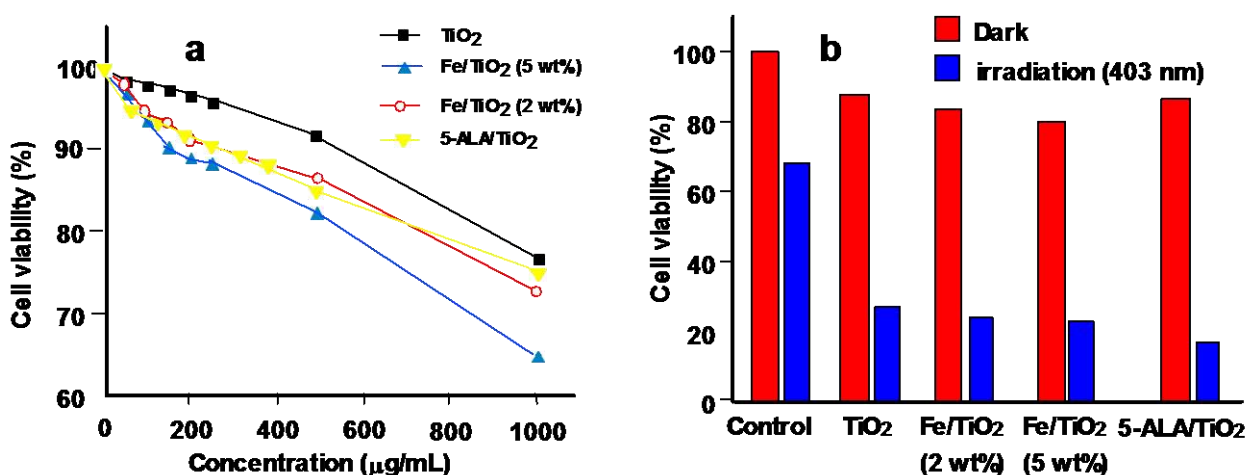


Fig. 12: (a) Dark toxicity of TiO_2 and modified TiO_2 NPs on HL60 cells at different concentrations. (b) Cell viability of TiO_2 and modified TiO_2 NPs on the HL60 cells upon irradiation (1 hour, 403 nm, 5 mW/cm^2 , 18 J/cm^2). Taken from reference (Lu et al. 2015)

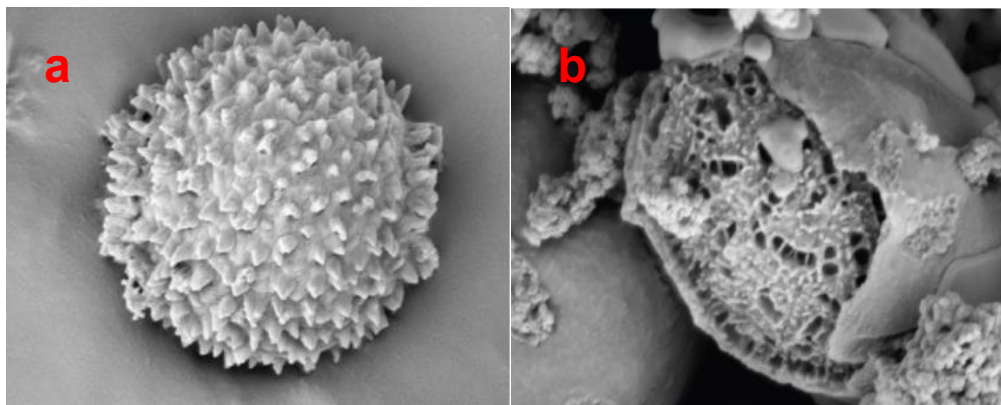


Fig. 13: Ultrastructural morphology of HL60 cells. a normal cultured cell. b PDT-treated cell cultured with 5-ALA/TiO₂ NPs. Reused with permission from reference (Lu et al. 2015)

In summary, TiO₂ is a semiconductor material extensively used in many domains including photocatalytic water treatment, solar cells, sterilization and more recently anti-cancer therapy. It embraces a wide range of advantageous properties such as low cost, availability and biological and chemical inertness. TiO₂ can produce a significant cytotoxic effect under UV illumination, accompanied with minor dark toxicity, high stability and good biocompatibility in vitro and in vivo. However, TiO₂ has a UV-limited photoresponse due to its wide band gap. The electronic properties of TiO₂ can be easily tuned by linking a PS to its surface. The PS can be either adsorbed or grafted covalently to the surface of TiO₂ NPs. The formed TiO₂-PS system induces an extension of the absorption profile of TiO₂ enabling the use of the visible light for different applications. TiO₂, in its nano-metric scale, possesses an appropriate size enabling its use as a carrier of PS to enhance the latter's uptake into the cells, such as Pc. In addition, conjugated TiO₂-PS system has evidenced a good ROS production (¹O₂ and other radicals). TiO₂-PS systems can also serve in the cellular bio-imaging. Despite all those good properties, such systems suffer from agglomeration and dispersion issues.

Table 3 below summarized the data available on the application of TiO₂ NPs grafted with or encapsulating PSs for PDT applications.

Table 3: Application of TiO₂ NPs in PDT

Type of NPs (size, nm)	PS (amount)	NPs-PS interactions	Irradiation conditions	Type of ROS	Cancer cell line		Ref.
					<i>In vitro</i>	<i>In vivo</i>	
NPs (32-37)	TSPP (1 per TiO ₂)	Conjugated <i>via</i> a silyl linker	Laser irradiation	¹ O ₂	–	Skin tumors from mice	(Ion and Brezoi 2005b; Ion 2005)
NPs (nd)	ZnPc (nd)	Encapsulated	Laser light 670 nm, 2.5 or 10 J/cm ² , or biological photoreactor 597-752 nm, 2.5 J/cm ²	¹ O ₂	THP-1 HepG2 Vero	–	(Lopez et al. 2010)
NPs (164.2)	DBMC (63.3 µg per TiO ₂)	Conjugated <i>via</i> an ether linker	UV- visible (≥ 410 nm), 0-60 min	¹ O ₂	MDA-MB-231	–	(Gangopadhyay et al. 2015)
NPs (25-40)	AlPcS ₄ (nd)	Electrostatic attraction	150-W Xe lamp (420-800 nm)	ROS	HeLa	–	(Pan et al. 2015)
NPs (nd)	ALA	H-bonds	403 ± 6 nm, 5 mW/cm ² , 18 J/cm ² , 60 min	nd	HL60	–	(Lu et al. 2015)
Nanowhiskers (> 100)	TSPP (15.7 wt%)	Physical absorption	Visible light 500-550 nm, 30 min	ROS ¹ O ₂	Fibroblast cells from RA joint of SD rats	Male SD strain rats and DBA- 1 mice with RA disease	(Zhao et al. 2015)

Table 3: continued

Type of NPs (size, nm)	PS (amount)	NPs-PS interactions	Irradiation conditions	Type of ROS	Cancer cell line		Ref.
					<i>In vitro</i>	<i>In vivo</i>	
Nanowhiskers (30)	TSPP (17.4 wt%)	Charge- transfer	Green light 500-550 nm, 5 mW/dm ² , 10 min	¹ O ₂	HSC RSC	–	(Zhao et al. 2016)
Nanowhiskers (nd)	TSPP (nd)	Ionic bonding	Visible LED light (500-550 nm), 5 mW/dm ² , 5 min for <i>in vitro</i> and 60 min for <i>in vivo</i>	ROS ¹ O ₂	RA infected BMS cells	BMS cells from the RA infected murine models	(Rehman et al. 2015)
Nanowhiskers (nd)	TSPP (concentr ation TiO ₂ :TSP P, 6:1)	Solution mixture	Green light 500–550 nm, 60 min	ROS ¹ O ₂	Fibroblast primary cells from SD rats	Male SD rats	(Rehman et al. 2016b)
Nanowhiskers (nd)	TSPP (concentr ation TiO ₂ :TSP P, 10:1)	Absorption	Visible light 500-550 nm, 60 min	ROS ¹ O ₂	–	Diabetes mellitus murine model (type I and type II)	(Rehman et al. 2016a)

NPs nanoparticles, PS photosensitizer, ROS reactive oxygen species, nd not disclosed, TSPP meso-tetra(4-sulfonatophenyl) porphyrin, ZnPc zinc phthalocyanine, DBMC 7,8-dihydroxy-4-bromomethylcoumarin, UV ultraviolet, AlPcS₄ aluminum phthalocyanine chloride tetrasulfonate, ALA 5-aminolevulinic acid, SD Sprague-Dawley

4. Fullerene

Fullerene C₆₀ has been evidenced in 1985 by Kroto et al. who were awarded the 1996 Nobel Prize in Chemistry for this important discovery (Kroto et al. 1985). From that point, this redox-active chromophore and its analogues were thoroughly studied for their electron and energy-transfer ability to form artificial photosynthetic systems (Martin et al. 1998). Thus a large number of intermolecular C₆₀ charge-transfer dyads were described either with electron-donor molecules such as ferrocenes (Crane et al. 1992), cobaltocenes (Stinchcombe et al. 1993) or polymers (Zhang et al. 2014). In addition, numerous covalently linked C₆₀-Donor dyads have been synthesized by several ways (Hirsch 1995) *i.e.* 1,3-dipolar cycloaddition (Maggini et al. 1993; Meier and Poplawska 1996), Diels-Alder (Belik et al. 1993) or Bingel–Hirsch (Bingel 1993; Cho et al. 2014) reactions.

Functionalized fullerenes alone can be considered as PSs usable for the medical applications as, for example, the treatment of mice infected by Gram-negative bacteria (Huang et al. 2014; Sharma et al. 2011). PDT applications also have been investigated and various cancers such as metastatic cancer in peritoneal cavity were studied. As early as 1993, Tokuyama et al. were the first to show that fullerenes substituted by carboxylic acids could be phototoxic for HeLa cells (Tokuyama et al. 1993). In the same way, it has been shown that the action of pristine C₆₀ and light could be used for the treatment of Ehrlich carcinoma cells or infected thymocytes eradication in rat (Burlaka et al. 2004). Currently, research focuses more on the treatment of pathogenic infections by substituted fullerenes in the presence of light than on light mediated PDTs of cancers and only few research articles have been submitted the two last years, the most important being cited in the following references (Li et al. 2015b; Liu et al. 2015b; Shi et al. 2016; Shi et al. 2014; Wang et al. 2014; Yu et al. 2016)

As already mentioned, the subject of this review concerns the use of dyads in which a PS (electron donor) and a fullerene (electron attractor) can give rise to a PDT effect mainly due to a light-induced electron transfer. An interesting review untitled “Fullerene–porphyrin nanostructures in photodynamic therapy” has been published in 2010 (Constantin et al. 2010).

One general protocol to functionalize a fullerene is the Bingel-Hirsch reaction (Bingel 1993) which is a two-steps cyclopropanation by a Michael addition of a α -halocarbonyl followed by the expulsion of the halogen and subsequent malonate formation (Fig. 14).

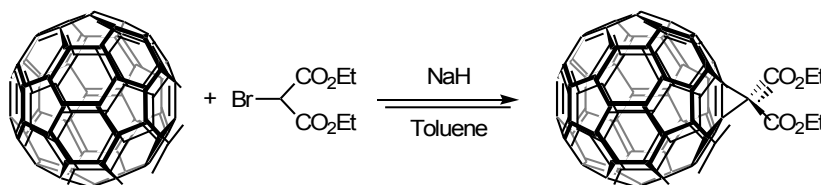


Fig. 14: Example of malonic functionalization of fullerene

This malonic functionalization of fullerene has been widely studied to design new molecules usable for PDT application. However it is known that [C₆₀] fullerene malonic acid derivatives (MA-C₆₀) can induce damages to cytoplasmic and mitochondrial membranes (Yang et al. 2007).

The other classical protocol to substitute a fullerene is the Prato reaction (Maggini et al. 1993) which can proceed by two ways involving an addition of azomethine ylide to fullerene (Fig. 15).

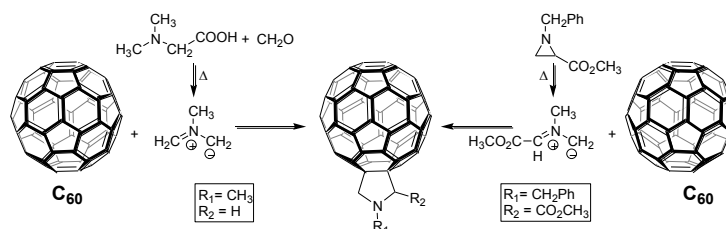


Fig. 15: Substitution of fullerene by Prato reaction

In 2005, Durantini's group designed 5-(4-amidophenyl)-10,15,20-tris(4-methoxyphenyl)porphyrin-fullerene dyads (P-C₆₀) free base or metallated by Zn(II) (Fig. 16a) (Milanesio et al. 2002). The synthesis involved the condensation of 1,2-dihydro-1,2-methanofullerene[60]-61-carboxylic acid (Fungo et al. 2001) and an aminoporphyrin (Fungo et al. 2000). Compared to porphyrin alone, the P-C₆₀ dyads exhibited a lower emission than that of the porphyrin alone, resulting from a quenching of the fullerene entity (Milanesio et al. 2005). ¹O₂ production quantum yield (Φ_{Δ}) was dependent of the polarity of the solvent and Φ_{Δ} diminished considerably in DMF ($\Phi_{\Delta} = 0.18$) vs toluene ($\Phi_{\Delta} = 0.80$). For the *in vitro* studies on Hep-2 human larynx-carcinoma cell line, the dyads were added from a liposomal solution due to their low solubility in PBS. Only the free base porphyrin P-C₆₀ exhibited interesting properties (Alvarez et al. 2006) and was further studied. The P-C₆₀ was uptaken at a concentration of < 1.5 nM/10⁶ cells after 5-8 hours. After incubation with P-C₆₀ (1 μ M) and irradiation at a wavelength range between 350 and 800 nm and 54 J/cm², the cell survival was about 20% and 50% under atmosphere of air or argon, respectively (Alvarez et al. 2009; Alvarez et al. 2006) (Fig. 16b).

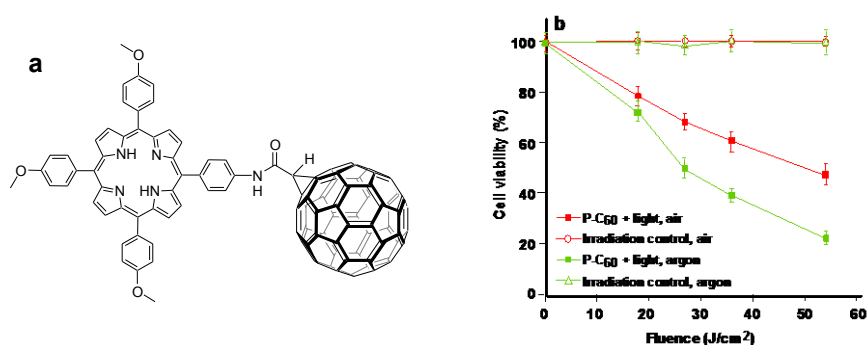


Fig. 16: (a) Chemical structure of free base P-C₆₀ dyad. (b) Inactivation of Hep-2 cells irradiated with visible light (0-54 J/cm²) in atmosphere of air or argon (1 μ M of P-C₆₀, incubation time 24 hours). Taken from reference (Alvarez et al. 2009; Alvarez et al. 2006)

In 2014, the same group described the synthesis of a similar porphyrin-fullerene dyad P-C₆₀ (Fig. 17a) via a Prato reaction in which a *N*-ethylcarbazole moiety was introduced at the *meso* positions (Belen Ballatore et al. 2014). This dyad was investigated for the photoinactivation of *S. aureus* and *E. coli*. The bacterial suspensions were incubated and irradiated by visible light at different time intervals. This dyad inactivated more than 99% of *S. aureus* at a concentration of 5 μ M in 30 minutes at 37°C (Fig. 17b). The activity (25%) against the Gram-negative *E. coli* was found to be lower but significant in the same conditions.

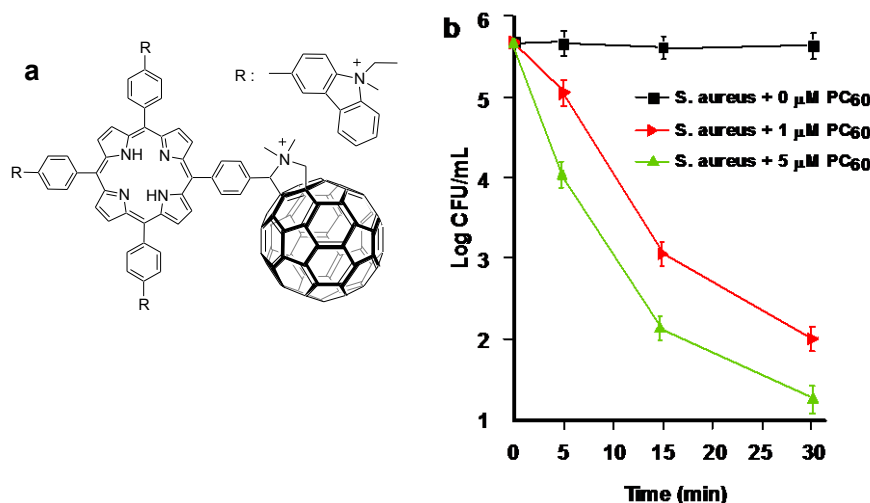


Fig. 17: (a) Chemical structure of P-C₆₀ dyad. (b) Photoinactivation of *S. aureus* by P-C₆₀ fullerene at different concentrations and at a wavelength range between 350 and 800 nm. Taken from reference (Belen Ballatore et al. 2014)

Recently, Shu's group included P-C₇₀ dyads in upconversion NPs (UCNPs) (Guan et al. 2015a) which included a core of lanthanide (Gd, Y, Tm) wrapped electrostatically by P-C₇₀ (P = TMPyP) and finally coated by folic acid-modified PEG. This UCNP-PEG-FA/P-C₇₀ nanocomposite can act as theranostic tool with folic acid (FA) as targeting agent, PEG for furtivity, lanthanide for trimodal imaging (fluorescence/upconversion luminescence/magnetic resonance imaging) and P-C₇₀dyad for photoinduced therapy. The UV emission of UCNP matched with the absorption at 290 nm, 345 nm, 361 nm, and the visible emission at 451 nm, 475 nm of P-C₇₀. The *in vitro* viability of HeLa-*luc* cells decreased with the concentration of UCNP-PEG-FA/P-C₇₀ and 95% of cell death were obtained at a concentration of 0.2 mg/mL upon NIR irradiation (980 nm, 480 J/cm²) (Fig. 18a). Only 50% of cell death was reached in hypoxia condition. As illustrated in Fig. 18b, the *in vivo* growth of tumor cells was considerably decreased with UCNP-PEG-FA/P-C₇₀ in presence of light compared to controls.

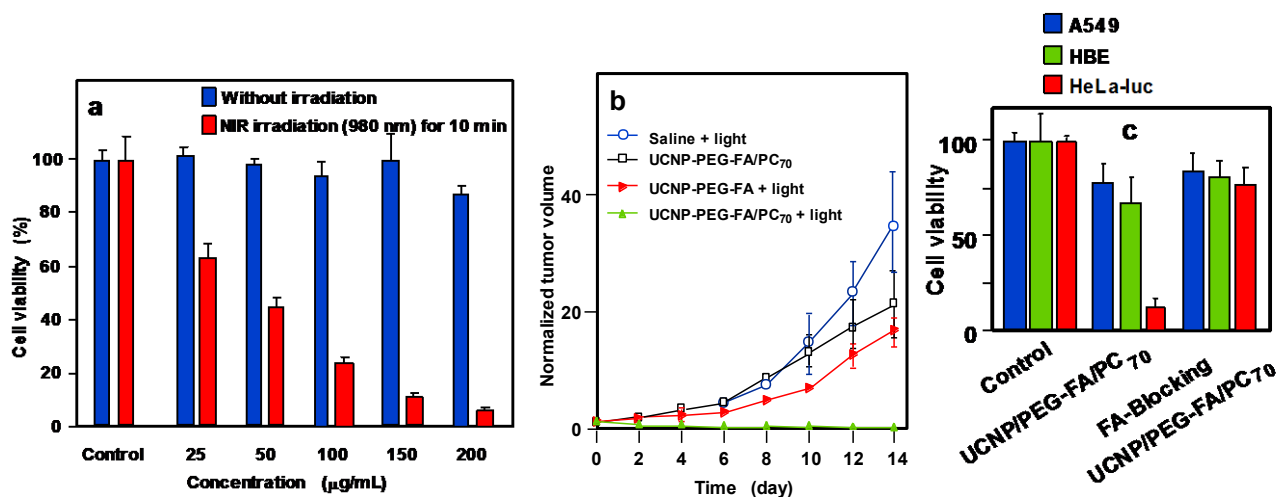


Fig. 18: (a) Cell viability of HeLa-luc cells incubated with UCNP–PEG–FA/PC₇₀ at various concentrations. (b) Growth of tumors after treatments. The relative tumor volumes were normalized to their initial sizes. Taken from reference (Guan et al. 2015a). (c) Cell viability of A549, HBE and HeLa-Luc) incubated with either UCNP-PEG-FA/PC₇₀ or the mixture of UCNP-PEG-FA/P₇₀ and an excess of folate (980 nm, 480 J/cm²). Taken from reference (Guan et al. 2015a)

During the same year, Shu's group (Guan et al. 2015b) revisited also the results on P-C₆₀ dyad obtained by Alvarez and co-workers (Alvarez et al. 2006) and synthesized an amphiphilic dyad porphyrin-C₇₀ (P-C₇₀) according to a previous methodology (Xu et al. 2011) by coupling trimethylpyridylporphyrin (TMPyP) with fullerene C₇₀ *via* a Prato reaction (Maggini et al. 1993) (**Fig.19a**). The P-C₇₀ dyad formed a self-assemble liposomal structure with a diameter of *ca.* 30 nm. The P-C₇₀ cellular uptake by A549 cells was three folds better than that of the porphyrin alone (TMPyP) and confocal microscopy showed that P-C₇₀ was localized as small clusters in the cytoplasm. After 3 hours incubation and under 10 minutes irradiation at 405 nm (17 mW/cm²), the efficacy of killing was about 98% at a concentration of 1 µM/L under air atmosphere (**Fig.19b**). More interesting is the efficiency of PDT under anaerobic conditions. In the same conditions, but under nitrogen, the damages reached 80% for P-C₇₀ and 22% only for TMPyP alone. Mechanism of this surprising PDT effect has been studied. While ¹O₂ is responsible of the damages in aerobic conditions, the formation of other ROS is involved under hypoxia condition, particularly from P-C₇₀. The longer triplet lifetime of P-C₇₀ (211.3 µs) can be assigned to the exciplex formed by energy transfer between the excited porphyrin and the ground state C₇₀. All of these properties made P-C₇₀ dyad an ideal candidate for anticancer PDT under shallow and hypoxia tissues. It has to be noted that Lee et al. published the synthesis of similar covalently linked chlorin-fullerene dyads formed by coupling methyl-pyropheophorbide-a and a C₆₀ in toluene at reflux (Lee et al. 2001) without performing any PDT assays.

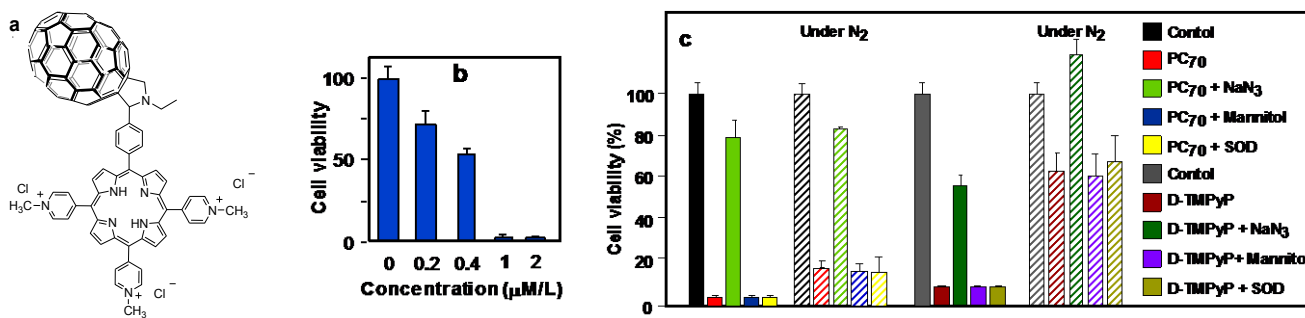


Fig.19: (a) Chemical structure of P-C₇₀dyad. (b) Cell viability of A549 cells incubated with P-C₇₀ at gradient concentrations for 3 hours and exposed to light irradiation (17 mW/cm², 10 min) (c) Cell viability of A549 cells incubated for 3 hours with P-C₇₀ and D-TMPyP (2 μM concentration) alone or in the presence of different ROS quenchers upon light irradiation for 10 min (white light irradiation, 17 mW/cm²) under air or nitrogen conditions. Taken from reference (Guan et al. 2015b)

Very recently, the same group (Guan et al. 2016) described the production and the properties of nanovesicles (noted FCNVs) made from C₇₀-oligo ethyleneglycol-Ce6 (**Fig. 20a**) which contained both hydrophilic and hydrophobic parts. These FCNVs have a high loading efficiency of Ce6 (57 wt% on TFC₇₀) and efficient absorption in near infrared could be observed. The diameter was estimated to be 31 nm as assessed by SEM and AFM images indicated that the FCNVs are hollow spheres. *In vitro* experiments on A549 cells in presence of NaN₃ (¹O₂ quencher) clearly showed that cell death was due to ¹O₂. The ¹O₂ production was higher for the FCNVs than for Ce6 alone due to a better absorption at 660 nm. Furthermore, negligible cytotoxicity was observed at concentration up to 0.2 mg/mL. **Fig. 20b** clearly showed the excellent ability of the FCNVs to kill A549 cells as compared to Ce6 and TFC₇₀ alone. **Fig. 20c** showed the relative tumor volume 4 hours after *i.v.* injection (10 mg/kg) and irradiation with 660 nm laser (0.1 W/cm² for 10 minutes). The half-life of the FCNVs was shown to be 73.6 hours (13.2 hours for Ce6) indicating a longer blood circulation than for the free Ce6.

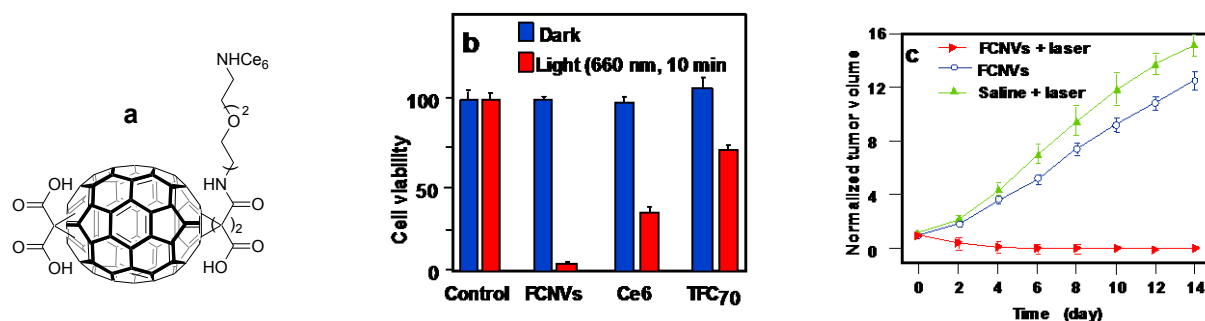


Fig. 20: (a) Chemical structure of FCNVs. (b) Cell viabilities of A549 cells incubated with FCNVs, free Ce6 and TFC₇₀ (0.1 mg/mL). (c) Growth of tumors after treatments. The relative tumor volumes were normalized to their initial sizes. Taken from reference (Guan et al. 2016)

Rancan's team proposed fullerene-pyropheophorbide-a conjugates as new tools for PDT. Her team synthesized different complexes starting from bis-malonato-pyropheophorbide-a up to decakis-pyropheophorbide-a[5:1]fullerene hexaadduct (Rancan et al. 2007a; Rancan et al. 2007b; Rancan et al. 2005). They compared the uptake, photoinduced cytotoxicity and photosensitizing activity of mono- (FP1) and hexa-adducts (FHP1) towards human leukemia T-lymphocytes (Jurkat cells) with free pyropheophorbide-a (Pyro-a) as a reference (**Fig. 21**) (Rancan et al. 2005).

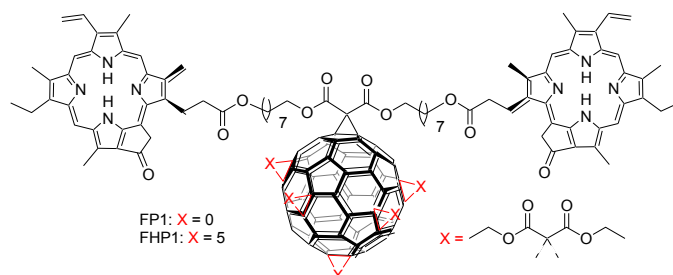


Fig. 21: Chemical structures of mono- (FP1) and hexa-adducts (FHP1). Taken from reference (Rancan et al. 2005).

Intracellular uptake of these derivatives showed a better accumulation than that of Pyro-a alone. This can be due to the size of adducts and a better diffusion through the plasma membranes of the small molecules when compared to bigger ones, which can be only uptaken by endocytosis or pinocytosis. Nevertheless, the adduct FHP1 showed a better cytotoxic activity than FP1 with a 58% cell death when irradiated at 688 nm and 400 mJ/cm².

Two years later, the same group (Rancan et al. 2007a; Rancan et al. 2007b) described the synthesis of hexamalonato-fullerenes bearing 6 (FHP6) and 12 Pyro-a moieties (FHP12) (**Fig. 22**).

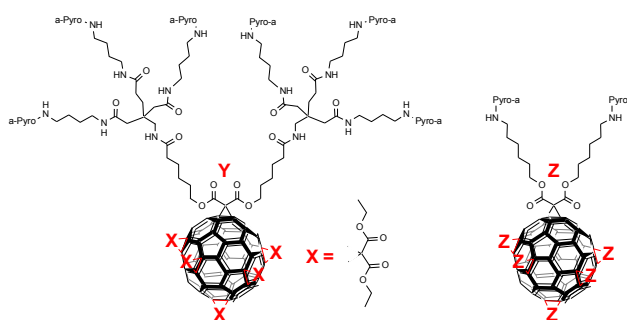


Fig. 22: Chemical structures of hexamalonato-fullerenes with 6 Pyro-a units (FHP6) and 12 Pyro-a units (FHP12). Taken from reference (Rancan et al. 2007a; Rancan et al. 2007b)

They showed that FHP6 exhibited a 5 times higher intracellular uptake than FHP1 and 40 times higher than FHP12 but significantly lower than Pyro-a alone (Rancan et al. 2007b). In a last assay, they conjugated the decakis-pyropheophorbide-a [5:1]fullerene hexaadduct adipinic acid active ester with the monoclonal antibody Rituximab as addressing unit. This antibody binds to the membrane of the CD20 receptor, which is overexpressed by cancer B-cells. The affinity for the receptor was conserved as assessed by confocal microscopy (Rancan et al. 2007a). Unfortunately, the

cell viability was 70% with Rituximab and the hexaadduct adipinic ester. No further results were published.

In 2010, Ion et al. synthesized a tetraphenyl-porphyrin (TPP)-poly(vinylpyrrolidone) (PVP)-C₆₀ (TPP-PVP-C₆₀) triad formulation (Fig. 23) (Ion et al. 2010). The system was stabilized by electrostatic interactions between the three components, donor-acceptor bonds between C₆₀, TPP and PVP. *In vitro* studies have been performed on K562 leukemia cell lines: no dark toxicity was observed with a concentration up to 0.5 μM after 18 hours of incubation. In the same conditions and under irradiation (436 nm, 0-1 J/cm², 20-200 mW/cm²) only 20% of cells remained alive (80% without triad).

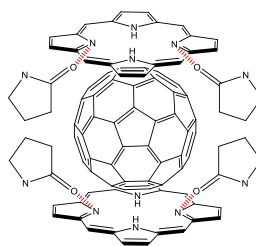


Fig. 23: Chemical structure of TPP-PVP-C₆₀ triad. Taken from reference (Ion et al. 2010).

The *in vivo* experiments were performed on tumor bearing rats (Walker 256 carcinoma) treated with TPP-PVP-C₆₀ (10 mg/kg) (Ion et al. 2012). In tumor, lipid peroxides and protein carbonyls concentration significantly increased while thiol groups level decreased indicating a strong tumoral oxidative process. No further results were given.

In 2014, Guo et al. co-encapsulated malonic acid-fullerene (MA-C₆₀) and docetaxel (DTX) in PEG-PLA micelles as delivery carriers (Guo et al. 2014). The average diameter was about 37 nm as assessed by TEM images. The cell viability of HeLa cells decreased with the co-entrapping of both MA-C₆₀ and DTX (40% in the dark and 10% upon light irradiation at 339 nm after 72 hours). After *i.v.* injection in S180 tumor-bearing mice, bioavailability of the MA-C₆₀/DTX NPs was 2.25-fold higher than DTX micelles and a tumor growth inhibition rate of 81.3% at a 15 mg/kg dose was observed after 14 days (61.2% for DTX micelles).

In 2014, Zhang's group described 5-ALA-loaded fullerene vesicles (C₆₀-5-ALA) (Li et al. 2014) obtained by dripping 5-ALA sodium salt into a toluene solution of fullerene C₆₀. The diameter of the NPs has been estimated to be about 80-200 nm by DLS and the loading of 5-ALA at the periphery of C₆₀ was found to be 45 wt% as assessed by thermal gravimetric analysis. The PpIX generation was estimated after incubation, disruption and extraction of B16-F10 cells (Fig. 24a). In tumor-bearing mice, PpIX induced by 5-ALA alone was found in almost all the tissue while it is more selective for the tumoral tissue and lungs with C₆₀-5-ALA. With 5-ALA alone PpIX formation reached a maximum at 2 hours and then rapidly decreased while C₆₀-5-ALA induced the maximum after 4 hours. Furthermore the authors observed an enhanced cell-killing effect with C₆₀-5-ALA after

irradiation at 630 nm (49% for C₆₀-5-ALA and 32% for 5-ALA alone). Moreover, the tumor volume was stable after 11-days treatment, which was not the case for 5-ALA or irradiation alone (Fig. 24b).

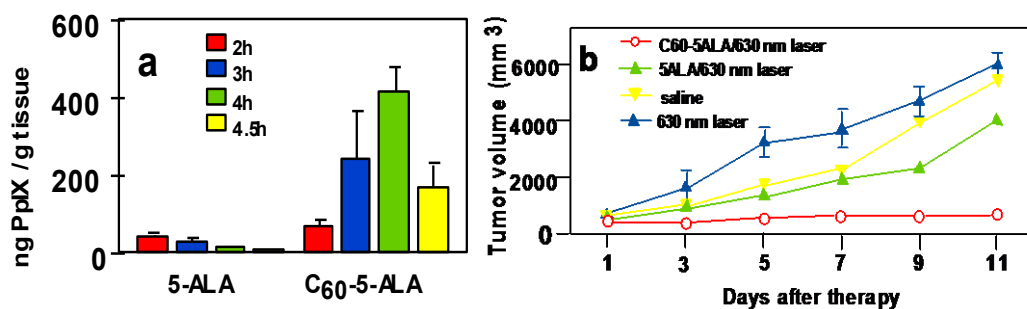


Fig. 24: (a) PpIX synthesis from 5-ALA or C₆₀-5-ALA in tissues as a function of time. (b) Growth of tumors after PDT treatment (630 nm, 0.1 W/cm², 0.5 min) with 5-ALA or C₆₀-5-ALA. Taken from reference (Li et al. 2014)

In 2009, Laptev et al. (Laptev et al. 2009) applied for a patent in which they described a pharmaceutical formulation for PDT of malignant tumors. They described the synthesis and the PDT assays of C₆₀ PSs covalently bound to an amino acid or a dipeptide (Arg-Arg) and their combination with biocompatible synthetic biopolymers. Toxicity was only observed after 3-5 hours post-administration (adynamia, ruffling of hair and absence of protecting reflex) but the animals returns quickly to a normal state as assessed by histological analyses of liver, kidney, spleen.... after one week of administration. The *in vivo* PDT bioassays (615-680 nm region) were carried out on Balb/c mice with lymphogenically metastazing or hybrid mice F1 (CBA+C57/B6) with intraperitoneally transplanted embryocarcinoma. Qualitatively, the administration of the composition was characterized by the formation of a scab the first 3-5 days and the necrosis in the tumor node which can reach 7 to 9 mm in depth.

Fullerene: Potential conjugates

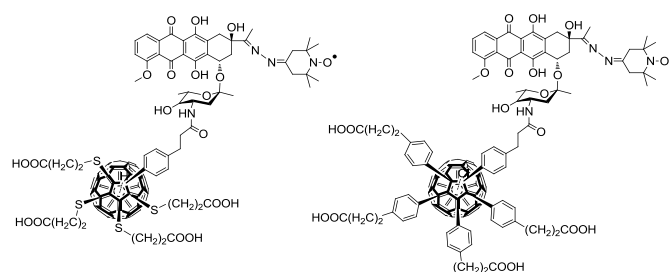


Fig. 25: Conjugates between C₆₀ and ruboxyl. Taken from reference (Kotelnikov et al. 2013)

In 2013, Kotelnikov et al. described two covalently linked conjugates between C₆₀ and ruboxyl (Kotelnikov et al. 2013) (Fig. 25). While ruboxyl and fullerene alone exhibit no or low PDT activity when irradiated at 500 nm, ruboxyl can interact with the fullerene moiety *via* energy and/or electron transfer. Thus under visible irradiation at 500 nm, the resulting excited fullerene produced

superoxide radical anion ($O_2^{\bullet-}$). Furthermore the presence of a chlorine atom on the fullerene induced a 30% gain of the $O_2^{\bullet-}$ production as assessed by NBT test. These potential PDT properties could be of interest for biomedical applications in cancer, virus or bacteria treatments.

As a promising tool in PDT and triplet-triplet annihilation upconversion (TTA-UC), Zhao's team described the photophysical behavior of two light-harvesting fullerene dyads as triplet PS (**Fig. 26**) (Wu et al. 2012). Two conjugates BDP-C₆₀ and Bis-DBP-C₆₀ were synthesized from boron-dipyrromethene (BDP) and C₆₀ by a Prato reaction. These heavy atom free molecules are efficient and exhibited an upconversion quantum yields up to 7% and a strong absorption of visible light at 515 nm for BDP-C₆₀ dyad or 590 nm for Bis-BDP-C₆₀ dyad.

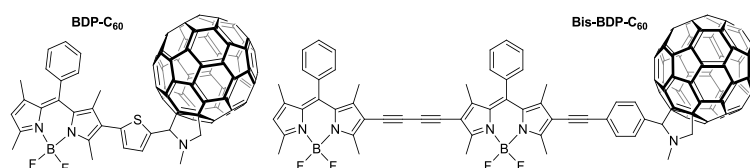


Fig. 26: Light-harvesting fullerene dyads BDP-C₆₀ and Bis-DBP-C₆₀. Taken from reference (Wu et al. 2012)

In the PDT field, the measurement of oxygen concentration during PDT is a particularly challenging problem due to real-time changes in oxygen demand and supply during the treatment. Starting from similar P-C₆₀ dyad, Mermut et al. (Mermut et al. 2009) studied its use as a novel optical oxygen sensor in PDT. They related the measurement of O₂ concentration during PDT by analyzing the magnetic field effect which can discriminate between the type I and II photodynamic pathways, and proposed a new tool for controlling the intersystem crossing between singlet and triplet states by using a fullerene-linked to Zn or Cu porphyrin in liposome cell phantom.

Since their discovery in the 1980s, fullerenes (C₆₀ and C₇₀) have fascinated researchers. Fullerenes are semiconductor materials and are used as organic photovoltaics, catalysts, to purify water, in biohazard protection, antioxidants... and, quite recently, as nanomedicines. The formulation of this kind of nanomaterials involving fullerenes can be done by several ways, e.g. liposomes, micelles, dendrimers or nanovesicles, and can be used in various fields of medicine such as antibacterial, PDT and PTT, or dual PDT/PTT agents. For example, functionalized fullerenes with carboxylic acid groups have found application in PDT as PSs due to their electron and energy transfer ability. Fullerenes can also act as n-type semiconductors (electron acceptors) and be conjugated with p-type porphyrins (electron donors) to develop dyads giving rise to a PDT effect mainly due to a light-induced electron transfer. At present, some researchers have started to develop bimodal protocols involving diagnosis/therapy, PDT/PTT or aerobic/hypoxia conditions and these bimodal approaches seem to be the most promising.

Table 4 below summarized the data available on the application of fullerene NPs grafted with or encapsulating PSs in PDT applications.

Table 4: Application of fullerene NPs in PDT

Type of NPs (size, nm)	PS (amount)	NPs-PS interactions	Irradiation conditions	Type of ROS	Cancer cell line		Ref.
					<i>In vitro</i>	<i>In vivo</i>	
Liposomes (nd)	ATMP (1 per C ₆₀)	Conjugated	150W lamp 350-800 nm, 54 J/cm ²	¹ O ₂	Hep-2	–	(Alvarez et al. 2006)
Liposomes (nd)	AcTMP	Conjugated	150W lamp 350-800 nm, 54 J/cm ²	¹ O ₂	Hep-2	–	(Alvarez et al. 2009)
Reversed micelles (nd)	FTEP (1 per C ₆₀)	Conjugated <i>via</i> 1,3- dipolar cycloaddition	Visible light (350- 800 nm), 0.2 W/cm ² , 8 J/cm ²	¹ O ₂	<i>S. aureus</i> <i>E. coli</i>	–	(Belen Ballatore et al. 2014)
Liposomes (30)	TMPPyP (1 per C ₇₀)	Conjugated	White light 400-700 nm, 17 mW/cm ² , 5- 20 min	ROS ¹ O ₂	A549 HaCaT	–	(Guan et al. 2015a)
Liposomes (20)	TMPPyP (1 per C ₇₀)	Conjugated	Laser 980 nm, 0.8 W/cm ² , 10 min	¹ O ₂	HeLa- <i>luc</i> A549	HeLa- <i>luc</i> tumor- bearing female Balb/cnude mice	(Guan et al. 2015b)
Nanovesicles (31)	Ce6 (57 wt%)	Conjugated to C ₇₀ <i>via</i> the OEG2 linker	Laser 660 nm, 20 mW/cm ² (<i>in vitro</i>) or 0.1 W/cm ² (<i>in vivo</i>),	¹ O ₂	A549	4T1- <i>luc</i> tumor- bearing female Balb/c mice	(Guan et al. 2016)
Micelles (37)	DTX (< 80 wt%)	Encapsulated	Diode laser 532 nm, 0.1 W/cm ² , 5 min	ROS	HeLa	S180 tumor-bearing mice	(Guo et al. 2014)

Table 4: continued

Type of NPs (size, nm)	PS (amount)	NPs-PS interactions	Irradiation conditions	Type of ROS	Cancer cell line		Ref.
					<i>In vitro</i>	<i>In vivo</i>	
Supramolecular assemblies (nd)	TPP (nd)	H-bonds Electrostatic	Hg lamp, equipped with an UV39 filter, 436 nm, 20-200 mW/cm ² , 0-1 J/cm ²	nd	K562	–	(Ion et al. 2010)
Supramolecular assemblies (nd)	TPP (2 per C ₆₀)	H-bonds Electrostatic	Red light 635 nm, 50 J/cm ² , 15 min	ROS	–	Walker 256 tumor-bearing Wistar rats	(Ion et al. 2012)
Complexes (nd)	Ce6 and ZnCe6 (nd)	nd	A) Laser 662 nm and 890 nm, 100 J/cm ² B) Laser 615-680 nm	¹ O ₂	–	A) Embryocarcinoma bearing F1 hybrid female mice (CBA and C57/B6) B) Lymphogenically metastazing embryocarcinoma bearing female Balb/c mice	(Laptev et al. 2009)
Complexes (nd)	Pyro	Conjugated	Laser diode 668 nm,	¹ O ₂	Jurkat	–	(Rancan et
Dendrimers (nd)	Pyro (6 or 12 per C ₆₀)	Conjugated	nd	¹ O ₂	Jurkat	–	(Rancan et al. 2007a)
					Ramos		
					EBV transformed B-		

Table 4: continued

Type of NPs (size, nm)	PS (amount)	NPs-PS interactions	Irradiation conditions	Type of ROS	Cancer cell line	In vivo		Ref.
						In vitro	In vivo	
Dendrimers (nd)	Pyro (2, 6 or 12 per C ₆₀)	Conjugated	Laser diode 668 nm, 2.12 mW/cm ² ,	¹ O ₂	Jurkat	–	–	(Rancan et al. 2007b)
NPs (80-200)	ALA (45.12 wt%)	ALA complexed with C ₆₀	Laser 630 nm, 0.1 W/cm ² , 0.5 min	nd	B16-F10	B16-F10 mice melanoma	–	(Li et al. 2014)

NPs nanoparticles, PS photosensitizer, ROS reactive oxygen species, *nd* not disclosed, *ATMP* 5-(4-amidophenyl)-10,15,20-tris(4-methoxyphenyl) porphyrin, *AcTMP* 5-(4-acetamidophenyl)-10,15,20-tris(4-methoxyphenyl) porphyrin, *FTEP* 5-(4-formylphenyl)-10,15,20-tris[3-(*N*-ethylcarboxoyl)] porphyrin, *TMPyP* trismethylpyridylporphyrin, *Ce6* chlorin e6, *OEG2* 1,10-diamino-4,7-dioxadecane, *DTX* docetaxel, *TPP* tetraphenylporphyrin, *UV* ultraviolet, *Pyro* pyropheophorbide a, *ALA* 5-aminolevulinic acid

5. Graphene and graphene oxide

Graphene is a relatively new material recently isolated in 2004 by Kostya, Novoselov and Geim (Novoselov et al. 2004), which has an extremely huge potential. It is a single layer of graphite, and its structure and physico-chemical properties permit its applications in different areas ranging from flexible electronics to DNA sequencing (Ahn and Hong 2014; Ojha et al. 2014; Raccichini et al.). Starting from graphene, there are different two and three-dimensional structures that can be produced and used as drug carriers (Fig. 27). Among these structures, we can cite single-walled carbon nanotubes (SWCNTs, rolled-up graphene monolayers), fullerenes (wrapped-up graphene, see fullerene NPs part), and graphite (stacked-up graphene monolayers). Graphene oxide (GO) and reduced graphene oxide (rGO) are, meanwhile, obtained after oxidation and oxidation/reduction processes, respectively (Fig. 27). Graphene is known, among other things, for its good electrical conductivity properties thanks to a two-dimensional (2D) network of sp^2 - hybridized carbon atoms.

Oxidation of graphene to GO causes the loss of the sp^2 carbon network, *i.e.* GO becomes electrical insulator, and the formation of several oxygen containing functional groups (hydroxyl, carboxyl and epoxy groups). The presence of oxygen atoms gives the GO better hydrophilicity than graphene, making it easier to disperse in organic solvents, water, and different matrixes. The reduction of the GO to rGO is needed to restore electrical conductivity but this causes a considerable reduction of its dispersity due to its tendency to produce aggregates.

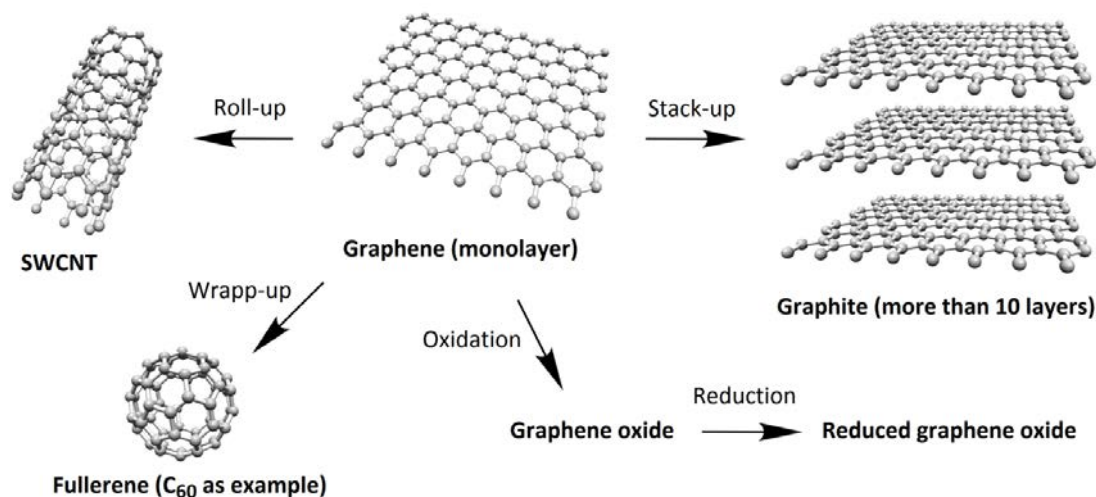


Fig. 27: Chemical structures of graphene and its descendants.

Numerous reviews reports on the use of graphene or graphene oxide (GO) as drug carriers (Dong et al. 2014; Krishna et al. 2013; Wu et al. 2015). A first advantage relies on their large surface area. Another advantage arises from the $\pi - \pi$ structure of graphene which can easily bind to aromatic structures which is often the case for PS. In the field of cancer therapy and/or diagnosis, 73% of the articles focuses on drug delivering applications and 27% on theranostic applications (Orecchioni et al. 2015). In cancer therapy and particularly in PDT, some reviews such as

(Goncalves et al. 2013; Li et al. 2015a; Rahman et al. 2015; Shen et al. 2012) can be useful for scientists.

5.1. Graphene and single wall carbon nanotubes (SWCNTs)

5.1.1. Graphene for PDT applications

Liu et al. (Liu et al. 2015a) published an interesting article describing the direct one-pot synthesis of graphene (G) loaded with Ce6 *via* $\pi - \pi$ stacking interactions by a simple sonification of Ce6 and graphite in an aqueous solution (loading efficiency 160 wt% and exfoliation yield 9%). During the Ce6 loading, graphite is progressively exfoliated to graphene to form G-Ce6 nanocomposite. In addition to having the advantage of direct producing graphene-based PS without going through an oxidizing step to generate graphene oxide (GO), the authors found that the G-Ce6 displays remarkable characteristics. First, the Ce6 loading for G is ten-fold higher than GO analogous, and no functionalization of graphene is required to obtain a good dispersibility in physiological conditions. The *in vitro* study of G-Ce6 (HeLa cells, laser irradiation 660 nm for 2 minutes) provided evidence of ROS generation and showed that the concentration necessary to kill cells with G-Ce6 is 6-75 times lower than in any other Ce6 composites including GO-Ce6. This result opens the path to the drawing up of new graphene-based as PS nanocarriers for PDT.

Wu et al. studied the synergistic activity of polylysine-graphene (G-PLL) formulated with doxorubicin (Dox) and Zn(II)phthalocyanine (ZnPc) (Wu et al. 2014). The nanocomplex was easily prepared by self assembling ZnPc and Dox on G-PLL and showed high solubility and stability in biological media. It was found that the $^1\text{O}_2$ production was lower than that of ZnPc alone but besides it was also shown that the activity of the PS may be restored after releasing (Tian et al. 2011; Zhu et al. 2008). The cytotoxicity on HeLa cells was found to be negligible; however when subjected to irradiation (660 nm, 0.15 W/cm² for 10 minutes) a 90% loss of viability was observed with an IC₅₀ = 0.14 $\mu\text{g}/\text{mL}$. This synergistic effect was also observed with MCF-7 (IC₅₀ = 0.21 $\mu\text{g}/\text{mL}$) and B16 mouse melanoma cells (IC₅₀ = 0.28 $\mu\text{g}/\text{mL}$).

5.1.2. SWCNTs and PDT applications

In 2012, Zhu's team studied the chemical characteristics and PDT efficacy of SWCNTs-Ce6-chitosan nanorods (Xiao et al. 2012). The obtained nanorods had an overall diameter of 6-7 nm with a thickness of PS of about 1.2 nm. The dark toxicity of SWCNTs-Ce6-chitosan (100 $\mu\text{g}/\text{mL}$) was found to be less than 20% after 48 hours incubation with NIH/3T3 normal cells. The PDT effect of SWCNTs-Ce6-chitosan to HeLa cells was determined *in vitro* by WST-1 assay and showed that IC₅₀ of free Ce6 is about $8.80 \pm 0.059 \mu\text{g}/\text{mL}$, while that one of the nanocomposite is only $5.98 \pm 0.064 \mu\text{g}/\text{mL}$ probably due to a better hydrophilicity (Fig.28).

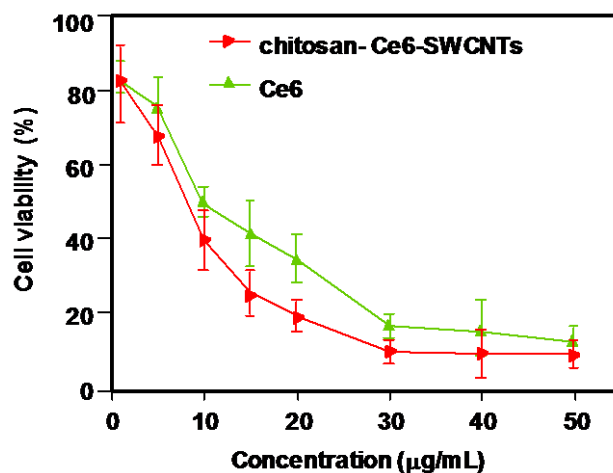


Fig.28: *In vitro* PDT effect of SWCNTs-Ce6-chitosan to HeLa cells (663 nm, 150 mW/cm², 10 min). Taken from reference (Xiao et al. 2012)

Ogobodu and co-workers (Ogobodu et al. 2013b, 2013a; Ogobodu et al. 2015a; Ogobodu et al. 2015b; Ogobodu and Nyokong 2014) studied SWCNTs with 1-5 nm in diameter and 1-5 µm length as nanocarrier of several zinc phthalocyanine-X (ZnPc-X) conjugates (**Table 5**). These conjugates were adsorbed onto SWCNT *via* $\pi - \pi$ stacking interactions. They presented better photophysical properties than the ZnPc alone. The *in vitro* phototoxicity experiments were performed with ZnMAPc-FA-SWCNT and ZnMAPc-spermine-SWCNT on human skin melanoma A375 and MCF-7 breast cancer cells respectively. After diode laser irradiation (676 nm, 98 mW/cm², 5 J/cm²) in the presence of ZnMAPc-FA-SWCNT at 10 µM, a PDT effect was observed with a 37% cell viability compared to 40% with ZnMAPc-FA and 77% with SWCNT-FA, showing that SWCNT does not have a significant PDT or PTT effect to the cell (**Fig. 29**).

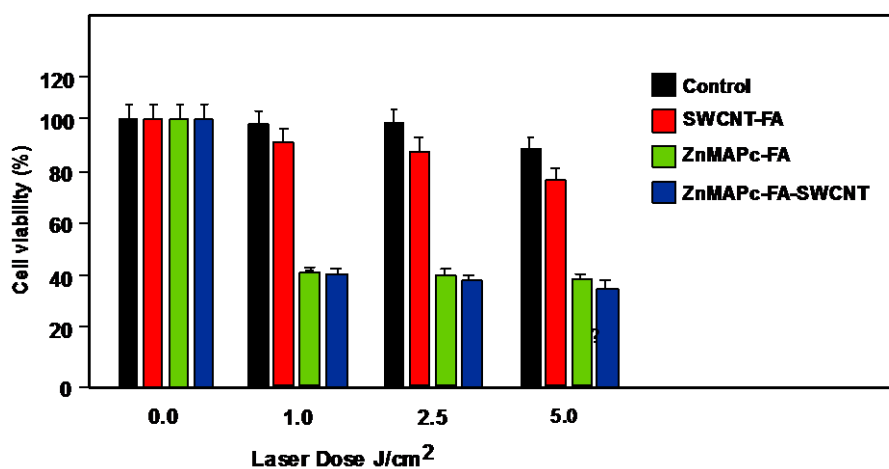


Fig. 29: Cell viability of melanoma cells incubated with SWCNT-FA, ZnMAPc-FA and ZnMAPc-FA-SWCNT under irradiation (676 nm, 98 mW/cm², 5 J/cm²). Taken from reference (Ogobodu et al. 2015b)

Concerning ZnMAPc-spermine-SWCNT, the same authors decided to use a quartz lamp that can absorb sunlight from about 600 nm and beyond 1000 nm in order to investigate the PDT and PTT effects of ZnMAPc and SWCNT by varying different parameters, such as concentration of ZnMCPPc, ZnMCPPc-spermine or ZnMCPPc-spermine-SWCNT (from 5 to 40 μM) and time irradiation (5, 10 or 20 minutes) equivalent to an irradiation dose of 28 to 112 J/cm^2 . The best results were obtained at a 40 μM concentration after 20 minutes irradiation. These results indicated that ZnMCPPc-spermine-SWCNT allowed a 5% cell viability but 3% and only 36% with ZnMCPPc-spermine and ZnMCPPc respectively. ZnMCPPc-spermine has a better PDT effect compared to ZnMCPPc-spermine-SWCNT, as it possesses higher triplet and $^1\text{O}_2$ quantum yield values and no clear PTT effect of SWCNTs was observed (Fig. 30).

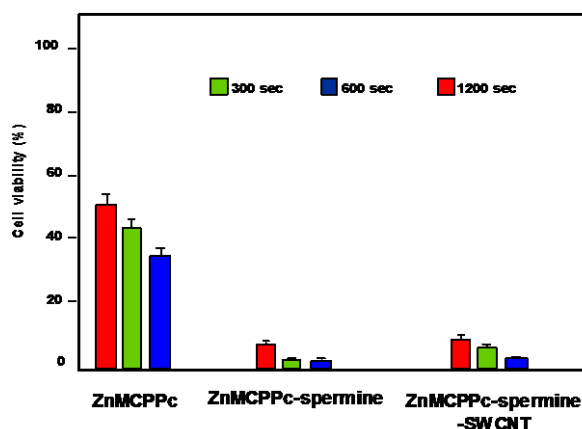


Fig. 30: Cell viability of MCF-7 breast cancer cells incubated with ZnMCPPc (a), ZnMCPPc-spermine (b) and ZnMCPPc-spermine-SWCNT (c) at 40 μM concentration under irradiation (600-1000 nm, 93 mW/cm^2 , 112 J/cm^2) for 20 min. Taken from reference (Ogobodu et al. 2015a)

Table 5: ZnPc-X conjugates

ZnPc	X	Ref.
ZnMAPc	Pyrene	(Ogobodu et al. 2013b)
ZnMAPc	Folic acid	(Ogobodu et al. 2013a; Ogobodu et al. 2015b)
ZnOPc	Bovine serum albumine	(Ogobodu and Nyokong 2014)
ZnMCPPc	Spermine	(Ogobodu et al. 2015a)

ZnMAPc zinc monoamino phthalocyanine, *ZnOPc* zinc octacarboxy phthalocyanine, *ZnMCPPc* zinc mono carboxy phenoxyphthalocyanine

Also in respect to SWCNTs, Safar et al. (Safar et al. 2015) wished to combine chirality enriched (6,5) single-walled carbon nanotubes (E-SWCNTs) and some porphyrins for estimating the potential PDT effect of these new hybrid systems. To achieve this goal, *meso*-tetrakis(4-pyridyl)porphyrin tosylate salt ($\text{H}_2\text{TM4PyP}$ (OTs)₄, POR) and its myristil analogous *meso*-

tetrakis(*N*-myristyl-4-pyridinium)porphyrin tosylate salt ($H_2TMy4PyP$ (OTs)₄, MYR). Commercial Verteporfin (VER) was used as the reference. After studying the optical absorption of porphyrins and E-SWCNT (Table 6), the production of ¹O₂ for each hybrid systems was evaluated using a white 5-LEDs lamp with yellow or red filter (wavelength = 570 and 630 nm respectively) or 940 nm. The authors observed that E-SWCNT alone can produce ¹O₂, involving very likely a direct energy transfer from E-SWCNT excitons to dissolved oxygen, but less than the hybrid systems. Furthermore, it has been shown in some cases that the hybrid systems have a better ¹O₂ production efficiency than the free porphyrins in the therapeutic window.

Table 6: Optical absorption of porphyrins and E-SWCNT

Compounds ^a	Absorption bands (nm) ^b
POR	521, 556, 587 and 641
MYR	530 and 570
VER (commercial, reference)	575, 630 and 695
E-SWCNT	572 and 992 ^c

^a porphyrin aqueous solutions at 55 μM and aqueous suspension of E-SWCNT, ^b for all porphyrins, another weak band can be observed from 900 to 1000 nm, ^c bands attributed to E22 and E11 optical transitions, (Weisman and Bachilo 2003) *POR* meso-tetrakis(4-pyridyl)porphyrin tosylate salt, *MYR* meso-tetrakis(*N*-myristyl-4-pyridinium)porphyrin tosylate salt, *VER* verteporfin, *E-SWCNT* chirality enriched (6,5) single-walled carbon nanotube

5.1.3. PDT/PTT applications

Some research teams worked on the use of photothermal effect of PS-graphene nanocomposites for the development of new theranostic nanoplatfoms by combining photodynamic therapy (PDT) and photothermal therapy (PTT) (Yang et al. 2010) to improve the efficacy against cancer.

In 2014, Jiang and co-workers synthesized two new PS nanocarriers with a dual phototherapy effect (PDT/PTT) in one sonication step by coating tetrasulfonic acid tetrasodium salt copper phthalocyanine (TSCuPc) onto graphene sheets (GR) (Jiang et al. 2014b) and single-walled carbon nanohorns (SWNHs) (Jiang et al. 2014a) *via* π – π interactions. The loading efficiencies of TSCuPc were 27 and 38 wt% for GR-TSCuPc and SWNHs-TSCuPc nanohybrids, respectively. Both nanohybrid systems produce ROS, such as superoxide radical anion (O₂^{•-}) and hydroxyl radical (OH[•]) and their *in vitro* dual phototherapeutic effects (PDT/PTT) at the TSCuPc equivalent of 10 μg/mL using human cervix cancer HeLa cells were highlighted by using a single wavelength (laser irradiation at 650 nm, 3 W/cm² for 5 minutes) (Fig.31).

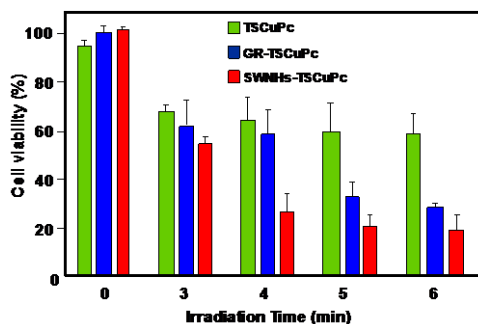


Fig. 31: Cell viability of HeLa cells incubated with free TSCuPc, GR-TSCuPc and SWNHs-TSCuPc nanohybrids (650 nm, 3 W/cm²). Taken from references (Jiang et al. 2014a; Jiang et al. 2014b)

In 2014, Gollavelli et al. (Gollavelli and Ling 2014) used a graphene derivative loaded with a PS by $\pi - \pi$ stacking interactions in order to develop a new theranostic nanoplatform combining phototherapy (PDT and/or PTT) and imaging for cancer treatment and detection. Water dispersible magnetic and fluorescent graphene NPs (MFG) and hydrophobic silicon naphthalocyanine bis (trihexylsilyloxiide) (SiNc₄) as PS were chosen to achieve their goals (MFG size \approx 40 nm, loading efficiency of PS 8.5 wt%). The Magnetic Resonance Imaging (MRI) measurements and the *in vitro* phototherapy study (PDT and PTT) were conducted on human cervical cancer HeLa cells (Fig. 32). The authors proved that MGF-SiNc₄ were well internalized in HeLa and T₂-weighted MRI measurements revealed a great luminescence image and T₂-weighted MRI contrast due to the fluorescence and superparamagnetic properties of MFG. It should be noted that MFG and SiNc₄ can together absorb \approx 775 nm light and it was demonstrated a dual phototherapy effect (PDT and PTT) is possible to kill cells by using an inexpensive single light source (tungsten halogen lamp equipped with a long pass filter capable of providing a light range of 750-1380 nm and delivers a power of 0.3 W/cm² during 1 hour). This experiment indicated a cancer cell killing efficacy of \approx 97.9% (PDT \approx 64.7% and PTT \approx 33.2%).

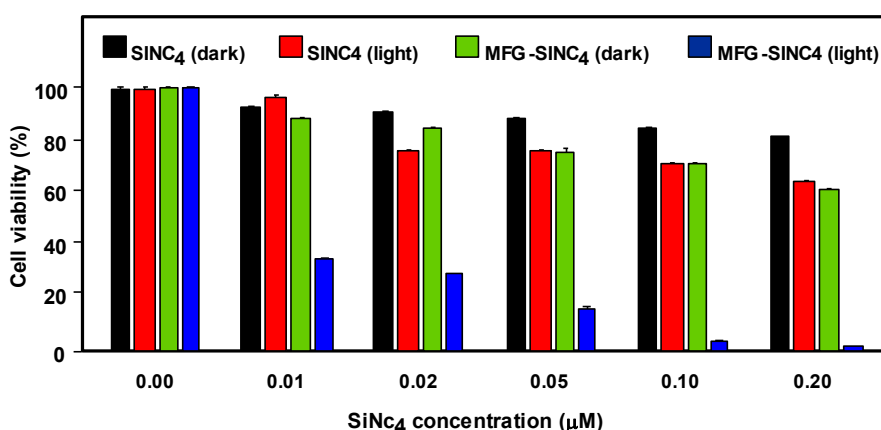


Fig. 32: Comparative cell viabilities by MTT assay of HeLa cells treated with different concentrations of SiNc₄/MFG-SiNc₄ under dark/phot irradiation conditions (750-1380 nm, 0.3 W/cm², 1h). Taken from reference (Gollavelli and Ling 2014)

5.2. Graphene oxide

5.2.1. PDT applications

In 2010, Dong et al. (Dong et al. 2010) described the use of methoxy-poly(ethylene glycol) conjugated nano-graphene oxide (NGO-mPEG) as a potential PS nanocarrier for anticancer PDT. Hydrophilic mPEG was conjugated to the NGO for increasing the solubility and stability of NGO in cell culture media. The authors found that the structure of NGO is a single-layer sheets with size down to 200 nm and thickness about 2-3 nm and the cytotoxicity of NGO-mPEG towards human breast cancer MCF-7 cells was negligible. Zinc phthalocyanine (ZnPc) as PS was loaded onto NGO-mPEG by $\pi - \pi$ stacking and hydrophobic interactions (loading efficiency 14 wt%) to evaluate the *in vitro* photodynamic effect of NGO-mPEG/ZnPc. Human MCF-7 breast cancer cells were treated by different concentrations of NGO-mPEG/ZnPc for 24 hours followed by an exposition to the UV band-path filtered Xe light irradiation for 10 minutes (60 J/cm^2). Without light irradiation, the authors observed cell viability of $> 85\%$ and, with irradiation, this value decreases from about 80% to 60% when the concentration was increased from 3.8 to 60 mg/L.

In 2013, Wojtoniszak et al. showed that graphene oxide (GO) loaded with Methylene Blue (MB) as PS by adsorption had a much higher $^1\text{O}_2$ generation capacity than graphene after irradiation with 785 nm laser. They concluded that MB-GO could be used as potential PS delivery system in PDT. No *in vitro* and *in vivo* studies have been conducted yet.

In 2014, Miao et al. (Miao et al. 2013) demonstrate that polyethylene glycol-grafted graphene oxide (pGO) nanosheets can be employed as multimodal nanocarrier to co-deliver a PS Ce6 and Dox. The PEGylation of pGO is necessary to increase aqueous stability of pGO. Ce6 and Dox were co-loaded onto pGO nanosheets by $\pi - \pi$ stacking and hydrophobic interactions (loading efficiencies 51.9 ± 5.1 and 61.7 ± 4.4 wt%, respectively) to form multimodal nanophysiorplexes (Ce6/Dox/pGO) with a size of 148.0 ± 18.0 nm. The *in vitro* cytotoxicity of GO and pGO nanosheets towards murine SCC7 squamous carcinoma cells was evaluated after treatment with a concentration of $40 \mu\text{g/mL}$ and the cell viability is around 90% for both. Conversely, the *in vivo* cytotoxicity, after treating mice by intravenous bolus injection of nanosheets at 80 mg/kg dose, showed no cytotoxicity for pGO nanosheets compared to the 10% survival rate for GO nanosheets. The authors proved by *in vivo* and *in vitro* studies (irradiation with LED 660 nm with luminous intensity of 8000 mCd during 30 minutes) that the co-delivery of Ce6 and Dox by the pGO nanosheets induces a synergistic photodynamic anticancer effect and the best result was obtained at a Dox-Ce6 molar ratio of 1:2.

As did Dong and co-workers (Dong et al. 2010), Zeng et al. (Zeng et al. 2015) synthesized PEGylated nano-graphene oxide (NGO-PEG). The PEG-amine was covalently attached to NGO sheets for the dispersibility improvement of NGO in physiological conditions. The size of NGO-PEG is around 20-40 nm with a thickness ≈ 1.4 nm. The loading of Ce6 onto NGO-PEG by $\pi - \pi$

stacking and hydrophobic interactions (loading efficiency ≈ 13 wt% at the feeding concentration of 2 mM) and *in vitro* PDT study (HeLa cells, laser irradiation 660 nm, 0.2 W/cm^2 for 5 minutes) showed that NGO-PEG can be used as PS nanocarrier. Furthermore when coupled to polyethylenimine (BPEI) the resulting positively charged NGO-PEG-BPEI showed a better cellular uptake by HeLa cell and the loading ratio of Ce6 reached a 26 wt% value. For the cellular uptake by HeLa cells cytometric analysis, confocal microscopy and fluorescence experiments were carried out. **Fig. 33a** shows the cell viability of HeLa cells after light irradiation by 662 nm laser at a power density of 0.2 W/cm^2 for 5 minutes and **Fig.33b** shows the changes of Ce6 fluorescence intensity in cells as a function of incubation time. It can be noted that the mean fluorescence intensity of Ce6 in NGO-PEG-BPEI-Ce6 system was 2.6-fold higher than that in NGO-PEG-Ce6, and 30-fold better than that in free Ce6 system. This preliminary study indicated that NGO-PEG-BPEI-Ce6 could target delivery the Ce6 into lysosome.

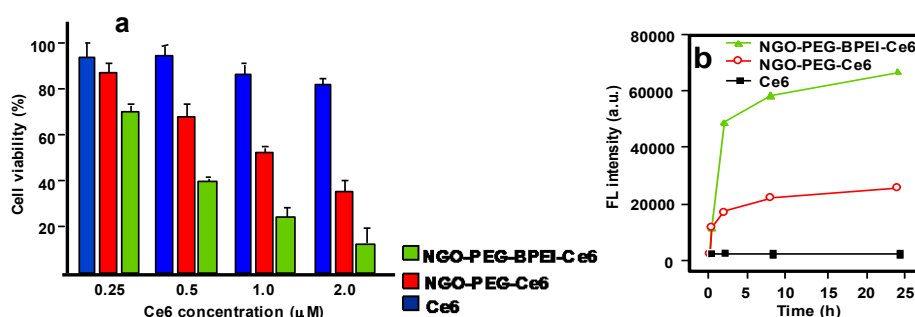


Fig. 33: (a) Cell viability of HeLa cells treated with free Ce6, NGO-PEG-Ce6 and NGO-PEG-BPEI-Ce6 at different concentrations of Ce6. (b) Ce6 fluorescence intensity in HeLa cells treated with Ce6, NGO-PEG-Ce6 and NGO-PEG-BPEI-Ce6 at various times. Taken from reference (Miao et al. 2013)

Yang et al. (Yang et al. 2012) described a scaffold for PDT and drug delivery in which GO is the carrier, folic acid modified cyclodextrin (FA- β CD) is a targeting agent, Dox is the drug, and adamantanyl porphyrin (AdaTPP) is a linker. The assembly of the nanocomposite resulted from successive mixings of GO, AdaTPP and Dox to form GO-Dox/AdaTPP then with FA- β CD by strong hydrophobic interaction between the CD cavity and adamantane moiety. The resulting assembly called 1/2/Dox/GO showed no cytotoxicity towards normal cells over a 1-day period but induced a tumor-growth inhibition *in vivo* in HeLa bearing BALB/c nude mice as illustrated in **Fig.34**.

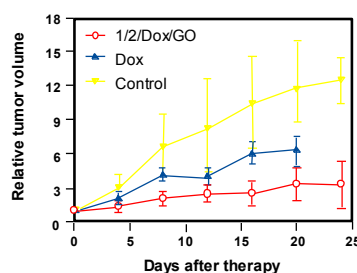


Fig. 34: Tumor growth curves for BALB/c nude mice with HeLa cancer cells. Taken from reference (Yang et al. 2012)

Yan et al. (Yan et al. 2014) reported the regulation of $^1\text{O}_2$ production probe using the binding properties of an aptamer (AP). The concept of this molecular beacon (for a review, see (Verhille et al. 2010)) is based on a non-covalent binding of a cDNA aptamer-Ce6 (AP-Ce6) moiety with GO as efficient fluorescence and SOG quenching probe. In the absence of a target, the PS is not active due its close proximity with GO. Once the AP hybridizes with the target the $^1\text{O}_2$ production is restored (Fig.35).

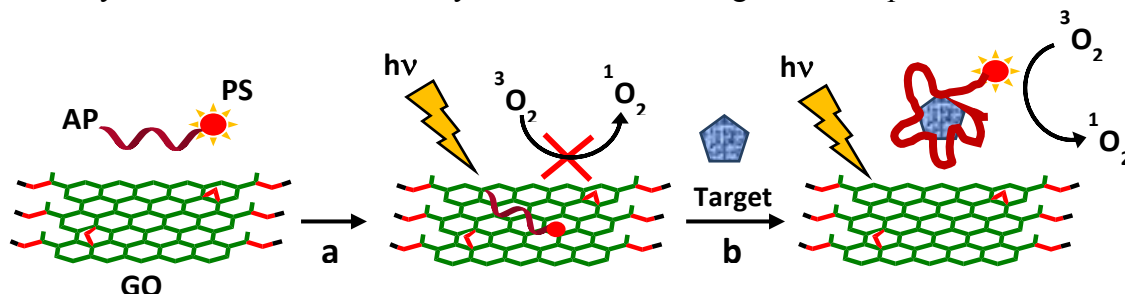


Fig. 35: Concept of photomolecular beacon. Taken from reference (Zhu et al. 2008)

Adenosine 5'-triphosphate (ATP), which is overexpressed on the extracellular surface of cancer cells besides the mitochondrial matrix, was used as a proof-of concept target molecule. The graphic based GO / AP-Ce6 was prepared by mixing GO and AP-Ce6 and exhibited a size of 80 nm and a thickness of about 1.2 nm. The quenching by graphene is clearly evidenced in Fig. 36a and it can be noted that the presence of ATP as a target restored the ability of Ce6 to produce $^1\text{O}_2$ owing to stronger interactions between ATP and AP-Ce6 than those of GO and the PS. In Human HepG2 cells $^1\text{O}_2$ was detected using DCFH-DA method and the results evidenced the restoration of $^1\text{O}_2$ production in the presence of ATP (Fig. 36b). These results are comforted by cell viability after light irradiation at 404 nm for 10 minutes (Fig. 36c).

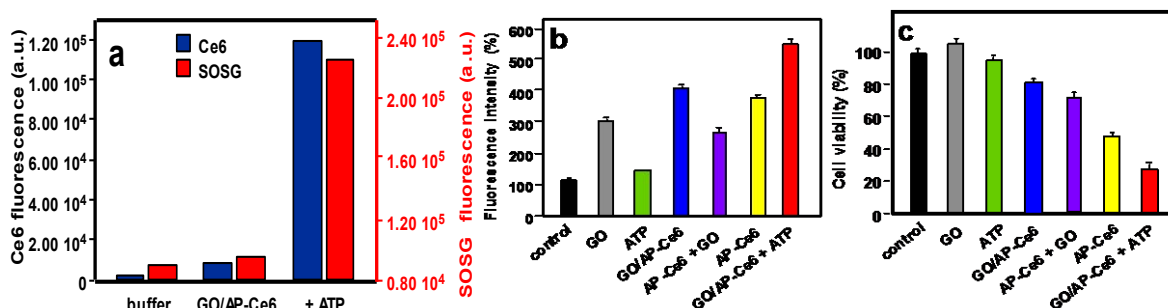


Fig. 36: (a) The Ce6 and SOSG signal readouts after irradiation condition (404 nm, 10 min). (b) DCF-fluorescence intensity in HepG2 cells. (c) Cellular viability of HepG2 cells treated with light. Taken from reference (Yan et al. 2014)

A targeted ligand is often required to provide a better selectivity of the PS. Within this scope, some teams developed targeted nanocarrier systems for the PS delivery.

In 2011, Huang and co-worked (Huang et al. 2011) prepared GO as single-layer sheet (sheet-like shapes) with thickness about 1.2 nm covalently linked to folic acid (FA). The PS (Ce6) was then loaded onto FA-GO (loading efficiency ≈ 80 wt%) via hydrophobic interactions and $\pi - \pi$ stacking.

The *in vitro* cytotoxicity of FA-GO and FA-GO-Ce6 was measured after 24 hours incubation with MGC803 cells and showed that GO-FA does not have any dark toxicity and the dark cytotoxicity of FA-GO-Ce6 is dependent upon Ce6 concentration. The intracellular distribution study revealed a higher accumulation of Ce6 inside the tumor. The *in vitro* PDT effect was studied after the exposure of MGC803 cells to FA-GO-Ce6 at different ratios (FA-GO:Ce6, 10:1 to 1:1 wt%) followed by irradiation with He-Ne laser (632.8 nm, $\approx 30 \text{ mW/cm}^2$) for 10 minutes. Without irradiation, cell viability above 80% was observed and after light exposure, only $\approx 10\%$ of cell viability was detected for 1:1 and 2:1 ratios.

The same team in 2015 (Huang et al. 2015) described the preparation of reduced graphene oxide (rGO) nanosheets covalently linked to polyvinylpyrrolidone (PVP). PVP was used for increasing aqueous dispersibility and biocompatibility of rGO. The rGO-PVP is a sheet-like shape with PVP layers of thickness $\approx 0.85 \text{ nm}$ on each side of the $0.96 \pm 0.05 \text{ nm}$ thick rGO layers (total thickness for rGO-PVP $2.81 \pm 0.18 \text{ nm}$). The ACDCRGDCFCG peptide (RGD4C), used as vectors for $\alpha_v\beta_3$ integrin targeted delivery of PSs, was covalently anchored to rGO-PVP and the result rGO-PVP-RGD was loaded with Ce6 by hydrophobic interactions and π - π stacking (loading efficiency $\approx 80 \text{ wt}\%$). No dark cytotoxicity of rGO-PVP and rGO-PVP-RGD on MGC803 cells was observed in the concentration range of 0-500 $\mu\text{g/mL}$ (cell viability higher than 95%). The authors also observed that rGO-PVP-RGD-Ce6 induced a better PDT effect on cells as compared to free Ce6 and rGO-PVP-Ce6 at all tested concentrations (0-50 μM Ce6, i.e. 0.6-30 $\mu\text{g/mL}$ Ce6) after laser irradiation (671 nm, 30 mW/cm^2 for 3 minutes) (Fig. 37). These results demonstrated the active targeting ability of RGD. The $^1\text{O}_2$ generation from rGO-PVP-RGD-Ce6 has been detected by measuring the fluorescence signal of singlet oxygen sensor green (SOSG).

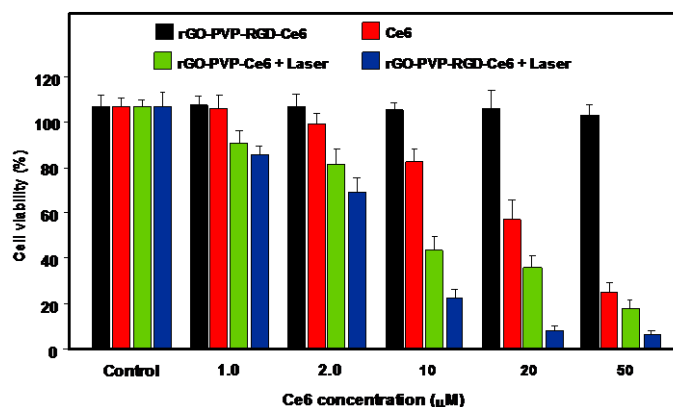


Fig. 37: Cell viability of MGC803 cells treated with different concentrations of Ce6, rGO-PVP-Ce6 or rGO-PVP-RGD-Ce6 for 24 hours at 37°C without or with irradiation (671 nm , 30 mW/cm^2). Taken from reference (Huang et al. 2015)

Li et al. (Li et al. 2013) covalently attached hyaluronic acid (HA) into the surface of GO nanosheets in order to target cancer cells with overexpressed HA receptors. The hydrodynamic

diameter of GO nanosheets is 59.3 nm and the average diameter of HA-GO nanocarrier is 78.1 nm. Ce6 was loaded onto HA-GO *via* $\pi - \pi$ stacking and/or hydrophobic interactions (loading efficiency 115 wt% at the feeding concentration of 1.5 mg/mL). The *in vitro* phototoxicity study (laser irradiation 670 nm, 1.8 J/cm²) of HA-GO/Ce6 nanohybrids towards human cervical cancer HeLa cells showed a photodynamic efficacy times greater than free Ce6 (IC₅₀ shifted from 1 μ g/mL to 0.1 μ g/mL).

In 2015, Xu et al. described a dual-targeting nanosystem comprising a modified nanographene oxide (NGO) as the carrier and a PS ((5-(p-(4-Trimethylammonium)-butoxyphenyl)-10,15,20-triphenylporphyrin Bromide abbreviated MitoTPP) (Xu et al. 2015). The NGO nanocomposite was modified as follow: Firstly, 4-arm PEG-amine was covalently coupled as described by Li (Li et al. 2013) to enhance dispersibility and biocompatibility, and secondly folic acid (FA) NHS ester was grafted on NGO-PEG to give the modified NGO-PEG-FA composite. Finally, an overnight mixing of NGO-PEG-FA and MitoTPP afforded the desired nanosystem NGO-PEG-FA/MitoTPP (loading of MitoTPP was estimated to 37.2 wt%). The *in vitro* release of MitoTPP strongly depended on the pH. Due to the nonionized carboxyl groups in NGO at pH 5.0, the electrostatic attraction is much weaker and promotes the release of MitoTPP from NGO and permits to escape from the acidic endosome/lysosome compartments and then diffuse into mitochondria. Confocal microscopy showed that the intracellular localization for MitoTPP was found to be mitochondria. ¹O₂ generation was observed using ABDA indicator at pH 7.4 and 5.0 under irradiation and over different periods. While the absorbance for ABDA did not change at pH 7.4 for 1 hour, that one at pH 5.0 dramatically decreased within the initial 15 minutes irradiation, indicating that MitoTPP can induce ¹O₂ after being released from NGO. The presence of FA in the nanocomposite induced a much brighter fluorescence than with NGO-PEG/MitoTPP demonstrating the dual targeting. The phototoxicity caused by PDT is represented in Fig.38 which clearly shows the greater effectiveness of this double targeting after 30 minutes of light irradiation (650 nm, 10 mW/cm²).

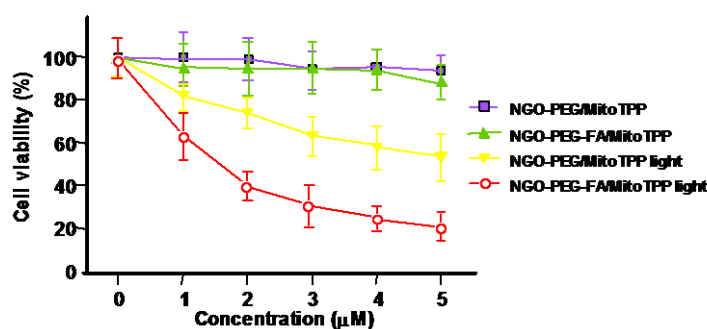


Fig. 38: Cell viability of HeLa cells after treatment with NGO-PEG/MitoTPP in presence/absence of FA and light (650 nm, 10 mW/cm², 30 min). Taken from reference (Xu et al. 2015)

In 2015, Zhou and co-workers (Zhou et al. 2015) worked on the development of photosensitive and magnetic targeted PS delivery system by dispersing in a uniform size the Fe_3O_4 magnetic nanoparticles on the GO surface by co-precipitation method. The thickness of the single-layer sheet was about 0.8 nm and the saturation magnetization value of the resulting GO- Fe_3O_4 nanocomposite was about 15 emu/g, preventing any Fe_3O_4 aggregation on GO. Hematoporphyrin (HP) was loaded onto GO- Fe_3O_4 by hydrophobic interactions and $\pi - \pi$ stacking (loading efficiency 23.6 wt%). The authors determined that GO- Fe_3O_4 produces $^1\text{O}_2$ but in smaller quantities compared to HP alone (63.4% of the value obtained with free HP), which is in agreement with the literature (Tian et al. 2011). The *in vitro* study on human cervical cancer Hela cells highlighted the fact that IC_{50} of GO- Fe_3O_4 -HP decreased from 189.24 $\mu\text{g}/\text{mL}$ (dark cytotoxicity) to 10.12 $\mu\text{g}/\text{mL}$ after incubating cells with GO- Fe_3O_4 -HP during 24 hours followed by laser irradiation at 671 nm ($0.1 \text{ W}/\text{cm}^2$) for 5 minutes and continued incubation to 72 hours. These results clearly demonstrate that the magnetic GO- Fe_3O_4 nanocomposite could be used as tumor-targeted PS delivery system under proper external magnetic field and as photosensitive PDT agent under laser irradiation at 671 nm to produce $^1\text{O}_2$.

Recently, Chang et al. (Chang et al. 2015) described a new concept using near-infrared (NIR) irradiation as stimuli for the formation of the hydrogel shells inducing cell death. The developed hydrogel precursor (rGO/AE/AuNPs) was composed of reduced graphene oxide (rGO), amaranth extract (AE) and gold nanoparticles (AuNPs). AuNPs and rGO were used for their PTT properties and ability to speed up the $^1\text{O}_2$ generation. AE was used as PS (due to the chlorophyll derivatives contained in the extract) and as cross-linking agent. The authors showed that the hydrogel precursor was initially in the form of a viscous oil, but that the rapid hydrogel formation was observed upon 10 minutes NIR irradiation. This hydrogel formation can be ascribed to several interactions between the various constituents of the hydrogel precursor, i.e. excess of AE inducing reduction of GO to rGO, formation of dewatered rGO sheets caused by an increase in the temperature of precursor under NIR irradiation, improvement of the 1140 π - π stacking and hydrophobic interactions among rGO sheets and finally electrostatic attraction between positively charged Au NPs and negatively charged GO sheets. *In vitro* studies on Chinese hamster ovary (CHO) and HeLa cancerous cells showed an *in situ* hydrogel shell formation on cells after laser irradiation (600 nm, $2 \text{ W}/\text{cm}^2$ for 10 minutes), which led to an enrichment of PS and PTT agents around tumor cells resulting in the cell death *via* a dual PDT/PTT treatment with minimal side effects (Fig.39).

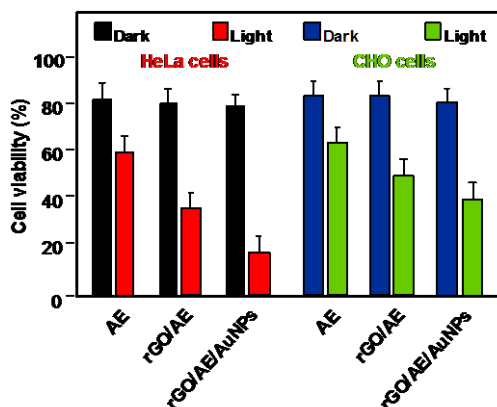


Fig. 39: Cell viabilities of (a) HeLa and (b) CHO cells treated with AE, rGO/AE and rGO/AE/AuNPs in the dark or after light irradiation (600 nm, 2 W/cm² for 10 min). Taken from reference (Chang et al. 2015)

The same year, Rong and co-workers (Rong et al. 2014) used polyethylene glycol-functionalized graphene oxide (PEG-GO) as PS delivery system. PEG-GO was loaded with 2-(1-hexyloxyethyl)-2-devinylpyropheophorbide- α (HPPH, Photochlor[®]) as PS (loading efficiency 131 wt%) by supramolecular $\pi - \pi$ stacking. The PEG-GO system was of about 50 nm and has a thickness around 1.5 nm, which reaches up to 2 nm after HPPH loading (Fig. 40).

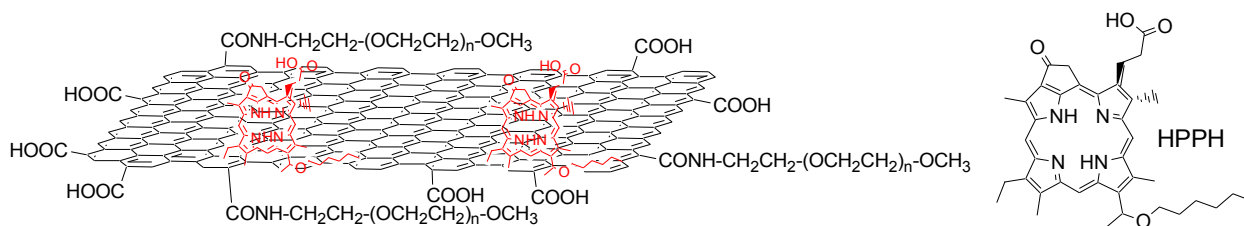


Fig. 40: Schematic structure of the GO-PEG-HPPH system. Taken from reference (Rong et al. 2014)

The *in vitro* PDT studies of GO-PEG-HPPH, GO-PEG and HPPH alone towards murine breast cancer 4T1 cells were performed after incubation with GO-PEG-HPPH (1 μ m equivalent of HPPH and 0.49 μ g/mL of GO-PEG) during 24 hours followed by laser irradiation at 671 nm (4 mW/cm²) for 3 minutes. No dark cytotoxicity was observed, and after irradiation GO-PEG-HPPH caused a greater cell death than HPPH alone (Fig. 41a). The *in vivo* HPPH delivery and PDT effects of GO-PEG-HPPH and free HPPH were studied in 4T1 tumor-bearing mice with both fluorescence and PET imaging. While there was a reduction of the generation of ¹O₂ by GO-PEG-HPPH compared to the free HPPH, a better accumulation of HPPH into tumor region was observed. The *in vivo* PDT study was carried out after *i.v.* injection of GO-PEG-HPPH or free HPPH ([HPPH] = 1 mg/kg in both cases) followed by laser irradiation at 24 hours post-injection (671nm, 75 mW/cm² for 20 minutes). A marked improvement in average life expectancy has been also observed (35% after

60 days). Subsequently, the volume of tumors in the GO-PEG-HPPH-treated mice decreased the first two days and remained unchanged for at least 14 days (Fig. 41b).

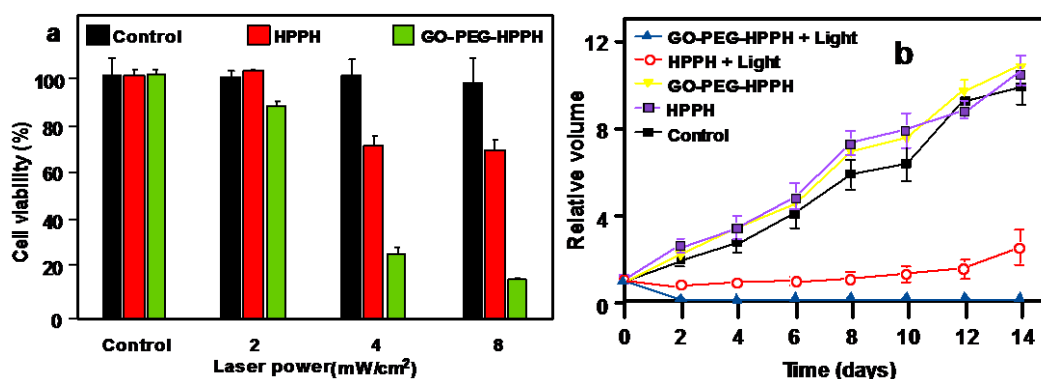


Fig. 41: (a) Cell viability of 4T1 cells incubated with various concentrations of free HPPH, GO-PEG, GO-PEG-HPPH after irradiation at 671 nm (4 mW/cm², 3 min). (b) Tumor growth curves of different groups of tumor-bearing mice after PDT treatment. The tumor volumes were normalized to their initial. Taken from reference (Rong et al. 2014)

In 2012, Cho et al. (Cho and Choi 2012) linked GO to Ce6 with disulfide bond (SS) to generate GO-SS-Ce6 system having an average hydrodynamic size around 102.4 ± 15.2 nm and a homogeneous dispersion with 1-2 nm thickness, showing a single- or double-layered graphene structures. Glutathione (GSH) or dithiothreitol (DTT) were used as redox-responsive cleavable disulfide linkers. These compounds did not present any fluorescence and phototoxic properties, even upon light irradiation. The UV/Vis and fluorescence spectroscopy studies demonstrated the quenching effect of GO on the fluorescence yield of Ce6 and the cleavage of the disulfide bonds. The fluorescence intensity of GO-SS-Ce6 was 9-fold greater after incubation in 1 mM DTT solution during 3 hours. The authors also studied the ¹O₂ generation of several solutions (free Ce6, GO-SS-Ce6 and GO-SS-Ce6 + 1 mM DTT) under CW laser beam irradiation (670 nm, 100 mW/cm²) and found that the simultaneous treatment of GO-SS-Ce6 by 1 mM DTT and laser irradiation produces a significant increase of ¹O₂ generation compared to the GO-SS-Ce6 solution alone, reaching around the same level as the free Ce6 solution. The *in vitro* GSH-activatable fluorescence imaging and PDT studies of free Ce6 and GO-SS-Ce6 towards human lung cancer A549 cells (dark incubation during 24 hours followed by diode laser irradiation at 670 nm, 20 J/cm²) showed an effective cellular internalization and a preferential accumulation of Ce6 in the cancer cells, especially in the lysosomes (Fig. 42).

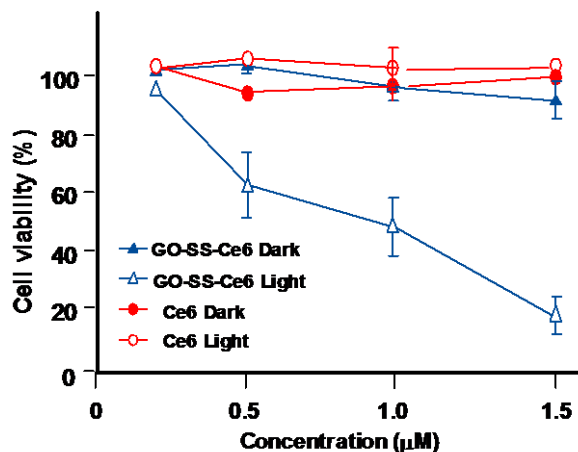


Fig. 42: *In vitro* PDT efficacy on A549 cells of free Ce6 and GO–SS–Ce6 system under dark or light irradiation conditions (670 nm, 20 J/cm²). Taken from reference (Cho and Choi 2012)

In 2015, Tian et al. (Tian et al. 2015) synthesized GO coupled to FA, a PS and to an enzyme-responsive substrate (peptide) to control the selective release of PS at the specific site. The folate based conjugate and the PS-labeled peptide substrate consist of 1,2-distearoyl-sn-glycero-3-phosphoethanolamine-N-[folate(poly ethylene glycol)-2000] (DSPE-PEG2000-FA) and Ce6-GRRGKGGFFFF (Ce6-Pep) respectively and loaded onto GO by $\pi - \pi$ and hydrophobic interactions. The peptide GRRGKGGFFFF is known to be a Cathepsin B (CaB)-activatable substrate with a specific cleavage of the RR peptide bond. GO sheets have a size less than 100 nm and a dispersion with 0.4 nm thickness, showing a single-layered graphene structure. The successive loading of Ce6-Pep and DSPE-PEG2000-FA were observed with the increase of thickness, rising from 0.4 to 0.7 then 1.2 nm respectively. The Ce6-Pep loading of Ce6-Pep/DSPE-PEG2000-FA/GO nanoprobe represents was 35 wt% loading. The fluorescence intensity of Ce6-Pep/GO increased by a factor of 18 after addition of CaB, the fluorescence of Ce6-Pep was not restored by adding Cathepsins D or L with Ce6-Pep/GO. Lysosome-targeting and CaB-activatable fluorescence nanoprobe for imaging cancer cells have been shown with *in vitro* studies by using FR-positive HeLa or KB cells and FR-negative HaCaT or A549 cells. Others *in vitro* and *in vivo* studies (HacaT and/or HeLa cells) were also performed to demonstrate the PDT effect (660 nm, 250 mW/cm², 50 J/cm² during 200 seconds) and *in vivo* tumor imaging.

5.2.2. PDT and PTT applications

In 2011, Tian and co-workers (Tian et al. 2011) combined the PTT effect and PDT by using PEGylated graphene oxide (GO-PEG) loaded with Ce6 *via* supramolecular $\pi - \pi$ stacking. The size of the NPs was down to 50 nm and the thickness about 1 nm. The maximal Ce6 loading capacity of GO-PEG was 15 wt% at the feeding concentration of 3 mM. The *in vitro* study was carried out after the exposure of KB cells with GO-PEG-Ce6 followed by different possible laser irradiations: (i) at

660 nm (15 J/cm^2) for 5 minutes to test the PDT effect, (ii) at 808 nm (0.3 W/cm^2 , 360 J/cm^2 , 20 minutes) for the PTT effect or (iii) both with PTT irradiation before PDT treatment. Despite a reduction of the $^1\text{O}_2$ generation for GO-PEG-Ce6 compared to free Ce6, the photodynamic effect was significantly increased thanks to a synergistic combination of PDT and PTT effects (**Fig. 43**).

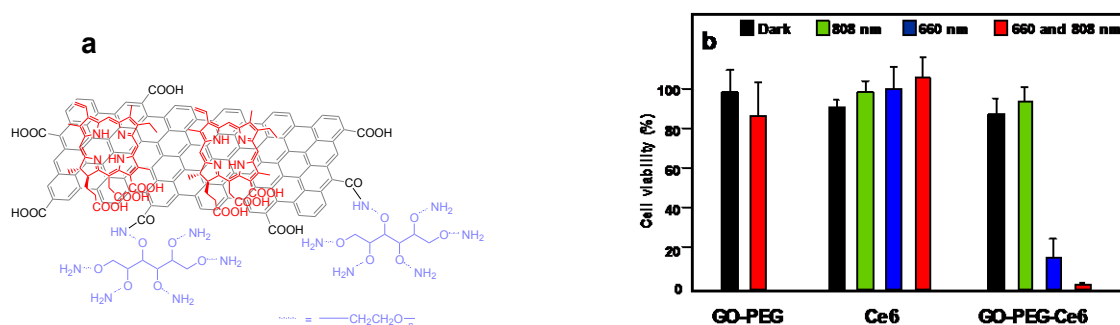


Fig. 43: (a) Schematic structure of GO-PEG-Ce6. (b) Cell viability of KB cells under different light irradiations (Ce6 concentration: $5 \mu\text{M}$). Taken from reference (Tian et al. 2011)

In 2015 Cao and co-workers (Cao et al. 2016) used the same GO-PEG-Ce6 NPs to apply tandem PDT/PTT treatment on the murine breast cancer cell line 4T1. The authors obtained similar results than Tian et al. (*vide supra*). Interestingly, after PTT treatment they observed a greater tumor apparent diffusion coefficient (ADC) value in diffusion-weighted imaging (DWI) maps. Furthermore, after PDT treatment the apparent transverse relaxation rate (R_2^*) was enhanced and allowed blood oxygenation level-dependent magnetic resonance imaging (BOLD MRI). They clearly demonstrated that the tandem DWI and BOLD MRI after PTT/PDT treatment is a very promising tool for monitoring and prognosis.

In 2013, Sahu et al. (Sahu et al. 2013) developed nano-graphene oxide (NGO) coated with pluronic block copolymer to stabilize the NPs in biological fluids. The hydrodynamic size of NGO was $38.4 \pm 3.1 \text{ nm}$, while the hydrodynamic size was $40.6 \pm 2.8 \text{ nm}$ after coating with Pluronic. Methylene Blue (MB) was loaded onto coated NGO (NGO-MB) *via* electrostatic interactions. The maximal MB loading capacity was $22.7 \pm 0.6 \text{ wt}\%$ at the feeding ratio of 70:30 (NGO/MB) with hydrodynamic size of $43.5 \pm 5.1 \text{ nm}$ and large aggregates were observed when the feeding ratio is 50:50. The *in vitro* study (PDT irradiation: CW laser at 655 nm for 3 minutes, PTT irradiation: NIR laser at 808 nm for 3 minutes or dual treatment) was performed with human cervical HeLa cells and mouse normal fibroblast cells (NIH/3T3) and the *in vivo* study (PDT irradiation: CW laser at 650 nm, $\approx 150 \text{ mW/cm}^2$, for 10 minutes, PTT irradiation: NIR laser at 808 nm, 2 W/cm^2 for 3 minutes) with HeLa cells. NGO-MB generates less $^1\text{O}_2$ generation than free MB but, as seen previously, the photodynamic effect is dramatically increased *in vitro* with dual treatment (**Fig.44a**). Concerning the *in vivo* photodynamic effect on mice, the PDT treatment showed a small decrease in tumor growth while it has been significantly reduced by the PTT treatment (incomplete tumor ablation) (**Fig.44b**).

The combination of PDT/PTT treatments revealed a complete regression of tumor even after 15 days of treatment.

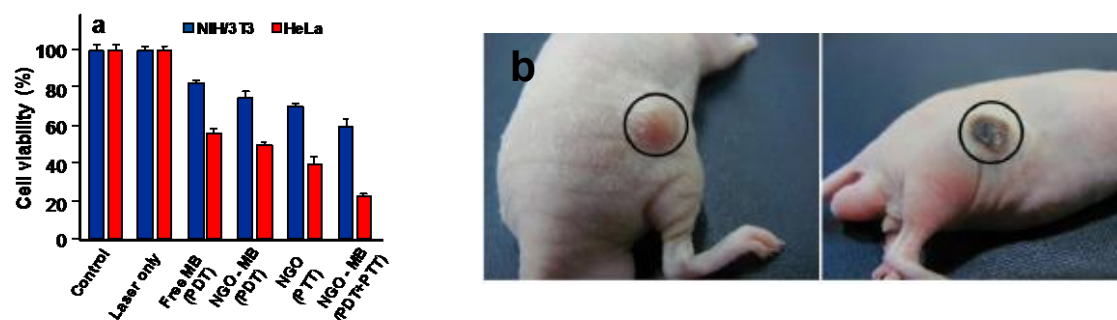


Fig. 44: (a) *In vitro* cytotoxicity effect of MB, NGO and NGO-MB in NIH/3T3 and HeLa cells after PDT, PTT and PDT+PTT treatments. (b) PTT treatment effect on the tumor tissue before (left) and after 1-day irradiation (right). Reused with permission from reference (Sahu et al. 2013)

In two recent publications (Yan et al. 2015a; Yan et al. 2015b), Chen's team described new nanocomposites made from a PEGylated graphene oxide (PEG-GO) loaded by sinoporphyrin sodium (DVDMS, Fig. 45a). The DVDMS loading capacity reaches a maximum of 201.2 wt% in the resulting GO-PEG-DVDMS nanodevice. Interestingly, the fluorescence intensities of GO-PEG-DVDMS are 3-8 times higher than that of the free DVDMS. This can be due to the two sterically hindered porphyrin rings in the PS, one being involved in the $\pi - \pi$ interactions with GO, the other being hanging out and responsible of this phenomena. $^1\text{O}_2$ generation of GO-PEG-DVDMS is slightly lower than that of DVDMS at the same concentration. In the first paper (Yan et al. 2015a), the authors showed a slight dose-dependent cytotoxicity to U87MG cells in the range of 0.3-5 mg/mL of DVDMS. Concerning the PDT efficiency they found that GO-PEG-DVDMS induced a quasi-total cell death at the dose of 5 mg/mL of DVDMS upon 630 nm laser irradiation, after 24 h incubation (Fig. 45b).

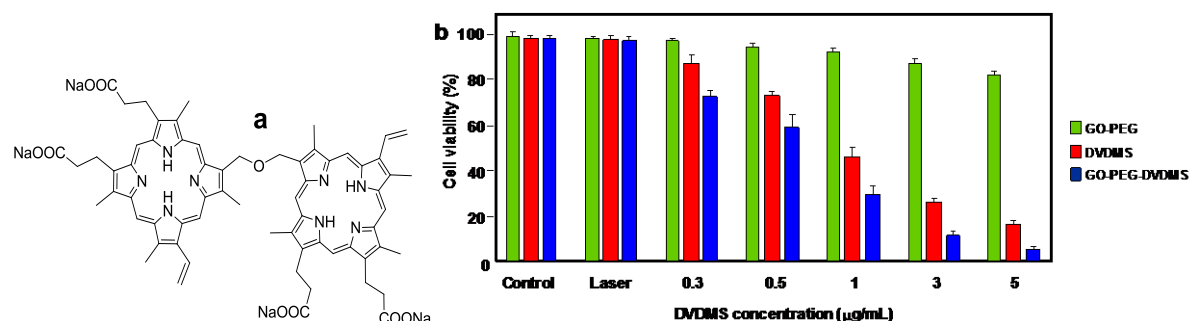


Fig. 45: (a) Chemical structure of DVDMS. (b) Cell viability of U87MG cells incubated with various concentrations of free DVDMS, GO-PEG, or GO-PEG-DVDMS after irradiation by 630 nm laser (2 J). Taken from references (Yan et al. 2015a; Yan et al. 2015b)

In this first paper (Yan et al. 2015a) the *in vivo* PDT experiments were carried out on U87MG tumor-bearing mice with 630 nm laser irradiation at dose of 50 J. The GO-PEG-DVDMS laser group showed a life span longer than 30 days as compared to 22 days for the DVDMS laser group. In the second paper (Yan et al. 2015b) they studied the dual-modality imaging guided synergistic PDT/PTT therapies on PC9 cells for *in vitro* and PC9 tumor-bearing mice for *in vivo*. They noticed a high accumulation of GO-PEG-DVDMS in the tumor tissues due to EPR effect. 24 hours post-injection, PTT alone (808 nm, 1 W/cm² for 10 minutes) induced an increase of tumor temperature up to 57 °C while that of the healthy tissues only reached 32 °C. The synergistic effect of PDT/PTT is shown in Fig. 46.

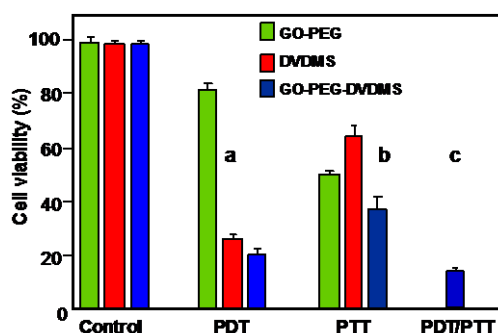


Fig. 46: Effect of irradiation conditions (PDT and/or PTT) on HeLa cell viability by using free DVDMS, GO-PEG, or GO-PEG-DVDMS ($m_{\text{GO-PEG}}:m_{\text{DVDMS}} = 1:2$, GO-PEG concentration = 3 $\mu\text{g}/\text{mL}$). (a) PDT effect (630 nm, 2 J per well). (b) PTT effect (808 nm, 1 W/cm², 3 min per well). (c) Synergetic PDT/PTT effect. Taken from reference (Yan et al. 2015b)

In 2013, Wang et al. developed a new concept of NIR imaging and PTT/PDT therapy (Wang et al. 2013). Upconversion nanoparticles (UCNPs) were obtained as previously described (Bogdan et al. 2011) and treated by poly(allylamine) as surface coating agent. The modified UCNPs were then covalently coupled to NGO *via* carbodiimide cross-linking. The UCNPs-NGO was mixed with ZnPc to give the final composition (Fig. 47) with ZnPc loading amount of 11 wt% and an average diameter of 40 nm as assessed by TEM.

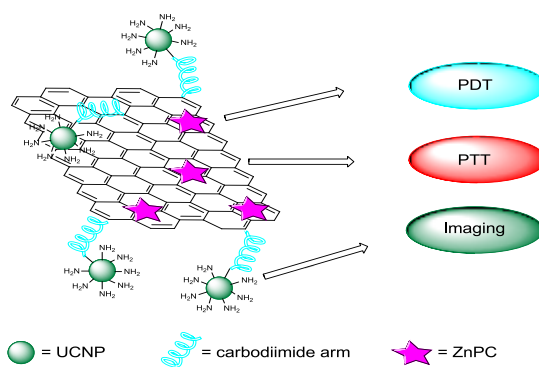


Fig. 47: Schematic illustration of UCNPs-NGO/ZnPC as a multifunctional theranostic nanoplatform for cancer treatment. Taken from reference (Wang et al. 2013)

The $^1\text{O}_2$ production (DPBF (1,3-Diphenylisobenzofuran) method) of UCNPs-NGO/ZnPc was lower than that of ZnPc alone due to the presence of NGO but was still 60%. Furthermore, the good biocompatibility and the low cytotoxicity allowed using these NPs for PDT treatment. Fig. 48 shows the PDT and PTT effects after irradiation. It can be seen clearly that the PDT effect (green) is the main phenomena as compared to the PTT effect (red) but the combined PDT/PTT effect reduced the viability of HeLa cells to 15% (blue).

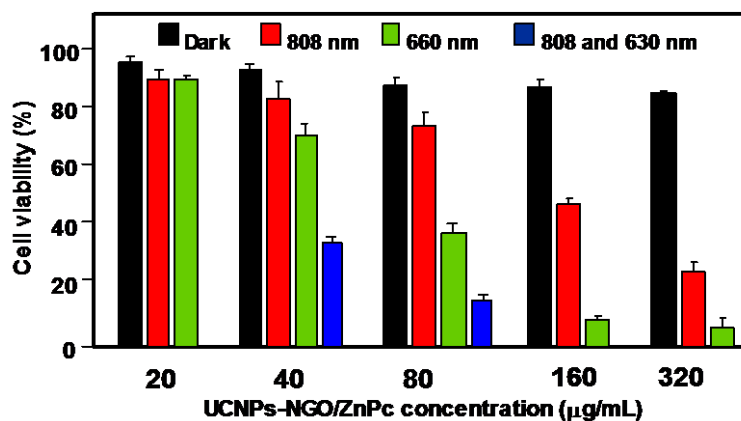


Fig. 48: *In vitro* cell viability assay in HeLa cells of UCNPs-NGO/ZnPc at different concentrations without irradiation (black) and after PDT (green), PTT (red) or combined PDT/PTT (blue) treatments. Taken from reference (Wang et al. 2013)

One year later, the same team (Cho et al. 2013) described the elaboration of GO-HA-Ce6 nanoplatform, as was the case with Li et al., (Li et al. 2013) but based this time on a covalently linked hyaluronic acid-chlorin e6 (HA-Ce6) loaded into the surface of nano-sized GO *via* $\pi - \pi$ and hydrophobic interactions (average hydrodynamic size 441.1 ± 48.8 nm). The objective of this work was to develop an enzyme-activatable theranostic agent by using HA, which is known to preferentially accumulate in the extracellular matrix and to be degraded quickly in the presence of hyaluronidase (HAdase) enzyme. The quenching effect of GO on the fluorescence yield of Ce6 and the cleavage of the glycosidic bonds were demonstrated by comparing the fluorescence emission spectra of GO, HA-Ce6, and GO-HA-Ce6 at a same Ce6 concentration. When GO-HA-Ce6 is treated with HAdase (800 U/mL), the fluorescence signal increased by a factor of 5, indicating a Ce6 release of approximately 21% from the GO surface. The *in vitro* studies (Fig.49) of GO-HA-Ce6 were performed with human lung cancer A549 cells and a synergistic phototherapy effect (PDT: CW laser beam irradiation, 670 nm, 50 mW/cm², 4 J/cm² and PTT: 810 nm, 4 W/cm², 250 J/cm²) was observed, making it an interesting HAdase-activatable theranostic agent combining phototherapy (PDT/PTT) and activatable fluorescence imaging guided tumor for cancer treatment.

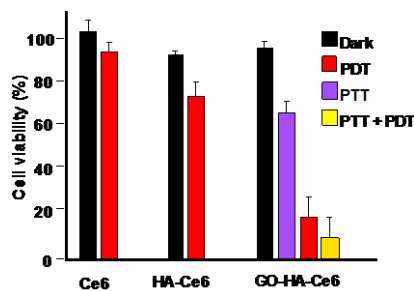


Fig.49: *In vitro* cell viability assay in A549 cells of free Ce6, HA-Ce6 and GO-HA-Ce6 at a same Ce6 concentration (1.8 μM equivalent) without irradiation (black) and after PDT (670 nm, red), PTT (810 nm, purple) or combined PDT/PTT (670 and 810 nm, yellow) treatments. Taken from reference(Cho et al. 2013)

In 2015, Taratula and co-workers (Taratula et al. 2015) described a new targeted graphene-based nanoplatfrom combining phototherapy (PDT/PTT) and imaging guided tumor for ovarian cancer treatment. In a first time, the monosubstituted silicon phthalocyanine Pc(OH)(mob) was loaded onto polypropylenimine generation 4 (PPIG4) dendrimer and the resulted adduct was covalently attached to low-oxygen graphene (LOGr) nanosheets through the amine functions of the dendrimer affording LOGr-Pc. Finally, the luteinizing hormone-releasing hormone (LHRH) peptide was grafted to give LOGr-Pc-LHRH nanoplatfrom. PEGylation and peptide were necessary to increase biocompatibility and to target LHRH receptors overexpressed on the membranes of both primary and metastatic ovarian cancer cells. The hydrodynamic diameter of LOGr-PC-LHRH was 78.3 ± 9.54 nm (≈ 15 and 62 nm for the LOGr and Pc-LHRH respectively) and the Pc loading efficiency onto PPIG4 was approximately 20 wt%. The *in vitro* combination phototherapy effect (PDT/PTT) of the nanoplatfrom ([Pc] = 1.0-4.0 $\mu\text{g}/\text{mL}$ and [LOGr] = 1.8-7.0 $\mu\text{g}/\text{mL}$) towards LHRH-positive A2780/AD ovarian cancer cells has been demonstrated by using a single wavelength (laser diode irradiation at 690 nm, $0.3 \text{ W}/\text{cm}^2$ during 15 minutes) to induce $^1\text{O}_2$ generation by Pc and PTT effect by LOGr (Fig. 50a). The *in vivo* NIR fluorescence imaging was also highlighted after administration of LOGr-Pc-LHRH into mice bearing A2780/AD tumor (Fig. 50b).

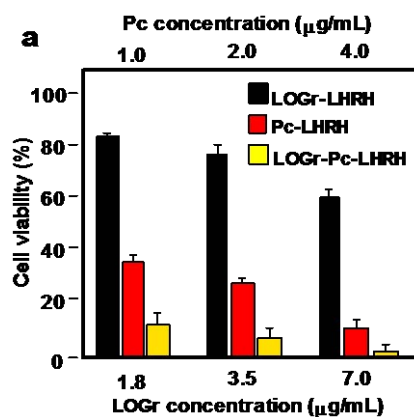


Fig. 50: (a) *In vitro* cell viability assay in A2780/AD cells of LOGr-LHRH, Pc-LHRH and LOGr-Pc-LHRH at different LOGr concentrations after combined PDT/PTT treatment (690 nm, $0.3 \text{ W}/\text{cm}^2$, 15 min). Taken from reference (Taratula et al. 2015)

In the same year, Kim and co-workers (Kim et al. 2015) opted to use core and shell NPs (core@shell) to report a “one-pot synthesis” of a new theranostic nanoplatform combining Raman bioimaging and phototherapy (PDT/PTT). These core@shell NPs are comprised of Au core and graphene oxide nanocolloid (GON) shells, onto which PEG and ZnPc have been grafted and loaded respectively. The PEG was added to have a better colloidal stability in biological media and the PS was loaded onto Au@GON NPs *via* $\pi - \pi$ interactions (loading efficiency $1.9 \cdot 10^6$ ZnPc per NP). The size of the Au@GON NPs, approximately spherical in shape, is 60 ± 15 nm with 2-3 nm GON shell thickness. The *in vitro* evaluation of Raman Imaging and dual PDT/PTT effect of the resulting ZnPc-PEG-Au@GON NPs in human cervical cancer HeLa cells were investigated and demonstrated that these NPs can be intended to conduct Raman Imaging and have a synergistic phototherapy effect (PDT: LED irradiation at 660 nm, 0.2 mW/cm^2 for 10 minutes and PTT: laser irradiation at 808 nm, 0.67 W/cm^2 for 20 minutes) with $^1\text{O}_2$ generation (Fig.51).

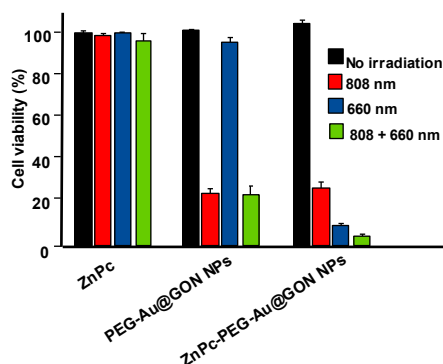


Fig. 51: *In vitro* cell viability assay in HeLa cells of free ZnPc, PEG-Au@GON NPs and ZnPc-PEG-Au@GON NPs without irradiation (black) and after PDT (660 nm, 0.2 W/cm^2 , 10 min, blue), PTT (808 nm, 0.67 W/cm^2 , 20 min, red) or combined PDT/PTT (green) treatments. Taken from reference (Kim et al. 2015)

Graphene is a new material but is already called a «new wonder material» thanks to many advantages. Its structure and its physico-chemical properties make him an excellent candidate for different applications from solar cells to cancer treatment. In the field of PDT, the first paper was published in 2010 and since this date, more than 35 papers have been edited. Thanks to its large surface area, it is possible to use it as an efficient PS carrier. Its π - π structure can easily bind to aromatic PS. Graphene presents also a high dispersability in water and good stability in biological media. We can notice that it is a very good conductor of heat and it can be used to perform both PDT and PTT. One of the disadvantages might be its size compared to small NPs, except nanorods. One of the advantages of the graphene oxide (GO) is its easy dispersability in water and other organic solvents due to the presence of oxygen atoms. Moreover, It is very easy to functionalize it and even one publication describes the covalent binding of Ce6 onto GO. Folic acid, hyaluronic acid, or peptides have already been successfully bound onto GO. Few papers describes the use of reduced graphene oxide (rGO), might be due to its tendency to aggregate.

Table 7 below summarized the data available on the application of graphene NPs with grafted or encapsulated PSs in PDT and/or PTT applications.

Table 7: Application of graphene NPs in PDT and/or PTT

Type of NPs (size, nm)	PS (amount)	NPs-PS interactions	Irradiation conditions	Type of ROS	Cancer cell line		Ref.
					In vitro	In vivo	
Nanosheets (200)	ZnPc (14 wt%)	π - π stacking Hydrophobic	UV band-path filtered Xe light, 60 J/cm ² , 10 min	nd	MCF-7	–	Dong et al. (2010)
Nanosheets (nd)	MB (nd)	nd	Laser 785 nm	¹ O ₂	–	–	Wojtoniszak et al. (2013)
Nanosheets (148)	Ce6 (51.9 wt%)	π - π stacking Hydrophobic	LED 660 nm, 8000 mCd, 30 min	nd	SCC7	SCC7 bearing mice C3H/HeN mice	Miao et al. (2013)
Nanosheets (20–40)	Ce6 (26 wt%)	π - π stacking Hydrophobic	Laser 660 nm, 0.2 W/cm ² , 5 min	ROS ¹ O ₂	HeLa	–	Zeng et al. (2015)
Nanosheets (nd)	Ce6 (160 wt%)	π - π stacking	Laser 660 nm, 2 min	ROS	HeLa	–	Liu et al. (2015a)
Nanosheets (200)	ZnPc (60 wt%)	π - π stacking Hydrophobic	Light 660 nm, 0.15 W/cm ² , 10 min	¹ O ₂	HeLa MCF-7	–	Wu et al. (2014)
Nanosheets (120)	MitoTPP (37.2 wt%)	π - π stacking Electrostatic	LED 650 nm, 10 mW/cm ² , 30 min	¹ O ₂	HeLa	–	Xu et al. (2015)
Nanosheets (nd)	HP (23.6 wt%)	π - π stacking Hydrophobic	Laser 671 nm, 0.1 W/cm ² , 5 min	¹ O ₂	HeLa	–	Zhou et al. (2015)
Nanosheets (300–400)	AdaTPP (nd)	π - π stacking	Visible light	ROS	HeLa OCT-1	HeLa-bearing BALB/c nude mice	Yang et al. (2012)
Nanosheets (80)	AP-Ce6 (23.1 wt%)	π - π stacking	Light 650 nm, 50 mW/cm ² , 20 min	¹ O ₂	HepG2	–	Yan et al. (2014)
Nanosheets (nd)	Ce6 (80 wt%)	π - π stacking Hydrophobic	He-Ne laser 632.8 nm, 30 mW/cm ² , 10 min	nd	MGC803	–	Huang et al. (2011)
Nanosheets (nd)	Ce6 (80 wt%)	π - π stacking Hydrophobic	Laser 671 nm, 30 mW/cm ² , 3 min	¹ O ₂	MGC803	–	Huang et al. (2015)
Nanosheets (78.1)	Ce6 (115 wt%)	π - π stacking Hydrophobic	Laser 670 nm, 1.8 J/cm ²	¹ O ₂	HeLa	–	Li et al. (2013)
Nanosheets (50)	Ce6 (15 wt%)	π - π stacking	Laser 660 nm, 15 J/cm ² , 5 min (PDT); Laser 808 nm, 0.3 W/cm ² , 360 J/cm ² (PTT)	¹ O ₂	KB	–	Tian et al. (2011)
Nanosheets (38.4)	MB (22.7 wt%)	Electrostatic	CW laser 650 nm, 0.15 W/cm ² , 10 min (PDT); NIR laser 808 nm, 2 W/cm ² , 3 min (PTT)	¹ O ₂	HeLa NIH/3T3	HeLa	(Sahu et al. 2013)
Nanosheets (nd)	TSCuPc (27 wt%)	π - π stacking	Laser 650 nm, 3 W/cm ² , 5 min	ROS	HeLa	–	Jiang et al. (2014b)
Nanorods (nd)	TSCuPc (38 wt%)	π - π stacking	Laser 650 nm, 3 W/cm ² , 5 min	ROS	HeLa	–	Jiang et al. (2014a)
Nanosheets (20.5)	DVDMS (100 wt%)	π - π stacking	Laser 630 nm, 50 J (PDT); NIR laser 808 nm, 1 W/cm ² , 10 min (PTT)	¹ O ₂	PC9	PC9 tumor-bearing mice	Yan et al. (2015a)
Nanosheets (50)	DVDMS (201.2 wt%)	π - π stacking Hydrophobic	Laser 630 nm, 50 J	¹ O ₂	U87MG	U87MG tumor-bearing mice	Yan et al. (2015b)
Nanorods (1–5)	ZnMAPc (nd)	nd	Diode laser 676 nm, 98 mW/cm ² , 5 J/cm ²	¹ O ₂	A375	–	Ogobodu et al. (2013a, b, 2015b)
Nanorods (1–5)	ZnMAPc (nd)	nd	602 nm	¹ O ₂	–	–	Ogobodu et al. (2013b)

Table 7: Continued

Type of NPs (size, nm)	PS (amount)	NPs-PS interactions	Irradiation conditions	Type of ROS	Cancer cell line		Ref.
					In vitro	In vivo	
Nanorods (1–5)	ZnMCPPc (nd)	nd	Quartz lamp 600–1000 nm, 28–112 J/cm ² , 5–20 min	¹ O ₂	MCF-7	–	Ogobodu et al. (2015a)
Nanorods (1–5)	ZnOCPC (nd)	nd	610 nm	¹ O ₂	–	–	Ogobodu and Nyokong (2014)
Nanorods (nd)	POR, MYR (nd)	π - π stacking	LED lamp 570 nm (yellow filter), 630 nm (red filter) or 940 nm	¹ O ₂	–	–	Safar et al. (2015)
Nanorods (nd)	Ce6 (11.3 wt%)	π - π stacking	Laser 630 nm, 0.15 W/cm ² , 10 min	nd	HeLa NIH/3T3	–	Xiao et al. (2012)
Nanosheets (40)	ZnPc (11 wt%)	π - π stacking	Laser 630 nm, 50 mW/cm ² , 10 min (PDT); NIR laser 808 nm, 2 W/cm ² , 10 min (PTT)	¹ O ₂	HeLa KB	–	Wang et al. (2013)
Hydrogel shells (35)	AE (nd)	π - π stacking Hydrophobic	Laser 600 nm, 0.2 W/cm ² , 10 min	¹ O ₂	HeLa CHO	–	Chang et al. (2015)
nd (40)	SiNc4 (8.5 wt%)	π - π stacking	Halogen lamp 775 nm, 0.3 W/cm ² , 60 min	ROS ¹ O ₂	HeLa	–	Gollavelli and Ling (2014)
Nanosheets (50)	HPPH (131 wt%)	π - π stacking	Laser 671 nm, 2–8 mW/cm ² , 3 min (in vitro) and 75 mW/cm ² , 20 min (in vivo)	¹ O ₂	4T1	4T1-bearing mice	Rong et al. (2014)
Nanosheets (102.4)	Ce6 (nd)	Grafted with disulfide bond (SS)	CW laser beam 670 nm, 0.1 W/cm ² , 20 J/cm ²	¹ O ₂	A549	–	Cho and Choi (2012)
Nanosheets (441.1)	Ce6 (nd)	Hydrophobic	CW laser beam 670 nm, 0.1 W/cm ² , 20 J/cm ²	¹ O ₂	A549	–	Cho et al. (2013)
Nanosheets (100)	Ce6-Pep (35 wt%)	π - π stacking Hydrophobic	Laser 660 nm, 0.25 W/cm ² , 200 s	¹ O ₂	KB A549 HeLa HaCaT	HeLa-bearing mice	Tian et al. (2015)
Nanosheets (15)	PcSi(OH) (mob) (20 wt%)	Encapsulated into PPIG4 dendrimer	Laser diode 690 nm, 0.3 W/cm ² , 15 min (PDT/PTT, in vitro)	¹ O ₂	A2780/AD	A2780/AD-bearing mice	Taratula et al. (2013, 2015)
Nanocolloid Core@Shell NPs (15)	ZnPc (1.9 10 ⁶ ZnPc/Au@GON NP)	π - π stacking	LED 660 nm, 0.2 W/cm ² , 10 min (PDT); NIR laser 808 nm, 0.67 W/cm ² , 20 min (PTT)	¹ O ₂	HeLa	–	Kim et al. (2015)

NPs nanoparticles, PS photosensitizer, ROS reactive oxygen species, nd not disclosed, ZnPc zinc phthalocyanine, UV ultraviolet, MB methylene blue, Ce6 chlorin e6, MitoTPP 5-(p-(4-bromo)butoxyphenyl)-10,15,20-triphenylporphyrin, HP hematoporphyrin, AdaTPP adamantanyl porphyrin, AP aptamer, CW continuous wave, TSCuPc tetrasulfonic acid tetrasodium salt copper phthalocyanine, DVDMS sinoporphyrin sodium, NIR near-infrared, ZnMAPc zinc monoamino phthalocyanine, ZnMCPPc zinc monocarboxyphenoxy phthalocyanine, ZnOCPC zinc octacarboxy phthalocyanine, POR meso-tetrakis(4-pyridyl)porphyrin tosylate salt, MYR meso-tetrakis(N-myristyl-4-pyridinium)porphyrin tosylate salt, AE chlorophyll derivatives in amaranth extract, SiNc4 silicon naphthalocyanine bis (trihexylsilyloxy), HPPH 2-(1-hexyloxyethyl)-2-devinyl pyropheophorbide- α , SS disulfide, HA hyaluronic acid, Pep peptide, PcSi(OH)(mob) monosubstituted phthalocyanine derivative, PPIG4 polypropylenimine generation 4, GON graphene oxide nanocolloid

6. Conclusion

Nanoparticles (NPs) hold great promise for design of new compounds for PDT. In this field many biodegradable NPs have been formulated with the problem of controlling the NPs' degradation and the release of the PS. Non-degradable NPs such as TiO₂, ZnO, fullerene and graphene are very promising NPs for PDT applications even if they are already well known in the field of photocatalysis. Their small size, low toxicity and easy functionalization make them very good candidates for bio-imaging and cancer therapy (PDT and/or PTT treatments). According to the results presented in this review and in the best of worlds, the ideal approach would allow us to develop theranostic platforms combining both bio-imaging to localize tumor cells and a dual PDT/PTT treatments to eradicate tumor cells by using a single wavelength while minimizing as much as possible the side effects. In order to achieve this ambitious goal, it will be necessary to modify the NP surface with i) a contrast agent suitable for MRI, PET or X-ray imaging, 2) PDT and PTT agents having a photodynamic and photothermal activity in hypoxic and non-hypoxic areas and 3) a vector to target tumor cells.

References of Subchapter I.2

- Ahn J-H and Hong BH. Things you could do with graphene. *Nat Nanotech.* 2014;9:737-47.
- Alvarez MG, Milanesio M, Rivarola V, Durantini E, Batlle A and Fukuda H. Endogenous and exogenous porphyrins as photosensitizers in the Hep-2 human carcinoma cell line. *Cell Mol Biol.* 2009;55:8-14.
- Alvarez MG, Prucca C, Milanesio ME, Durantini EN and Rivarola V. Photodynamic activity of a new sensitizer derived from porphyrin-C-60 dyad and its biological consequences in a human carcinoma cell line. *Int J Biochem Cell Biol.* 2006;38:2092-101.
- Atif M, Fakhar-e-Alam M and Al Salhi MS. Role of sensitivity of zinc oxide nanorods (ZnO-NRs) based photosensitizers in hepatocellular site of biological tissue. *Laser Phys.* 2011;21:1950-61.
- Belen Ballatore M, Spesia MB, Elisa Milanesio M and Durantini EN. Synthesis, spectroscopic properties and photodynamic activity of porphyrin-fullerene C-60 dyads with application in the photodynamic inactivation of *Staphylococcus aureus*. *Eur J Med Chem.* 2014;83:685-94.
- Belik P, Gugel A, Kraus A, Spickermann J, Enkelmann V, Frank G and Mullen K. The Diels-Alder adduct of C-60 and 4,5-dimethoxy-*o*-quinodimethane synthesis, crystal-structure, and donor-acceptor behavior. *Adv Mater.* 1993;5:854-6.
- Benachour H, Seve A, Bastogne T, Frochot C, Vanderesse R, Jasniewski J, Miladi I, Billotey C, Tillement O, Lux F and Barberi-Heyob M. Multifunctional peptide-conjugated hybrid silica nanoparticles for photodynamic therapy and MRI. *Theranostics.* 2012;2:889-904.
- Berg K, Nordstrand S, Selbo PK, Diem TTT, Angell-Petersen E and Hogset A. Disulfonated tetraphenyl chlorin (TPCS2a), a novel photosensitizer developed for clinical utilization of photochemical internalization. *Photochem Photobiol Sci.* 2011;10:1637-51.
- Bingel C. Cyclopropylation of fullerenes. *Chem Ber Recl.* 1993;126:1957-9.
- Blanco E, Shen H and Ferrari M. Principles of nanoparticle design for overcoming biological barriers to drug delivery. *Nat Biotechnol.* 2015;33:941-51.
- Bogdan N, Vetrone F, Ozin GA and Capobianco JA. Synthesis of ligand-free colloiddally stable water dispersible brightly luminescent lanthanide-doped upconverting nanoparticles. *Nano Lett.* 2011;11:835-40.
- Bulin AL, Truillet C, Chouikrat R, Lux F, Frochot C, Amans D, Ledoux G, Tillement O, Perriat P, Barberi-Heyob M and Dujardin C. X-ray induced singlet oxygen activation with nanoscintillator coupled porphyrins. *J Phys Chem C.* 2013;117:21583-9.
- Burlaka AP, Sidorik YP, Prylutska SV, Matyshevska OP, Golub OA, Prylutsky YI and Scharff P. Catalytic system of the reactive oxygen species on the C60 fullerene basis. *Exp Oncol.* 2004;26:326-7.
- Calixto GMF, Bernegossi J, de Freitas LM, Fontana CR and Chorilli M. Nanotechnology-based drug delivery systems for photodynamic therapy of cancer: A review. *Molecules.* 2016;21:Article Number: 342
- Cao JB, An HQ, Huang XL, Fu GF, Zhuang RQ, Zhu L, Xie J and Zhang F. Monitoring of the tumor response to nano-graphene oxide-mediated photothermal/photodynamic therapy by diffusion-weighted and BOLD MRI. *Nanoscale.* 2016;8:10152-9.
- Chang GR, Wang YL, Gong BY, Xiao YZ, Chen Y, Wang SH, Li SK, Huang FZ, Shen YH and Xie AJ. Reduced graphene oxide/amaranth extract/AuNPs composite hydrogel on tumor cells as integrated platform for localized and multiple synergistic therapy. *ACS Appl Mater Interfaces.* 2015;7:11246-56.
- Chang H-I and Yeh M-K. Clinical development of liposome-based drugs: formulation, characterization, and therapeutic efficacy. *Int J Nanomedicine.* 2012;7:49-60.
- Chen W and Zhang J. Using nanoparticles to enable simultaneous radiation and photodynamic therapies for cancer treatment. *J Nanosci Nanotechnol.* 2006;6:1159-66.
- Cho HY, Ansems RBM and Scott LT. Site-selective covalent functionalization at interior carbon atoms and on the rim of circumtrindene, a C₃₆H₁₂ open geodesic polyarene. *Beilstein J Org Chem.* 2014;10:956-68.
- Cho WS, Duffin R, Thielbeer F, Bradley M, Megson IL, Macnee W, Poland CA, Tran CL and Donaldson K. Zeta potential and solubility to toxic ions as mechanisms of lung inflammation caused by metal/metal oxide nanoparticles. *Toxicol Sci.* 2012;126:469-77.

- Cho Y and Choi Y. Graphene oxide-photosensitizer conjugate as a redox-responsive theranostic agent. *Chem Commun.* 2012;48:9912-4.
- Cho Y, Kim H and Choi Y. A graphene oxide-photosensitizer complex as an enzyme-activatable theranostic agent. *Chem Commun.* 2013;49:1202-4.
- Chouikrat R, Seve A, Vanderesse R, Benachour H, Barberi-Heyob M, Richeter S, Raehm L, Durand JO, Verelst M and Frochot C. Non polymeric nanoparticles for photodynamic therapy applications: Recent developments. *Curr Med Chem.* 2012;19:781-92.
- Chu X, Li K, Guo H, Zheng H, Shuda S, Wand X, Zhang J, Chen W and Zhang Y. Exploration of graphitic-C₃N₄ quantum dots for microwave-induced photodynamic therapy. *ACS Biomater Sci Eng.* 2017;3:1836-44.
- Colombeau L, Acherar S, Baros F, Arnoux P, Gazzali AM, Zaghoudi K, Toussaint M, Vanderesse R and Frochot C. Inorganic nanoparticles for photodynamic therapy. *Top Curr Chem.* 2016;370:113-34.
- Constantin C, Neagu M, Ion R-M, Gherghiceanu M and Stavaru C. Fullerene-porphyrin nanostructures in photodynamic therapy. *Nanomedicine.* 2010;5:307-17.
- Couleaud P, Bechet D, Vanderesse R, Barberi-Heyob M, Faure AC, Roux S, Tillement O, Porhel S, Guillemain F and Frochot C. Functionalized silica-based nanoparticles for photodynamic therapy. *Nanomedicine.* 2011;6:995-1009.
- Crane JD, Hitchcock PB, Kroto HW, Taylor R and Walton DRM. Preparation and Characterization of C-60(Ferrocene)₂. *J Chem Soc, Chem Commun.* 1992;24:1764-5.
- D'Souza S, Moeno S and Nyokong T. Effects of ZnO nanohexagons and nanorods on the fluorescence behavior of metallophthalocyanines. *Polyhedron.* 2015;85:476-81.
- De Jong WH and Borm PJA. Drug delivery and nanoparticles: Applications and hazards. *Int J Nanomedicine.* 2008;3:133-49.
- Dong HQ, Dong CY, Ren TB, Li YY and Shi DL. Surface-engineered graphene-based nanomaterials for drug delivery. *J Biomed Nanotechnol.* 2014;10:2086-106.
- Dong HQ, Zhao ZL, Wen HY, Li YY, Guo FF, Shen AJ, Frank P, Lin C and Shi DL. Poly(ethylene glycol) conjugated nano-graphene oxide for photodynamic therapy. *Sci China Chem.* 2010;53:2265-71.
- Fakhar-e-Alam M, Ali SMU, Ibpoto ZH, Kimleang K, Atif M, Kashif M, Loong FK, Hashim U and Willander M. Sensitivity of A-549 human lung cancer cells to nanoporous zinc oxide conjugated with Photofrin. *Lasers Med Sci.* 2012;27:607-14.
- Fakhar-e-Alam M, Firdous S, Atif M, Khan Y, Zaidi SSZ, Suleman R, Rehman A, Khan RU, Nawaz M and Ikram M. The potential applications of ZnO nanoparticles conjugated with ALA and photofrin as a biomarker in HepG2 cells. *Laser Phys.* 2011a;21:2156-64.
- Fakhar-e-Alam M, Kishwar S, Khan Y, Siddique M, Atif M, Nur O and Willander M. Tumoricidal effects of nanomaterials in HeLa cell line. *Laser Phys.* 2011b;21:1978-88.
- Fakhar-e-Alam M, Kishwar S and Willander M. Photodynamic effects of zinc oxide nanowires in skin cancer and fibroblast. *Lasers Med Sci.* 2014a;29:1189-94.
- Fakhar-e-Alam M, Rahim S, Atif M, Aziz MH, Malick MI, Zaidi SSZ, Suleman R and Majid A. ZnO nanoparticles as drug delivery agent for photodynamic therapy. *Laser Phys Lett.* 2014b;11:article id. 025601.
- Fungo F, Otero LA, Sereno L, Silber JJ and Durantini EN. Synthesis of a porphyrin-C-60 dyad for potential use in solar energy conversion. *Dyes Pigm.* 2001;50:163-70.
- Fungo F, Otero LA, Sereno L, Silber JJ and Durantini EN. Synthesis of porphyrin dyads with potential use in solar energy conversion. *J Mater Chem.* 2000;10:645-50.
- Gangopadhyay M, Mukhopadhyay SK, Karthik S, Barman S and Singh NDP. Targeted photoresponsive TiO₂-coumarin nanoconjugate for efficient combination therapy in MDA-MB-231 breast cancer cells: Synergic effect of photodynamic therapy (PDT) and anticancer drug chlorambucil. *Medchemcomm.* 2015;6:769-77.
- Gollavelli G and Ling YC. Magnetic and fluorescent graphene for dual modal imaging and single light induced photothermal and photodynamic therapy of cancer cells. *Biomaterials.* 2014;35:4499-507.

- Goncalves G, Vila M, Portoles MT, Vallet-Regi M, Gracio J and Marques P. Nano-graphene oxide: A potential multifunctional platform for cancer therapy. *Adv Healthc Mater.* 2013;2:1072-90.
- Gu Y (2013) Microwave induced photodynamic therapy. WO2013006176-A1
- Guan M, Dong H, Ge J, Chen D, Sun L, Li S, Wang C, Yan C, Wang P and Shu C. Multifunctional upconversion-nanoparticles-trimethylpyridylporphyrin- fullerene nanocomposite: a near-infrared light-triggered theranostic platform for imaging-guided photodynamic therapy. *Npg Asia Mater.* 2015a;7:e205.
- Guan M, Qin T, Ge J, Zhen M, Xu W, Chen D, Li S, Wang C, Su H and Shu C. Amphiphilic trimethylpyridylporphyrin-fullerene (C-70) dyad: An efficient photosensitizer under hypoxia conditions. *J Mat Chem B.* 2015b;3:776-83.
- Guan MR, Ge JC, Wu JY, Zhang GQ, Chen DQ, Zhang W, Zhang Y, Zou TJ, Zhen MM, Wang CR, Chu TW, Hao XJ and Shu CY. Fullerene/photosensitizer nanovesicles as highly efficient and clearable phototheranostics with enhanced tumor accumulation for cancer therapy. *Biomaterials.* 2016;103:75-85.
- Guo X, Ding R, Zhang Y, Ye L, Liu X, Chen C, Zhang Z and Zhang Y. Dual role of photosensitizer and carrier material of fullerene in micelles for chemo-photodynamic therapy of cancer. *J Pharm Sci.* 2014;103:3225-34.
- Hirsch A. Addition-reactions of buckminsterfullerene (C-60). *Synthesis.* 1995895-913.
- Høgset A, Prasmickaite L, Selbo PK, Hellum M, Engesaeter BB, Bonsted A and Berg K. Photochemical internalisation in drug and gene delivery. *Adv Drug Del Rev.* 2004;56:95-115.
- Hu Z, Li J, Li CY, Zhao SJ, Li N, Wang YF, Wei F, Chen L and Huang YD. Folic acid-conjugated graphene-ZnO nanohybrid for targeting photodynamic therapy under visible light irradiation. *J Mat Chem B.* 2013;1:5003-13.
- Huang P, Wang SJ, Wang XS, Shen GX, Lin J, Wang Z, Guo SW, Cui DX, Yang M and Chen XY. Surface functionalization of chemically reduced graphene oxide for targeted photodynamic therapy. *J Biomed Nanotechnol.* 2015;11:117-25.
- Huang P, Xu C, Lin J, Wang C, Wang XS, Zhang CL, Zhou XJ, Guo SW and Cui DX. Folic acid-conjugated graphene oxide loaded with photosensitizers for targeting photodynamic therapy. *Theranostics.* 2011;1:240-50.
- Huang Y-Y, Sharma SK, Dai T, Chung H, Yaroslavsky A, Garcia-Diaz M, Chang J, Chiang LY and Hamblin MR. Can nanotechnology potentiate photodynamic therapy? *Nano Rev.* 2012;1:111-46.
- Huang Y-Y, Sharma SK, Yin R, Agrawal T, Chiang LY and Hamblin MR. Functionalized fullerenes in photodynamic therapy. *J Biomed Nanotechnol.* 2014;10:1918-36.
- Ion R-M and Brezoi D-V. New Nano-Sized Sensing Drug and Its Clinical Application *Solid State Phenomena.* 2005a;1006:79-82.
- Ion RM. Porphyrinic nano-sensitizers encapsulated into colloidal carriers. *Rom.J.Phys.* 2004;49:867-71.
- Ion RM, Daicovicu D, Filip AG, Clichici S and Muresan A. Oxidative stress effects of fullerene-porphyrin derivatives in photodynamic therapy. *J Porphyrins Phthalocyanines.* 2012;16:870-7
- Ion RM, Fierascu RC, Neagu M, Constantin C and Stavaru C. Porphyrin (TPP)-polyvinylpyrrolidone (PVP)-fullerene (C-60) triad as novel sensitizer in photodynamic therapy. *Sci Adv Mater.* 2010;2:223-9.
- Jia X and Jia L. Nanoparticles improve biological functions of phthalocyanine photosensitizers used for photodynamic therapy. *Curr Drug Metab.* 2012;13:1119-22.
- Jiang BP, Hu LF, Shen XC, Ji SC, Shi ZJ, Liu CJ, Zhang L and Liang H. One-step preparation of a water-soluble carbon nanohorn/phthalocyanine hybrid for dual-modality photothermal and photodynamic therapy. *ACS Appl Mater Interfaces.* 2014a;6:18008-17.
- Jiang BP, Hu LF, Wang DJ, Ji SC, Shen XC and Liang H. Graphene loading water-soluble phthalocyanine for dual-modality photothermal/photodynamic therapy via a one-step method. *J Mat Chem B.* 2014b;2:7141-8.
- Kim YK, Na HK, Kim S, Jang H, Chang SJ and Min DH. One-pot synthesis of multifunctional Au@graphene oxide nanocolloid core@shell nanoparticles for Raman bioimaging, photothermal, and photodynamic therapy. *Small.* 2015;11:2527-35.

- Kotelnikov AI, Rybkin AY, Khakina EA, Kornev AB, Barinov AV, Goryachev NS, Ivanchikhina AV, Peregudov AS, Martynenko VM and Troshin PA. Hybrid photoactive fullerene derivative-ruboxyl nanostructures for photodynamic therapy. *Org Biomol Chem*. 2013;11:4397-404.
- Krishna KV, Menard-Moyon C, Verma S and Bianco A. Graphene-based nanomaterials for nanobiotechnology and biomedical applications. *Nanomedicine*. 2013;8:1669-88.
- Kroto HW, Heath JR, O'Brien SC, Curl RF and Smalley RE. C-60 - Buckminsterfullerene. *Nature*. 1985;318:162-3.
- Laptev VP, Petrov VV, Andreev SM, Panferova NG, Romanova VS and Ovchinnikov AE (2009) Composition for photodynamic therapy of malignant tumors comprises a fullerene amino acid or dipeptide derivative. WO2007075119-A1; RU2323722-C2; US2009012008-A1,
- Lee JC, Kim TY, Kang SH and Shim YK. Synthesis of covalently linked chlorin-fullerene dyads. *Bull Korean Chem Soc*. 2001;22:257-8.
- Lee KP, Trochimowicz HJ and Reinhardt CF. Pulmonary response of rats exposed to titanium dioxide (TiO₂) by inhalation for two years. *Toxicol Appl Pharmacol*. 1985;79:179-92.
- Li F, Park S-J, Ling D, Park W, Han JY, Na K and Char K. Hyaluronic acid-conjugated graphene oxide/photosensitizer nanohybrids for cancer targeted photodynamic therapy. *J Mat Chem B*. 2013;1:1678-86.
- Li Y, Dong HQ, Li YY and Shi DL. Graphene-based nanovehicles for photodynamic medical therapy. *Int J Nanomedicine*. 2015a;10:2451-9.
- Li Z, Pan L-L, Zhang F-L, Zhu X-L, Liu Y and Zhang Z-Z. 5-Aminolevulinic acid-loaded fullerene nanoparticles for in vitro and in vivo photodynamic therapy. *Photochem Photobiol*. 2014;90:1144-9.
- Li Z, Zhang FL, Pan LL, Zhu XL and Zhang ZZ. Preparation and characterization of injectable mitoxantrone poly(lactic acid)/fullerene implants for in vivo chemo-photodynamic therapy. *J Photochem Photobiol B: Biol*. 2015b;149:51-7.
- Liu G, Qin HM, Amano T, Murakami T and Komatsu N. Direct fabrication of the graphene-based composite for cancer phototherapy through graphite exfoliation with a photosensitizer. *ACS Appl Mater Interfaces*. 2015a;7:23402-6.
- Liu XM, Que I, Kong XG, Zhang YL, Tu LP, Chang YL, Wang TT, Chan A, Lowik C and Zhang H. In vivo 808 nm image-guided photodynamic therapy based on an upconversion theranostic nanoplatform. *Nanoscale*. 2015b;7:14914-23.
- Liu Y, Zhang Y, Wang S, Pope C and Chen W. Optical behaviors of ZnO-porphyrin conjugates and their potential applications for cancer treatment. *Appl Phys Lett*. 2008;92:Article Number: 143901.
- Lohani A, Verma A, Joshi H, Yadav N and Karki N. Nanotechnology-based cosmeceuticals. *ISRN Dermatology*. 2014Article ID 843687.
- Lopez T, Ortiz E, Alvarez M, Navarrete J, Odriozola JA, Martinez-Ortega F, Paez-Mozo EA, Escobar P, Espinoza KA and Rivero IA. Study of the stabilization of zinc phthalocyanine in sol-gel TiO₂ for photodynamic therapy applications. *Nanomed Nanotechnol Biol Med*. 2010;6:777-85.
- Lu KQ, He QY, Chen L, Ai BQ and Xiong JW. The comparative PDT experiment of the inactivation of HL60 on modified TiO₂ nanoparticles. *J Nanomater*. 2015Article ID 540247.
- Lucky SS, Soo KC and Zhang Y. Nanoparticles in photodynamic therapy. *Chem Rev*. 2015;115:1990-2042.
- Luo MD, Shen CC, Feltis BN, Martin LL, Hughes AE, Wright PFA and Turney TW. Reducing ZnO nanoparticle cytotoxicity by surface modification. *Nanoscale*. 2014;6:5791-8.
- Maggini M, Scorrano G and Prato M. Addition of azomethine ylides to C-60 - Synthesis, characterization, and functionalization of fullerene pyrrolidines. *J Am Chem Soc*. 1993;115:9798-9.
- Martin N, Sanchez L, Illescas B and Perez I. C-60-based electroactive organofullerenes. *Chem Rev*. 1998;98:2527-47.
- Meier MS and Poplawska M. The addition of nitrile oxides to C60. *Tetrahedron*. 1996;52:5043-52.
- Mermut O, Diamond KR, Cormier JF, Gallant P, Ho N, Leclair S, Marois JS, Noiseux I, Morin JF, Patterson MS and Vernon ML. The use of magnetic field effects on photosensitizer luminescence as a novel probe for optical monitoring of oxygen in photodynamic therapy. *Phys Med Biol*. 2009;54:1-16.

- Miao W, Shim G, Lee S, Lee S, Choe YS and Oh YK. Safety and tumor tissue accumulation of pegylated graphene oxide nanosheets for co-delivery of anticancer drug and photosensitizer. *Biomaterials*. 2013;34:3402-10.
- Milanesio ME, Alvarez MG, Rivarola V, Silber JJ and Durantini EN. Porphyrin-fullerene C-60 dyads with high ability to form photoinduced charge-separated state as novel sensitizers for photodynamic therapy. *Photochem Photobiol*. 2005;81:891-7.
- Milanesio ME, Gervaldo M, Otero LA, Sereno L, Silber JJ and Durantini EN. Synthesis and photophysical properties of Zn(II) porphyrin-C-60 dyad with potential use in solar cells. *J Phys Org Chem*. 2002;15:844-51.
- Monge-Fuentes V, Muehlmann LA and de Azevedo RB. Perspectives on the application of nanotechnology in photodynamic therapy for the treatment of melanoma. *Nano Reviews*. 2014;5:10.3402/nano.v5.24381.
- Novoselov KS, Geim AK, Morozov SV, Jiang D, Zhang Y, Dubonos SV, Grigorieva IV and Firsov AA. Electric field effect in atomically thin carbon films. *Science*. 2004;306:666-9.
- Ogobodu RO, Antunes E and Nyokong T. Physicochemical properties of zinc monoamino phthalocyanine conjugated to folic acid and single walled carbon nanotubes. *Polyhedron*. 2013a;60:59-67.
- Ogobodu RO, Antunes E and Nyokong T. Physicochemical properties of a zinc phthalocyanine-pyrene conjugate adsorbed onto single walled carbon nanotubes. *Dalton Trans*. 2013b;42:10769-77.
- Ogobodu RO, Limson JL, Prinsloo E and Nyokong T. Photophysical properties and photodynamic therapy effect of zinc phthalocyanine-spermine-single walled carbon nanotube conjugate on MCF-7 breast cancer cell line. *Synth Met*. 2015a;204:122-32.
- Ogobodu RO, Ndhunduma I, Karsten A and Nyokong T. Photodynamic therapy effect of zinc monoamino phthalocyanine-folic acid conjugate adsorbed on single walled carbon nanotubes on melanoma cells. *Spectrochim Acta, Pt A: Mol Biomol Spectrosc*. 2015b;137:1120-5.
- Ogobodu RO and Nyokong T. Effect of bovine serum albumin and single walled carbon nanotube on the photophysical properties of zinc octacarboxy phthalocyanine. *Spectrochim Acta, Pt A: Mol Biomol Spectrosc*. 2014;121:81-7.
- Ojha K, Anjaneyulu O and Ganguil AK. Graphene-based hybrid materials: synthetic approaches and properties. *Curr Sci*. 2014;107:397-418.
- Olivo M, Bhuvaneshwari R, Lucky SS, Dendukuri N and Thong PSP. Targeted therapy of cancer using photodynamic therapy in combination with multi-faceted anti-tumor modalities. *Pharmaceuticals*. 2010;3:1507-29.
- Orecchioni M, Cabizza R, Bianco A and Delogu LG. Graphene as cancer theranostic tool: Progress and future challenges. *Theranostics*. 2015;5:710-23.
- Osmond-McLeod MJ, Oytam Y, Osmond RIW, Sobhanmanesh F and McCall MJ. Surface coating protect against the *in vitro* toxicity of zinc oxide nanoparticles in human hepatic stellate cells. *J Nanomed Nanotechnol*. 2014;5:232.
- Pan XB, Xie J, Li Z, Chen MX, Wang MY, Wang PN, Chen L and Mi L. Enhancement of the photokilling effect of aluminum phthalocyanine in photodynamic therapy by conjugating with nitrogen-doped TiO₂ nanoparticles. *Colloids Surf B Biointerfaces*. 2015;130:292-8.
- Pandurangan M and Kim DH. In vitro toxicity of zinc oxide nanoparticles: a review. *J Nanopart Res*. 2015;17:Article Number: 158
- Raccichini R, Varzi A, Passerini S and Scrosati B. The role of graphene for electrochemical energy storage. *Nat Mater*. 2015;14:271-9.
- Rahman M, Akhter S, Ahmad MZ, Ahmad J, Addo RT, Ahmad FJ and Pichon C. Emerging advances in cancer nanotheranostics with graphene nanocomposites: opportunities and challenges. *Nanomedicine*. 2015;10:2405-22.
- Rancan F, Helmreich M, Moelich A, Ermilov EA, Jux N, Roeder B, Hirsch A and Boehm F. Synthesis and in vitro testing of a pyropheophorbide-a-fullerene hexakis adduct immunoconjugate for photodynamic therapy. *Bioconj Chem*. 2007a;18:1078-86.

- Rancan F, Helmreich M, Moelich A, Jux N, Hirsch A, Roeder B and Boehm F. Intracellular uptake and phototoxicity of 3(1),3(2)-didehydrophytychlorin-fullerene hexaadducts. *Photochem Photobiol.* 2007b;83:1330-8.
- Rancan F, Helmreich M, Molich A, Jux N, Hirsch A, Roder B, Witt C and Bohm F. Fullerene-pyropheophorbide a complexes as sensitizer for photodynamic therapy: Uptake and photo-induced cytotoxicity on Jurkat cells. *J Photochem Photobiol B: Biol.* 2005;80:1-7.
- Reddy JA, Allagadda VM and Leamon CP. Targeting therapeutic and imaging agents to folate receptor positive tumors. *Curr Pharm Biotechnol.* 2005;6:131-50.
- Rehman FU, Zhao CQ, Jiang H, Selke M and Wang XM. Photoactivated TiO₂ Nanowhiskers and Tetra Sulphonatophenyl Porphyrin Normoglycemic Effect on Diabetes Mellitus During Photodynamic Therapy. *J Nanosci Nanotechnol.* 2016a;16:12691-4.
- Rehman FU, Zhao CQ, Jiang H, Selke M and Wang XM. Protective effect of TiO₂ nanowhiskers on Tetra Sulphonatophenyl Porphyrin (TSPP) complexes induced oxidative stress during photodynamic therapy. *Photodiagnosis Photodyn Ther.* 2016b;13:267-75.
- Rehman FU, Zhao CQ, Wu CY, Jiang H, Selke M and Wang XM. Influence of photoactivated tetra sulphonatophenyl porphyrin and TiO₂ nanowhiskers on rheumatoid arthritis infected bone marrow stem cell proliferation in vitro and oxidative stress biomarkers in vivo. *Rsc Advances.* 2015;5:107285-92.
- Roblero-Bartolon GV and Ramon-Gallegos E. Use of nanoparticles (NP) in photodynamic therapy (PDT) against cancer. *Gac Med Mex.* 2015;151:85-98.
- Rong PF, Yang K, Srivastan A, Kiesewetter DO, Yue XY, Wang F, Nie LM, Bhirde A, Wang Z, Liu Z, Niu G, Wang W and Chen XY. Photosensitizer loaded nano-graphene for multimodality imaging guided tumor photodynamic therapy. *Theranostics.* 2014;4:229-39.
- Sadjadpour S, Safarian S, Zargar SJ and Sheibani Nr. Antiproliferative effects of ZnO, ZnO-MTCP, and ZnO-CuMTCP nanoparticles with safe intensity UV and X-ray irradiation. *Biotechnol Appl Biochem.* 2016;63:113-24.
- Safar GAM, Gontijo RN, Fantini C, Martins DCS, Idemori YM, Pinheiro MVB and Krambrock K. Enhanced oxygen singlet production by hybrid system of porphyrin and enriched (6,5) single-walled carbon nanotubes for photodynamic therapy. *J Phys Chem C.* 2015;119:4344-50.
- Sahu A, Choi WI, Lee JH and Tae G. Graphene oxide mediated delivery of methylene blue for combined photodynamic and photothermal therapy. *Biomaterials.* 2013;34:6239-48.
- Sega EI and Low PS. Tumor detection using folate receptor-targeted imaging agents. *Cancer Metastasis Rev.* 2008;27:655-64.
- Senthilkumar S, Hariharan R, Suganthi A, Ashokkumar M, Rajarajan M and Pitchumani K. Synergistic photodynamic action of ZnO nanomaterials encapsulated meso-tetra (4-sulfonatophenyl) porphyrin. *Powder Technol.* 2013;237:497-505.
- Sharma SK, Chiang LY and Hamblin MR. Photodynamic therapy with fullerenes in vivo: reality or a dream? *Nanomedicine.* 2011;6:1813-25.
- Shen H, Zhang LM, Liu M and Zhang ZJ. Biomedical applications of graphene. *Theranostics.* 2012;2:283-94.
- Shen Y, Shuhendler AJ, Ye D, Xu J-J and Chen H-Y. Two-photon excitation nanoparticles for photodynamic therapy. *Chem Soc Rev.* 2016;45:6725-41.
- Shi H, Magaye R, Castranova V and Zhao J. Titanium dioxide nanoparticles: a review of current toxicological data. *Part Fibre Toxicol.* 2013;10:Article Number: 15
- Shi JJ, Chen ZY, Wang L, Wang BH, Xu LH, Hou L and Zhang ZZ. A tumor-specific cleavable nanosystem of PEG-modified C60@Au hybrid aggregates for radio frequency-controlled release, hyperthermia, photodynamic therapy and X-ray imaging. *Acta Biomater.* 2016;29:282-97.
- Shi JJ, Wang L, Gao J, Liu Y, Zhang J, Ma R, Liu RY and Zhang ZZ. A fullerene-based multi-functional nanoplatfrom for cancer theranostic applications. *Biomaterials.* 2014;35:5771-84.
- Stallivieri A, Baros F, Arnoux P, Vanderesse R, Barberi-Heyob M and Frochot C, Production of singlet oxygen by nanoparticle-bound photosensitizers, In: Nonell and Flors (eds), *Singlet Oxygen:*

Applications in Biosciences and Nanosciences, Volume 1: The Royal Society of Chemistry, 2016, pp. 209-23.

- Stinchcombe J, Penicaud A, Bhyrappa P, Boyd PDW and Reed CA. Buckminsterfulleride(1-) salts - Synthesis, EPR, and the Jahn-Teller distortion of C-60. *J Am Chem Soc.* 1993;115:5212-7.
- Taratula O, Patel M, Schumann C, Naleway MA, Pang AJ, He HX and Taratula O. Phthalocyanine-loaded graphene nanoplatfrom for imaging-guided combinatorial phototherapy. *Int J Nanomedicine.* 2015;10:2347-62.
- Taratula O, Schumann C, Naleway MA, Pang AJ, Chon KJ and Taratula O. A Multifunctional theranostic platform based on phthalocyanine-loaded dendrimer for image-guided drug delivery and photodynamic therapy. *Mol Pharm.* 2013;10:3946-58.
- Tian B, Wang C, Zhang S, Feng L and Liu Z. Photothermally enhanced photodynamic therapy delivered by nano-graphene oxide. *ACS Nano.* 2011;5:7000-9.
- Tian JW, Ding L, Wang QB, Hu YP, Jia L, Yu JS and Ju HX. Folate receptor-targeted and cathepsin B-activatable nanoprobe for in situ therapeutic monitoring of photosensitive cell death. *Anal Chem.* 2015;87:3841-8.
- Tokuyama H, Yamago S and Nakamura E. Photoinduced biochemical activity of fullerene carboxylic acid. *J Am Chem Soc.* 1993;115:7918-9.
- Vanderesse R, Frochot C, Barberi-Heyob M, Richeter S, Raehm L and Durand JO, Nanoparticles for photodynamic therapy applications, In: Prokop (ed), *Intracellular Delivery: Fundamentals and Applications*: Springer Netherlands, 2011, pp. 511-65.
- Verhille M, Couleaud P, Vanderesse R, Brault D, Barberi-Heyob M and Frochot C. Modulation of photosensitization processes for an improved targeted photodynamic therapy. *Curr Med Chem.* 2010;17:3925-43.
- Voon SH, Kiew LV, Lee HB, Lim SH, Noordin MI, Kamkaew A, Burgess K and Chung LY. In vivo studies of nanostructure-based photosensitizers for photodynamic cancer therapy. *Small.* 2014;10:4993-5013.
- Wang SZ, Gao RM, Zhou FM and Selke M. Nanomaterials and singlet oxygen photosensitizers: potential applications in photodynamic therapy. *J Mater Chem.* 2004;14:487-93.
- Wang X, Yang CX, Chen JT and Yan XP. A dual-targeting upconversion nanoplatfrom for two-color fluorescence imaging-guided photodynamic therapy. *Anal Chem.* 2014;86:3263-7.
- Wang YH, Wang HG, Liu DP, Song SY, Wang X and Zhang HJ. Graphene oxide covalently grafted upconversion nanoparticles for combined NIR mediated imaging and photothermal/photodynamic cancer therapy. *Biomaterials.* 2013;34:7715-24.
- Wang GD, Nguyen HT, Chen H, Cox PB, Wang L, Nagata K, Hao Z, Wang A, Li Z and Xie J. X-ray induced photodynamic therapy: A combination of radiotherapy and photodynamic therapy. *Theranostics.* 2016;6:2295-305.
- Weisman RB and Bachilo SM. Dependence of optical transition energies on structure for single-walled carbon nanotubes in aqueous suspension: An empirical Kataura plot. *Nano Lett.* 2003;3:1235-8.
- Wojtoniszak M, Roginska D, Machalinski B, Drozdziak M and Mijowska E. Graphene oxide functionalized with methylene blue and its performance in singlet oxygen generation. *Mater Res Bull.* 2013;48:2636-9.
- Wu CH, He QM, Zhu AN, Li D, Xu M, Yang H and Liu YY. Synergistic anticancer activity of photo- and chemoresponsive nanoformulation based on polylysine-functionalized graphene. *ACS Appl Mater Interfaces.* 2014;6:21615-23.
- Wu SY, An SSA and Hulme J. Current applications of graphene oxide in nanomedicine. *Int J Nanomedicine.* 2015;10:9-24.
- Wu W, Zhao J, Sun J and Guo S. Light-harvesting fullerene dyads as organic triplet photosensitizers for triplet-triplet annihilation upconversions. *J Org Chem.* 2012;77:5305-12.
- Xia T, Zhao Y, Sager T, George S, Pokhrel S, Li N, Schoenfeld D, Meng H, Lin S, Wang X, Wang M, Ji Z, Zink JI, Madler L, Castranova V and Nel AE. Decreased dissolution of ZnO by iron doping yields nanoparticles with reduced toxicity in the rodent lung and zebrafish embryos. *ACS Nano.* 2011;5:1223-35.

- Xiao HR, Zhu BS, Wang DL, Pang Y, He L, Ma XF, Wang RB, Jin CY, Chen Y and Zhu XY. Photodynamic effects of chlorin e6 attached to single wall carbon nanotubes through noncovalent interactions. *Carbon*. 2012;50:1681-9.
- Xu JS, Zeng F, Wu H, Yu CM and Wu SZ. Dual-targeting nanosystem for enhancing photodynamic therapy efficiency. *ACS Appl Mater Interfaces*. 2015;7:9287-96.
- Xu W, Feng L, Wu YS, Wang TS, Wu JY, Xiang JF, Li B, Jiang L, Shu CY and Wang CR. Construction and photophysics study of supramolecular complexes composed of three-point binding fullerene-trispyridylporphyrin dyads and zinc porphyrin. *PCCP*. 2011;13:428-33.
- Yan L, Chang YN, Yin WY, Tian G, Zhou LJ, Liu XD, Xing GM, Zhao LN, Gu ZJ and Zhao YL. On-demand generation of singlet oxygen from a smart graphene complex for the photodynamic treatment of cancer cells. *Biomater Sci*. 2014;2:1412-8.
- Yan X, Hu H, Lin J, Jin AJ, Niu G, Zhang S, Huang P, Shen B and Chen X. Optical and photoacoustic dual-modality imaging guided synergistic photodynamic/photothermal therapies. *Nanoscale*. 2015a;7:2520-6.
- Yan XF, Niu G, Lin J, Jin AJ, Hu H, Tang YX, Zhang YJ, Wu AG, Lu J, Zhang SL, Huang P, Shen BZ and Chen XY. Enhanced fluorescence imaging guided photodynamic therapy of sinoporphyrin sodium loaded graphene oxide. *Biomaterials*. 2015b;42:94-102.
- Yang K, Zhang SA, Zhang GX, Sun XM, Lee ST and Liu ZA. Graphene in mice: Ultrahigh in vivo tumor uptake and efficient photothermal therapy. *Nano Lett*. 2010;10:3318-23.
- Yang X, Chen L, Qiao X and Fan C. Photo-induced damages of cytoplasmic and mitochondrial membranes by a [C-60] fullerene malonic acid derivative. *Int J Toxicol*. 2007;26:197-201.
- Yang Y, Zhang YM, Chen Y, Zhao D, Chen JT and Liu Y. Construction of a graphene oxide based noncovalent multiple nanosupramolecular assembly as a scaffold for drug delivery. *Chem Eur J*. 2012;18:4208-15.
- Yano S, Hirohara S, Obata M, Hagiya Y, Ogura S-i, Ikeda A, Kataoka H, Tanaka M and Joh T. Current states and future views in photodynamic therapy. *J Photochem Photobiol C*. 2011;12:46-67.
- Yao M, Ma L, Li L, Zhang J, Lim RX, Chen W and Zhang Y. A new modality for cancer treatment-nanoparticle mediated microwave induced photodynamic therapy. *J Biomed Nanotech*. 2016;12:1835-51.
- Yu C, Avci P, Canteenwala T, Chiang LY, Chen BJ and Hamblin MR. Photodynamic therapy with hexa(sulfo-n-butyl)[60]fullerene against sarcoma in vitro and in vivo. *J Nanosci Nanotechnol*. 2016;16:171-81.
- Zeng YP, Yang ZY, Luo SL, Li H, Liu C, Hao YH, Liu J, Wang WD, Li R. Fast and facile preparation of PEGylated graphene from graphene oxide by lysosome targeting delivery of photosensitizer to efficiently enhance photodynamic therapy. *Rsc Advances*. 2015;5:57725-34.
- Zhang W, Gong X, Liu C, Piao Y, Sun Y and Diao G. Water-soluble inclusion complex of fullerene with gamma-cyclodextrin polymer for photodynamic therapy. *J Mat Chem B*. 2014;2:5107-15.
- Zhang Y, Chen W, Wang S, Liu Y and Pope C. Phototoxicity of zinc oxide nanoparticle conjugates in human ovarian cancer NIH: OVCAR-3 cells. *J Biomed Nanotechnol*. 2008;4:432-8.
- Zhao CQ, Rehman FU, Jiang H, Selke M, Wang XM and Liu CY. Titanium dioxide-tetra sulphonatophenyl porphyrin nanocomposites for target cellular bio-imaging and treatment of rheumatoid arthritis. *Sci China Chem*. 2016;59:637-42.
- Zhao CQ, Rehman FU, Yang YL, Li XQ, Zhang D, Jiang H, Selke M, Wang XM and Liu CY. Bio-imaging and photodynamic therapy with tetra sulphonatophenyl porphyrin (TSPP)-TiO₂ nanowhiskers: New approaches in rheumatoid arthritis theranostics. *Sci Rep*. 2015;5:Article Number: 11518.
- Zhou YH, Wang Y, Zhang XL, Peng JJ, Li HM and Li Z. Preparation and characterization of photosensitive and magnetic targeting graphene oxide nanocomposite. *J Nanosci Nanotechnol*. 2015;15:2009-14.
- Zhu Z, Tang Z, Phillips JA, Yang R, Wang H and Tan W. Regulation of singlet oxygen generation using single-walled carbon nanotubes. *J Am Chem Soc*. 2008;130:10856-7.

Chapter II:

Photocatalytic Water Treatment by Modified Titania and Silica Nanoparticles

This chapter describes the synthesis and characterization of modified TiO_2 and SiO_2 NPs with silane reagents and organic PS (P1-COOH and Ce6). The synthesized NPs are tested for their efficiency in the photocatalytic degradation of model pollutants, methylene blue and methyl orange under solar and visible light irradiation. The reactive oxygen species involved in the photocatalytic process under visible light were also studied.

Comparison of two procedures for the design of dye-sensitized nanoparticles targeting photocatalytic water purification under solar and visible light

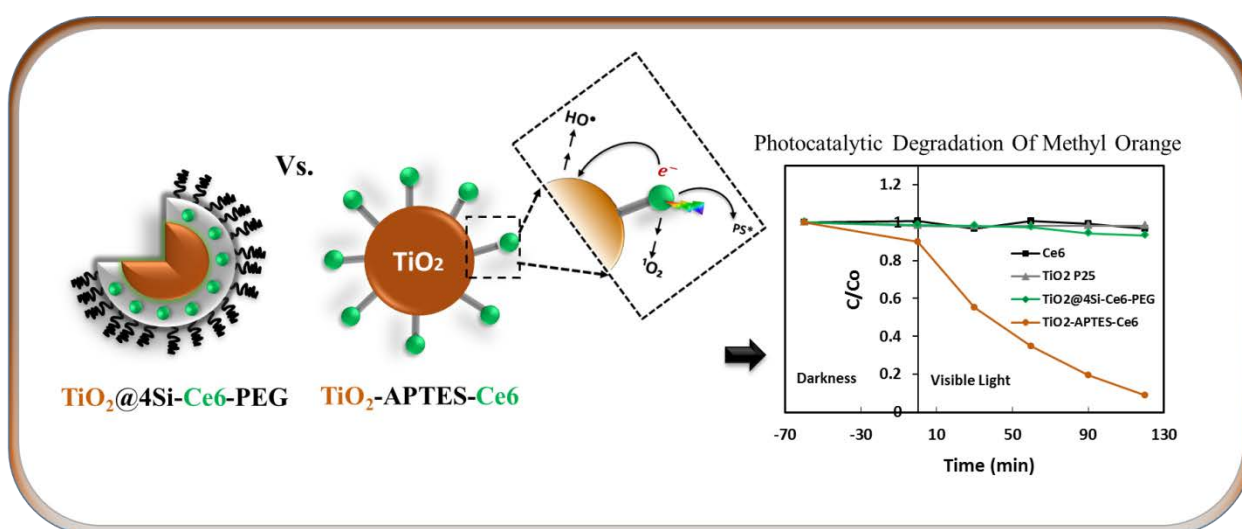
Zahraa Youssef,^{1,2} Philippe Arnoux,¹ Ludovic Colombeau,¹ Joumana Toufaily,² Tayssir Hamieh,²

Céline Frochot,¹ Thibault Roques-Carmes^{1,*}

¹ Laboratoire Réactions et Génie des Procédés (LRGP), UMR CNRS 7274, Université de Lorraine, 1 rue Grandville 54001 Nancy, France.

² Laboratory of Materials, Catalysis, Environment and Analytical Methods, Faculty of Sciences I, Lebanese University, Campus Rafic Hariri, Beirut, Lebanon.

Article submitted to Journal of Photochemistry and Photobiology A: Chemistry



Abstract

In this study, light-sensitive photosensitizers are coupled to titanium dioxide and silicon dioxide nanoparticles in order to develop new kinds of visible light photocatalysts for water treatment applications. The influence of the mode of surface modification of the nanoparticles and the nature of the linked photosensitizer (PS) on the photocatalytic activity under visible and solar light was considered. The TiO₂ Degussa P25 core was either coated with a polysiloxane layer formed by two silane reagents (3-aminopropyl tetraethoxysilane (APTES) and tetraethyl orthosilicate (TEOS) emerging a core-shell nanosystem, or simply modified by APTES alone. In both systems, the APTES mediated the amide covalent linkage between the TiO₂ and the PS. Monocarboxylic tetraphenyl porphyrin (P1-COOH) and chlorin e6 (Ce6) were used to sensitize the TiO₂ semiconductor. Those photosensitizers serve as visible light antenna, thus modifying the UV-limited photoresponse properties of the hybridized TiO₂ nanoparticles. The morphological and structural properties of the synthesized nanosystems were investigated through TEM, XRD, DLS, FTIR, zeta potential and UV–visible absorption. The photophysical properties (fluorescence emission and singlet oxygen formation) were also probed. The photodegradation of two model pollutants, methylene blue and methyl orange, was used to assess the photocatalytic efficiency of the prepared catalysts under simulated solar and pure visible lights. Similar sensitized nanosystems with a SiO₂ core were also prepared and characterized in order to assess the contribution of the support in the photocatalytic degradation process. The reactive oxygen species involved in the photodegradation process were also studied.

Keywords: Photocatalysis; Water treatment; Photosensitizers; Titanium dioxide

1. Introduction

Water bodies such as oceans, lakes and rivers can be contaminated naturally by soil erosion and volcanic eruptions for instance, as well as through man-made doings. Over the last century, human activities have vastly contributed to the emerging water quality concern, threatening the human health and the community. Wastes from industrial, residential, pharmaceutical, agricultural and municipal sources are daily discharged into water [1–4].

Among the available environmental remediation technologies, photocatalysis has gained the spotlight for being an economical and ‘green’ technology targeting a wide variety of water pollutants specially the toxic organic ones [5–11]. Owing to its great UV-photocatalytic activity accompanied by low toxicity, low cost and good chemical and photostability, TiO₂ semiconductor is considered to be one of the most promising photocatalysts for the mineralization of organic pollutants [12–17]. However, due to its wide band gap, the photoresponse of TiO₂ strictly lies in the UV region of light, which hampers the efficient employment of solar irradiation reaching earth containing only 4-6 % of UV light [6, 7]. Besides, the high recombination rate of photogenerated holes and electrons also limits the efficacy of TiO₂ [18–21].

Many efforts have been devoted to develop visible-light activated TiO₂ photocatalysts. Such approaches include transition metal and non-metal doping, ion implantation, semiconductor coupling and dye-sensitization [21–23]. The photosensitization of the surface of titania by organic dyes extends the former’s absorption profile towards the visible zone of light. Chlorophylls and their derivatives already occur in natural systems and are involved in many vital processes such as photosynthesis. Based on their primary role in plant photosynthesis and efficient light harvesting capability, the use of porphyrins and chlorins for TiO₂ sensitization appears attractive. On the one hand, porphyrins are macrocyclic molecules with a structure stabilized by highly delocalized π electrons system. On the other hand, chlorin e6 (Ce6) is also considered as a promising photosensitizer due to its high sensitizing efficiency. Both PSs exhibit an intensive visible light absorption capacity in the region between 400-800 nm. Although Ce6 PS embraces the required properties for the design of an efficient Ce6/TiO₂ system for photocatalytic water treatment, yet, to our best knowledge, no such application is witnessed. However, this system has been efficiently employed in dye-sensitized solar cells (DSSC) for photovoltaic applications [24–26].

Photosensitizers can be linked to the surface of titania either by adsorption or by covalent coupling. Most of the PS/TiO₂ systems in the literature rely on the physical adsorption mode for connecting the PS to the TiO₂ nanoparticles (NPs). Those systems proved their efficiency in the

photocatalytic degradation of a wide range of pollutants [27, 28]. Though, linking the PS to titania by the means of physical adsorption may jeopardize the stability and the photocatalytic efficiency of such systems as the PS may easily desorb from the surface of TiO_2 during the photocatalytic process [22]. To overcome this issue, a covalent bond established between the PS and the TiO_2 NPs *via* an anchoring group is thought to be appealing. Such anchoring group can be primarily attached either to the PS or to TiO_2 itself. Several porphyrins holding anchoring groups could create a steady covalent bond with the surface of TiO_2 upon sensitization. However, it seems complicated and time-consuming to synthesize such kinds of PSs [29, 30]. The covalent bonding can be performed between the TiO_2 and the PS *via* carboxyl, phosphonato, amido or silyl functionalities primarily attached to the catalyst surface. Among those, silyl anchoring groups draw much curiosity for their unique properties of upholding a covalent connection that reveals no dissociation or de-chelation. In addition, the high affinity between the hydroxyl groups occupying the surface of TiO_2 and the silyl functionalities supports the choice of silyl anchoring groups for the surface modification of TiO_2 . As a result, chemically inert Ti-O-Si bonds are established between the PS and titania [19, 31–34].

In the light of these deliberations, monocarboxylic tetraphenyl porphyrin (P1-COOH) and chlorin e6 (Ce6) were chosen to sensitize TiO_2 P25 NPs in order to extend the photoresponse of titania to the visible light region. In this work, the influence of the nature of the PS and the mode of surface modification of TiO_2 were studied. The titania was modified *via* two silanization approaches for studying the effect of the surface modification and the mode of silanization. The first approach is the core-shell nanosystem constituting of a TiO_2 core encapsulated in a polysiloxane matrix molded by the two silane reagents, *i.e.* 3-aminopropyl triethoxysilane (APTES) and tetraethyl orthosilicate (TEOS) [35]. In the second approach, only APTES reagent was used to silanize TiO_2 . The PSs were linked to the surface of both nanosystems through grafting *via* an amide covalent bond. To explore the effect and the contribution of the catalyst support, non-photoactive SiO_2 NPs, are modified and sensitized following a similar approach than those employed with TiO_2 . The photocatalytic efficiency of the prepared catalysts was evaluated towards the degradation of two model pollutants, *i.e.* methylene blue (MB) and methyl orange (MO), under simulated solar and pure visible light sources. The reactive oxygen species involved in the photocatalytic process were also investigated.

2. Experimental procedures

2.1. Materials

The titanium dioxide used was commercial Degussa P25 constituted of 75 % anatase and 25 % rutile. It possessed a BET specific surface area of $50 \text{ m}^2 \text{ g}^{-1}$ and a diameter of about 21 nm. Silicon

dioxide nanoparticles (amorphous, 10-20 nm particle size), 3-aminopropyl triethoxysilane (APTES), tetraethyl orthosilicate (TEOS), Poly(ethylene glycol) bis(carboxymethyl) ether (PEG 250-COOH), triethylamine (TEA), N-hydroxysuccinimide (NHS), dimethyl sulfoxide (DMSO), dichloromethane (DCM), N,N'-dicyclohexylcarbodiimide (DCC) and 1-hydroxybenzotriazole (HOBt) were purchased from Aldrich. Diethylene glycol (DEG) and *N*-(3-dimethylaminopropyl)-*N'*-ethylcarbodiimide hydrochloride (EDC) were bought from Alfa Aesar. Dimethylformamide (DMF) was supplied by Fisher chemical. The photosensitizers (PS) employed in those experiments were monocarboxylic tetraphenylporphyrin (P1-COOH, Porphychem) Chlorin e6 (Ce6, Frontier Scientific). Methylene blue (MB, Fluka) and methyl orange (MO, Sigma-Aldrich) were used as model pollutants. Singlet oxygen sensor green (SOSG) and hydroxyphenyl fluorescein (HPF) probes were purchased from Invitrogen and Molecular Probes, respectively. Titania and silica nanoparticles were used without additional purification.

2.2. Preparation of the photosensitizer-nanoparticles

2.2.1. Activation of the photosensitizers

An equivalent of porphyrin P1-COOH (**Fig. 1A**) was activated with an excess of both three equivalents of EDC and NHS. The reaction was conducted under an inert atmosphere in dichloromethane (DCM) at 40 °C for 4 hours. The crude product was further purified by silica column (**Fig. S1** in the supporting information).

Concerning the coupling of Ce6 (**Fig. 1A**), in order to activate only one carboxyl group of Ce6, 1.2 equivalents of both of DCC and HOBt were added to one equivalent of Ce6 and stirred in dimethylformamide (DMF) at room temperature for one hour (**Fig. S2** in the supporting information).

2.2.2. Synthesis of the core-shell functionalized silica-based nanoparticles

Firstly, a polysiloxane shell was grown around the TiO₂ NPs. The NPs (1 mmol, 10 mM) were dispersed in 100 mL diethylene glycol (DEG) for 1 hour at 40 °C. 44.5 μL (0.2 mmol) of TEOS and 70 μL (0.3 mmol) of APTES were added into the TiO₂ dispersion while stirring at 40 °C. One hour later, 170 μL of a DEG solution (0.2 mM TEA, 10 mM water) was added. The dispersion was stirred for about 10 hours and the same volumes of silane reagents and DEG solution were added in the same order. The growth of the polysiloxane layer on the TiO₂ core was induced by the hydrolysis-condensation of those two silane reagents: APTES and TEOS (ratio APTES/TEOS = 1.5) in the presence of a basic triethylamine (TEA) catalyst. The whole pre-mentioned process of the addition of

the silane reagents and TEA was repeated for three more times. Between the single additions, the dispersion was left under stirring for 12 hours at 40 °C (**Fig. S3** of the Supporting information).

Secondly, the photosensitizer was grafted into the polysiloxane layer. Hence, prior to the addition of the fourth portion of silane reagents (89 μL TEOS, 140 μL APTES and 340 μL TEA solution in DEG), a solution containing the activated photosensitizer (0.02 mmol) and 140 μL of APTES (0.6 mmol, corresponding to the amount of APTES assigned for the last addition, $\text{APTES}^{4\text{th}} / \text{PS} = 30$) dissolved in 3 mL of DMSO was prepared and stirred overnight at room temperature. After TEOS, the solution containing the APTES-PS was added instead of free APTES. After the addition of all the silane reagents and the DEG solution, the dispersion was left under stirring at 40 °C for 48 hours. Highly hydrophilic PEG-250 was then coupled to the NPs covalently *via* an amide bond between the free amine groups of APTES and the carboxylic groups of the PEG. An excess of PEG-250 (0.6 mmol) was added to a 5 mL solution of DEG containing EDC (6 mmol, 1 PEG / 10 EDC). The two components were stirred together for 15 min. Then, the excess of NHS (12 mmol, 1 PEG / 20 NHS) was added and they were all left under stirring for an hour at room temperature. The mixture was added to the TiO_2 dispersion and stirred overnight at room temperature to produce the grafting of activated PEG-250 onto the functionalized NPs (**Fig. 1B** and **Fig. S3** in the supporting information). To assure better solid-phase precipitation of the PEGylated NPs, about 350 mL of acetone were added into the dispersion. The solvent was discarded by vacuum filtration. The dried PEGylated NPs were re-dispersed in Milli-Q water, and were washed thoroughly several times with water, and a final time with ethanol. Finally, the hybrid NPs were centrifuged at 4000 rpm for 20 min and dried in the vacuum oven at 60 °C. The resultant samples were named as $\text{TiO}_2@4\text{Si-PS-PEG}$. It should be noted that before PEGylation, in the particular case of core-shell NPs coupled to P1-COOH, half of the content of the batch was taken and recovered and PEG-250 was only coupled to the other half. This was done for the aim of comparing and investigating the role of PEG.

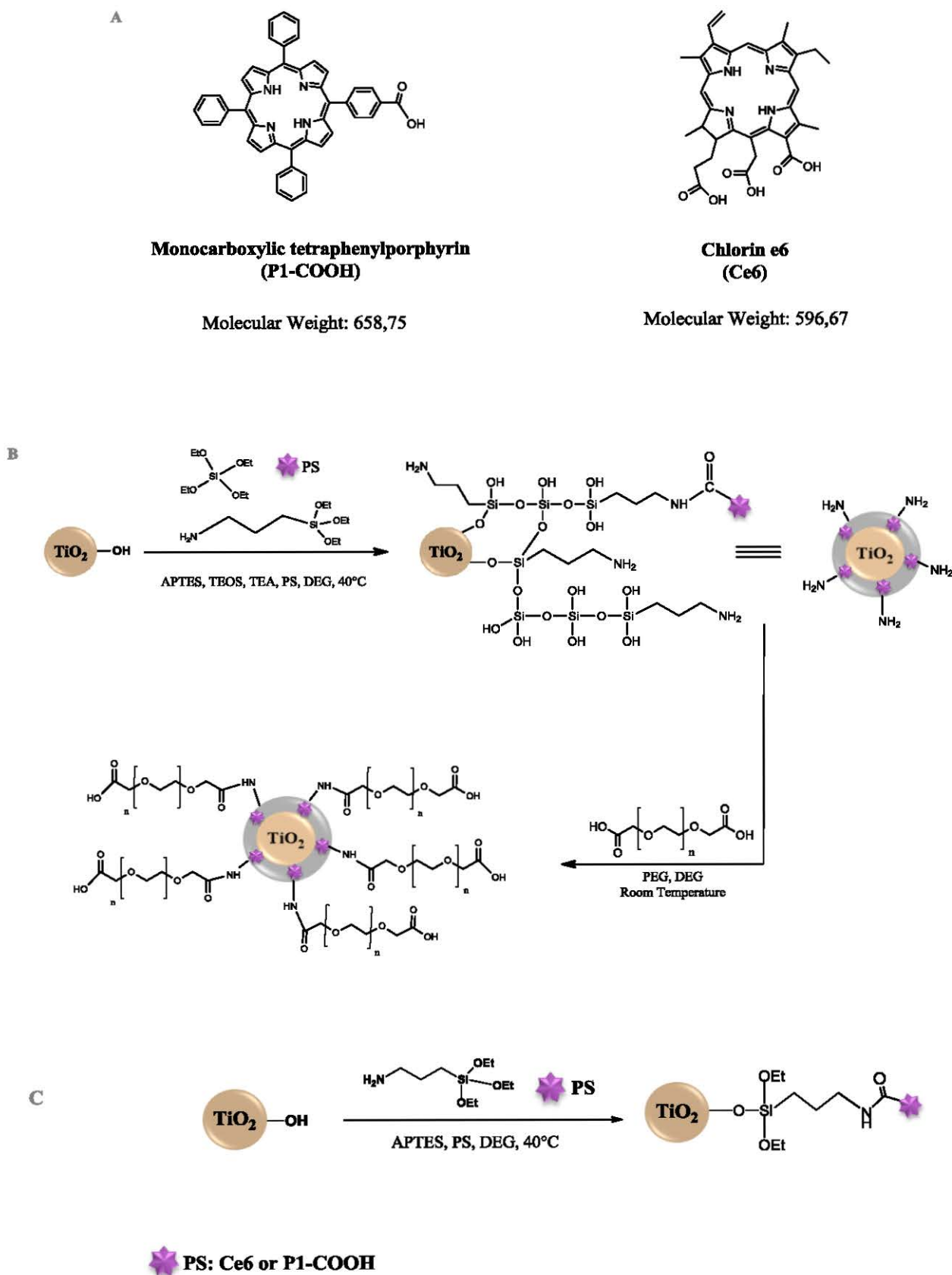


Fig.1: (A) The molecular structures of P1-COOH and Ce6 photosensitizers. (B) The strategy of preparation of $\text{TiO}_2@4\text{Si-PS-PEG}$ NPs. (C) The strategy of preparation of $\text{TiO}_2\text{-APTES-PS}$ NPs.

2.2.3. Preparation of APTES modified hybrid NPs

In a simpler approach for functionalizing the NPs, TiO₂ NPs were modified by one silane reagent, *i.e.* APTES. Thus, the surface of titania would not be totally coated or embedded within a shell. The quantity of grafted APTES onto the NPs was assessed by modifying the surface of TiO₂ by different amounts of APTES and studying the effect of this surface modification on the BET specific surface area, the point of zero charge and the photocatalytic activity of the material (See [Annex I](#)). Similarly, to attain the photosensitizer-nanoparticle coupling *via* the APTES bridge, a 3 mL of DMSO solution with APTES (0.375 mmol, 87.5 μ L, APTES / PS = 30) and PS (0.0125 mmol) was prepared as precursor and stirred overnight at room temperature. The TiO₂ NPs (1 mmol, 10 mM) were dispersed in 100 mL of DEG for 1 hour at 40 °C. The APTES-PS solution was then added into the TiO₂ dispersion. The final mixture was left under continuous stirring for 48 hours at 40 °C. Those NPs were recovered similarly to the core-shell ones. About 350 mL of acetone were added into the batch to enhance the precipitation of the hybrid NPs. Then, the solvent was removed by vacuum filtration and the obtained NPs were washed with water and ethanol to be finally centrifuged at 4000 rpm for 20 min and dried under vacuum at 60 °C ([Fig. 1C](#) and [Fig. S4](#) in the supporting information). The as-synthesized materials were denoted as TiO₂-APTES-PS.

2.2.4. Control nanoparticles

The term ‘control nanoparticles’ was assigned to the NPs modified either by APTES alone or enclosed within a polysiloxane layer in the absence of any photosensitizer molecule. They were typically synthesized as mentioned above but without the step of PS coupling. The control NPs were referred to as TiO₂@4Si-PEG for core-shell NPs and as TiO₂-APTES for the APTES-modified NPs.

2.2.5. Silicon dioxide NPs: silane modification and PS grafting

Amorphous silicon dioxide nanoparticles were also used in this study for comparative reasons. The SiO₂ NPs were functionalized *via* the two pre-mentioned approaches under the same conditions as for TiO₂, *i.e.* core-shell and simple APTES modification, and were sensitized by Ce6 PS ([Fig. S3](#) and [S4](#) in the supporting information).

2.3. Characterization of the modified NPs

2.3.1. Physico-chemical characterizations

The hydrodynamic diameters of the nanoparticles were measured by dynamic light scattering (DLS) using an HPPS setup (High Performance Particle Sizer) from Malvern. For the measurements, the NPs were dispersed in Milli-Q water. The zeta-potential of the NPs was determined using a Zetasizer NanoZS equipped with a He-Ne laser at 633 nm (Malvern). The NPs were first dispersed in milli-Q water, and then, diluted in an aqueous solution of NaCl (0.01 M) adjusted to the required pH. The transmission electronic microscopy (TEM) and high-resolution TEM (HR-TEM) imaging were realized on a JEOL Atomic Resolution 200F cold FEG (TEM / STEM) instrument. The samples were prepared by administering the NP suspension onto a 300-mesh Formvar-coated copper grid that had been previously hydrophilized under UV light (Electron Microscopy Sciences, Hatfield, PA). FTIR spectra were recorded on a FTIR ATR BRUCKER instrument between 400 and 4000 cm^{-1} . To analyze the crystallinity of the NPs, an X-ray diffractometer with Cu $K\alpha$ radiation ($\lambda = 0.15406$ nm) was used.

2.3.2. Photophysical measurements

The absorption spectra were recorded on a UV-3600 UV-visible double beam spectrophotometer (Shimadzu). The measurements were performed in quartz cuvettes with an optical path of 10 mm. The wavelength range was 200–800 nm.

The fluorescence spectra were recorded on a Fluorolog FL3-222 spectrofluorimeter (HORIBA Jobin Yvon) equipped with a 450 W Xenon lamp, a thermo-stated cell compartment (25 °C), a UV-visible photomultiplier R928 (Hamamatsu), and an InGaAs infrared detector (DSS-16A020L Electro-Optical System Inc). The excitation beam was diffracted by a double ruled grating SPEX monochromator (1200 grooves/mm blazed at 330 nm). Singlet oxygen emission was detected through a double ruled grating SPEX monochromator (600 grooves/mm blazed at 1 μm) and a long-wave pass (780 nm). All spectra were measured in 4 faces quartz cuvette. All the emission spectra (fluorescence and singlet oxygen luminescence) were displayed with the same absorbance (less than 0.2) with the lamp and photomultiplier correction.

The generation of singlet oxygen ($^1\text{O}_2$) upon the excitation of the hybrid NPs was determined either directly, as mentioned above, or indirectly through the use of a chemical probe. Singlet oxygen sensor green (SOSG) is a chemical probe that possesses a great selectivity for $^1\text{O}_2$ and shows no appreciable response to other reactive oxygen species, including hydroxyl radical (HO^\bullet), superoxide ($\text{O}_2^{\bullet-}$) and nitric oxide (NO^\bullet). Before reacting with singlet oxygen, this probe initially exhibited weak

blue fluorescence with excitation peaks at 372 and 393 nm, and emission peaks at 395 and 416 nm. However, after excitation at 504 nm and in the presence of $^1\text{O}_2$, it emitted a green fluorescence at 525 nm. Besides the detection of $^1\text{O}_2$, we were interested in investigating the possibility of the formation of hydroxyl radicals (HO^\bullet), upon the excitation of the hybrid NPs. Another chemical probe, hydroxyphenyl fluorescein (HPF), which is capable of detecting HO^\bullet , was used for this purpose. HPF is a fluorescein derivative. It is non-fluorescent until it reacts with the HO^\bullet or peroxyxynitrite anion. Upon oxidation, HPF exhibited bright green fluorescence at 515 nm after excitation at 490 nm, making it compatible with any instrument that can detect fluorescein.

The experiments for the detection of $^1\text{O}_2$ and HO^\bullet species were conducted under the following conditions. A 3 mL dispersion of the TiO_2 or SiO_2 sensitized by Ce6 and its negative control, *i.e.* surface modified non-sensitized TiO_2 or SiO_2 NPs, were prepared in Milli-Q water at a concentration of 10 $\mu\text{g}/\text{mL}$. As for Ce6 PS, a 3 mL of an aqueous solution of 1 μM was diluted in water from a 4 mM Ce6 solution prepared in DMSO. The initial concentration of HPF and SOSG probes was 5 mM. 3 μL of HPF or SOSG were added to the prepared NP's dispersion. The final concentration of probe was equal to 5 μM . The UV-Visible absorption spectrum of each sample was recorded prior to the fluorescence experiments. The excitation wavelengths chosen were 420 nm, 450 nm and 492 nm to record the fluorescence of the NPs, HPF and SOSG, respectively. The fluorescence was recorded between 510 and 610 nm for SOSG, and 460 and 630 nm for HPF. In the case of SOSG, seven cycles of excitation were applied on the sample: at 492 nm during 100 s to excite SOSG with a detection at 525 nm, and then, at 420 nm during 30 s to excite Ce6 with a detection at 670 nm. Similarly, for HPF, seven cycles of excitation were applied on the sample: at 450 nm during 85 s to excite HPF with a detection at about 414 nm, and then, at 420 nm during 30 s to excite Ce6 with a detection at 670 nm.

2.4. Photocatalytic tests

The photocatalytic efficiency of the NPs was evaluated towards the degradation of two model pollutants (**Annex II**), namely methylene blue (MB) in the case of TiO_2 NPs sensitized by P1-COOH PS and methyl orange (MO) in the case of TiO_2 and SiO_2 NPs sensitized by Ce6 PS. Some of the photocatalytic tests were performed under simulated solar light and others under pure visible light.

2.4.1. Solar light

The photocatalytic experiments under simulated solar light were performed as follows. 30 mg of the NPs were dispersed and magnetically stirred in an aqueous solution of model pollutants (MO or

MB, 10 mg L⁻¹, 30 mL) in a 50 mL crystallizer. The dispersion was kept under stirring in the dark for 1 hour in order to attain the equilibrium between the rates of adsorption and desorption of the pollutant on the surface of the NPs [13]. The reaction media was illuminated with two neon tubes placed horizontally 3 cm far from both sides of the crystallizer (**Fig. S5** in the supporting information). The two JBL neon tubes T5 Solar Ultra Color (24 Watts, 438 nm) were used to closely simulate solar light with a total fluence of about 5 mW cm⁻² reaching the reaction media. The photocatalytic experiments were conducted at room temperature and without bubbling oxygen or adding any oxidant. To monitor the degradation of the pollutant an aliquot of the suspension at defined time intervals was taken and centrifuged to separate the catalyst from the solution. Quantitative determination of MB and MO concentrations was performed through measuring their absorption at 664 and 463 nm, respectively, with a UV–Vis spectrophotometer.

2.4.2. Visible light

The degradation of MO was employed to evaluate the photocatalytic efficiency of TiO₂ and SiO₂ NPs sensitized by Ce6 under pure visible light. The source of visible light was an OmniCure[®] S2000 platform equipped with a 200 W lamp with an emission wavelength ranging from 250 to 500 nm. The UV emission of the lamp (below 400 nm) was filtered out by a polycarbonate plate placed between the light source and the reaction medium. The irradiation fluence of the light emerging from the lamp was 500 mW cm⁻². However, the crystallizer was placed 30 cm away from the light source (**Fig. S6** of the supporting information), so the actual irradiation fluence of the light reaching the reaction media was less than 500 mW cm⁻². As previously described, 30 mg of NPs were dispersed in a 30 mL aqueous solution of MO (10 mg L⁻¹), magnetically stirred in dark for 1 hour, then exposed to visible light for MO photodegradation assay. Similarly, the degradation of MO was checked by measuring the absorption of MO at 463 nm at defined time intervals by the means of a UV–Vis spectrophotometer.

3. Results and discussion

3.1. Characterization of the modified catalysts

3.1.1. Transition electron microscopy (TEM) and high resolution-TEM (HR-TEM)

To investigate the morphology of the NPs, TEM images of bare and silanized TiO₂ coupled to Ce6 are performed (**Fig. 2** and **Fig. S7** in the supporting information). Upon silanization and sensitization, TiO₂-APTES-Ce6 and TiO₂@4Si-Ce6-PEG NPs seem to possess a similar morphology

as that of TiO_2 . However, the size of the NPs slightly changes from about 21 nm in the case of bare TiO_2 to about 25 and 30 nm in the case of TiO_2 -APTES-Ce6 and $\text{TiO}_2@4\text{Si-Ce6-PEG}$ NPs, respectively. The conservation of the crystalline structure of the TiO_2 core through all the modifications is also validated by TEM and HRTEM. For $\text{TiO}_2@4\text{Si-Ce6-PEG}$ NPs, the ‘core-shell’ structure can be evidenced from the pictures (**Fig. 2B, C**). The amorphous silica matrix coating the TiO_2 core is about 3-5 nm thick (**Fig. 2D**).

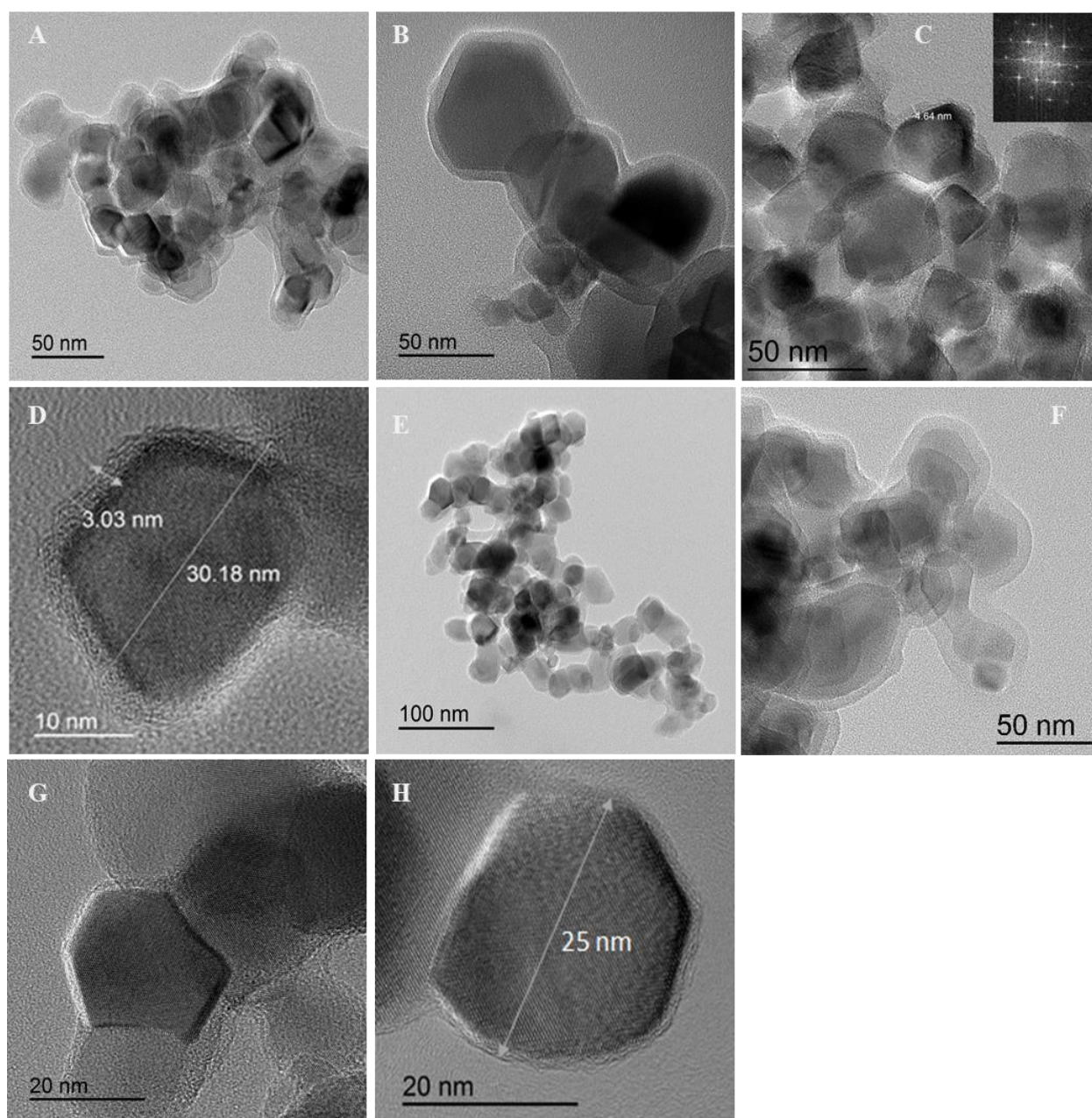


Fig. 2: TEM and HRTEM (insets) images of (A-D) $\text{TiO}_2@4\text{Si-Ce6-PEG}$ NPs, and (E-H) TiO_2 -APTES-Ce6 NPs.

3.1.2. X-ray diffraction (XRD)

XRD analysis is used to investigate the crystallinity and the crystalline phases of the modified NPs. The Fig. 3 displays the XRD patterns of the bare TiO₂ P25 and the nanosystems modified by APTES alone or encapsulated within a silica shell. The employed Degussa P25 titanium dioxide is constituted of a mixture of 75 % anatase and 25 % rutile crystalline phases. It appears that all the diffraction patterns corresponding to the silanized TiO₂ NPs (TiO₂-APTES and TiO₂-APTES-Ce6 NPs) and to the core-shell systems (TiO₂@4Si-PEG and TiO₂@4Si-Ce6-PEG NPs) display all the diffraction peaks originally reported by the unmodified P25 powder. Those diffraction peaks that are localized at $2\theta = 25.42^\circ$, 37.96° , 48.54° , 55.12° , 62.8° , 69° , 70.52° and 75.3° correspond, respectively, to the (101), (004), (200), (105), (211), (204), (116), (220) and (215) planes of the anatase phase (JCPDS No. 84-1286). In addition, the diffraction peaks that are situated at $2\theta = 27.56^\circ$, 36.22° and 41.32° are assigned, respectively, to the (110), (101) and (111) planes of the rutile phase (JCPDS No. 88-1175). Neither shift nor modification can be witnessed in the diffraction peaks of the XRD patterns of TiO₂-APTES-Ce6 and TiO₂@4Si-Ce6-PEG NPs. Based on those outcomes, it appears that the silanization and the sensitization of the TiO₂ NPs does not alter the crystalline structure of the titania. Similar observation was already reported in several instances [3, 33].

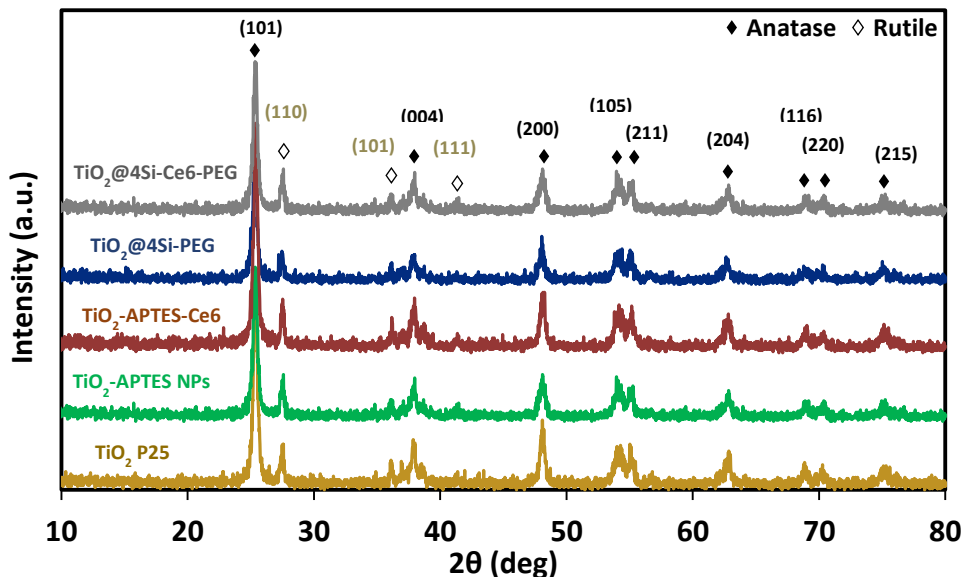


Fig. 3: X-ray diffraction patterns of bare and modified TiO₂ NPs.

3.1.3. Dynamic light scattering (DLS)

DLS is a well-suited technique for investigating the agglomeration state of the nanoparticles as a function of time or suspending solution. The bare TiO_2 NPs used possess a diameter of about 21 nm as determined by TEM (Fig. S7 in the supporting information). However, the DLS can give an idea about the behavior of those NPs when dispersed in solution (Fig. 4A). It appears that the TiO_2 NPs tend to aggregate in solutions since the size analysis gives a hydrodynamic diameter of about 340 nm. On the contrary, the modified NPs display lower sizes. On the one hand, the NPs silanized by APTES possess a hydrodynamic diameter of 210 nm. This indicates a lower state of aggregation which reveals a better dispersion due to the improvement of the hydrophilic character thanks to the NH_2 groups of the aminosilane. On the other hand, the TiO_2 core surrounded by the polysiloxane layer displays a hydrodynamic diameter of 170 nm. Consequently, it presents the bottommost state of aggregation among all three. This is definitely due to the highly-hydrophilic PEG chains grafted onto the polysiloxane matrix (Fig. 4A).

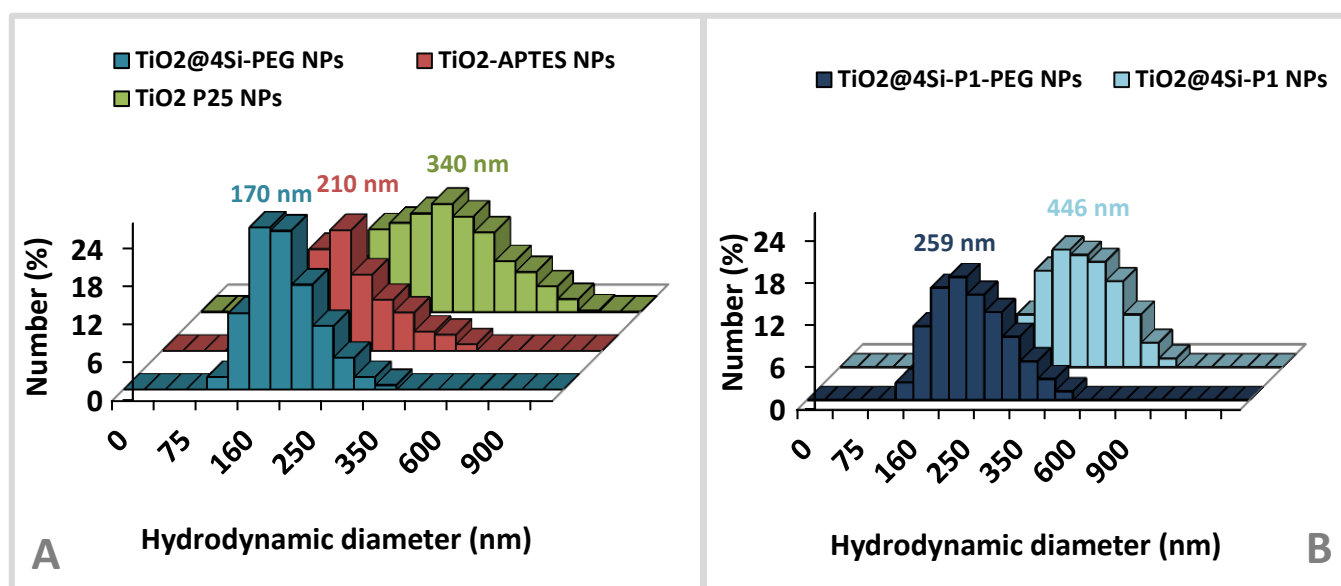


Fig. 4: The hydrodynamic diameter, measured by DLS in water, of (A) the bare and modified TiO_2 P25, (B) core-shell TiO_2 nanosystem coupled to P1-COOH with and without PEG.

In order to confirm this aspect, it seems interesting to investigate the effect of grafting a hydrophilic PEG shell onto the periphery of the core-shell nanoparticles. To this aim, the hydrodynamic diameters of $\text{TiO}_2@4\text{Si-P1}$ and $\text{TiO}_2@4\text{Si-P1-PEG}$ were measured in water by DLS

(Fig. 4B). In the absence of PEG, the average diameter reaches 446 nm. Conversely, when PEG is grafted onto those NPs, the average diameter drops to 259 nm indicating smaller aggregates.

3.1.4. Fourier Transform Infrared Spectroscopy (FTIR)

FTIR analysis is employed to investigate the characteristic active functional groups, and the coordination between those functions and the TiO₂ NPs (Fig. 5). Referring to the IR spectra of both the bare and the APTES-modified TiO₂ nanoparticles, a broad band between 3200-3400 cm⁻¹ and a small peak at 1640 cm⁻¹ can be observed. Those peaks correspond, respectively, to the O-H stretching vibrations of adsorbed water and to the bending vibration of hydroxyl groups (OH) at the surface of TiO₂. For the TiO₂ NPs modified with APTES, the IR spectrum reveals the apparition of new absorption peaks. The peak at 1560 cm⁻¹ can be ascribed to the vibration of the amine NH₂ group of the APTES. Besides, a weak band is also revealed at 2926 cm⁻¹ which corresponds to the alkyl groups of the aminosilane. As the silanol groups of the APTES tend to react with the hydroxyl groups of TiO₂ through condensation, Ti-O-Si moieties are formed and the stretching vibration of those moieties creates an absorption band at 1020 cm⁻¹. Consequently, the amine group occupies the terminal position of the propyl chain. It should be noted that the broad band between 400 and 600 cm⁻¹ observed in all the three spectra can be attributed to the Ti-O-Ti bonds. The IR spectrum of the core-shell nanosystem displays a peak at 1061 cm⁻¹ which can be assigned to the bending and stretching vibrations of Si-O-Si. Upon the addition of the silane reagents, Ti-O-Si bonding between titania NPs and silica is created replacing the Ti-O-H bonding. The Ti-O-Si bonding is expressed in the corresponding FTIR spectrum at 935 cm⁻¹ revealing that the polysiloxane shell is firmly bound to the oxide core. For this nanosystem, the peak localized at 1487 cm⁻¹ may be ascribed to the bending vibration of -NH₂ [36, 37].

In the presence of the photosensitizer, the FTIR spectra of the sensitized NPs exhibit new peaks in addition to the characteristic bands of TiO₂. The bands appearing at 1539, 1541, 1560, and 1559 cm⁻¹ correspond to the stretching vibration of C=N bonds belonging to the pyrrole moieties for TiO₂-APTES-Ce6, TiO₂@4Si-Ce6-PEG, TiO₂-APTES-P1, and TiO₂@4Si-P1-PEG, respectively. The C=O band localized at 1686 cm⁻¹ in Ce6, is shifted to lower wavenumbers, at 1637 and 1646 cm⁻¹, for TiO₂-APTES-Ce6 and TiO₂@4Si-Ce6-PEG, respectively. This difference of 9 cm⁻¹ may indicate different binding modes of the Ce6 onto the NPs through one, two or three carboxylate groups. As for P1-COOH, the $\nu(\text{C}=\text{O})$ band at 1683 cm⁻¹ is shifted to lower wavenumbers at 1652 and 1639 cm⁻¹ for TiO₂-APTES-P1 and TiO₂@4Si-P1-PEG, respectively. The spectra also reveal bands localized at 1386, 1389, 1390 and 1389 cm⁻¹ corresponding to the C-N bond for TiO₂-APTES-

Ce6, TiO₂@4Si-Ce6-PEG, TiO₂-APTES-P1 and TiO₂@4Si-P1-PEG, respectively. Those results confirm that the PSs, *i.e.* Ce6 and P1-COOH, are successfully grafted onto the silanized TiO₂ NPs [11, 38–40].

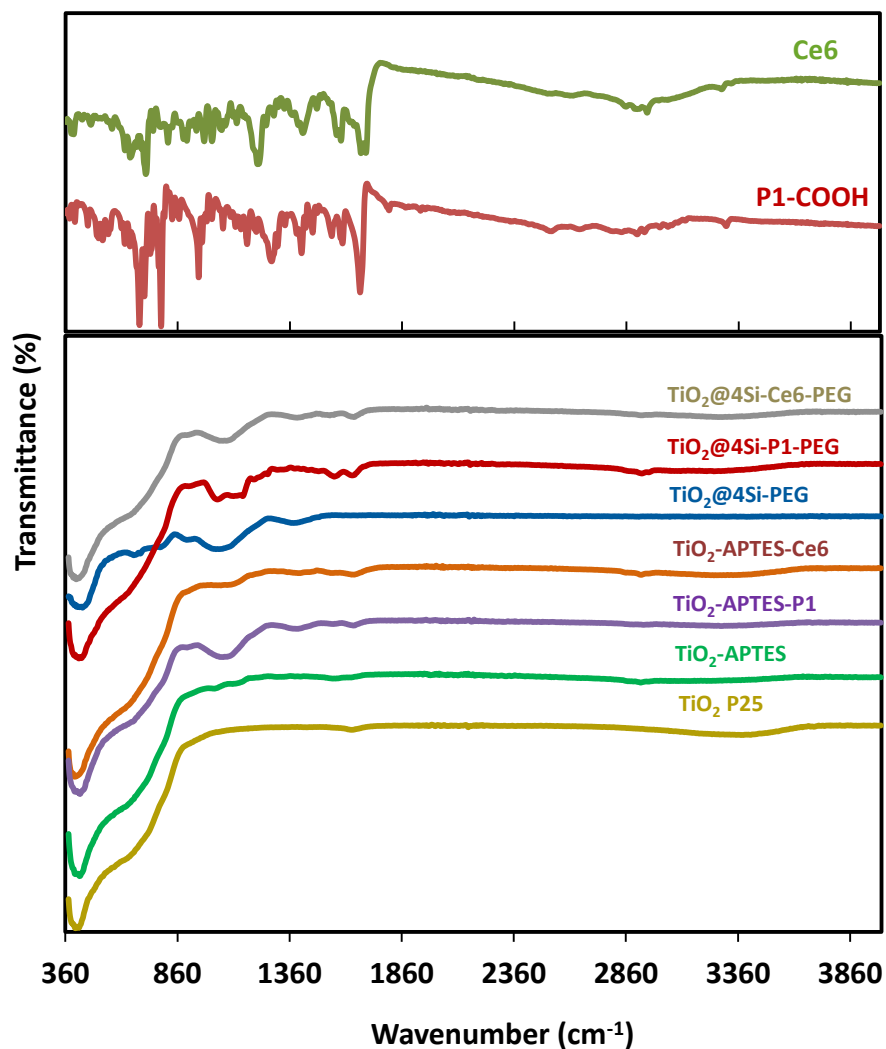


Fig. 5: FTIR spectra of TiO₂@4Si-Ce6-PEG, TiO₂@4Si-P1-PEG, TiO₂@4Si-PEG, TiO₂-APTES-Ce6, TiO₂-APTES-P1, TiO₂-APTES, and TiO₂ NPs in addition to Ce6 and P1-COOH PSs

3.1.5. Zeta-potential (ζ -potential)

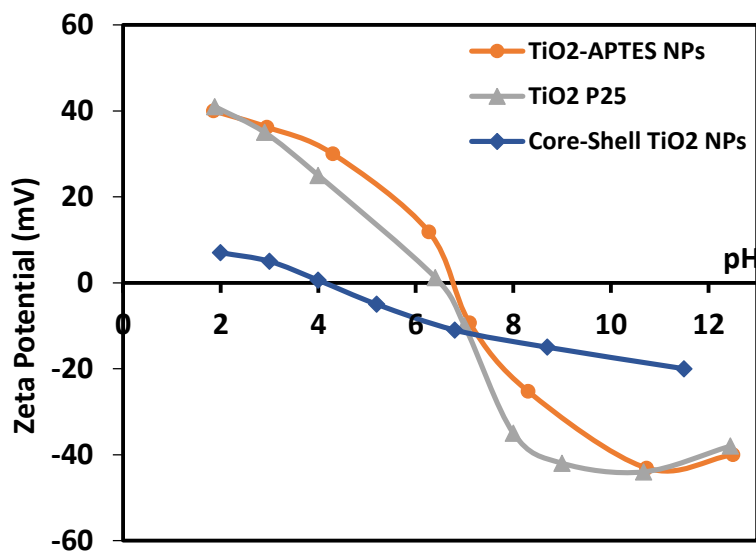


Fig. 6: Variation of the zeta potential of the bare and modified TiO₂ NPs versus pH.

Zeta potential-pH curves are obtained to investigate the surface charge of the bare and the modified titania nanoparticles (Fig. 6). For all the three curves, the zeta potential tends to decrease as the pH increases from positive to negative values in acidic and basic mediums, respectively. As they decrease, the curves pass through the point of zero charge (pzc). After modification with APTES, the corresponding zeta potential-pH curve adopts a very similar trend as obtained with bare TiO₂. In details, at basic pH values between 9 and 12, the curves corresponding to bare and APTES-modified TiO₂ witness a sharp drop to a potential value of about -43 mV. As the pH evolves to values greater than 10, a plateau is reached. This implies that the zeta potential becomes independent of the pH in this range. Modifying the surface of TiO₂ with APTES silane triggers a slight increase in the pzc of those NPs (6.7) as compared to that corresponding to bare TiO₂ (6.4). This weak difference may be attributed to the insignificant diminution of the hydroxyl groups occupying the surface TiO₂. This outcome indicates a low surface coverage of TiO₂ by APTES [34]. However, the pzc tends to increase, and not decrease as familiar in the case of TiO₂ modified by other silane reagents, such as HTS, this may be due to the effect of the NH₂ periphery groups of APTES [34]. Nevertheless, for core-shell TiO₂ nanosystem, the shape of the curve becomes different. Actually, the majority of the hydroxyl groups of titania lessens as the polysiloxane layer grows and encapsulates the TiO₂ core. This may lie behind the variation in the pzc (4.1) and the high reduction of the zeta potential values in the positive region (acidic) in comparison to pure titania. However, in the negative region (pH > 4.1), the negative zeta potential (-15 mV) exhibited by those NPs may be ascribed to the presence of both, the negatively charged silane and the hydrophilic PEG chains. Concerning the the PEG, the

negative charge comes from the deprotonation of the carboxylic groups (pK_a (COOH/COO⁻) \sim 5) in addition to the occurring steric hindrance [35].

3.2. Photophysical properties

3.2.1. UV-visible absorption spectroscopy

UV-vis absorption spectroscopy is used to characterize the optical properties of the powder materials. Fig. 7 represents the influence of the mode of surface modification and the nature of the photosensitizer on the UV-Vis solid absorbance of bare and modified TiO₂. The silanization of TiO₂ NPs with silane reagents through the two different approaches promotes no change in the absorption profile of TiO₂ (Fig. 7A). Similarly to bare TiO₂, both silanized NPs, *i.e.* TiO₂-APTES and core-shell TiO₂ NPs, have a photoresponse restricted to the UV light. All the three spectra merge into a unique master curve. Thus, the silanization of TiO₂ does not induce any shift in the band gap. This behavior is in accordance with results reported in literature [34, 41].

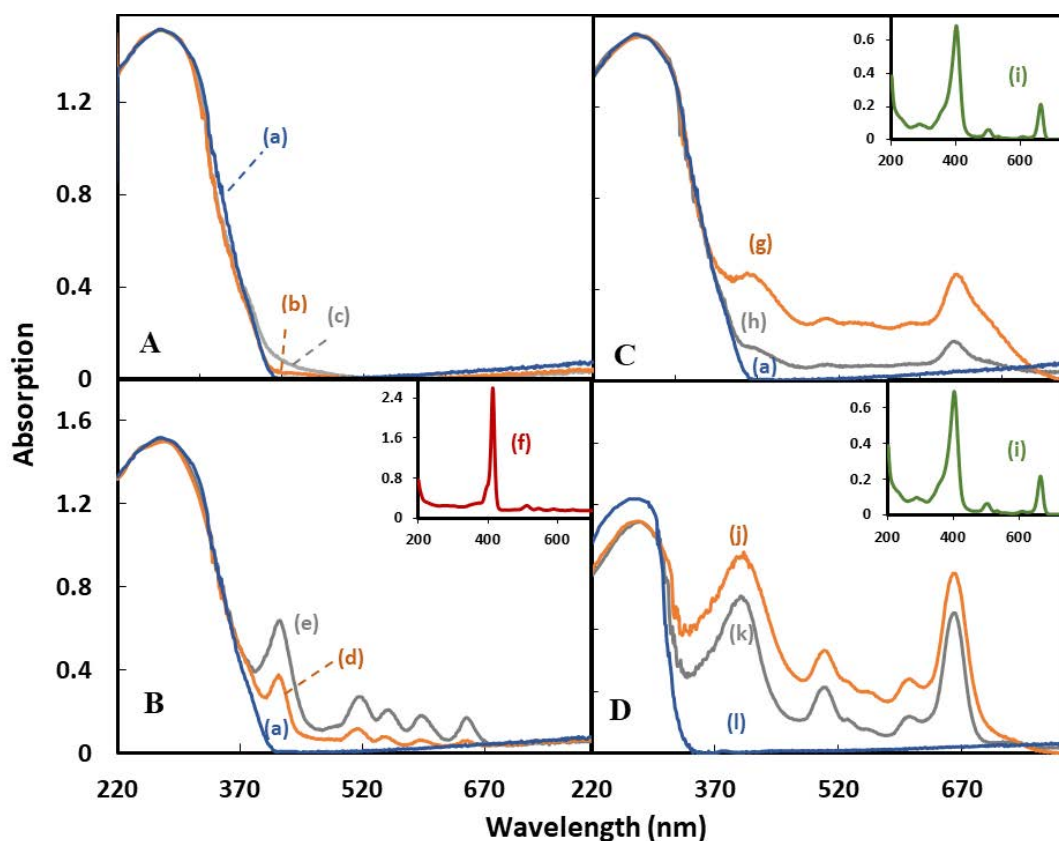


Fig. 7: UV-visible absorption spectra of (A) (a) TiO₂, (b) TiO₂-APTES, (c) TiO₂@4Si-PEG; (B) (d) TiO₂-APTES-P1, (e) TiO₂@4Si-P1-PEG; (C) (g) TiO₂-APTES-Ce6, (h) TiO₂@4Si-Ce6-PEG; (D) (j) SiO₂-APTES-Ce6, (k) SiO₂@4Si-Ce6-PEG, and (l) SiO₂ NPs. In the insets: (f) P1-COOH and (i) Ce6 PS dissolved in ethanol.

The UV-Visible absorption spectra of the free photosensitizers dissolved in ethanol (insets in **Fig. 7B, C & D**) display a major Soret or B-band and four Q-bands between 500 and 700 nm. In details, for P1-COOH PS, the Soret band is evidenced at a wavelength of 414 nm, while the Q-bands occur at 512, 546, 590, and 645 nm. For Ce6 PS, the Soret band takes place at 401 nm, while the Q-bands occur at 501, 530, 605 and 663 nm.

The UV-Visible absorption spectra of APTES-modified and the core-shell TiO₂ nanosystems hybridized by porphyrin are shown in **Fig. 7B (d, e)**. While the photoresponse of bare TiO₂ is restricted to the UV light region, the absorption spectra of both APTES-modified and the core-shell TiO₂ nanosystems hybridized by porphyrin witness the appearance of new peaks in the region between 400-800 nm. Those peaks are compatible with the Soret and Q-bands of P1-COOH (**Fig. 7B inset f**) [42]. Similarly, the UV-visible absorption spectra of TiO₂-APTES-Ce6 and TiO₂@4Si-Ce6-PEG NPs exhibit the characteristic peaks of Ce6 besides the UV-localized peak of TiO₂ (**Fig. 7C**) [43]. So, it can be concluded that P1-COOH and Ce6 are linked to the surface of both types of modified TiO₂ (silanized by APTES or core-shell), and that the photoresponse of the hybridized TiO₂ is successfully extended to the visible region of light. Also, it is noteworthy to mention that the sensitization of TiO₂ NPs by the PS left the band gap intact since all the spectra retained the maximum absorption value of the UV band which is the characteristic peak of TiO₂. This result is very similar to that described in the literature [41, 44].

As far as silica is concerned, the absorption spectra are reported in the **Fig. 7D**. Logically, the bare SiO₂ NPs present no absorption peak in the visible light region. However, the spectra of the sensitized SiO₂-APTES-Ce6 and SiO₂@4Si-Ce6-PEG NPs reveal the absorption peaks of Ce6 PS. Likewise to TiO₂, after sensitization with Ce6, the silica NPs can absorb in the visible light zone. Similar observations were already reported in the literature [43].

3.2.2. Fluorescence and singlet oxygen measurements

In order to calculate valid fluorescence and singlet oxygen quantum yields for free PS and sensitized NPs, the optical density (OD) of the Soret band should be adjusted at about 0.2. Unfortunately, it is difficult to attain this OD in the absorption spectra of the hybridized NPs dispersed in solutions. Such absorption spectra are unreliable due to the problem of light diffusion and scattering. Despite this, with TiO₂ NPs sensitized with P1-COOH, we try to regulate the OD of the Soret band of P1-COOH at 0.2 and we measure the fluorescence and singlet oxygen intensities depending on those values. The resulting absorption spectra appear noisy (**Fig. S8** of the Supporting information), thus, the calculation of the quantum yields based on those spectra is not consistent.

On the one hand, it can be observed that no alteration in the shape of the fluorescence emission spectra between the free P1-COOH and that grafted onto TiO₂ (Fig. 8A). Besides that, the P1-hybridized TiO₂ NPs are capable of ¹O₂ formation (Fig. 8B). On the other hand, and unlike with silica, the light diffusion totally masks the Soret band of Ce6 in the case of Ce6-hybridized TiO₂ NPs dispersed in ethanol (Fig. S9 in the Supporting information), which renders it impossible to extract any data concerning the optical density of the Soret band. Thus, we try to have an idea about the fluorescence and singlet oxygen intensities by dispersing 200 μg/mL of each type of NPs in ethanol. Referring to the fluorescence spectra (Fig. 8C), no modification in the shape of the emission spectra could be witnessed between free Ce6 and that grafted onto TiO₂ and SiO₂ under the two synthesis approaches. Besides, the Ce6-hybridized TiO₂ and SiO₂ NPs are capable of ¹O₂ formation (Fig. 8D).

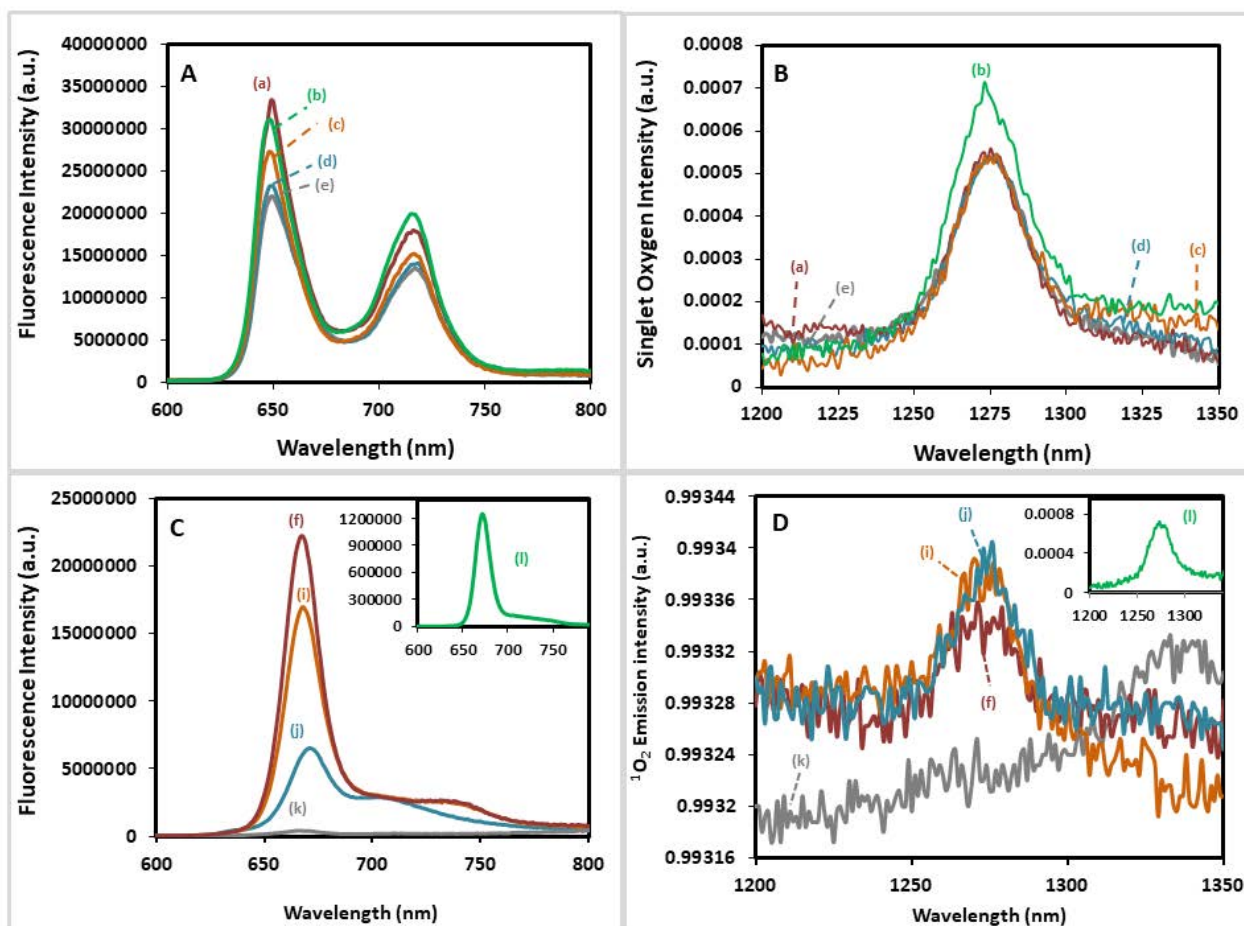


Fig. 8: The fluorescence spectra (A) and singlet oxygen spectra (B) of: (a) TiO₂-APTES-P1, (c) TiO₂-APTES-P1-PEG, (d) TiO₂@4Si-P1-PEG, (e) TiO₂@4Si-P1 NPs, and (b) free (non-attached) P1-COOH PS at an optical density of about 0.2 excited at 420 nm. The fluorescence intensity (C) and singlet oxygen intensity (D) of: (f) SiO₂@4Si-Ce6-PEG, (i) SiO₂-APTES-Ce6, (j) TiO₂-APTES-Ce6, (k) TiO₂@4Si-Ce6-PEG NPs at 200 μg/mL, and in the insets (l) free (non-grafted) Ce6 PS at an optical density of about 0.2 excited at 420 nm.

4. Photocatalytic activity

The photocatalytic activity of the prepared titania and silica samples has been tested on the photodegradation of MO and MB. It has been widely described in the literature that the nature of the incident light has a significant effect on both the photodegradation of organic compounds and the ROS production [40, 45, 46]. For this reason, the photocatalytic performance of the hybrid nanomaterials activated under solar light and pure visible are studied separately.

4.1. Photocatalysis under solar light

Preliminary experiments are performed to test the photocatalytic activity of the bare NPs in the absence of any grafted photosensitizer towards the degradation of MO under simulated solar light (Fig. 9A). For the core-shell titania NPs ($\text{TiO}_2@4\text{Si-PEG}$), a solar irradiation over 250 minutes produces no appreciable reduction in the MO concentration. The TiO_2 NPs modified with APTES ($\text{TiO}_2\text{-APTES}$), induce a decrease in the MO amount by 30%, yet their photocatalytic efficiency remains inferior to that of the bare TiO_2 that significantly reduces the amount of MO by 75%. Thus, in the absence of PS, the bare titania produces better photocatalytic activity than the modified materials. Actually, the bare TiO_2 semiconductor utilizes efficiently the small amount of UV light from the solar illumination (4-6 %) to be excited, and to produce the active ROS species, mainly HO^\bullet and $\text{O}_2^{\bullet-}$, capable of degrading the contaminant. However, it can also be attributed to the rutile crystalline phase of P25 which is assumed to be capable of visible light absorption. It is noteworthy to shed light on the fact that TiO_2 P25 possesses a very high level of photocatalytic activity in a wide range of photocatalytic reaction system. Such property encourages the extensive use of TiO_2 P25. More than thousand papers have been issued on the photocatalytic applications of those NPs since 1990. It is said that finding a catalyst exhibiting a superior photoactivity over TiO_2 P25 is not easy, that is why it is considered as a “de facto standard” TiO_2 photocatalyst [47]. On the opposite, the diminution of the photoactivity for the APTES-modified TiO_2 NPs can be explained by the reduction of the number of photocatalytic sites caused by grafting of the APTES molecules onto the surface hydroxyl groups [34]. More precisely, the surface-silanization of TiO_2 by APTES leads to the formation of Ti-O-Si bonds causing the loss of some hydroxyl Ti-OH groups normally abundant on the surface of those NPs. In addition, the partial coverage of the surface of TiO_2 by APTES may hinder the light penetration into the NPs. Those reasons prompt the weakened photocatalytic activity of $\text{TiO}_2\text{-APTES}$ NPs. On the contrary, surrounding the TiO_2 core with a polysiloxane layer causes the loss of the majority of the Ti-OH groups and somehow masks the surface of titania. This can explain the suppression of photoactivity of the core-shell nanosystem ($\text{TiO}_2@4\text{Si-PEG}$).

The photodegradation of MO in the presence of free P1-COOH or Ce6 PSs not grafted onto any support experimented under simulated solar light is shown in **Fig. 9B, C & D**. Despite the fact that both Ce6 and P1-COOH PSs can be activated by the visible portion of the solar light to produce a significant amount of $^1\text{O}_2$ (quantum yields of $^1\text{O}_2$ in ethanol: $\phi_{\Delta} = 0.63$ and 0.56 for Ce6 and P1-COOH, respectively), the PS alone (P1-COOH or Ce6) appears to be incapable of photodegrading the pollutants. This outcome can be most probably attributed to the lack of a support for pollutants to be adsorbed on. This confirms that to achieve the photocatalytic degradation of a pollutant, the PS needs to be linked to a support either through adsorption or covalent grafting. Hence, during the photocatalytic process, the pollutants may adsorb onto the support, thus allowing the contact between the ROS produced by the PS and the pollutants.

The effect of modifying the surface of titania by photosensitizers (P1-COOH or Ce6) on the time course of the photocatalytic degradation of the two pollutants is illustrated in **Fig. 9B and 9C**, respectively. When the PS is attached to the surface of titania, the hybridized catalysts show superior photocatalytic efficiency over that of the silanized PS-free titania. Thus, the sensitization of the titania surface has some beneficial influence on the overall degradation performances under solar light irradiation. In parallel, it seems interesting to discuss the impact of the mode of grafting (APTES-modified or core-shell) and the content of PS on the kinetics of the photodegradation of the pollutants. All the sensitized titania NPs (TiO_2 -APTES-P1, TiO_2 -APTES-P1-PEG $\text{TiO}_2@4\text{Si}$ -P1, $\text{TiO}_2@4\text{Si}$ -P1-PEG, TiO_2 -APTES-Ce6 and $\text{TiO}_2@4\text{Si}$ -Ce6-PEG) enable the degradation of the contaminants dissolved in water. This indicates that the hybrid nanosystems display a photocatalytic activity under solar light. Nevertheless, the maximum efficiencies towards the degradation of MB and MO are obtained by both the bare unmodified titania and the TiO_2 -APTES-PS nanosystems for P1-COOH (TiO_2 -APTES-P1) and Ce6 photosensitizers (TiO_2 -APTES-Ce6), respectively.

Those results can be explained in terms of the production of radicals which is intimately linked to the mode of grafting of the PS. The $^1\text{O}_2$ is the first type of ROS that we consider. Although it is difficult to evaluate the $^1\text{O}_2$ quantum yields ($\lambda = 420$ nm) due to the light diffusion issue, such analysis may give us a lot of pertinent information about the $^1\text{O}_2$ photoproduction under visible light. All the P1-COOH hybridized nanosystems, namely $\text{TiO}_2@4\text{Si}$ -P1-PEG and TiO_2 -APTES-P1, appear to induce similar $^1\text{O}_2$ production (**Fig. 8B**). Consequently, the variation in the photocatalytic degradation performances between those two systems cannot be related to $^1\text{O}_2$. Similar conclusion can be drawn with the Ce6 sensitized titania NPs ($\text{TiO}_2@4\text{Si}$ -Ce6-PEG and TiO_2 -APTES-Ce6). Therefore, the higher photocatalytic efficiency of TiO_2 -APTES-PS NPs over the other hybridized core-shell nanosystems may be attributed to the presence of another type of ROS species beside $^1\text{O}_2$, such as hydroxyl radicals (HO^\bullet) or superoxide anions ($\text{O}_2^{\bullet-}$), being involved in this catalytic system.

As the PS contributes solely to the generation of $^1\text{O}_2$, it appears logical that the other ROS are produced by the TiO_2 semiconductor itself. The low APTES surface coverage enables the partial penetration of solar light into the TiO_2 core. Thus in the TiO_2 -APTES-PS nanosystems, titania can absorb the UV portion of the solar light and become activated hence producing ROS. Another pathway for the activation of TiO_2 under solar light may be achieved by the PS through electron transfer process. Where the PS can absorb in the visible portion of the solar light, get excited, and injects the produced electrons into the conduction band (CB) of the TiO_2 semiconductor initiating ROS production.

The proposed mechanisms of ROS production *via* both pathways may be as follows:

TiO_2 activation by solar light (UV) absorption



TiO_2 activation by electron transfer from the PS



In order to validate all the above conclusions, it appears interesting to investigate the photodegradation of MO by SiO_2 , SiO_2 -APTES-Ce6, and $\text{SiO}_2@4\text{Si}$ -Ce6-PEG NPs (**Fig. 9D**). Silica is not a semi-conductor and it cannot take advantage of the light to be activated, thus it lacks any photocatalytic activity towards the degradation of MO. However, when coupled to Ce6, hybridized APTES-modified and core-shell SiO_2 NPs result in a decrease of the initial amount of the MO pollutant by 19.9 % and 30 %, respectively, after 240 minutes of solar irradiation. Since SiO_2 is not photoactive, this decrease is logically triggered by the $^1\text{O}_2$ produced by the grafted Ce6 photosensitizer.

As compared to the lifetime of HO^\bullet (ca. 10 μs), $^1\text{O}_2$ possesses a short lifetime (2 μs). This is due to the rapid deactivation of $^1\text{O}_2$ at the surface of the NPs. Thus, $^1\text{O}_2$ cannot migrate towards the targeted pollutant [48]. In addition, most catalytic reactions involving heterogeneous catalysts occur either on the surface of the catalysts or at the interface of the active species and the support [49]. Hence, it appears that coupling Ce6 to a support (SiO_2) helped in the adsorption of the pollutants in order to establish the contact between the $^1\text{O}_2$ produced by the coupled Ce6 and MO adsorbed on the

SiO₂ support for a photocatalytic reaction to occur. This result illustrates the previous assumption concerning the lack of the photocatalytic activity in terms of pollutant degradation in the presence of free PS.

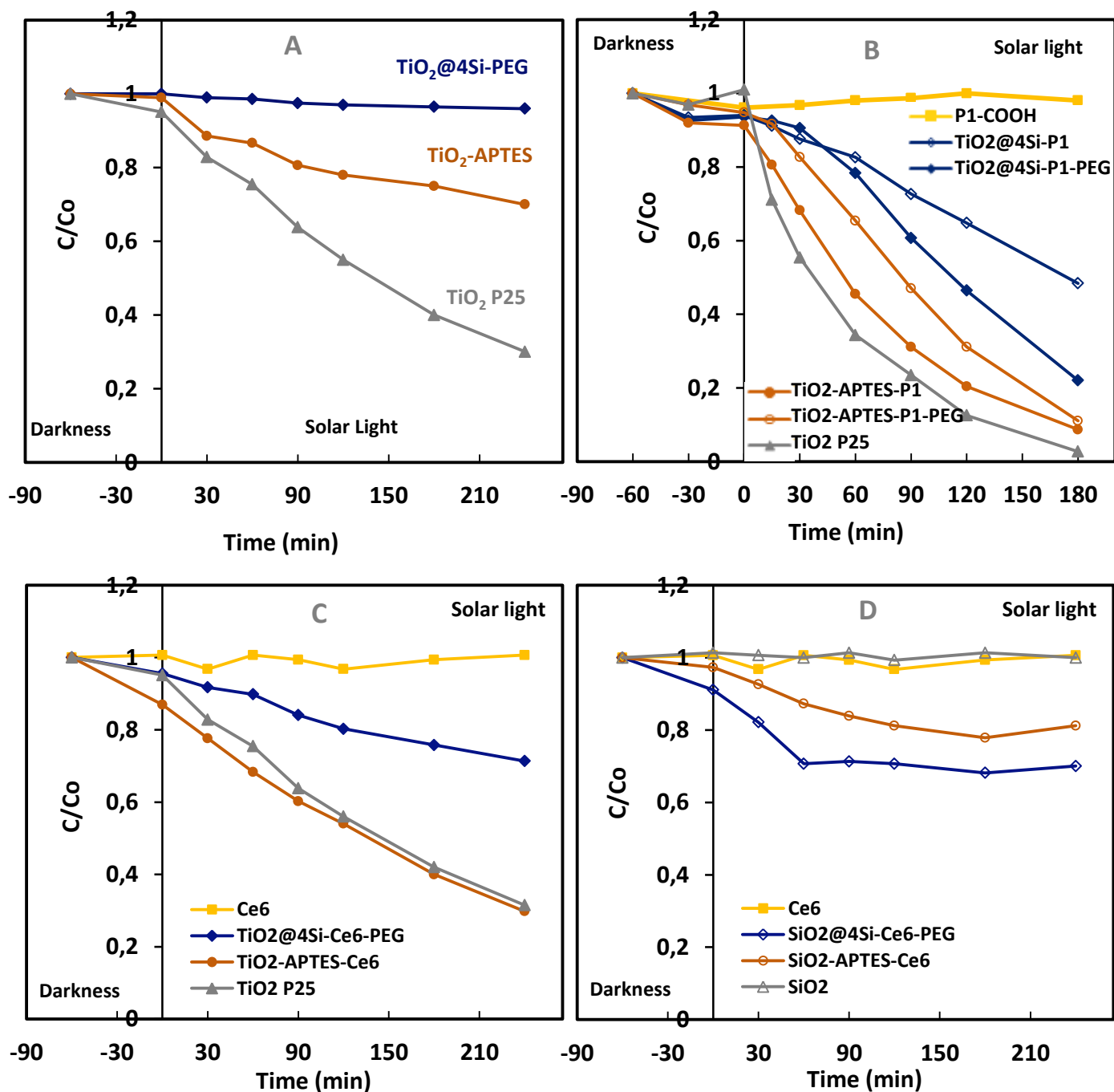


Fig. 9: Photocatalytic activity under simulated solar light. (A) Photodegradation of MO by bare and modified TiO₂ NPs in the absence of PS. (B) Photodegradation of MB by TiO₂ sensitized by P1, and free P1-COOH PS. (C) Photodegradation of MO by TiO₂ sensitized by Ce6, and free Ce6 PS. (D) Photodegradation of MO by bare SiO₂ and silica NPs sensitized by Ce6.

More interestingly, for the core-shell nanosystems ($\text{TiO}_2@4\text{Si-Ce6-PEG}$ and $\text{SiO}_2@4\text{Si-Ce6-PEG}$) it appears that the photodegradation of the pollutant is not strongly affected by the nature of the support, *i.e.* TiO_2 or SiO_2 (**Fig. S11** of the Supporting information), both leading to a final decrease of the MO amount by 30 % after 240 minutes of solar light irradiation. This confirms that the coverage with the polysiloxane shell layer masks the majority of the active sites of the core (TiO_2), and consequently, the latter almost plays no role in the ROS generation. On the opposite, the photocativity of $\text{TiO}_2\text{-APTES-Ce6}$ remains significantly higher than that of $\text{SiO}_2\text{-APTES-Ce6}$ NPs. The difference indicates the contribution of the other radicals produced by titania in the photodegradation process beside $^1\text{O}_2$ produced by the PS itself.

Putting on side the nature of the support and the PS content, grafting PEG onto the surface of the NPs offers certain advantageous properties that enhance their use especially in the biological applications. When grafted onto the NPs, highly hydrophilic PEG can maintain better dispersion that normally leads to better photocatalytic performance of the NPs. Thus, it is also interesting to evaluate the effect of grafting PEG onto the surface of our NPs on their photocatalytic performances. In the presence and absence of PEG grafted to their surfaces, APTES-modified NPs coupled to P1-COOH ($\text{TiO}_2\text{-APTES-P1}$ and $\text{TiO}_2\text{-APTES-P1-PEG}$) generate almost the same $^1\text{O}_2$ amount (**Fig. 8B**) and possess a similar dispersion behavior in water. In addition, no substantial difference in their photodegradation activity can be detected. Both NPs lead to the same final amount of pollutant after 180 minutes of solar light illumination. Conversely, in the presence of PEG, $\text{TiO}_2@4\text{Si-P1-PEG}$ NPs seem to generate more $^1\text{O}_2$ (**Fig. 8B**) and exhibit better photocatalytic degradation of MO as compared to that in the absence of PEG ($\text{TiO}_2@4\text{Si-P1}$ NPs). Such outcomes agree with the results from DLS (**Fig. 4B**) where it was clear that grafting PEG improved the dispersion behavior of the core-shell NPs in aqueous media. The hybridized NPs in the absence of PEG agglomerate into larger aggregates. This coalescence produces a significant diminution of the available catalyst surface for the light and the pollutants. Consequently, an inferior photocatalytic activity of $\text{TiO}_2@4\text{Si-P1}$ NPs towards the degradation of MB is attained.

4.2. Photocatalysis under visible light

The stability/instability of MO under pure visible light (400-500 nm) is preliminary assessed and the corresponding figure is shown in supporting information (**Fig. S13**). Under visible light and in the absence of any catalyst no degradation of MO is witnessed.

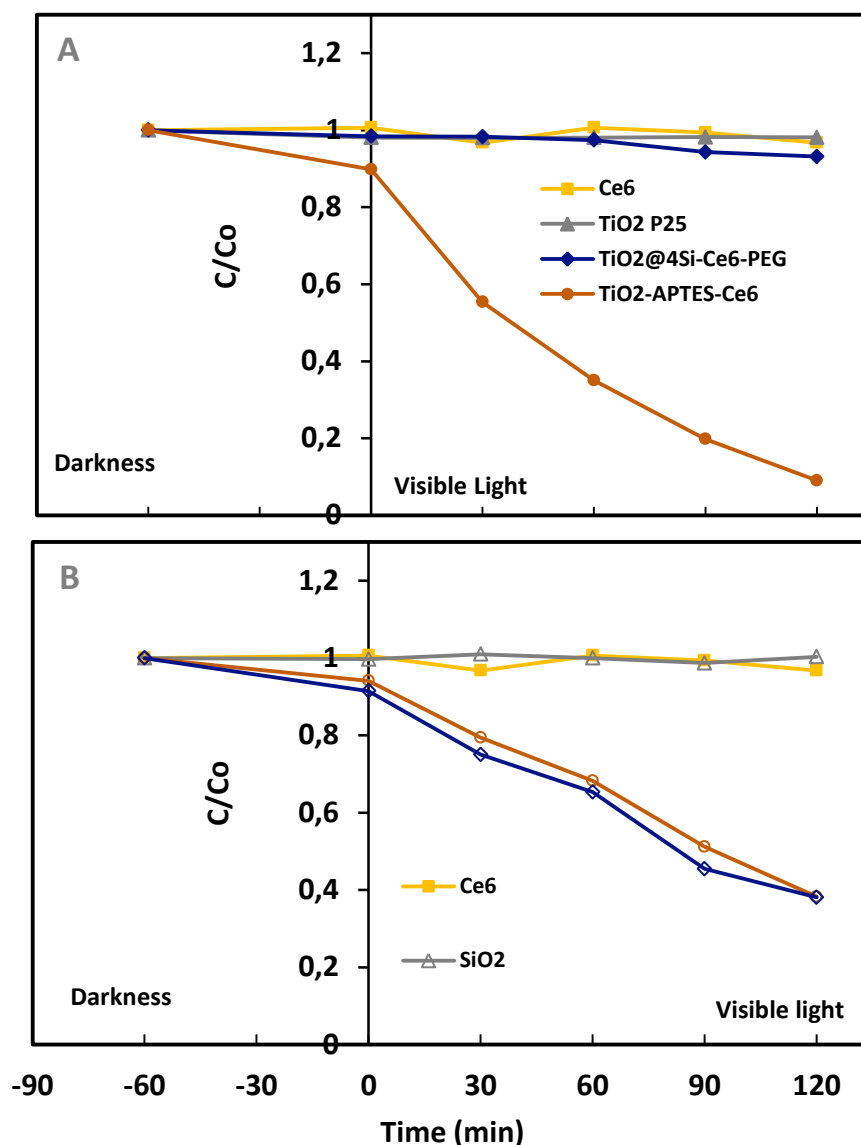


Fig. 10: Photocatalytic degradation of MO under pure visible light by (A) TiO₂, TiO₂-APTES-Ce6, TiO₂@4Si-Ce6-PEG NPs and Ce6 PS, (B) SiO₂, SiO₂-APTES-Ce6, SiO₂@4Si-Ce6-PEG NPs and Ce6 PS

The photocatalytic degradation of MO using PS grafted titania (**Fig. 10A**) and silica (**Fig. 10B**) NPs is reported in **Fig. 10**. Under pure visible light, the bare TiO₂ NPs cannot be activated, thus, it appears inefficient towards the photocatalytic degradation of MO. No degradation can be obtained with the TiO₂@4Si-Ce6-PEG NPs. This is probably due the pre-mentioned shielding effect of the silica shell grown around the TiO₂ core. However, only the TiO₂-APTES-Ce6 NPs possess a photocatalytic efficiency among all the tested titania NPs (**Fig. 10A**). 91 % of MO degradation is achieved after 120 minutes of visible light irradiation. The abundance of visible light irradiation

prompts an enhanced photocatalytic activity in the degradation of the pollutant. On the other hand, for the bare silicon dioxide nanoparticles, it appears that no degradation of MO is witnessed under visible light. However, with SiO₂ NPs coupled to Ce6, both the core-shell (SiO₂@4Si-Ce6-PEG) and the APTES-modified nanosystems (SiO₂-APTES-Ce6) possess a similar efficiency in the photocatalytic degradation of MO under pure visible light (**Fig. 10B**). A percentage of degradation of 38 % is recorded at the end of the process. Furthermore, in order to understand the origin of the superior photocatalytic efficiency of the TiO₂-APTES-Ce6 NPs and also to assess the contribution of each element (core particles, PS), the ROS production is investigated through the use of probes.

5. ROS measurements: HO[•] and ¹O₂

Two kinds of analysis are performed to evaluate the photoproduction of ROS. On the one hand, the hydroxyl radicals (HO[•]) production is detected by HPF probe. On the other hand, SOSG probe is used to evaluate the singlet oxygen (¹O₂) content.

The temporal evolution of the fluorescence intensity of HPF alone, and in the presence of free Ce6, Ce6 grafted onto the NPs (TiO₂-APTES-Ce6 and SiO₂-APTES-Ce6) and control NPs without PS (TiO₂-APTES and SiO₂-APTES) is reported in **Fig. S14** (supporting information). The HPF fluorescence results generated by each type of NPs are monitored at the emission wavelength of 514 nm. A ratio between the variation of the fluorescence intensity (F.I.) of HPF at time *t* and the initial fluorescence intensity at *t*₀ normalized by the the initial fluorescence intensity at *t*₀ (ratio of F.I. variation = (F.I.(*t*) - F.I.(*t*₀)) / F.I.(*t*₀)) is established for all the samples in order to compare the trend of the evolution of these fluorescences with the excitation time. In other words, such ratio becomes necessary since we want to compare the potential to produce HO[•] between the different types of NPs when irradiated by visible light (420 nm). The results are displayed in the **Fig. 11A**.

For the free Ce6 PS, control TiO₂-APTES and SiO₂-APTES-Ce6 NPs, a negligible increase in the HPF fluorescence intensity over time is witnessed. No variation at all is revealed in the case of control SiO₂-APTES NPs. This indicates the absence or the weak production of HO[•] for all these systems. Conversely, the TiO₂-APTES-Ce6 NPs induce a large progression in the fluorescence intensity of HPF with time when excited at 420 nm. This outcome proves the existence of HO[•] elaborated from the excited TiO₂-APTES-Ce6 nanosystem. As we are exciting in the visible light region, and keeping in mind that Ce6 PS alone is not capable of producing this significant amount of HO[•], it seems that an indirect excitation of TiO₂ is taking place. This is possible through an electron transfer process from the excited PS into the conduction band of the TiO₂ semiconductor (**Fig. 11C**).

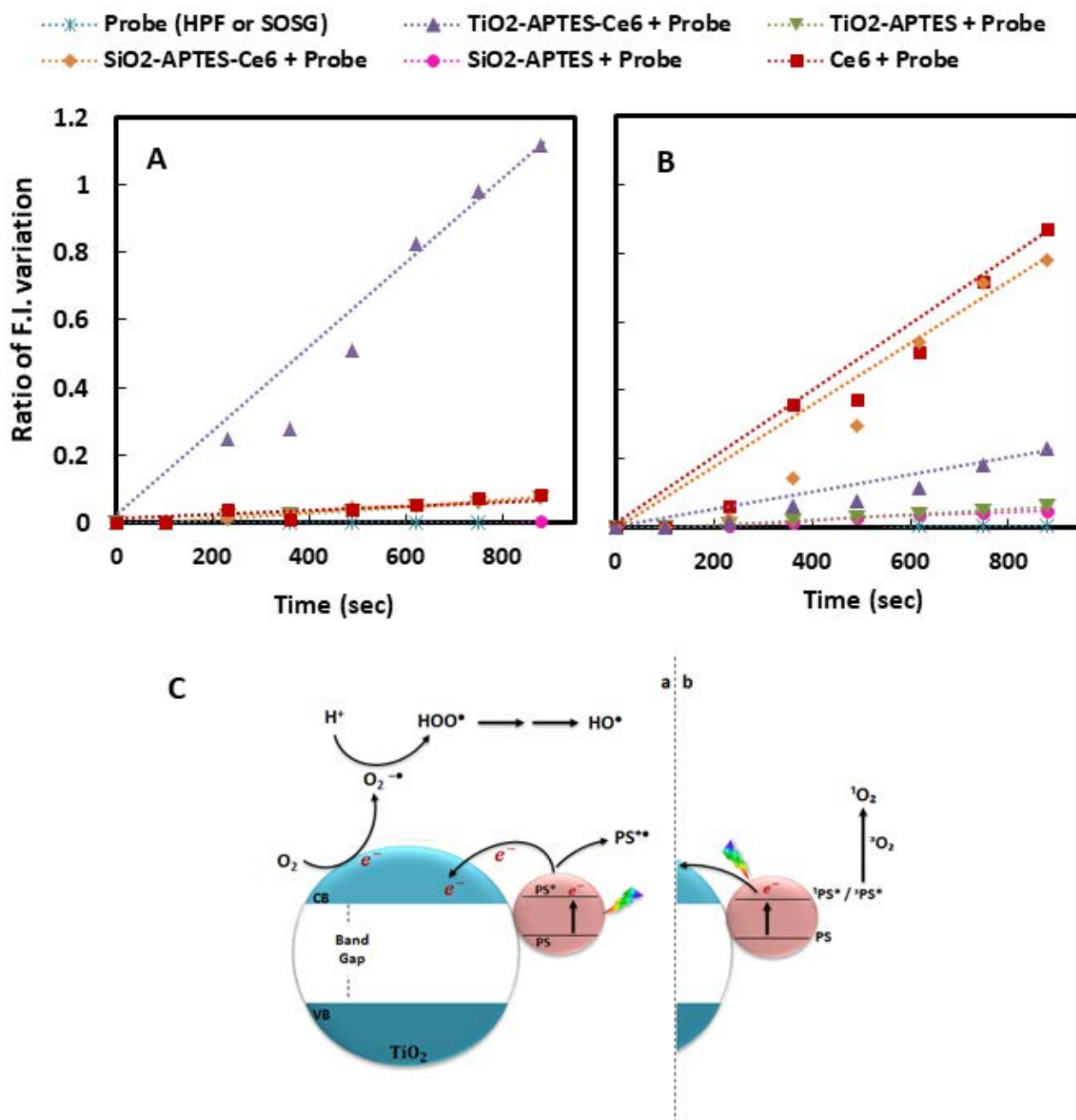


Fig. 11: The evolution of the ratio of fluorescence of (A) HPF at 514 nm in the case the HPF alone, Ce6 PS, TiO₂-APTES, TiO₂-APTES-Ce6, SiO₂-APTES and SiO₂-APTES-Ce6 NPs all in the presence of the HPF probe in water and of (B) SOSG at 525 nm in the case the SOSG alone, Ce6, TiO₂-APTES, TiO₂-APTES-Ce6, SiO₂-APTES and SiO₂-APTES-Ce6 all in the presence of the HPF probe in water. A ratio between the variation of the fluorescence intensity (F.I.) of HPF at time t and the initial fluorescence intensity at t_0 normalized by the the initial fluorescence intensity at t_0 (ratio of F.I. variation = $(t - t_0) / t_0$). The mechanism of sensitization and electron transfer process occurring in the TiO₂ NPs sensitized with Ce6 (C).

Concerning the $^1\text{O}_2$ content, SOSG probe was utilized. **Fig. S15** (supporting information) shows the evolutions of the fluorescence intensity of SOSG alone, and in the presence of free Ce6, Ce6 grafted onto the NPs ($\text{TiO}_2\text{-APTES-Ce6}$ and $\text{SiO}_2\text{-APTES-Ce6}$) and control NPs without PS ($\text{TiO}_2\text{-APTES}$ and $\text{SiO}_2\text{-APTES}$). The SOSG fluorescence results generated by each type of NPs are monitored at the emission wavelength of 525 nm. Following the same approach employed with the HO^\bullet , the ratio between the variation of the fluorescence intensity (ratio of F.I. variation = $(\text{F.I.}(t) - \text{F.I.}(t_0)) / \text{F.I.}(t_0)$) is employed. The temporal evolution of the ratio is reported in the **Fig. 11B** for the various modified particles. A negligible increase in the SOSG fluorescence intensity is witnessed for control $\text{TiO}_2\text{-APTES}$ and $\text{SiO}_2\text{-APTES}$ NPs. However, the slight progression in the fluorescence intensity of SOSG in the presence of $\text{TiO}_2\text{-APTES-Ce6}$ NPs corresponds to a small production of $^1\text{O}_2$ (~15%). The coupled Ce6 PS is responsible for the production of $^1\text{O}_2$ in the $\text{TiO}_2\text{-APTES-Ce6}$ nanosystem (**Fig. 11B**). Conversely, the large increase in the fluorescence intensity of SOSG in the presence of Ce6 PS and $\text{SiO}_2\text{-APTES-Ce6}$ NPs reveals the generation of significant amounts of $^1\text{O}_2$ produced by this free PS and the hybridized silica NPs upon excitation in the visible range of light (420 nm). Since SiO_2 is not photoactive by itself, the elaborated $^1\text{O}_2$ is generated by visible-light sensitive Ce6 PS grafted to its surface. The larger amount of $^1\text{O}_2$ produced by the $\text{SiO}_2\text{-APTES-Ce6}$ can be attributed to the greater PS surface coverage onto silica as compared to that on titania.

The ROS investigation makes it possible to explain the photocatalytic results under visible light. It appears that the $\text{TiO}_2\text{-APTES-Ce6}$ nanosystem can be active under the solar light as well as under the visible one. As the $\text{TiO}_2\text{-APTES-Ce6}$ NPs are irradiated under pure visible light, only Ce6 PS absorbs this light (**Fig. 11C**). Thus, Ce6 is excited to appropriate singlet and triplet states and is converted into cationic radicals. Besides, the excited PS generates electrons. Those electrons are injected into the conduction band of TiO_2 . Consequently, the TiO_2 semiconductor becomes indirectly photo-activated through electron transfer process. The injected electron interacts with the pre-adsorbed molecular oxygen causing the production of reactive oxygen species (HO^\bullet , HOO^\bullet , $\text{O}_2^{\bullet-}$) through photo-redox reactions (**Fig. 11C(a)**). Accordingly, we can say that $\text{TiO}_2\text{-APTES-Ce6}$ nanosystems elaborate an abundant amount of ROS predominantly HO^\bullet under visible light irradiation. At the same time, lower amount of $^1\text{O}_2$ are generated by the grafted PS (**Fig. 11C(b)**). Therefore, all the components of the system, TiO_2 core and Ce6 PS, contribute to the high photocatalytic efficiency. On the opposite, $\text{SiO}_2\text{-APTES-Ce6}$ NPs are not capable to create any HO^\bullet radicals. Actually, the electron transfer from the grafted PS to the silica NPs does not occur because silica NPs are not semiconductor materials. However, $\text{SiO}_2\text{-APTES-Ce6}$ NPs produce a significant amount of $^1\text{O}_2$. The $^1\text{O}_2$ elaboration is attributed to the grafted Ce6 PS which acts as an antenna to

harvest visible light (**Fig. 11C(b)**). Thus, SiO₂ core only serves as a support for the adsorption of pollutants and does not contribute in the ROS production.

6. Conclusions

In this work, the surface of the TiO₂ and the SiO₂ cores was modified through silanization *via* two different approaches, the core-shell and the APTES-modified. Light-sensitive organic molecules, P1-COOH and Ce6 photosensitizers, were covalently grafted onto the surface of the NPs *via* the amine group of the APTES bridging molecule. Non-photoactive SiO₂ NPs were used for comparative reasons. The morphological, structural and photophysical properties of the obtained NPs were studied. The crystalline structure of the TiO₂ core remained intact after silanization and sensitization as confirmed by HR-TEM and XRD. The photoresponse of all the hybridized NPs was extended towards the visible region of light as revealed by UV-visible spectrophotometry. FTIR analysis proved that the PS was linked onto the surface of the hybridized NPs *via* amide covalent bond. Upon sensitization with P1-COOH and Ce6 PSs, the elaborated NPs were capable of fluorescing under visible light irradiation.

The photocatalytic activity of those NPs was evaluated by the degradation of MB and MO model pollutants. The photocatalytic experiments were conducted under simulated solar and pure visible light. The APTES-modified nanosystems coupled to P1-COOH and Ce6 PSs possessed superior photocatalytic efficiency towards the degradation of the pollutants over the sensitized core-shell nanosystems under both solar and visible light. In particular, TiO₂-APTES-Ce6 NPs lead to a remarkable efficiency in the photocatalytic destruction of the pollutant (91% of degradation) under visible light irradiation. In this nanosystem, Ce6 played a double role. First, it absorbs the visible light and is excited to produce ¹O₂ and electrons. Second, those electrons are injected into the conduction band of TiO₂ triggering a series of redox reactions producing HO[•]. SOSG and HPF probes were used to detect the generation of HO[•] and ¹O₂. The significant generation of HO[•] in the case of TiO₂-APTES-Ce6 validates the theory of the electron transfer. The concomitant roles played by Ce6 and TiO₂ in this nanosystem yielded abundant production of different ROS that conceded a superior photoactivity over the core-shell nanosystem and the bare titania. As for the SiO₂-APTES-Ce6 NPs, only ¹O₂ generation was detected. The source of the ¹O₂ was Ce6, where SiO₂ played only the role of a support for the adsorption of the pollutants but did not contribute in the ROS production, unlike TiO₂ semiconductor. The results obtained with silica confirmed the role of the TiO₂ core as an effective component in the TiO₂-APTES-Ce6 nanosystem contributing to both the adsorption of the pollutants and the elaboration of ROS mainly HO[•] under both solar and visible light.

References for chapter II

- [1] D. Fatta-Kassinos, S. Meric, A. Nikolaou, Pharmaceutical residues in environmental waters and wastewater: current state of knowledge and future research, *Anal. Bioanal. Chem.*, 399 (2011), 251–275.
- [2] M. Grassi, L. Rizzo, A. Farina, Endocrine disruptors compounds, pharmaceuticals and personal care products in urban wastewater: implications for agricultural reuse and their removal by adsorption process, *Environ. Sci. Pollut. Res.*, 20 (2013), 3616–3628.
- [3] S. D. Richardson, S. Y. Kimura, *Water Analysis: Emerging Contaminants and Current Issues*, *Anal. Chem.*, 88 (2016), 546–582.
- [4] M. Trapido, I. Epold, J. Bolobajev, N. Dulova, Emerging micropollutants in water/wastewater: growing demand on removal technologies, *Environ. Sci. Pollut. Res.*, 21 (2014), 12217–12222.
- [5] G. Charles, T. Roques-Carmes, N. Becheikh, L. Falk, J.-M. Commenge, S. Corbel, Determination of kinetic constants of a photocatalytic reaction in micro-channel reactors in the presence of mass-transfer limitation and axial dispersion, *J. Photochem. Photobiol. Chem.*, 223 (2011), 202–211.
- [6] J.-M. Herrmann, Heterogeneous photocatalysis: state of the art and present applications In honor of Pr. R.L. Burwell Jr. (1912–2003), Former Head of Ipatieff Laboratories, Northwestern University, Evanston (Ill)., *Top. Catal.*, 34 (2005), 49–65.
- [7] J.-M. Herrmann, Photocatalysis fundamentals revisited to avoid several misconceptions, *Appl. Catal. B Environ.*, 99 (2010), 461–468.
- [8] G. Charles, T. Roques-Carmes, N. Becheikh, L. Falk, S. Corbel, Impact of the design and the materials of rectangular microchannel reactors on the photocatalytic decomposition of organic pollutant, *Green Process. Synth.*, 1 (2012), 363–374.
- [9] A. K. Fung, B. K. Chiu, M. H. Lam, Surface modification of TiO₂ by a ruthenium(II) polypyridyl complex via silyl-linkage for the sensitized photocatalytic degradation of carbon tetrachloride by visible irradiation, *Water Res.*, 37 (2003), 1939–1947.
- [10] X. Su, J. Li, Z. Zhang, M. Yu, L. Yuan, Cu(II) porphyrins modified TiO₂ photocatalysts: Accumulated patterns of Cu(II) porphyrin molecules on the surface of TiO₂ and influence on photocatalytic activity, *J. Alloys Compd.*, 626 (2015), 252–259.
- [11] X. Lü, W. Sun, J. Li, W. Xu, F. Zhang, Spectroscopic investigations on the simulated solar light induced photodegradation of 4-nitrophenol by using three novel copper(II) porphyrin–TiO₂ photocatalysts, *Spectrochim. Acta. A. Mol. Biomol. Spectrosc.*, 111 (2013), 161–168.
- [12] U. I. Gaya, A. H. Abdullah, Heterogeneous photocatalytic degradation of organic contaminants over titanium dioxide: A review of fundamentals, progress and problems, *J. Photochem. Photobiol. C Photochem. Rev.*, 9 (2008), 1–12.
- [13] J.-L. Blin, M.-J. Stébé, T. Roques-Carmes, Use of ordered mesoporous titania with semi-crystalline framework as photocatalyst, *Colloids Surf. Physicochem. Eng. Asp.*, 407 (2012), 177–185.
- [14] A. Fujishima, T. N. Rao, D. A. Tryk, Titanium dioxide photocatalysis, *J. Photochem. Photobiol. C Photochem. Rev.*, 1 (2000), 1–21.
- [15] K. Assaker, C. Carteret, T. Roques-Carmes, J. Ghanbaja, M.-J. Stébé, J.-L. Blin, Influence of Zn ion addition on the properties of ordered mesoporous TiO₂, *New J. Chem.*, 38 (2014), 2081, 2014.
- [16] X. Zhao, X. Liu, M. Yu, C. Wang, J. Li, The highly efficient and stable Cu, Co, Zn-porphyrin–TiO₂ photocatalysts with heterojunction by using fashioned one-step method, *Dyes Pigments*, 136 (2017), 648–656.
- [17] G. Yao, J. Li, Y. Luo, W. Sun, Efficient visible photodegradation of 4-nitrophenol in the presence of H₂O₂ by using a new copper(II) porphyrin–TiO₂ photocatalyst, *J. Mol. Catal. Chem.*, 361–362 (2012), 29–35.

- [18] M. R. Hoffmann, S. T. Martin, W. Choi, D. W. Bahnemann, Environmental Applications of Semiconductor Photocatalysis, *Chem. Rev.*, 95 (1995), 69–96.
- [19] S. Afzal, W. A. Daoud, S. J. Langford, Self-cleaning cotton by porphyrin-sensitized visible-light photocatalysis, *J. Mater. Chem.*, 22 (2012), 4083–4088.
- [20] A. Kruth, S. Peglow, N. Rockstroh, H. Junge, V. Brüser, K.-D. Weltmann, Enhancement of photocatalytic activity of dye sensitized anatase layers by application of a plasma-polymerized allylamine encapsulation, *J. Photochem. Photobiol. Chem.*, 290 (2014), 31–37.
- [21] C. Wang, J. Li, G. Mele, G. M. Yang, F. X. Zhang, L. Palmisano, G. Vasapollo, Efficient degradation of 4-nitrophenol by using functionalized porphyrin-TiO₂ photocatalysts under visible irradiation, *Appl. Catal. B Environ.*, 76 (2007), 218–226.
- [22] B. Yao, C. Peng, W. Zhang, Q. Zhang, J. Niu, J. Zhao, A novel Fe(III) porphyrin-conjugated TiO₂ visible-light photocatalyst, *Appl. Catal. B Environ.*, 174–175 (2015), 77–84.
- [23] W. Sun, J. Li, G. Yao, F. Zhang, J.-L. Wang, Surface-modification of TiO₂ with new metalloporphyrins and their photocatalytic activity in the degradation of 4-nitrophenol, *Appl. Surf. Sci.*, 258 (2011), 940–945.
- [24] G. Calogero, G. Di Marco, S. Caramori, S. Cazzanti, R. Argazzi, C. A. Bignozzi, Natural dye sensitizers for photoelectrochemical cells, *Energy Environ. Sci.*, 2 (2009), 1162–1172.
- [25] S. Afzal, W. A. Daoud, S. J. Langford, Photostable Self-Cleaning Cotton by a Copper(II) Porphyrin/TiO₂ Visible-Light Photocatalytic System, *ACS Appl. Mater. Interfaces*, 5 (2013), 4753–4759.
- [26] P. Huang, C. Xu, J. Lin, C. Wang, X. Wang, C. Zhang, X. Zhou, S. Guo, D. Cui, Folic acid-conjugated graphene oxide loaded with photosensitizers for targeting photodynamic therapy. *Theranostics*, 1 (2011), 240–250.
- [27] G. Granados-Oliveros, E. A. Páez-Mozo, F. M. Ortega, C. Ferronato, J.-M. Chovelon, Degradation of atrazine using metalloporphyrins supported on TiO₂ under visible light irradiation, *Appl. Catal. B Environ.*, 89 (2009), 448–454.
- [28] B. U. Jang, J. H. Choi, S. J. Lee, S. G. Lee, Synthesis and characterization of Cu - phthalocyanine hybrid TiO₂ sol, *J. Porphyr. Phthalocyanines*, 13 (2009), 779–786.
- [29] C. J. P. Monteiro, M. M. Pereira, M. G. H. Vicente, L. G. Arnaut, Photophysical properties of unsymmetric meso-substituted porphyrins synthesized via the Suzuki coupling reaction, *Tetrahedron*, 68 (2012), 8783–8788.
- [30] G. Granados-Oliveros, E.A. Páez-Mozo, F.M. Ortega, M. Piccinato, F.N. Silva, C.L.B. Guedes, E. Di Mauro, M.F. da Costa, A.T. Ota, Visible light production of superoxide anion with MCarboxyphenylporphyrins (M=H, Fe, Co, Ni, Cu, and Zn) free and anchored on TiO₂: EPR characterization, *J. Mol. Catal. Chem.*, 339 (2011), 79–85.
- [31] H. Alloul, T. Roques-Carmes, T. Hamieh, A. Razafitianamaharavo, O. Barres, J. Toufaily, F. Villiéras, Effect of chemical modification on surface free energy components of Aerosil silica powders determined with capillary rise technique, *Powder Technol.*, 246 (2013), 575–582.
- [32] H. Alloul, T. Roques-Carmes, J. Toufaily, M. Kassir, M. Pelletier, A. Razafitianamaharavo, T. Hamieh, F. Villiéras, Towards a better description of organosilane grafting onto silica particles using volumetric techniques based on molecular probing, *Adsorption*, 22 (2016), 923–937.
- [33] M. Kassir, T. Roques-Carmes, T. Hamieh, A. Razafitianamaharavo, O. Barres, J. Toufaily, F. Villiéras, Surface modification of TiO₂ nanoparticles with AHAPS aminosilane: distinction between physisorption and chemisorption, *Adsorption*, 19 (2013), 1197–1209.
- [34] M. Kassir, T. Roques-Carmes, T. Hamieh, J. Toufaily, M. Akil, O. Barres, F. Villiéras, Improvement of the photocatalytic activity of TiO₂ induced by organic pollutant enrichment at the surface of the organografted catalyst, *Colloids Surf. Physicochem. Eng. Asp.*, 485 (2015), 73–83.
- [35] P. Couleaud, D. Bechet, R. Vanderesse, M. Barberi-Heyob, A.C. Faure, S. Roux, O. Tillement, S. Porhel, F. Guillemain, C. Frochot, Functionalized silica-based nanoparticles for photodynamic therapy, *Nanomed.*, 6 (2011), 995–1009.

- [36] F. Cheng, S. M. Sajedin, S. M. Kelly, A. F. Lee, A. Kornherr, UV-stable paper coated with APTES-modified P25 TiO₂ nanoparticles, *Carbohydr. Polym.*, 114 (2014), 246–252.
- [37] X. Feng, S. Zhang, H. Wu, X. Lou, A novel folic acid-conjugated TiO₂–SiO₂ photosensitizer for cancer targeting in photodynamic therapy, *Colloids Surf. B Biointerfaces*, 125 (2015), 197–205.
- [38] A. Fidalgo-Marijuan, E. Amayuelas, G. Barandika, B. Bazán, M. K. Urtiaga, M. I. Arriortua, Coordination and Crystallization Molecules: Their Interactions Affecting the Dimensionality of Metalloporphyrinic SCFs, *Molecules*, 20 (2015), 6683–6699.
- [39] R. Rahimi, S. Saadati, E. Honarvar Fard, Fluorine-doped TiO₂ nanoparticles sensitized by tetra(4-carboxyphenyl)porphyrin and zinc tetra(4-carboxyphenyl)porphyrin: Preparation, characterization, and evaluation of photocatalytic activity, *Environ. Prog. Sustain. Energy*, 34 (2015), 1341–1348.
- [40] S. Murphy, C. Saurel, A. Morrissey, J. Tobin, M. Oelgemöller, K. Nolan, Photocatalytic activity of a porphyrin/TiO₂ composite in the degradation of pharmaceuticals, *Appl. Catal. B Environ.*, 119–120 (2012), 156–165.
- [41] M.Y. Duan, J. Li, G. Mele, C. Wang, X.F. Lü, G. Vasapollo, F.X. Zhang, The photocatalytic activity of novel, substituted porphyrin/TiO₂-based composites, *Dyes Pigments*, 84 (2010), 183–189.
- [42] A.L. Bulin, C. Truillet, R. Chouikrat, F. Lux, C. Frochot, D. Amans, G. Ledoux, O. Tillement, P. Perriat, M. Barberi-Heyob, C. Dujardin, X-ray-Induced Singlet Oxygen Activation with Nanoscintillator-Coupled Porphyrins, *J. Phys. Chem. C*, 117 (2013), 21583–21589.
- [43] A. Kay, R. Humphry-Baker, M. Graetzel, Artificial Photosynthesis. 2. Investigations on the Mechanism of Photosensitization of Nanocrystalline TiO₂ Solar Cells by Chlorophyll Derivatives, *J. Phys. Chem.*, 98 (1994), 952–959.
- [44] C. Peng, B. Yao, W. Zhang, J. Niu, J. Zhao, Synthesis of CuAPTPP-TDI-TiO₂ Conjugated Microspheres and its Photocatalytic Activity, *Chin. J. Chem. Phys.*, 27 (2014), 200–208.
- [45] H. Huang, X. Gu, J. Zhou, K. Ji, H. Liu, Y. Feng, Photocatalytic degradation of Rhodamine B on TiO₂ nanoparticles modified with porphyrin and iron-porphyrin, *Catal. Commun.*, 11 (2009), 58–61.
- [46] X.-T. Zhou, H.-B. Ji, X.-J. Huang, Photocatalytic Degradation of Methyl Orange over Metalloporphyrins Supported on TiO₂ Degussa P25, *Molecules*, 17 (2012), 1149–1158.
- [47] B. Ohtani, O. O. Prieto-Mahaney, D. Li, R. Abe, What is Degussa (Evonik) P25? Crystalline composition analysis, reconstruction from isolated pure particles and photocatalytic activity test, *J. Photochem. Photobiol. Chem.*, 216 (2010), 179–182.
- [48] A. Fujishima, X. Zhang, D. Tryk, TiO₂ photocatalysis and related surface phenomena, *Surf. Sci. Rep.*, 63 (2008), 515–582.
- [49] Z. Rui, S. Wu, C. Peng, H. Ji, Comparison of TiO₂ Degussa P25 with anatase and rutile crystalline phases for methane combustion, *Chem. Eng. J.*, 243 (2014), 254–264.

Supporting information

Supporting information S1: Activation of P1-COOH

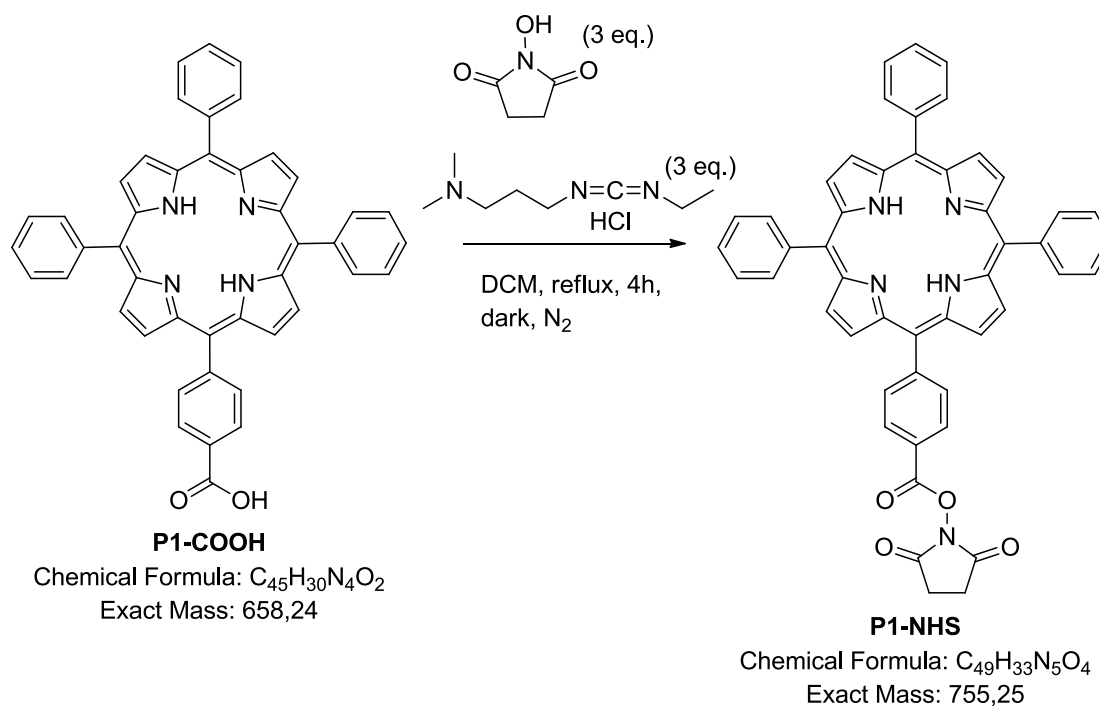


Fig. S1: Scheme representing the steps of the activation of the P1-COOH PS.

In dark and under inert atmosphere, in a 50 mL round bottomed flask, photosensitizer P1-COOH (100 mg) was dissolved in dichloromethane (DCM, CH_2Cl_2) (30 mL) and *N*-hydroxysuccinimide (3 eq.) and *N*-(3-dimethylaminopropyl-*N'*-ethyl carbodiimide hydrochloride (3 eq.) were added. The mixture is stirred at 40 °C for 4 hours, under nitrogen. The reactional mixture (DCM) was evaporated. Then the crude is taken off in chloroform (50 mL), the organic fraction was washed with water (50 mL x 2), followed by decantation. After that, the organic fraction was dried with anhydrous sodium sulfate (flask covered with aluminum foil and stirred for about 10 min), and the solvent was removed under vacuum. The chloroform was then evaporated. For purification with silica column, the crude product was dissolved in DCM. The purification of the crude material was performed using a silica gel column with DCM. The product was collected and the DCM solvent was then evaporated. Afterwards, a minimum amount of DCM was added to dissolve the crude material, and then hexane was added in a dropwise manner until crystals started to form. The product was placed in the fridge overnight for recrystallization to be finally obtained by vacuum filtration.

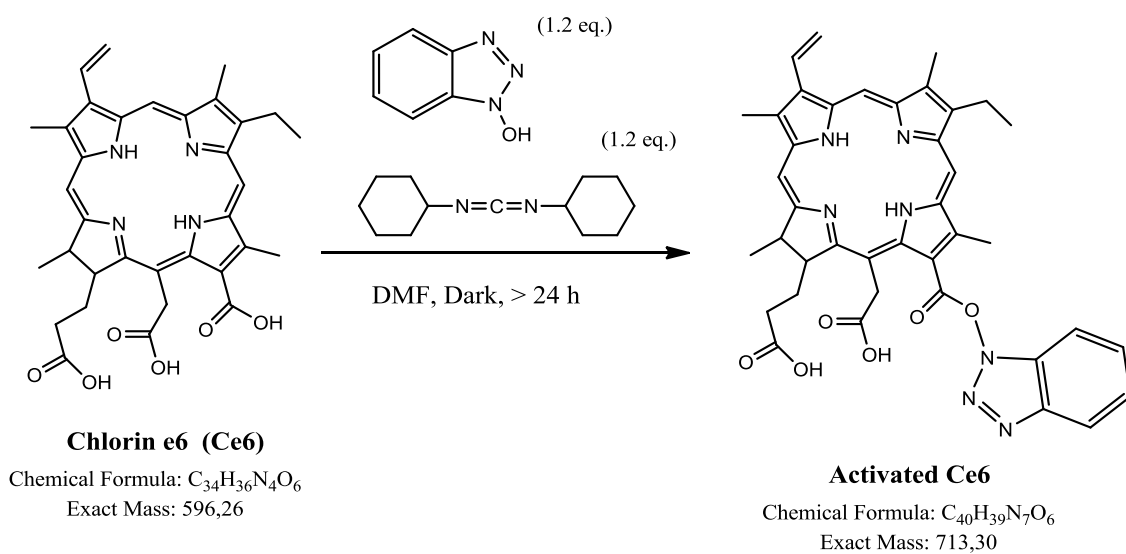
Supporting information S2: Activation of Ce6

Fig. S2: Scheme representing the steps of the activation of the Ce6.

First, DCC (1.2 eq.) was dissolved in DMF (30 mL), and HOBT (1.2 eq.) was added into the solution. After that, the Ce6 PS (1 eq.) was added and all the solution was stirred at room temperature for at least 24 hours. The activated PS was used directly.

Supporting information S3: Preparation of the core-shell nanosystem

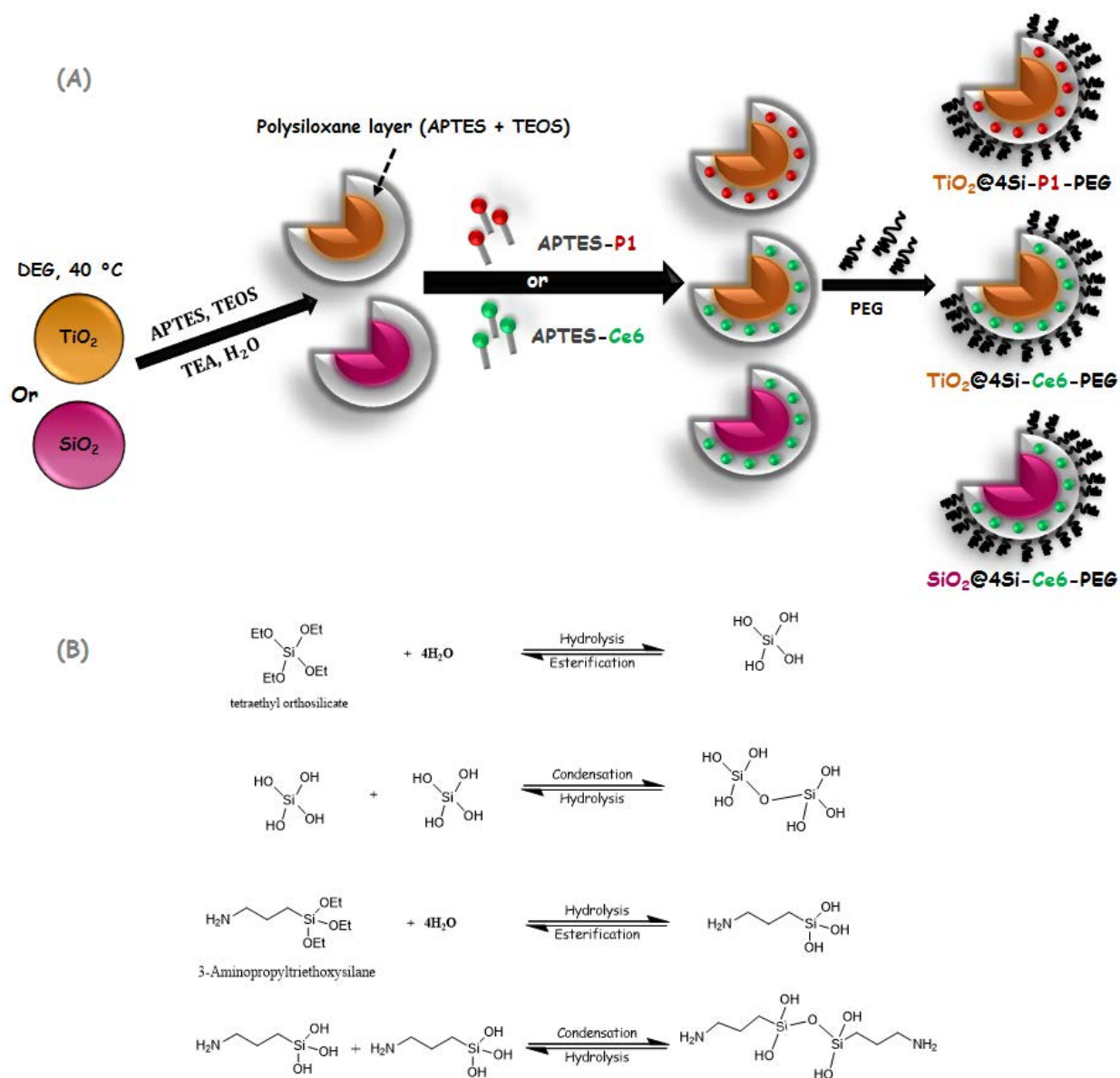


Fig. S3: (A) Scheme representing the steps of the formation of the core-shell nanosystem. (B) The steps of the hydrolysis and condensation of the APTES and TEOS silane reagents constituting the polysiloxane layer.

The encapsulation of the TiO_2 or SiO_2 core into a polysiloxane shell was accomplished by the use of two silane reagents. Thus, the silica shell was constituted of 60% of aminopropyltriethoxysilane (APTES) and 40% of tetraethoxysilane (TEOS). Under soft conditions as low temperature (40 °C) and in the presence of a basic catalyst, *i.e.* triethylamine (TEA), and traces of water, the formation of the polysiloxane layer was possible via hydrolysis-condensation reactions of the silane groups. First, the ethoxy groups (Si-OEt) of the silane reagents hydrolyzed and formed hydroxyl groups (Si-OH).

After that, the silane precursors tend to condense thus forming the polysiloxane network around the TiO_2 or SiO_2 core promoted by the occurrence of TEA catalyst. However, those NPs can be functionalized by different species due to the presence of the aminopropyl arm of APTES. So this amine group was employed to graft the PS and the hydrophilic PEG-250 onto the NPs via an amide bond involving the carboxyl group of the PS and PEG.

Supporting information S4: Preparation of the APTES-modified nanosystem

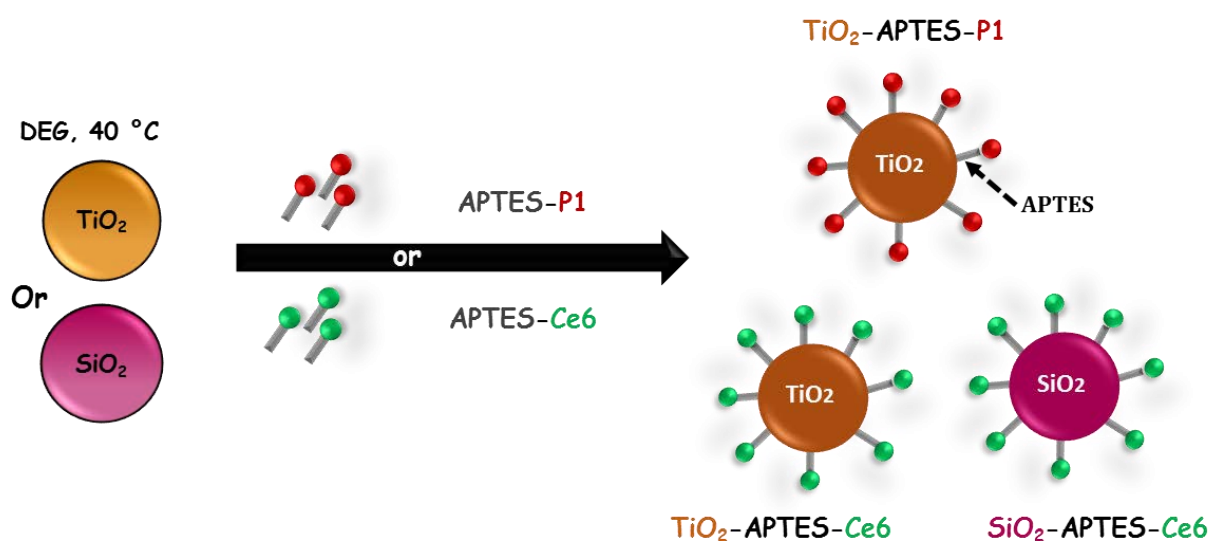


Fig. S4: Scheme representing the steps of the formation of the APTES-modified nanosystem.

Upon silanization, APTES tend to interact with the hydroxyl ($-\text{OH}$) functions on TiO_2 or SiO_2 surface. APTES owns two distinctive terminal functional groups that are the amine ($-\text{NH}_2$) and the hydrolysable silane ($-\text{Si}(\text{OEt})_3$) groups. The $-\text{OH}$ groups at the surface of the NPs may interact with the ethoxy groups of APTES. It is considered a normal attachment with free terminal amine groups oriented away from the surface of TiO_2 NPs.

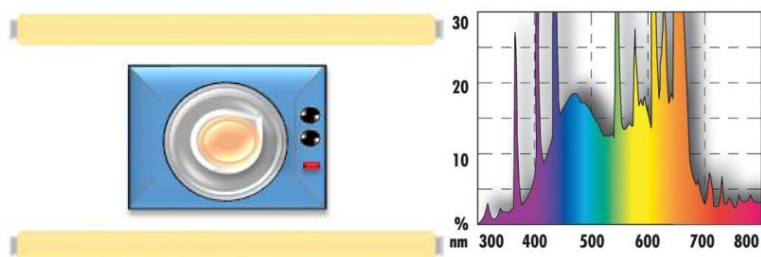
Supporting information S5: Photocatalytic tests performed under solar light

Fig. S5: The experimental setup of the photocatalytic tests performed under simulated solar light and the spectrum of the used lamp.

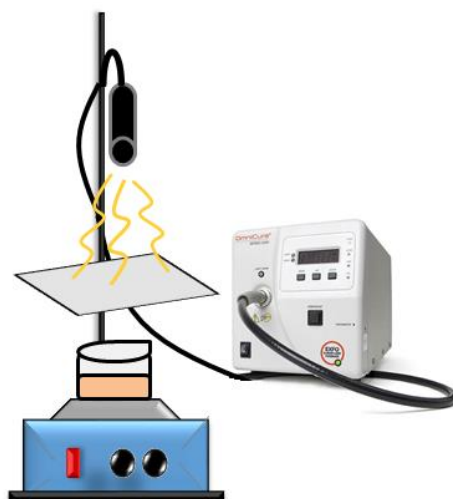
Supporting information S6: Photocatalytic tests performed under visible light

Fig. S6: The experimental setup employed for the photocatalytic tests performed under visible light.

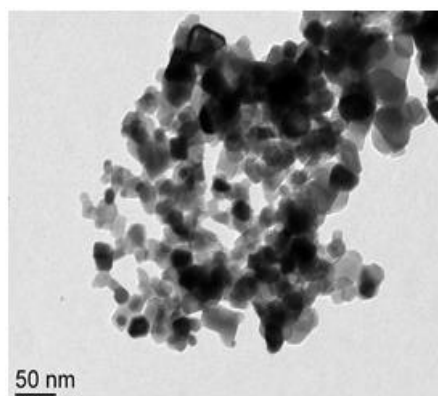
Supporting information S7: Transmission Electron Microscopy (TEM) of bare TiO₂ P25

Fig. S7: TEM image of bare TiO₂ P25.

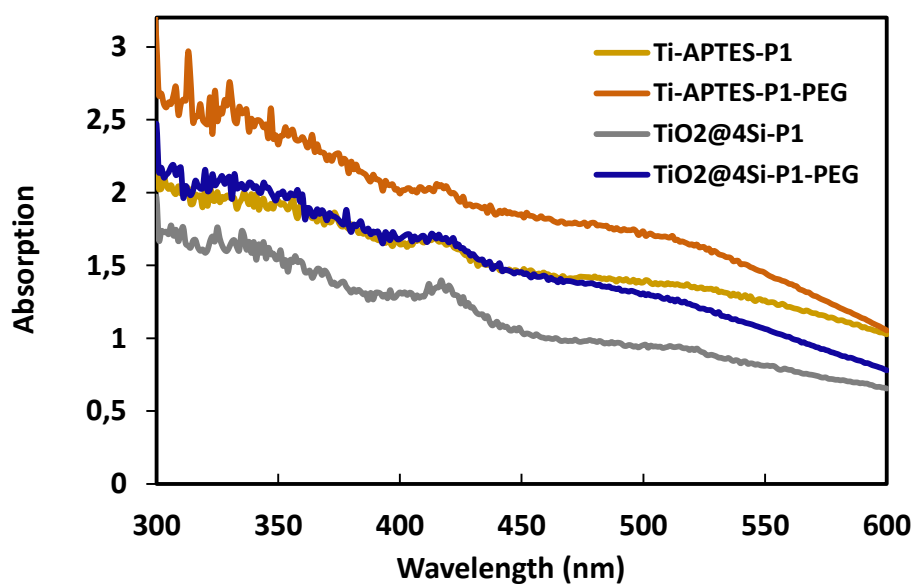
Supporting information S8: UV-Visible absorption spectra of NPs modified by P1-COOH PS in the absence and presence of PEG

Fig. S8: UV-Visible absorption spectra of core-shell and APTES-modified TiO₂ NPs sensitized by P1-COOH PS in the absence and in the presence of PEG. The NPs are dispersed in ethanol.

Supporting information S9: UV-Visible absorption spectra of TiO₂ and SiO₂ NPs modified by Ce6 PS

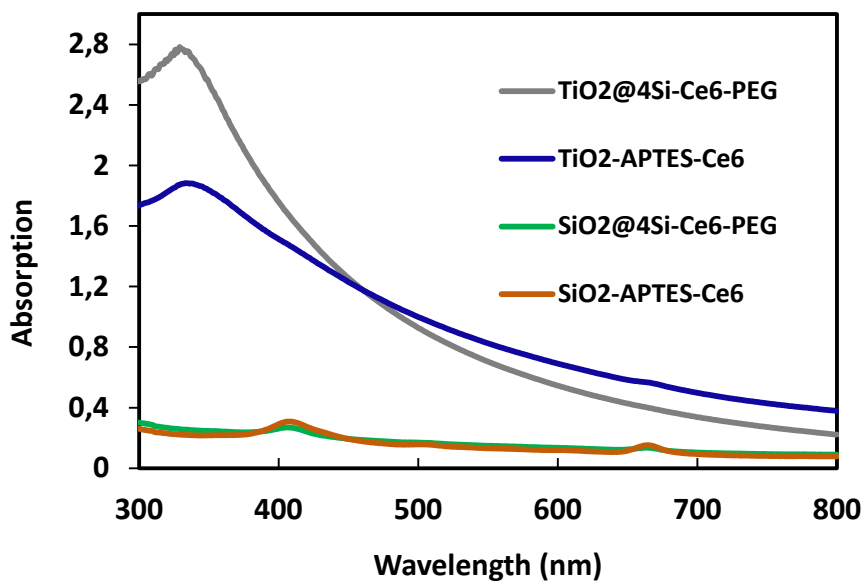


Fig. S9: UV-Visible absorption spectra of core-shell and APTES-modified TiO₂ and SiO₂ NPs sensitized by Ce6 PS dispersed in ethanol.

Supporting information S10: Photocatalytic degradation of methyl orange by free (non-attached) Ce6 and P1-COOH PSs under simulated solar light

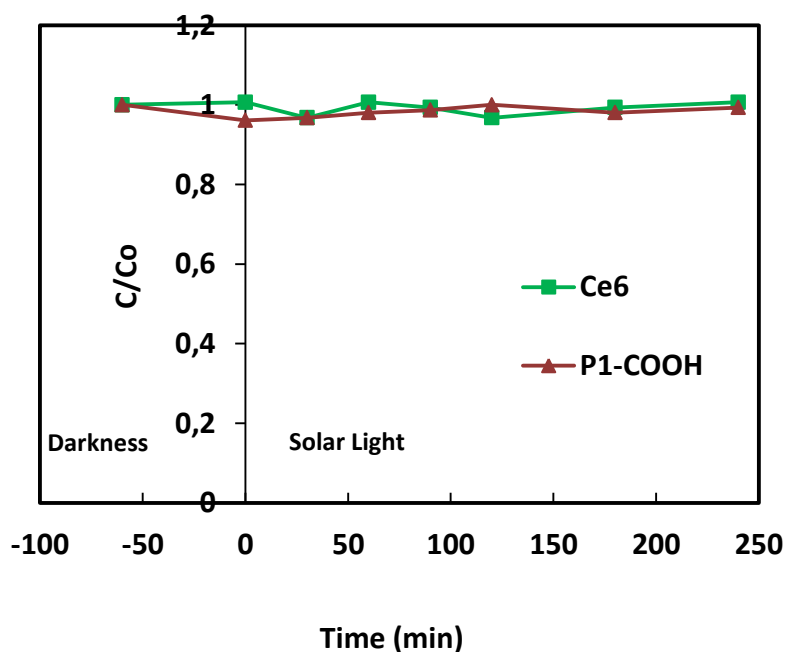


Fig. S10: Photocatalytic degradation of MO by free (non-grafted) Ce6 and P1-COOH PSs under simulated solar light.

Supporting information S11: Photocatalytic degradation of methyl orange under solar light

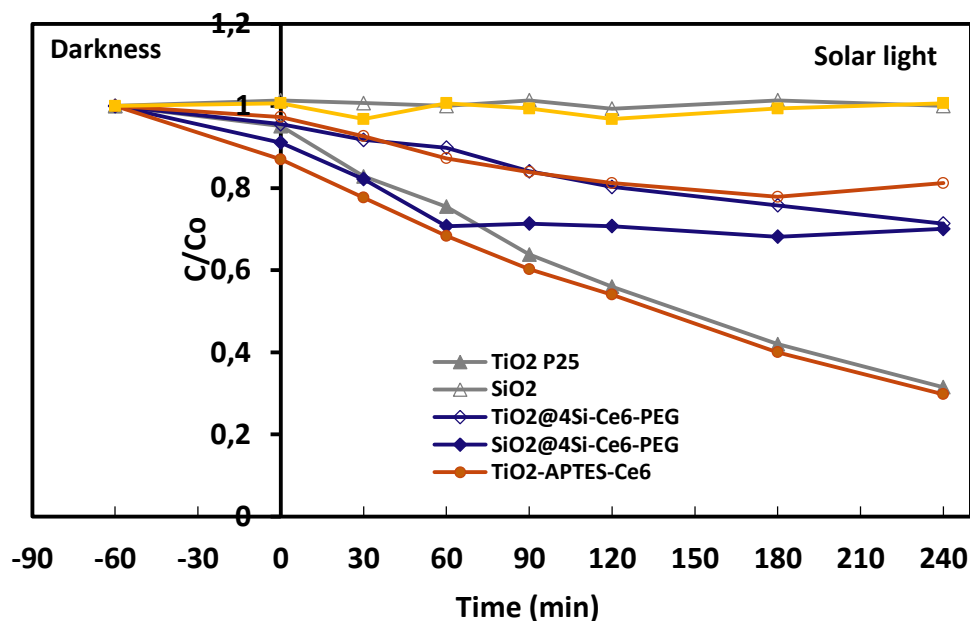


Fig. S11: Comparison of the photocatalytic degradation of methyl orange by TiO₂, TiO₂-APTES-Ce6, TiO₂@4Si-Ce6-PEG, SiO₂, SiO₂-APTES-Ce6, SiO₂@4Si-Ce6-PEG NPs, and free (non-grafted) Ce6 PS under simulated solar light irradiation.

Supporting information S12: Photocatalytic degradation of methyl orange under visible light

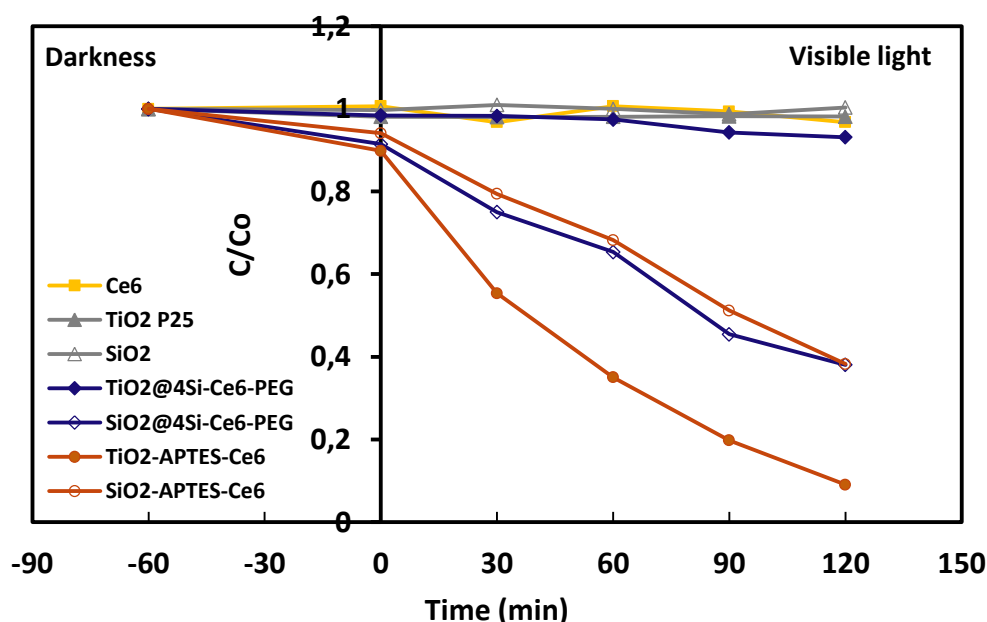


Fig. S12: Comparison of the photocatalytic degradation of methyl orange by TiO₂, TiO₂-APTES-Ce6, TiO₂@4Si-Ce6-PEG, SiO₂, SiO₂-APTES-Ce6, SiO₂@4Si-Ce6-PEG NPs, and free (non-attached) Ce6 PS under pure visible light irradiation.

Supporting information S13: Stability/instability of methyl orange under visible light in the absence of a catalyst

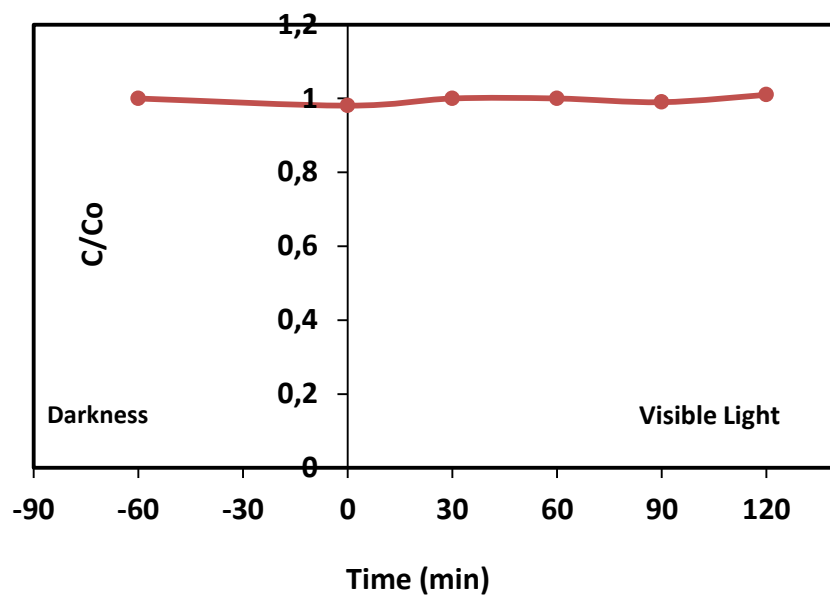


Fig. S13. The photocatalytic degradation of methyl orange in the absence of any catalyst under pure visible light irradiation.

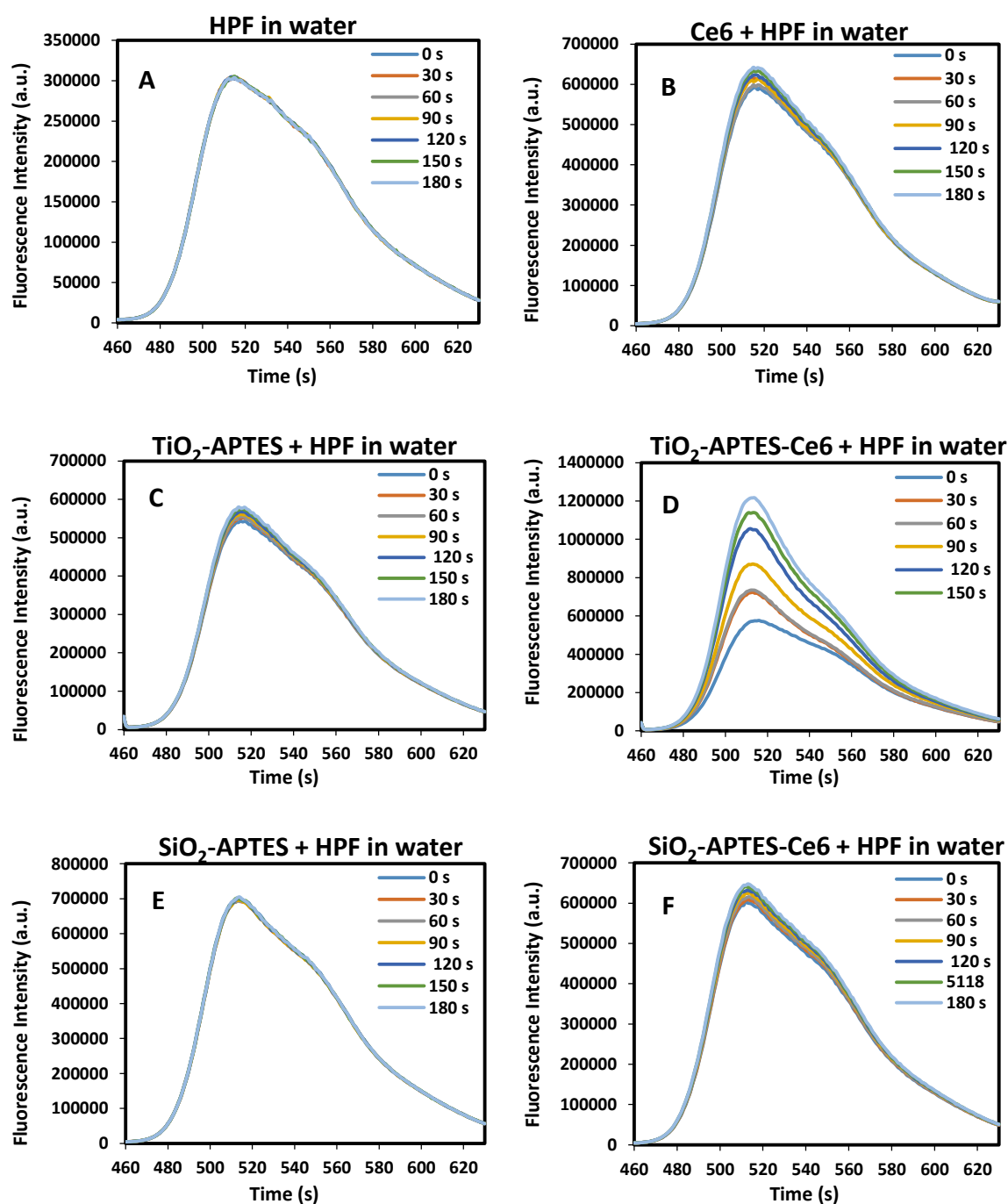
Supporting information S14: Measurement of hydroxyl radicals (HO \cdot) by HPF probe

Fig. S14. The temporal evolution of the fluorescence intensity of (A) HPF alone, and HPF in the presence of (B) Ce6, (C) control TiO₂-APTES NPs, (D) TiO₂-APTES-Ce6 NPs, (E) control SiO₂-APTES NPs, and (F) SiO₂-APTES-Ce6 NPs.

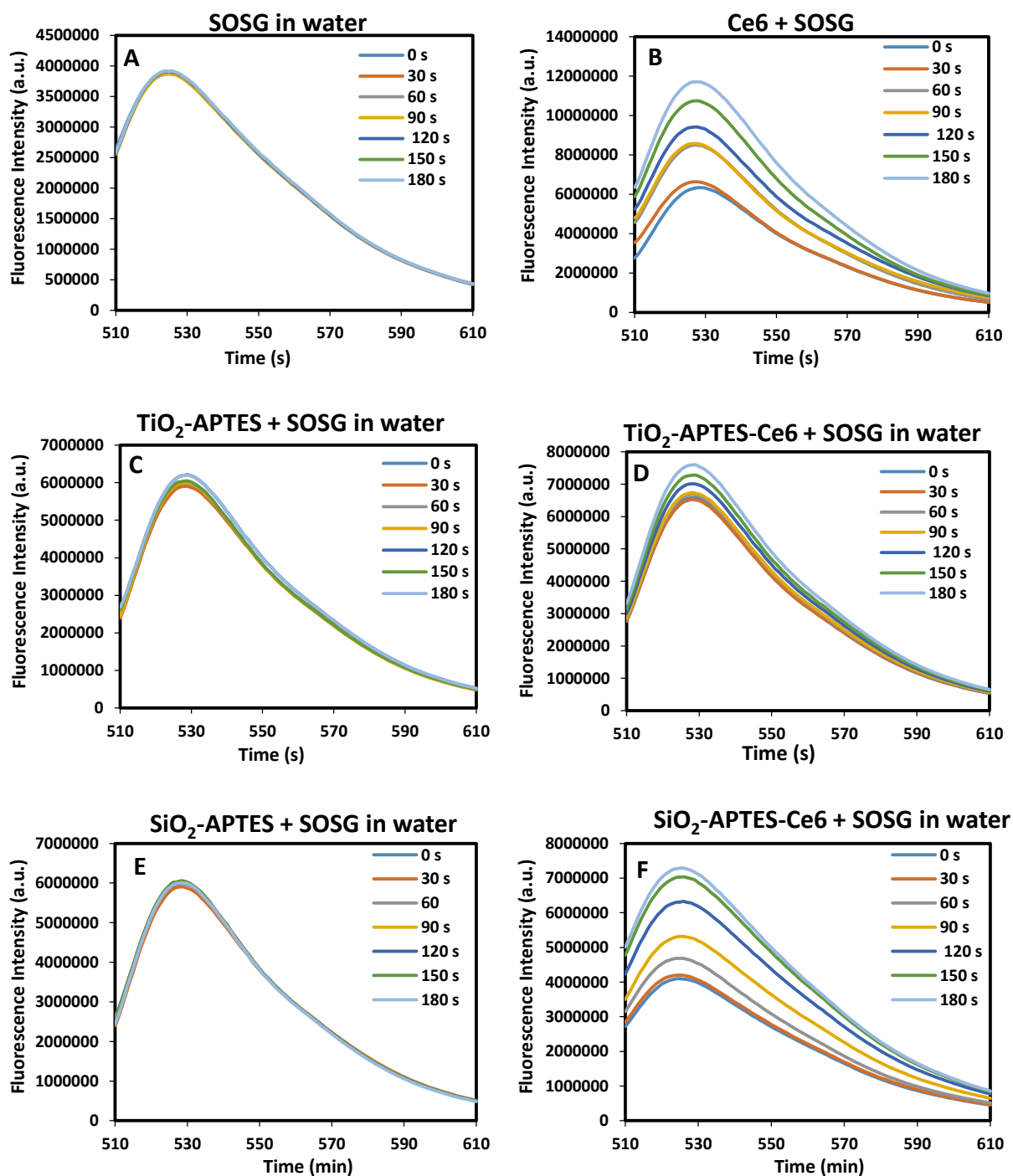
Supporting information S15: Measurement of singlet oxygen ($^1\text{O}_2$) by SOSG probe

Fig. S15. The temporal evolution of the fluorescence intensity of (A) SOSG alone, and SOSG in the presence of (B) Ce6, (C) control TiO₂-APTES NPs, (D) TiO₂-APTES-Ce6 NPs, (E) control SiO₂-APTES NPs, and (F) SiO₂-APTES-Ce6 NPs.

Annexes

Annex I: Surface modification of TiO₂ by APTES

The surface of TiO₂ P25 NPs was modified by grafting different amounts of APTES silane. **Table A1** summarizes the amounts of grafted APTES. The results obtained are shown in **Table A2**.

Table A1: APTES silane linked onto the surface of TiO₂ semiconductor.

Ti: 1 mmol					
Sample	n (APTES) mmol	n (Ti) mmol	n (APTES) mmol	V (APTES) mL	V (xylene) mL
TiO ₂ -APTES 1	0.05	18.78	0.939	0.219	150
TiO ₂ -APTES 2	0.1	18.78	1.878	0.438	150
TiO ₂ -APTES 3	0.15	18.78	2.817	0.657	150
TiO ₂ -APTES 4	0.2	18.78	3.756	0.876	500
TiO ₂ -APTES 5	0.4	18.78	7.512	1.752	150
TiO ₂ -APTES 6	0.6	18.78	11.268	2.629	150
TiO ₂ -APTES 7	0.8	18.78	15.024	3.505	150
TiO ₂ -APTES 8	1	18.78	18.781	4.381	150
TiO ₂ -APTES 9	1.2	18.78	22.537	5.257	150

Table A2: Different amounts of APTES silane grafted onto the surface of TiO₂ P25.

NPs	S _{BET} (m ² /g)	C _{BET}	Pore volume (cm ³ /g) at P/P ₀ = 0.99	Pore size (Å°)
TiO ₂ P25	48.8	96.1	0.154	125.9
TiO ₂ -APTES 1	45.0	56.9	0.179	159.0
TiO ₂ -APTES 2	44.9	55.6	0.175	155.4
TiO ₂ -APTES 3	44.2	56.5	0.181	164.0
TiO ₂ -APTES 4	44.4	53.2	0.178	159.9
TiO ₂ -APTES 5	45.5	51.5	0.173	151.7
TiO ₂ -APTES 6	46.1	48.8	0.239	207.5
TiO ₂ -APTES 7	46.6	45.0	0.239	205.3
TiO ₂ -APTES 8	46.3	46.8	0.251	216.6
TiO ₂ -APTES 9	46.3	40.0	0.171	147.2

AI.1. The variation of the BET specific surface area as a function of the APTES surface coverage

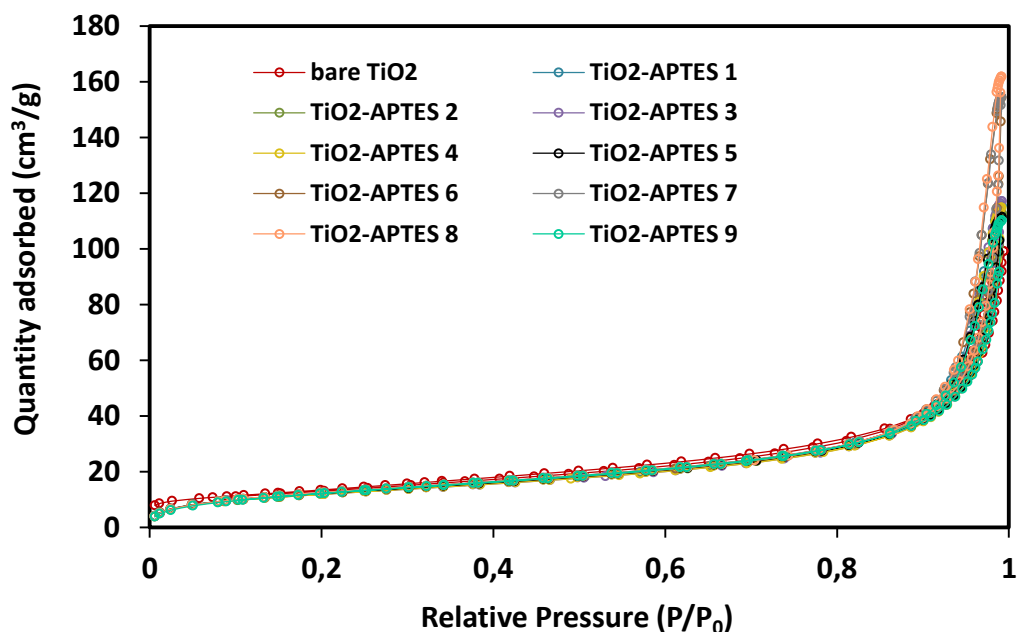


Fig. A1: The BET specific surface area of APTES-modified and bare TiO₂ obtained from nitrogen adsorption-desorption isotherm.

The surface area of TiO₂ before and after modification is about $45 \pm 2 \text{ m}^2/\text{g}$. It appears that grafting APTES into the surface of the NPs induced no effect on the BET surface area. The S_{BET} graphs corresponding to bare TiO₂ and TiO₂ modified with different amounts of APTES are similar and are all of type II isotherm according to IUPAC. Very small, almost negligible, hysteresis can be observed, this is linked with the non-porous or micro-porous property of the TiO₂ P25 material [A1].

AI.2. The variation of the BET constant (C_{BET}) as a function of the APTES surface coverage

Fig. A2 shows that grafting APTES onto the surface of TiO₂ causes a reduction of the BET constant (C_{BET}). The observed drop in the C_{BET} constant confirms the alteration of the TiO₂ surface chemistry in the presence of APTES. Thus, the C_{BET} remains high for polar surfaces and becomes low for non-polar surfaces or those possessing a lower hydrophilic character (*Kassir colloids and surfaces*).

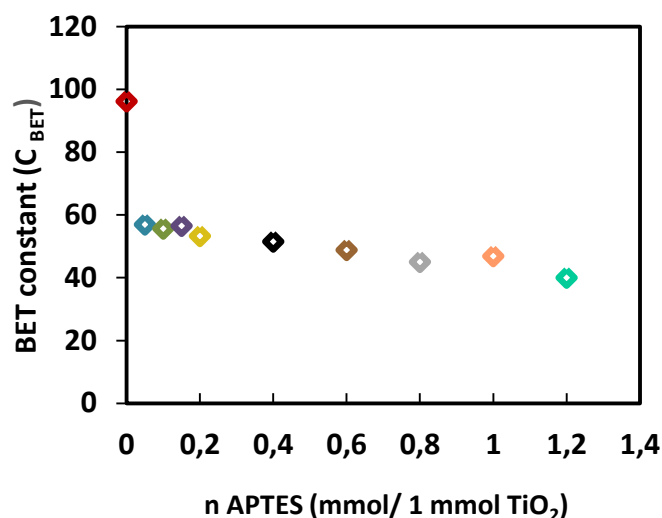


Fig. A2: The variation of the BET constant (C_{BET}) as a function of the APTES surface coverage.

AI.3. The variation of the point of zero charge (PZC) as a function of the APTES surface coverage

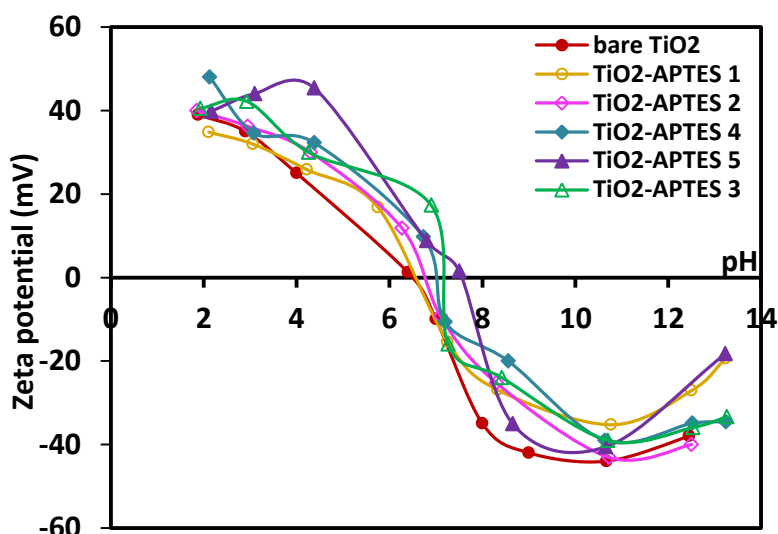


Fig. A3: The variation of the zeta-potential with pH for bare and APTES-modified titania.

The zeta potential of the bare and the modified titania nanoparticles tend to decline as the pH rises from positive to negative values in acidic and basic mediums, respectively. After modification with different amounts of APTES, the corresponding zeta potential-pH curves embrace a very similar trend as obtained with bare TiO₂. As the pH increases to values higher than 10, a plateau is reached. Modifying the surface of TiO₂ with different amounts of APTES induces an increase in the pzc of

those NPs as compared to that corresponding to bare TiO_2 . The PZC increases as the amount of grafted APTES increases.

AI.4. The effect of grafting different amounts of APTES on the photocatalytic activity of the NPs towards the degradation of methyl orange under solar light

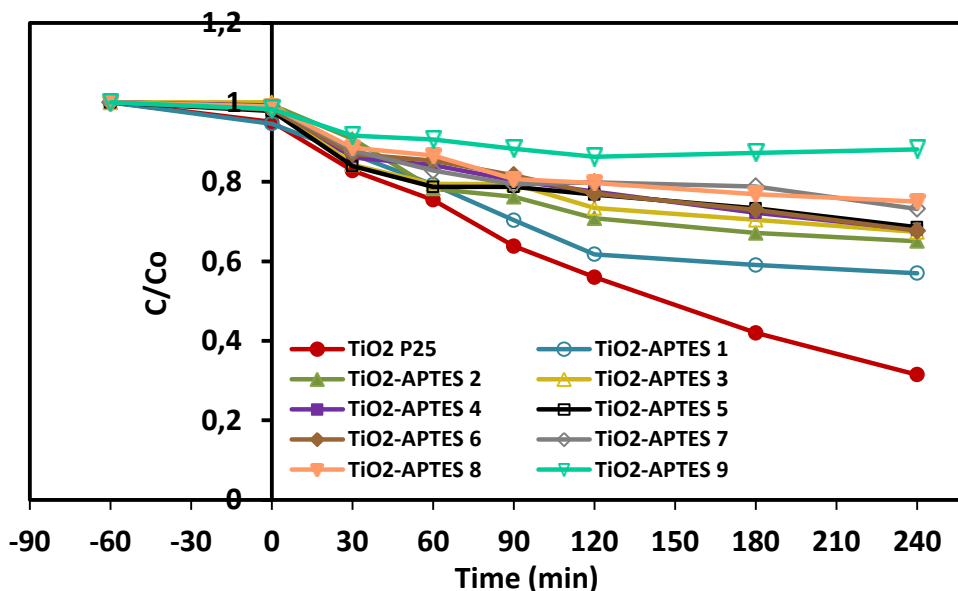


Fig. A4: The variation in the photocatalytic activity of bare and APTES-modified TiO_2 NPs towards the degradation of methyl orange.

The photocatalytic activity of the APTES-modified TiO_2 tends to decrease as the amount of grafted APTES increases. This is due to the decrease in the number of the hydroxyl groups occupying the surface of the semiconductor which lie at the core of the good photocatalytic activity of TiO_2 . Thus the chosen amount of APTES has to be moderate assuring the incomplete shielding of TiO_2 and producing enough $-\text{NH}_2$ groups for grafting the PS onto the TiO_2 NPs.

Annex II: Model water pollutants (methylene blue and methyl orange)

Methylene blue (MB) is used in many domains including textiles, biological microscopic staining, medical sector, etc [A2]. Methyl orange (MO) is frequently used as a pH-indicator in titration [A3].

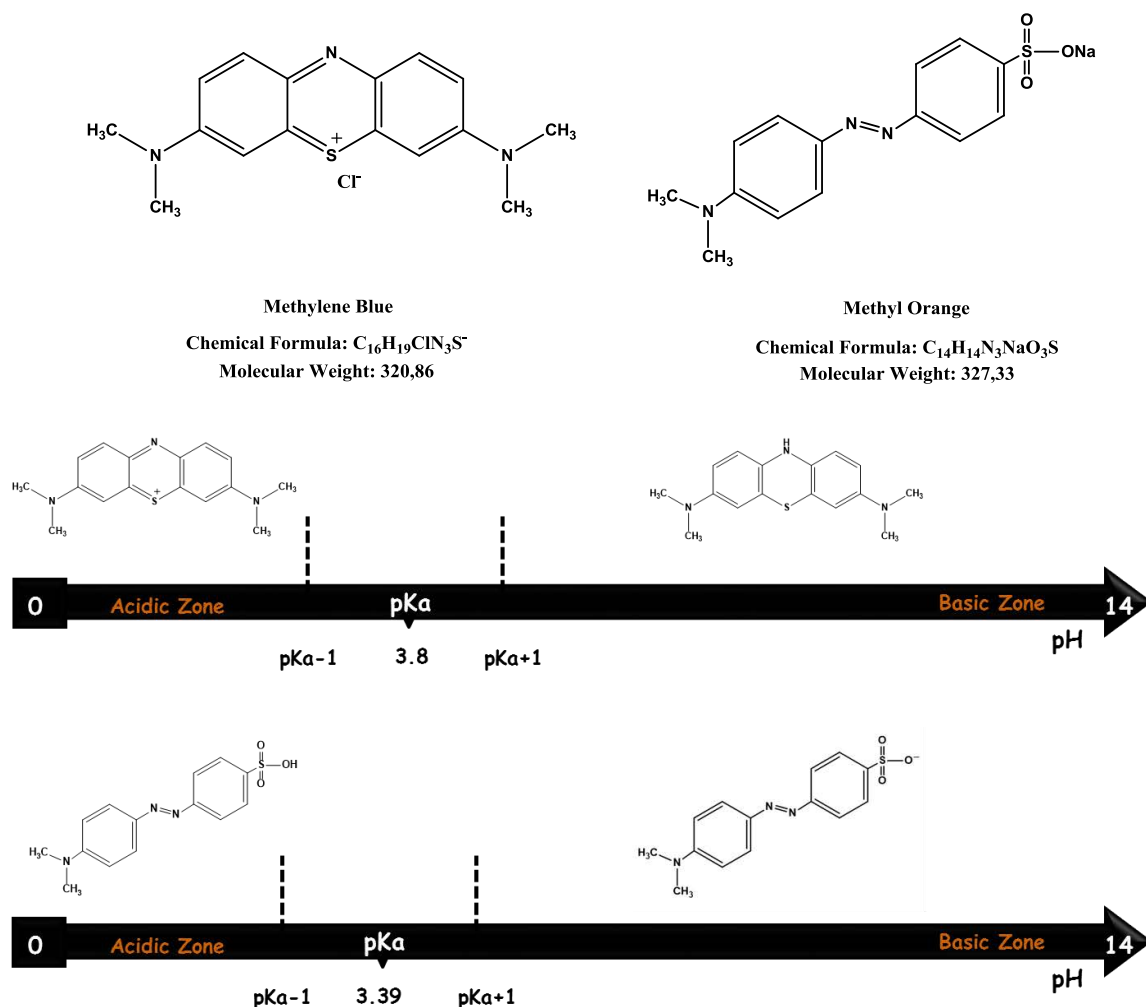


Fig. A5: The chemical structures of MB and MO and the zone of predominance of MB and MO and their conjugated bases as a function of pH.

References for Annexes

- [A1] K. Kaneko, "Determination of pore size and pore size distribution: 1. Adsorbents and catalysts." *Journal of membrane science* 96.1-2 (1994): 59-89
- [A2] <https://healdove.com/health-care-industry/Methylene-Blue-Uses-in-Medicine-and-Biology-Benefits-and-Risks>
- [A3] Generalic, Eni. "Methyl orange." *Croatian-English Chemistry Dictionary & Glossary*. 29 Aug. 2017. KTF-Split. 11 Sep. 2017. <<https://glossary.periodni.com>>

Chapter III:

Photodynamic Therapy Of Glioblastoma By Modified Titania And Silica Nanoparticles

This chapter describes the synthesis and characterization of Ce6-hybridized TiO₂ and SiO₂ NPs after modification with silane reagents. The elaborated NPs are tested for their photodynamic efficiency towards the eradication of glioblastoma U87 cells under visible light exposure in the presence of different amounts of NPs. The reactive oxygen species that induce the photodynamic effect were investigated.

Titania And Silica Nanoparticles Coupled To Chlorin e6 For Anti-Cancer Photodynamic Therapy

Zahraa Youssef^{1,2}, Valérie Jouan-Hureau³, Ludovic Colombeau¹, Philippe Arnoux¹, Albert Moussaron^{1,4}, Francis Baros¹, Joumana Toufaily², Tayssir Hamieh², Thibault Roques-Carmes¹, Céline Frochot*¹

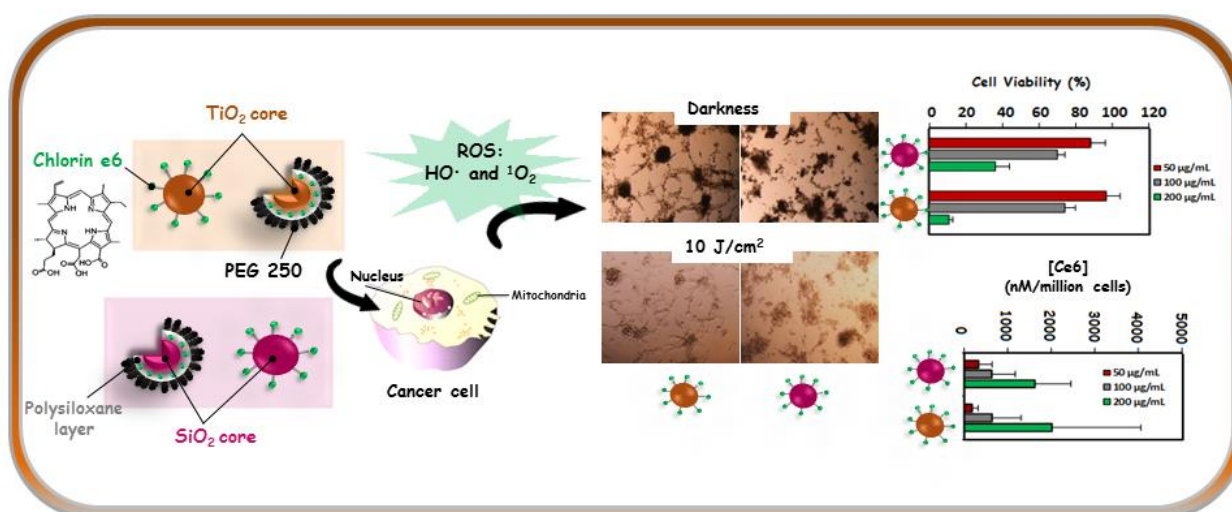
¹Laboratoire Réactions et Génie des Procédés, UMR 7274, Université de Lorraine-CNRS, Nancy, France

²Laboratory of Materials, Catalysis, Environment and Analytical Methods, Faculty of Sciences I, Lebanese University, Campus Rafic Hariri, Beirut, Lebanon.

³Université de Lorraine, CRAN, UMR 7039, Vandœuvre-lès-Nancy, France, CNRS, CRAN, UMR 7039, Vandœuvre-lès-Nancy, France

⁴Univ Lyon, Université Claude Bernard Lyon 1, CNRS, Institut Lumière Matière, F-69622, LYON, France

Article to be submitted to Photochemistry and Photobiology B: Biology Journal



Abstract

Photodynamic therapy (PDT) is a modality for treatment of cancer. In the search for new types of photosensitizers, nanoparticles are considered very promising especially as drug-delivery systems in PDT. Using Titanium dioxide nanoparticles (TiO₂ NPs) can be an option to improve passive targeting in PDT thanks to their strong oxidizing power, high stability, good *in vitro* and *in vivo* biocompatibility and minor dark cytotoxicity. They have been compared to SiO₂ NPs which are not photoactive unlike UV-active TiO₂ semiconductor in order to investigate the relationship between the composition and PDT efficiency. In this study, the TiO₂ or SiO₂ core were silanized either by the growth of a silica shell constituting of two silane reagents ((3-aminopropyl)triethoxysilane (APTES) and tetraethyl orthosilicate (TEOS)) around the core (TiO₂@4Si-Ce6-PEG, SiO₂@4Si-Ce6-PEG) or simply modified by APTES alone (TiO₂-APTES-Ce6, SiO₂-APTES-Ce6). After silanization, Ce6 was covalently coupled to the surface of TiO₂ and SiO₂ *via* an amide bond. *In vitro* experiments on U87 glioblastoma cell line were performed to evaluate the PDT efficiency of the NPs. The cells were exposed to different concentrations of NPs and illuminated ($\lambda_{\text{exc}} = 652 \text{ nm}$, fluence 10 J/cm^2). In contrast to the core-shell NPs, APTES-modified nanosystems were found to be more efficient for PDT. An interesting photodynamic effect was observed in the case of TiO₂-APTES-Ce6 NPs. After illumination, the viability of U87 was decreased by 90% when they were exposed to 200 $\mu\text{g/mL}$ of TiO₂-APTES-Ce6 NPs, which corresponds to 0.22 μM of Ce6. The same effect can be obtained with free photosensitizer but using a higher concentration (10 μM of Ce6).

Keywords

Nanoparticles; photodynamic therapy; TiO₂; SiO₂; Reactive Oxygen species.

1. Introduction

Photodynamic therapy (PDT) has emerged as an alternative and promising minimally invasive treatment modality for certain types of cancers and is becoming adapted in clinics nowadays. For example, in dermatology, PDT is gradually becoming the reference treatment for actinic keratoses (KA), superficial basal cell carcinomas and Bowen's disease [1]. In ophthalmology, PDT with Visudyne[®] has been very popular in the treatment of patients with Age-related macular degeneration [2]. In urology, the French company Steba-Biotech developed a new PS, Tookad[®] for the treatment of prostate cancer [3]. In gastroenterology, the demonstration of its effectiveness has been done for the treatment of i) superficial cancers of the esophagus in patients inaccessible to another treatment, with post-radiotherapy recurrence, ii) dysplasia and iii) inoperable cholangiocarcinoma [4]. In gynecology, the interest of PDT has been shown in the treatment of low and high grade cervical dysplastic lesions [5]. In neurosurgery, several studies report encouraging results in human clinical use to treat glioblastomas. Survival for 2 years after treatment with iPDT has been reported whereas the median survival in case of relapse in the literature is estimated at 3 months [6]. In pulmonology, PDT appears as a promising treatment for malignant pleural mesothelioma (MPM), or primitive cancer of the pleura [7]. PDT is based on the excitation of a photoactivatable molecule, called a photosensitizer (PS) which will, in the presence of light, transfer its energy to the surrounding oxygen to form mainly singlet oxygen (1O_2) or others types of ROS responsible for cell death. Thus the efficacy of PDT depends on the photosensitizer's ability to produce reactive oxygen species (ROS), oxygen availability, light dose and photosensitizer's (PS) concentration in the treated area [8].

The term nanoparticles (NPs) encompass a wide range of nanospheres and nanocapsules possessing a diameter less than 100 nm [9]. In 1976, Birrenbach and Speiser seem to be the first who conceived the term 'nanoparts' as they introduced there nanometric-scaled micelles entrapping bioactive drugs [10]. The use of NPs in PDT mainly as vehicles for drug delivery has been increasing recently. The PS can either be encapsulated into NPs, adsorbed or covalently grafted onto the NPs' surface. The PSs are mostly hydrophobic inducing some selectivity and aggregation hindering issues, thus using NPs facilitates their delivery in blood and diminishes such issues. Interestingly, thanks to the Enhanced Permeability and Retention (EPR) effect, NPs are usually more efficiently internalized into cells, which allow the use of lower PS amounts for the photodynamic therapeutic process. NPs are characterized by large surface area and the chemical and biochemical properties of this surface can be easily tuned. Functional groups can be linked to the surface of NPs which allows the

attachment of a wide range of PSs and targeting molecules for enhanced tumor selectivity. NPs can be synthesized through various strategies and their diameter can be controlled [9, 11].

Our team proved, for example, that the use of ultrasmall nanoparticles [12, 13] or Polymer-lipid-PEG nanoparticles [14] improved the efficiency of PDT.

TiO₂ nanoparticles were applied in the field of phototherapy of malignant cells, and have been regarded as the potential photosensitizing agents for anti-cancerous PDT due to their unique phototoxic effect upon the irradiation by UV light [15, 16]. This semiconductor can absorb UV light thus initiating a series of redox reaction through generated electrons and holes. Those reactions produce various ROS such as hydroxyl radicals (HO[•]), superoxide anions (O₂^{•-}), hydrogen peroxide (H₂O₂), etc. However, UV light is not always convenient for PDT as it has a limited penetration depth and a lower light content. In addition, it can be dangerous to expose patients to UV light [17]. On this basis, various efforts were dedicated to extend the photoresponse of TiO₂ to the visible light region.

Modifying the surface of TiO₂ with organic dyes, especially porphyrins, have gained much attention as it can widen the absorption range of titania from UV to visible. Chlorin e6 (Ce6) is a porphyrin-based photosensitizer with a high sensitizing efficiency [18]. Ce6 can either be adsorbed onto the surface of TiO₂ [19] or linked covalently such as through silane reagents [20]. Adsorption of the PS onto the surface of TiO₂ may encounter a problem of desorption which may limit the efficiency of the nanosystem. However, covalent bonding of the PS to TiO₂ maintains a stable nanosystem, especially through silyl anchoring groups of high affinity towards the hydroxyl groups of TiO₂ [21–25].

Silica-based nanoparticles have been widely described by our team and appear to be efficient in PDT. Those embrace a wide variety of silica-based NPs including core-shell NPs with a gadolinium oxide or terbium oxide core encapsulated within a silica matrix [8, 26–28].

In PDT, silica is mostly used in its mesoporous form because their surface area is large and can be easily chemically modified [26]. However, in our experiments we used commercial amorphous silicon dioxide of a diameter (10-20 nm) close to that of TiO₂ P25 (21 nm). SiO₂ is not photoactive, so as compared to UV-active TiO₂ semiconductor we can comprehend the influence of the choice of the support on the photodynamic efficiency of the NPs.

In this study, we decided to elaborate two kinds of TiO₂ and SiO₂ nanoparticles: first functionalized nanoparticle system is constituted of a core-shell structure, where the TiO₂ or SiO₂

core is surrounded by polysiloxane shell formed by the hydrolysis and condensation of the silane reagents aminopropyl triethoxysilane (APTES) and tetraethyl orthosilicate (TEOS) with photosensitizers and polyethylene glycol molecules (PEG) grafted on the NPs. As for the second approach, the surface of TiO₂ or SiO₂ core is only modified by APTES that acts as anchorage groups for the grafting of the PS molecules. As a photosensitizer, we decide to choose commercial Ce6 which is a very efficient PS in the field of PDT even coupled to silica NPs [29]. We compared the photophysical properties of Ce6 coupled to the different nanoparticles, the physico-chemical properties of the NPs. We have also studied the photodynamic properties of these NPs by measuring their uptake, dark cytotoxicity and phototoxicity after illumination in an *in vitro* model using U87 cell line. The ROS involved in the photodynamic process induced by NPs were also investigated.

2. Materials and methods

2.1. Materials

Titania and silica nanoparticles were used as supplied without additional purification. The titanium dioxide is commercial Degussa P25 (75% anatase and 25% rutile, ~ 21 nm, $S_{\text{BET}} \approx 50 \text{ m}^2 \text{ g}^{-1}$). Silicon dioxide nanoparticles (amorphous, 10-20 nm particle size by BET), aminopropyl triethoxysilane (APTES), tetraethoxysilane (TEOS), polyethylene glycol 250 (PEG 250), triethylamine (TEA), dimethyl sulfoxide (DMSO), N,N'-dicyclohexylcarbodiimide (DCC) and 1-hydroxybenzotriazole (HOBt) were purchased from Aldrich. Diethylene glycol (DEG) and dimethylformamide (DMF) were bought respectively from Alfa Aesar and Fisher chemical. Chlorin e6 PS (Ce6) is supplied by Frontier Scientific, Logan. Hydroxyphenyl fluorescein (HPF) and singlet oxygen sensor green (SOSG) were purchased from Molecular Probes and Invitrogen, respectively. Hanks' Balanced Salt solution (HBSS buffer), Trypsin, Thiazolyl Blue Tetrazolium Bromide (MTT), Fetal Calf Serum (FCS) and the antibiotic (penicillin-streptomycin) were purchased from Sigma-Aldrich, France. Dulbecco's Modified Eagle's Medium (DMEM) was obtained from Gibco BRL, France. U87 MG glioblastoma cell lines (HTB-14TM) were provided by ATCC, USA.

2.2. Preparation of the titania and silica NPs

The TiO₂ and SiO₂ nanoparticles were tuned by two silanization approaches, either embedded within a polysiloxane layer (core-shell) or only modified by APTES, and then hybridized by Ce6.

2.2.1. Activation of Chlorin e6 PS

1.2 equivalents of DCC and HOBt were added to 1 equivalent of Ce6 and were stirred in DMF at room temperature for about 1 h.

2.2.2. Preparation of core-shell NPs coupled to Ce6

The synthesis of the core-shell NPs by embedding the gadolinium oxide (Gd_2O_3) and terbium oxide (Tb_2O_3) cores within a polysiloxane layer have been described by our team thoroughly elsewhere [27, 28, 30]. The same synthesis was implemented onto TiO_2 core. A polysiloxane layer (4 mmol constituting of 2.4 mmol of APTES and 1.6 mmol of TEOS) was grown around TiO_2 NPs (1 mmol, 10 mM) in DEG.

A solution containing the activated Ce6 (0.02 mmol) and 140 μ L (0.6 mmol) of APTES dissolved in 3 mL of DMSO was prepared as a precursor and stirred overnight at room temperature. The Ce6-APTES solution and 89 μ L of TEOS (0.4 mmol) were added in the dispersion containing the core-shell TiO_2 NPs and stirred in DEG at 40°C. 1 h later, 340 μ L of DEG solution containing 0.2 mM TEA and 10 mM water was added. The final suspension was stirred for 48 h at 40 °C.

The carboxylic groups of PEG 250 (0.6 mmol, $M = 250$ g/mol, $d = 1.302$ g/mL) were activated by adding EDC (6 mmol) and NHS (12 mmol) in 5 mL solution of DEG. Activated PEG was then added to the reaction mixture and stirred overnight at room temperature. The NPs were then precipitated in acetone (350 mL). The acetone was removed by vacuum filtration. The dried PEGylated NPs were re-dispersed in Milli-Q water and were washed and centrifuged thoroughly three times with water and a final time with ethanol. Finally, the hybrid NPs were centrifuged at 4000 rpm for 20 min and dried in the vacuum oven at 60°C. The same procedure was performed to synthesize core-shell Ce6- SiO_2 NPs.

2.2.3. Preparation of APTES-modified NPs coupled to Ce6

In contrary to the core-shell functionalization approach, TiO_2 NPs were modified by one silane reagent; *i.e.* APTES. The activated Ce6 (0.0125 mmol) was mixed with APTES (0.375 mmol, 87.5 μ L) in 3 mL of DMSO and stirred overnight at room temperature. The APTES-Ce6 solution was then added to the TiO_2 NPs (1 mmol) previously dispersed in 100 mL of DEG for 1 h at 40 °C. The final mixture was left under continuous stirring for 48 h at 40°C. Those NPs were recovered similarly

to the core-shell ones. The same procedure was performed to synthesize APTES-modified-Ce6 SiO₂ NPs. Control NPs are TiO₂ and SiO₂ nanoparticles modified either by APTES alone or surrounded with a polysiloxane layer without any Ce6 (TiO₂-APTES, TiO₂@4Si-Ce6-PEG, SiO₂-APTES, SiO₂@4Si-PEG).

2.3. Physico-chemical and photophysical characterizations

The synthesized nanoparticles were characterized morphologically *via* Transmission Electronic Microscopy (TEM) and High-Resolution TEM (HR-TEM) imaging. TEM, HRTEM images and selected area electron diffraction (SAED) patterns were realized on a JEOL Atomic Resolution 200F cold FEG (TEM / STEM) instrument. The crystallinity of the nanoparticles was examined *via* X-ray diffraction (XRD) using X-ray diffractometer with Cu K α radiation ($\lambda = 0.15406$ nm). Infrared (FTIR) spectra were recorded on a FTIR ATR BRUCKER instrument between 400 and 4000 cm⁻¹. The evolution of the zeta-potential of the NPs was studied using a Zetasizer NanoZS equipped with a He-Ne laser at 633 nm from Malvern. Nanoparticle dispersions were prepared in milli-Q water and diluted in a sodium chloride aqueous solution (0.01 M) having a pH of 6.8.

The setup and the protocol to evaluate the photophysical characterizations including the absorption, fluorescence and singlet oxygen spectra in addition to the fluorescence and singlet oxygen lifetimes has been described elsewhere [31].

2.4. *In vitro* studies

2.4.1. Cell culture conditions

U87 cells (ATCC[®] HTB-14[™]) were cultured in Dulbecco's modified eagle's medium (DMEM) supplemented with sodium pyruvate 1.5mM, MEM AA, MEM NE AA, MEM vitamins, L-Ser 14 μ g/mL, L-asp 25 μ g/ml, L-Glu 2.5mM, 100U/mL penicillin, 100 μ g/mL streptomycin and 20% FCS under standard cell culture conditions at 37 °C in a humidified atmosphere (80 %) containing 5 % CO₂.

2.4.2. Cellular uptake

The cellular uptake of free Ce6 and Ce6 grafted onto NPs were investigated by fluorescence spectroscopy as previously reported [14].

Briefly, U87 cells were seeded into 6-well plates at a density of 10×10^3 cells/cm² and cultivated during 48 h. The old culture medium was discarded and cells were exposed to NPs or their PS-free control NPs (50, 100 and 200 µg/mL) or free Ce6 (1 and 10 µM) during 24 h. U87 cells were then detached from their support by trypsination and a numeration was performed using Thoma's chamber. The remaining cells were centrifuged for 10 min at 300 G and washed once with HBSS. Afterwards cells were resuspended into DMSO to solubilize Ce6 and lysed by sonication in a water bath during 10 min. The fluorescence signal of samples was measured in duplicate with an excitation wavelength of 405 nm and an emission wavelength of 670 nm (Tecan Infinite M200 Pro spectrofluorometer, Tecan). Concentrations were determined from a standard calibration curve obtained using diluted concentrations of free Ce6 into DMSO. The results of cellular uptake was expressed as the amount of Ce6 (nmol) incorporated per one million of cells

2.4.3. Estimation of Ce6 concentration in each dose of NPs

The concentration of Ce6 present per NPs were evaluated using their fluorescence properties. Three concentrations of each type of NPs were prepared in DMSO (50, 100 and 200 µg/mL). The fluorescence of each sample was measured using a spectrofluorimeter multiplate reader (TECAN) at an excitation wavelength of 405 nm and an emission wavelength of 670 nm. The concentration of Ce6 present per NPs was determined using a standard calibration curve obtained using different concentrations of free Ce6 diluted in DMSO.

2.4.4. Fluorescence microscopy

The localization of free Ce6 and Ce6 grafted onto NPs into U87 cells was investigated by fluorescence microscopy.

U87 cells were seeded at the density of 2×10^4 cells/cm² into 4-well glass chamber recovered by poly-D-lysine and cultivated during 48 h. The old culture medium was then discarded and cells were exposed to NPs or their PS-free control NPs (100 µg/mL) or free Ce6 (10 µM) during 24 h. After that, U87 cells were then washed twice with HBSS, fixed in 4% paraformaldehyde during 20 min before the labelling of the nucleus using DAPI. Finally, the chamber was mounted by antifade reagent (Prolong diamond antifade mountant, Molecular Probes) using glass coverslip. Fluorescence microscope images were taken at 20x magnification using Cy3 and DAPI filters (Nikon Eclipse Ci, Nikon, France).

2.4.5. Photodynamic therapy efficiency

The cytotoxicity and phototoxicity of NPs or their PS-free control were investigated in U87 after cultivation in the dark or after light exposure respectively. The viability of cells was determined *via* the measurement of the mitochondrial dehydrogenase activity of living cells (MTT assay) as previously described [14].

Briefly, U87 were plated at 2×10^4 cells/cm². After 48 h, old culture media were discarded and cells were exposed to NPs or their PS-free control (50, 100 and 200 µg/mL) or free Ce6 (1, 3 and 10 µM) during 24 h. U87 cells were then washed three times by HBSS. To assess the photo-induced toxicity of NPs, cells were exposed to light (fluence rate: 4.54 mW/cm²; fluence: 10 J/cm²) using a 652 nm diode laser system (Ceralas, Biolytec). U87 cells treated the same as above except for lack of light exposure were used to evaluate the cytotoxicity. After treatment, cells were incubated for additional 24 h under the standard culture conditions before to evaluate their viability using MTT assay. Shortly, cells were incubated with 0.4 mg/mL MTT (3-(4,5-dimethylthiazol-2-yl)-2,5-diphenyltetrazolium bromide) during 3 h at 37°C. The formazan crystals developing in living cells were dissolved by dimethylsulfoxide (DMSO) and absorbance was measured at 570/630nm (Multiscan Ascent microplate reader, Thermo Fisher). The results of cell viability were expressed as a percentage of variation with values obtained for untreated cells.

2.4.6. Statistical analysis

All *in vitro* experiments were realized in triplicate and the results were given as mean +/- standard deviation (SD). Differences among groups were evaluated using the Mann-Whitney U test (GraphPad Prism 6.0 software). A value of $p < 0.05$ was considered as statistically significant.

2.4.7. ROS measurement

The ROS measurement was achieved indirectly through the use of chemical probes, HPF and SOSG. Those measurements were conducted at the same conditions of PDT test but in the absence of cells. Briefly, different concentrations of the Ce6-hybridized NPs or their PS-free control NPs (50, 100 and 200 µg/mL) or free Ce6 (10 µM) were prepared in milli-Q water and added into 24-well plate in presence and absence of HPF or SOSG for the detection of hydroxyl radicals or singlet oxygen, respectively, and in the presence and absence of sodium azide. The plate was illuminated with light (fluence rate: 4.54 mW/cm²; fluence : 10 J/cm²) using a 652 nm diode laser system (Ceralas, Biolytec). The fluorescence signal of HPF was measured at an excitation wavelength of

485 nm and an emission wavelength of 515 nm. The fluorescence signal of SOSG was measured at an excitation wavelength of 505 nm and an emission wavelength of 540 nm (Tecan Infinite M200 Pro spectrofluorometer, Tecan). Prior to irradiation, the fluorescence of HPF and SOSG in each well was also measured in order to detect the evolution in the intensity of the probes in case of ROS production.

3. Results and discussion

3.1. Physico-chemical characterization

As revealed by TEM and HR-TEM (**Fig. 1**), the crystalline structure of TiO_2 remained intact and no morphological changes are observed after silanization and Ce6 coupling on both TiO_2 -APTES-Ce6 and $\text{TiO}_2@4\text{Si-Ce6-PEG}$ NPs. The SAED analysis (**Fig. 1e, i**) permits the calculation of the d-spacings from the ring patterns (**Table 1**). The extracted d-spacings from the patterns corresponding to TiO_2 -APTES-Ce6 and $\text{TiO}_2@4\text{Si-Ce6-PEG}$ NPs indicate that those NPs possess a crystalline structure of anatase and rutile TiO_2 phases [32]. **Table 2** presents the diameter of the NPs after the surface functionalization. The “core-shell” structure appeared clear on the morphology of $\text{TiO}_2@4\text{Si-Ce6-PEG}$ NPs. Those NPs possess a total diameter of about 30 nm with the amorphous polysiloxane matrix being about 3-5 nm thick. As for TiO_2 -APTES-Ce6 NPs, the diameter slightly changed from 21 nm to about 25 nm as compared to pure TiO_2 .

Table 1: The d-spacing values of the anatase and rutile crystalline phases of TiO_2 -APTES-Ce6 and $\text{TiO}_2@4\text{Si-Ce6-PEG}$ NPs extracted from SAED patterns as compared to the d-spacing values reported in the JCPDS card no. 01-084-1286 and 01-088-1172 for anatase and rutile, respectively.

		Anatase					Rutile				NPs
Crystal phase	<i>Hkl</i>	101	004	200	204	215	110	210	211	112	-
<i>d</i> -spacings/nm	JCPDS	0.3514	0.2375	0.1891	0.1479	0.1263	0.3228	0.2042	0.1678	0.1340	TiO_2
	SAED	0.3504	0.2366	0.1900	0.1480	0.1270	0.3253	0.2047			TiO_2 -APTES-Ce6
	SAED	0.3494	0.2365	0.1879	0.1480	0.1252	0.3256		0.1686	0.1339	$\text{TiO}_2@4\text{Si-Ce6-PEG}$

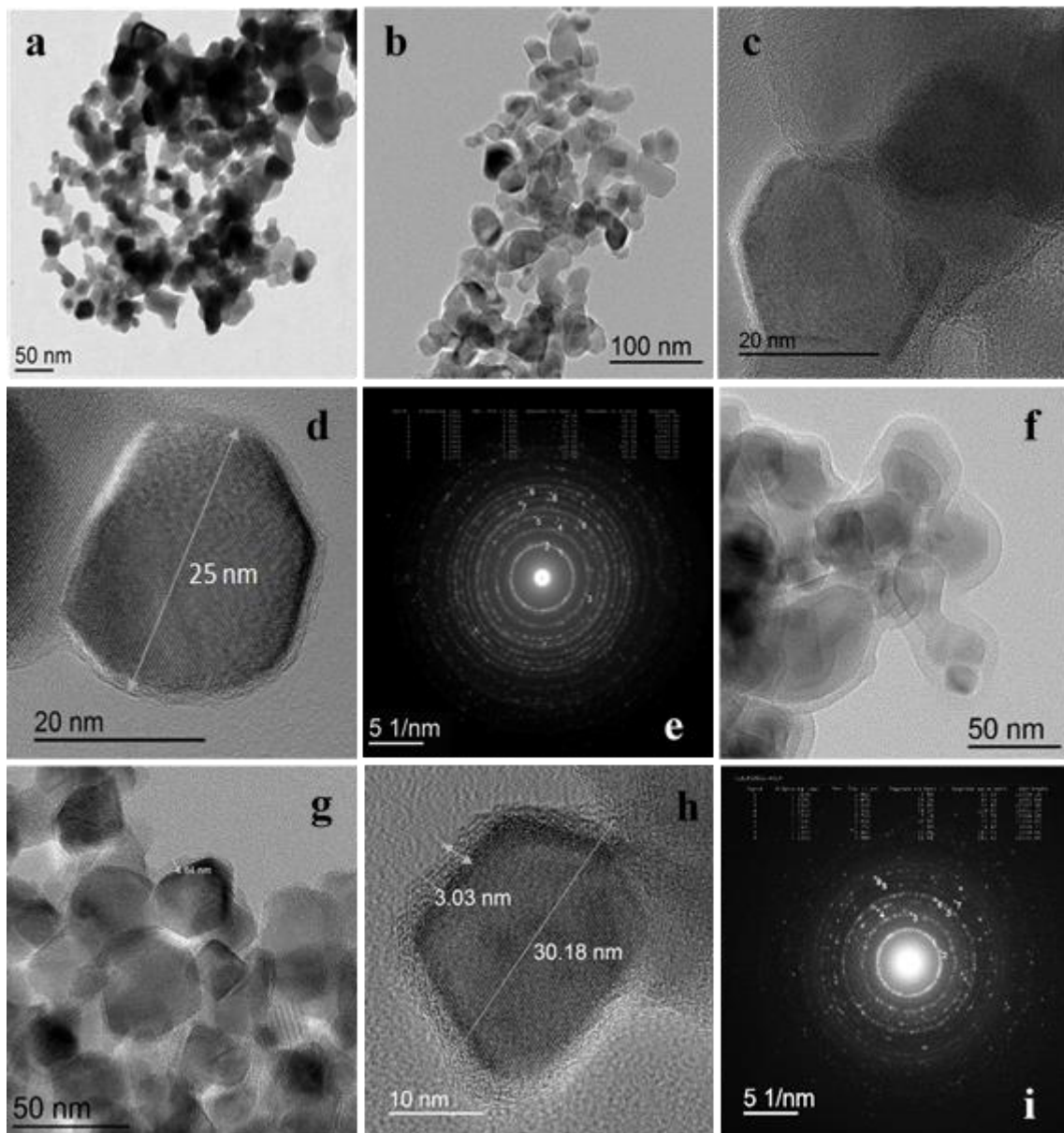
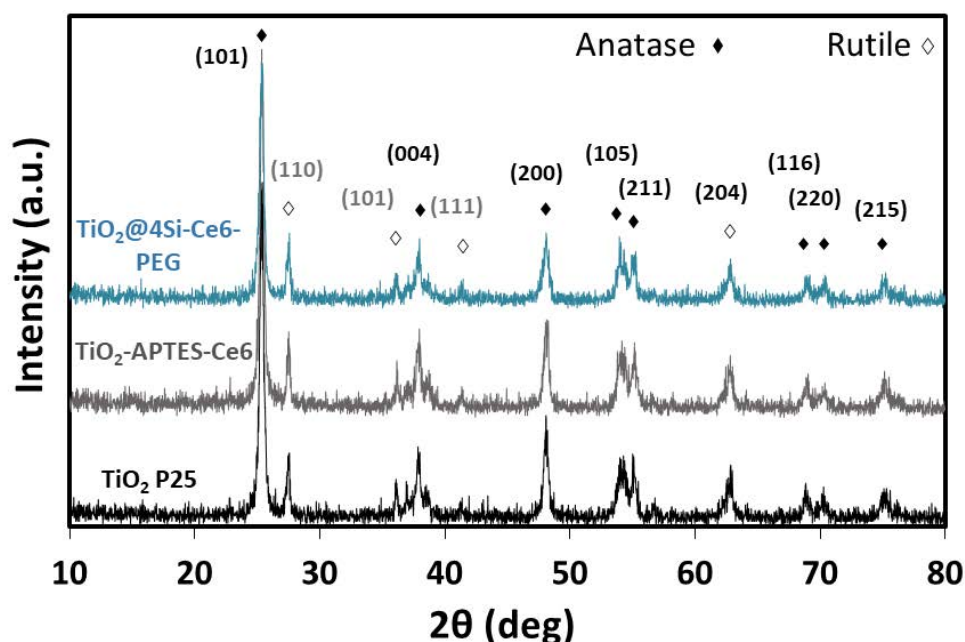


Fig. 1: TEM, HRTEM images and SAED patterns of (a) TiO_2 , (b-d) (e) TiO_2 -APTES-Ce6 and (f-h) (i) $\text{TiO}_2@4\text{Si}$ -Ce6-PEG NPs prepared in ethanol.

Table 2: The diameter of the bare TiO₂, TiO₂-APTES-Ce6 and TiO₂@4Si-Ce6-PEG NPs by TEM.

NPs	Diameter (nm)	Shell thickness (nm)
TiO ₂ P25	21	-
TiO ₂ -APTES-Ce6	25	-
TiO ₂ @4Si-Ce6-PEG	30	3-5

Fig. 2 presents the XRD patterns of bare and modified Ce6-TiO₂. All the patterns presented in **Fig. 2** are compatible to that of bare TiO₂ without any shift or modification after Ce6 grafting. They display the diffraction peaks corresponding to the anatase and rutile constituents of TiO₂ P25. Those conforming to the anatase phase are localized at $2\theta = 25.42, 37.96, 48.00, 54.00, 55.12, 62.80, 69.00, 70.52$ and 75.30 (JCPDS No. 84-1286). The diffraction peaks matching the rutile constituent are situated at $2\theta = 27.56, 36.22$ and 41.32 (JCPDS No. 88-1175) [33]. Those outcomes confirm the data extracted from TEM, HR-TEM and SAED patterns.

**Fig. 2:** X-ray diffraction patterns of TiO₂, TiO₂-APTES-Ce6 and TiO₂@4Si-Ce6-PEG NPs.

It is noteworthy to mention that TEM and XRD characterizations were performed for the samples with bare and modified TiO₂ in order to assure the preservation of the crystalline structure of TiO₂ after modification with the silane reagents and Ce6. However, this analysis was not performed on silica samples since the used SiO₂ NPs are amorphous.

Zeta potential measurements of bare and the modified TiO₂ and SiO₂ NPs is used to investigate the surface charge of the NPs in all the systems at pH = 6.8 (**Table 3**). Grafting APTES onto the negatively charged TiO₂ and SiO₂ induces a positively charged surface due to the presence of the cationic amino groups of APTES. Encapsulating the TiO₂ and SiO₂ cores within a polysiloxane shell with PEG grafted onto this shell induces a negative charge. The negative charge at a pH above 4 for those NPs result mainly from the deprotonation of the carboxyl groups and the steric hindrance prompted by the highly hydrophilic PEG. Upon grafting Ce6 in all four types of NPs, the surface charge decreases to lower positive charges in the case of TiO₂-APTES-Ce6 and SiO₂-APTES-Ce6 NPs and to negative values for both TiO₂@4Si-Ce6-PEG and SiO₂@4Si-Ce-PEG NPs [27, 34].

Table 3: Zeta-potential values of the bare and modified titania and silica nanoparticles.

NPs	ζ-potential (mV)	NPs	ζ-potential (mV)
TiO ₂ P25	-8 ± 1.62	SiO ₂	-57 ± 0.35
TiO ₂ -APTES	23 ± 0.24	SiO ₂ -APTES	34 ± 1.56
TiO ₂ -APTES-Ce6	12 ± 0.05	SiO ₂ -APTES-Ce6	8 ± 0.12
TiO ₂ @4Si-PEG	-10 ± 1.70	SiO ₂ @4Si-PEG	-3 ± 1.12
TiO ₂ @4Si-Ce6-PEG	-21 ± 0.30	SiO ₂ @4Si-Ce6-PEG	-24 ± 0.07

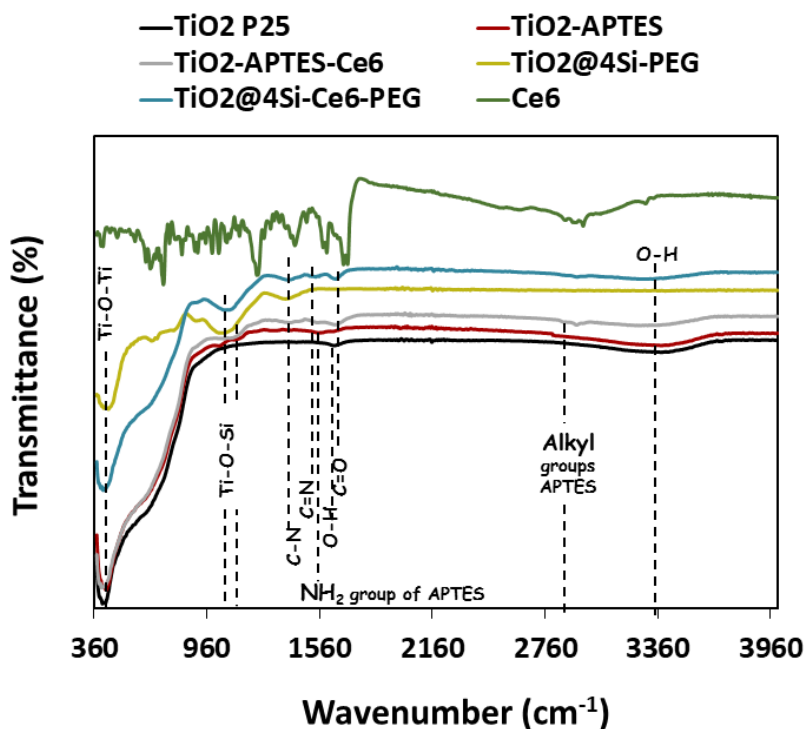


Fig. 3: FTIR spectra of Ce6 PS, TiO₂@4Si-Ce6-PEG, TiO₂@4Si-PEG, (f) TiO₂-APTES-Ce6, TiO₂-APTES and TiO₂ NPs.

FTIR analysis was also used as an effective analytical method for identifying the presence of specific functional groups and characterizing covalent bonding. **Fig. 3** and **table 3** present the FTIR bands expressed by the spectra of bare and modified TiO₂ NPs. In the spectrum of the core-shell nanosystem (TiO₂@4Si-PEG), the occurrence of the bending and stretching vibrations of Si-O-Si is revealed with a peak localized at 1061 cm⁻¹. However, the existence of an absorption peak at 935 cm⁻¹ corresponding to Ti-O-Si bonds, confirms that the silica matrix is strongly linked to the titania core. The FTIR spectra of the NPs coupled to Ce6 witness the evolution of new peaks besides those of bare and silanized TiO₂. The spectra of TiO₂-APTES-Ce6 and TiO₂@4Si-Ce6-PEG NPs exhibit peaks at 1539 and 1541 cm⁻¹, respectively, corresponding to the stretching vibration of C=N bonds belonging to the pyrrole moieties. For free Ce6, the C=O band appears at 1686 cm⁻¹. However, this band tends to shift to lower wavenumber when Ce6 is linked to TiO₂ as it appears at 1646 and 1637 cm⁻¹ for TiO₂@4Si-Ce6-PEG and TiO₂-APTES-Ce6 NPs respectively. Diverse linking modes through different number of carboxylic groups (*via* one, two or three) are established by the Ce6 onto the surface of TiO₂ which may lie behind the 9 cm⁻¹ difference between the C=O bands displayed by both nanosystems. Bands signifying the presence of C-N bond are detected at 1389 and 1386 cm⁻¹

for $\text{TiO}_2@4\text{Si-Ce6-PEG}$ and $\text{TiO}_2\text{-APTES-Ce6}$ NPs respectively. In addition, in the case of $\text{TiO}_2@4\text{Si-PEG}$ and $\text{TiO}_2@4\text{Si-Ce6-PEG}$ NPs, very weak features appear in the ranges 1400-1450 cm^{-1} corresponding to the C-H vibrations of the amino-siloxane groups. Thus, it can be concluded that Ce6 has been efficiently grafted onto the surface of the TiO_2 semiconductor [35–38].

For bare and modified SiO_2 NPs, FTIR could not give us an idea since we obtained the same spectra with all NPs (See supporting information Fig. S1).

Table 4: The main FTIR bands corresponding to TiO_2 , $\text{TiO}_2\text{-APTES}$, $\text{TiO}_2\text{-APTES-Ce6}$, $\text{TiO}_2@4\text{Si-PEG}$ and $\text{TiO}_2@4\text{Si-Ce6-PEG}$ NPs.

NPs	FTIR bands (cm^{-1})				
TiO_2	3374 (broad) $\nu\text{O-H}$	404 Ti-O-Ti			
$\text{TiO}_2\text{-APTES}$	3388 (broad) $\nu\text{O-H}$	424 Ti-O-Ti	1560 νNH_2 groups of APTES	2926 Alkyl groups of APTES	1020 Ti-O-Si moieties
$\text{TiO}_2\text{-APTES-Ce6}$	3253 (broad) $\nu\text{O-H}$	400 Ti-O-Ti	1539 $\nu\text{C=N}$ of pyrole	1637 C=O bond	1386 C-N bond
$\text{TiO}_2@4\text{Si-PEG}$	436 Ti-O-Ti	1063 $\nu\text{Si-O-Si}$	935 Ti-O-Si bonds of silica shell linked to Ti	1487 νNH_2 of APTES constituent of the shell	
$\text{TiO}_2@4\text{Si-Ce6-PEG}$	3289 (broad) $\nu\text{O-H}$	408 Ti-O-Ti	1541 $\nu\text{C=N}$ of pyrole	1646 C=O	1389 C-N bond

Upon silanization of the surface of the TiO_2 semiconductor, the absorption spectra of both nanosystems in their solid state remain similar to that of bare TiO_2 . As bare titania, core-shell and APTES-modified TiO_2 NPs possess one UV-localized absorption peak with no shift. It can be concluded that the band gap of TiO_2 is not affected by silanization (See supporting information Fig. S2) [39]. However, the UV-visible absorption spectra of $\text{TiO}_2@4\text{Si-Ce6-PEG}$ and $\text{TiO}_2\text{-APTES-Ce6}$

NPs reveal the characteristic peaks of Ce6 comprising a Soret or B-band and four Q-bands between 400 and 800 nm besides the UV-localized peak of TiO₂ (Fig. 4A) [40].

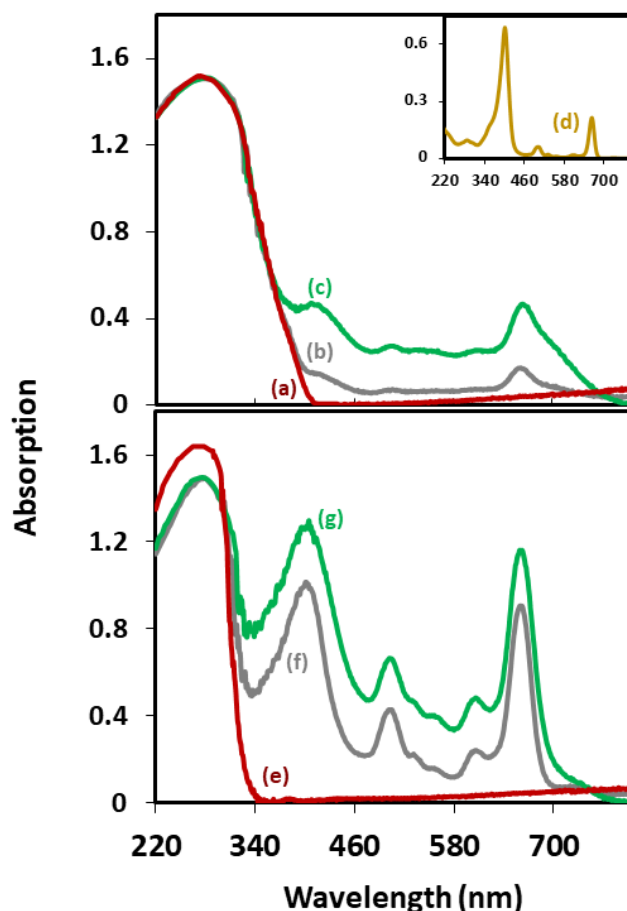


Fig. 4: UV-visible absorption spectra of (a) TiO₂, (b) TiO₂@4Si-Ce6-PEG, (c) TiO₂-APTES-Ce6, (e) SiO₂ NPs, (f) SiO₂@4Si-Ce6-PEG and (g) SiO₂-APTES-Ce6 NPs in their solid state and in the insets (d) Ce6 PS dissolved in ethanol.

Hence, the photoresponse of both Ce6-TiO₂ NPs is effectively prolonged towards the visible light zone as the Ce6 is bonded to their surfaces. Linking Ce6 to the TiO₂ NPs also left the band gap intact. In Fig. 4B, the absorption spectra of SiO₂@4Si-Ce6-PEG and SiO₂-APTES-Ce6 NPs display the peaks of Ce6 likewise to TiO₂ [40].

3.2. Photophysical properties

Fluorescence lifetimes of free Ce6 or Coupled into the NPs have been measured. The lifetime is not affected by the coupling and does not differ too much from the lifetime of free Ce6 (4.8 ns) in ethanol.

Table 5: The fluorescence and singlet oxygen lifetimes of TiO₂-APTES-Ce6, TiO₂@4Si-Ce6-PEG, SiO₂-APTES-Ce6, SiO₂@4Si-Ce6-PEG NPs and Ce6 PS in ethanol excited at 410 nm.

Sample	λ_{\max} (nm)	τ_f (ns)	τ_{Δ} (μ s)
TiO ₂ -APTES-Ce6	410	$\tau_1 = 4.7$ (59%) $\tau_2 = 0.6$ (41%)	$\tau_1 = 12$
TiO ₂ @4Si-Ce6-PEG	410	$\tau_1 = 5.2$ (65%) $\tau_2 = 1.5$ (35%)	-
SiO ₂ -APTES-Ce6	410	$\tau_1 = 4.5$ (56%) $\tau_2 = 1.7$ (44%)	$\tau_1 = 13$
SiO ₂ @4Si-Ce6-PEG	410	$\tau_1 = 4.3$ (100%)	$\tau_1 = 13$
Ce6	410	$\tau_1 = 4.8$	$\tau_1 = 15$

Absorption, fluorescence emission and singlet oxygen formation have been studied for Ce6 coupled to the four types of nanoparticles and compared to Ce6 alone (Table 5 and Fig. 5).

In Fig. 5A, a large band at 350 nm typical of TiO₂ can be observed. Due to the large size of the NPs in solution the baseline of the spectra do not allow the detection of the absorption bands of Ce6. On the contrary, the Soret band around 400 nm and the Q₁ band at 660 nm can be detected for SiO₂ NPs.

All the NPs present a fluorescence emission even if it is very low for TiO₂@4Si-Ce6-PEG. Fluorescence lifetime of Ce6 is similar in all the nanoparticles and close to the lifetime of free Ce6 (4.8 ns). Nevertheless, a shorter lifetime appears in TiO₂-APTES-Ce6 (0.6 ns), TiO₂@4Si-Ce6-PEG (1.5 ns), SiO₂-APTES-Ce6 (1.7 ns) but not in SiO₂@4Si-Ce6-PEG. Ce6 might be in different environment into the NPs. The PSs that are more at the surface of the NPs are mainly in ethanol whereas Ce6 inside the shell are surrounded by silane. That could explain the different lifetimes observed. In fact, Ce6 owns three carboxylic functions that can react with APTES. These different lifetimes might be due to different populations due to the way Ce6 is grafted onto the nanoparticles. All NP still produce ¹O₂ upon irradiation ($\lambda_{\text{exc}} = 420$ nm) except TiO₂@4Si-Ce6-PEG. As expected, the ¹O₂ lifetime does not change since it has been measured all the time in ethanol (between 12 and 15 μ s). It seems that ¹O₂ does not react with the PSs.

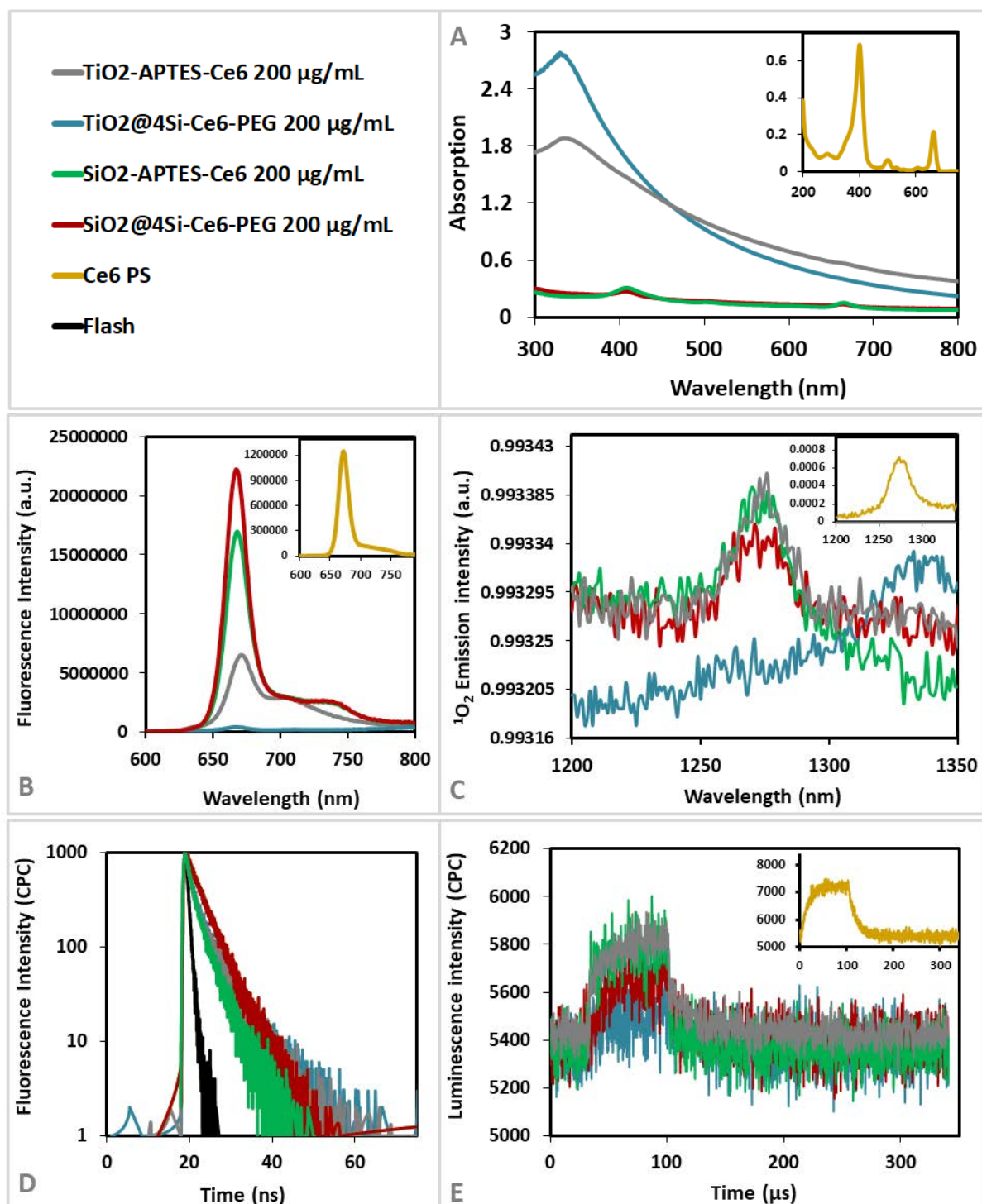


Fig. 5: The UV-visible absorption spectra (A), the fluorescence spectra ($\lambda_{\text{exc}} = 420 \text{ nm}$) (B), the singlet oxygen emission spectra ($\lambda_{\text{exc}} = 420 \text{ nm}$) (C), the fluorescence lifetime ($\lambda_{\text{exc}} = 410 \text{ nm}$) (D) and the singlet oxygen lifetime ($\lambda_{\text{exc}} = 410 \text{ nm}$) (E) of TiO₂@4Si-Ce6-PEG NPs, TiO₂-APTES-Ce6, SiO₂-APTES-Ce6 and SiO₂@4Si-Ce6-PEG NPs at 200 μg/mL in ethanol and in the insets Ce6 (optical density of 0.2).

3.3. Cellular uptake of NPs

The uptake of free Ce6 or Ce6 grafted onto NPs was presented in Fig. 6.

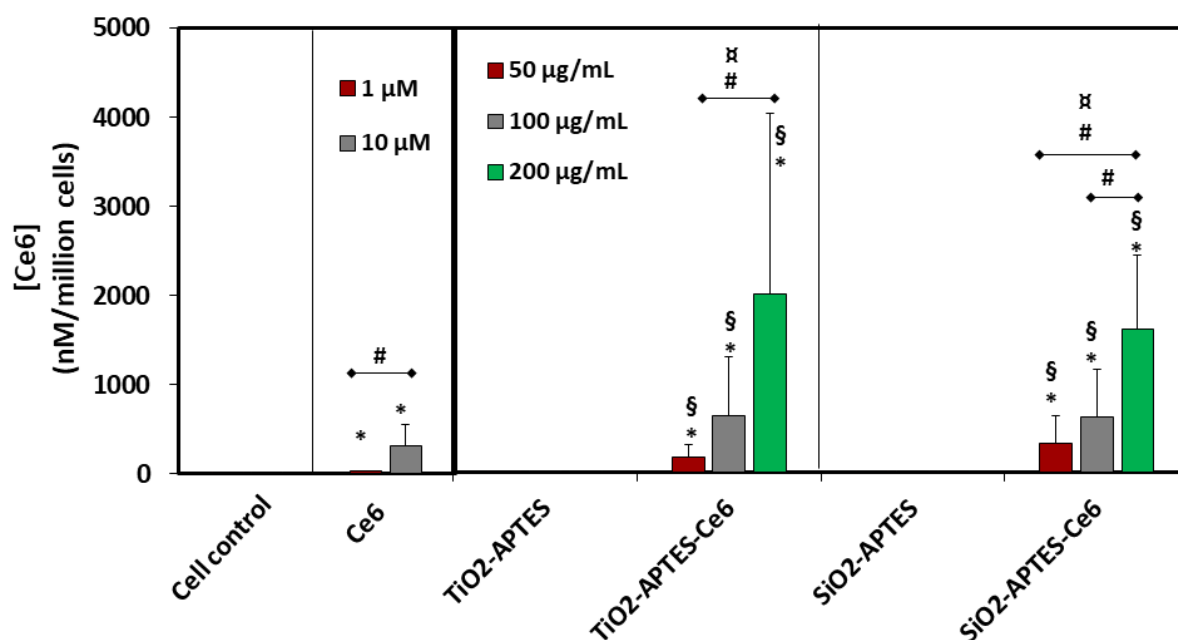


Fig. 6: Uptake of free Ce6 and Ce6 grafted onto APTES-modified TiO₂ and SiO₂ nanoparticles into U87 cells (Mean \pm SD, n = 4, * versus control cells, * p < 0.05, § versus NPs-APTES without Ce6, # versus NP-APTES-Ce6 200 $\mu\text{g/mL}$ and □ versus Ce6 10 μM).

The cellular uptake of a PS is a key factor for the PDT's efficiency. To explore the ability of NPs to be incorporated into cells, we have measured the concentration of Ce6 incorporated by U87 cells using fluorescence proprieties of the PS. As expected, Ce6 was not detected when cells were exposed to Ce6-free NPs. The cellular uptake of free Ce6 or Ce6 grafted onto NPs appears to be dose-dependent.

We have tried to estimate the amount of Ce6 grafted onto each NP system by fluorimetry using a standard calibration curve of free Ce6 (See supporting information Fig. S3). Those concentrations represent an estimation to better analyze the uptake result and compare with the literature. However, concerning the amount of NPs introduced into the wells for PDT, almost all authors use the same mass of different types of NPs for their tests ($\mu\text{g mL}^{-1}$) rather than using the same concentration of PS in each type of NPs. Thus, we used the mass of NPs as in literature for our PDT tests [34, 41–44]. In terms of cellular uptake, 200 $\mu\text{g mL}^{-1}$ of TiO₂-APTES-Ce6 NPs and SiO₂-

APTES-Ce6 NPs correspond to 0.22 and 0.74 μM of Ce6, respectively. Thus, the concentration of Ce6 found in U87 cells was more elevated when cells were exposed to Ce6 grafted onto NPs at 200 $\mu\text{g}/\text{ml}$ (**Fig. 6**) whatever the NPs used (SiO_2 or TiO_2). Hence, the type of NPs (TiO_2 and SiO_2) did not influence the concentration of Ce6 incorporated into U87 cells. This outcome is in agreement with literature stating that commonly, the NPs can enable high accumulation of the PS in the tumor as they can be efficiently uptaken by cells [9, 11, 34, 45, 46].

The use of titania and silica NPs as carriers of the PS seems to be efficient in the delivery of Ce6 into U87 cells and hence improving the uptake of Ce6 by those cells. Besides the good biocompatibility of TiO_2 described in literature, the greater cellular internalization witnessed in the case of TiO_2 -APTES-Ce6 NPs may be attributed to their superior surface positive charge over SiO_2 -APTES-Ce6 NPs. The membrane of cancer cells is negatively charged. Thus, as the surface charge of the NPs becomes more positive, the more facilitated their adherence and internalization is [34].

3.4. Fluorescence microscopy

In order to know if Ce6 grafted onto NPs were adsorbed onto the cell surface or completely internalized into cells, we have performed a fluorescence microscopy imaging. When U87 cells were exposed to free Ce6, PS was found diffused into the cytoplasm of cells (**Fig. 7A**). When Ce6 was grafted onto the NPs, PS was found more clustered into vesicles regardless of the type NPs used (SiO_2 or TiO_2) (**Fig. 7B, C**). These results indicated that the cellular localization of Ce6 is different when PS is grafted onto NPs. This can explain the difference found in the PDT efficacy.

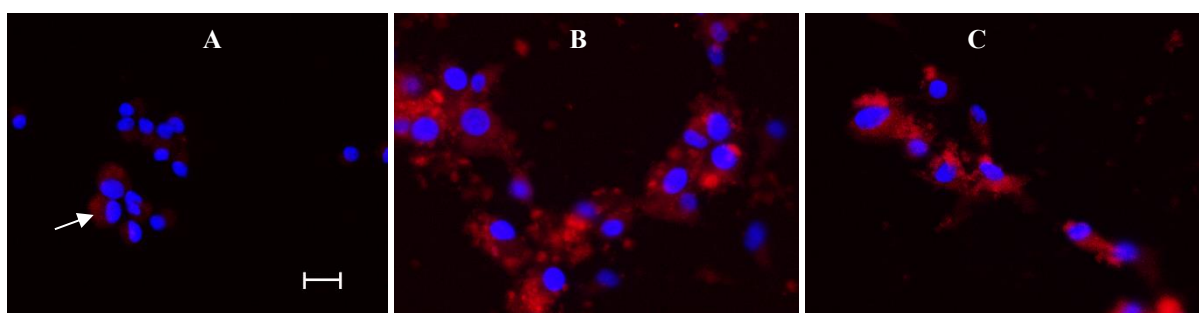


Fig. 7: Fluorescence microscopy of U87 exposed to free Ce6 PS (A), SiO_2 -APTES-Ce6 (B) and TiO_2 -APTES-Ce6 NPs (C). Free Ce6 or Ce6 grafted onto NPs appeared in red while nucleus labelled with DAPI appeared in blue. Scale bar: 20 μm .

3.5. Photodynamic therapy

The evaluation of the mitochondrial activity of cells was used to estimate the cytotoxicity and phototoxicity of the hybridized TiO₂ and SiO₂ NPs as well as free Ce6 towards the U87 cells *in vitro*.

In darkness, both core-shell and APTES-modified NPs induced a 20% to 30% decrease of the viability of the U87 cells, for TiO₂ and SiO₂ respectively (Fig. 8A and supporting information Fig. S4A). This cytotoxic effect displayed by all the tested NPs seems to be independent of the concentration of NPs administrated into the cells. In addition, grafting Ce6 PS onto the NPs does not influence their cytotoxic effect. On the contrary, Ce6 alone is not toxic even at 10 μM.

Both core-shell nanosystems (TiO₂@4Si-Ce6-PEG and SiO₂@4Si-Ce6-PEG) did not display any phototoxic effect (Supporting information Fig. S4B). Grafting Ce6 onto the surface of those NPs induced an increase of absorption into the visible light region (Fig. 4) and the photophysical measurements reveal that, at least SiO₂@4Si-Ce6-PEG NPs (200 μg mL⁻¹) can generate ¹O₂ (Fig. 5).

Stabilizing molecules such as deoxyribonucleic acid (DNA), albumin and polyethylene glycol (PEG) have been used to functionalize the surface of the NPs for their advantages in decreasing the ionic strength and enhancing the NPs' dispersion by inhibiting their aggregation and agglomeration in the biological media [45]. Another advantage of grafting PEG onto the NPs is that it reduces the possibility of those NPs to be taken up by the macrophages thus increasing their time of circulation in blood [9]. Despite those merits, the surface chemistry of the nanoparticles can influence their efficacy and the pathway of cellular uptake. Thus, it is described in the literature that PEGylated NPs and those holding neutral charge are internalized more slowly than the negatively and positively charged ones [45]. In our case, it seems that highly hydrophilic PEG grafted onto the surface of the NPs promotes better dispersion, but probably lies behind the absence of any photodynamic effect for core-shell nanosystems.

Based on the lack of any PDT effect displayed by both core-shell TiO₂ and SiO₂ NPs, we decided to go further with the APTES-modified nanosystems and study their uptake by cells, localization and ROS generation.

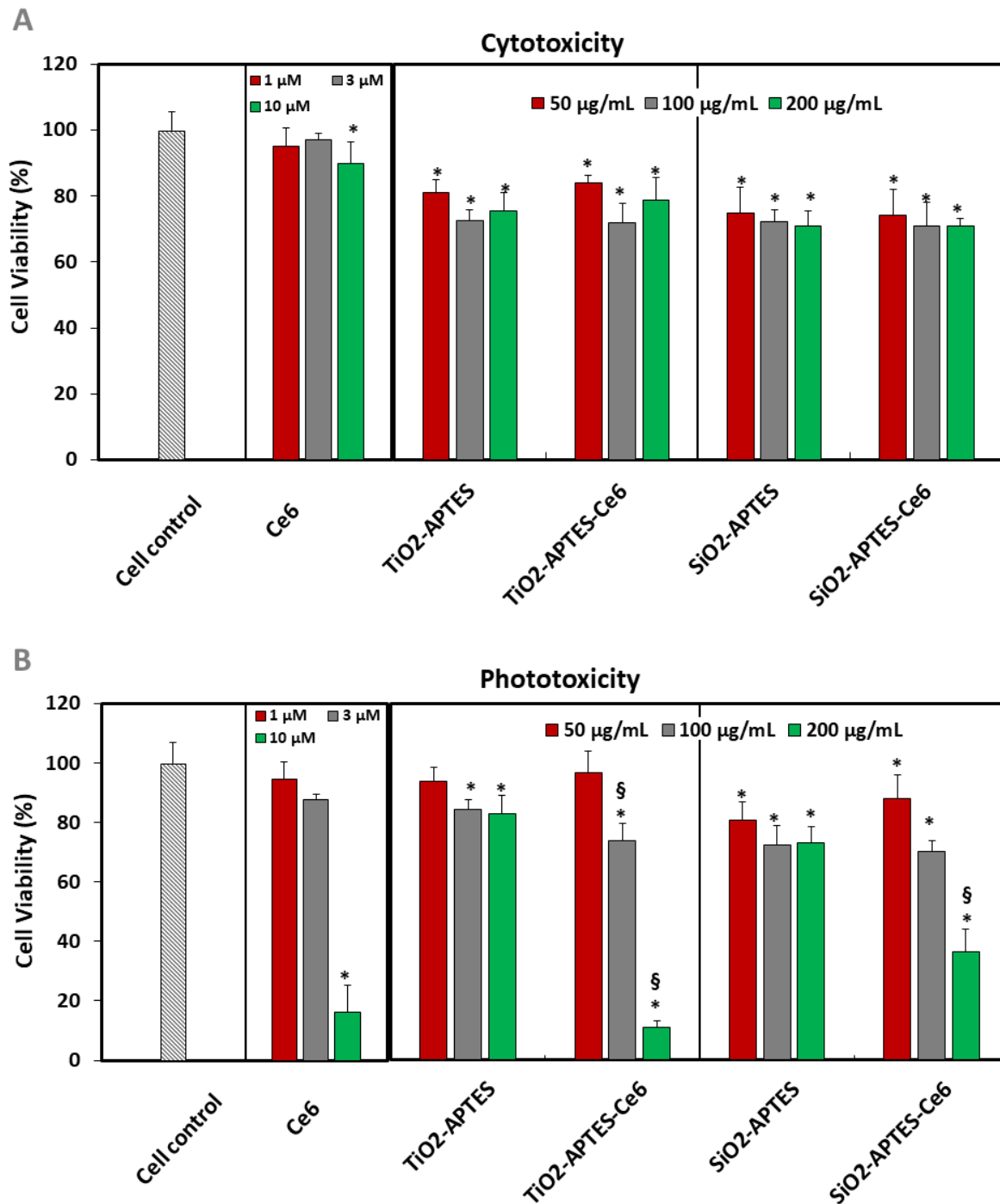


Fig. 8: Cell viability of U87 cells treated with free Ce6, TiO₂-APTES, TiO₂-APTES-Ce6, SiO₂-APTES and SiO₂-APTES-Ce6 NPs and incubated into the dark (A, dark toxicity) or after irradiation with a light dose of 10 J/cm² (B, phototoxicity). Results were expressed as percentage of values obtained from untreated cells and given by mean \pm SD, n = 3. * versus control cells, * p < 0.05, § versus NPs without PS.

When cells were exposed to light (**Fig. 8B**), the SiO₂-APTES-Ce6 NPs (200 µg mL⁻¹) induced a 64% decrease of the U87 viability. However, a more drastic photodynamic effect was found using TiO₂-APTES-Ce6 NPs (200 µg mL⁻¹) which induced an 89% decrease of cell viability. Thus the modification of the NPs by APTES alone in the absence of PEG induced an interesting photodynamic activity of the NPs towards the cancer cells.

Ce6 alone used at 10 µM induced the same photodynamic effect than Ce6 grafted onto TiO₂ NPs (84% decrease of cell viability after light exposure).

As mention before, the concentration of Ce6 grafted onto NPs (200 µg mL⁻¹) of TiO₂-APTES-Ce6 NPs and SiO₂-APTES-Ce6 NPs respectively correspond to 0.22 and 0.74 µM of Ce6. These results indicate that Ce6 grafted onto NPs was more efficient than Ce6 alone for PDT. Consequently, lower levels of the Ce6 can be used for PDT by grafting to nanoparticle-based drug delivery systems.

The enhanced cellular uptake of the TiO₂-APTES-Ce6 and SiO₂-APTES-Ce6 NPs is also in agreement with the enhanced photodynamic effect of those NPs as compared to Ce6-free TiO₂ and SiO₂ NPs.

3.6. ROS measurement

The capability of TiO₂-APTES-Ce6 and SiO₂-APTES-Ce6 NPs to produce multiple ROS when irradiated at 652 nm is also studied and compared to free Ce6. HPF and SOSG are used to detect the production of HO[•] and ¹O₂, respectively. **Fig. 9A, B** presents the fluorescence intensity of HPF and SOSG, respectively, demonstrating the ROS production upon PDT treatment (10 J/cm², 652 nm) by TiO₂-APTES-Ce6, SiO₂-APTES-Ce6 NPs (200 µg/mL) and free Ce6 (10 µM). By observing the absorption spectra of TiO₂-APTES-Ce6 and SiO₂-APTES-Ce6 NPs (**Fig. 4**), a relatively broad peak localized at about 660 nm corresponding to the grafted Ce6 overlap well with the emission wavelength (652 nm) permitting the activation of Ce6. Upon irradiation, no evolution in the fluorescence intensity of SOSG in the case of TiO₂-APTES and SiO₂-APTES control NPs appears. Thus they are not photoactive at 652 nm. However, the fluorescence intensity of SOSG increases in the case of TiO₂-APTES-Ce6 and SiO₂-APTES-Ce6 NPs signifying the production of ¹O₂ by activated Ce6. TiO₂-APTES-Ce6 NPs produce more ¹O₂ than SiO₂-APTES-Ce6 NPs. The amount of ¹O₂ elaborated by both types of NPs is much less than that produced by free Ce6 at 10 µM, yet it is

still detectable. After addition of sodium azide, which is a quencher of $^1\text{O}_2$, the fluorescence intensity of SOSG is decreased for both NPs and free Ce6. This confirms that the produced ROS is $^1\text{O}_2$ (Fig. 9A).

Fig. 9B presents the evolution of the fluorescence intensity of HPF upon the irradiation of the NPs and Ce6 at 652 nm. Control TiO_2 -APTES, SiO_2 -APTES NPs and free Ce6 are incapable of triggering an increase in the fluorescence intensity of HPF, which indicates the lack of HO^\bullet production. However, TiO_2 -APTES-Ce6 and SiO_2 -APTES-Ce6 NPs seem to significantly produce HO^\bullet as the fluorescence intensity of HPF increases. TiO_2 -APTES-Ce6 NPs produces about 2.5 more times HO^\bullet than SiO_2 -APTES-Ce6 NPs. HO^\bullet can be elaborated through the indirect activation of the NPs by the injection of the electrons from the excited Ce6 into the NPs [47]. TiO_2 is a semiconductor possessing a wide band gap. In the TiO_2 -APTES-Ce6 nanosystem, the grafted Ce6 absorbs the visible light rather than UV-limited TiO_2 . Thus, Ce6 gets excited into suitable singlet and triplet states and is converted into a cationic radical [48]. Subsequently, the injection of the excited electrons from the Ce6 to the conduction band (CB) of TiO_2 is favored due to the proper energy state of this PS with respect to TiO_2 [49]. The electrons react with molecular oxygen that is pre-adsorbed onto the surface of TiO_2 and initiate the production of ROS especially superoxide anions and hydroxyl radicals [48]. It is also stated that TiO_2 in both its crystalline forms, anatase and rutile, might interact with the components of the cell leading to the generation of ROS. Thus, the cytotoxicity induced by the ROS occurs when the generated amount of ROS overcomes the antioxidant cellular defense or trigger the mechanisms of mitochondrial apoptosis [50]. Hence, the fact that TiO_2 is a semiconductor may have enhanced the electron transfer process thus elaborating more HO^\bullet unlike non-photoactive silica.

Consequently, the production of good amounts of multiple ROS especially HO^\bullet and the efficient internalization into the U87 cells induced the good photodynamic effect of TiO_2 -APTES-Ce6 NPs and proved that SiO_2 -APTES-Ce6 NPs can be considered as potential nanosystem for anti-cancer PDT.

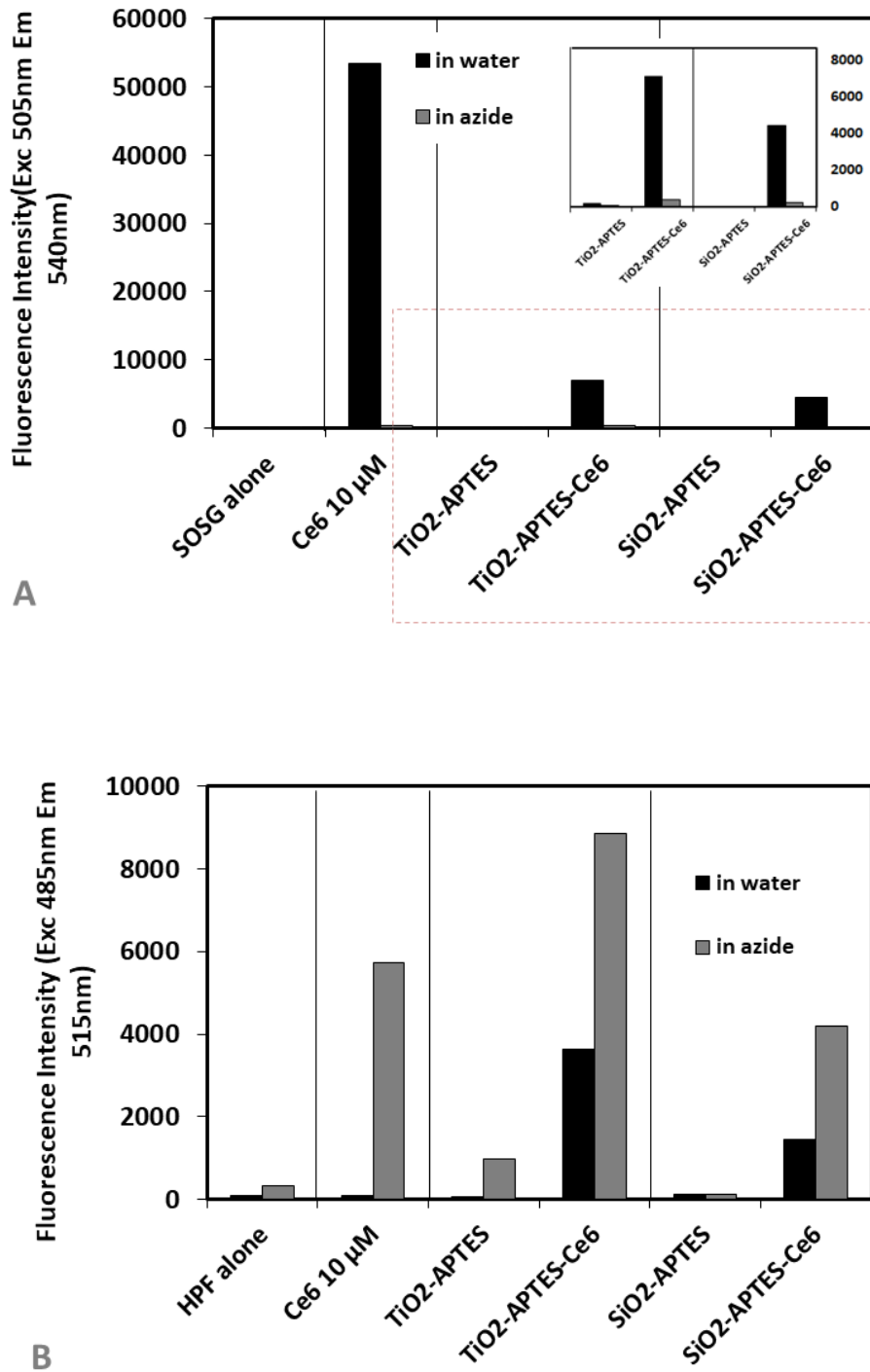


Fig. 9: $^1\text{O}_2$ (A) and HO^\bullet (B) detection by TiO₂-APTES, TiO₂-APTES-Ce6, SiO₂-APTES and SiO₂-APES-Ce6 NPs (200 $\mu\text{g}/\text{mL}$) and free Ce6 (10 μM) upon treatment by PDT through HPF and SOSG, respectively.

4. Conclusion

In this study, the TiO₂ or SiO₂ NPs were modified either by the growth of a silica shell constituting of two silane reagents ((3-aminopropyl)triethoxysilane (APTES) and tetraethyl orthosilicate (TEOS)) around the core (TiO₂@4Si-Ce6-PEG, SiO₂@4Si-Ce6-PEG) or simply modified by APTES alone (TiO₂-APTES-Ce6, SiO₂-APTES-Ce6). Ce6 was covalently coupled onto the modified TiO₂ and SiO₂ *via* an amide bond which successfully extended the absorption profile of the NPs to the visible region of light. The physicochemical and photophysical characteristics of the NPs were investigated. TEM, HR-TEM and XRD proved the preservation of the TiO₂ crystallinity upon modification with silane reagents and Ce6-coupling. The covalent grafting of Ce6 onto the NPs was confirmed by FTIR. The synthesized NPs became fluorescent and exhibit ¹O₂ production when irradiated in visible. *In vitro* experiments on U87 glioblastoma cell line were performed to assess the PDT efficacy of those NPs. The cells were exposed to different concentrations of NPs and illuminated ($\lambda_{exc} = 652$ nm, fluence 10 J/cm²). Unlike the core-shell NPs, NPs modified with APTES alone proved to be more efficient for PDT. In the case of TiO₂-APTES-Ce6 NPs, a remarkable PDT effect was observed. The viability of U87 cells was decreased by 90% after visible light illumination in the presence of 200 μ g/mL of TiO₂-APTES-Ce6 NPs, which corresponds to 0.22 μ M of Ce6. The same PDT effect can be obtained with free Ce6 but using a higher concentration of 10 μ M. The use of TiO₂ and SiO₂ NPs as carriers of the PS seems to be efficient in the delivery of Ce6 into the U87 cells as the uptake of Ce6 by those cells was enhanced. The cellular localization differs between free Ce6 and Ce6 linked to the NPs. Regardless the type of NPs is, TiO₂ or SiO₂, Ce6 seemed to be localized into vesicles. Both TiO₂-APTES-Ce6 and SiO₂-APTES-Ce6 produced good amounts of multiple ROS (HO[•] and ¹O₂). The efficient uptake of the NPs by the U87 cells and the good ROS production seemed to induce the good PDT effect of TiO₂-APTES-Ce6 NPs and demonstrated that SiO₂-APTES-Ce6 can be regarded potential NPs for PDT.

References of chapter III

- [1] K. L. Du, S. Both, J. S. Friedberg, R. Rengan, S. M. Hahn, and K. A. Cengel, “Extrapleural pneumonectomy, photodynamic therapy and intensity modulated radiation therapy for the treatment of malignant pleural mesothelioma,” *Cancer Biol. Ther.*, vol. 10, no. 5, pp. 425–429, Sep. 2010.
- [2] G. C. Brown, M. M. Brown, J. Campanella, and G. R. Beauchamp, “The Cost-Utility of Photodynamic Therapy in Eyes With Neovascular Macular Degeneration—A Value-Based Reappraisal With 5-Year Data,” *Am. J. Ophthalmol.*, vol. 140, no. 4, p. 679.e1-679.e10, Oct. 2005.
- [3] A.-R. Azzouzi *et al.*, “TOOKAD[®] Soluble vascular-targeted photodynamic (VTP) therapy: determination of optimal treatment conditions and assessment of effects in patients with localised prostate cancer: TOOKAD[®] soluble vascular targeted photodynamic (VTP) therapy in patients with localised prostate cancer,” *BJU Int.*, vol. 112, no. 6, pp. 766–774, Oct. 2013.
- [4] H. Moole *et al.*, “Success of photodynamic therapy in palliating patients with nonresectable cholangiocarcinoma: A systematic review and meta-analysis,” *World J. Gastroenterol.*, vol. 23, no. 7, p. 1278, 2017.
- [5] P. Soergel, M. Loning, I. Staboulidou, C. Schippert, and P. Hillemanns, “Photodynamic Diagnosis and Therapy in Gynecology,” *J. Environ. Pathol. Toxicol. Oncol.*, vol. 27, no. 4, pp. 307–320, 2008.
- [6] A. F. Degen *et al.*, “Photodynamic endometrial ablation for the treatment of dysfunctional uterine bleeding: A preliminary report: PHOTODYNAMIC ENDOMETRIAL ABLATION,” *Lasers Surg. Med.*, vol. 34, no. 1, pp. 1–4, Jan. 2004.
- [7] K. Moghissi and K. Dixon, “Is bronchoscopic photodynamic therapy a therapeutic option in lung cancer?,” *Eur. Respir. J.*, vol. 22, no. 3, pp. 535–541, Sep. 2003.
- [8] D. Bechet, P. Couleaud, C. Frochot, M.-L. Viriot, F. Guillemain, and M. Barberi-Heyob, “Nanoparticles as vehicles for delivery of photodynamic therapy agents,” *Trends Biotechnol.*, vol. 26, no. 11, pp. 612–621, Nov. 2008.
- [9] D. K. Chatterjee, L. S. Fong, and Y. Zhang, “Nanoparticles in photodynamic therapy: An emerging paradigm,” *Adv. Drug Deliv. Rev.*, vol. 60, no. 15, pp. 1627–1637, Dec. 2008.
- [10] G. Birrenbach and P. P. Speiser, “Polymerized Micelles and Their Use as Adjuvants in Immunology,” *J. Pharm. Sci.*, vol. 65, no. 12, pp. 1763–1766, Dec. 1976.
- [11] N. Mehraban and H. Freeman, “Developments in PDT Sensitizers for Increased Selectivity and Singlet Oxygen Production,” *Materials*, vol. 8, no. 7, pp. 4421–4456, Jul. 2015.
- [12] E. Thomas *et al.*, “Ultras-small AGuIX theranostic nanoparticles for vascular-targeted interstitial photodynamic therapy of glioblastoma,” *Int. J. Nanomedicine*, vol. Volume 12, pp. 7075–7088, Sep. 2017.
- [13] M. Toussaint *et al.*, “Proton MR Spectroscopy and Diffusion MR Imaging Monitoring to Predict Tumor Response to Interstitial Photodynamic Therapy for Glioblastoma,” *Theranostics*, vol. 7, no. 2, pp. 436–451, 2017.

- [14] S. Pramual *et al.*, “Polymer-lipid-PEG hybrid nanoparticles as photosensitizer carrier for photodynamic therapy,” *J. Photochem. Photobiol. B*, vol. 173, pp. 12–22, Aug. 2017.
- [15] J. Xu *et al.*, “Photokilling cancer cells using highly cell-specific antibody–TiO₂ bioconjugates and electroporation,” *Bioelectrochemistry*, vol. 71, no. 2, pp. 217–222, Nov. 2007.
- [16] T. Lopez *et al.*, “Study of the stabilization of zinc phthalocyanine in sol-gel TiO₂ for photodynamic therapy applications,” *Nanomedicine Nanotechnol. Biol. Med.*, vol. 6, no. 6, pp. 777–785, Dec. 2010.
- [17] Z. Fei Yin, L. Wu, H. Gui Yang, and Y. Hua Su, “Recent progress in biomedical applications of titanium dioxide,” *Phys. Chem. Chem. Phys.*, vol. 15, no. 14, p. 4844, 2013.
- [18] P. Huang *et al.*, “Folic Acid-conjugated Graphene Oxide loaded with Photosensitizers for Targeting Photodynamic Therapy,” *Theranostics*, vol. 1, pp. 240–250, 2011.
- [19] Y. Tokuoka, M. Yamada, N. Kawashima, and T. Miyasaka, “Anticancer Effect of Dye-sensitized TiO₂ Nanocrystals by Polychromatic Visible Light Irradiation,” *Chem. Lett.*, vol. 35, no. 5, pp. 496–497, May 2006.
- [20] Z. Yu, W. Pan, N. Li, and B. Tang, “A nuclear targeted dual-photosensitizer for drug-resistant cancer therapy with NIR activated multiple ROS,” *Chem Sci*, vol. 7, no. 7, pp. 4237–4244, 2016.
- [21] A. K. . Fung, B. K. . Chiu, and M. H. . Lam, “Surface modification of TiO₂ by a ruthenium(II) polypyridyl complex via silyl-linkage for the sensitized photocatalytic degradation of carbon tetrachloride by visible irradiation,” *Water Res.*, vol. 37, no. 8, pp. 1939–1947, Apr. 2003.
- [22] H. Alloul *et al.*, “Effect of chemical modification on surface free energy components of Aerosil silica powders determined with capillary rise technique,” *Powder Technol.*, vol. 246, pp. 575–582, Sep. 2013.
- [23] H. Alloul *et al.*, “Towards a better description of organosilane grafting onto silica particles using volumetric techniques based on molecular probing,” *Adsorption*, vol. 22, no. 7, pp. 923–937, Oct. 2016.
- [24] M. Kassir *et al.*, “Surface modification of TiO₂ nanoparticles with AHAPS aminosilane: distinction between physisorption and chemisorption,” *Adsorption*, vol. 19, no. 6, pp. 1197–1209, Dec. 2013.
- [25] M. Kassir *et al.*, “Improvement of the photocatalytic activity of TiO₂ induced by organic pollutant enrichment at the surface of the organografted catalyst,” *Colloids Surf. Physicochem. Eng. Asp.*, vol. 485, pp. 73–83, Nov. 2015.
- [26] Frochot C., Sève A., Vanderesse R., Toussaint M., Barberi-Heyob M., “Silica-based nanoparticles for PDT, Applications of Nanosciences in Photomedecine, , Michael Hamblin and Pinar Avci,” in *Woodhead Publishing Series in Biomedicine*, 2014.
- [27] P. Couleaud *et al.*, “Functionalized silica-based nanoparticles for photodynamic therapy,” *Nanomed.*, vol. 6, no. 6, pp. 995–1009, Aug. 2011.
- [28] A.-L. Bulin *et al.*, “X-ray-Induced Singlet Oxygen Activation with Nanoscintillator-Coupled Porphyrins,” *J. Phys. Chem. C*, vol. 117, no. 41, pp. 21583–21589, Oct. 2013.

- [29] S. Bharathiraja, M. S. Moorthy, P. Manivasagan, H. Seo, K. D. Lee, and J. Oh, "Chlorin e6 conjugated silica nanoparticles for targeted and effective photodynamic therapy," *Photodiagnosis Photodyn. Ther.*, vol. 19, pp. 212–220, Sep. 2017.
- [30] F. Lux *et al.*, "Ultrasmall Rigid Particles as Multimodal Probes for Medical Applications," *Angew. Chem. Int. Ed.*, vol. 50, no. 51, pp. 12299–12303, Dec. 2011.
- [31] A. Stallivieri *et al.*, "Synthesis and photophysical properties of the photoactivatable cationic porphyrin 5-(4-N-dodecylpyridyl)-10,15,20-tri(4-N-methylpyridyl)-21H,23H-porphyrin tetraiodide for anti-malaria PDT," *Photochem Photobiol Sci*, vol. 14, no. 7, pp. 1290–1295, 2015.
- [32] M. Rehan, X. Lai, and G. M. Kale, "Hydrothermal synthesis of titanium dioxide nanoparticles studied employing in situ energy dispersive X-ray diffraction," *CrystEngComm*, vol. 13, no. 11, p. 3725, 2011.
- [33] S. D. Richardson and S. Y. Kimura, "Water Analysis: Emerging Contaminants and Current Issues," *Anal. Chem.*, vol. 88, no. 1, pp. 546–582, Jan. 2016.
- [34] X. Pan *et al.*, "Enhancement of the photokilling effect of aluminum phthalocyanine in photodynamic therapy by conjugating with nitrogen-doped TiO₂ nanoparticles," *Colloids Surf. B Biointerfaces*, vol. 130, pp. 292–298, Jun. 2015.
- [35] G. Charles, T. Roques-Carmes, N. Becheikh, L. Falk, J.-M. Commenge, and S. Corbel, "Determination of kinetic constants of a photocatalytic reaction in micro-channel reactors in the presence of mass-transfer limitation and axial dispersion," *J. Photochem. Photobiol. Chem.*, vol. 223, no. 2–3, pp. 202–211, Sep. 2011.
- [36] J.-M. Herrmann, "Heterogeneous photocatalysis: state of the art and present applications In honor of Pr. R.L. Burwell Jr. (1912–2003), Former Head of Ipatieff Laboratories, Northwestern University, Evanston (Ill).," *Top. Catal.*, vol. 34, no. 1–4, pp. 49–65, May 2005.
- [37] J.-M. Herrmann, "Photocatalysis fundamentals revisited to avoid several misconceptions," *Appl. Catal. B Environ.*, vol. 99, no. 3–4, pp. 461–468, Sep. 2010.
- [38] G. Charles, T. Roques-Carmes, N. Becheikh, L. Falk, and S. Corbel, "Impact of the design and the materials of rectangular microchannel reactors on the photocatalytic decomposition of organic pollutant," *Green Process. Synth.*, vol. 1, no. 4, Jan. 2012.
- [39] X. Lü, W. Sun, J. Li, W. Xu, and F. Zhang, "Spectroscopic investigations on the simulated solar light induced photodegradation of 4-nitrophenol by using three novel copper(II) porphyrin–TiO₂ photocatalysts," *Spectrochim. Acta. A. Mol. Biomol. Spectrosc.*, vol. 111, pp. 161–168, Jul. 2013.
- [40] U. I. Gaya and A. H. Abdullah, "Heterogeneous photocatalytic degradation of organic contaminants over titanium dioxide: A review of fundamentals, progress and problems," *J. Photochem. Photobiol. C Photochem. Rev.*, vol. 9, no. 1, pp. 1–12, Mar. 2008.
- [41] K. P. Lee, H. J. Trochimowicz, and C. F. Reinhardt, "Pulmonary response of rats exposed to titanium dioxide (TiO₂) by inhalation for two years," *Toxicol. Appl. Pharmacol.*, vol. 79, no. 2, pp. 179–192, Jun. 1985.

- [42] H. Shi, R. Magaye, V. Castranova, and J. Zhao, "Titanium dioxide nanoparticles: a review of current toxicological data," *Part. Fibre Toxicol.*, vol. 10, no. 1, p. 15, 2013.
- [43] C. Zhao *et al.*, "Bio-imaging and Photodynamic Therapy with Tetra Sulphonatophenyl Porphyrin (TSPP)-TiO₂ Nanowhiskers: New Approaches in Rheumatoid Arthritis Theranostics," *Sci. Rep.*, vol. 5, no. 1, Sep. 2015.
- [44] C. Zhao, F. U. Rehman, H. Jiang, M. Selke, X. Wang, and C.-Y. Liu, "Titanium dioxide-tetra sulphonatophenyl porphyrin nanocomposites for target cellular bio-imaging and treatment of rheumatoid arthritis," *Sci. China Chem.*, vol. 59, no. 5, pp. 637–642, May 2016.
- [45] J. H. Park and N. Oh, "Endocytosis and exocytosis of nanoparticles in mammalian cells," *Int. J. Nanomedicine*, p. 51, May 2014.
- [46] A. M. Pekkanen, M. R. Dewitt, and M. N. Rylander, "Nanoparticle Enhanced Optical Imaging and Phototherapy of Cancer," *J. Biomed. Nanotechnol.*, vol. 10, no. 9, pp. 1677–1712, Sep. 2014.
- [47] W. Lei, Q. Zhou, Z. Li, X. Wang, and B. Zhang, "Photodynamic Activity of Ascorbic Acid-modified TiO₂ Nanoparticles upon Visible Illumination (>550 nm)," *Chem. Lett.*, vol. 38, no. 12, pp. 1138–1139, Dec. 2009.
- [48] S. Rehman, R. Ullah, A. M. Butt, and N. D. Gohar, "Strategies of making TiO₂ and ZnO visible light active," *J. Hazard. Mater.*, vol. 170, no. 2–3, pp. 560–569, Oct. 2009.
- [49] G. Granados-Oliveros, E. A. Páez-Mozo, F. M. Ortega, C. Ferronato, and J.-M. Chovelon, "Degradation of atrazine using metalloporphyrins supported on TiO₂ under visible light irradiation," *Appl. Catal. B Environ.*, vol. 89, no. 3–4, pp. 448–454, Jul. 2009.
- [50] C. Jin *et al.*, "Cellular Toxicity of TiO₂ Nanoparticles in Anatase and Rutile Crystal Phase," *Biol. Trace Elem. Res.*, vol. 141, no. 1–3, pp. 3–15, Jun. 2011.

Supporting information

Supporting information S1: FTIR spectra of bare and modified silica NPs

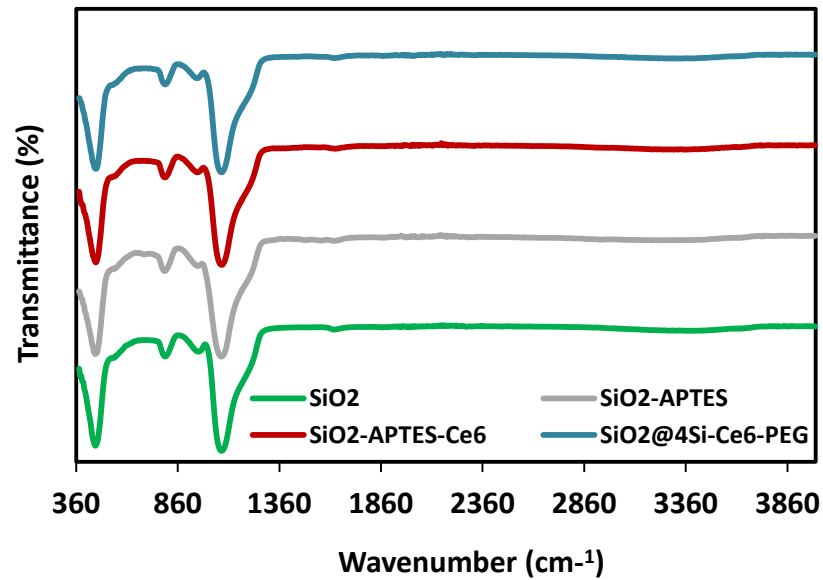


Fig S1: FT-IR spectra of bare and Ce6-coupled SiO₂ NPs

Supporting information S2: Absorption spectra of control NPs

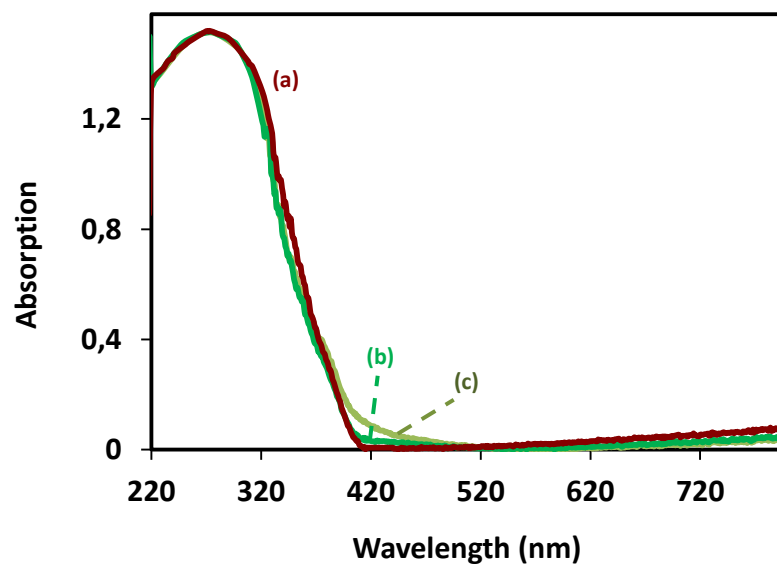


Fig. S2: The UV-Visible absorption spectra of solid (a) TiO₂, (b) TiO₂-APTES and (c) TiO₂@4Si-PEG NPs.

Supporting information S3: Concentration of Ce6 in each dose of NPs

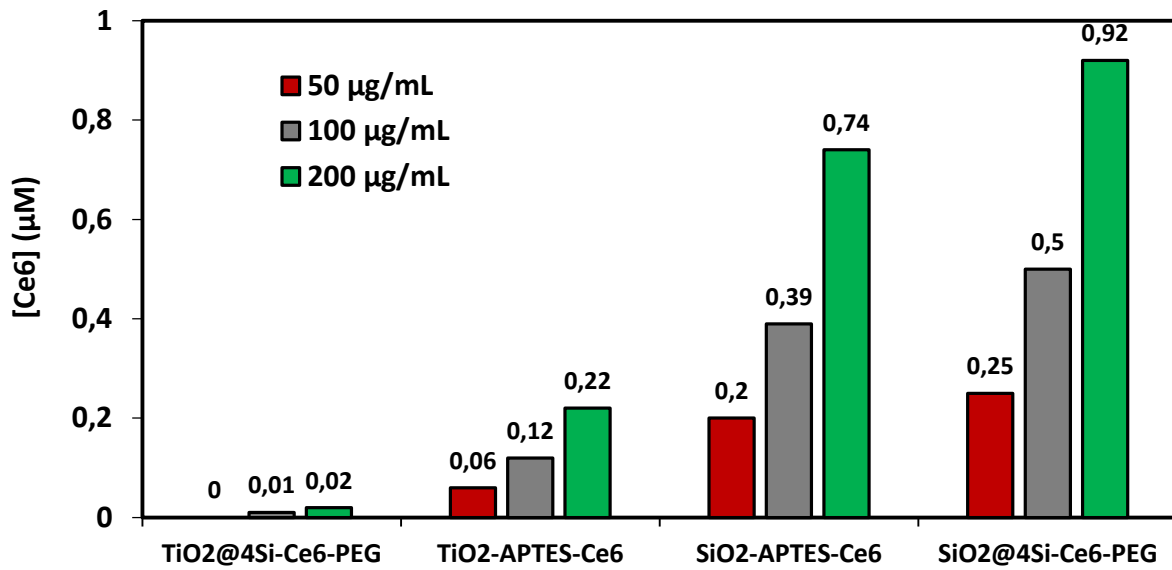


Fig. S3: The concentration of Ce6 in each amount of Ns introduced into the wells

Supporting information S4: Cell viability assessment

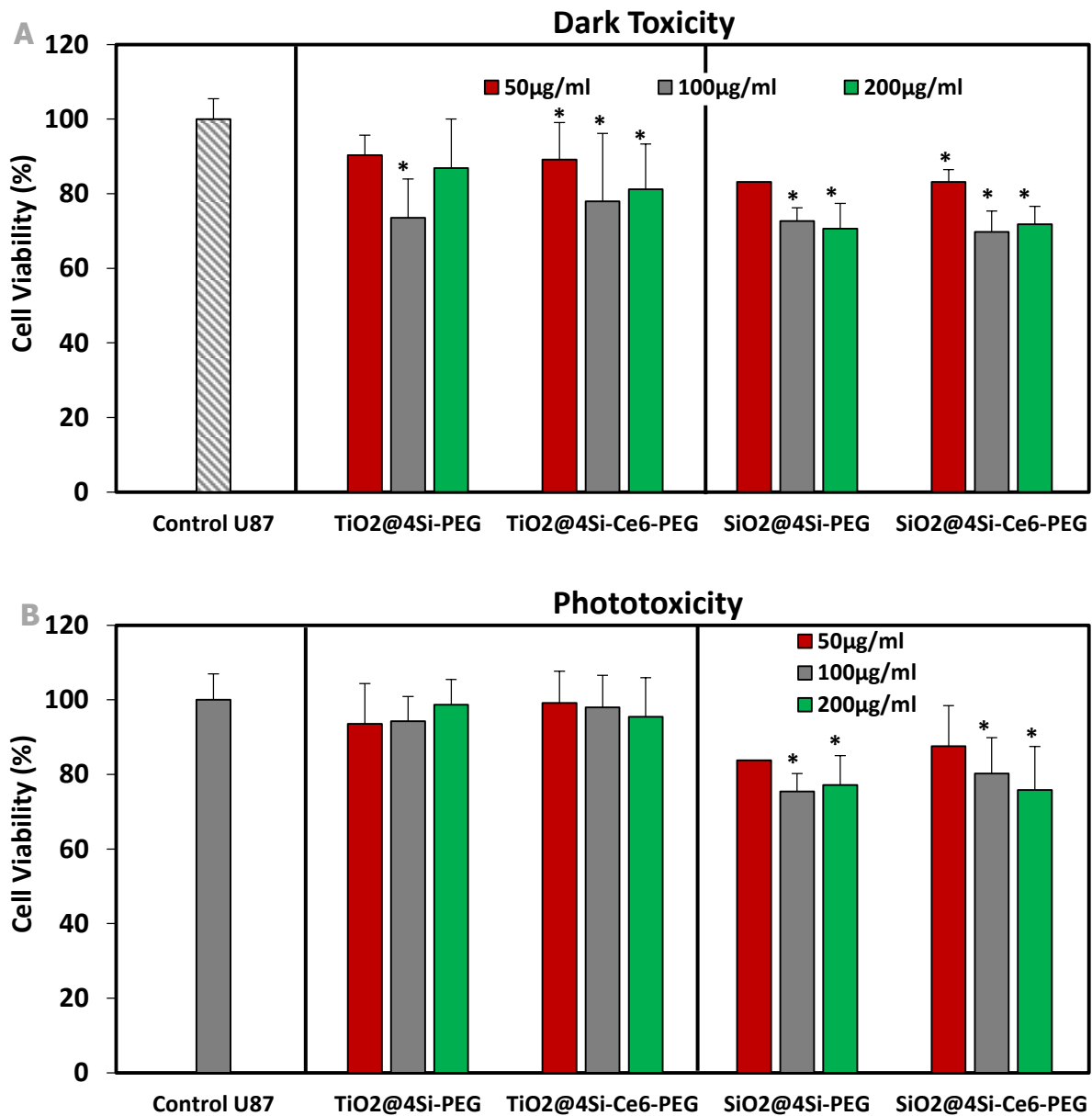


Fig. S4: Percentage of cell viability of U87 cells treated with free Ce6 PS, TiO₂@4Si-PEG, TiO₂@4Si-Ce6-PEG, SiO₂@4Si-PEG and SiO₂@4Si-Ce6-PEG, NPs (A) dark toxicity and (B) after irradiation with a light dose of 10 J/cm². Results were expressed as percentage of values obtained from untreated cells and given by mean ± SD, n = 3. * versus control cells, * p < 0.05.

Annexes

Annex I: Contrast phase imaging

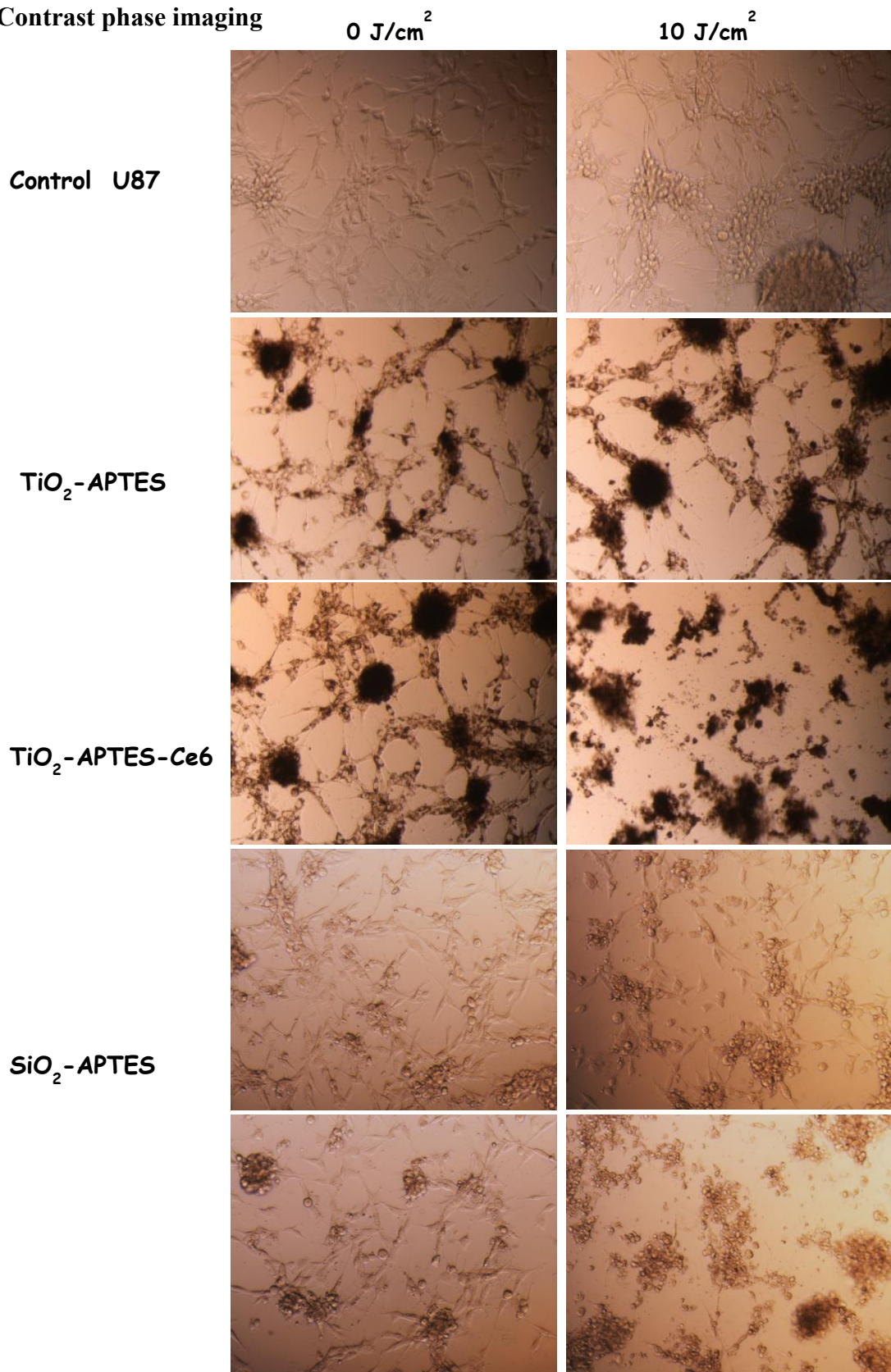


Fig. A1: Phase contrast imaging of cells exposed to different types of NPs before and after illumination (APTES-modified NPs)

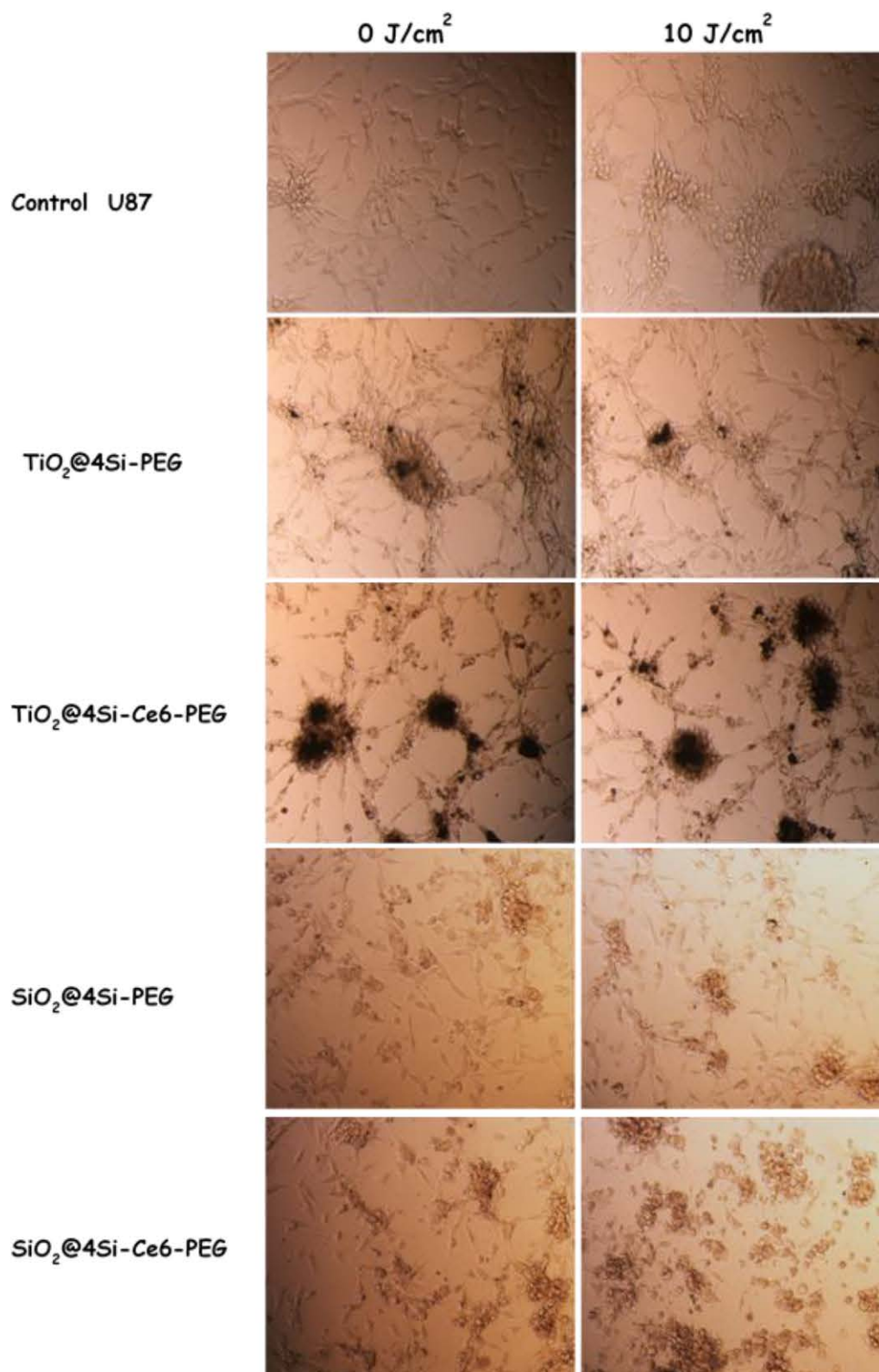


Fig. A2: Phase contrast imaging of cells exposed to different types of NPs before and after illumination

CONCLUSION AND PERSPECTIVES

The synthesis and characterization of new titania- and silica-based NPs was conducted throughout this work. The synthesized NPs were employed in two distinct fields, environmental and biological.

To widen the domain of use and commercialization of TiO₂, the restricted UV-activation property and electron-hole recombination issue should be resolved. In this study, we were interested in the strategy dye-sensitization of NPs by visible light-sensitive organic molecules for rendering hybridized TiO₂ NPs active under visible light. For this purpose, monocarboxylic tetraphenyl porphyrin (P1-COOH) and chlorin e6 (Ce6) were selected as the organic PSs. Despite the debate, coupling through a covalent bond appeared to establish a more stable linkage between the NPs and the PS over the adsorption. For this reason, the PS was covalently grafted onto the surface of the TiO₂ NPs through covalent coupling. To assure the covalent grafting, the surface of the TiO₂ NPs needed to be functionalized. Silyl anchoring groups were chosen to functionalize TiO₂ since, depending on literature; there exist a high affinity between the silyl functionalities and the surface OH groups of TiO₂ forming chemically inert Ti-O-Si bonds and it seemed to be the only group preserving a covalent linkage that exhibits no dissociation or de-chelation. Thus, prior to dye-sensitization, the TiO₂ core was modified with silane reagents through two approaches. In the first approach, the core-shell nanosystem was synthesized. The TiO₂ core was embedded in a polysiloxane shell formed by the condensation and polymerization of two silane reagents (3-aminopropyl)triethoxysilane (APTES) and tetraethyl orthosilicate (TEOS)) in presence of a basic catalyst triethylamine. The PS is then grafted onto the core-shell NPs followed by grafting highly hydrophilic PEG, thus elaborating TiO₂@4Si-PS-Ce6 NPs. In the second approach, the APTES-modified nanosystem was synthesized. The TiO₂ core was functionalized with only APTES before linking the PS to its surface elaborating TiO₂-APTES-Ce6. APTES mediates the formation of the covalent linkage between the TiO₂ NPs and the PS via amide bond. Amorphous silicon dioxide NPs were modified and hybridized similarly to TiO₂. Those NPs were used in this study for comparative reasons with TiO₂ to elucidate the effect of the type of the support and the contribution of the latter in the different applications.

The physicochemical characterization of the synthesized NPs proved by TEM and XRD that the crystallinity and the morphology of the TiO₂ core remained intact after surface functionalization with silane and hybridization with organic PSs. Imaging by HR-TEM revealed clearly the core-shell structure of NPs with a shell thickness ranging between 3-5 nm. The size of the NPs slightly changes from about 21 nm in the case bare TiO₂ to about 25 nm and 30 nm in the case of TiO₂-APTES-PS and TiO₂@4Si-PS-PEG NPs, respectively. Analysis by FT-IR showed that the PS was linked onto

the surface of the hybridized NPs *via* amide covalent bond. Functionalization of TiO₂ by its encapsulation into a polysiloxane layer with grafted PEG or by APTES alone triggered a better dispersion of the NPs into aqueous solutions compared to bare TiO₂ as demonstrated by DLS. The photophysical properties characterization proved that the photoresponse of all the hybridized TiO₂ and SiO₂ NPs was extended towards the visible region of light as revealed by UV-visible spectrophotometry. Upon sensitization with P1-COOH and Ce6 PSs, the elaborated NPs were capable of fluorescing and producing ¹O₂ under visible light irradiation.

The photocatalytic activity of the synthesized NPs was assessed by the degradation of model organic pollutants, methylene blue and methyl orange, under simulated solar and pure visible light. The APTES-modified nanosystems coupled to P1-COOH and Ce6 PSs influenced a superior photocatalytic activity towards the degradation of the pollutants over those coupled to core-shell nanosystems under both solar and visible light. To be more specific, TiO₂-APTES-Ce6 NPs induced a significant photocatalytic degradation of the pollutant (91% of degradation) under visible light irradiation.

The efficiency of the elaborated NPs in PDT was assessed through *in vitro* experiments on U87 glioblastoma cell line under visible light irradiation at 652 nm in the presence of different amounts of NPs. The same trend demonstrated by photocatalysis was confirmed by PDT experiments where APTES-modified NPs proved to be much more efficient for PDT than core-shell NPs. In the case of SiO₂-APTES-Ce6 NPs (200 μg mL⁻¹, 0.74 μM Ce6), a potential PDT effect was observed as the viability of U87 cells was decreased by 64% when exposed to light. However a stronger photodynamic effect was induced by TiO₂-APTES-Ce6 NPs (200 μg mL⁻¹, 0.22 μM Ce6) where the cell viability was decreased by 89% under visible light. When the PS was conjugated to the NPs, their uptake by the U87 cells was enhanced. The fluorescence microscopy showed that the NP-APTES-PS nanosystems appeared clustered into vesicles regardless of the type NPs used (SiO₂ or TiO₂) while free PS diffused into the cytoplasm.

Both TiO₂-APTES-Ce6 and SiO₂-APTES-Ce6 produced significant amounts of multiple ROS (HO[•] and ¹O₂). In TiO₂-APTES-Ce6 NPs, Ce6 played a double role 1) it absorbed the visible light and was excited to produce ¹O₂ and electrons, 2) those electrons are injected into the conduction band of TiO₂ triggering a series of redox reactions producing HO[•]. The significant generation of HO[•] in the case of TiO₂-APTES-Ce6 validates the theory of the electron transfer. The concomitant roles played by Ce6 and TiO₂ in this nanosystem yielded abundant production of different ROS that conceded a superior photoactivity over the core-shell nanosystem and the bare titania in both applications. In photocatalysis, the TiO₂ core in the TiO₂-APTES-Ce6 NPs contribute to both the

adsorption of the pollutants and the elaboration of ROS mainly HO[•] under both solar and visible light.

In this work, an example of a product design approach was employed to design efficient functionalized nanoparticle system for two different applications. This study indicates that the recent advances in photocatalytic materials can be easily implemented in PDT and *vice versa*. Such systems may be also used in other applications such as H₂ production through water splitting.

Currently the number of publications concerning the synthesis, characterization, and applications of the photocatalytic materials for the remediation of the environmental issues has been increasing exponentially. The use of photocatalytic materials for those purposes might provide a route to the evolution of a sustainable technology that guarantees a safe and effective cleaning of the environment. Due to the current issues of water scarcity and pollution, together with the growth of the population, the development of such technologies is challenging. On this basis, in the future, the synthesized NPs may be tested for the photocatalytic degradation of wide array of pollutants including the pharmaceuticals and micropollutants such as ibuprofen, carbamazepine, sulfamethoxazole, diclofenac, etc.

In the fields of PDT, the NPs are functionalized by APTES that possess an amine arm enabling the linkage various specific targeting molecules such as antibodies, folic acid, peptides, etc. it would be interesting to couple targeting unit to improve the selectivity of the NPs for cancerous cells. If achieved, the amount of injected PS will be decreased and the accumulation of the NPs into the malignant cells will be more selective leaving more healthy cells intact. It is also known the the depth of X-ray light penetration exceeds that of visible light, so as a perspective, TiO₂ or SiO₂ may be linked to PSs may be used for PDT under X-ray irradiation. This will enable reaching deeply localized tumors.

AcH	Acetaldehyde	MTAP	meso-tetra(o-amino phenyl) porphyrin
(OH)AlPcSmix	mixture of the di-, tri- and tetra-sulfonated phthalocyanine derivatives	MTCP	meso-tetra (4-carboxyphenyl) porphyrin
[RuII(py-pzH)₃]²⁺	py-pzH=3-(20-pyridyl)pyrazole	MTCPP	Metallo tetra(4-carboxyphenyl)porphyrin (M= Fe(II), Cu(II), Zn(II))
2,4-DCP	2,4-dichlorophenol	MTPP	Metallo tetraphenyl porphyrin (M = Cu, Zn)
4-NP	4-Nitrophenol	MTT	methylthiazolyl tetrazolium
5-ALA	5-aminolevulinic acid	NBT	nitroblue tetrazolium
ABDA	9,10-anthracenediyl-bis(methylene)dimalonic acid	NGO	nano-graphene oxide
AcTMP	5-(4-acetamidophenyl)-10,15,20-tris(4-methoxyphenyl) porphyrin	NHS	N-hydroxysuccinimide
AdaTPP	adamantanyl porphyrin	NiP	Nickel porphyrin
ADC	apparent diffusion coefficient	NIR	near infrared
AE	amaranth extract	NPs	nanoparticles
AFM	atomic force microscopy	NR	nanorod
AlPcS4	aluminum phthalocyanine chloride tetrasulfonate	N-TiO₂	nitrogen-doped TiO ₂
AO7	Acid Orange 7	NV	nanovesicle
AP	aptamer	NW	nanowhisker
APTES	3-aminopropyl triethoxysilane	P	Porphyrin
APTES	3-aminopropyl triethoxysilane	PBS	phosphate buffer saline
ATMP	5-(4-amidophenyl)-10,15,20-tris(4-methoxyphenyl) porphyrin	Pc	phthalocyanine
ATP	adenosine-5'-triphosphate	Pc	Phthalocyanine
βXA	beta-cyclodextrin	Pc(OH)(mob)	monosubstituted silicon phthalocyanine
BDP	boron-dipyrromethene	P-C60	porphyrin-[C60] fullerene dyads
BOLD	blood oxygenation level-dependent	P-C70	porphyrin-[C70] fullerene dyads
BPEI	branched polyethylenimine	PdP	Palladium porphyrin
CaB	cathepsin B	PDT	photodynamic therapy
CBC	complete blood cells count	PEG	polyethylene glycol
CC50	cytotoxic concentration that induces 50% of cell death	Pep	peptide
Ce6	chlorin e6	PET	positron emission tomography
CM-H₂DCFDA	2,7- dichlorodihydrofluorescein diacetate acetyl ester	pGO	polyethylene glycol-grafted graphene oxide
CoTPPS	Cobalt tetrakis (4-sulfonatophenyl) porphyrin	PLA	polylactide
CoTSP	Cobalt tetrasulfophthalocyanine	PLL	polylysine
CuAPTPP	Copper 5-(4-aminophenyl)-10,15,20-triphenylporphyrin	PPDME	protoporphyrin dimethyl ester
CuP	Copper porphyrin	PPIG4	polypropylenimine generation 4

CuPcTs	Copper phthalocyanine tetrasulfonate	PpIX	protoporphyrin IX
CW	continuous wave	PS	photosensitizer
DBMC-CmbI	7,8-dihydroxy-4-bromomethylcoumarin-chlorambucil	PSTs	tetrasulfonated phthalocyanine
DCFH-DA	2',7'-dichlorodihydrofluorescein diacetate	PtP	Platinum porphyrin
DLS	dynamic light scattering	PTT	photothermal therapy
DNA	deoxyribonucleic acid	PVP	poly(vinylpyrrolidone)
Dox	doxorubicin	Pyro	pyropheophorbide
DPBF	1,3-diphenylisobenzofuran	RB	Rose bengal
D-TMPyP	5-(4-formylphenyl)-10,15,20-tris(4-pyridyl)-porphyrin	rGO	Reduced graphene oxide
DTT	dithiothreitol	RhB	Rhodamine B
DTX	docetaxel	RhG	Rhodamine 6G
DVDMS	sinoporphyrin sodium	ROS	reactive oxygen species
DWI	diffusion-weighted imaging	Ru(bpy)₃²⁺	Tris(bipyridine)ruthenium(II)
EPR	enhanced permeability and retention	SA	Salicylic Acid
E-SWCNT	chirality enriched (6,5) single-walled carbon nanotube	SEM	scanning electron microscopy
FA	folic acid	Sil	silane arm
FCNV	fullerene C70 nanovesicle	SiNc₄	silicon naphthalocyanine bis (trihexylsilyloxy)
FDA	food and drug administration	SLPDT	self-lighting photodynamic therapy
FeP	Iron porphyrin	SnP	Tin porphyrin
FP	fine particle	SOG	singlet oxygen generation
FRET	fluorescence resonance energy transfer	SOSG	singlet oxygen sensor green
FTEP	5-(4-formylphenyl)-10,15,20-tris[3-(N-ethylcarbozoyl)] porphyrin	SSA	2-hydroxy-5-sulfosalicylic acid
FTIR	Fourier transform infrared	SWCNT	single-walled carbon nanotube
GO	Graphene oxide	SWNH	single-walled carbon nanohorn
GON	graphene oxide nanocolloid	TAPPI	Tetrakis(4-trimethyl aminophenyl) porphyrin
GR or G	Graphene	TCB-Zn/Pc	2,3 tetra(carbazol-2-yloxy) phtalocyaninate Zinc (II)
GSH	glutathione	TCPP	Metal-free tetrakis(4-carboxyphenyl)porphyrin
H₂EtPp	5,15-di[4-(carboethoxymethyleneoxy)phenyl]-10,20-di(4butylphenyl) porphyrin	TDI	Toluene diisocyanate
H₂Pc	29H,31H- phthalocyanine	TEM	transmission electron microscopy
H₂TCIPP	5,10,15,20-tetrakis(4-chlorophenyl) porphyrin	TEOS	Tetraethyl orthosilicate
		TEA	Triethylamine

H₂TM₄PyP (OTs)₄	meso-tetrakis(4-pyridyl)porphyrin tosylate salt (POR)	TFC70	tri-malonate derivative of fullerene C70
H₂TMy₄PyP (OTs)₄	meso-tetrakis(N-myristyl-4-pyridinium)porphyrin tosylate salt (MYR)	TMA	Trimethylamine
H₂TPP	Metal-free tetraphenyl porphyrin	TMPyP	trimethylpyridylporphyrin
HA	hyaluronic acid	TNCuPc	Copper tetranitrophthalocyanine
HP	hematoporphyrin	TPP	tetraphenyl-porphyrin
HPPH	2-(1-hexyloxyethyl)-2-devinylpyropheophorbide-alpha	TSCuPc	tetrasulfonic acid tetrasodium salt coper phthalocyanine
IC₅₀	concentration that induces 50% of parasite inhibition	TSPP	meso-tetra (4-sulfonatophenyl) porphyrin
IR	infrared	TTA-UC	triplet-triplet annihilation upconversion,
LED	light-emitting diode	UCNP	upconversion nanoparticles
LHRH	luteinizing hormone-releasing hormone	UV	ultraviolet
LOG_r	low-oxygen graphene	VER	verteporfin
MA	malonic acid derivatives	Vis	visible
MB	Methylene Blue	WST-1	water-soluble tetrazolium salt
MCPp	Metal porphyrin corresponding to H ₂ EtPp	wt	weight
ME	2-Mercaptoethanol	ZnMAPc	zinc monoamino phthalocyanine
MFG	magnetic and fluorescent graphene	ZnMCPPc	zinc mono carboxy phenoxy phthalocyanine
MitoTPP	(5-(p-(4-trimethylammonium)-butoxyphenyl)-10,15,20-triphenylporphyrin bromide	ZnOPc	zinc octacarboxy phthalocyanine
MO	Methyl Orange	ZnPc	zinc phthalocyanine
MP	Metallo porphyrin (M = Fe, Cu, Zn)	ZnTMAAPc	2,(3),9(10),16(17),23(24)-tetrakis-(mercaptoacetic acid phthalocyaninato) zinc(II)
MPc	Metallo phthalocyanine (M = Cu, Zn, Co, Ni)	ZnTMPAPc	2,(3),9(10),16(17),23(24)-tetrakis-(mercaptopropanoic acid phthalocyaninato) zinc(II)
mPEG	methoxy-poly(ethylene glycol)	Φ_Δ	singlet oxygen production quantum yield
MRI	magnetic resonance imaging		

Nanoparticules De TiO₂ Couplées à Des Photosensibilisateurs Pour Des Applications En Photocatalyse Et En Thérapie Photodynamique

Mots-clés: TiO₂; photosensibilisateurs; photocatalyse; PDT

Résumé : Ce travail concerne le développement de nanoparticules de TiO₂ et de SiO₂ sensibilisées aux photosensibilisateurs pour application dans la photocatalyse et la thérapie photodynamique (PDT). Les NP ont été soit recouverts d'une coquille de polysiloxane, soit modifiés par l'aminopropyltriéthoxysilane (APTES) seul. Les PSs de tétraphényl monocarboxylphosphine (P1-COOH) ou de chlorine e6 (Ce6) ont été couplés aux NP par liaison amide. En photocatalyse, les NP hybrides modifiées par l'APTES, en particulier TiO₂-APTES-Ce6, présentent une activité photocatalytique supérieure vis-à-vis de la dégradation du bleu de méthylène et de l'orange de méthyle sur les systèmes cœur-coquille sous lumière solaire et visible. Pour la PDT, des tests *in vitro* ont été désignés sur la lignée cellulaire de glioblastome U87 à différentes concentrations de NP éclairées à 652 nm. TiO₂-APTES-Ce6 a révélé une bonne phototoxicité car la viabilité cellulaire a diminué de 89% après illumination. L'incorporation cellulaire et la localisation de ces NP et de leurs analogues de la silice ont été explorées. Les ROS impliqués dans la photocatalyse et la PDT ont été étudiés.

TiO₂ Nanoparticles Coupled To Photosensitizers For Applications In Photocatalysis And Photodynamic Therapy

Key words: TiO₂; photosensitizers; photocatalysis; PDT

Abstract: This work addresses the development of dye-sensitized TiO₂ and SiO₂ nanoparticles (NPs) for application in photocatalysis and photodynamic therapy (PDT). The NPs were either coated with a polysiloxane shell or modified by aminopropyl triethoxysilane (APTES) alone. Monocarboxylic tetraphenyl porphyrin (P1-COOH) or chlorin e6 (Ce6) PSs were coupled to the NPs by amide bond. In photocatalysis, The APTES-modified sensitized NPs, particularly TiO₂-APTES-Ce6, exhibit a superior activity towards the degradation of methylene blue and methyl orange over the core-shell systems under solar and visible light. For PDT, *in vitro* tests were conducted on the glioblastoma cell line U87 at different NPs' concentrations illuminated at 652 nm. TiO₂-APTES-Ce6 revealed a good phototoxicity as the cell viability decreased by 89% after illumination. The cellular uptake and localization of those NPs and their silica analogues were explored. The ROS involved in photocatalysis and PDT were investigated.